Experimental and Computational Determination of Wind Loads on Netted/Sheeted Scaffolds

Hassan Irtaza

Thesis submitted in partial fulfilment of the requirements of
Oxford Brookes University for the Degree of
Doctor of Philosophy

School of Built-Environment
Oxford Brookes University
Oxford, UK

Director of Studies
Dr. R G Beale, School of Technology, OBU, Oxford

Co-Director of Studies
Dr. M H R Godley, School of Built-Environment, OBU, Oxford

October 2009

ABSTRACT

This thesis describes an investigation into the wind loading on access scaffolds erected around a cubical building, clad by impermeable sheeting or permeable debris netting. The subject was investigated experimentally by tests in a wind-tunnel and theoretically using computational fluid dynamics techniques. The results were verified from the wind tunnel tests and computational analyses on the Silsoe Experimental Building (SEB) using data from the full-scale tests made in 1993-94 at Silsoe, U.K.

The lower portion of the Atmospheric Boundary Layer exhibits different flow properties to the upper elevations. A procedure is presented for modelling the atmospheric surface layer flow properties in a boundary-layer wind-tunnel at useful model scales. The full-scale data available from the cubical 6m x 6m x 6m SEB was used to validate the results presented in this study. A model scale of 1:30 were used both for experiments in a wind-tunnel and in the computational analyses undertaken in the study. Pressure data obtained from the wind-tunnel experiments on the SEB model were compared to full-scale data with good agreement. These data were also compared with various computational fluid dynamics techniques available commercially and the conclusions drawn on the use of the different techniques.

The wind-tunnel simulations on an SEB model and on a sheet/elevated sheet clad scaffold models were undertaken based on a duplication of the turbulence intensities and small-scale turbulence of the incidence flow. It is very difficult to achieve equality of Reynolds number in the wind-tunnel as it is very difficult to achieve exactly the same integral scales of turbulence. Two different types of terrain and inflow boundary conditions were simulated in the wind-tunnel for the models and results are reported here.

Large suctions (separation of flows) occur near the leading edges and roof corners. The modelling of these phenomena in the wind-tunnel remains a problem. Because of the limited space near the corners and leading edges, it is difficult to make reliable measurements by introducing probes in these areas. This difficulty can be overcome by modelling the flow with Large Eddy Simulation (LES) numerical techniques. However, the disparity between the large and small scales, especially under extreme wind conditions, makes it extremely difficult to resolve the entire range of dynamic scales.

The pressure force on bare pole access scaffolds are further influenced by the presence of the building façade which induces a shielding effect. A 2-D model of bare pole scaffolds surrounding the SEB using CFD techniques was successfully achieved whereas a 3-D model could not be produced because of the limitations of the meshing-software GAMBIT available to the author.

Cladding increases the wind loads on scaffold structures above the pressure force on bare pole access scaffolds. To determine the wind forces on net/sheet clad scaffolds the Silsoe Experimental Building was used as a base model and simulated scaffolds erected around it. Although, sheeting/netting exhibits aero-elastic behaviour under wind load, an assumption was made to treat the cladding (sheeting/netting) surrounding the scaffold as being made of static solid thin plates. Models were tested in a wind-tunnel and the same assumptions were used in the computational fluid dynamics analyses.

For the sheet clad scaffolds, two models were made, one with sheeting touching the ground and the other with an elevated sheet surrounding the building. These models were tested in a wind-tunnel to determine the pressure coefficients on the outer and inner faces of the sheeting. The permeability of the two types of net were successfully obtained from wind-tunnel tests. The simulated data from the wind-tunnel tests were used as input for different computational techniques with good agreement. A new procedure was developed to extend the computational model to net clad scaffolds (both elevated and touching the ground) with the netting simulated as porous media. The author presents new results of the pressure coefficients on sheeted scaffolds obtained using CFD and wind-tunnel techniques and also CFD results on netted scaffold structures.

This thesis is the result of research undertaken to assess various methods available for the numerical simulation of turbulent fluid flow using the Fluent Software Package and to see their applicability in computational wind engineering. Investigations have concentrated on analysing the accuracy and numerical stability of a number of different turbulence models including both widely available models and state of the art techniques.

Furthermore, Large Eddy Simulations using the dynamic kinetic energy sub-grid-scale model have been completed on some models, in order to account for the four dimensional nature of turbulent flow and to show the best correlation between wind-tunnel, full-scale and sheeted scaffolds.

The author has detailed and tested all the above techniques and gives recommendations on the appropriate turbulence model to be used for successful computational wind engineering.

Finally the author has given recommendations on the wind pressures to be used in analysing the scaffold structures.

Dedicated to my Father

Late Abdus Salam, Advocate

ACKNOWLEDGEMENTS

I owe a deep sense of gratitude to Dr. Robert Beale and Dr. Mike Godley for providing me an opportunity to work in one of the best modern universities of United Kingdom. Sirs, I do not find words which can truly express my thanks for your invaluable guidance, comments, support, patience and for sparing time out of your busy schedule for me during this work. Your constant motivation has been responsible for the successful completion of this work. Your caring hearts and always willing to help attitude has oppressed my awkwardness to approach you in the situation of any difficulty and hardship.

I express my sincere appreciation to Dr. Ramin Kievani (Research Coordinator), Dan Bell, Andy Glass, Mark Collett, Ray Salter, and Gareth Brown for their technical support, constructive criticism and suggestions.

My special thanks are due to Dr. Faye Michele for her support in setting up the Unix cluster of parallel computers in the School of Technology for me to carry out my research.

I will not be able to forget all my friends related either directly or indirectly to my research making this task an enjoyable process and making my stay in Oxford a memorable experience.

My greatest debt is, of course, to my loving mother (*Ammi*). It extremely saddens me for being away at Oxford in her moment of grief when my father (*Abba*) left for his heavenly abode. May God (*Allah*) give peace to his soul.

My lovely children Fatima, Faiz and Bilal deserve special mention for their frequent greetings and nice talks over phone relaxing me at times of tension and frustration.

Last but not least, my lovely and beautiful wife Huma is the most important person to me in this world I need to appreciate who represented me before my mother on the sad demise of my father and provided me all support during the course of this work.

Chapter 4 Computational Fluid Dynamics and Turbulence Modelling

LIST OF FIGURES

LIST OF TABLES

The following symbols are used throughout this chapter. Symbols are defined when they appear for the first time. Occasionally a symbol has been used for more than one parameter for common practice. Where this was applied the exact meaning of the symbol is made clear when it appears in the text.

A_i	Reference area [m^2]
A_{open}	Total area of openings in the building façade taking into account the most open face of the building perpendicular to the wind face [m^2]
A_{total}	Total area of the building face
$A\|\|_r$	Total area of all round parts and toeboards projected onto a plane parallel to the supporting structures [m^2]
$A\|\|_s$	Area of parts of a particular cross-section (other than those included in $A\|\|_r$) projected to a plane parallel to the supporting structures [m^2]
$A\perp_r$	Total area of all round parts and toeboards projected onto a plane at right angles to the supporting structures [m^2]
$A\perp_s$	Area of parts of a particular cross-section (other than those included in $A\perp_r$) projected onto a plane at right angles to the supporting structures [m^2]
A^+	A constant equal to 25
b	Constant between 0.015 and 0.03
B	Length/width of sheet/net clad scaffolds surrounding SE
c_i	Position coefficient in relation to the position of the scaffolding in conjunction with the structure
c_f	Aerodynamic force coefficient appropriate to the cross-section of the parts in question, as given in annexes B of HD 1000: 1988
$c\|\|$	Overall pressure coefficient for forces parallel to the supporting structure and has the value 1.1
$c_\perp$	Overall pressure coefficient for forces perpendicular to the supporting structure and has the value 0.9 (see annex C of HD 1000: 1988) and represents a façade which is 60% open
$c_\perp closed$	Overall pressure coefficient of the scaffold beside a closed building façade, and has the value 0.3
$C_{\varepsilon 1}, C_{\varepsilon 2}, C_{1RNG}, C_\mu$	Constants in turbulence transport equations
C_{ij}	Convection term of $\overline{u_i' u_j'}$
C_s	Model constant
C_{ij}	Prescribed matrices in the momentum equations
C_2	Inertial resistance factor
C_0	User defined empirical coefficients
C_1	User defined empirical coefficient

d	Effective displacement height of zero-plane above ground due to surrounding obstacles
d	Van Driest damping factor
D	Permeability of the building façade, calculated as A_{open}/A_{total}
D	Length/width of sheet clad scaffolds
D_{ij}	Diffusion term of $\overline{u_i' u_j'}$
D_{ij}	Prescribed matrices in the momentum equations
e_{ij}	Rate of deformation of tensor
F	Resulting static wind force
F	Body force per unit volume
F_{ij}	Stress production of $\overline{u_i' u_j'}$ by action of rotational or body forces
f	Coriolis parameter $\left(f = 2\Omega \sin\varphi\right)$, $[rad/s]$
h	Boundary layer height $[m]$ $\left(= u_*/6f\right)$
H	Model Height
I_i	Turbulence intensity, $\left(= \sigma_i/U_i\right)$
i	General values of u, v or w component at point in space at time t
k	Turbulent kinetic energy, $k = \frac{1}{2}\left(u_i' u_j'\right)$
${}^{x}L_u, {}^{x}L_v, {}^{x}L_\omega$	Length scales of turbulence in x-direction relating to u, v or w components respectively $[m]$
l	Length scale
n	Frequency [Hz]
n_i	${}^{x}L_i n / U_z$
N_{CFL}	The Courant-Friedrichs-Lewy or CFL number
P	Horizontal force
P_i	Cumulative probability that any value of i will be less than a particular value, i_p
p_i	Probability density functions of u-, v- or w-component
$\overline{P}$	Mean pressure
p_k	Production of turbulent kinetic energy
P_{ij}	Production term in algebraic stress model
q_i	Dynamic pressure (velocity pressure)
$S(n)$	Spectral density function at frequency n
S_{uu}, S_{vv}, S_{ww}	Length scales of turbulence in x-direction relating to $u-, v-$ and $w-$components respectively
S_{ij}	Strain rate tensor
S_i	i^{th} Source term for the momentum equation
T	Averaging time or response period of measuring instrument
T_0	Duration of sample or wind-speed record
t	Time step
$U(z)$	Mean wind speed at height z above the ground
$U(z_{ref})$	Mean wind speed at reference height above the ground

$\overline{u}$	Mean velocity
$u^{'}$	Random fluctuating component of velocity
u^{+}	Velocity scale (non-dimensional)
u_i	The filtered resolvable scale velocity field
$u_i^{'}$	The sub-grid scale (SGS) components
$\overline{u_i^{'}u_j^{i}}$	Reynolds stresses
u_* or u_τ	Friction velocity, $\sqrt{\tau_0/\rho}$ $[m/s]$
u, v, w	Fluctuating component of wind speed at time t along $x-, y-$ and $z-$ axes respectively
v_i, v_j	Velocity in i or j direction
v_{mag}	Absolute velocity
W	Appropriate wind pressure [N/m^2]
x, y, z	System of rectangular Cartesian co-ordinates
y^{+}	The distance from the wall in non-dimensional wall units
y	The distance from a point in the fluid to the nearest wall
z	Height above the ground
z_0 or Z_0	Roughness length, which is measure of the eddy size at the ground
z_1	Height above the ground up to which log law is valid
z_{ref}	Reference height above the ground

Greek Symbols

α	Power law exponent
α	Permeability
δ	Local member imperfection
δ	Boundary layer or gradient height
δ_{ij}	Kronecker delta
Δ	Global geometrical imperfection
Δ	The filter width
Δ_t	Time step size or duration
Δ_x	Grid spacing
ε	Dissipation rate of k
ε_{ij}	Dissipation term of $\overline{u_i^{'}u_j^{'}}$
μ_l	Laminar viscosity
μ	Dynamic viscosity of air
μ_t	Eddy or turbulent viscosity
ϕ_{ij}	Pressure-strain correlation term
ν	The laminar kinematic viscosity
ν_{sgs}	The sub-grid viscosity
χ	Exposure factor
κ	Von Karman's constant equal to 0.41
Ω	Angular rotation of the earth = $72.9\times10^6 rad/s$

Ω	Vorticity (equal to twice the instantaneous rate of spin of a fluid element, determined by lateral velocity gradients)
φ	Angle of latitude at site
σ_i	Standard deviation of i-component at height z for $T \to 0$ and $T_0 \to \infty$
$\sigma_k, \sigma_\varepsilon$	Turbulent Prandtl numbers for k and ε for the $k-\varepsilon$ turbulence model
τ	Shear stress
τ	Time lag
τ_{ij}	Turbulent stress tensor
ρ	Air density

Abbreviations

ABL	Atmospheric Boundary Layer
ASL	Atmospheric Surface Layer
CFD	Computational Fluid Mechanics
CWE	Computational Wind Engineering
DNS	Direct Numerical Simulation
LES	Large Eddy Simulation
LETOT	Large Eddy Turnover Time
RANS	Reynolds Average Navier-Stokes
RNGKE	Renormalization group (RNG) $k-\varepsilon$ model
RKE	Realizable $k-\varepsilon$ model
RSM	Reynolds Stress Model
SEB	Silsoe Experimental Building
SGS	Sub-grid-scale
SKE	Standard $k-\varepsilon$ model
SST	Shear Stress Transport
WALE	Wall-adapting Local Eddy-Viscosity

LIST OF PUBLICATIONS

1. H. Irtaza, R.G. Beale and M.H.R. Godley, 'Determination of the effects of the wind load on bare tube access scaffold structures using computational fluid dynamics', 5th International Conference on Advances in steel structures, Singapore, pp. 627-632, 4-7 December 2007.

2. H. Irtaza, R.G. Beale and M.H.R. Godley, 'Experimental and numerical evaluation by computational fluid dynamics of wind loads on sheeted scaffolds', Proceedings of the 12th International Conference on Civil, Structural and Environmental Engineering Computing, Madeira, Portugal, paper No. 261, pages 19, 1-4 September 2009.

3. H. Irtaza, R.G. Beale and M.H.R. Godley, 'Wind loads on netted metal access scaffolds', 6th International Conference on Advances in steel structures, Hong Kong, 16-18 December, 2009 (accepted for publications).

CHAPTER 1
Introduction

1.1 Introduction

Steel scaffolds are extensively used to provide access and support to permanent works during different stages of construction in the UK and other parts of the world. Figure 1.1 shows a typical scaffold system. Scaffold systems are light in weight, easy to maintain, install, and dismantle. They are mostly fabricated from hot rolled steel tubes. The basic components of a tube-and-fitting scaffold are standards, ledgers and transoms as shown in Figure 1.2. 'The vertical tubes transfer the entire mass of the structure to the ground [1.2]' and are called standards or uprights. Each standard has a base plate underneath to spread the load. The standards are connected by horizontal tubes, called

Figure 1.1 A typical tube and fitting scaffold system

ledgers. These members run parallel to the building and also act as support to the transoms. Reference [1.2] states that 'transoms are horizontal tubes that rest upon the ledgers at right angles and main transoms are placed next to the standards. They hold the standards in place and provide support for boards. Intermediate transoms are those placed between the main transoms to provide extra support for boards'. In proprietary scaffolds, other shaped members are used to provide the transom and ledger elements but have the same purpose. The stability for these structures is provided by tie and bracing members. The loading applied to the scaffold consists of self weight of the structure, imposed loads including men and materials and wind loads.

Figure 1.2 Components of scaffold system [1.1]

Much research, both experimental and computational has been done to determine the exact mechanism of scaffold failure under different conditions of loading. This includes analyses based on the effective length method in the early stages of research to more advanced non-linear force displacement effects (both $P-\delta$ and $P-\Delta$) taking into account the influence of semi-rigid standard-ledger and standard-transom connections including finite element analyses taking both material and geometric non-linearity into account. It is clear/imperative that most of the research done in the past aimed at understanding the behavior of scaffold under load. Limited research has been reported on the magnitude of loads actually acting on the scaffold including wind load.

Scaffolds are often clad with nets (Figure 1.3) or wind proof sheets (Figure 1.4) to protect both the passers-by and work force from falling debris and also to shield workers from extreme weather. The cladding increases wind loads on the scaffold leading scaffold structures susceptible to damage or collapse under stormy conditions. Very little published research is reported on the wind loads on access scaffolds. The UK Health and Safety Executive published a few reports of casualties and damage to both scaffold structures and building structures during storms and high winds [1.3]. In current design and analysis of scaffolds, the wind loads, apart from dead loads and superimposed loads, are derived from experiments conducted on permanent structures and no allowance is made for the presence of the façades of the building to which the scaffold is attached. No research using Computational Fluid Dynamics has been reported to determine the wind loads on temporary structures.

Figure 1.3 Typical scaffolds surrounded by net [1.4]

Figure 1.4 Typical scaffolds surrounded by wind proof sheet [1.4]

The reason why wind-tunnel tests on bare-pole scaffold structures have not been undertaken in the past is because of the scaling effect. A scale of 1:50 will lead the diameter of the scaffold tube to be less than 1 mm. It is very difficult to maintain the stiffness of the scaled scaffold tube to that of original one. Also it is very difficult to fix pressure taps on the scaled scaffold tubes and that on the nets/sheets. The aeroelastic nature of netting/sheeting compels aeroelastic wind-tunnel tests on clad scaffolds. Any question regarding static or dynamic stability of the fabric, can only be accurately answered by an aeroelastic wind tunnel test. A rigid model test gives no information regarding the possibility of divergence or flutter, but can be used to predict fluctuating wind pressure due to buffeting.

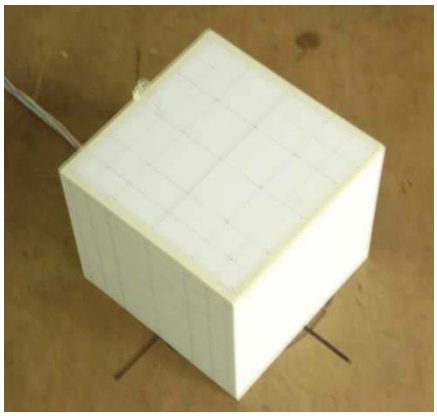

Figure 1.5 Scaled cubical SEB

Keeping all these in mind, wind-tunnel tests were carried out on a scale model of the cubical Silsoe Experimental Building (SEB) as shown in Figure 1.5 and that on a sheet clad scaffold as shown in Figure 1.6 and 1.7 surrounding the SEB. In the model, the sheeted scaffold surrounding the building was 4 mm thick (with a tapered top) with pressure taps implanted both on the inner and outer face of the sheeting to measure pressure coefficients. The reason for this experiment was that there were neither full-scale nor model-scale sheeted results available for the SEB.

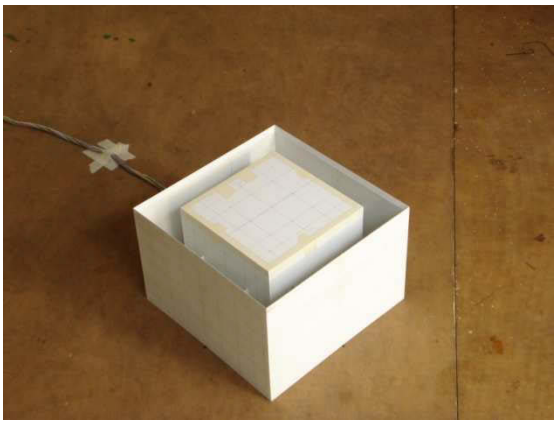

Figure 1.6 Scaled cubical SEB surrounded by sheet clad scaffold

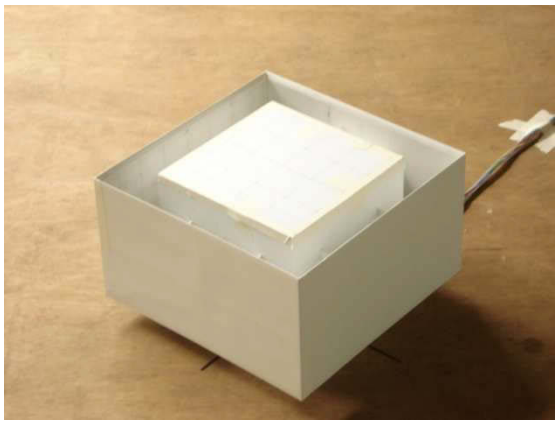

Figure 1.7 Scaled cubical SEB surrounded by by elevated sheet clad scaffold

The ultimate purpose of wind-tunnel testing of sheeted scaffold models is to contribute significantly to the knowledge of forces we cannot otherwise assess pertaining, in particular, to wind loads.

These experimental tests have been validated by simulating the above model using Computational Fluid Dynamics (CFD). Although it is new area of study, particularly in its application to external flow, the model has been used to find pressure coefficients on sheets/nets surrounding a scaffold. The net was modeled as a porous media and porous jump boundary conditions were used to simulate a net. Prior to this, wind tunnel tests were conducted on two types of net commonly used in construction industries to determine their permeability.

The advances made in high speed digital computer technology had enabled the solution of flow problem which were described mathematically by a set of coupled non-linear partial differential equations and the appropriate boundary conditions, in a relatively short span of time and for a low financial cost. Initially the wind engineering community largely ignored this technique due to the need for powerful computers and the errors in early modelling techniques [1.5]. Nevertheless, the rapidly falling costs of computer hardware and further advances in technology in the late 1980s and 1990s enabled CFD to be applied to the complex field of wind engineering [1.6].

In theory, it is numerically possible to completely resolve all aspects of fluid dynamics problem including the rapid spatial and temporal variations of turbulence in the flow using a CFD technique known as direct numerical simulation. This technique involves discretizing the equations using the finite volume method at a mesh size below the smallest eddies in turbulent flow, the Kolmogorov length scale, and therefore resolving the flow down to the smallest spatial and temporal variations. Unfortunately, the direct numerical simulation of practical turbulent fluid flows using the time dependent Navier-Stokes equations in their simplest forms is well beyond the capabilities of even the present day of computing power. This is due to the fact that the amount of computer processing (CPU) time required is dependent on the degree of resolution of the small scale eddies. The smallest eddies in turbulent flow, the so-called 'Kolmogorov microscales' are very small at about 0.1 to 1mm for natural wind [1.5]. Therefore the numerical discretization of an entire wind engineering flow field with a complex geometry at high Reynolds numbers is at present well beyond the capabilities of even the most powerful supercomputers available.

The only economically feasible way to solve this problem is to employ statistically averaged equations which govern the mean flow equations. Turbulence models are then required to achieve closure of the averaged equations and represent the action of

turbulent stresses on the mean flow. Unfortunately the mathematical models used in CFD are only able to perform as well as the physical assumptions and knowledge built into them will allow. In particular, the assumptions made regarding the modelling of the turbulent component of engineering flows have proved to be a major source of error in wind engineering simulations.

Presently, 'the most popular and widely used models use equations representing a single length and velocity scales; and are based on Reynolds averaging and the isotropic eddy viscosity concept' [1.5]. Although many of these turbulence models have been used successfully in aeronautical applications, where fluid flow without separation may be a regular occurrence, the same is not true of wind engineering applications. Wind engineering flow fields are highly complex and are 'characterized by the presence of multiple recirculation zones embedded within a uni-directional flow. The addition of streamline curvature and favourable and adverse pressure gradients lead to flow fields possessing very different turbulence scales and structures. Consequently such turbulence models have great difficulty in simulating wind engineering flow fields which are essentially transient and highly anisotropic. It is, therefore, apparent that one of the main obstacles in the use of CFD in wind engineering is that of turbulence modelling' [1.7].

In view of these shortcomings one of the aims of this work has been to conduct research into the various turbulence modelling methods available with a view of comparing the different turbulence models available for computational wind engineering. This project has also concentrated on a number of different turbulence models and analyses their effects on the accuracy of the results obtained for bluff body flow simulations from the CFD package Fluent 6.30 [1.8]. A number of bluff body test cases have been used, all of which have also been analyzed experimentally at 'model-scale' to allow direct comparisons of the available data. As far as the author is aware these tests represent the first comparison of experimental data from a model-scale surface mounted cube and sheeted cube.

1.2 Aims of Present Investigation

The aims of this project are:

- To calculate the pressure coefficients on sheeted scaffold structures by testing a scaled model in a wind-tunnel.

- To calculate the permeability of the common nets used in the construction industry.
- To develop a mathematical model of scaffolds subjected to wind loads.
- To incorporate the mathematical model in Computational Fluid Dynamics programs such as Fluent.
- To explore an effective and reliable approach for the determination of pressure/ force coefficients for the design of scaffolds subjected to wind loads.
- To obtain revised wind load pressures for scaffolds for inclusion in new/ revised design codes and to obtain an understanding of the influence of the attached structures.

1.3 Outline of Dissertation

This thesis is structured as follows:

Chapter 1 introduces the idea and purpose of the present study. Besides that, a description of the project strategy is stated. The aims of the project are discussed.

Chapter 2 discusses the information obtained from the literature review on scaffold structures. This includes causes of failure of scaffold structures and discusses the current UK and German practices in the design of scaffold structures. This also includes the name and number of common British and EU codes uses for design of scaffold structures. In brief an attempt has been made to demonstrate the aeroelastic nature of netted/-sheeted scaffolds under wind loads. Very little published research is reported on the wind effects on scaffolding.

Chapter 3 introduces the reader to the subjects of wind and its nature. A brief history of the development of wind engineering has been presented. The behavior of wind under atmospheric flows, its turbulent nature and its statistical properties is discussed. Bluff body aerodynamics of cubical building to explain its turbulent nature has been discussed.

Chapter 4 describes computational fluid dynamics (CFD), giving a brief history of its development, the governing equations involved and the methods of simulation of turbulence. The advantages and disadvantages of various turbulence models are

discussed. In addition the turbulence models available within Fluent are described and the reasons why the particular methods used in this thesis for the solution of the bluff body aerodynamics have been adopted are given.

Chapter 5 discusses the simulation of the actual wind properties at the Silsoe Research Site for wind tunnel tests including wind profile and turbulence, etc. The same wind conditions were used in the CFD analyses for inlet boundary conditions, outflow boundary conditions, near wall treatment. The various solution strategies adopted for successful solutions were discussed.

In Chapter 6 a simulation of netted scaffold as porous media is presented together with its limitations and assumptions. The governing equations for the simulation have been established. A few examples have also been illustrated to calculate the permeability and guide to the use of derived data for the solution of net simulation problems by Fluent.

Chapter 7 describes the performance of the three models chosen for the analysis in CFD for a number of different bluff body flow fields. It compares the results obtained against the wind tunnel data obtained from the experiments on the scaled Silsoe Experimental Building and on the building surrounded with sheeted scaffolds. A full analysis and discussion of the results is offered based on the ability of the models to meet certain criteria (described in Chapter 4 and 5), in order to assess their applicability as wind engineering turbulence model.

Chapter 8 draws conclusions on the present work and recommendations are made for further research.

CHAPTER 2
Literature Review

2.1 Introduction

Tubular steel scaffolds have been widely used in the building construction in the U.K. They are light in weight, easy to maintain, install, and dismantle. They are mostly fabricated from hot rolled steel tubes. Scaffold structures are often slender and constructed of elements with semi-rigid connections and are prone to fail by buckling. Vast amounts of research have been carried out to study the performance of scaffolds using conventional linear analyses (stability check were often undertaken using the effective length approach), buckling analyses, non-linear geometric/material analyses, etc. However, in reality the connections are semi-rigid in nature. Their stability largely depends on flexural, shear and axial deformation of the members, performance of the connections and the support conditions. The behaviour of the connection is often non-linear even when the components remain in an elastic state of stress. Further, due to slender nature of the members, the loads acting on the deformed shape of the structure amplifies the forces and the lateral displacement of the structure ($P-\Delta$ effects). These effects cannot be calculated using linear analysis methods. In addition, it is difficult to estimate the effective lengths of the members due to the non-linear behaviour of the connections. Thus the effective length approach can be very conservative and lead to uneconomical design [2.1].

Furthermore, in the last 20 years we have seen a significant increase in the use of debris netting (Figure 2.1a) and impermeable wind proof sheeting (Figure 2.1b) for cladding temporary scaffold structures used in building construction work in the U.K. Plastic nets are generally woven fabric of varying air penetrability where as sheet cladding can be made from windproof tarpaulins or plastic sheeting. The main benefits of sheeting are an improvement in working conditions and shielding workers from extreme weather. It also protects both the general public and the workforce from falling debris. The main disadvantage of using these materials is that there is an increase in the wind load on the structure, particularly on the scaffold to building ties. Such increases in the wind load on the scaffolds make such structures susceptible to damage or collapse under storm conditions. This has led to a number of incidents reported over the past two decades,

such as Uppark House, Surrey, which claimed two lives on 25th January 1990 [2.2]. Building damage is often caused by windblown scaffolding as well.

British Standards BS 5973: 1993, BS 6399-2: 1997 and European Codes BS EN 12810-1 & 2: 2003, BS EN 12811-1, 2 & 3: 2003, etc. includes techniques for assessing the increase in tie loading. Despite this, there have been a number of incidents in recent years where scaffolding has fallen from buildings during storm conditions.

(a) Debris netting **(b) Impermeable sheeting**

Figure 2.1 Net and sheet clad scaffolds

A. Maitra [2.2] in his paper reported that of the scaffolds which collapsed in windy conditions, a disproportionate number were sheeted and that most of these collapses could have been prevented by better design and site control, concluding that the effects of sheeting a scaffold are not fully understood. He went on to draw attention to the fact that the practice of sheeting scaffolds is on the increase and, consequently, that there is a need to ensure that information is available to designers and users of such scaffolds to ensure that they are of adequate strength, when supplied and throughout their intended life. It was also observed that sheeting scaffolds may have prevented a significant number, almost 50%, of falls of persons from height and may also have prevented in excess of 60% of objects/articles which fell off the edge of a scaffold and struck somebody working or passing nearby.

In one such report [2.2] by the investigating inspector of the UK Health and Safety Executive (HSE) that where wind velocity was responsible for scaffold damage, 29% of these were catastrophic collapses. Furthermore, of this number of scaffold collapses, 54% were sheeted of which nearly two thirds collapsed because they were inadequately tied (35% were reported as never having had sufficient ties while in 25% of the cases ties had been removed by operatives and never replaced). This number of collapses is

disproportionate to the number of scaffolds that were sheeted during the period in question (April 1986 to December 1993), and does give cause for concern.

2.2 Wind Storm Classification by Scale

The UK is one of the windiest parts of the Europe and every year many thousands of temporary and permanent structures suffer wind damage. Wind damage in the UK occurs in three distinct scales which in ascending order are [2.3]:

***2.2.1 Tornado Damage*:** This is highly localised damage occurring along a narrow tract typically 50m wide and 200m long continuing intermittently over distances of up to 20 Km as the tornado 'skips' over the ground.

***2.2.2 Background Damage*:** This is the damage that occurs during windstorm of low to medium severity at wind speeds below the design values. The damage is distributed throughout the UK, mainly as many isolated events. Background damage occurs at a consistent level of between 100,000 to 150,000 instances per year; at least an order of magnitude higher than tornado damage [2.3].

***2.2.3 Storm Damage*:** This is the damage that occurs during severe windstorms when the wind speed approaches or exceeds design values. The damage is widespread over the area covered by the storm and includes all classes and ages of buildings. These storms are infrequent but generally cause an order of magnitude more damage than from background damage.

2.3 General Causes of Failure of Scaffolding Structures

There are basically two main causes of failure of scaffolding structures:

1. Inadequate tying back to the main structure, and
2. Failure to design for the appropriate wind load.

The latter includes failure caused by sheeting the scaffold to provide weatherproofing or security without taking the increased wind loads into account. Even sheeting the roof can significantly increase the wind load and in such cases the scaffold should be treated as a clad or partially clad structure for the calculation of wind load.

2.4 Recent UK Practice for Wind Load on Bare-poles and Clad Scaffolding

According to BS 1139-5: 1990/ HD 1000: 1988 [2.4] wind load should be calculated for wind acting parallel and perpendicular to the façades served by the scaffold. According to the code the design wind pressure adopted for these calculations shall be as follows:

(a) *Maximum Wind Conditions*: A design wind pressure of 600 N/m^2 at the base of the scaffold increasing uniformly to 770 N/m^2 to the height of 24 m and then constant 770 N/m^2 to the height of 30 m at acting over the projected area of the scaffold.

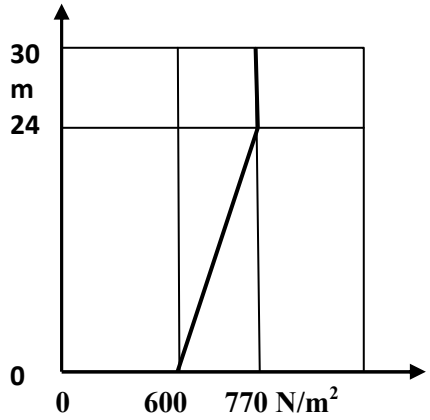

Figure 2.2: Design wind pressure applying to the height above the ground level

(b) Working Wind Conditions: A design wind pressure of 200 N/m^2 uniformly distributed over the projected area of the scaffold. For the purpose of this calculation only, a nominal area shall be added to the area normal ($A\perp_r$) and parallel ($A\|_r$). This area results from an obstruction to the wind 400 mm high minus the height of a toeboard. This area is to be considered acting at the surface of the platform.

The force parallel to the façade $F\|$ in N , shall be calculated from the expression:

$$F\| = W.c\|.\left[A\perp_r + \sum_1^n \frac{A\perp_s .c_f}{1.2}\right] \tag{1.1}$$

The force perpendicular to the façade in N , shall be calculated from the expression

$$F_\perp = W.c_\perp.\left[A\|_r + \sum_1^n \frac{A\|_s .c_f}{1.2}\right] \tag{1.2}$$

Where the scaffold crosses in front of large openings in the façade or extends beyond the sides or top, higher forces perpendicular to the façade may occur and the design of the scaffold shall permit these extra loads to be allowed for (see annex C of HD 1000:

1988).

Calculation of the overall pressure coefficient perpendicular to the building façade $c_{\perp}$ for facades of varying permeability for a structure comprising circular members and toe boards is calculated from the expression:

$$c_{\perp} = c_{\perp} closed + D \tag{1.3}$$

Nets can reduce wind loads on scaffolds for operatives. The general reduction factor is about 40% which is good protection and also nets provide some resistance to rain penetration. The design procedure is to reciprocate the wind reduction, coming back to porosity, and then design the scaffold structure and its fixing for 60% of the equivalent sheeted surface [2.5].

In areas of high local suction which frequently occur near to the edges of walls and roofs the coefficients for local effects should only be used to calculate the loads on these local areas. They should not be used for calculating the load on the entire structural elements such as roofs, walls or the structure as a whole.

The advantage of solid soft plastic sheeting over debris netting is that the wind within the scaffold is reduced still further. A reduction of 90% is a commonly accepted figure. The operating environment then nearly becomes what is the draught factor for operatives. For a number of years contractors have occasionally heated sites, with solid sheeting this becomes a practical consideration further enhancing the working environment. Whatever form of cladding is employed it is important to specify this at the earliest stage possible as this will affect the design , the period of construction and of course the cost.

2.4.1 Erection of Cladding

Erection methods have become fairly standardised and are fully described in section 10.2 of British Standard 8093: 1991 [2.6]. The erection of containment netting should only be carried out once the structure to which it is to be fixed has been boarded out at each lift, allowing safe access to complete the tying.

2.4.1.1 Method One:

This method is suitable where only weather protection and dust protection duties are required. ‘Take the complete roll of containment netting of the required length to the

highest boarded out point at which it is required. Using standard nylon straps fix one end of the roll at both corners and at intermediate points where necessary to the highest ledger. Carefully lower the remainder of the roll down the outside of the scaffold. Tie off at the lowest point to prevent the netting flapping around and causing obstruction. Then tie to ledgers at each lift and 'stitch' the vertical joints' [2.6].

2.4.1.2 Method Two:

This method is preferable for enabling containment nets to restrict falls by men and materials. Use netting of a pre-determined width to suit the scaffolding lift height.

'To fix on the inside take the net to the height at which it is required and lays it on the boarded level. Starting at one end tie the two corners to the upper and lower ledgers of the lift. Fix additional ties at required centres as the netting is unrolled. It is not advisable to unroll the net fully on a boarded level before fixing' [2.6].

'To fix the outside two people are required. Take the roll of containment netting to the level at which it is required. One person takes the free end of netting while the other gradually unrolls from the main roll. The free end is then passed around the outside of the standards. When the required length of netting is unrolled, fix the free end to the framework. Cut the netting at the required length and pull taut. Insert the remainder of the fixings' [2.6].

Typical fixing arrangements of nets and sheets are shown in Figure 2.3 (a & b), while the lap details for nets and sheets are shown in Figure 2.4.

(a)

(b)

Figure 2.3 (a & b) Typical fixing arrangements of nets and sheets

Figure 2.4 Typical lap details of nets and sheets

2.5 Design Codes in Practice

The design of temporary structures over the years has seen many changing concepts. In early years, the late 1940s and the early 1950s ENGINEERING was introduced into the industry since when considerable experience as well as knowledge had been gained. Equipment and components were sometimes evaluated by simple calculation half married to custom and practice. The industry then gradually adopted a policy of testing both components and complete scaffold structures. Scaffolding contractors and institutions later were frequently found to possess the largest testing rigs in the UK.

Today there are a number of codes and reference documents that are widely used by designers in industries, even though some of the codes have been withdrawn:

BS 5973: 1993	Code of practice for access and working scaffold and special scaffold structures in steel.
BS EN 12810-1&2: 2003	Façade scaffolds made of prefabricated components – Part 1: Product specifications, Part 2: Particular methods of structural design.
BS EN 12811-1,2 & 3:2003	Temporary works equipment –Part 1: Scaffolds – Performance requirements and general design, Part 2: Information on materials & Part 3: Load testing.
BS 1139-1.1: 1990	Metal Scaffolding Tubes – Specification for steel tubes.
BS 1139-2.1: 1991/ EN 74: 1988	Metal Scaffolding Couplers – Specification for steel couplers, loose spigots and base plates for use in working scaffolds and false work made of steel tubes.
BS 1139-2.2: 1991	Metal Scaffolding Couplers – Specification for steel and aluminium couplers, fittings and accessories for use in tubular scaffolding.
BS 6399-2: 1997	Loading for Buildings – Code of practice for wind loads.
CP3: Chapter V-2: 1972	Code of basic data for the design of buildings-Loading: Wind loads.
BS 8093: 1991	Code of practice for the use of safety nets, containment nets and sheets on constructional works.
BS 1139 – 5: 1990/ HD 1000: 1988	Metal Scaffolding–Specification for materials, dimensions design loads and safety requirements for service and working scaffolds made of prefabricated elements.
NASC	National Association of Scaffolding Contractors - Guidance Notes

Wind Loading Handbook – Newberry and Eaton.

Manufacturers and Suppliers Information.

Of the above British Codes only BS 5973: 1993 contains guidance on the strength and number of ties between a fabrics clad scaffold and a building. Only recommendations for sheeted scaffolds are made. Currently all nets are considered to be sheets for the purpose of tie strength calculations.

2.6 Recent German Practices in Cladding Scaffold Structures

Cladding of temporary structures has been used in Germany for many years for weather protection purposes. Therefore the cladding material has to be fairly impermeable. These requirements are well met with sheets.

In recent times façade scaffolds were often clad, where in addition to impervious sheets less permeable nets were also used. This cladding was mainly provided to protect the environment from dust or noise. Sometimes it was also used as a side protection facility to protect persons from falling down.

Structures which are clad by sheets or nets are substantially loaded by wind forces. Until now, however, the air penetrability of the cladding materials has largely been ignored. For economic, as well as for safety reasons, a more realistic knowledge of the parameters influencing the wind load on the cladding is needed.

2.6.1 German Code Provisions

The resultant static wind forces acting on a clad structure were usually calculated according to the following formula given in DIN 4420- Part 1: 1990 [2.7]:

$$F = q_i . \chi . c_i . \sum c_{f,i} . A_i \tag{1.4}$$

In calculating wind forces a temporary structure has to be treated like a permanent structure. The German Guidelines for weather protection halls specified aerodynamic coefficients by referring to the national wind loading code for usual structures and by supposing that the cladding of the walls as well as of the roofs is impermeable. Up to a height of $12\,m$ a constant velocity pressure of $0.5\,KN/m^2$ was used which meant that a wind velocity of $28\,m/s$ had to be applied. It was also assumed that the internal pressure corresponded to the current atmospheric pressure so that no additional wind forces due to over or under pressure within the hall could occur.

Specifications for façade scaffold in general were given in the German standard DIN 4420- Part1: 1990. This standard also specified values for claddings. Corresponding aerodynamic force coefficients are given as $c_{f\perp} = 1.3$ and $c_{f\parallel} = 0.1$. $c_{f\perp}$ and $c_{f\parallel}$ describes the action of the wind perpendicular and parallel to the plane of the sheeting

respectively. The value of $c_{f\perp} = 1.3$ also applied to permeable nets unless detailed wind tunnel tests on a special net type showed favourable values. The same procedure applied to the corresponding aerodynamic force coefficient $c_{f\parallel}$ which has to be taken as $c_{f\parallel} = 0.2$ if no other information is available. Wind-tunnel testing on nets of different types produced by various manufacturers, which are used very often for scaffold cladding, has been reported by H Nieser [2.8]. The results of some of them are given in Table 2.1 below. They show medium values of $c_{f\perp} = 0.6$ and $c_{f\parallel} = 0.1$, that meant in comparison with sheets a substantial reduction of the wind forces perpendicular to the plan of the cladding was assumed. These forces had to be assumed to act at full magnitude in both directions, i.e. towards as well as away from the façade. The standard allowed a reduction due to the influence of the more or less open scaffolded façade only for non clad-scaffolds. To neglect this influence for clad scaffolds seems to be very conservative, especially considering the wind action away from the façade, where a substantial reduction will be given by the sheltering effect of the façade. The reason for this sometimes very strong specification is that fact that there was no assured knowledge of such an influence when preparing the standards. Therefore, values lying on the safe side were adopted.

Table 2.1 Difference of pressure coefficients across nets

Designation of the net	Aerodynamic Force Coefficient	
	$c_{f\perp}$	$c_{f\parallel}$
Delta Tex B	0.49	0.12
Euro-Net	0.50	0.14
733.735,7331	0.55	0.18
Hate-Net	0.50	0.14
Nicofence 40	0.85	0.08
Nicoprotect	1.00	0.06
Plana-Net Type B	0.50	0.14
Austronet 313	0.77	0.06
Austronet 202G	0.69	0.13
Secura Quality 03	0.62	0.05
Secura Quality 67	0.47	0.05
Tegunet	0.50	0.14

The wind force that acts on the material covering scaffolding depends essentially on the parameters of air penetrability of the netting and penetrability of the building. In the case of buildings with closed façades the wind forces perpendicular to the façade acting on the scaffolding covered with air penetrable netting are slight. As the penetrability of the building increases the aerodynamic force coefficients increase in a roughly linear pattern. The force coefficients determined for a penetrability of 100% for the force perpendicular to the netting plane is roughly equivalent to those calculated for individual netting samples. As a matter of principle, coverings made of largely windproof material behave differently from wind penetrable coverings. Significant wind forces occur for these materials even where the building façade is closed.

Whether or not the front face of the scaffolding is covered plays an important part when evaluating the wind forces parallel to the building façade. The wind force on the front face covering corresponds to the wind force perpendicular to the netting plane. In addition to this wind forces made up of that proportion of the force parallel to the netting plane that is produced during flow through and pure frictional forces become active in the netting plane parallel to the façade.

2.7 Aeroelastic Nature of Net or Sheet Clad Scaffolds

If a structure changes shape in a wind, this will in turn modify the wind pressures on the structure. However, it is not just the change in shape which is important, but also the velocity and acceleration of the structure and its recent past history of motion **[**2.9**]**.

Aeroelasticity is the study of the interaction of aerodynamic loads and elastic structural behaviour. Aeroelastic phenomena are unimportant in the design of many building and civil engineering structures. This means that the wind loads are effectively independent of the motion of the structure. However, certain structures, such as suspension bridges, slender towers and fabric structures may undergo large scale motion caused by aeroelastic phenomena.

Aeroelasticity manages to combine all the complexity of structural analysis and fluid dynamics. The fundamental differential equations of fluid dynamics and elasticity are virtually identical, but in fluid dynamics there is no equivalent of St. Venants's principle which applies in elasticity. In essence St. Venant's principle states that small deformations of a structure or approximations in the analysis of a structure only have a

localised effect – making a small saw cut in a loaded table top has a large effect on stresses locally, but a few centimetres away the effect is negligible.

In fluid dynamics small changes in the shape of an object can have a large effect on the way in which the fluid flows over the object as a whole. Similarly small approximations in the analysis can lead to large errors. This explains why wind tunnel tests have now been replaced by numerical methods, although there are still problems in scaling the results from wind tunnel tests.

When wind flows past objects, vortices may be shed into the flow. Fluid flows in a circular manner in a vortex, eddies that can be seen in the flow of a river are examples of vortices. Vortices moving with the flow cause the flow to become unsteady that is the flow varies with time. Vortices are responsible for the gusts and lulls that we experience in a wind.

The presence of vortices produces a dynamic load even on rigid structures and this phenomenon might be called buffeting. The vortices may be present in the wind before it arrives at the structure or may be formed in passing over the structure itself. The frequency of loading depends upon the speed of the wind and the spacing of the vortices.

When the fluid flows past an object, the flow may or may not separate from the object. For example a flow over the wing of an aircraft should remain attached, that is not separate. However, if the angle of attack, that is the slope of the wing relative to the airflow, is too great than the flow will separate from the top of the wing leading to stalling which is the sudden loss of lift. Wind flow separates from virtually all civil engineering and building structures.

Flutter is an aeroelastic phenomenon in which a structure oscillates and extracts energy from the wind to build up and maintain oscillation. Thus when flutter occurs, the dynamic load is caused by motion of a ‘flexible’ structure, whereas buffeting can produce dynamic loads on a ‘rigid’ structure. Flutter and buffeting can occur simultaneously and it is often difficult to distinguish between them.

Flutter can be further characterised as classical flutter or stall flutter. In classical flutter the flow remains attached to the object. In stall flutter it separates, making analysis even more complicated.

The extraction of energy from airflow to build up and maintain an oscillation is termed negative aerodynamic damping.

Divergence is a static aeroelastic phenomenon which is rather akin to buckling. When a structure buckles, the negative geometric stiffness balances the elastic and possibly geometric stiffness of the structure. Aerodynamic stiffness can be explained as follows. If the shape of the structure changes in a wind, the wind pressure also changes. The change in pressure will be dependent upon the magnitude of the change in shape leading to stiffness like term. The aerodynamic stiffness may be positive or negative in that it may either tend to return the structure to its equilibrium configuration or destabilize it [2.9].

When a structure oscillates in a fluid, the fluid contained within and surrounding the structure also oscillates. The mass of the fluid moving with the structure is known as the added or virtual mass. The density of air is approximately is 1.3 Kg/m^3 and therefore a 10 x 10 x 10 m^3 of air has a mass of over a tonne. For fabric structures the added mass is often much greater than the mass of the fabric.

The behaviour of a fabric structure in a wind can be extremely complex. There is no one satisfactory design method and it is a question of combining experimental results with simple theories and experience with similar structures.

If there is any question regarding static or dynamic stability of the fabric, it can only be accurately answered by an aeroelastic wind tunnel test. A rigid model test gives no information regarding the possibility of divergence or flutter, but can be used to predict fluctuating wind pressure due to buffeting.

2.8 Research into Scaffolding

Many research studies have been reported to improve the analyses and design of scaffolds. Prior to the mid 1970s scaffold structures were normally analysed by hand calculation techniques using effective length calculations of the scaffold standards. It was known, however, that the effective lengths of the standards were strongly influenced by the lateral support to the standard afforded by the horizontal members attached to them [2.10]. Following the collapse of various scaffold and falsework structures in the United Kingdom (UK) in the late 1960s [2.11, 2.12] the United

Kingdom Science Research Council commissioned a study of scaffold structures at Oxford University commencing in1971 under the supervision of Professor Lightfoot. The results of this study were published in 1975 and 1977 [2.13-2.16] and showed that scaffold systems primarily fail due to elastic instability. Research by Harung et al [2.16] created models of single storey 'tube-and-fitting' towers and loaded them with dead load on top of the tower. The models were analysed using a geometrically non-linear finite element program. All the models analysed had either rigid or pinned connections. No eccentricity of the connection was included. The failure of models occurred by buckling. The results were compared with experiment, the theoretical results being between 10% and 15% higher than the experiments. The program was applied to three full-scale tests on a three storey scaffold with similar precision. The discrepancies between theory and experiment can be attributed to material and geometrical imperfections in the structures tested and to neglecting the semi-rigid nature of the scaffold connections. Harung et al concluded that the effective lengths of scaffold columns should be taken larger than 1 due to additional effects of imperfections in member geometry.

In 1980 a scaffold supplied by SGB was tested at Stuttgart as part of a European project to develop a new code for proprietary access scaffolds. The results of these tests were used by German and British researchers to test analytical procedures to model scaffold assemblies [2.17-2.20]. The results showed that scaffold assemblies are examples of slender structures and analyses must include local member imperfection $(P-\delta)$ effects and overall global geometrical $(P-\Delta)$ imperfection effects as well as incorporating the rotational stiffness of the semi-rigid connections.

Research into wind loading has been predominantly into permanent structures and the results codified into national and international standards such as CP3 [2.21] and BS 6393-2 [2.22]. A conference was held under the auspices of Health and Safety Executive (HSE) at Buxton, UK in 1994 [2.23] on wind loads on temporary structures. During the conference it was stated that wind loads could only be determined through the use of wind tunnel procedures. Various papers on the Buxton Conference commented on the differences between the earlier wind load code CP3 [2.21] and the current UK code BS 6399-2 [2.22] which showed that, depending upon season and location, the new code gave pressures that could be greater or less than those of the original code [2.24]. The author, Blackmore, commented that the new code made

allowance for temporary structures by reducing the probabilities of high wind speeds which in the main code were derived on 50-year return periods, far in excess of the life of a scaffold. Blackmore [2.25], in another paper presented a brief review of collapses due to wind damage and showed that scaffold collapses were a small proportion of collapses and primarily due to inadequate tying to the façade or to inadequate calculations of the wind load on the scaffold.

Williams [2.9] in his research paper discussed the aerodynamic behaviour of fabric sheets suggesting that due to the complexity of fabric behaviour that modelling could only be achieved by wind tunnel tests.

Hoxey et al [2.26] were primarily concerned with experimentally determining drag coefficients on light-weight semi-permanent structures but pointed out that for scaffold structures the maximum wind pressure could arise for the end wall of the long scaffold by wind acting between 30^{o}-40^{o} from the plane of the façade.

Schnabel [2.27] reported on wind tunnel experiments on a model of dimensions 0.6m x 0.3m x 0.6m and a supplemental model of size 0.6m x 0.6m x 0.6m conducted in Bravia [2.28] in accordance with the German Code DIN 4420 Part 1 [2.7]. The experiments determined the force coefficients on a cladded scaffolds. Experiments were conducted with scaffolding attached to one side of the building only and attached around the whole building. Effects of permeability of the debris netting were included. Permeability was shown to reduce the total force for the netting used by 20% over that acting on an impermeable cladding. The paper concluded by noting that fully cladding a building on all four sides reduced total scaffold loads.

Wilson and Hollis [2.29] conducted field tests on a large putlog scaffold 13.7m high by 13.2m wide at Buxton. The scaffold was sheeted with different cladding materials and consisting of single face, the rear being open. The forces on various locations on the scaffold were recorded using the method described by Gylltoft [2.30]. The data was compared with wind tunnel tests in Hull with little correlation between the results. Research still required at that time into scaffolding and other temporary structures was summarised by James [2.31].

Bamboo scaffolds have been widely used in construction in South East Asia, in particular, Southern China and Hong Kong for many years. A pilot study was carried

out by Chung and Yu [2.32, 2.33] 'to examine the variation of compressive strength against various physical properties along the length of bamboo culms of two locally available bamboo species Kao Jue and Mao Jue and to establish characteristic values of both the strength and the Young's modulus of each bamboo species for limit state structural design. Due to the slenderness of bamboo members, column buckling is always critical in bamboo scaffolds, and thus, extensive and systematic experimental investigations on column buckling for both species over a wide range of practical member lengths were executed to examine their axial bucking behaviour [2.34, 2.35 and 2.36]. In accordance with existing structural design philosophy on column buckling for both steel and timber structures, a design method based on modified slenderness was proposed for general design after careful calibration against test data'. Axial buckling of bamboo columns in bamboo scaffold is the latest published work by Yu et al [2.37].

Chan et al [2.38] proposed a non-linear analysis method for the elastic buckling analysis of scaffolding systems. However, the connection stiffness was taken into account by manually changing the effective length of elements. The connection stiffness was assumed to be constant until lateral instability occurred. Similar approaches have been used by Peng et al [2.39-2.41]. Godley and Beale [2.20] demonstrated the effect relatively small joint stiffnesses have on the overall behaviour of a scaffold structures using 2D and 3D modelling of scaffolds. Further work by the same authors emphasised the need to incorporate the nonlinear behaviour of joint stiffness and the second order analysis of the scaffolds [2.42-2.43]. They also demonstrated that the performance of 2D models could be improved by the use of springs modelling the interactions between the faces parallel to the façade and between the adjacent frames perpendicular to the façade and nonlinear second order analysis incorporating geometric nonlinearities. Nonlinear joint models have been shown to work for large scaffold assemblies [2.44].

Test on scaffold tower shoring systems were reported by Kao [2.45] and Yen et al [2.46-2.49]. These tests were conducted on scaffold systems up to five storeys in height. In [2.48] Yen suggested an empirical equation which could model the experimental results. However, as tests had not been conducted on systems of more than five storeys the formula could not be used for high systems. Huang et al [2.50] used Yen's experimental results on shoring systems to validate a finite element analysis using two-dimensional models. The modes of failure found from the theoretical analysis were identical to those found in the experiments. However, the theoretical calculations

produced failure loads which were about 20% higher than the experiments. No account was made of any three-dimensional interaction which may reduce the overall capacity or of the effects of semi-rigid connections. In a companion paper [2.51] Huang et al developed an approximate two dimensional model of the failure of the scaffold structure under the assumption that the experimental failures were due to sway in the lowest member and its closed form solution was proposed for the 2D Numerical model. Chan and Chu [2.45] propose a computer simulation for the design of scaffolding systems using stability functions there by eliminating the effective length approach, which was found to be unreliable.

In 2002 the US Department of Labour published a safety note [2.53] on the wind effects on scaffolding. The note emphasised that the frequency and adequacy of ties and anchors must be determined when considering wind effects. They also gave a 'rule-of-thumb' that ties should be doubled up when scaffolds are sheeted.

Yue et al [2.54] in his paper 'wind load on integral-lift scaffolds for tall building construction', advocates [2.54] that the wind load on scaffolds are much greater than dead loads and may be the dominant effect as the scaffolds climb over 150m in height. The shape coefficients and vibration coefficients are important factors in calculating wind loads. However, there is no available approach at present for determining the two coefficients for calculating the wind loads on scaffolds'.

Recently Kaveh et al used 'an efficient force method of frame analysis by generating special cycle bases for the formation of localized self-equilibrating systems, leading to sparse flexibility matrices' [2.55]. A study on 2D building with bare-pole scaffolding tubes all around were conducted by the author [2.56] and it was found that the pressures in general are significantly lower than those given in the Eurocode which does not allow for the shielding effects on the tubes of the building to which the scaffold is attached. Higher pressures than those given in the code were found on the corner standards. These standards, however, are the most lightly loaded standards in general and hence this higher pressure is unlikely to cause problems. A review of the extensive research into the analysis and design of scaffold structures has been given by Beale [2.57], reviewing all research undertaken between 1970 and 2006 and citing 145 references. This review shows that analyses procedures are well developed and usually require second-order geometric and material non-linearity properties to be considered.

Peng et al [2.58] carried out experimental investigations on door shaped modular scaffolds and concluded that the eccentric load significantly reduces the load carrying capacity. Also when the base of scaffold is flexible, 'the critical load of the structure slightly decreases with an increase in the number of stories. A fixed support can significantly increase the critical load of the scaffolding system' [2.58].

Jack E. Cermark in [2.59] studied the wind tunnel testing of the World Trade Centre, New York. A manuscript by the American Society of Civil Engineers (1996) [2.60] discusses in detail about testing of structures in wind–tunnels. Emil Simiu (2005) [2.61] in his technical notes throws lights on wind tunnel testing and a sector-by-sector approach to wind directionality effects of various types of structures. Huang et al. [2.62] made use of the Computational fluid Dynamics (CFD), such as large Eddy Simulation (LES) and Reynolds Averaged Navier-Stokes Equations (RANS) Model for the study of wind effects on the Commonwealth Advisory Aeronautical Council standard tall building. 'The main objective of this study was to explore an effective and reliable approach for evaluation of wind effects on tall buildings by CFD techniques' [2.62]. With the exception of author [2.56] no one has reported the use of CFD techniques in studying the behaviour of scaffolds under wind load.

The present study on the 'Experimental and computational determination of wind loads on clad scaffolds' has been undertaken to quantify the effects of wind on scaffolds. It requires model scaffolds to be analysed both experimentally and computationally using *CWE* (Computational Wind Engineering). CWE as a branch of Computational Fluid Dynamics has been developed rapidly over the last 30 years to evaluate the interaction between wind and structures numerically, offering an alternative technique for practical application and is described in detail in the next chapter. The study will determine the pressure loads due to wind that real scaffolds are subjected to, taking into account the influence of the building to which the scaffold is attached. Limited research into wind loads on scaffolds has been done in the past which has led to current codes being based upon the effects of wind loads on permanent structures. The objective of this research is to obtain revised wind load pressures for scaffolds for inclusion in new/revised design codes and to obtain an understanding of the influence of the attached structure on wind loads.

2.9 Conclusions

This chapter has focussed on the general practices used in the design of scaffolds and on the major research undertaken into scaffolding. Most of the published research into scaffolding has been concerned with load carrying capacity and failure modes. No major research has been done in the past to calculate wind forces on the scaffolds by CFD.

Safety is important issue in civil engineering construction. Wind effects may become the dominant factor that will influence the operational safety of scaffolds. The phenomena associated with wind loads on bare tube scaffolds and clad scaffolds are very little understood till date. The various codes discussed in this chapter give guidance in calculating the wind forces on bare tubes scaffolds based on the projected area of tubes, toe boards etc. without taking into consideration any shielding effects on the tubes because of building (presence of a building may increase or decrease the force coefficients/pressure coefficients). The wind forces on sheeted scaffolds are based on the frontal area without considering the suction forces on the leeward of the sheeted scaffolds. The effects of permeability of nets on the wind forces on scaffolds have not been explained properly by any researchers. The author has tried to overcome some of the limitations of the previous research into wind loading in the following chapters.

CHAPTER 3
Wind and its Nature

3.1 Introduction

This chapter provides a general introduction into the field of wind engineering with a brief overview of this complex and diverse subject. The reader is offered a brief history in the development of the subject and the prominent figures who have contributed to this subject. The significant effects of the atmospheric boundary layer on the flow pattern around buildings are graphically demonstrated. Also various statistical parameters which define the random nature of wind are also discussed. the majority of the data is drawn from references [3.1] to [3.3].

The development of modern materials and construction techniques has resulted in the emergence of a new generation of buildings and structures that are often, to a degree unknown in the past, remarkably flexible, lower in damping, and light in weight [3.1]. Thus these buildings, as well as various types of rigid and semi-rigid structures, exhibit a tremendous susceptibility to the effects of wind. Accordingly, wind engineering as a fast evolving discipline aims to develop tools which will enable the designer to estimate the wind effects with a higher degree of refinement than in the past. Structural engineers have the task of ensuring that the performance of the structures subjected to the action of the wind will be adequate during their designed life for safety and serviceability. Thus a knowledge of the wind environment, the relation between wind and the forces it induces on the structures and the behaviour of the structures under those forces are primary key factors to designers.

The wind environment normally includes knowledge about elements derived from meteorology, micrometeorology and climatology. Meteorology provides a description and explanation of the fundamental features of atmospheric flow on this planet. Some meteorology features need to be considered in the design procedures, such as hurricane information for coastal building design, or tornado characteristics for the design of nuclear plant, etc. Micrometeorology describes the characteristics of the atmospheric flow near the ground, such as the variation of mean wind speeds with the height above the ground, the correlation of the mean wind speed and the turbulence upon the roughness of the terrain. This topic i.e. micrometeorology, is directly the concern of

structural engineers. Climatology, as applied to the wind environment, is concerned with the prediction of wind conditions at given geographical locations. Probability statements on future wind speeds from climatological studies may be summarised in wind maps in various building codes such as ASCE 7, BS 6399-2:1997 etc.

3.2 Brief History of Wind Engineering

To discuss developments related to boundary layer wind-tunnel studies of bluff bodies in general, and low-rise studies in particular, it is pertinent to consider a brief history of wind to support present research.

'As a natural force, wind was often personified as one or more wind gods or as an expression of the supernatural in many cultures. Vayu is the Hindu God of wind [3.2]'. 'One of the earliest gods of wind dates back five thousand years to the Assyro-Babylonian culture and was referred to as Enlil. Since winds were often associated with the souls of the dead, human sacrifices were occasionally offered to calm violent storm winds' [3.3].

'A practical use of wind was achieved in some early Egyptian cities. The prevailing winds influenced the layout of the city of Kahun (circa 2000 BC). The orientation of dwellings to the cooler north winds favoured those with power and wealth in that society. More recently in Hyderabad, India, houses are designed with tall airshafts and modified air scoops on the roof that draw the breeze from above the city down into the homes [3.3]'.

'The Greek philosophers, Aristotle and Theophrastus in the third century B.C., contributed their ideas to the cause of weather and its prediction. Aristotle's treatise, '*Meteorologica*', had little basis in physics but was very imaginative and, as Melaragno notes, '*it lasted undisputed until beyond the sixteenth century*'. However, it was not until Leonardo da Vinci (1452-1519) produced, by quantitative observation and deduction, a genuine appreciation of the phenomena that any real progress was made. He grasped the concept of conservation of mass for an incompressible fluid and developed some early sketches of a variety of flying/gliding machines [3.3]'.

'Further development in the physics behind atmospheric motion became possible as instrumentation was invented to record the atmosphere's properties and characteristics. By the early 1600s Galileo had invented the thermometer and Torricelli in 1643 the

barometer. The apparatus allowed works, such as Sir Francis Bacon's '*Historia Ventorum*', to challenge Aristotle's writings [3.3]'.

'No real attempts to quantify the motion and properties of fluids were possible until Sir Isaac Newton had developed his concepts of mechanics. For example, he correctly observed that the resistive force on an object in a fluid is proportional to the square of the velocity of the fluid passing it. The result is of particular use for bluff bodies (not streamlined) at modest to high Reynolds numbers (ratio of inertial to viscous forces). The analysis of continuum mechanics was developed by great mathematicians and hydraulicians, such as Bernoulli, Euler, d' Alembert, Navier, Stokes, Cauchy, Poisson, Reynolds and Joukowski to mention a few (see Table 3.1). The most general formulation of the equations of motion is attributed to the French mathematician, Claude Louis Marie Henri Navier (1785-1836), and the British physicist, Sir George Gabriel Stokes (1819-1903). The analytical solutions of these equations are limited to simple geometries and well defined fluid properties. Examples of these flows may be found in many fluid dynamics texts [3.3]'. 'Since, for most engineering applications, the ideal fluid solution is analytically unobtainable or apparently in conflict with common sense many designers had to resort to physical testing. One case in point is the design and construction of the Parisian Eiffel Tower, which subsequently resulted in considerable atmospheric science and aeronautical research. Eiffel's experiments in bluff body aerodynamics and his wind load design assumptions for the Paris Exposition Tower were amongst the earliest attempts to understand static wind loading [3.3]'.

'At about the same time Ludwig Prandtl (1875-1953) presented his seminal paper, '*Uber Flüssigkeitsbewegung bei sehr kleiner Reibung*', at the 1904 meeting of the International Mathematical Congress in Heidelberg. An apparent impasse existed between the theoretical, newly termed field of 'fluid mechanics' and the empirical results of hydraulics. The most dramatic example of the inconsistency between theory and practice is referred to as d'-Alembert's paradox. The apparent lack of drag predicted by the mathematical analysis of irrotational flow around a body was at odds with practical experience. Prandtl's proposal to consider two adjacent, asymptotic regions of a fluid acting around a body resulted in reconciliation between observation and the equations of motion. Prandtl constructed a small wind tunnel in 1908 at Gottingen, and so the concept of aerodynamic model testing was put on a more scientific footing. Prior

to this work some bluff-body building studies had been attempted in primitive wind tunnels by Kernot, Irminger and Eiffel, as noted above [3.3]'.

'Prandtl's work suggested that the viscous components in the equation of motion were assumed to be significant in a thin region of flow at a close proximity to the surface over which the fluid moved. This allowed for a non-slip condition at the surface with progressively increasing velocities as one moves from the surface into the free stream flow. The region was described by the term, '*boundary layer*', and its asymptotic nature required some definition of extent. One that is commonly in use is the distance from the surface at which the velocity assumes ninety-nine percent of the free stream flow. Outside this boundary layer it was proposed that the classical inviscid solutions could be applied. Note that a boundary may exist near the surface of the structure or adjacent to the Earth itself. The latter, planetary boundary layer is immensely larger, but is still 'thin' compared to the depth of the atmosphere [3.3]'.

'One of the most famous students of Prandtl, Theodore Von Kármán, studied solid mechanics before moving on to make great contributions to the field of aerodynamics' [3.4].

'However, the application of wind tunnel testing to ground based structures took five more decades to become a useful engineering tool. In fact, the term '*Wind Engineering*' was not coined until the early 1970s at what became known as the first United States National Conference on Wind Engineering Research. This meeting was held at Cal Tech (organised by Anatol Roshko) and resulted in the formation of the United States Wind Engineering Research Council (WERC), with Jack Cermak elected its first president. Prior to this development, the field was a subset of the larger topic of 'Industrial Aerodynamics' influenced greatly by Kit Scruton in Great Britain [3.3]'.

'Initially studies were performed in a uniform flow which produced spurious results. Probably the most quoted example is a paper by Bailey, 1935. By the 1950s atmospheric studies of the Earth's turbulent boundary layer had led to a greater understanding of its complexity and the establishment of a better set of modelling criteria. Cermak, 1958 demonstrated the criteria for Reynolds number independence when modelling an atmospheric boundary layer flow at a reduced scale. The application of statistical concepts, developed by Davenport was an essential contribution to physical modelling in wind engineering [3.3]'. Building studies began in the early 1960s, and the

theoretical justification for such work was contained in papers by Cermak. ‘In brief, it had been observed that the drag dependence on Reynolds number for bluff, sharp edges bodies (and the boundary layer itself) was small when performed above a critical Reynolds number. Thus, a major similarity requirement could be waived and the test results would still be of value’ [3.3].

Other similarity requirements include an equating of the Rossby, Richardson, Prandtl and Eckert numbers between models and prototypes. The significance of these non-dimensional quantities depends on the situation being modelled. However, the insensitive nature of load coefficients to Reynolds number meant that boundary-layer wind-tunnel modelling was viable at moderate wind speeds. The strict adherence to Reynolds number equality between the model and prototype at many useful model scales would have demanded velocities so high that compressibility would be considered. In essence, Mach numbers exceeding 0.3, or velocities greater than 100m/s, would be required.

‘Concurrent studies into the effects of turbulence and how to measure them had been progressing from as early as Schubauer and Dryden (1935) and Taylor (1935) to more recent works by Van der Hoven (1957), Monin and Obukhov (1954), and Melbourne (1979)’. The turbulent spectrum (i.e. distribution of eddy sizes and energies) of the natural wind led to a growth of modelling in a wind-tunnel from static building studies to dynamic investigations. The description of the energy content of the wind via the turbulence spectrum by Davenport was a crucial concept that pushed Wind Engineering into the arena of dynamic studies. During the 1940s and 1950s dynamic wind-tunnel studies were generally limited to flexible, long-span bridge structures; particularly after the dramatic failure of the Tacoma Narrows Bridge. It is worth noting that this mechanism of torsional failure was not a new phenomenon [3.3] (see Table 3.1)’.

The transition from dynamic bridge to dynamic building studies was principally motivated by the decision to build the twin towers of the World Trade Centre in New York [3.5, 3.6].

The World Trade Centre was designed by the firm Skilling, Helle, Christiansen and Robertson and is one of the several landmark developments in the interdisciplinary areas of structural and wind engineering. For leading edge design such as: the World Trade Centre (417m, with over 10000 visco-elastic dampers per tower), the Sears Tower

(443m, designed by Fazlur Khan with a “bundled tube” concept), the Citicorp Centre (280m, designed by Le-Messurier and the first to use a tuned mass damper which, in this case, reduced horizontal acceleration by 38%) and the One Shell Plaza in Houston (218m, using the framed tube concept which was a precursor to the bundled tubes of the Sears Tower) ‘the structural engineer has to be somewhat of an architect and the architect somewhat of an engineer’[3.7]. Designs of a challenging height and/or form have resulted in a rapid evolution of the dynamic aspects of high-rise, wind tunnel testing.

‘Instrumental in the development of dynamic studies was the ability to observe the passing turbulence structure using hot-wire anemometry. The initial heat transfer analysis was performed by King, but the technique was seriously limited by practical electronic considerations for two more decades (Dryden and Kuethe, 1929). The work of Schubauer and Klebanoff showed that the high frequency response possible with more advanced electronics was of practical value [3.3]’. The technique evolved into two approaches: the constant current and the constant-temperature procedures. Both incorporate the use of a Wheatstone-Bridge [The Wheatstone-Bridge was invented by the mathematician Christie. Charles Wheatstone, Professor of Experimental Philosophy at King’s College, London in 1834 simply popularized its use]. In recent times the development of a constant-temperature, hot-wire anemometer has become the most common technique used. The instantaneous temperature of the hot wire is maintained at a constant value and thus the resistance remains constant too. The current required to maintain this constant temperature feedback provides a measure of the heat loss and hence the velocity of the fluid passing the wire. The inherent instability of the feedback system required to keep the wire resistance and temperature constant can now be controlled by modern electronics. Thus, the constant-temperature method is now widely accepted for air-flow studies. A brief discussion of hot-wire anemometry is given by Hinze [3.8], Bradshaw [3.9].

To date, an analytical solution to the Navier-Stokes equation is possible for only the simplest geometries. However, recourse to numerical procedures such as finite difference and finite element techniques allow more complex shapes to be tackled. Lin and Apelt [3.10] discuss a numerical solution of flow over a two dimensional solid fence. More sophisticated computer studies in Japan by Murakami [3.11, 3.12] have produced detailed flow patterns around isolated buildings and building components. To

date, numerical studies of flow around structures have been limited to low Reynolds numbers. In order to achieve a Reynolds number comparable to the full scales being modelled a very fine grid is required. As the Reynolds number (R_e) increases the turbulence structure becomes finer. Tennekes and Lumley [3.13] point out that the range of turbulence scales depends on $R_e^{-3/4}$ and so '*the separation in scales widens as the Reynolds number increases*'. This problem and, the issue of the turbulence model closure used, have both served to slow the use of Computational Fluid Dynamics (CFD) in architectural aerodynamics. Obviously significant computer and methodological developments are required before successful computer simulations of building flows in a complex city-escape is commonplace. Wind-tunnel and CFD research will continue to complement one another for some time to come.

A recent review by Tieleman and Baker [3.14, 3.15] in the field of wind engineering covers all aspects from origin to the present level development. H. W. Tieleman [3.14] in a review paper on wind-tunnel simulation of wind loading on low-rise structures has discussed the development of wind-tunnels over the time to the simulation by wind-tunnels of atmospheric flow characteristics near the surface under a variety of atmospheric and upwind terrain conditions. He discussed in detail the recommendations and requirements for the appropriate conduct of wind-tunnel experiments and justification for wind-tunnel simulation.

C. J. Baker [3.15] in his paper wind engineering – past, present and future discussed in detail the history of wind engineering by arbitrarily dividing the time period in five epochs as the 'traditional' period (up to 1750), the 'empirical' period (1750-1900), the 'establishment' period (1900-1960), the period of growth (1960-1980) and the modern period (1980 onwards). He considered the development of the wind engineering in terms of the socio-economic and intellectual contexts of the time. He describes the current state of the discipline and looks forward for the possible development taking into consideration the likely socio-economic and intellectual changes in the decades to come.

Table 3.1 Some key events in the development of wind engineering

1100s		**Development of flying buttress to resist wind loads on cathedrals**
1643	Torricelli	invents barometer
1687	Newton	discovers viscosity, laws of motion, calculus, Principia
1738	Bernoulli	defines conservation of energy applied to fluids, Hydrodynamica
1755	Euler	forms inviscid equations of fluid motion
1806	Beaufort	defines Beaufort scale of wind speed in terms of its visible effects
1836		**Collapse of the Brighton Chain Pier by oscillatory motion**
1845	Stokes	formulates the Navier-Stokes equations of fluid motion
1846	Robinson	invents cup anemometer
1879		**Collapse of the Tay Bridge in Scotland**
1883	Reynolds	develops a dimensionless parameter to investigate the onset of turbulence
1888	Dines	invents pressure tube anemometer
1904	Prandtl	develops boundary layer concept
1912	Von Karman	identifies vortex shedding in wakes
1914	King	gives equation for cooling hot-wires (hot cylinders)
1928	Fisher and Tippet	develop theory of extreme value
1934		**Highest measured gust at Mt. Washington (370 km/h)**
1935	Taylor	develop statistical theory of turbulence
1940	Rathbun	collected full-scale deflections data on the Empire State Building
1940		**Collapse of the Tacoma Narrow Bridge by oscillatory motion**
1954	Cermak	builds first large boundary-layer wind tunnel
1954	Jensen	formulates model scaling laws, Jensen number
1957		Van der Hoven compiles wide frequency range spectrum of the wind
1958	Cermak	describes Reynolds number independence for modelling atmospheric boundary layer
1961	Davenport	develops statistical concept to wind loadings, 1st International Conference on Wind Effects on Building
1963		**First international conference on wind effects on buildings**
1964	Cermak & Davenport	first major building study in a boundary-layer wind tunnel- World Trade Centre Twin Tower, New York
1965		**Collapse of three cooling towers at Ferrybridge**
1970		**Term 'Wind Engineering' coined**
1974	Eaton & Mayne	Aylesbury house study in Great Britain - full scale low-rise building
1976	Deaves & Harris	develop mathematical model for strong winds
1979	Melbourne	Shows importance of turbulence in bluff body aerodynamics
1984	Holmes	Define wind-tunnel pressure tubing response characteristics
1986		Amarube Tekkyo rail bridge disaster in Japan
1987	Mehta	Texas Tech University Experimental Building is built
1988	Robertson & Glass	Silsoe Structural Building is built.
1992	Murakami	1st Computational Wind Engineering Symposium, Tokyo
2003	Tieleman	Wind-tunnel simulation of wind loading on low-rise structures: a review
2007	Baker	Wind engineering – Past, present and future.

Sources: Cochran [3.3], Cermak [3.16], Cook [3.17],

3.3 Description of Atmospheric Flows

Wind, or the motion of the air with respect to the surface of the earth, is fundamentally caused by variable solar heating of the earth's atmosphere. It is initiated, in a more immediate sense, by differences of pressure between points of equal elevation. The energy required for the occurrence of these phenomena is provided by the sun in the

form of radiated heat. Whilst the sun is the original source**,** the source of energy most directly influential upon the atmosphere is the surface of the earth [3.1].

High wind speeds resulting from Extra tropical cyclones, Tornadoes, Hurricanes are associated with a neutral atmosphere (no thermal gradients). This is because the high turbulence present mixes the layers so that the thermal stratification cannot be maintained [3.1].

The need to provide mathematical representation of wind speeds is paramount so that calculations can be performed to demonstrate the suitability of a structure or its environment. The data must be sanitized.

The Earth's surface exerts on the moving air a horizontal drag force, whose effect is to retard the flow. This effect is diffused by turbulent mixing throughout a region referred to as the atmospheric boundary layer. The depth of the boundary layer normally ranges in the case of neutrally stratified flows from a few hundred metres to several kilometres, depending upon wind intensity, roughness of terrain, and the angle of latitude. Within the boundary layer, the wind speed increases with elevation; its magnitude at the top of the boundary layer is often referred to as the gradient speed. Outside the boundary layer, that is, in the free atmosphere, the wind flows approximately with gradient speed along the isobars [3.1].

Atmospheric flows can generally be separated into a mean flow and fluctuations about the mean. The fluctuations about the mean are interpreted as turbulence or gusts. Mean flow profiles in the atmospheric boundary layer (ABL) are described by either the log law or the power law. Turbulence in the ABL is normally described by its turbulence intensity, its integral scale and its spectral density.

The atmospheric boundary layer is further sub-divided into two regions: an inner layer called Atmospheric Surface Layer (ASL) and outer layer. The atmospheric boundary layer can also be further divided into a number of sub-layers as shown in Figure 3.1. The mean flow in the lower and upper region is described by the law of the wall and by the velocity defect law respectively.

Roughness Sub-layer **–** This layer extends from the surface to the average height of the roughness elements that may range from snow and grass to trees and buildings.

Inertial Sub-layer – This layer extends from the roughness layer to a height that is dependent on the degree of roughness of the surface retarding the flow. Both the roughness and inertial sub-layers are encompassed within the surface layer.

Ekman layer – Extends from the top of the surface layer to a height where the wind is unaffected by the Earth's surface. This height is commonly referred to as the gradient height.

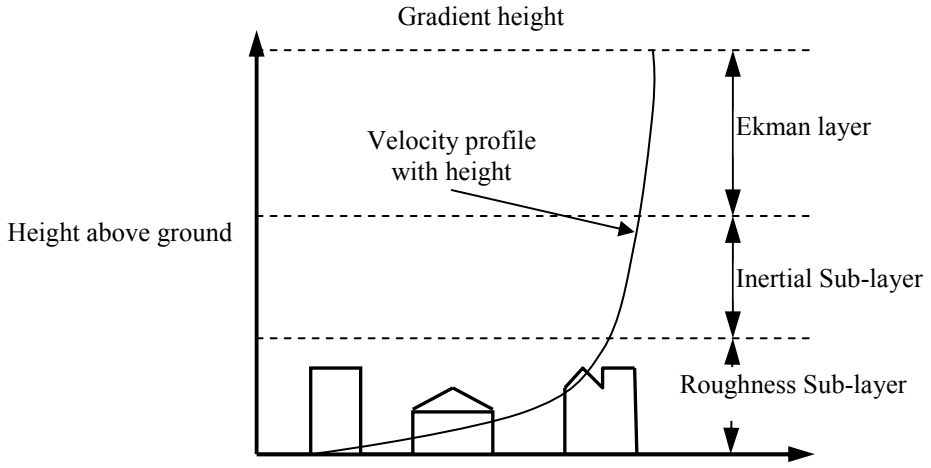

Figure 3.1 Mean velocity profile for the atmospheric flows

The region of the atmospheric boundary layer where the law of the wall is applicable is closest to the earth surface. The mean flow in this region can be described by a logarithmic law. For the neutral thermal stability, the log law states:

$$U(z) = \frac{u_*}{\kappa} \ln\left(\frac{z-d}{z_0}\right) \tag{3.1}$$

where κ is defined as Von Karman's constant, normally taken as 0.41; u_* is called shear velocity or friction velocity and is related to the ground roughness and therefore to the shear stress at the surface $\tau_0 = \rho u_*^2$; z is the height above the ground; and z_0 is the roughness length, which is measure of the eddy size at the ground; d is the displacement height; ρ is the density of air.

The log law is valid up to a height, z_1 of approximately

$$z_1 = b\frac{u_*}{f} \tag{3.2}$$

where b is a constant between 0.015 and 0.03 and f is the Coriolis parameter, which is defined as:

$$f = 2\Omega \sin \varphi \tag{3.3}$$

where Ω is the angular rate of rotation of earth and is equal to $72.9 \times 10^{6}\, rad / \sec$ or in other words the angular rotation of flow in the lowest part of the boundary layer.

The power law states that the mean flow at height z is

$$U(z) = U(z_{ref}) \left(\frac{z}{z_{ref}} \right)^{\alpha} \tag{3.4}$$

where $U(z)$ and $U(z_{ref})$ are the mean wind speeds at heights z and at reference height z_{ref} respectively; α is defined as the power law exponent.

In the outer regions of the boundary layer, the log law was found to be unrepresentative, the law of the wall was found to be more suitable. Work by Deaves and Harris [3.18] established the composite expression

$$U(z) = \left(\frac{u_*}{\kappa} \right) \left[\ln \left\{ \frac{(z-d)}{z_o} \right\} + 5.75 \left(\frac{z}{\delta} \right) \right] \tag{3.5}$$

where δ is the height of the boundary layer, or the gradient height of the atmospheric boundary layer, which varies with the ground roughness but is usually considered to be in between 500 -1000 m.

The power law exponent is a function of the terrain roughness and atmospheric stability. At the Silsoe Research Institute, UK, the average power law exponent was in the range 0.15-0.17 [3.19]. Simiu and Scanlan [3.1] provide appropriate values of α for other terrains as well.

Table 3.2 Values of α and δ recommended

Referred by	Open Terrain		Suburban Terrain		Centres of Large Cities	
	α	δ (m)	α	δ (m)	α	δ (m)
A.G. Davenport	0.16	275	0.28	400	0.4	520
J. Vellozi and E. Cohen	1/7	275	1/ 4.5	400	1/3	460

Turbulent flow in the region of the earth's surface i.e. the flow in boundary layer is influenced by the roughness of the earth's surface, thermal heating of the surface and atmosphere, etc. For the case where the winds are intense (i.e. where there is high wind speed) the contribution of convection to the atmospheric turbulence is small in comparison to the mechanically generated turbulence. This case is called a neutral stable condition. For the case of neutral stability, the turbulence generated by heating of the atmosphere can be ignored.

3.3.1 Probability Density

This property describes how the magnitudes of the fluctuating velocity components are distributed. A common assumption, which is reasonable in many applications, is that atmospheric turbulence is a 'normal' or Gaussian process with a probability density function for which

$$p_i = \frac{1}{\sigma_i (2\pi)^{1/2}} \exp\left[\left(\frac{-i^2}{2\sigma_i^2}\right)\right] \tag{3.6}$$

where $i = u, v$ or w. The integral

$$P_i = \int_{-\infty}^{i_p} p_i di \tag{3.7}$$

gives the proportion of all values which can be expected to have values below a particular value i_p.

'In practice, atmospheric turbulence contains '*patches*' of a significantly non-Gaussian nature (particularly in the lower 30 m) when larger gusts and longer lulls may occur more frequently than indicated by the Gaussian distribution' [3.20], as shown below in Figure 3.2.

For the calculation of wind loads on and the response of, buildings in strong winds it has been found to be generally satisfactory in most applications to assume that the probability distribution is Gaussian. In the calculation or simulation of aircraft response to atmospheric turbulence this is not necessarily so and there have been several attempts to develop non-Gaussian models that are applicable to the '*patches*' mentioned earlier. One method is to generate a non-Gaussian random process by the multiplication of two

Gaussian processes. An alternative is to represent wind fluctuations as a statistical aggregate of '*discrete gusts*'.

Figure 3.2 Probability density function

3.3.2 Turbulence

Atmospheric turbulence is typically described by its turbulence intensity, its integral scale and its spectra. Turbulence intensity is a measure of the magnitude of the fluctuating velocity component compared to the hourly-mean wind speed at the same height. It is a non-dimensional quantity derived from the variance $\left(\sigma_i^2\right)$ and for the *u*-component is

$$I_u = \frac{\sigma_u}{U(z)} \tag{3.8}$$

where I_u is the turbulence intensity at height z; σ_u is the standard deviation of the wind speed at height z and $U(z)$ is the mean wind speed in the *u*-direction at height z. In general, the turbulence intensity for the smooth terrain is less than the turbulence intensity for a rough terrain.

For the situation where the terrain is uniform upwind of the site for at least 30 km (i.e. the atmospheric boundary layer is in dynamic equilibrium with the underlying surface) the values of I_u according to ESDU 85020 [3.20] are given by the following equations.

$$I_u = \frac{\sigma_u}{u_*} \cdot \frac{u_*}{U_z} \tag{3.9}$$

where

$$\frac{\sigma_u}{u_*} = \frac{7.5\eta\left[0.538 + 0.09\ln\left(z/z_0\right)\right]^p}{1 + 0.156\ln\left(u_*/\left(f \times z_0\right)\right)} \tag{3.10}$$

$$\eta = 1 - \frac{6fz}{u_*} \quad ; \quad p = \eta^{16} \tag{3.11}$$

and

$$U_z/u_* = 2.5\left[\ln\left(z/z_0\right) + 34.5\left(f \cdot z/u_*\right)\right] \tag{3.12}$$

3.3.3 $v-$ and $w-$ components of turbulence intensity

Data from sources where both σ_u and σ_v, σ_u and σ_w have been measured simultaneously for neutral atmospheric conditions indicate that near the ground the ratios σ_v/σ_u and σ_w/σ_u are essentially constant irrespective of the nature of the terrain. Thus, values of I_v and I_w (I_{vx} and I_{wx}) can be obtained by evaluating I_u (or I_{ux} if roughness changes are to be considered) for the site in question and then multiplying this value by the ratio σ_v/σ_u or σ_w/σ_u. These are represented by [3.20] as:

$$\frac{\sigma_v}{\sigma_u} = 1 - 0.22\cos^4\left(\frac{\pi z}{2\delta}\right) \tag{3.13}$$

and

$$\frac{\sigma_w}{\sigma_u} = 1 - 0.45\cos^4\left(\frac{\pi z}{2\delta}\right) \tag{3.14}$$

where δ can be taken as $u_*/(6f)$

This procedure assumes that the effect of any upwind roughness changes on σ_v and σ_w can be accounted for, to a first approximation, through the effect on the *u*-component. At large heights above the ground, as $z \to \delta$, σ_v/σ_u and σ_w/σ_u both tend to unity.

3.3.4 Integral Length Scale

Integral scales of turbulence are a measure of the average size of the gusts carried in the mean flow. There are nine integral length scales of turbulence corresponding to the three spatial dimensions and they are used to give a single measure of the frequency

content of the atmospheric winds. The scales of turbulence represent the length, width, and height of the gust in each of the spatial three dimensions. Of interest to the structural engineer are the integral scales in the direction of the mean flow (longitudinal direction), L_u^x, L_u^y and L_u^z, which are the gust size in the along-wind direction, in the across-wind direction and in the vertical direction respectively. The longitudinal integral scale, L_u^x is evaluated using

$$L_u^x = U(z)\int_0^\infty R(\tau)d\tau \tag{3.15}$$

where $U(z)$ is the mean longitudinal wind speed at height z, $R(\tau)$ is the auto-correlation function for fluctuations in the longitudinal direction. The length of the record time from which $R(\tau)$ is estimated should be as the same as that used to estimate the mean wind speed [3.1, 3.21].

3.3.5 Spectral Density

The spectrum for the turbulence provides an indication of the amount of turbulent energy which is presented at a given frequency. The classical spectral density for the wind was presented by Van der Hoven [3.18]. He combined the measurements at Brookhaven, NY for many investigators to cover the range of frequencies for 5Hz to 1/(11 years). A spectral density of the form proposed by Kaimal, 1988 [3.22] is generally used for engineering purposes. Specifically the Blunt Model proposed by Tieleman, 1991 [3.23] can be used as a reference here [3.24]. The Blunt Model is presented as:

$$\frac{nS_u(n)}{u_*^2} = \frac{252.6f}{(1+60.62f)^{5/3}} \tag{3.16}$$

where $S_u(n)$ is the spectral density function at frequency n; u_* is the shear velocity; f is the reduced frequency which is equal to $nz/U(z)$; z is the height above ground. It is to be noted that the energy content at a given frequency is a function of elevation and shear velocity.

The spectra are often presented in a 'Normalised' form in which the spectral density function is divided by the variance. This has the advantage that the area under the curve

is unity. Similarly if $nS(n)/\sigma^2$ is graphed against $\log_e(n)$ the area under the curve is always 2.303.

3.3.6 Reynolds Stresses

Retarding forces exerted on the wind at the surface of the earth are transmitted upwards through the atmospheric boundary layer by shear forces, called Reynolds Stresses, and also by the exchange of momentum, due to the movement of air. In applications to wind loading on ground-based structures knowledge of Reynolds stresses is only required in special cases.

Reynolds stresses are obtained from the co-variances $\overline{uv}$, $\overline{vw}$ and $\overline{uw}$ and are zero for isotropic turbulence (for isotropic turbulence the statistical properties do not change when the reference co-ordinates are rotated i.e., the properties are independent of direction in the turbulence field). Near the ground surface friction distorts the symmetry of turbulence and non-isotropic conditions result. However, in practice, the co-variances $\overline{uv}$ and $\overline{vw}$ are small and can be ignored but this is not so for the $\overline{uw}$ co-variance.

The co-variance $\overline{uw}$ is defined by the shear stress,

$$\tau_z = -\rho\overline{uw} = \rho u_*^2\left(1-\frac{z}{\delta}\right)^2 \tag{3.17}$$

Thus for heights up to about 300m

$$\frac{-\overline{uw}}{\sigma_u\sigma_w} \approx \frac{u_*^2\left(1-2\frac{z}{\delta}\right)}{\sigma_u\left(\frac{\sigma_w}{\sigma_u}\right)\sigma_u} = \frac{\left(1-2\frac{z}{\delta}\right)}{\left(\frac{\sigma_u}{u_*}\right)^2\left(\frac{\sigma_w}{\sigma_u}\right)} \tag{3.18}$$

where, for an equilibrium boundary layer, σ_u/u_* is given by the above equation and $\sigma_w/\sigma_u \approx 0.55$. Reported values of $-\overline{uw}(\sigma_u/\sigma_w)$ in the literature tend to be slightly higher than the values given by above. The probable reason is the response characteristics of typical anemometers used to measure the vertical component of wind speed [3.20].

3.4 Bluff Body Aerodynamics

A vast majority of buildings and structures are within the lowest part of the atmospheric boundary layer (ABL) where wind flow is highly turbulent. Instantaneous wind speed and its directions vary with time and are unpredictable by any deterministic function. When an incident wind impinges a building, wind flow cannot negotiate the edges of roofs, eaves, and walls smoothly, thus it separates sharply from these edges. This interaction between the building and the approaching flow brings additional turbulence to the flow near the building surfaces. Wind induced turbulence is generally random. Wind pressures at any specific location of a building are influenced by many factors, e.g. wind speed, wind direction, surroundings, overall building shape and architect features. Resulting flows around buildings are complicated enough that no closed-form solutions currently exist. Wind tunnel tests have been used extensively in investigating the aerodynamic phenomena around three dimensional obstacles with sharp edges. A conceptual model of the flow pattern near a cubic building in an atmospheric boundary layer has been developed by Woo et al, as shown in Figure 3.3.

The term, windward wall, is used to define the surface on a building that faces an approaching wind. The windward wall is the surface of a building that experiences inward acting or positive pressure. It is conventional to designate inward acting pressure as positive and outward acting pressure (suction) as negative. Illustrated by Figure 3.4 is the flow structure in front of a building immersed in an atmospheric boundary layer flow and pressure distribution on the windward wall. The stagnation point is formed at about two-thirds of the total building height. The flow above this stagnation point goes up and separates along the upper edge of the building surface. The flow below the stagnation point goes downward until it hits the ground and rolls up into a vortex in front of the windward wall. This vortex is termed a horseshoe vortex. It has been found that the existence of this vortex has a significant effect on the distribution of wind pressure on the wind-ward surface [3.25].

The two side walls are under the action of negative pressures or suctions due to the flow separation along the edge of the windward surfaces. The flow pattern on side walls caused by an atmospheric boundary layer is illustrated in Figure 3.5 a. The flow above two-thirds of the building height is denoted as Flow A. Flow B is designated for the flow below the Flow A. Flow B moves faster than the incident wind at the corresponding height because of the horseshoe vortices formed in front of the windward

surface. For an elongated building, the separated streamlines reattach to the building surfaces in the manner shown in Figure 3.5 b. This is named as reattachment. The zone covering the leading edge of the building to the reattachment point is usually defined as the separation bubble. In reattachment regions, wind pressures recover their low values (more negative in magnitude) in separation bubbles. Buildings encounter less suction in reattachment regions than in separations bubbles.

Figure 3.3 A conceptual model for the flow pattern (Woo et al., 1977)

Figure 3.4 Flow structure in the windward wall (after Cook, 1990)

(a) (after Cook,1985)

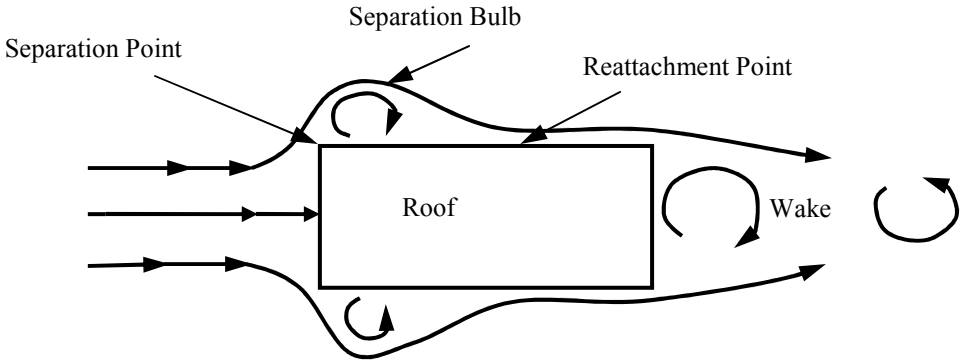

(b) Separation on the sides of the elongated building

Figure 3.5a, b Flow pattern on the sides of the walls

The roof pressure under wind effects has been discussed for the cases where the incident flow is normal to the building and where it is skewed at an angle. A separation bubble is formed along the upstream edge of the roof with a normal approaching flow. The streamline pattern is demonstrated graphically in Figure 3.6 for building in ABL flow. Only the flow above the stagnation point goes up and separates along the roof edge and is reattached to the roof. The joint effect of the wind profile, vortex in the shear layer along the separation boundary, and the Reynolds number of the ABL, is to lower the separated streamlines and lead to an earlier reattachment of the separated flow to the building roof [3.26]. Higher suctions are encountered along the leading edge of the roof than the rest of the roof. The suction decreases in magnitude downstream in a pattern similar to that on the side walls.

Figure 3.6 Flow separation and reattachment on the roof (after Cook, 1985)
(SP = Separation point, RP = Reattachment point)

Strong conical vortices are produced at the roof corner when the incident flow is skewed from the direction normal to the windward wall. These are usually termed delta wing vortices, from aerospace and aircraft engineering. The general pattern of the delta wing demonstrates strong three dimensionalities. The delta wing vortices contain primary and secondary vortices that roll up to form a pair of trailing vortices, as shown in Figure 3.7 a. Bienkiewicz and Sun (1992) verified this observation with the aid of both flow visualization and pressure measurements under delta-wing vortices. Along the axis of the primary vortex, denoted as AP in Figure 3.7 b, highly negative pressures are developed under the delta-wing vortices near the corner as a result of centrifugal force acting on the rotating fluid. Mean pressures under delta-wing vortices decrease rapidly in magnitude as the distance from the corner of the roof increases. Fluctuating pressures below the vortex centre are judged to be independent of the turbulent intensity level in the incident flow [3.27].

(a) (Cook, 1985)

(b) (The Japanese Society of Mechanical Engineering)

Figure 3.7 Delta wing vortex and its three dimensionalities

The flow trailing the building is termed the wake. The flow pattern in the wake immediately after the leeward side is illustrated in Figure 3.8. A pair of vertical vortices is induced by the horseshoe vortex through the shear layers on the side walls of a building. A relatively uniform pressure distribution has been observed in the region close to the vertical sides of the leeward face [3.23]. The flow marked as B is driven by the shear layer over the roof. The flow in the wake is also found to be highly turbulent.

Figure 3.8 Flow structure in the wake of a building (after Cook, 1990)

3.5 Conclusions

'Over the last two decades Wind Engineering has increasingly focussed on modest low-rise structures, since much of the damage and financial loss associated with extreme wind events happens to minimally engineered buildings. As some of the model- and full-scale wind engineering data filters into design codes and standards one may expect to see reduced hurricane/cyclone damage. However, when one combines the more rapid increase in population along the world's tropical coasts with a generally unacceptably low standard of new building construction inspection, it seems quite likely that loss of life, as well as insured and uninsured property losses will continue to be the norm in the foreseeable future. The wind engineering community needs to be more responsible in forcefully transferring its technical knowledge to the designer and builder. A booklet with the aim of explaining, in simple terms, the wind effects on structures to the architect, builder and inspector should be produced. This sort of direct information, along with passionate political lobbying, is needed to mitigate the unacceptable loss of life and financial loss caused by extreme wind events [3.3]'.

CHAPTER 4
Computational Fluid Dynamics and Turbulence Modelling

4.1 Introduction

> *'Computational Fluid Dynamics (CFD) is the analysis of systems involving fluid flow, heat transfer and associated phenomenon such as chemical reactions by means of computer-based simulations'* [4.1].

The technique is very powerful and spans a wide range of industries and academic institutions. The ultimate aim of developments in the CFD field is to provide a capability comparable with other computer-aided engineering tools such as stress analysis codes. The main reason why CFD has lagged behind is the tremendous complexity of the underlying behaviour, which precludes a description of fluid flows that is at the same time economical and sufficiently complete. The availability of affordable high-performance computing hard-ware and the introduction of user-friendly interfaces have led to a recent upsurge of interest and CFD has entered into the wider industrial community since the 1990s.

Because of the complexity of the atmospheric wind and of little understood phenomenon, every year we encounter wind induced failure of structures, and the ensuing financial and human costs. Scientists and engineers have for many years studied the results of full scale and wind tunnel tests of models, and developed an understanding of how the wind in the atmospheric boundary layer (ABL) interacts with complex ground based structures which has led our knowledge of wind engineering to its present level. Much is known about the interaction of wind and structures, but there is obviously still much more to learn to accurately assess the effects of atmospheric wind on ground based structures.

The application of CFD to wind engineering started approximately 25 years ago; the overall progress in computational wind engineering (CWE) is slower. It seems apparent that the traditional methods will dominate for many years to come. 'This is mainly due to: (i) large Reynolds number, (ii) impinging at the front, (iii) sharp edges of the bluff bodies, (iv) remaining effect of flow obstacle at outflow boundary, (v) computing power, (vi) poor understanding of the phenomena known as turbulence, etc.' [4.2]. These problems associated with the numerical solution of fluid flow are unfortunately

further highlighted when this technique is applied to wind engineering flows due to the highly turbulent nature of the ABL, the non-aerodynamic bluff bodies and the need for a large computational domain for external flow fields.

4.2 The Beginning of Computational Wind Engineering

The very first use of CFD in wind engineering occurred in the mid to late 1980s by Summers et al [4.3], Mathews [4.4] and Murakami & Mochida [4.5] with the application of the standard $k-\varepsilon$ model to flows around building shapes. Early attempts were undertaken by Murakami et al in the late 1980s to apply Large Eddy Simulation (LES) to wind engineering problems [4.6]. These tests were in fact the first to fully analyse the results of a simulation that involve flow impingement and thus showed the fundamental flaws in the standard $k-\varepsilon$ model based on the isotropic eddy viscosity model. This early discovery initiated one of the most attractive research targets since the start of CFD that of improved turbulence modelling. The main areas of interest included the following [4.7]:

1. The improvement of the standard $k-\varepsilon$ model and the introduction of a more sophisticated Reynolds Averaged Navier Stokes (RANS) models.
2. The development of easier methods for applying Large Eddy Simulation to Computational Wind Engineering problems

The results of this intense research effort to improve the application of CFD to wind engineering, or to engineering applications in general, have included a number of new turbulence models. These range from ad-hoc modifications to the $k-\varepsilon$ model to more advance RANS models such as the Reynolds Stress Model (RSM). In addition Large Eddy Simulation technique has allowed for significant improvements in the predictive accuracy of CFD when applied to wind-engineering. Invaluable work over the past 25 years by researchers and academics such as Leschziner, Speziale, Launder, Rodi, and Murakami [4.1] from different engineering disciplines, have significantly contributed in improving the accuracy and applicability of CFD techniques.

Unfortunately, although CWE has progressed a long way from the early days of the 1980s, there is still a long way to go before the same confidence can be placed on CWE as with finite element analysis in structural engineering. There are still many problems in CWE, including errors in wall boundary conditions and near wall functions, and

although much has been achieved, the biggest problem is still that of turbulence modelling in the highly turbulent and complex flow fields encountered.

Nevertheless, even at the current stage of development, the theoretical advantages of 'virtual' computer based 'model scale' tests such as the ones undertaken in this project are significant. So much so that according to Murakami and Mochida [4.7], CWE has evolved into a powerful tool for analysing wind engineering flow fields.

Generally the benefits brought about by the use of CFD in other engineering disciplines have proved a strong incentive to improve the performance of CFD in wind engineering. The eventual aim of all CFD wind engineering researchers is to able to exactly match a computational solution to the real situation. While it is unclear at this time whether or not this goal will ever be achieved, it is apparent that continued research is required to, at the very least, attain success in CWE comparable to that found in, say, aeronautical engineering where CFD is routinely used. As such the author is of the opinion that the work detailed in the following chapters is very useful to the wind engineering community in attempting to offer possible improvements to the problem of turbulence modelling and therefore advancing the use of CFD in wind engineering.

4.3 Governing Equations of Fluid Flow

The numerical solution of any fluid flow problem requires the solution of the general equations of fluid motion, i.e. the Navier-Stokes and continuity equations. Fluid flow problems are described mathematically which are a set of coupled non-linear partial differential equations with appropriate boundary conditions. These equations are derived from Newton's Second Law and describe the conservation of momentum in the flow.

4.3.1 The Navier-Stokes Equations

'The Navier-Stokes equations, named after Claude-Louis Navier and George Gabriel Stokes, describe the motion of fluid substances such as liquids and gases. These equations establish that changes in momentum in infinitesimal volumes of fluid are simply the sum of dissipative viscous forces (similar to friction), changes in pressure, gravity, and other forces acting inside the fluid' [4.8].

The general form of three dimensional incompressible instantaneous Navier-Stokes equations is as follows, in Cartesian tensor form (details of the derivation of these equations are referred to Young [4.9]):

$$\underbrace{\frac{\partial(\rho u_i)}{\partial t}}_{\text{acceleration term}} = \underbrace{-\frac{\partial(\rho u_i u_j)}{\partial x_j}}_{\text{convection term}} \underbrace{-\frac{\partial P}{\partial x_j}}_{\text{pressure gradient}} + \underbrace{\frac{\partial}{\partial x_j}\left[\mu\left(\frac{\partial u_i}{\partial x_j}+\frac{\partial u_j}{\partial x_i}\right)\right]}_{\text{effects of viscosity}} + \underbrace{F}_{\text{body force}} \tag{4.1}$$

and the continuity equation:

$$\frac{\partial \rho}{\partial t} + \frac{\partial \rho u_i}{\partial x_i} = 0 \tag{4.2}$$

'They are one of the most useful sets of equations because they describe the physics of a large number of phenomena of academic and economic interest. They may be used to model weather, ocean currents, water flow in a pipe, flow around an airfoil (wing), and the motion of stars inside a galaxy. As such, these equations in both full and simplified forms are used in the design of aircraft and cars, the study of blood flow, the design of power stations, the analysis of the effects of pollution, etc. Coupled with Maxwell's equations, they can be used to model and study magneto-hydrodynamics' [4.9].

'The Navier-Stokes equations are also of great interest in a purely mathematical sense. Somewhat surprisingly, given their wide range of practical uses, mathematicians have yet to prove that in three dimensions solutions always exist (existence), or that if they do exist they do not contain any infinities, singularities or discontinuities (smoothness). These are called the Navier-Stokes existence and smoothness problems' [4.10].

'Contrary to what is normally seen in solid mechanics, the Navier-Stokes equations dictate not position but rather velocity. A solution of the Navier-Stokes equations is called a velocity field or flow field, which is a description of the velocity of the fluid at a given point in space and time. Once the velocity field is solved for, other quantities of interest (such as flow rate, drag force, or the path a 'particle' of fluid will take) may be found' [4.10].

All flows encountered in engineering practice become unstable above a certain Reynolds number (which gives a measure of the relative importance of inertia forces and viscous forces). At low Reynolds numbers, flows are ***laminar,*** i.e. flows are smooth

and adjacent layers of fluid slide past each other in an orderly fashion. If the applied boundary conditions do not change with time the flow is steady. At values of the Reynolds numbers above critical, a complicated series of events takes place which eventually leads to radical change of the flow character. 'A chaotic and random state of motion develops in which the velocity and pressure change continuously with time within substantial regions of flow' [4.1]. The motion becomes intrinsically unsteady even with constant imposed boundary conditions. This regime of flow is called ***turbulent***.

The simple cases of flow in a laminar regime can be solved analytically by using the continuity and Navier-Stokes equations [4.11]. Most of the flows of engineering significance are turbulent. Fluid engineers need access to viable tools capable of representing the effects of turbulence.

The random nature of a turbulent flow precludes an economical description of the motion of all fluid particles as shown in Figure 4.1. The velocity is decomposed into a steady mean value $\overline{u}_i$ with a fluctuating component $u_t^{'}(t)$ superimposed on it:

$$u_i(t) = \overline{u}_i + u_i^{'}(t) \tag{4.3}$$

where *i* denotes the *x, y* and *z* direction. This is called ***Reynolds decomposition***.

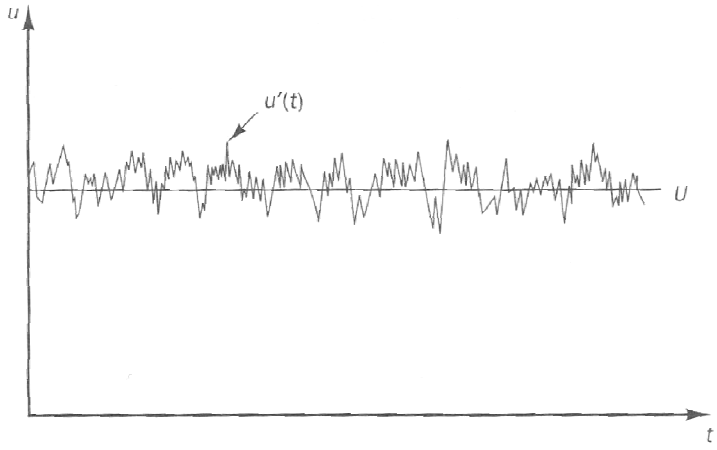

Figure 4.1 Typical point velocity measurements in turbulent flow [4.1]

'Even in flows where the mean velocities and pressures vary in only one or two space dimensions, turbulent fluctuations always have a three dimensional spatial character' [4.1]. Visualisations of turbulent flows reveal rotational flow structures as shown in Figure 4.2, so-called turbulent eddies, with a wide range of length scales. Particles of

fluid which are initially separated by a long distance can be brought close together by the eddying motions in turbulent flows. As a consequence, heat, mass and momentum are effectively exchanged. For example, a streak of dye which is introduced at a point in a turbulent flow will rapidly break up and be dispersed right across the flow. Such effective mixing gives rise to high values of diffusion coefficients for mass, momentum and heat.

Figure 4.2 Turbulent eddies; small and large eddies [4.12]

'The largest turbulent eddies interact with and extract energy from the mean flow by a process called **vortex stretching**. The presence of mean velocity gradients in sheared flows distorts the rotational turbulent eddies' [4.1]. Suitably aligned eddies are stretched because one end is forced to move faster than the other.

The characteristic velocity ϑ and characteristic length ℓ of the larger eddies are of the same order as the velocity scale U (or $\overline{u}_i$) and the length scale L of the mean flow. Hence a 'large eddy' Reynolds number $\mathrm{Re}_\ell = \dfrac{\vartheta \ell}{\nu}$ formed by combining these eddy scales with the kinematic viscosity will be large in all turbulent flows, since it is not very different in magnitude from UL/ν which itself is large [4.1]. This suggest that these large eddies are dominated by inertia effects and viscous effects are negligible.

The large eddies are therefore effectively inviscid, and angular momentum is conserved during vortex stretching. This causes the rotation rate to increase and the radius of their cross-sections to decrease. Thus the process creates motions at smaller transverse length scales and also at smaller time scales. 'The stretching work done by the mean flow on the large eddies during these events provides the energy which maintains the turbulence'. 'Smaller eddies are themselves stretched strongly by somewhat larger eddies and more weakly by the mean flow. In this way the kinetic energy is handed down from large eddies to progressively smaller and smaller eddies, what is termed the **energy cascade'** [4.1].

Large eddies are most energetic where as the smallest eddies have the lowest energy content. The smallest scales of motion in a turbulent flow (lengths of the order of 0.1 to 0.01 mm and frequencies around 10 kHz in typical engineering flows) are dominated by viscous effects. The Reynolds number of the smallest eddies based on the characteristic velocity and characteristic length is equal to one, so the smallest scale present in a turbulent flow are those for which the inertia and viscous effects are of equal strength. These scales are named the ***Kolmogorov microscales*** after the Russian Scientist who carried groundbreaking work on the structure of turbulence in 1940s. At these scales work is performed against the action of the viscous stresses, so that the energy associated with the small scale eddy motions is dissipated and converted into thermal internal energy. This dissipation results in ***increased energy losses*** associated with turbulent flows [4.1].

The Kolmogorov microscales can be expressed in terms of the rate of energy dissipation of a turbulent flow and the fluid viscosity, which uses the notion that in every turbulent flow the rate of production of turbulent energy has to be broadly in balance with its rate of dissipation to prevent unlimited growth of turbulence energy. This yields the following order of magnitude estimates of the ratios of small length, time and velocity scales η, τ, υ and large length, time and velocity scales ℓ, T, ϑ [4.13].

$$\begin{aligned} &\text{Length-scale ratio} && \frac{\eta}{\ell} \approx \mathrm{Re}_{\ell}^{-3/4} \\ &\text{Time-scale ratio} && \frac{\tau}{T} \approx \mathrm{Re}_{\ell}^{-1/2} \\ &\text{Velocity-scale ratio} && \frac{\upsilon}{\vartheta} \approx \mathrm{Re}_{\ell}^{-1/4} \end{aligned} \tag{4.4}$$

Typical values of Re_ℓ might be 10^3-10^6, so the length, time and velocity scales associated with small dissipating eddies are much smaller than those of large, energetic eddies, and the difference – the so-called scale-separation – increases as Re_ℓ increases.

The most accurate way to model fluid flow numerically is direct numerical simulation [4.14] which involves discretising the equations at a mesh size below the Kolmogorov length scales and applying Equation 4.1 along with suitable wall boundary conditions to the whole flow field. Unfortunately for practical wind engineering flows this is well beyond the capabilities of present day computers. Therefore to reduce the amount of computational effort the effect of turbulence has to be modelled. The starting point in this modelling process is to make the assumption 'that the velocity at a given point in space and time can be made up of the superposition of some mean velocity which varies slowly with time and a random component that varies rapidly' [4.15]. Therefore the instantaneous velocity component $u'(t)$ can be described by Equation 4.3. To incorporate the effect of turbulence on mean flow, Equation 4.3 is substituted into Equations 4.1 and 4.2 and integrated over time to obtain the mean flow equations. As the fluctuating components are random and do not show any preferential direction the integrals over time will be zero for the linear terms in the momentum equations. The convective terms in the momentum equations are in fact non-linear being the product of velocity and derivatives of the velocity component. As such the convective terms generate extra higher order terms for the products of fluctuating components. These terms are referred to as the ***Reynolds Stresses***.

4.4 The Reynolds Stresses

Proceeding with the averaging process results in the instantaneous values being replaced with the mean variables except for the case of the convenient transport term. Referring to the convection term, (in Equation 4.1) the substitution of the fluctuating component of velocity results in [4.16]:

$$\begin{aligned}\overline{u_j u_i} &= \overline{\left(\overline{u}_j + u_j'\right)\left(\overline{u}_i + u_i'\right)} \\ &= \overline{\overline{u}_j \overline{u}_i} + \overline{\overline{u}_j u_i'} + \overline{u_j' \overline{u}_i} + \overline{u_j' u_i'} \\ &= \overline{\overline{u}_j \overline{u}_i} + \overline{u_j' u_i'}\end{aligned} \tag{4.5}$$

where the over-bar indicates mean values per unit time.

Thus, the time averaged equation of fluid motion becomes [4.13]:

$$\frac{\partial(\rho\overline{u}_i)}{\partial t} = -\frac{\partial\left(\rho\overline{u}_j\overline{u}_i\right)}{\partial x_j} - \frac{\partial\overline{P}}{\partial x_i} + \frac{\partial}{\partial x_j}\left[\mu\left(\frac{\partial\overline{u}_i}{\partial x_j} + \frac{\partial\overline{u}_j}{\partial x_i}\right) - \rho\overline{u_i'u_j'}\right] + F_i \qquad (4.6)$$

Equation 4.6 is generally referred to as the Reynolds equation and differs from the equation describing a laminar flow only by the presence of the term containing averaged products of fluctuating velocity. The process it represents is the additional transfer of momentum due to turbulent fluctuations. The first term in the brackets is the viscous term and the second term $\rho\overline{u_i'u_j'}$ is the turbulent stress or the ***Reynolds stress tensor***.

$$\overline{u_i'u_j'} = \begin{bmatrix} \overline{u'u'} & \overline{u'v'} & \overline{u'w'} \\ \overline{v'u'} & \overline{v'v'} & \overline{v'w'} \\ \overline{w'u'} & \overline{w'v'} & \overline{w'w'} \end{bmatrix} \qquad (4.7)$$

where

$$\left.\begin{aligned} \tau_{xx} &= -\rho\overline{u'^2} \\ \tau_{yy} &= -\rho\overline{v'^2} \\ \tau_{zz} &= -\rho\overline{w'^2} \end{aligned}\right\}$$ - Three normal stresses

$$\left.\begin{aligned} \tau_{xy} = \tau_{yx} &= -\rho\overline{u'v'} \\ \tau_{yz} = \tau_{zy} &= -\rho\overline{v'w'} \\ \tau_{zx} = \tau_{xz} &= -\rho\overline{v'w'} \end{aligned}\right\}$$ – Three shear stresses (3 symmetrical pairs)

In turbulent flows the normal stresses are always non-zero because they contain squared velocity fluctuations. The shear stresses are associated with correlations between different velocity components.

It is therefore the main aim of the turbulence model to predict the effect of these Reynolds stresses on the mean flow. Consequently the next step in the turbulence modelling process is the formulation and application of a suitable model that can accurately represent these stresses over a range of flow fields.

4.5 Turbulence Modelling

Turbulence causes the appearance in the flow of eddies with a wide range of length and time scales that interact in a dynamically complex way. Given the importance of the avoidance or promotion of turbulence in engineering applications, it is no surprise that a substantial amount of research effort is dedicated to the development of numerical methods to capture the important effects due to turbulence. The methods can be grouped into the following three categories.

(i) Turbulence models for Reynolds averaged Navier-Stokes (RANS) equations
(ii) Large Eddy simulation (LES)
(iii) Direct Numerical Simulation (DNS)

Fluent 6.3, 2006 [4.17] provides the following turbulent models. Only a few have been discussed here, which have been used for simulation purposes.

1. RANS (Reynolds Average Navier-Stokes) Models
   - Spalart-Allmars model
   - k - ε models
     - Standard k - ε models
     - Renormalization-group (RNG) k - ε model
     - Realizable k - ε model
   - k - ω models
     - Standard k - ω model
     - Shear-stress transport (SST) k - ω model
   - $v^2 - f$ model
   - Reynolds Stress Model (RSM)
2. Detached Eddy Simulation (DES) Model
3. Large Eddy Simulation (LES) Model

4.5.1 Turbulence Models for Reynolds Averaged Navier-Stokes (RANS) Equations

Attention is focussed on the mean flow and the effects of turbulence on mean flow properties. Prior to the application of numerical methods the Navier-Stokes equations are time averaged (or ensemble averaged in flows with time-dependent boundary conditions). In general it can be said that these models calculate a mean, steady state

velocity and pressure field and account for the velocity and pressure fluctuations through additional modelled variables. These equations describe the movement of large scale eddies, thus allowing the use of coarse grids and making the models relatively economical to use. Extra terms appear in the time-averaged (or Reynolds-averaged) flow equations due to the interactions between various turbulent fluctuations. These extra terms are modelled with classical turbulence models; among the best known ones are the $k-\varepsilon$ model and the Reynolds stress model. The computing resources required for reasonably accurate flow computations are modest, so this approach has been the mainstay of engineering flow calculations over the last three decades. A number of models are available under this general heading which range from closure models based on the eddy viscosity concept to full second moment closure models which represent the effect of each component of the Reynolds stress tensor on the mean flow.

4.5.1.1 The Eddy Viscosity Concept

Newton's law of viscosity states that the viscous stresses are proportional to the rate of deformation of fluid elements, while, Boussinesq (1877) postulated that the Reynolds stresses might be proportional to the mean rates of deformation [4.1]. This is perhaps the most important research attributed to the earliest work in the field of turbulence modelling. This concept is based on the assumption that both the viscous stresses and the Reynolds stresses act on the mean flow in similar manner. Referring to the Equation 4.8 (shown below) it can be seen that these stresses appear on the right hand side of the momentum equation.

$$\frac{\partial\left(\rho\overline{u}_i\right)}{\partial t}=-\frac{\partial\left(\rho\overline{u}_j\overline{u}_i\right)}{\partial x_j}-\frac{\partial\overline{P}}{\partial x_i}+\frac{\partial}{\partial x_j}\left[\mu\left(\frac{\partial\overline{u}_i}{\partial x_j}+\frac{\partial\overline{u}_j}{\partial x_i}\right)-\rho\overline{u_i'u_j'}\right]+F_i \qquad (4.8)$$

For an incompressible fluid this relationship can be expressed in mathematical terms as:

$$\tau_{ij}=\mu S_{ij}=\mu\left(\frac{\partial u_i}{\partial x_j}+\frac{\partial u_j}{\partial x_i}\right) \qquad (4.9)$$

'It is experimentally observed that turbulence decays unless there is a shear in isothermal incompressible flows. Furthermore turbulent stresses are found to increase as the mean rate of deformation increases' [4.1]. Therefore, these statements led

Boussinesq to propose a linear relationship between Reynolds stresses and the rate of deformation of a fluid linked by a coefficient of proportionality μ_t as follows:

$$\tau_{ij} = -\rho\overline{u_i' u_j'} = \mu_t\left(\frac{\partial \overline{u}_i}{\partial x_j} + \frac{\partial \overline{u}_j}{\partial x_i}\right) \tag{4.10}$$

Bousssinesq's reasoning seems to be logical when one considers that the energy dissipation and transport of mass and momentum normal to the flow in laminar flows are all mediated by viscosity [4.1]. As the effect of turbulence is to greatly increase this process it seems a natural assumption to conclude that an extra viscosity can adequately represent the effect of turbulence [4.1].

The right hand side of Equations 4.9 and 4.10 are the same except for the coefficient linking the two sides of the equations. μ is a function of the fluid properties only while μ_t is a function of the turbulence. When Equation 4.10 is substituted into Equation 4.1 then the mean flow equation now has an enhanced additional viscosity μ_t due to the turbulence of the flow. Using this approach the modelling process can be completed if the turbulent viscosity can be from other variables (a full derivation of eddy viscosity can be found in the book by Gatski et al, 1996 [4.18]).

4.5.1.2 The Mixing Length Model

In the mixing length model, turbulence (turbulence viscosity) at a given point and time in the flow field can be characterised as a product of velocity scale ϑ and a turbulent length scale ℓ. Hence the turbulent viscosity is expressed in terms of these two scales as a function of position as follows [4.19]:

$$\mu_t = \rho C_\mu \ell^2 \left(\frac{\partial \overline{u}}{\partial y} + \frac{\partial \overline{v}}{\partial x}\right) \tag{4.11}$$

'Most of the kinetic energy of turbulence is contained in the largest eddies, and the turbulence length scale ℓ is therefore characteristic of these eddies which interact with the mean flow' [4.20]. If we accept that there is a strong connection between the mean flow and the behaviour of the largest eddies we can attempt to link the characteristic velocity scale of eddies with the mean flow properties. This has been found to work well in simple two-dimensional turbulent flows where the only significant Reynolds

stress is $\tau_{xy} = \tau_{yx} = -\rho\overline{u'v'}$ and the only significant mean velocity gradient is $\frac{\partial \overline{u}}{\partial y}$ (or $\frac{\partial U}{\partial y}$) [4.1]. These properties are very important for wind engineering flow fields, which include recirculatory flows. Consequently more complex statements are required involving fluid transport equations which may express these effects in terms of the dynamics of turbulence.

Advantages of the mixing length model:

- It is easy to implant and cheap in terms of computing resources.
- It gives a good prediction for thin shear layers: jets, mixing layers, wakes and boundary layers.
- It is well established.

Disadvantages of the mixing length model:

- It is completely incapable of describing flows with separation and recirculation
- It only calculates mean flow properties and turbulent shear stress

4.5.1.3 Spalart-Allmaras Model

The Spalart-Allmaras Model is a relatively simple one-equation model that solves a modelled transport equation for the kinematic eddy (turbulent) viscosity $\tilde{\nu}$ and a specification of a length scale by means of an algebraic formula, and provides economical computations of boundary layers in external aerodynamics [4.1]. 'This model is designed specifically for aerospace applications involving wall-bounded flows and has been shown to give good results for boundary layers subjected to adverse pressure gradients. However, this model is relatively new, and no claim is made regarding its suitability to all types of complex engineering flows. For instance, it cannot be relied on to predict the decay of homogeneous, isotropic turbulence [4.17]'.

4.5.1.4 The Standard $k-\varepsilon$ model

The standard $k-\varepsilon$ model has 'two model equations based on model transport equations for the turbulent kinetic energy k and its dissipation rate ε. In the derivation of the $k-\varepsilon$ model it is assumed that the flow is fully turbulent and the effects of molecular

viscosity are negligible. The standard $k-\varepsilon$ model is therefore valid only for turbulent flows' [4.17].

These values are used to define the velocity scale and the length scale at a given point and time in the flow field, representative of large scale turbulence as follows:

$$\text{Velocity scale} \quad \vartheta = k^{1/2} \tag{4.12}$$

$$\text{Length scale} \quad \ell = \frac{k^{3/2}}{\varepsilon} \tag{4.13}$$

Where k = Turbulent kinetic energy
ε = Rate of dissipation of turbulent kinetic energy

Applying dimensional analysis, the eddy viscosity can be specified as follows:

$$\mu_t = C_\mu \ell \vartheta = \rho C_\mu \frac{k^2}{\varepsilon} \tag{4.14}$$

where C_μ is a dimensionless constant.

Inserting the Boussinesq hypothesis into the momentum equation yields:

$$\frac{\partial \rho \overline{u}_i}{\partial t} = -\frac{\partial \rho \overline{u_j u_i}}{\partial x_j} - \frac{\partial \overline{P}}{\partial x_i} + \frac{\partial}{\partial x_j}\left[\mu_{eff}\left(\frac{\partial \overline{u}_j}{\partial x_j} + \frac{\partial \overline{u}_j}{\partial x_i}\right)\right] \tag{4.15}$$

where,

$$\mu_{eff} = \mu + \mu_t \tag{4.16}$$

The standard $k-\varepsilon$ model equation is obtained by multiplication of the instantaneous Navier-Stokes equations by the appropriate fluctuating velocity components (i.e. x – component equation is multiplied by u' etc.) and by the addition of all the results. This is followed by a repeat of this process on the time averaged Reynolds equations, subtracting of the two resulting equations and substantial re-arrangement yielding the equation for the turbulent kinetic energy k [4.20]. It is also possible to develop similar transport equations, from the Navier-Stokes equations, for other turbulence quantities including the rate of viscous dissipation ε. Nonetheless it should be noted that the energy dissipation equation is far more empirical and the modelling of terms is so severe that it is best to regard the entire equation as a model.

The standard $k-\varepsilon$ model uses the following transport equations for k and ε:

$$\rho\frac{\partial k}{\partial t}+\rho\overline{u}_j\frac{\partial k}{\partial x_j}=\tau_{ij}\frac{\partial \overline{u}_i}{\partial x_j}-\rho\varepsilon+\frac{\partial}{\partial x_j}\left[\left(\mu+\frac{\mu_t}{\sigma_\varepsilon}\right)\frac{\partial \varepsilon}{\partial x_j}\right] \tag{4.17}$$

$$\rho\frac{\partial \varepsilon}{\partial t}+\rho\overline{u}_j\frac{\partial \varepsilon}{\partial x_j}=C_{\varepsilon 1}\frac{\varepsilon}{k}\tau_{ij}\frac{\partial \overline{u}_i}{\partial x_j}-C_{2\varepsilon}\rho\frac{\varepsilon^2}{k}+\frac{\partial}{\partial x_i}\left[\left(\mu+\frac{\mu_t}{\sigma_\varepsilon}\right)\frac{\partial \varepsilon}{\partial x_j}\right] \tag{4.18}$$

In words the equations 4.17 and 4.18 are:

Rate of change of k or ε	+	Transport of k or ε by convection	=	Transport of k or ε by diffusion	+	Rate of production of k or ε	–	Rate of destruction of k or ε

The above equations contain five adjustable constants arrived at by comprehensive data fitting for a wide range of turbulent flows:

$$C_\mu=0.009 \qquad \sigma_k=1.00 \qquad \sigma_\varepsilon=1.30 \qquad C_{1\varepsilon}=1.44 \qquad C_{2\varepsilon}=1.92$$

'Production and destruction of turbulent kinetic energy are always closely linked. The dissipation rate ε is large where the production of k is large. The model Equation 4.18 for ε assumes that its production and destruction terms are proportional to the production and destruction terms of the k Equation 4.17' [4.21]. Adoption of such forms ensures that ε increases rapidly if k increases rapidly and that it decreases sufficiently fast to avoid (non-physical) negative values of turbulent kinetic energy if k decreases. The factor ε/k in the production and destruction terms make these terms dimensionally correct in the ε equation. To compute the Reynolds stress tensor in the $k-\varepsilon$ model a revised Boussinesq relationship is used from that shown in Equation 4.19.

$$-\rho\overline{u_i'u_j'}=\mu_t\left(\frac{\partial U_i}{\partial x_j}+\frac{\partial U_j}{\partial x_i}\right)-\frac{2}{3}\rho k\delta_{ij}=2\mu_t S_{ij}-\frac{2}{3}\rho k\delta_{ij} \tag{4.19}$$

where $\tau_{ij}=2\mu_t S_{ij}-\frac{2}{3}\rho k\delta_{ij}$ = Reynolds stress tensor

and $\delta_{ij}=$ the Kronecker delta (1 when $i=j$ and 0 when $i\neq j$)

$$S_{ij} = \left(\frac{\partial \overline{u}_i}{\partial x_j} + \frac{\partial \overline{u}_j}{\partial x_i} \right)$$

'The effect of extra term $\frac{2}{3}\rho k \delta_{ij}$ added to the Boussinesq relationship is to make the term applicable to the normal Reynolds stresses as the standard hypothesis deals only with shear stresses. This term effectively allocates an equal third of the sum of the normal Reynolds stresses to each normal stress' [4.1].

Advantages of the standard $k-\varepsilon$ model

- It is the simplest turbulence model for which only initial and/or boundary conditions need to be supplied.
- It has an excellent performance for many industrially relevant flows.
- It is well established, the most widely validated turbulence models.

Disadvantages of the standard $k-\varepsilon$ model

- It is more expensive to implement than mixing length model (two extra PDEs)
- It has a poor performance in a variety of important cases such as:
  - Some unconfined flows.
  - Flows with large extra strains (e.g. curved boundary layers or swirling flows).
  - Rotating flows.
  - Flows driven by anisotropy of normal Reynolds stresses (e.g. fully developed flows in non-circular ducts).

4.5.1.5 The Low Reynolds number $k-\varepsilon$ Model

The equations for this model are only slightly modified from the standard $k-\varepsilon$ model, the main difference occurs in the treatment of the near wall region. The high Reynolds number $k-\varepsilon$ model reduces the computational effort of a given flow simulation by making the use of the universal behaviour of the near wall flows. The low Reynolds number model does not use this method and integrates to the wall surface in the low Reynolds number region of the flow. The standard model therefore has to be revised to force the correct near wall conditions whereby the viscous stresses in the near wall region take over from the Reynolds stresses which are dominant in the flow at a much

greater distance from the wall. This is achieved by the use of wall damping functions that multiply the model constants C_μ , $C_{\varepsilon 1}$ etc.

For example:

$$\mu_t = \rho C_\mu f_\mu \, k^2 \Big/ \varepsilon \tag{4.20}$$

where

$$f_\mu = \exp\left(\frac{-3.4}{\left(1 + R_T \Big/ 50\right)^2} \right) \tag{4.21}$$

and

$$R_T = \frac{\rho k^2}{\mu \varepsilon} \tag{4.22}$$

Further damping functions are applied to the turbulence transport equations. Similar functions can be applied to any of the other models detailed in this section to allow them to resolve the flow in the low Reynolds, near wall region, of the flow. For further detail see Patel et al [4.22].

4.5.1.6 The $k-\omega$ Equation Model

This turbulence model, first proposed by Kolmogorov in 1941, was in fact the first model of turbulence. The variable k is, as usual, the turbulent kinetic energy and ω is the dissipation per unit turbulent kinetic energy. In the usual manner these two terms are modelled using partial differential equations. The advantage of replacing the ε equation with the ω equation is that the second is easier to integrate (more robust) and that it can be integrated through the sub-layer without the need for additional damping functions. For further details see Menter and Grotjans [4.23].

Eddy viscosity,

$$\mu_t = \rho \frac{k}{\omega} \tag{4.23}$$

Turbulent kinetic energy

$$\rho \frac{\partial k}{\partial t} + \rho \overline{u}_j \frac{\partial k}{\partial x_j} = \tau_{ij} \frac{\partial \overline{u}_i}{\partial x_j} - \beta^* \rho k \omega + \frac{\partial}{\partial x_j} \left[\left(\mu + \sigma^* \mu_T \right) \frac{\partial k}{\partial x_j} \right] \tag{4.24}$$

Specific dissipation rate

$$\rho\frac{\partial\omega}{\partial t}+\rho\bar{u}_j\frac{\partial\omega}{\partial x_j}=\alpha\frac{\omega}{k}\tau_{ij}\frac{\partial\bar{u}_i}{\partial x_j}-\beta\rho\omega^2+\frac{\partial}{\partial x_i}\left[(\mu+\sigma\mu_T)\frac{\partial\omega}{\partial x_j}\right] \tag{4.25}$$

where β,β^*,σ etc. are closure coefficients.

Although experimental evidence of the performance of this model is relatively scarce, Wilcox [4.24] showed that for a two dimensional backward facing step the reattachment length of the recirculation zone was within three percent of the experimentally measured location. This outperformed the standard $k-\varepsilon$ model, which significantly underestimated the reattachment length. The disadvantages of this model include the fact that the solutions produced are very sensitive to the values specified for ω at the inlet. Menter [4.23] has proposed a model that combines the advantages of $k-\varepsilon$ and $k-\omega$ models, thereby removing this deficiency.

4.5.1.7 The Renormalization Group (RNG) k − ε Turbulence Model

'The statistical mechanics approach has led to a new mathematical formalism, which, in conjunction with a limited number of assumptions regarding the statistics of small-scale turbulence, provides a rigorous basis for the extension of eddy viscosity models' [4.1]. 'The RNG based $k-\varepsilon$ turbulence model is derived from the instantaneous Navier-Stokes equations, using a mathematical technique called "renormalization group" (RNG) methods. The analytical derivation results in a model with constants different from those in the standard $k-\varepsilon$ model, and additional terms and functions in the transport equations for k and ε' [4.17]. The renormalization group devised by Yakhot and Orszag of Princeton University has attracted most interest. 'They represented the effects of the small-scale turbulence by means of a random forcing function in the Navier-Stokes equation. The RNG procedure systematically removes the small-scales of motion from the governing equations by expressing their effects in terms of larger scale motions and a modified viscosity. The mathematics is highly abstruse [4.25]'. This thesis only presents the RNG $k-\varepsilon$ model equations for high Reynolds number flows derived by Yakhot et al [4.25]:

$$\frac{\partial(\rho k)}{\partial t}+div(\rho kU)=div\left[\alpha_k\mu_{eff}gradk\right]+\tau_{ij}\cdot S_{ij}-\rho\varepsilon \tag{4.26}$$

$$\frac{\partial(\rho\varepsilon)}{\partial t} + div(\rho\varepsilon U) = div\left[\alpha_\varepsilon \mu_{eff} grad\,\varepsilon\right] + C_{1\varepsilon}^{*}\frac{\varepsilon}{k}\tau_{ij}\cdot S_{ij} - C_{2\varepsilon}\rho\frac{\varepsilon^2}{k} \qquad (4.27)$$

with

$$\tau_{ij} = -\rho\overline{u_i' u_i'} = 2\mu_t S_{ij} - \frac{2}{3}\rho k S_{ij} \qquad (4.28)$$

where

$$\mu_{eff} = \mu + \mu_t, \qquad \mu_t = \rho C_\mu {k^2}/{\varepsilon} \qquad (4.29)$$

and $C_\mu = 0.0845 \quad \alpha_k = \alpha_\varepsilon = 1.39 \quad C_{1\varepsilon} = 1.42 \quad C_{2\varepsilon} = 1.68$

and $C_{1\varepsilon}^{*} = C_{1\varepsilon} - \dfrac{\eta(1-\eta/\eta_0)}{1+\beta\eta^3} \qquad \eta = \dfrac{k}{\varepsilon}\sqrt{2S_{ij}\cdot S_{ij}} \qquad \eta_0 = 4.377 \qquad \beta = 0.012$

Only the constant β is adjustable; the above value is calculated from near wall turbulence data. All other constants are explicitly computed as part of the RNG processes.

Yakhot et al, 1992 [4.25] reported very good predictions of the flow over a back-ward facing steps. This performance improvement initially aroused considerable interest and a number of commercial CFD codes have now incorporated the RNG version of the $k-\varepsilon$ model. Performance of RNG $k-\varepsilon$ model is better than standard $k-\varepsilon$ model for general flow conditions.

4.5.1.8 The Realizable $k-\varepsilon$ Model

The realizable $k-\varepsilon$ model was developed by Shih et al [4.17]. 'The term "realizable" means that the model satisfies certain mathematical constraints on the normal stresses, consistent with the physics of turbulent flows. Shih et al intended to address the deficiencies of the traditional $k-\varepsilon$ by adopting the following:

(1) A new eddy-viscosity formula involving a variable C_μ originally proposed by Reynolds.
(2) A new model equation for dissipation of turbulent kinetic energy (ε) based on the dynamic equation of the mean-square vorticity fluctuations' [4.17].

The realizable $k-\varepsilon$ model satisfies certain mathematical constraints on the normal stresses, consistent with the physics of turbulent flows, combining the Boussinesq relationship with the eddy viscosity to obtain an expression for the normal Reynolds stress in an incompressible strained mean flow. These models have been validated for boundary layer flows, and separated flows on different models and perform substantially better than those of the standard $k-\varepsilon$ model.

4.5.1.9 The Reynolds Stress Model

A more complex version of the RANS equations is the Reynolds stress model of Launder, Reece and Rodi [4.26].

Second moment closure is based on exact transport equations for the individual Reynolds stresses and fluxes derived from the Navier-Stokes equations. The derivation of the Reynolds stress equations, detailed in full by Leschziner [4.27], results in a total of nine transport equations, six of which describe the Reynolds normal stresses and shear stresses and a further three which describe the Reynolds fluxes, which for an incompressible fluid gives:

$$\frac{\partial}{\partial x_k}\left(\rho\overline{u}_k\overline{u_iu_j}\right)=-\rho\left(\overline{u_ju_k}\frac{\partial\overline{u}_i}{\partial x_k}+\overline{u_iu_k}\frac{\partial\overline{u}_j}{\partial x_k}\right)+\left(\overline{u_if_j}+\overline{u_jf_i}\right)+p\overline{\left(\frac{\partial u_i}{\partial x_j}+\frac{\partial u_j}{\partial x_i}\right)}$$
$$-2\mu\overline{\frac{\partial u_i}{\partial x_k}\frac{\partial u_j}{\partial x_k}}-\frac{\partial}{\partial x_k}\left(\rho\overline{u_iu_ju_k}+\overline{pu}_i\delta_{jk}+\overline{pu}_j\delta_{ik}-\mu\frac{\partial\overline{u_iu_j}}{\partial x_k}\right) \quad (4.30)$$

this translates to

ρC_{ij}	=	ρP_{ij}	+	ρF_{ij}	+	$\rho\Phi_{ij}$	-	$\rho\varepsilon_{ij}$	-	ρd_{ij}
Transport of Reynolds stress By convection		Production of R.S		Stress production or destruction by action of rotation--al body forces		Redistribution of R.S due to pressure-strain interaction		Rate of dissipation by viscosity		Rate of diffusion

Wilcox [4.24] details the individual contents of the equations and lists some of the reasons for improvements over the eddy viscosity models as follows:

Firstly, since the equation automatically accounts for the convection and diffusion of the Reynolds stresses, a second order closure model will include effects of flow history. In turbulent shear flow large bodies of fluid migrate across the flow, carrying smaller scale disturbances. In addition to migrating across the flow, they have a lifetime so long that they persist for distances as much as 30 times the width of the flow [4.1]. Thus the

turbulent stresses at a given point depend upon upstream history and cannot be uniquely specified in terms of the local strain rate tensor, as is the case with the eddy viscosity formulation, and the linear Boussinesq relationship.

Secondly, Equation 4.30, being more complex than the eddy viscosity approximation, contains a greater number of terms enabling a great number of flow effects to be accounted for. The extra terms such as convection, production and body force allow representation of flows involving streamline curvature, system rotation and stratification. Thirdly, there is no reason why this model should give equal values for the normal and shear stresses as the individual components are calculated separately.

In a similar fashion to the models described previously, there is now a significant closure problem with the Reynolds stress model. In order to close the Reynolds stress equations it is necessary to eliminate third moment correlations that appear in the Equation 4.30 of the form $u_k u_i u_j$. Furthermore, it is necessary to model the dissipation tensor ε_{ij}, the turbulent transport tensor C_{ij} and the pressure strain correlation tensor Φ_{ij} in the Reynolds stress transport equation. As each of these forms is a tensor the approximation required for closure can assume much more elaborate forms compared to approximations used in k equation [4.24].

The diffusion term in the Reynolds stress transport equation is often modelled using Kolmogorov's (A.N. Kolmogorov, 'de l'Academia des Sci. de l'URSS 30:301, 1941) [4.1] hypothesis of local isotropy of small scales where directionality of the small scale eddies is damped due to the effects of viscosity. The model is formulated so that the normal Reynolds stresses only are affected [4.1].

$$\varepsilon_{ij} = \frac{2}{3}\varepsilon\delta_{ij} \qquad (i = j) \tag{4.31}$$

where $\varepsilon = \nu\left(\overline{\frac{\partial u_i}{\partial x_k}\frac{\partial u_i}{\partial x_k}}\right)$ = dissipation rate of the turbulent kinetic energy

It should be noted that this assumption is not always true and the dissipation of the turbulent kinetic energy may, in certain circumstances, be anisotropic. Rotta (J.C. Rotta, 'Turbulence Stromungen', B.G. Teubner, Stuttgart, 1972) [4.1] has attempted to account for this. The turbulent transport term is often modelled by the analogy that the rate of

transport of Reynolds stresses by diffusion is proportional to the gradients of the Reynolds stresses.

The pressure-strain correlation in the differential stress model has proven the most difficult term to account for and has received the greatest amount of attention from turbulence modellers. The physical process that cause pressure fluctuations to occur are detailed and complex and include interaction between neighbouring eddies and the effects of different mean velocities on the turbulent eddies [4.14]. The main effect of this term is to reduce the level of the Reynolds shear stresses and redistribute this energy amongst the normal stresses. This returns the normal stresses towards a state of isotropy. Unfortunately the presence of a solid boundary tends to increase the anisotropy of the turbulent eddies and decrease the magnitude of the Reynolds shear stresses in contrast to the role of the pressure strain term. Modifications to the pressure-strain term are thus required to enable the model to accurately predict the effect of the wall on the turbulent eddies.

4.5.2 Large Eddy Simulation (LES)

This is an intermediate form of turbulence calculations in which large eddies are explicitly computed (resolved) in a time dependent simulation using the 'filtered' Navier-Stokes equations. The rationale behind the LES is that by modelling less of the turbulence (and resolving more), the error introduced by turbulence modelling can be reduced. The method involves spatial filtering of the unsteady Navier-Stokes equations prior to the computations, which passes the larger eddies and rejects the smaller eddies. Filtering is essentially a mathematical manipulation of the exact Navier-Stokes equations to remove eddies that are smaller than a specified size. The effects on the resolved flow (mean flow plus large eddies) due to the smallest, unresolved eddies are included by means of a so-called sub-grid scale model. Unsteady flow equations must be solved, so the demands on computing resources in terms of storage and volume of calculations are large, but this technique is starting to address CFD problems with complex geometry [4.9].

The Large Eddy Simulation (LES) technique thus falls between the Direct Numerical Simulation (DNS) and the Reynolds averaged Navier-Stokes (RANS) equations in terms of the fraction of the resolved scales. 'The rationale behind the LES can be summarized as follows [4.17]:

- The momentum, mass, energy, and other passive scalars are transported mostly by large eddies.
- The large eddies are more problem-dependent. They are dictated by the geometries and boundary conditions of the flow involved.
- The small eddies are less dependent on the geometry, tend to be more isotropic, and are consequently more universal.
- The chance of finding a universal turbulence model is much higher for small eddies'.

Resolving only the large eddies allows the use of a much coarser mesh and larger time-step sizes in the LES technique than required by the DNS calculations. However, LES still requires substantially finer meshes than those typically used for RANS calculations. In addition, the LES calculations have to be run for a sufficiently long flow-time to obtain stable statistics of the flow being modelled. As a result, the computational cost involved with the LES technique is normally orders of magnitudes higher than those required for steady RANS calculations in terms of memory (RAM) and CPU time. Therefore, high-performance computing (e.g., parallel computing) is a necessity for LES, especially for industrial applications.

The theories behind the Large Eddy Simulation are based on the works of Jacobsen [4.28]. The methods used to implement and test the LES technique using Fluent 6.3 are based on the work of Jacobsen [4.28] and Ciofalo and Collins [4.29].

4.5.2.1 Spatial Filtering of Unsteady Navier-Stokes Equations

In the LES technique it is essential to define those quantities that are to be computed precisely. A velocity field is required that contains only the large scale components of the total field, which is best achieved by filtering the large or resolved scale field [4.9]. 'The governing equations employed for the LES are obtained by filtering the time-dependent Navier-Stokes equations in either Fourier (wave-number) space or configuration (physical) space. The filtering process effectively filters out eddies whose scales are smaller than the filter width or grid spacing used in the computations. The resulting equations thus govern the dynamics of large eddies [4.17]'. As such, in large eddy simulation, any physical quantity f is decomposed into two parts:

$$f = \bar{f} + f'' \tag{4.32}$$

Here, $\overline{f}$ is the resolvable scale component and $f^{"}$ is the sub-grid scale (SGS) component. Assuming that $f^{"}$ is the filtered velocity $\overline{u}_i$, then it is defined with a filter function $G\left(x,x^{'}\right)$ as follows:

$$\overline{u}_i\left(x\right)=\int G(x,x^{'})u_i(x^{'})dx^{'} \tag{4.33}$$

The filter kernel $G\left(x,x^{'}\right)$ is localised function and may include a Gaussian, box or cut off filter. Every filter has a length scale associated with it, that dictates large eddies are directly resolved and small eddies are therefore to be modelled.

Imposing the filter on the incompressible continuity and Navier-Stokes equations produces the following filter equations:

$$\frac{\partial\overline{u}_i}{\partial x}=0 \tag{4.34}$$

$$\frac{\partial\overline{u}_i}{\partial t}+\frac{\partial\overline{u_iu_j}}{\partial x_j}=-\frac{1}{\rho}\cdot\frac{\partial\overline{P}}{\partial x_i}+\frac{\mu}{\rho}\cdot\frac{\partial^2\overline{u}_i}{\partial x_j\partial x_j} \tag{4.35}$$

where the over-bar means a space filtered quantity.

In order to define the large scale velocity field that is separated out from the sub-grid-scale (SGS) components a Reynolds averaging type procedure is carried out:

$$u_i=\overline{u}_i+u_i^{'} \tag{4.36}$$

As described earlier, the main difficulties are due to the non-linear convection terms in the Navier-Stokes equations.

Putting Equation 4.37 into the non-linear terms and expanding gives:

$$\overline{u_ju_i}=\overline{\left(\overline{u}_j+u_j^{'}\right)\left(\overline{u}_i+u_i^{'}\right)} \tag{4.37}$$

$$=\overline{\overline{u}_i\overline{u}_j}+\overline{\overline{u}_iu_j^{'}}+\overline{u_i^{'}\overline{u}_j}+\overline{u_i^{'}u_j^{'}}$$

$$(1)\quad(2)\quad(3)\quad(4)$$

In general it must be noted that $\overline{u_k' u_l'} \neq 0$. In contrast to the time averaged approach all the four terms must now be considered. Terms 2 to 4 contain small scale, non-resolvable components u_i' which must be modelled. Term 1 is defined entirely in terms of the grid-resolved quantities by introducing the SGS stresses [4.27]:

$$\tau_{ij} = \overline{u_i u_j} - \overline{u}_i \overline{u}_j \tag{4.38}$$

Inserting Equation 4.38 into Equation 4.37 means that the convective term in the filtered Navier-Stokes Equation 4.35, will only depend on the resolved quantities [4.28].

The LES capability in Fluent 6.3 is also applicable to compressible flows. For the sake of concise notation, however, the theory is presented here for incompressible flows. Filtering the Navier-Stokes equations, one obtains

$$\frac{\partial \rho}{\partial t} + \frac{\partial}{\partial x_i}\left(\rho \overline{u}_i\right) = 0 \tag{4.39}$$

and

$$\frac{\partial}{\partial t}\left(\rho \overline{u}_i\right) + \frac{\partial}{\partial x_j}\left(\rho \overline{u}_i \overline{u}_j\right) = \frac{\partial}{\partial x_j}\left(\mu \frac{\partial \sigma_{ij}}{\partial x_j}\right) - \frac{\partial \overline{P}}{\partial x_i} - \frac{\partial \tau_{ij}}{\partial x_j} \tag{4.40}$$

where σ_{ij} is the stress tensor due to molecular viscosity defined by

$$\sigma_{ij} \equiv \left[\mu\left(\frac{\partial \overline{u}_i}{\partial x_j} + \frac{\partial \overline{u}_j}{\partial x_i}\right)\right] - \frac{2}{3}\mu \frac{\partial \overline{u}_l}{\partial x_l}\delta_{ij} \tag{4.41}$$

and τ_{ij} is the sub-grid-scale stress defined by

$$\tau_{ij} \equiv \rho\overline{u_i u_j} - \rho \overline{u}_i \overline{u}_j \tag{4.42}$$

The substantial portion of τ_{ij} is attributable to convective momentum transport due to interactions between the unresolved or SGS eddies; theses stresses are commonly termed the sub-grid scale stresses. We can also write the SGS stresses as follows [4.1]:

$$\tau_{ij} = \rho\overline{u_i u_j} - \rho \overline{u}_i \overline{u}_j = \left(\rho\overline{\overline{u}_i \overline{u}_j} - \rho \overline{u}_i \overline{u}_j\right) + \rho\overline{\overline{u}_i u_j'} + \rho\overline{u_i' \overline{u}_j} + \rho\overline{u_i' u_j'} \tag{4.43}$$

(I) (II) (III)

Thus we find that the SGS stresses contain three groups of contributions:

Term (I), Leonard stresses L_{ij} : $L_{ij} = \rho\overline{\overline{u}_i\overline{u}_j} - \rho\overline{u}_i\overline{u}_j$

Term (II), Cross-stresses C_{ij} : $C_{ij} = \rho\overline{\overline{u}_i u_j'} + \rho\overline{u_i'\overline{u}_j}$

Term (III), LES Reynolds stresses R_{ij} : $R_{ij} = \rho\overline{u_i' u_j'}$

These stresses are modelled in the following manner:

'Leonard (1974) has shown that the Leonard stress term removes significant energy from the resolved scales. They can be computed explicitly but it has been shown that they are of the same order as the truncation error when a finite difference scheme of order higher than two has been applied and thus they are implicitly represented (Wilcox, 1994). The remaining stresses have been modelled in different ways. Their properties are assumed to be identical with those arising in the Reynolds time-averaging approach. For the sub-grid scale turbulence the eddy viscosity model assumes that the sub-grid scale is proportional to the modulus of the strain rate tensor of the filtered large-scale flow [4.28]'.

4.5.2.2. Sub-grid-scale Models

The sub-grid-scale stresses resulting from the filtering operation are unknown, and require modelling. The sub-grid-scale turbulence models employ the Boussinesq hypothesis [4.17] as in the RANS models, computing sub-grid-scale turbulent stresses from

$$\tau_{ij} - \frac{1}{3}\tau_{kk}\delta_{ij} = -2\mu_t\overline{S}_{ij} \tag{4.44}$$

where is τ_{ij} the sub-grid-scale turbulent viscosity, and $\overline{S}_{ij}$ is the rate-of-strain tensor for the resolved scale defined by

$$\overline{S}_{ij} \equiv \frac{1}{2}\left(\frac{\partial\overline{u}_i}{\partial x_j} + \frac{\partial\overline{u}_j}{\partial x_i}\right) \tag{4.45}$$

Fluent 6.3 [4.17] offers four models for μ_t : the Smagorinsky-Lilly model, the dynamic Smagorinsky-Lilly model, the WALE model, and the dynamic kinetic energy sub-grid-scale model.

4.5.2.3 The Smagorinsky-Lilly Model

This simple model was first proposed by J. Smagorinsky [4.17], in which the eddy viscosity is modelled as:

$$\mu_t = \rho L_s^2 \left|\bar{S}\right| \tag{4.46}$$

Where L_s is the mixing length of the sub-grid-scales and $\left|\bar{S}\right| \equiv \sqrt{2\bar{S}_{ij}\bar{S}_{ij}}$

In Fluent 6.3, L_s is computed using

$$L_s = \min\left(\kappa d, C_s V^{1/3}\right) \tag{4.47}$$

where, κ is the Von-Kármán constant, d is the distance to the closest wall, C_s is the Smagorinsky constant, and V is the volume of the computational cell.

Lilly derived a value of 0.17 for C_s for homogeneous isotropic turbulence in the inertial sub-range. However, this value was found to cause excessive damping of large-scale fluctuations in the presence of mean shear and in transitional flows as near to solid boundaries, and has to be reduced in such regions [4.17]. In short, C_s is not a universal constant, which is the most serious shortcoming of this simple model. Nonetheless, a C_s value of around 0.1 has been found to yield the best results for a wide range of flows, and is the default value in Fluent 6.3.

The standard Smagorinsky model is simple and well designed and hence has been applied to many flow fields and with great success. However, the standard model has several shortcomings:

1. The model is overly dissipative.
2. The Smagorinsky constant C_s must be optimised for each flow field.
3. No, 'natural' account is taken of the effects of wall.
4. No account is made of the effects of negative SGS viscosities or the apparent transfer of energy from the small to large scale eddies, known as backscatter.

The second shortcoming represents the most serious problem in wind engineering flow fields. The rate of transfer from the large eddies to the small dissipative eddies varies

according to both the spatial and temporal point in the flow field as a consequence of the many different flow types encountered. Consequently dynamic SGS models have been devised that calculate values of the model constant depend on the spatial and temporal conditions in the flow field. For full details see [4.30].

4.5.2.4 The Dynamic Smagorinsky-Lilly Model

'Germano et al and subsequently Lilly conceived a procedure in which the Smagorinsky model constant, C_s is dynamically computed based on the information provided by the resolved scales of motion' [4.31]. The dynamic procedure thus obviates the need for users to specify the model constant C_s in advance. The details of the model implementation in Fluent and its validation can be found in S.-E. Kin technical report 2004 [4.32].

'The C_s obtained using the dynamic Smagorinsky-Lilly model varies in time and space over a fairly wide range. To avoid numerical instability in Fluent, C_s is clipped at zero and 0.23 by default' [4.17].

4.5.2.5 The Wall-Adapting Local Eddy-Viscosity (WALE) Model

This model was proposed by F. Nicoud and F. Ducros [4.33], in which the eddy viscosity is modelled as:

$$\mu_t = \rho L_s^2 \frac{\left(S_{ij}^d S_{ij}^d\right)^{3/2}}{\left(\bar{S}_{ij}\bar{S}_{ij}\right)^{5/2} + \left(S_{ij}^d S_{ij}^d\right)^{5/4}} \tag{4.48}$$

where L_s and S_{ij}^d in the WALE model are defined, respectively, as

$$L_s = \min\left(\kappa d, C_w V^{1/3}\right) \tag{4.49}$$

$$S_{ij}^d = \frac{1}{2}\left(\bar{g}_{ij}^2 + \bar{g}_{ji}^2\right) - \frac{1}{3}\delta_{ij}\bar{g}_{kk}^2 \quad , \quad \bar{g}_{ij} = \frac{\partial \bar{u}_i}{\partial x_j} \tag{4.50}$$

In Fluent 6.3, the default value of the WALE constant C_w is 0.325 and has been found to yield satisfactory results for a wide range of flow. The rest of the notation is the same as for the Smagorinsky-Lilly model. With this spatial operator, the WALE model is designed to return the correct wall asymptotic $\left(y^3\right)$ behaviour for wall bounded flows.

4.5.2.6 The Dynamic Kinetic Energy Sub-grid-Scale Model

The original and dynamic Smagorinsky-Lilly models discussed previously are essentially 'algebraic models in which sub-grid-scale stresses are parameterized using the resolved velocity scales. The underlying assumption is the local equilibrium between the transferred energy through the grid-filter scale and the dissipation of kinetic energy at small sub-grid-scales. The sub-grid-scale turbulence can be better modelled by accounting for the transport of the sub-grid-scale turbulence kinetic energy [4.34]'.

The dynamic SGS kinetic energy model in Fluent replicates the model proposed by Kim and Menon *in* the technical report submitted to American Institute of Aeronautics Astronautics, 35th Aerospace Sciences Meeting, Reno, NV [4.19].

The sub-grid-scale kinetic energy is defined as:

$$k_{sgs} = \frac{1}{2}\left(\overline{u_k^2} - \overline{u}_k^2\right) \tag{4.51}$$

This is obtained by contracting the sub-grid-scale stress in equation 4.52.

$$\tau_{ij} \equiv \rho\overline{u_i u_j} - \rho\overline{u}_i\overline{u}_j \tag{4.52}$$

The sub-grid-scale eddy viscosity μ_t is computed using k_{sgs} as:

$$\mu_t = C_k k_{sgs}^{1/2} \Delta_f \tag{4.53}$$

where Δ_f is the filter-size computed from $\Delta_f \equiv V^{1/3}$

The sub-grid-scale stress can then be written as

$$\tau_{ij} - \frac{2}{3}k_{sgs}\delta_{ij} = -2C_k k_{sgs}^{1/2}\Delta_f \overline{S}_{ij} \tag{4.54}$$

k_{sgs} is obtained by solving the following transport equation:

$$\frac{\partial \overline{k}_{sgs}}{\partial t} + \frac{\partial \overline{u}_j \overline{k}_{sgs}}{\partial x_j} = -\tau_{ij}\frac{\partial \overline{u}_i}{\partial x_j} - C_\varepsilon \frac{k_{sgs}^{3/2}}{\Delta_f} + \frac{\partial}{\partial x_j}\left(\frac{\mu_t}{\sigma_k}\cdot\frac{\partial k_{sgs}}{\partial x_j}\right) \tag{4.55}$$

In the above equations, the model constants C_k and C_ε are determined dynamically as proposed by Kim and Menon [4.19]. σ_k is hardwired to 1.0. The details of the implementation of this model in Fluent 6.3 and its validation are given by Kim [4.19].

4.5.3 Direct Numerical Simulation (DNS)

This technique is the easiest to define but is the most computationally expensive. Direct numerical simulation solves the instantaneous unsteady Navier-Stokes equations on spatial grids that are sufficiently fine and can resolve the Kolmogorov length scales at which energy dissipation takes place with time steps sufficiently small to resolve the period of the fastest fluctuations. This approach yields the complete spatial and temporal state of turbulent flow. These calculations are highly costly in terms of computing resources and large memory requirements, so the method is not used for industrial flow computations at the moment.

An excellent example of the massive computational requirements is given by Speziale [4.35], who states that a typical flow domain of 0.1m by 0.1m with high Reynolds number turbulent flow would contain eddies down to 10 to 100μm in size. These very small eddies would naturally have very high frequencies of approximately 10kHz, thus requiring time steps of about 100μs. In order to directly capture the details of the smallest eddies it has been calculated that a computational finite volume of 10^9 to 10^{12} points would be needed. The direct numerical simulation of such a turbulent flow at a Reynolds number of 500000 would require a computer 10 million times faster than a current generation supercomputer.

Due to the extremely high computational costs incurred, DNS is not able to calculate anything other than low Reynolds number flows in simple geometries. The simplest application of DNS requires access to a supercomputer. It is apparent that more practical applications of this technique await significant developments in computer technology. Nevertheless at present the DNS has proved invaluable in supplying computed statistics that can be used to test proposed closure approximations in engineering models. The DNS has been used at a fundamental level to obtain a greater understanding of turbulence structure and processes that are of value in developing turbulence theory that would be impossible to measure with traditional experimental techniques, for example the dissipation rate of turbulence [4.1].

4.6 Developments in Turbulence Modelling

At present the main areas identified as causing inaccuracies in flow predictions include the following:

1. The modelled turbulence energy dissipation equation.
2. The closure form of the pressure-strain tensor and the effect of wall reflection terms.
3. Numerical instabilities and difficulties in obtaining converged solutions for the modelled partial differential equations in complex flows.

The developments that have taken place in the recent past and the future research required in this area is discussed below:

4.6.1 The Murakami, Mochida and Kondo (MMK) $k-\varepsilon$ Turbulence Model

Many techniques have been applied by scientists and researchers to improve the results obtained by the standard $k-\varepsilon$ model due to the deficiencies of the eddy viscosity concept. The technique which is by far the most popular is to make flow specific ad-hoc modifications to the model closure constants to force it into agreement with experimentally derived flow fields. This technique, although popular, has the effect of reducing the universality of the model. There are many published revisions and ad-hoc changes to the model that successfully represent improvements over the standard model for certain flow fields. The following section will describe one of the more successful and extensive revisions appropriate to wind engineering flow fields, the MMK $k-\varepsilon$ model of turbulence [4.36].

The paper detailing this model proposes a $k-\varepsilon$ model that is said to resolve the problems encountered with the standard model (explained in section 4.5.1.4) by modifying the expression for the eddy viscosity approximation. The main k and ε model equations are unchanged. The revised $k-\varepsilon$ model is then applied to flow fields around bluff bodies including a surface mounted cube both normal and skewed to the flow.

4.6.1.1 Outline of the Revised Model

$$P_k = \nu_t \cdot s^2 \quad \text{where } \mu_t = C_\mu \frac{k}{\varepsilon^2} \tag{4.56}$$

The turbulent kinetic energy production term and the calculation of the eddy viscosity for the standard $k-\varepsilon$ are listed in the above equation.

For the MMK model, P_k and μ_t are as per equation 4.56 except that [4.36]:

$$C_\mu = C_\mu \frac{\Omega}{s} \text{ for values of } \frac{\Omega}{s} < 1 \tag{4.57}$$

$$C_\mu = C_\mu \text{ for } \frac{\Omega}{s} \geq 1 \tag{4.58}$$

In the standard $k-\varepsilon$ model, k is overestimated near the front edge of a surface mounted cube which gives rise to a large eddy viscosity. This discrepancy is caused by overestimation of the turbulence production term P_k caused by the eddy viscosity concept described by Murakami et al [4.37] as follows:

The full term (2-dimensional) for P_k:

$$P_k = -\overline{u'u'}\frac{\partial \bar{u}}{\partial x} - \overline{w'w'}\frac{\partial \bar{w}}{\partial z} - \overline{u'w'}\frac{\partial \bar{u}}{\partial z} - \overline{w'u'}\frac{\partial \bar{w}}{\partial x} \tag{4.59}$$

This term equates P_k to the difference between the turbulence production from the diagonal elements of the strain rate tensor and the production from off diagonal elements. This production term for the normal component of the Reynolds stress is as follows:

$$P_{kn} = \left(\overline{u'u'} - \overline{w'w'}\right)\frac{\partial \bar{u}}{\partial x} \tag{4.60}$$

Using the continuity equation and then the eddy viscosity concept this equation becomes:

$$P_{kn} = 4v_t\left(\frac{\partial \bar{u}}{\partial x}\right)^2 \tag{4.61}$$

When an anisotropic model is used such as the differential stress model, P_{kn} is calculated using the form as described in Equation 4.60 which involves two velocity components. When using the eddy viscosity concept these two normal stresses cannot be incorporated so they are simply expressed as Equation 4.61 by adding the two components of turbulence production [4.37]. Hence the value of turbulent production is always large and positive. Although the MMK model is still constrained by the eddy viscosity concept it attempts an ad-hoc correction to the over production of P_{kn}. The standard model constant C_μ becomes a variable that can reduce in magnitude dependent on the ratio of vorticity to shear. At flow impingement areas where there are high shear

stresses the ratio is less than one and a reduced value of C_μ is calculated thus reducing the eddy viscosity returned.

Tsuchiya et al [4.36] conducted tests using the MMK and the standard $k-\varepsilon$ model for flows over a two dimensional square rib and three dimensional cube. It has been reported that the MMK model outperformed the standard model for wind engineering flow fields in all aspects, including a better distribution of surface pressures.

Although this model has had encouraging reports it should be noted that it is still based on the fundamentally flawed assumption of isotropic eddy viscosity as used by the linear, standard $k-\varepsilon$ model. This model could be described as an ad-hoc modification to force the standard $k-\varepsilon$ model into agreement with wind engineering flows as the additions to the equations are not derived in any way from the Navier-Stokes equations.

4.6.2 Two Layer Turbulence Model

Low Reynolds number turbulence models, so called because they are able to integrate into the near wall low Reynolds number region of the flow are reported to require high degrees of numerical resolution in the sub-layer. This is due to the need to account for the steep gradients of the energy dissipation term ε [4.22]. As such the computational requirements of this model in complex three-dimensional wall bounded flows can become excessive, as previously discussed.

Due to these constraints, and in an attempt to improve the performance of turbulence models by taking a great account of the effects of the viscous sub-layer, two layer turbulence models have been formulated. These models make use of either a standard $k-\varepsilon$ or full Reynolds model to describe the near wall region. The advantages of this method are two-fold. Firstly a more accurate description of the sub-layer is given than with the use of wall functions and secondly a lower degree of numerical resolution is needed than with the low Reynolds model. In order to avoid the resolution problems encountered with the low Reynolds number model the sub-layer turbulence model usually avoids the use of the transport equation to determine ε in favour of determination from a prescribed length scale.

The sub-layer models tested and documented at this time consist of either a mixing length model, which is applicable for both the inner and outer flow regions, or more

usually a one-equation model [4.1]. For the one equation model a value of the eddy viscosity in the near wall region is calculated from:

$$v_t = C_\mu k^{1/2} l_\mu \tag{4.62}$$

Only one partial differential equation is solved in this model as the dissipation rate, ε is determined from a prescribed length scale distribution:

$$\varepsilon = \frac{k^{1/2}}{l_\varepsilon} \tag{4.63}$$

The length scales l_μ and l_ε are described by exponential functions that express a linear variation in the log law region until very near wall where deviations occur [4.9]. The length scale l_μ reduces rapidly in the region very close o the wall thus reducing the value of eddy viscosity determined in Equation 4.62.

The use of two layer turbulence models with the one equation model as described means that there are two descriptions of the turbulent kinetic energy k. Consequently the natural matching point of the two models appears to be at the outer edge of the log law sub-layer. Exact methods of matching the two models range from the specification of exact grid points away from the wall to the fulfilment of certain specific criteria. These include such factors as ratios of eddy viscosity to molecular viscosity and the value of l_μ, damping function relation close to unity i.e. very small effects [4.1].

4.6.3 Non-linear $k-\varepsilon$ Model

The standard $k-\varepsilon$ model uses the Boussinesq approximation and eddy viscosity expression. Hence:

$$-\rho\overline{u_i' u'}_j = \tau_{ij} = \tau_{ij}(S_{ij}, k, \varepsilon, \rho) \tag{4.64}$$

This relationship implies that the turbulent characteristics depend on local conditions only, i.e. the turbulence adjusts itself instantaneously as it is convected through the flow domain. The viscoelastic analogy holds that the adjustment does not take place immediately. In addition to the above dependence on mean strain rate S_{ij}, turbulence kinetic energy k, rate of dissipation ε and fluid density ρ the Reynolds stress should also be a function of the rate of change of mean strain following a fluid particle. So,

$$-\rho\overline{u_i'u_j'} = \tau_{ij} = \tau_{ij}\left(S_{ij}, \frac{DS_{ij}}{Dt}, k, \varepsilon, \rho\right) \tag{4.65}$$

A study of the RSM showed that τ_{ij} is actually a transported quantity, i.e. subject to rates of change, convective and diffusive redistribution and to production and dissipation. Bringing in a dependence on DS_{ij}/Dt could be regarded as a partial account of Reynolds stress transport, which recognises that the state of turbulence lags behind the rapid changes that disturb the balance between turbulence production and dissipation.

A group of researchers at NASA Langley Research Centre led by Speziale, 1987 elaborated this idea and proposed a non-linear $k-\varepsilon$. Their approach involves the derivation of asymptotic expansions for Reynolds stresses which maintain terms that are quadratic in velocity gradients [4.1].

$$\tau_{ij} = -\rho\overline{u_i'u_j'} = -\frac{2}{3}\rho k\delta_{ij} + \rho C_\mu \frac{k^2}{\varepsilon} 2S_{ij} - 4C_D C_\mu^2 \frac{k^3}{\varepsilon^2}\left(S_{im}\cdot S_{mj} - \frac{1}{3}S_{mn}\cdot S_{mn}\delta_{ij} + \overset{0}{S}_{ij} - \frac{1}{3}\overset{0}{S}_{mn}\delta_{ij}\right) \tag{4.66}$$

where $\overset{0}{S}_{ij} = \frac{\partial S_{ij}}{\partial t} + U.grad\left(S_{ij}\right) - \left(\frac{\partial U_i}{\partial x_m}\cdot S_{mj} + \frac{\partial U_j}{\partial x_m}.S_{mi}\right)$ and $C_D = 1.68$

The value of the adjustable constant C_D was found by calibration with experimental data [4.1].

Equation 4.66 is the non-linear extension of the $k-\varepsilon$ model to flows with moderate and large strains. Expression (4.19) for the Reynolds stresses in the standard $k-\varepsilon$ can be regarded as a special case of (4.66) at low rates of deformation when terms that are quadratic in velocity gradients may be dropped.

'Pope, 1975 stated that the non-linear eddy viscosity has the following advantages over the algebraic stress model, with which these models have often been incorrectly compared:

- The inter-relation between strain and stress is retained within the differential equation, thus increasing numerical stability.
- The time consuming solution of the algebraic stress simultaneous equations is not needed' [4.38].

This new model of eddy viscosity is therefore shown by Pope, 1975 [4.38] to correct the following fundamental weaknesses of the Boussinesq stress-strain relationship:

- Inability to capture normal stress anisotropy.
- Insufficient sensitivity to secondary strains.
- Excessive generation of turbulence at impingement zones.
- Violation of realisability at large ratios of strain.

4.7 2-D CFD Models

Before undertaking a 3-D study, simple 2-D analyses were done on scaffold tubes to understand the pattern of air flow around the scaffold tubes and the effect of shielding (interference of building) on the force/pressure coefficients. This work is fully described in reference 2.56. All the Figures related to this work can be found in Appendix-I. Two commonly used CFD models- the standard $k-\varepsilon$ and the RNG $k-\varepsilon$ (Renormalization group) were used for the 2-D analyses. The study was started on a single scaffold tube under a constant wind speed of 5 m/s and turbulence intensity of 15%. The force coefficients were determined and found to be 1.379 and 1.207 for the above two CFD models respectively. The higher value of the force coefficients obtained by using the standard $k-\varepsilon$ is due to the over production of turbulent kinetic energy on the windward face. The pressure coefficients around its circumference are shown in Figure A-I.13. The X-velocity contour and velocity vector of air flow around a single scaffold tube along the flow direction can be seen in Figure A-I.14. In case 2, two scaffold tubes were placed 1.2 m apart along the flow direction and force coefficients were determined. A plot of pressure coefficients on the perimeter of the scaffold tubes is shown in Figure A-I.15. The X-velocity contour and the development of turbulent kinetic energy around the tubes are shown in Figure A-I.16. The results are summarized in Table 7.1.

Table 4.1: Average Force Coefficient on Scaffold Tubes

CFD Model	Force Coefficients	
	Tube 1	Tube 2
Standard $k-\varepsilon$	1.378	0.825
RNG $k-\varepsilon$	0.958	0.609

From the above results it can be observed that shielding of one tube over the other affects the force coefficients to a great extent. When the tubes were placed at a distance

1.8-2.1 m apart (usual distance between scaffold tubes) across the flow direction and shown in Figure A-I.17, no interference was observed.

The force coefficients on the scaffold tubes around the cubical building square in plan were also determined using the standard $k-\varepsilon$ and RNG $k-\varepsilon$ methods. The force coefficients calculated on various tubes around the building are shown in Figure A-I.18 and Figure A-I.19. It is noticeable that the pressures in general are significantly lower than those given in the Eurocode which does not allow for the shielding effects on the tubes of the building to which the scaffold is attached.

When scaffold tubes are placed around the building the tubes do not appear to have the pressures applied to them which design codes require. This implies that in many cases scaffold design wind pressures are significantly overestimated. These pressures must be analysed in future.

Further research is required to investigate this shielding, particularly for oblique impacts and for buildings which exhibit porosity. This was not undertaken in the present study because of limitations of the software used for meshing, as every individual scaffold tube would need to be meshed along with the building in 3-D.

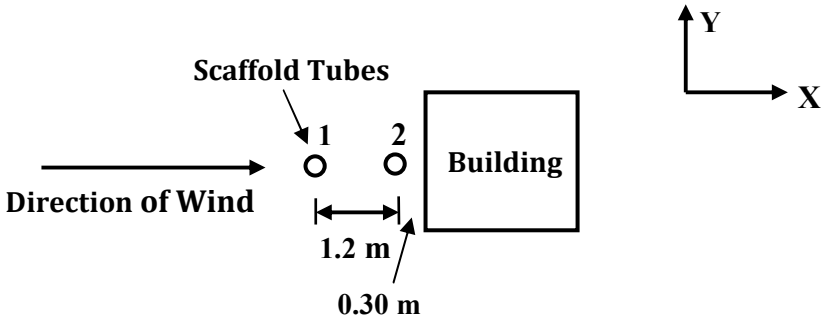

Figure 4.3 A simple model showing direction of wind

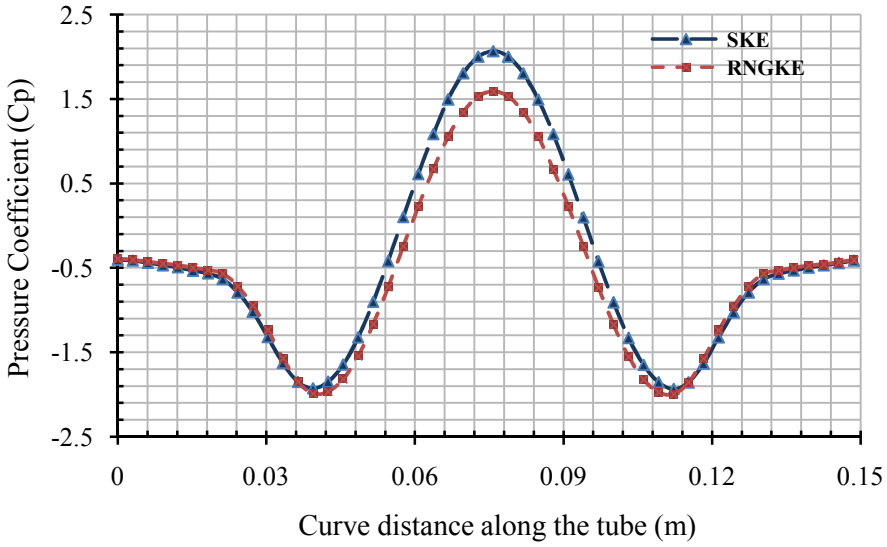

Figure 4.4 Pressure coefficients along the curve length of the tube along the flow direction

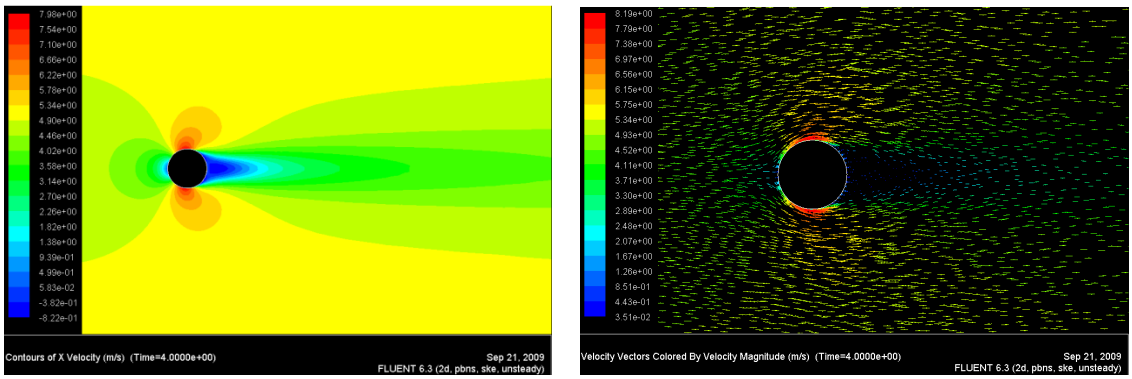

Figure 4.5 X-velocity contour and velocity vector around the scaffold tube along the flow direction

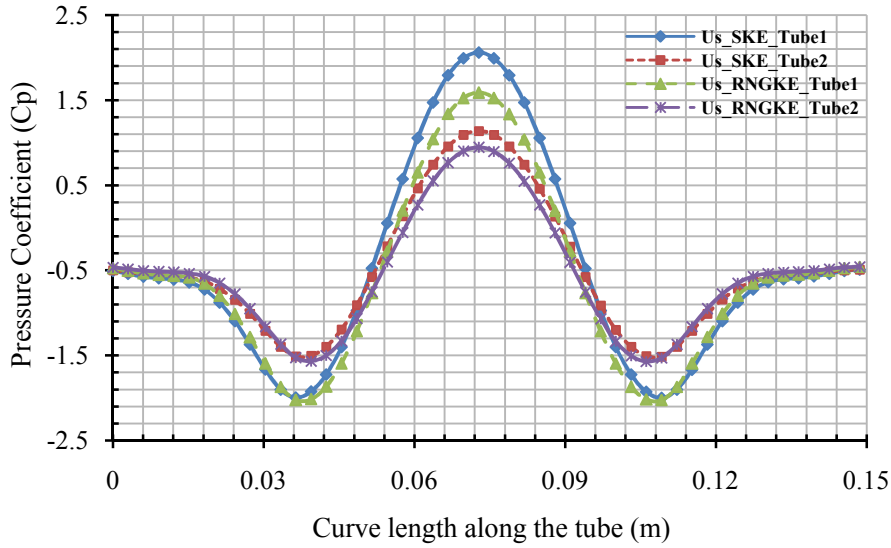

Figure 4.6 Pressure coefficients along the curve length of the tubes along the flow direction

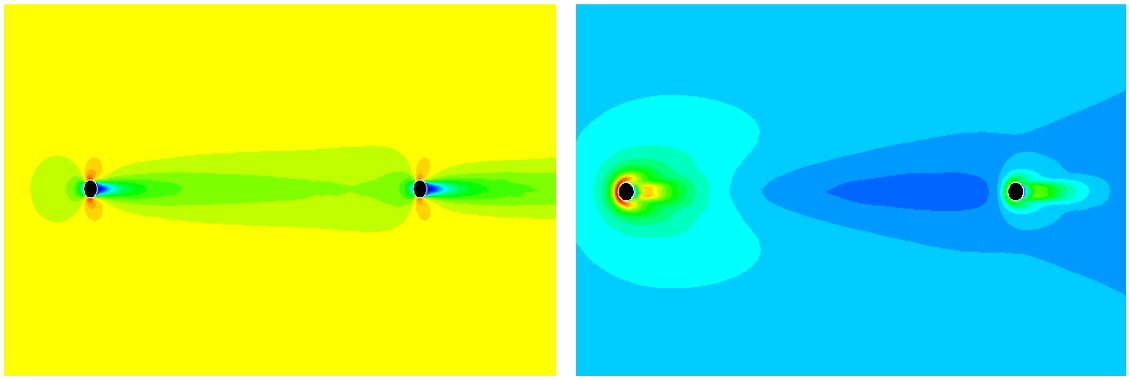

Figure 4.7 X-velocity contour and turbulent kinetic energy around the scaffold tubes along the flow direction for unsteady RNG $k-\varepsilon$ model

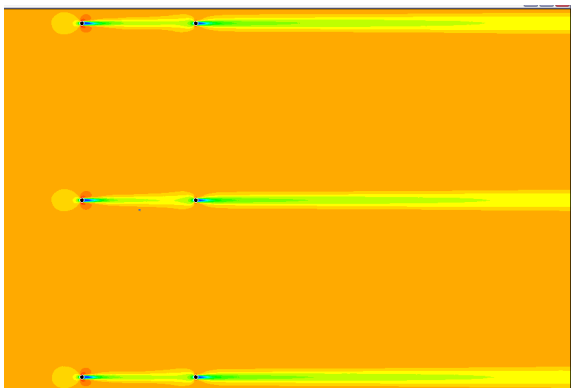

Figure 4.8 X-velocity contour around the scaffold tubes along and across the flow direction for unsteady RNG $k-\varepsilon$ model

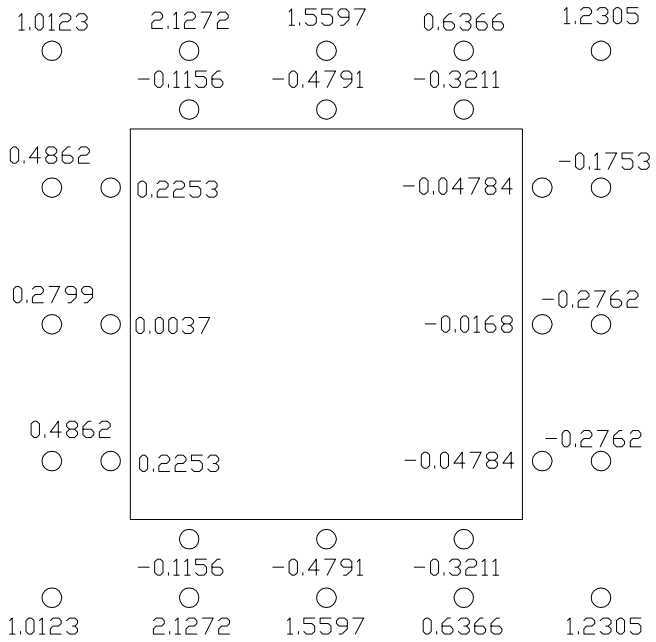

Figure 4.9 Force coefficients on the scaffold tubes around the building by unsteady Standard $k-\varepsilon$ model

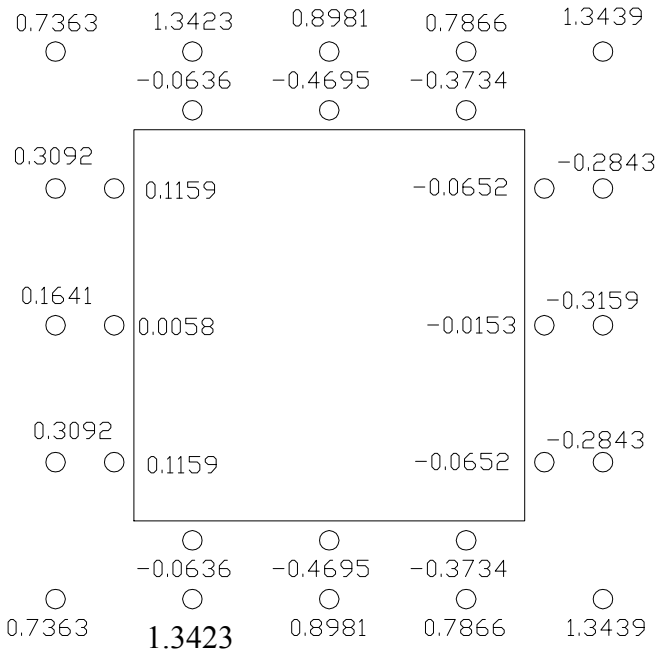

Figure 4.10 Force coefficients on the scaffold tubes around the building by unsteady RNG $k-\varepsilon$ model

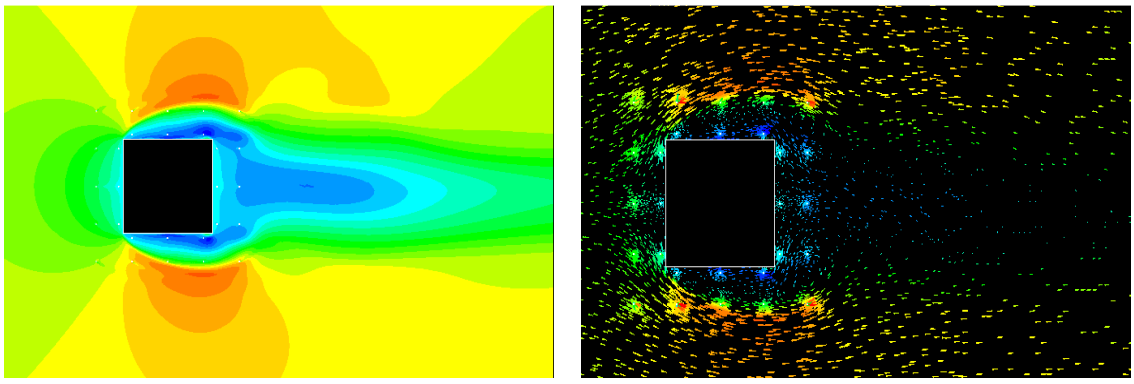

Figure 4.11 X-velocity contour and vector around the scaffold tubes surrounding SEB along the flow direction for unsteady RNG $k-\varepsilon$ method

4.8 Discussion

Of all the available turbulence models, the $k-\varepsilon$ model is by far the most widely used and has been tested for a vast number of flow fields. It is favoured in industrial applications due to its relatively low computational costs and generally better numerical stability than more complex turbulence models such as the Reynolds Stress Model. The model has proved a success in many applications, particularly in confined flows where the normal Reynolds stresses are relatively unimportant. Unfortunately the opposite is true of wind engineering flow fields and the $k-\varepsilon$ model performs poorly.

It is explained in a number of research papers by Murakami [4.7, 4.37] that the $k-\varepsilon$ model incorrectly estimates the level of turbulent kinetic energy around a surface mounted cube, in particular at the leading top edge. This fundamental error results in a poor representation of the flow field and pressure distribution around the cube. In addition, wind tunnel tests have revealed that the stream wise normal stress $u'u'$ dominates in the area of the roof and in the downstream free shear layer. Also the lateral normal stresses $v'v'$ dominates $u'u'$, with $w'w'$ the smallest, in the wake recirculation zone, where a Karman vortex street occurs [4.39]. Consequently the turbulent flow field in wind engineering applications is most definitely anisotropic. Therefore the assumption of a simple isotropic eddy viscosity term is insufficient to adequately describe the complexity of a highly anisotropic flow field and the results in the $k-\varepsilon$ model's failure to accurately predict many turbulent flow fields, not least in wind engineering applications. The main source of error in this model is therefore rooted in the linear Boussinesq approximation and the isotropic eddy viscosity concept.

Unfortunately there is little information available regarding testing of RNG $k-\varepsilon$ model in wind engineering flow fields. Orgaz [4.40] has reviewed papers on simulation and modelling of turbulent flows. The RNG $k-\varepsilon$ is one of the variants of the $k-\varepsilon$ model and as such is based on the flawed isotropic eddy viscosity assumption and Boussinesq approximations. There are some modified versions of the standard $k-\varepsilon$ model that may provide improved predictions for some applications.

The Reynolds stress model has a far greater universality than the models based on the eddy viscosity concept due to its more rigorous and detailed mathematical formulation. The inclusion of a great number of equations allows for a far greater description of the physics of turbulent flow.

Despite the considerable abilities of this model it still has many inadequacies and there are many years of development work to be undertaken on the Reynolds stress model closure forms before it will show its real potential. At present the main areas identified as causing inaccuracies in flow predictions include the following:

- The modelled turbulence energy dissipation equation.
- The closure form of the pressure-strain tensor and the effect of wall reflection terms.

- Numerical instability and difficulties in obtaining converged solutions for the modelled partial differential equations in complex flows.

The LES technique, vigorously pursued in Japan and USA, has the advantage of producing time dependent flow information of very high quality and accuracy even in complex flow fields such as those found in wind engineering. It has succeeded in reproducing the properties of a highly anisotropic flow field in wind engineering problems. It is widely felt by researchers that the LES technique is a promising tool for the future.

The present difficulties in using the LES technique mainly revolve around the constraints on available computer processing time and storage capacity which effectively hold back its use and advancement. This technique, although being more economical than DNS, is still very resource intensive and as such is not yet used outside of the research community. Further difficulties are apparent in the use of the sub-grid-scale model to dissipate the flow energy. Leschziner [4.27] reports that the sub-grid-scale eddies are not simply dissipative but can contribute significantly to turbulent mixing. Such processes as 'backscatter' can occur in which the small eddies combine with large eddies and transfer energy to them.

The present study on the SEB and sheet/net clad scaffolds started with the simulation of the most widely used turbulence model i.e. the standard $k-\varepsilon$ model. The model gave quite satisfactory results when used for internal flow. However, for wind engineering flow fields the standard $k-\varepsilon$ model performed poorly. This is due to the over production of turbulent kinetic energy around the leading edge of the SEB and sheet clad scaffolds surrounding the SEB. The RNG $k-\varepsilon$ model is based on flawed isotropic eddy viscosity assumptions and Boussinesq approximations (see the discussion on page number 66). Neither the RNG $k-\varepsilon$ model nor the Realizable $k-\varepsilon$ model accurately predicted the pressure coefficients on the side and leeward faces of the SEB and on sheet clad scaffolds surrounding the SEB. It was observed that due to the presence of unstructured meshes around the SEB and around sheet clad scaffolds surrounding the SEB the Reynolds stress method did not converge. This could be a Fluent limitation but the author did not have access to any other CFD package to see if convergence could be achieved. The main difficulties in using the LES technique are the availability of computer processing time and storage capacity. The convergence of solutions using the

LES is very difficult if the quality of the mesh around the corners is of not good quality and the sub-meshes are not fine near the walls. Of the available computer resources and time constraints the following turbulence methods were used for the following models:

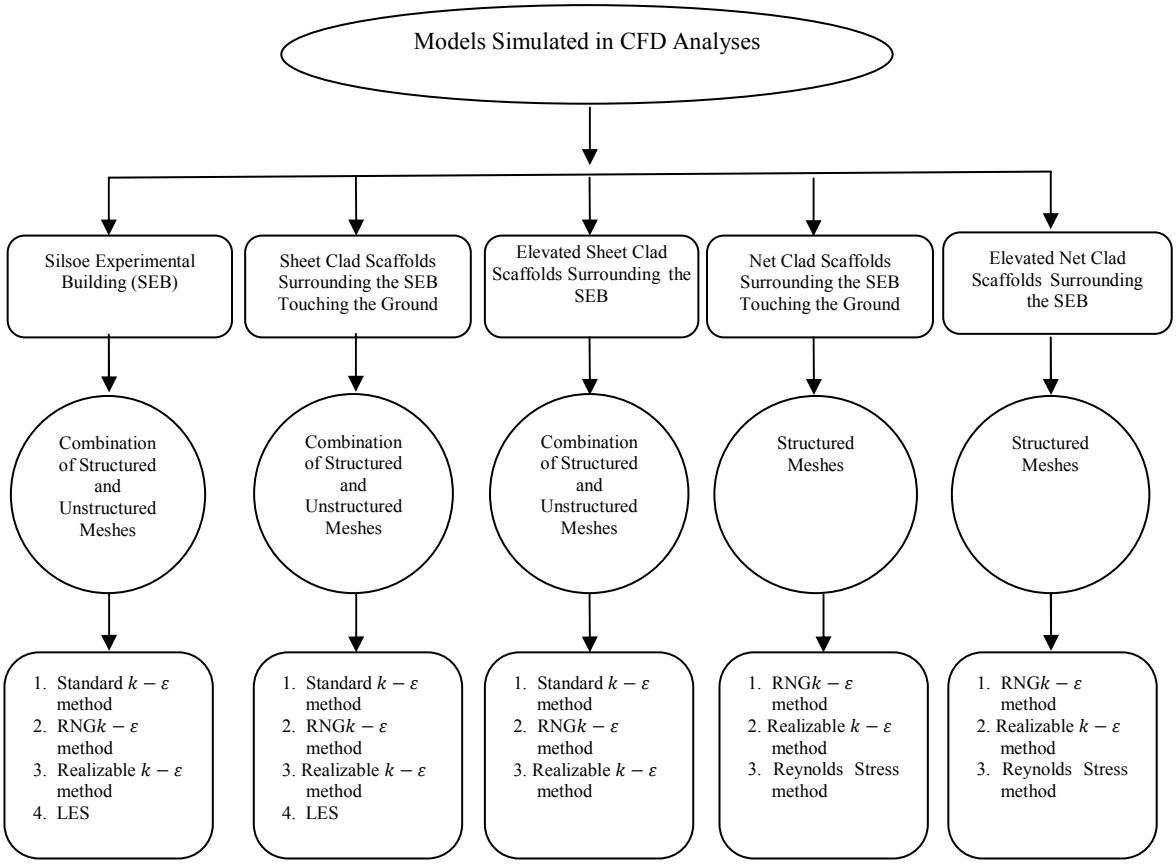

Figure 4.12 Flow chart showing the computational fluid dynamics techniques used for different models

CHAPTER 5
Wind and CFD Simulation

5.1 Introduction

This chapter discusses and provides a detailed justification for wind-tunnel simulations based primarily on the duplication of the turbulence intensities and the small scale turbulence of the incident flow acting on a test building erected at the Silsoe Research Institute Site [5.1]. 'Less emphasis has been placed on the duplication of the integral scale of turbulence, as duplication of both scales requires equality of the Reynolds numbers that cannot be achieved in the wind-tunnel easily' [5.2]. The simulated data in the wind-tunnel has been used for the inflow boundary conditions, the outflow boundary conditions, near wall treatment, etc. for the CFD analysis. Detailed solution strategies adopted for successful solutions for the CFD analyses of the problems are discussed. A flow chart showing the research methodologies used for the study on various models are shown in Figure 5.1.

5.2 Silsoe Full-Scale Experimental Data

The full scale Silsoe Experimental Building shown in Figure 5.2(a) was situated at the Silsoe Research Institute (SRI) in an exposed position in relatively flat terrain in South Bedfordshire. It was constructed in the late 1990s to allow the comparison of full scale rather than model scale wind tunnel data. The Silsoe Experimental Building (SEB) was positioned so that the boundary layer was generated from a fetch consisting of short grass with an effective roughness length of 0.006m - 0.01m. Checks undertaken in previous years have shown that the effective roughness length of the fetch is constant due to regular cutting of the grass [5.3].

The cube could be rotated through 360^{o} and pitched on the horizontal axis by 5^{o}. The cube surface consisted of sheet metal cladding with a smooth plastic coating to afford protection and avoid changes of the surface roughness due to rust. A photograph of the cube can be seen in Figure 5.2(b).

The cubical SEB was instrumented with surface tapping points on a vertical and horizontal centreline section on the windward face, roof and leeward face with additional tappings on

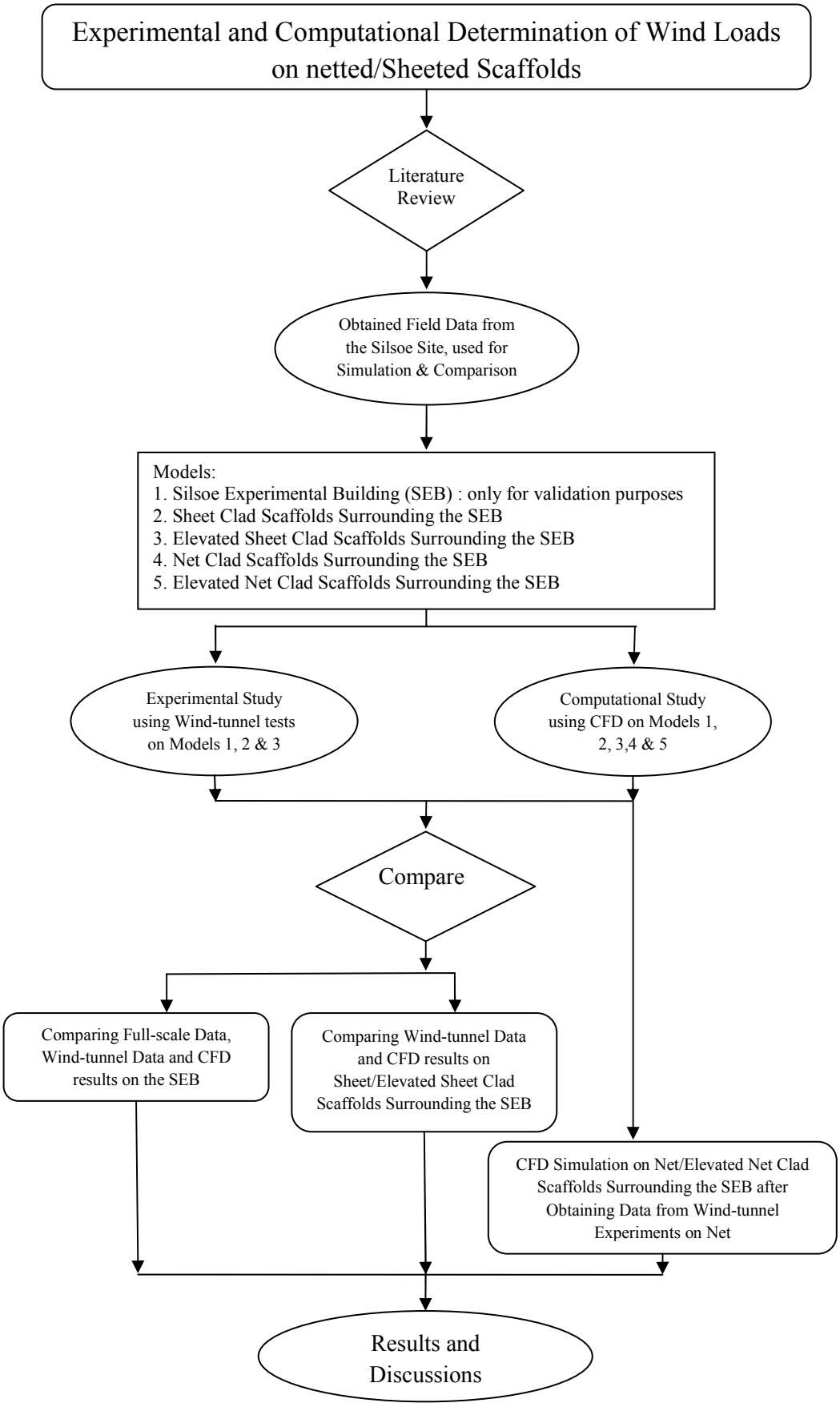

Figure 5.1 A flow chart showing the research methodologies used for the study on various models

(a) Open terrain with full scale buildings **(b) Cubical SEB**

Figure 5.2 Silsoe Experimental Buildings [5.3]

one quarter of the roof. 'Simultaneous measurements could be made of 32 pressures around the cube and the wind dynamic pressure and direction could be derived simultaneously from an ultrasonic anemometer positioned 25 m upstream of the building at roof height' [5.4]. The pressure tap locations could also be used to obtain data when the cube was skewed at 45^o to the incident wind. 'The tapping points were constructed of simple 7mm diameter holes (a size sufficient to prevent water blocking the tapping points) and the pressure signals were transmitted pneumatically, using a 6mm internal diameter plastic tube to transducers mounted centrally within the cube. Tube lengths of up to 10 metres were used in this system giving a frequency response of 3dB down at 8Hz [5.5]'.

The fully recorded information consisting of simultaneous measurements of the pressures at a sampling rate of 4.17 samples per second (~5Hz) together with three components of the wind speed. These were processed to give all the required experimental data including mean, fluctuating and spectral properties and can be found in the work by Richards et al [5.4]. A 36 minutes record length he used (9000 samples) which he sub-divided into three 12 minute segments. For some of the runs the cube was rotated to 45^o clockwise so that the instrumented corner could be towards the prevailing winds. In order to investigate the roof pressure distribution, measurements could be carried out with the corner roof taps in a variety of orientations. A polynomial fit was used to enable actual measurements of wind speed and direction to be manipulated to give a full quasi-steady prediction of surface pressure.

The velocity profile at the Silsoe Research Institute site (as shown in Figure 5.3a) was measured at various times [5.4] and is well matched by a simple logarithmic profile with a roughness length z_o = 0.006 - 0.01 m. This means that the cube had a Jensen

number of 600-1000. The longitudinal turbulence intensity at the roof height was typically 19% [5.4] as shown in Figure 5.3b.

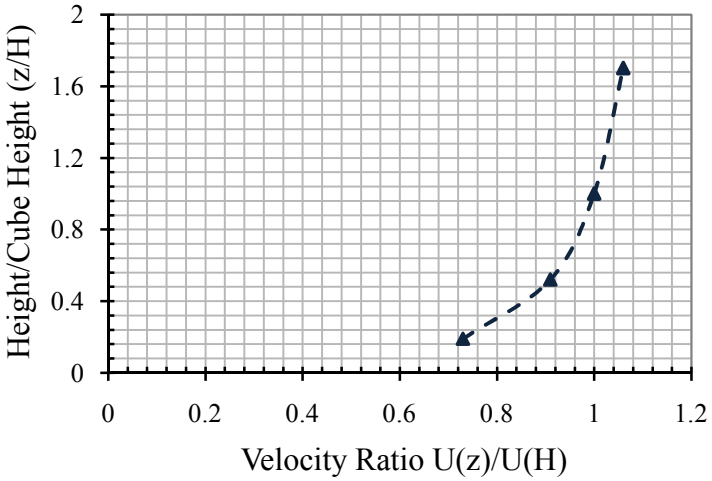

(a) Velocity profile

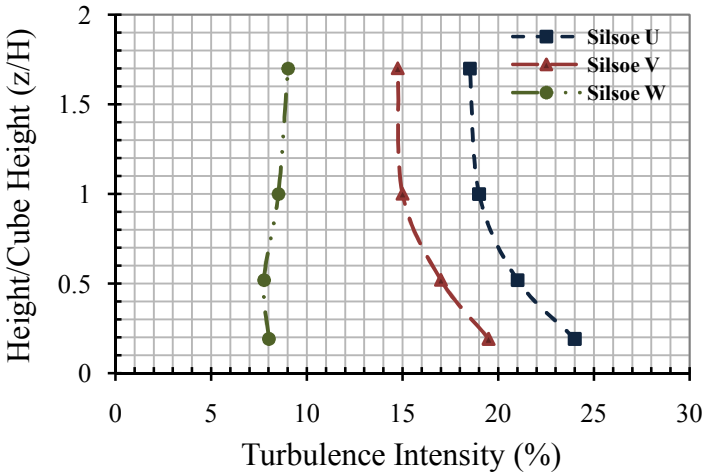

(b) Wind turbulence in all the three directions

Figure 5.3 Wind profile and wind-turbulence at Silsoe site

5.3 Description of Problem and Mode of Analysis

Both experimental (testing models in wind-tunnel) and computational (using computational fluid dynamics) methods have been used in this thesis to determine the forces on the scaled models. Models considered for wind-tunnel and computational fluid dynamics techniques are described below:

There were three wind-tunnel experiments conducted for finding the forces on the scaled model:

(i) A scaled cubical SEB (this test was undertaken for validation and calibration purposes) and is shown in Figure 5.4.
(ii) A sheet clad scaffold surrounding the scaled cubical SEB and shown in Figure 5.6.
(iii) An elevated sheet clad scaffold surrounding scaled cubical SEB and shown in Figure 5.9.

Both 2D and 3D models were simulated to find the pressure forces by using Computational Fluid Dynamic (CFD) techniques.

The 2D models used for CFD simulation are listed here. The complete analyses on bare pole scaffolds are described in chapter 4 where as those on 2-D net cladded scaffolds are described in chapter 6.

(i) A 2D bare pole scaffold.
(ii) A 2D bare poles scaffold placed along the flow direction.
(iii) A 2D bare poles scaffold along and across the flow direction.
(iv) A 2D bare poles scaffold surrounding a 2D plan of the cubical building.
(v) A 2D plan of a cladded permeable net scaffold (Simulated as a porous jump) surrounding a cubical building.

The 3D models used for the CFD simulation are:

(i) A scaled cubical SEB and shown in Figure 5.4.
(ii) A sheet clad scaffold surrounding a scaled SEB and shown in Figure 5.6.
(iii) An elevated sheet clad scaffold surrounding a scaled SEB and shown in Figure 5.9.
(iv) A net clad scaffold surrounding a scaled SEB and shown in Chapter 7.
(v) An elevated net clad scaffold surrounding a scaled SEB and shown in Chapter 7.

5.4 Experimental Solution Strategies

5.4.1 Position of Pressure Taps for the Experimental Models

The building models were fabricated using 2 mm thick white acrylic plastic. The stainless steel tubing pressure taps used were 10 mm long, 1.00 mm external diameter and 0.9 mm internal diameter. They were inserted into holes drilled in the plastic

sheeting with one end of the tap flush with the wall/roof surface. The tubing for measuring the pressures consisted of 300 - 400 mm vinyl tubes.

In Experiment Number 1 the observations were recorded on 1:30 scaled model of the scaled cubical SEB of dimension 200 x 200 x 200 mm as shown in Figure 5.4 both on the roof and the South walls. The location of pressure taps on the roof and on south vertical wall face are shown in the Figures 5.5a and 5.5b. The model was tested at every 15 degrees angle of rotation of the turn-table to produce a set of 24 observations around the building. A total of 61 taps (31 taps on the roof + 30 taps on a vertical wall face) were used for the first phase of experiment. The coding that was used throughout the experiments for tap positions was a four digit number.

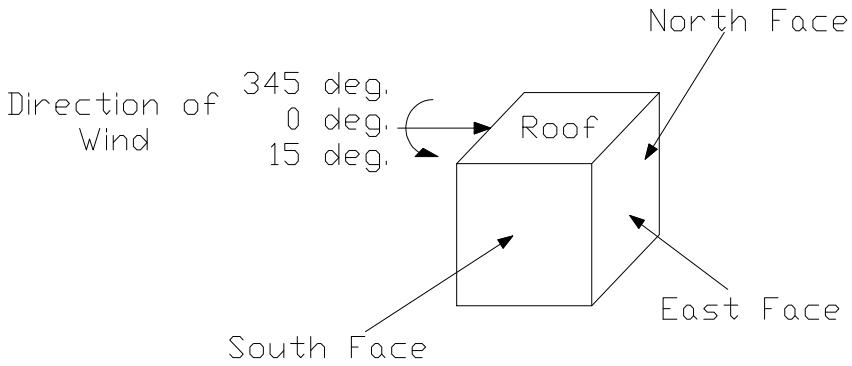

Figure 5.4 Scaled cubical SEB

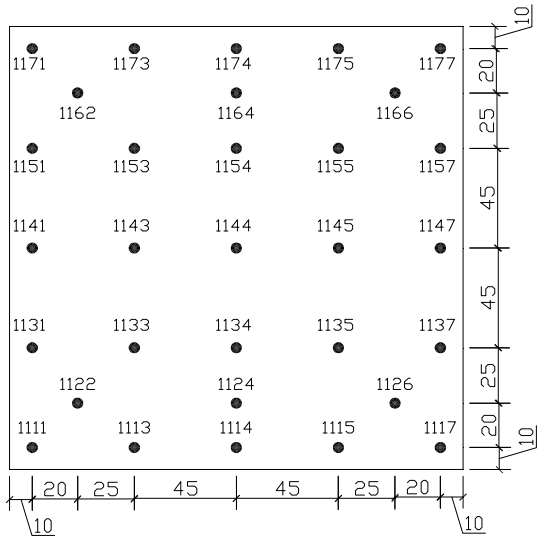

Figure 5.5(a) Pressure tap locations on roof

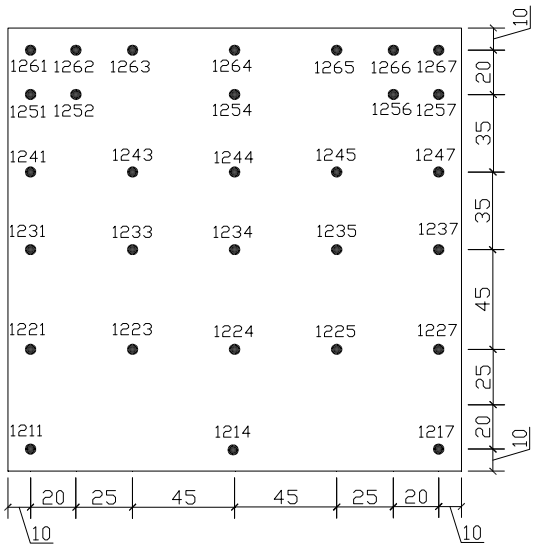

Figure 5.5(b) Pressure tap locations on the south wall face

In Experiment Number 2 the observations were recorded (two sets) on the sheet clad scaffolds surrounding scaled cubical SEB as shown in Figure 5.6. In set 1 the

observations were recorded on the outer south face, whereas, in set 2 the observations were recorded on the inner south face respectively and the location of pressure taps on the outer and inner south face of the sheeting are shown in Figure 5.7a and Figure 5.8a. Additional pressure taps were installed on the other two faces (North and East faces) to counter check the recordings of pressures and is shown in Figures 5.7b, 5.7c and 5.8b, 5.8c respectively. In a similar manner to Experiment 1 the observations were recorded by rotating the models at every 15 degrees until a complete rotation had occurred. In this case a total of 44 taps (36 taps on the outer main face of the sheeting + 4 taps each on the other two face of the sheeting) were used for the experiment.

In set 2 the distances shown in Figure 5.8a, b, c for the location of pressure taps were from the outer edge of the sheeting. Also the top 7 mm of the sheeting were tapered from the inside as shown by hatched lines.

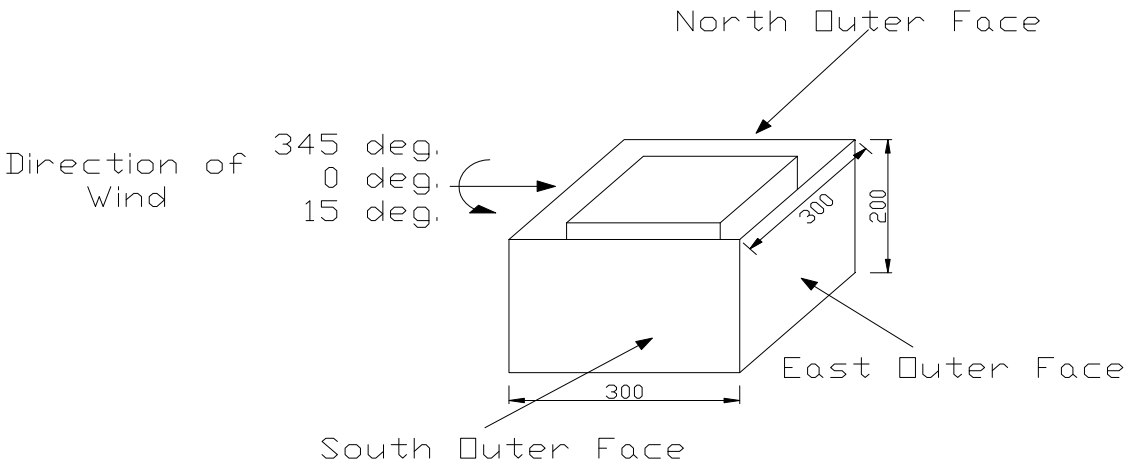

Figure 5.6 Scaled cubical SEB surrounded by sheet clad scaffold

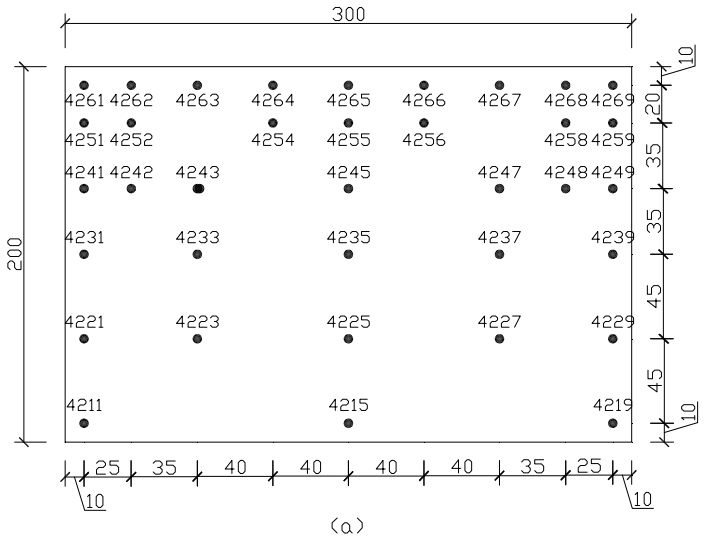

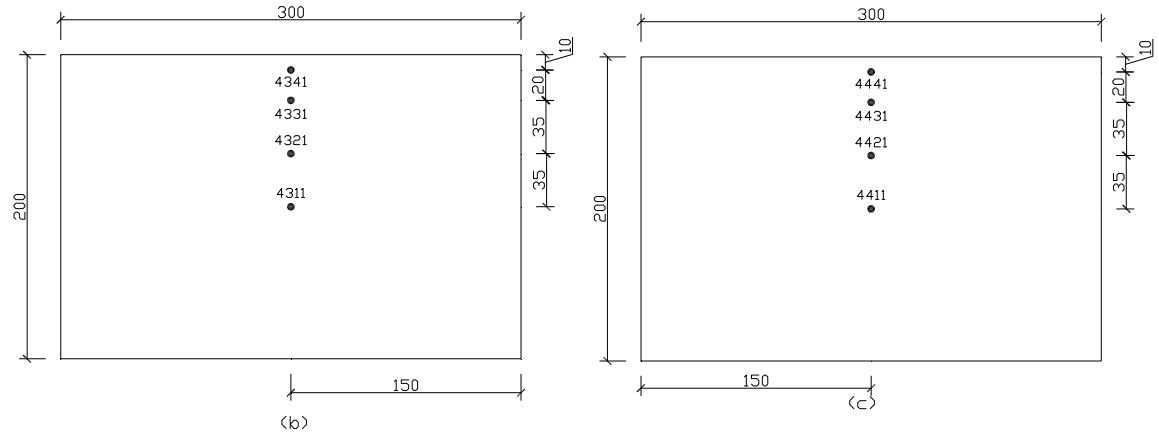

Figure 5.7a Pressure tap locations on the outer south face of the sheeting corresponding to Figure 5.6.

Figure 5.7b Pressure tap locations on the outer east face of the sheeting corresponding to Figure 5.6.

Figure 5.7c Pressure tap locations on the outer north face of the sheeting corresponding to Figure 5.6.

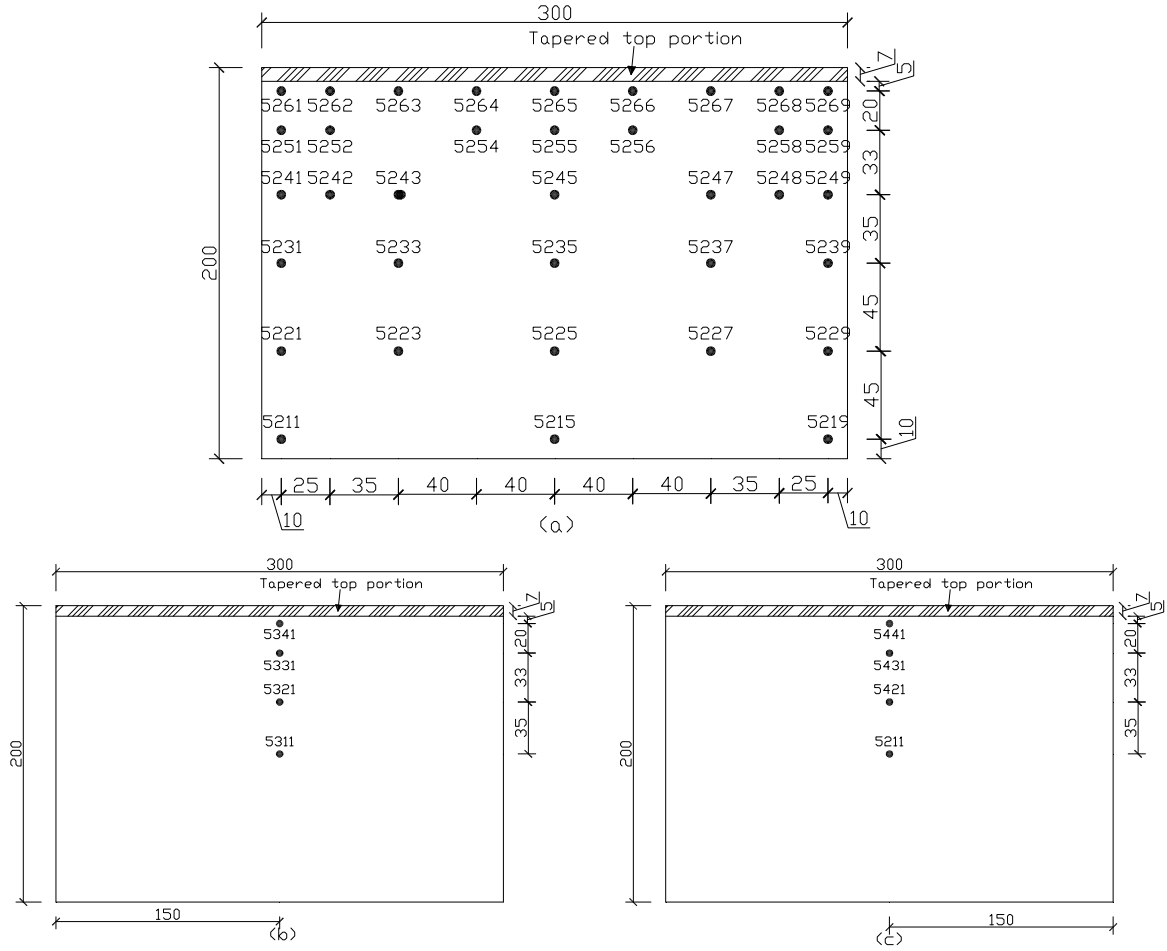

Figure 5.8a Pressure tap locations on the inner South face of the sheeting corresponding to Figure 5.6.

Figure 5.8b Pressure tap locations on the inner East face of the sheeting corresponding to Figure 5.6.

Figure 5.8c Pressure tap locations on the inner North face of the sheeting corresponding to Figure 5.6.

In Experiment Number 3 the observations were recorded (two sets) on the elevated sheeting surrounding scaled cubical SEB as shown in Figure 5.9. The bottom 33.3 mm (corresponding to a full-scale prototype of 1m) of the sheeting was open. In set 1 the observations were recorded on the outer South face, whereas, in set 2 the observations were recorded on the inner South face respectively and the location of pressure taps on the outer and inner South face of the sheeting are shown in Figure 5.10a and Figure 5.11a. Once again, additional pressure taps were installed on the other two faces (North and East face) to counter check the recordings of pressures and are shown in Figures 5.10b, c and Figures 5.11b, c respectively.

The distances of the pressure taps shown in Figure 5.11a, b, c were from the outer edge of the sheeting. The top 7 mm and bottom 7 mm of the sheeting were tapered from the inside as shown in Figure 5.11a, b, c. The models were again tested at every 15 degrees angle of rotation of the turn-table. In this case a total of 61 taps (47 taps on South inner face of the sheeting + 7 taps each on North and East vertical face of the sheeting) were used for the experiment.

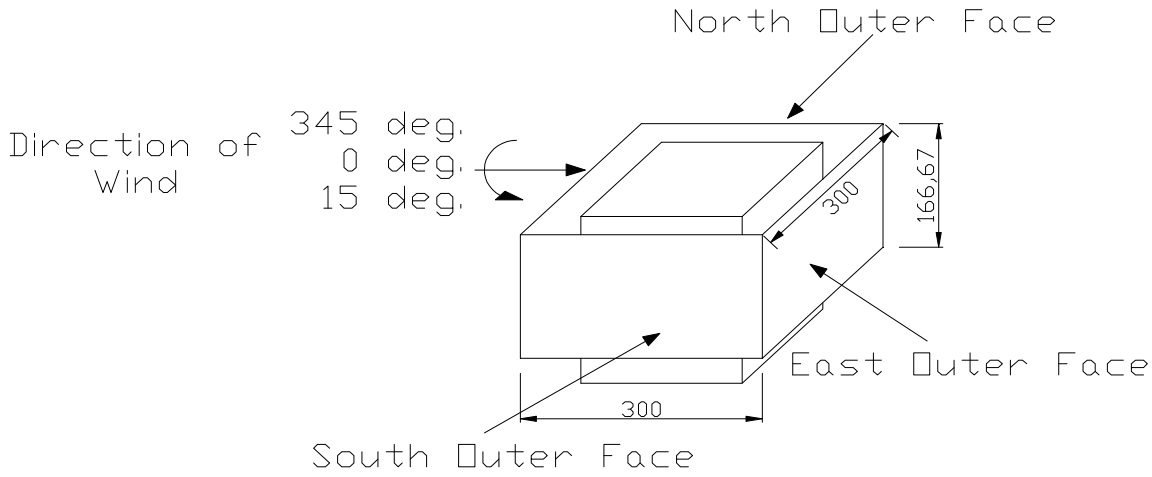

Figure 5.9 Scaled cubical SEB surrounded by elevated sheet clad scaffold

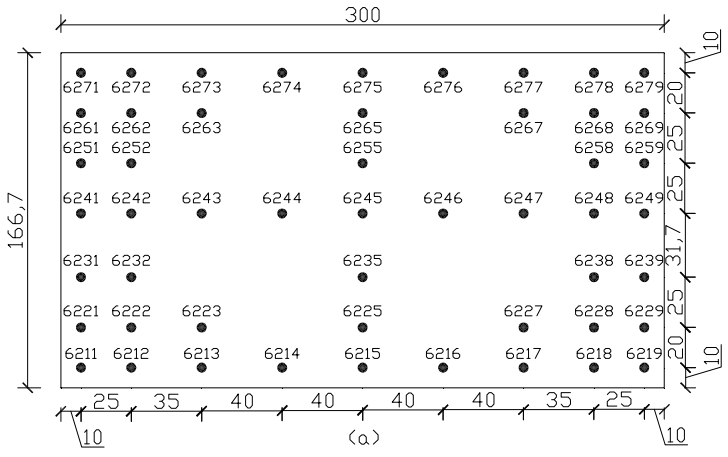

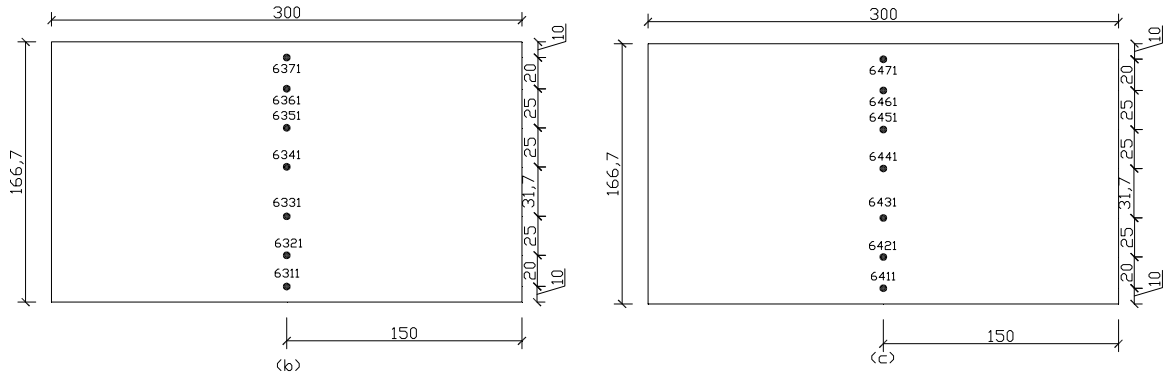

Figure 5.10a Pressure tap locations on the outer South face of the sheeting corresponding to Figure 5.9.

Figure 5.10b Pressure tap locations on the outer North face of the sheeting corresponding to Figure 5.9.

Figure 5.10c Pressure tap locations on the outer East face of the sheeting corresponding to Figure 5.9.

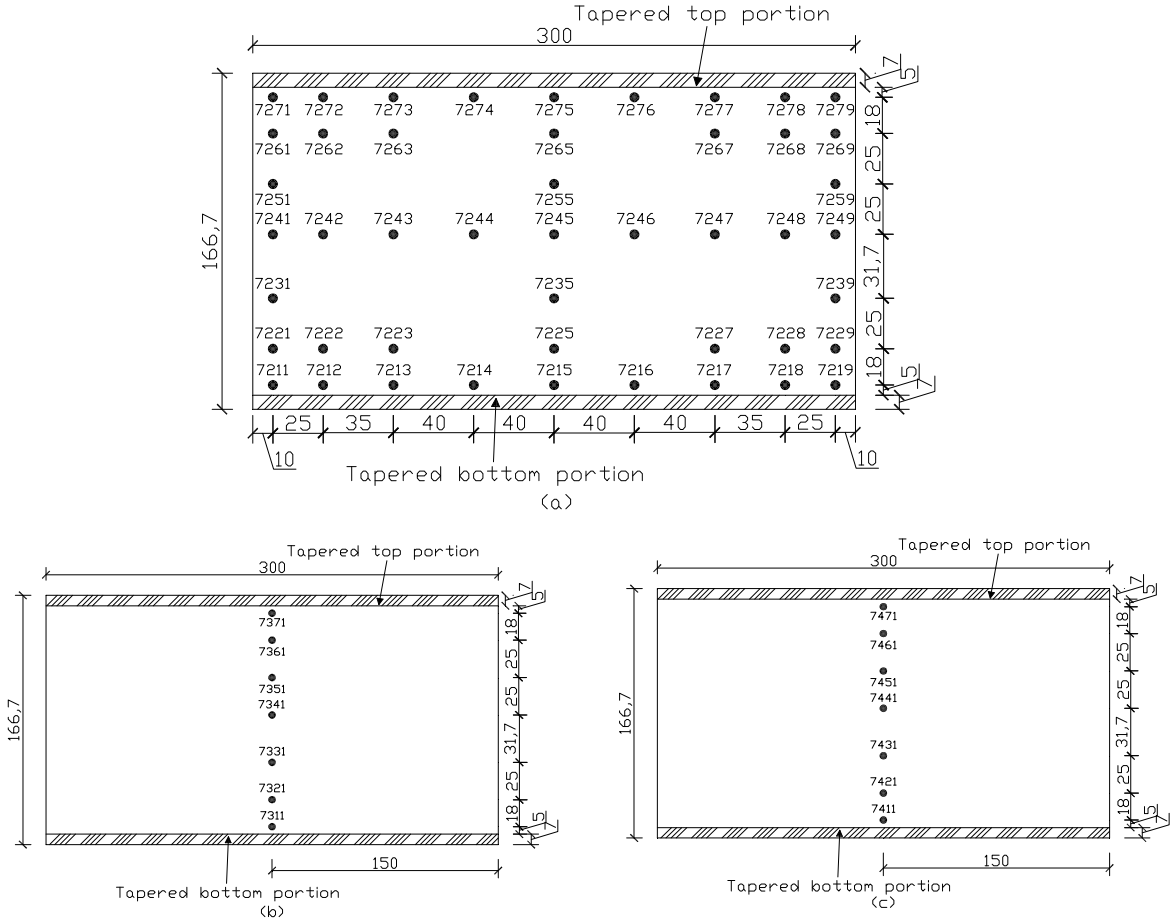

Figure 5.11a Pressure tap locations on the inner South face of the sheeting corresponding to Figure 5.9.

Figure 5.11b Pressure tap locations on the inner North face of the sheeting corresponding to Figure 5.9.

Figure 5.11c Pressure tap locations on the inner East face of the sheeting corresponding to Figure 5.9.

5.4.2 Testing Facilities and Equipments for Wind Pressure Study

The wind-tunnel used for testing the models was 26m long atmospheric boundary layer type as shown in Figure 5.12. This wind-tunnel was operated by Red Consultants Ltd, Hong Kong, working under the auspices of Department of Civil Engineering, Hong Kong Polytechnic University, Hong Kong [5.6]. The test section was 17.5 m long, 3.3 m wide and 2.2 m high. The roof of the test section could be raised up to a maximum height of 0.6 m to keep the pressure constant in longitudinal direction if required. The diameter of the turn table was 2.80 m. The maximum wind speed in the test section was around 15 m/s. The atmospheric boundary layer was simulated by using artificial roughness as shown in Figure 5.13 with spires and baffles as shown in Figure 5.14. The wind pressures were measured by a high frequency Esterline's electronic pressure scanner as shown in Figure 5.15. Simultaneous measurement of wind pressure up to 64 locations could be achieved with this pressure scanner.

Figure 5.12 Wind-tunnel

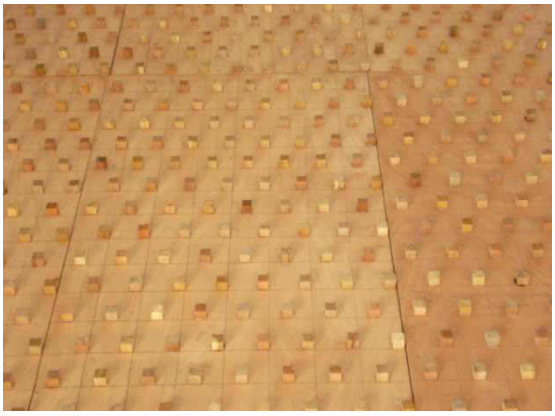

Figure 5.13 Artificial roughness

Figure 5.14 Spires and baffles in wind-tunnel Figure 5.15 Esterline's pressure scanner

5.4.3 Calibration and Validation Studies

It is necessary to check the flow characteristics and to calibrate them before using them for measuring the pressure coefficients on the model. The objective of checking the flow characteristics was to verify up to what level the predicted and desired flow characteristics could be achieved in the test section.

5.4.3.1 Tunnel Speed Setting

Before any calibration test were carried out, the wind speed in the tunnel should be properly set. For the purpose of wind tunnel speed calibration, four static pressure sensor ports each on the upstream and downstream of the contraction cone walls were installed. The ports were located at the centre of each wall. The pressure from four static pressure ports for both upstream and downstream stations, were averaged by interconnecting them. Pressure drop in 'Δp' (in mbar) across the contraction cone from upstream and downstream ports were measured using a digital manometer. A pitot static probe mounted at the centre of the test section was used to measure the dynamic pressure 'q_∞' by using another digital manometer. The pressure drop 'Δp' across the contraction cone is plotted against 'q_∞' is shown in Figure 5.16.

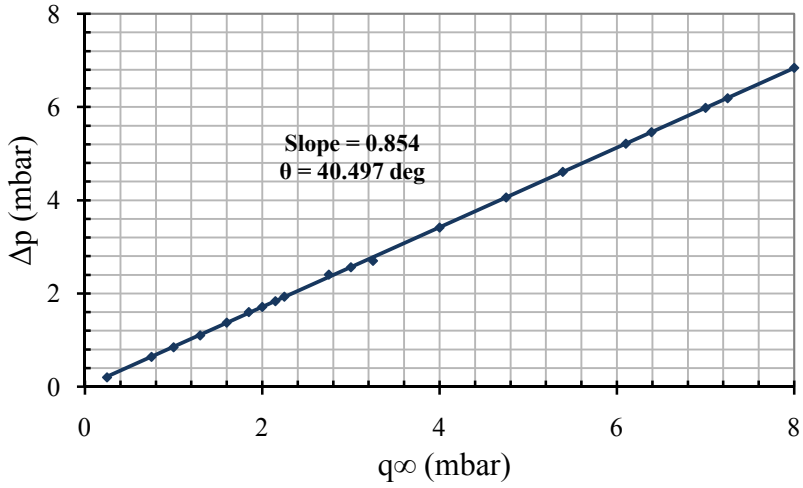

Figure 5.16 Speed calibration of wind-tunnel

5.4.3.2 Axial Static Pressure Gradient

The axial static pressure gradient affects the accuracy in predicting drag on a model in a wind-tunnel and an empirical correction is generally applied to the measured drag

values based on this parameter. However, this parameter should be as small as possible in the test section.

For the measurement of axial static pressure gradient an aluminium pipe of 50 mm diameter 3 m long was cut from the centre longitudinally and laid over the test section floor on either side from the centre of the turn-table. Equally spaced (200mm) 11 pressure ports along the length of the pipe were provided. The pressure ports were connected to the scanner with the help of nylon tube and the scanner was kept below the test section. Surface static pressures from the 11 ports were measured with reference to atmospheric pressure using an ESP -32 port electronic pressure scanner. Figure 5.17 gives the plot of $(p - p_{atm})/q_{\infty}$ *Vs* X for a tunnel speed of 5 m/sec. Near zero static pressure gradients exists in the wind-tunnel which is ideal.

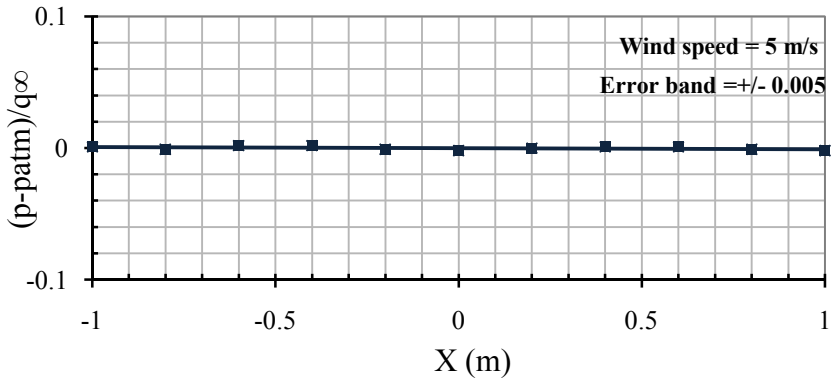

Figure 5.17 Static Pressure variations along the test section

5.4.3.3 Total Pressure Variation

To determine the total pressure variation along the wind tunnel height a pressure rake spanning half the tunnel section width was made using a 3-axis traverse system. The total pressure was measured by using a 32 port ESP pressure scanner. Atmospheric pressure was used as a reference. The accuracy of the differential pressure-measuring sensor was ± 0.03 mbar. Figure 5.18 shows the variation of $(p_0 - p_{atm})/q_{\infty}$ along the tunnel height for different span-wise locations. It can be observed that variation of 'p_0' with height is 0.3%.

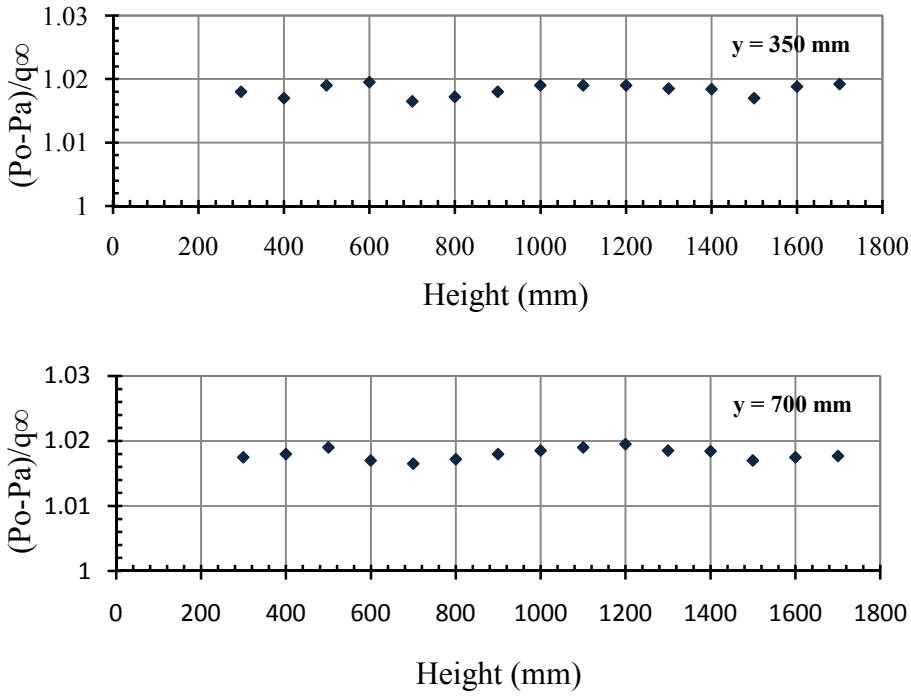

Figure 5.18 Variation of total pressure across tunnel height at different span-wise locations

5.4.3.4 Flow Angularity

The flow angularity in pitch and yaw planes, was measured by using a Standard Dynamic Model (SDM) attached to a sting balance. The flow angle calibration was obtained by the rotation of the drag polar. This method gives the flow angle of a finite region rather than a point.

The SDM model was instrumented with a tilt sensor to measure pitch angle and an internal balance to measure forces. For measuring flow angularity the test were carried out at model roll angles 0^o, 90^o, 180^o, and 270^o. Results of these measurements are shown in Figure 5.19 and Figure 5.20. Figure 5.19 shows the lift coefficient data for 0^o and 180^o roll angles. The intersection of the two curves in this figure gives the flow angularity in the pitch plane. The pitch plane flow angularity is observed to be -0.28 degree. Similarity, from Figure 5.20, which shows results for model roll angles 90^o and 270^o, yaw plane flow angularity is found to be 0.25 degree.

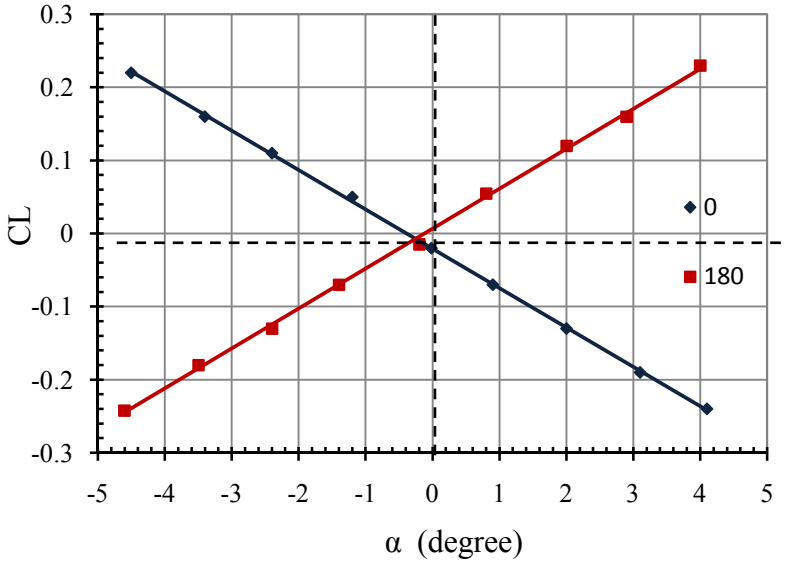

Figure 5.19 Variation of lift coefficient with angle of attack in pitch plane for model roll angles 0° and 180°

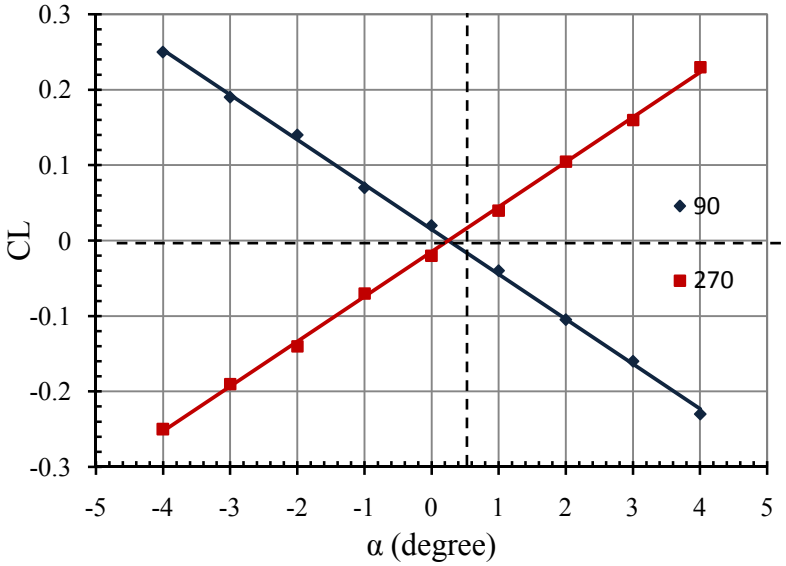

Figure 5.20 Variation of lift coefficient with angle of attack in yaw plane for model roll angles 90° and 270°

5.4.4 Experimental Program

To obtain the wind pressure distribution on the exterior cladding of the structures, 1:30 scale acrylic models of the structures were constructed to include all surface details. Sufficient numbers of pressure transducers were installed on the model structures to comply with the requirement. It was the rainy season in Hong Kong during experimental work. Most of the time it was either raining or the humidity of the air was more than 90% during recording of most of the observations in the wind-tunnel.

Natural wind was developed for the 1:30 scale model to simulate the wind over open country terrain using roughness blocks of different sizes. The simulation was done on the basis of Silsoe Research Institute (SRI) full-scale data. The velocity profile and the longitudinal turbulence intensities simulated in the wind-tunnel and data obtained from SRI site [5.4] shown in Figure 5.21 and 5.22. The wind history at model height recorded for 60 seconds in wind-tunnel are shown in Figure 5.23. Pressure measurements were carried out by using Esterline's 64 port electronic pressure scanner. 'The outputs of the sensors were electronically multiplexed through a single onboard instrumentation amplifier at rates up to 20,000 Hz using binary addressing. The multiplexed amplified analog output was capable of being driven through long lengths of cable to a remote A/D converter [5.7]'. The sampling rate was kept at 100 samples per second per channel and the duration of each run was kept to 249 seconds. This was equivalent to one hour data in the field. The pressure measurements obtained and plotted in Figure 5.22 were mean pressures at a given height as they were measured by pitot tube as opposed to the sonic anemometer pressure readings used at Silsoe.

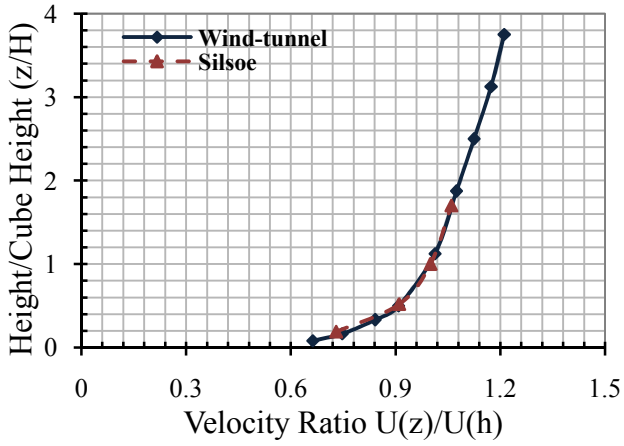

Figure 5.21 Mean velocity profile of full-scale and wind-tunnel [5.4]

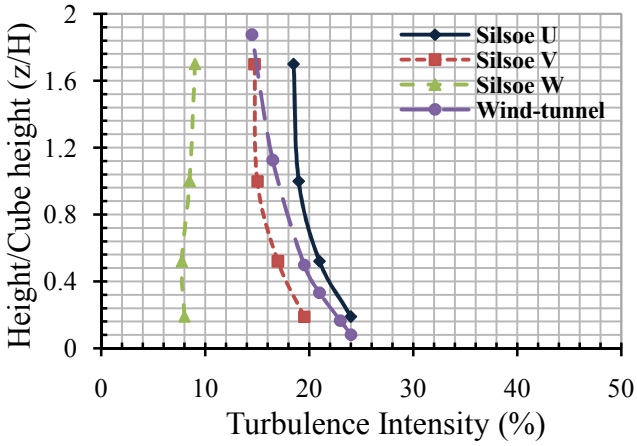

Figure 5.22 Turbulent intensity profile comparison between full-scale and wind-tunnel [5.4

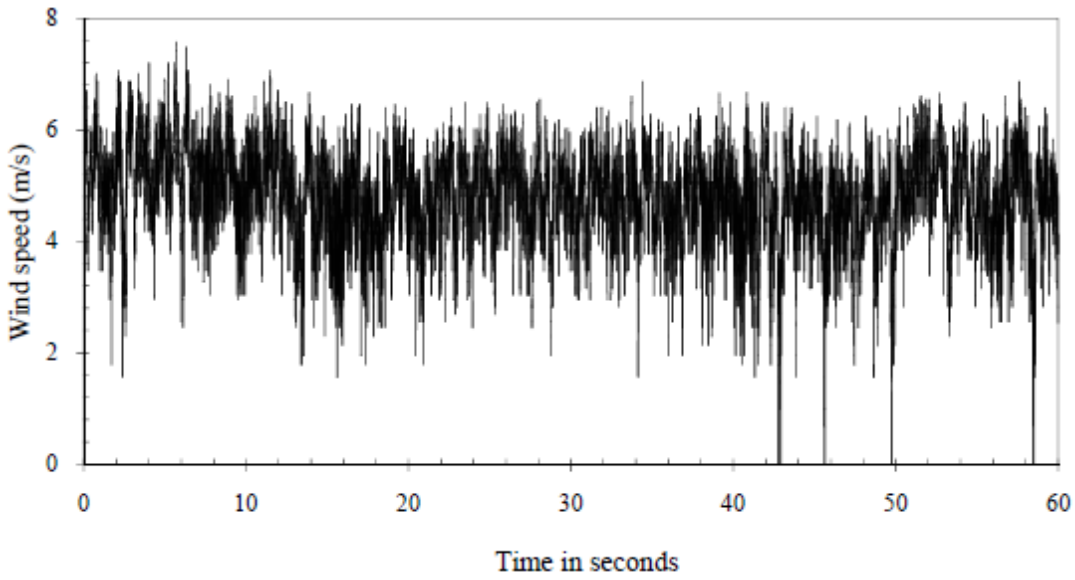

Figure 5.23 Wind history at model height

The mean longitudinal wind speed profile measured in the wind-tunnel was in good agreement with the SRI full-scale profile with a power-law exponent of 0.17. The longitudinal turbulence was slightly less than the SRI full-scale data. A lot of iterations (by changing the size and position of roughness) were done to achieve the same turbulence at the model height during the testing process but was not possible to achieve the exact turbulence.

The small-scale turbulence content (S) which is defined as $S = \left[nS_u(n) / \sigma_u^2 \right] \cdot \left[\sigma_u / U \right]^2 \times 10^6$ evaluated at $n = 10U / L_p$ where, n is frequency, $S_u(n)$ is spectral density, σ_u is the standard deviation of the longitudinal mean velocity (U) and L_p is the characteristic model dimension, was found to be 89. The model eave height was taken as the characteristic dimension. The reduced spectra plot at the model eave height is shown in Figure 5.24. The integral scale in the wind tunnel was also evaluated at the model eave height for the longitudinal wind speed and found to be 0.30 m. The auto-correlation plot to find the integral scale is shown in Figure 5.25. The integral scale is defined as area under the auto-correlation curve of the fluctuating velocity component. Since the auto-correlation measurements are usually temporal measurements at a fixed point, Taylor hypothesis can be used to convert the area under the auto-correlation function into a unit of length as given by the equation given below:

$$L_{ux} = U \int_0^\infty R(\tau) d\tau \tag{5.1}$$

where L_{ux} is the integral length scale, U is the mean wind speed, τ is the time and $\int_0^\infty R(\tau)d\tau$ is the area under the auto-correlation curve [5.6].

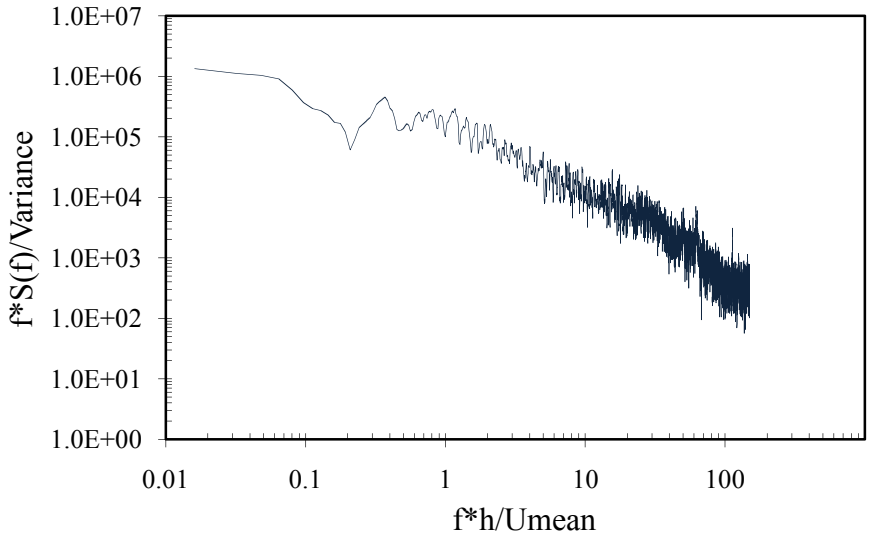

Figure 5.24 Normalised reduced spectrum plot at eave height

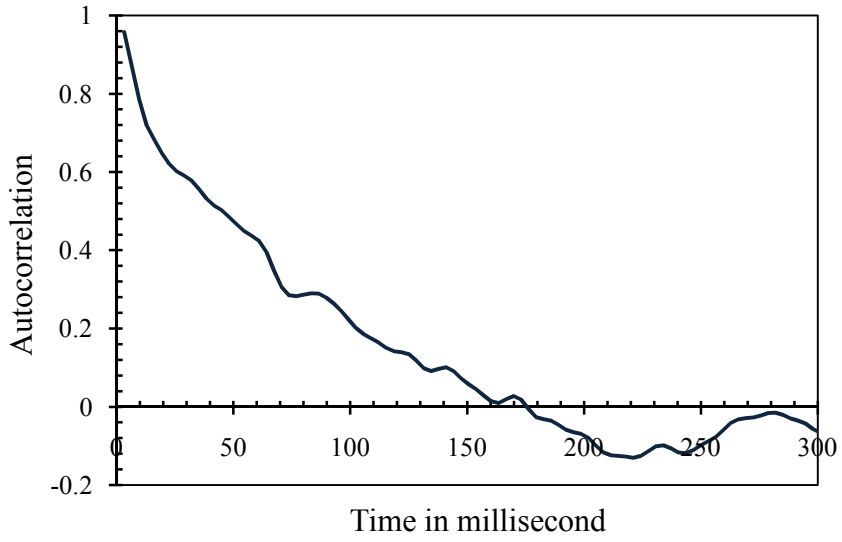

Figure 5.25 Auto-correlation plot at eave height

The major problem with this integral scale method is that the auto-correlation function is often highly oscillatory, and the area under the curve tends to cancel out, which will give an unrealistically small length scale. A common method of overcoming this problem is to define the integral scale as the area under the auto-correlation curve for the value occurring before the first zero crossing and procedure was adopted to calculate the integral length scale of the wind-tunnel experiments.

For each run, wind pressures measured on the models were expressed in the form of a non-dimensional pressure coefficient, defined as follows:

$$C_p(t) = \frac{p(t) - p_0}{\frac{1}{2}\rho U^2} \tag{5.2}$$

where, p_0 is the static (ambient/atmospheric) reference pressure and it is chosen as the pressure of a point far away from the building model (the reference pressure were measured at mid height of the tunnel), U the mean longitudinal wind speed at the reference height (eave height) and ρ the air density.

The instantaneous wind pressures at each location were measured at 24 wind directions in 15 degree intervals. The mean, RMS (root-mean-squares) and the maximum and minimum pressure coefficients, with reference to the gradient wind pressure, were derived from the wind tunnel data. The maximum and minimum pressures were determined by using the method proposed by Cook and Mayne, 1979 [5.8]. The maximum and minimum pressures are representative of the wind pressure of 4 minutes 9 seconds (equal to hourly wind data in the field) averages.

5.5 Computational Solution Strategies

5.5.1 Computational Domain and Mesh Arrangement

The dimension of the cubical Silsoe Experimental Building was 6 m x 6 m x 6 m and the reduced scale used here for the simulation is 1:30. This model was studied for calibration and validation purposes only. Apart from this, a model of a sheeted clad scaffold with sheeting 1.5 m away from the building face was simulated (as described in section 5.3). The Reynolds numbers involved in the simulations were in the range of 0.72×10^5 to 1.09×10^5 for both wind-tunnel experiments and computational analyses. As shown in Figure 5.26 and 5.27 the computational domain covers 29D or 29B (where D is the width of the building and B is the outer dimension of sheeted/netted clad scaffold) in the stream wise X direction $\left[-6.5 < \left(x/D \, or \, x/B\right) < 22.5\right]$, 13D or 13B in the lateral or normal (Z) direction $\left[-6.5 < \left(x/D \, or \, x/B\right) < 6.5\right]$ and 3H to 4H in the vertical (Y) direction. The percentage obstructions were 2.564 and 1.92 for the two cases described below which are less than the maximum 3% of obstruction required for

good wind-tunnel models. The reason for such a choice is to eliminate the flow obstacle effect on the inflow and outflow boundary conditions.

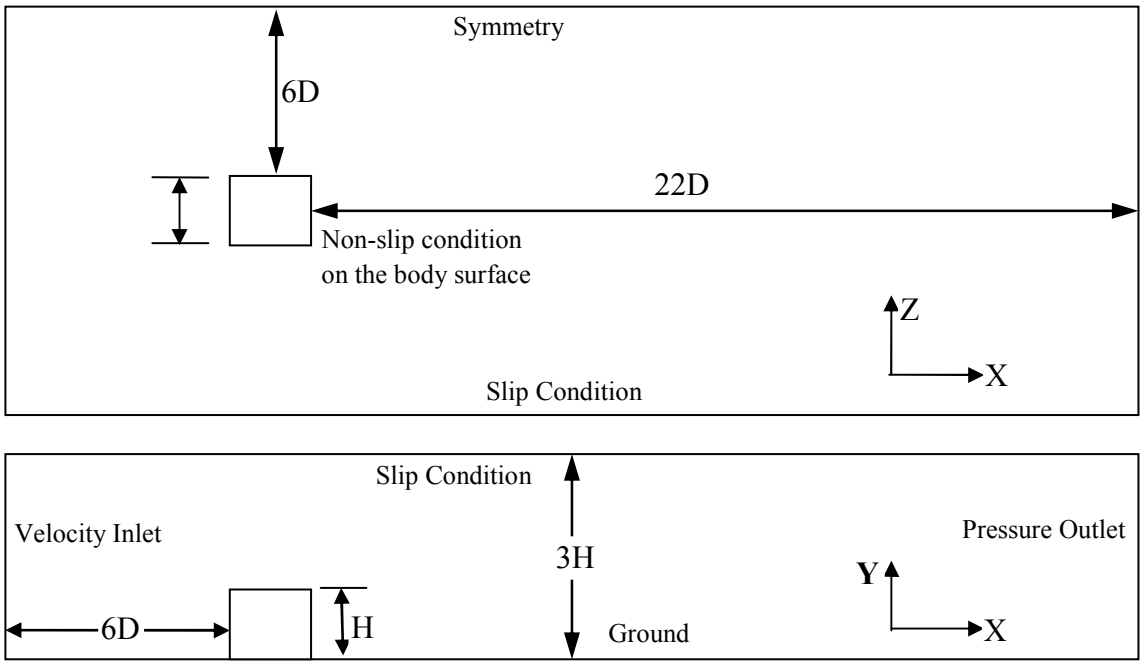

Figure 5.26 Computational domain and boundary conditions for the scaled cubical SEB

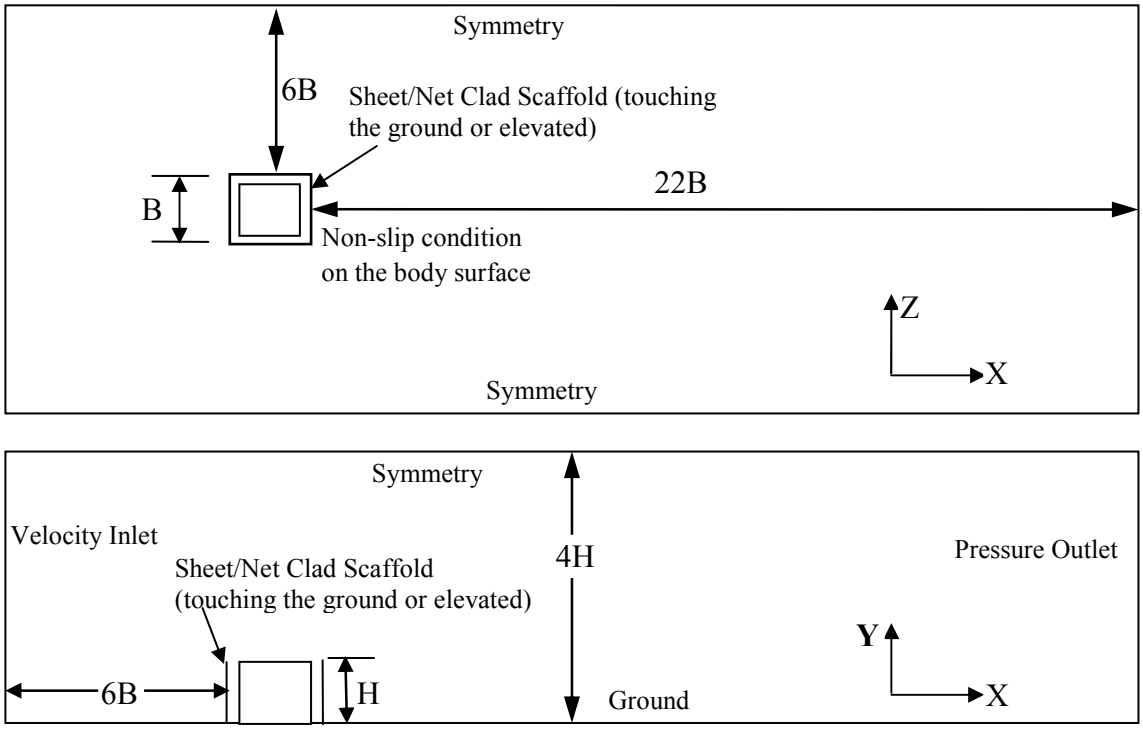

Figure 5.27 Computational domain and boundary conditions for the scaled sheet/net clad (or elevated sheet/net clad) scaffold surrounding the cubical SEB

If the building model is a simple cube, its computational mesh generation is straightforward in consideration of boundary layer conditions and wind attack angle but for the sheeted/netted clad scaffold (touching the ground or elevated) the generation of a quality mesh is very difficult. This can only be achieved by experience and requires a number of iterations to generate a good quality mesh. 'However, the number of mesh elements must be as low as possible for fast and efficient computation. The traditional finite difference method uses a structured grid, which requires a body-fitted grid transformation from the physical domain to the computational domain. The mesh near and aligned with the wall surfaces must be refined and stretched with the viscous boundary layer grid. Because the Fluent 6.30 code which was adopted in this study is based on the finite volume method (FVM), with the capacity of dealing with both structured and unstructured grids in its solver, there are a variety of different methods of mesh generation' [5.9]. Figures 5.28 to 5.32 show the mesh arrangement for all types of model. Two types of meshes, both structured and unstructured, were used in all the models. Unstructured meshes were generated in the core region around the scaled cubical SEB or sheet clad scaffold (or elevated sheet clad scaffold) and structured meshes were generated for the rest of the domain. For the net clad scaffold (or elevated net clad scaffold) structured meshes were used as it was easier to generate. 'This arrangement makes it easier to generate a mesh fine enough in the neighbourhood of the model while keeping the mesh in zones far away from the model surfaces unchanged or in a proper coarse state. An important advantage of this arrangement is that the mesh aligned to the model surfaces does need to be stretched with the wall boundary layer grid as the structured mesh does. Besides, a grid point at a sharp corner is a singular point in a structured grid with Finite Difference Method (FDM), which lead to unphysical wiggles in computation and needs special treatment. However, for Fluent 6.3 code, this can be avoided with the FVM discretisation [5.9]'.

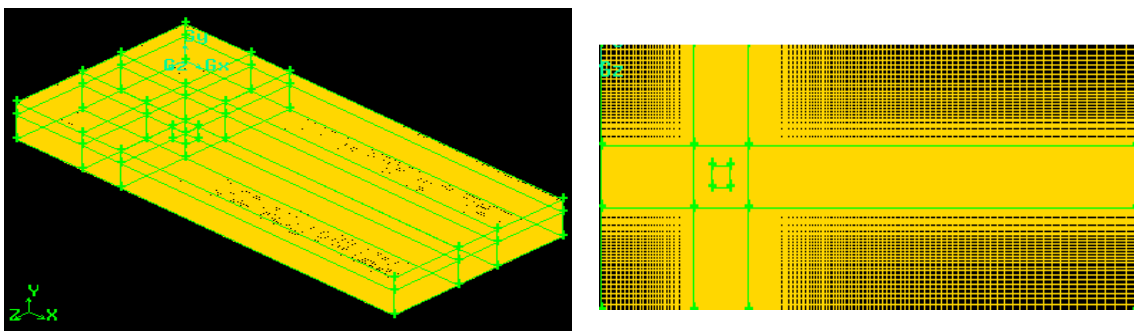

Figure 5.28 Overall grid distribution and grid distribution in plan

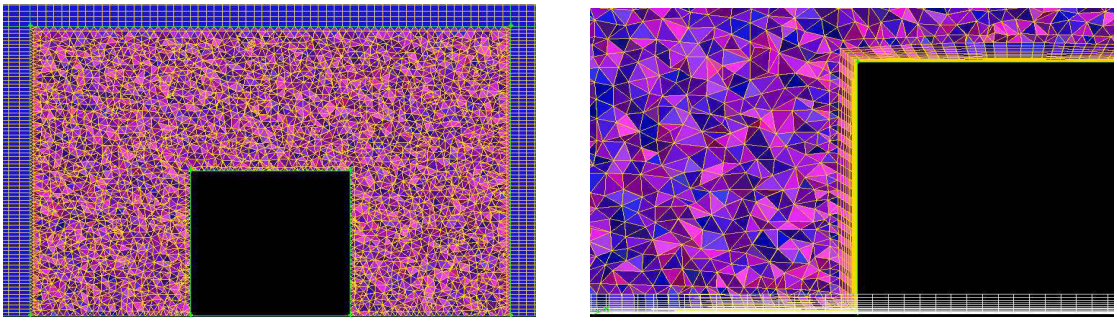

Figure 5.29 Typical mesh arrangements around the scaled cubical SEB with and without boundary layer

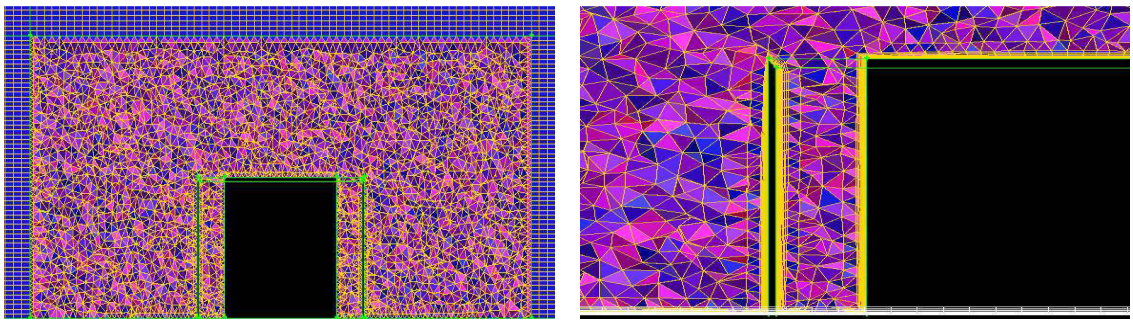

Figure 5.30 Typical mesh arrangements around sheet clad scaffold surrounding SEB with and without boundary layer

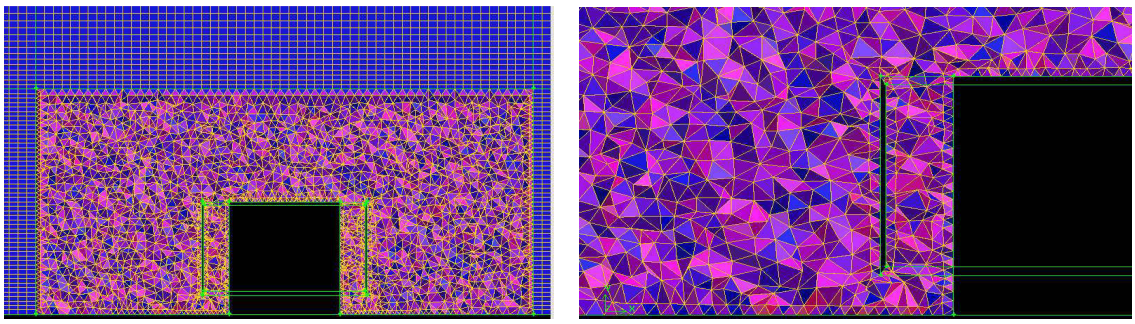

Figure 5.31 Typical mesh arrangements around elevated sheet clad scaffold surrounding SEB

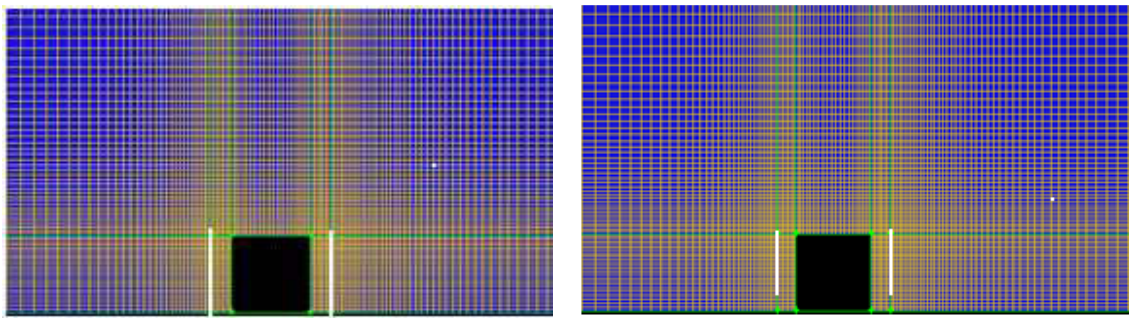

Figure 5.32 Typical mesh arrangements around the net clad scaffold (touching the ground and elevated) surrounding SEB

5.5.2 Near Wall Boundary Conditions (mesh arrangements near walls)

'Turbulent flows are significantly affected by the presence of walls. The mean velocity field is also affected by the no-slip condition that has to be satisfied at the wall. Very close to the wall, viscous damping reduces the tangential velocity fluctuations, while kinematic blocking reduces the normal fluctuations. Towards the outer part of the near wall region, however, the turbulence is rapidly augmented by the production of turbulence kinetic energy due to large gradients in mean velocity field' [5.10]. The $k-\varepsilon$ models, The RSM and the LES models are primarily valid for turbulent core flows (i.e. the flow in the regions somewhat far from walls). Considerations therefore need to be given as to how to make these models suitable for wall-bounded flows [5.11].

'Near wall regions can be largely sub-divided into three layers. In the innermost layer, called the viscous sub-layer, the flow is almost laminar and molecular viscosity plays a dominant role in momentum, heat and mass transfer. In the outer layer, called the fully-turbulent layer, turbulence plays a major role. Finally, there is an interim region between the viscous sub-layer and the fully turbulent-layer where the effects of molecular viscosity and turbulence are equally important. Figure 5.33 and 5.34 below illustrates these subdivisions of the near wall region, plotted in semi-log coordinates' [5.11].

Figure 5.33 Subdivisions of the Near-Wall region [5.11]

(a) Wall function approach (b) Near-wall model approach

Figure 5.34 Near Wall treatments in Fluent 6.30 [5.11]

As discussed in Chapter 4, the majority of the turbulence models can be used in high Reynolds number flows. This requires an economical method of modelling the effects of wall on the momentum and turbulence transport equations. This is particularly important in wind engineering applications as these are often high Reynolds number flows with complex wall bounded geometries.

Normally wall boundary conditions are specified using wall functions. This is necessary to avoid the need for very fine grids to resolve the large energy dissipation gradients in the near wall region and thus reduce the computational overheads of a given wall bounded problem. Wall functions are based on the universal assumptions that a constant shear stress exists in the near wall region and that the length scale of a typical eddy in this region is proportional to the distance from the wall. These assumptions result in a logarithmic velocity profile near the wall.

The wall law relates the shear stress τ to the turbulent kinetic energy [5.11]:

$$\tau = \rho \cdot C_{\mu}^{1/2} \cdot k \tag{5.3}$$

This is used to define a velocity scale:

$$u^{+} = \frac{(\rho.\tau)^{1/2}}{\tau}.u \tag{5.4}$$

and the scaled wall distance:

$$y^{+} = \frac{y_p}{\nu} \cdot \sqrt{\frac{\tau}{\rho}} = \frac{\rho u_{\tau} y_p}{\mu} \tag{5.5}$$

For any high Reynolds number turbulence model the implementation of wall boundary conditions start with the evaluation of y^+ (from equation 5.5) where y_p is the distance of the centre of a near wall node to the solid surface. A near wall flow is taken to be laminar if $y^+ \leq 11.63$ and the wall shear stress is assumed to be entirely viscous in origin. If $y^+ > 11.63$ the flow is turbulent and the wall function is used and the finite volume node is considered to be in the log law region of the turbulent boundary layer. In this region wall function formulae associated with the log law are used to calculate shear stress, heat flux and other variables [5.11].

'High Reynolds number turbulence models usually employ the assumption that if 'y' is the coordinate direction normal to the wall, the mean velocity at a point y_p with $30 < y^+ < 500$ satisfies the log-law. Measurements of turbulent kinetic energy budgets indicate that the rate of turbulence production equals the rate of dissipation. Using these assumptions and the eddy viscosity formula, it is possible to develop the following wall functions' [5.10].

$$u^+ = \begin{cases} y^+, & y^+ < y_0^+ \\ \frac{1}{k}\log\left(E \cdot y^+\right), & y^+ > y_0^+ \end{cases} \tag{5.6}$$

$$k = \frac{u_*^2}{\sqrt{C_\mu}} \tag{5.7}$$

$$\varepsilon = \frac{u_*^3}{\kappa \cdot y} \tag{5.8}$$

where y_0^+ defines the cross over point between the laminar sub-layer and the logarithmic region. E is the log layer constant and κ is the Von Karman constant, both of which are empirical values found from experiments. If the walls were not smooth, as discussed above, E should be adjusted accordingly and a new limiting value of y^+ would result.

'The wall function approach is not completely satisfactory for several reasons. Most importantly, numerical solutions are sensitive to the point above the surface where the wall functions are used, i.e. the point where the matching occurs. In addition, the law of the wall

does not always hold for the flow near solid boundaries, most notably for separated flows' [5.12].

At the solid surface the fluid is stationary and turbulent eddying motions also stop very close to the wall. In the absence of turbulent (Reynolds) shear stress effects the fluid closest to the wall is dominated by viscous shear. This layer is in practice extremely thin $\left(y^+ < 5\right)$ and we may assume that the shear stress is approximately constant and equal to the wall shear stress τ_w throughout the layer. As there is a linear relationship between u^+ and y^+ this region is referred to as the linear sub-layer [5.11].

For Large Eddy Simulation the value of wall unit y^+ should be around 1. The number of cells should have at least 10 within the viscosity-affected near-wall region ($\mathrm{Re}_y < 200$) to be able to resolve the mean velocity and turbulent quantities in that region [5.11].

5.5.3 Numerical Solvers and Interpolation Methods

There are two kinds of solver available in Fluent 6.30 namely pressure based and density based [5.8]. Pressure based solvers take momentum and pressure (or pressure correction) as the primary variables and use a pressure–velocity coupling algorithm derived from the continuity equation. In density based coupled solvers the continuity, momentum, energy and species equations are solved in vector form. There are two algorithm available with the pressure based solver, namely segregated solvers which solve for pressure corrections and momentum sequentially and a coupled solver which solves pressure and momentum equations simultaneously.

The pressure based solver is applicable to a wide range of flow regimes from low speed incompressible flow to high speed compressible flow. The pressure based coupled solver is applicable for most single phase flows and yields superior performance to the pressure-based (segregated) solver. The density based coupled solver is applicable when there is strong coupling or interdependence between density, energy, momentum and/or species.

Pressure-velocity coupling refers to the numerical algorithm which uses a combination of continuity and momentum equations to derive an equation for pressure (or pressure correction) when using pressure based solver. 'The Pressure Implicit with Splitting of Operators (PISO) algorithm involves one predictor step and two corrector steps and can be

regarded as an extension of the Semi-Implicit Method for Pressure-Linked Equations (SIMPLE), with a further corrector step to enhance it. PISO is useful for unsteady flow problems or for meshes containing cells with higher than average skewness' [5.10]. Therefore, PISO has a better performance in unsteady simulations than the SIMPLE and SIMPLEC (SIMPLE-Consistent) series algorithm. The second order implicit scheme could be used for time discretization. Second order upwind discretization uses large stencils for 2^{nd} order accuracy, essential with triangular or tetrahedral meshes or when the flow is not aligned with the grid. The only drawback it has that if using second order upwind discretization then convergence will be slower. A third order Quadratic Upwind Interpolation for Convective Kinematics (QUICK) difference scheme is used for spatial discretization. It can be applied to quadrilateral or hexahedral and hybrid meshes because it is useful for rotating/swirling flows. It gives a third order of accuracy if uniform meshes are used throughout. In particular, when the LES model is adopted, a bounded central difference is used to discretize the convective terms of momentum equations [5.8].

5.5.4 Boundary Conditions

As mentioned earlier, it is very difficult to simulate the open wind characteristics exactly in a wind-tunnel. 'Small differences in experimental conditions may also cause discrepancies between measurement results from different wind-tunnels. In order to obtain better agreement between experimental and numerical results, the boundary conditions adopted in the numerical simulations should be the same as those in the experiments, especially for the inflow boundary conditions' [5.9].

There are two kinds of expression to describe the velocity profile of atmospheric boundary layer simulated in wind tunnel tests. One is a power law and other is a log law. The velocity profile of the atmospheric boundary layer in the wind tunnel test conducted takes the following power law:

$$\frac{U}{U_H} = \left(\frac{Z}{Z_H} \right)^{\alpha} \tag{5.9}$$

where U_H is the wind speed at the height of the building model, which was 4.81 m/s in the experiments. α is the exponent of the velocity profile, which was 0.17 for the present case. Below are the plots of wind speed versus the natural log of scaled-up height and normal height above the working platform in the wind-tunnel. From these plots the shear

stress and the roughness length near the ground in the open terrain and in the wind-tunnel have been calculated and shown in Figures 5.35 and 5.36.

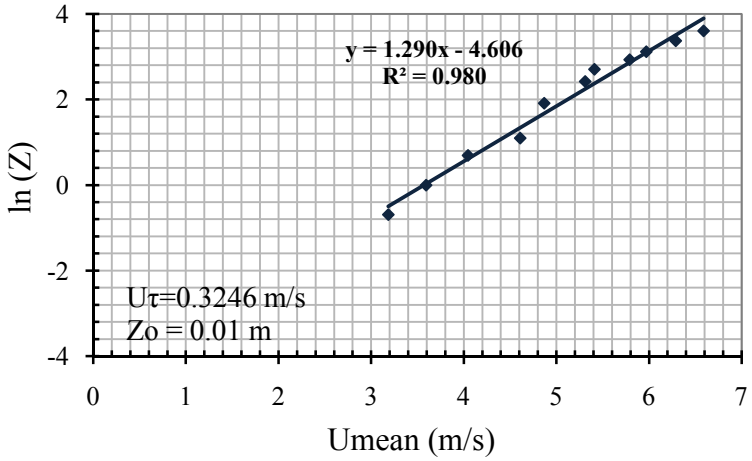

Figure 5.35 Natural log of scaled-up heights above the platform in the wind-tunnel versus wind speed

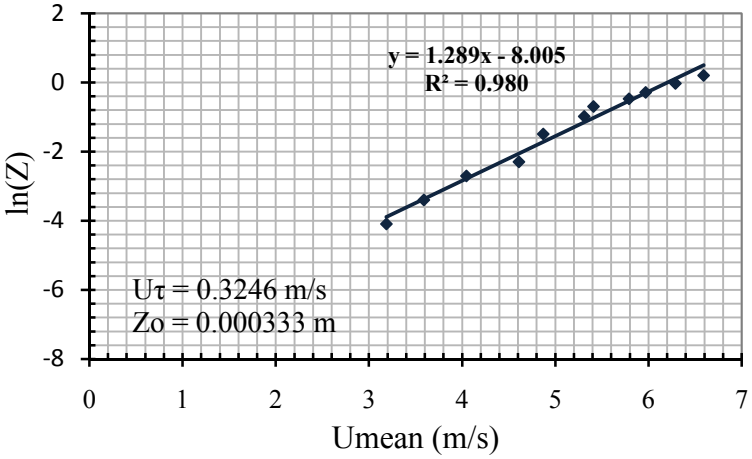

Figure 5.36 Natural log of heights above the platform in the wind-tunnel versus wind speed

The parameters derived from the present velocity profile for the present numerical simulation are $U_\tau = 0.3246$ m/s, $Z_0 = 10$ mm. The inlet velocity corresponding to the building height is 4.81 m/s.

The log law velocity profile has been simulated for the inlet boundary conditions for the CFD analysis from the simulated atmospheric boundary layer in the wind-tunnel study is given as follows:

$$\frac{U}{U_\tau} = \frac{1}{\kappa} \ln\left(\frac{Z + Z_0}{Z_0}\right) \tag{5.10}$$

where U_τ is the friction velocity, κ is Von Karman's constant and Z_0 is the surface roughness length parameter. Figure 5.37 shows the differences between wind-tunnel wind profile and the simulated wind profile for inlet boundary conditions for CFD analysis. The simulated wind profile for the CFD analysis nearly matches that of the wind profile simulated for the wind-tunnel testing.

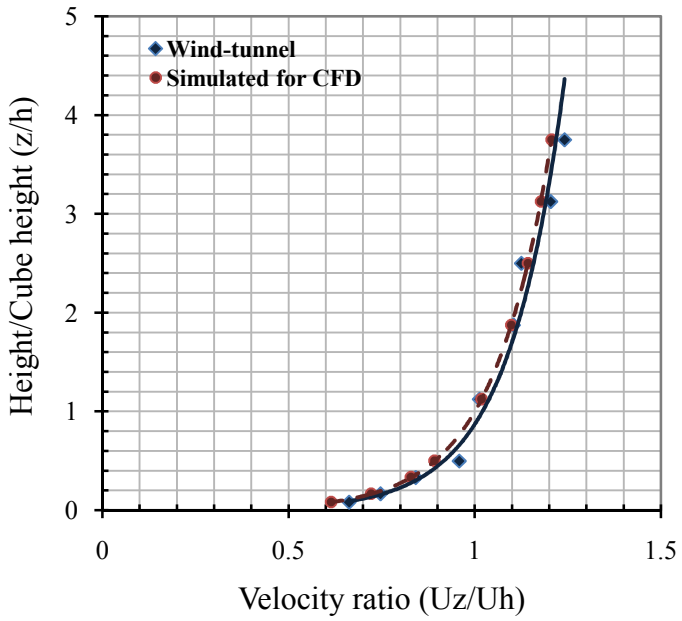

Figure 5.37 Simulated wind-tunnel wind profile and wind profile simulated for CFD

'Turbulence intensity in the approaching flow has a significant effect on the stream wise distributions of the wind-induced pressures on building models. Hence the turbulence intensity profile should be properly modelled in order to obtain accurate simulation results. The turbulence intensity profile of the wind-tunnel test conducted' [5.9] is shown in Figure 5.22.

The kinetic energy of turbulence and its dissipation rate at the inlet section were calculated according to the following equations:

$$k = \frac{3}{2}\left(U_{avg} I\right)^2 \tag{5.11}$$

$$\varepsilon = C_\mu^{3/4} \frac{k^{3/2}}{l} \tag{5.12}$$

where U_{avg} is the mean wind speed at inlet, I is the turbulence intensity, which was interpolated from the profiles given in Figure 5.21 at different heights and l is the turbulence integral length scale. The value of l measured in the wind-tunnel test at the model height was 0.30 m.

'In an LES study, apart from the mean velocity specifications, information on the fluctuating velocity of incident wind is also needed. The spectral synthesizer in the Fluent code was used to generate fluctuating velocity components, based on the random flow generation technique modified by Smirnov et al [5.13]. In this method, fluctuating velocity components are computed by synthesizing a divergence-free velocity vector field from the summation of Fourier harmonics on the basis of the input turbulence boundary conditions. In the implementation of the Fluent code, the number of the Fourier harmonics is fixed to 100 [5.11]'.

5.5.5 Determination of Time-step and Turnover Time

The appropriate time step was determined using the Crank-Nicolson scheme and using the simple Courant-Friedrichs-Lewy or CFL criterion to obtain a stable solution. This states that:

$$N_{CFL} = \frac{u.\Delta t}{\Delta x} < 1.0 \tag{5.13}$$

If the implicit Crank-Nicolson method is used the CFL can then be exceeded by factors as large as 5 [5.12] thus allowing for larger time-step for the same model simulation. The findings of Choi and Moin [5.14] show that too large a time step will effectively damp the turbulent fluctuations leading to a laminar solution. For the present study, a number of time steps were chosen, depending on the model geometry used, ranging from approximately 0.001 to 0.0005 seconds.

The simulations have to be run for a period that ensures that the turbulent structures have fully developed before any averaging can be performed [5.15]. This period is a multiple of the large eddy turnover time (LETOT) which refers to the time it will take for the large eddies in the simulation to do one revolution.

In the simulations in this thesis - the largest eddies in the flows were assumed to be approximately the size of the building, consequently the time for one LETOT is as follows for test case:

LETOT = Building dimension, (*H*)/ Velocity at roof height

Therefore, one LETOT = 0.2/5.0 (approximate) = 0.04 seconds

It is necessary to run the simulations for a time that ensured that sustained and statistically stationary turbulence levels were generated beyond the initial conditions set. This required approximately 20 to 30 LETOTS prior to the averaging of the results. For the present study a 4.0 seconds LETOTS has been used.

The entire computations were performed on a supercomputer (cluster of CPUs) in the School of Technology of Oxford Brookes University, Oxford. A total of 25 CPUs (Duo Core 2 processor) were used in parallel for the simulations.

5.6 Conclusions

The measurements of atmospheric surface flows together with related wind loads have contributed greatly to the fundamental knowledge of building aerodynamics. The wind-tunnel study further enhanced our knowledge by studying various aspects of bluff body aerodynamics.

The wind-tunnel simulations on the Silsoe Experimental Building and on net/sheet clad scaffolds were undertaken primarily based on the duplication of turbulence intensities and of the small-scale turbulence of the incident flow. It is very difficult to achieve equality between the Reynolds number in the wind-tunnel and the full-scale Reynolds number and hence it is very difficult to achieve exactly the same integral scales of turbulence.

Large suctions (separation of flows) occur near the leading edges and at roof corners. The investigation of these phenomena in the wind-tunnel remains a problem. Because of the limited space near corners and leading edges, it is difficult to make reliable measurements by introducing probes in these areas. This difficulty can be overcome by possible modelling the flow with Large Eddy Simulation (LES) numerical techniques. However, the disparity between the large and small scales, especially under extreme wind conditions, makes it extremely difficult to resolve the entire range of dynamic scales.

For successful simulation and convergence of a numerical solution of the problem, certain guidelines should be adopted:

- The quality of mesh should be examined before the CFD simulation. The skewness of the mesh should not be more than 0.97 in any case.
- Use node-based gradients with unstructured tetrahedral meshes. The node based averaging scheme is known to be more accurate than the default cell-based scheme for unstructured meshes, most notably for triangular and tetrahedral meshes.
- The input data for the CFD should be very near to the actual value; otherwise it will give unpredictable results.
- Second order discretization should be used for better accuracy rather than a faster solution when running the CFD simulation.

This chapter has described the application of the above principles to produce a successful wind-tunnel simulation and CFD models of the Silsoe Experimental Building and the extension to simulate sheeted scaffolds. Full details of the results will be given in the following chapters.

CHAPTER 6
Simulation of Nets as Porous Media

6.1 Introduction

This chapter provides a general theory behind the simulation of nets as porous media. A net can neither be tested as an aeroelastic model nor as a scaled model in a wind tunnel. This is because a thin net cannot be scaled further and also instrumentation is not available at the moment to be used for wind-tunnel modelling within nets. The author offers a brief description of the physics behind the development of this subject and its application in CFD modelling and the prominent figures who have contributed in this area. A 2D plan of the Silsoe Research Building surrounded by a net clad scaffold is discussed in this chapter. The 3D simulation of netting as cladding of scaffolding is discussed in the next chapter.

'The porous media model can be used for a wide variety of problems, including flows through packed beds, filter papers, perforated plates, flow distributors, etc' [6.1]. In this chapter and the next the author presents the first CFD simulation of the debris nets used for cladding scaffolds. The debris nets are modelled as porous media. A cell zone is generally defined in which a porous media model is to be applied and the loss in the flow is determined. 'Heat transfer through the medium can also be represented, subject to the assumption of thermal equilibrium between the medium and the fluid flow' [6.2].

'A 1D simplification of the porous media model, termed the "porous jump," can be used to model a thin membrane with known velocity/pressure-drop characteristics' [6.3]. A thin net can be considered as a 1D model (2D thin plane in 3D models). The porous jump model is applied to a face zone (not to a cell zone, as a cell zone is applied to porous media conditions) and should be used (instead of the full porous media model) whenever possible because it is more robust and yields better convergence.

6.2 Limitations and Assumptions of the Porous Media Model

'The porous media model incorporates an empirically determined flow resistance in a region of model defined as "porous". In essence, the porous media model is nothing more than an added momentum sink in the governing momentum equations' [6.3].

'Since the volume blockage that is physically present is not represented in the model, by default Fluent uses and reports a superficial velocity inside the porous medium, based on the volumetric flow rate, to ensure continuity of the velocity vectors across the porous medium interface. A more accurate alternative is to instruct Fluent 6.3 to use the true (physical) velocity inside the porous medium. Also the effect of the porous medium on the turbulence field is only approximated [6.3]'.

6.3 Momentum Equations for Porous Media

'Porous media are modelled by the addition of a momentum source term to the standard fluid flow equations. The source term is composed of two parts: a viscous loss term and an inertial loss term' [6.3].

$$S_i = -\left(\sum_{j=1}^{3} D_{ij} \mu v_j + \sum_{j=1}^{3} C_{ij} \frac{1}{2} \rho v_{mag} v_j \right) \tag{6.1}$$

'where S_i is the source term for the i^{th} (x, y or z) momentum equation, and D and C are prescribed matrices. This momentum sink contributes to the pressure gradient in the porous cell, creating a pressure drop that is proportional to the fluid velocity (or velocity squared) in the cell' [6.3].

To recover the case of a simple homogeneous porous media

$$S_i = -\left(\frac{\mu}{\alpha} v_i + C_2 \frac{1}{2} \rho v_{mag} v_i \right) \tag{6.2}$$

where α is the permeability and C_2 is the inertial resistance factor, D and C are specified as diagonal matrices with $1/\alpha$ and C_2, respectively, on the diagonals (and zero for the other elements).

Fluent 6.3 also allows the source term to be modelled as a power law of the velocity magnitude as:

$$S_i = -C_0 |v|^{C_1} = -C_0 |v|^{(C_1 - 1)} v_i \tag{6.3}$$

where C_0 and C_1 are user-defined empirical coefficients.

6.3.1 Darcy's Law in Porous Media

In laminar flows through porous media, the pressure drop is typically proportional to velocity [6.4] and the constant C_2 can be considered to be zero. 'Ignoring convective acceleration and diffusion, the porous media model then reduces to Darcy's Law' [6.3]:

$$\nabla p = -\frac{\mu}{\alpha}\vec{v} \tag{6.4}$$

'The pressure drops that Fluent computes in each of the three (x, y, z) coordinate directions within the porous region are then

$$\Delta p_x = \sum_{j=1}^{3} \frac{\mu}{\alpha_{xj}} v_j \Delta n_x \tag{6.5}$$

$$\Delta p_y = \sum_{j=1}^{3} \frac{\mu}{\alpha_{yj}} v_j \Delta n_y \tag{6.6}$$

$$\Delta p_z = \sum_{j=1}^{3} \frac{\mu}{\alpha_{zj}} v_j \Delta n_z \tag{6.7}$$

where $1/\alpha_{ij}$ are the entries in the matrix D in Equation 6.1, v_j are the velocity components in the x, y and z directions and $\Delta n_x, \Delta n_y$ and Δn_z are the thicknesses of the medium in the x, y and z directions' [6.3].

Here, the thickness of the medium ($\Delta n_x, \Delta n_y$ or Δn_z) is the actual thickness of the porous region, if the thicknesses used in the model differ from the actual thicknesses, one must make adjustments in the inputs for $1/\alpha_{ij}$ [6.3].

6.3.2 Inertial Losses in Porous Media

'At high flow velocities, the constant C_2 in Equation 6.1 provides a correction for inertial losses in the porous medium. This constant can be viewed as a loss coefficient per unit length along the flow direction, thereby allowing the pressure drop to be specified as a function of the dynamic head [6.3]'.

If modelling a perforated plate or tube bank, the permeability term can be eliminated from Equation 6.1 (because of large open area) and the inertial term remains, yielding the following simplified form of the porous media equations:

$$\nabla p = -\sum_{j=1}^{3} C_{2ij}\left(\frac{1}{2}\rho v_j v_{mag}\right) \tag{6.8}$$

or when written in terms of the pressure drop in the *x, y* and *z* directions:

$$\begin{aligned}
\Delta p_x &\approx \sum_{j=1}^{3} C_{2_{xj}} \Delta n_x \frac{1}{2}\rho v_j v_{mag} \\
\Delta p_y &\approx \sum_{j=1}^{3} C_{2_{yj}} \Delta n_y \frac{1}{2}\rho v_j v_{mag} \\
\Delta p_z &\approx \sum_{j=1}^{3} C_{2_{zj}} \Delta n_z \frac{1}{2}\rho v_j v_{mag}
\end{aligned} \tag{6.9}$$

The thickness of the medium ($\Delta n_x, \Delta n_y$ or Δn_z) is the thickness defined in the model and not the thickness of the original full scale body.

6.4 Treatment of Turbulence in Porous Media

Fluent 6.3 [6.3] will, 'by default, solve the standard conservation equations for turbulence quantities in porous media. In this default approach, therefore, turbulence in the medium is treated as though the solid medium has no effect on the turbulence generation or dissipation rates. This assumption may be reasonable if the medium's permeability is quite large and the geometric scale of the medium does not interact with the scale of the turbulent eddies'. In other instances, however, the effects of turbulence in the medium may be suppressed.

'When using one of the $k-\varepsilon$ turbulence models, the $k-\omega$ model, or the Spalart-Allmaras model, the effect of turbulence in a porous region is suppressed by setting the turbulent contribution to viscosity, μ_t equal to zero. By doing so, Fluent 6.3 [6.1] will transport the inlet turbulence quantities through the medium, but their effect on the fluid mixing and momentum will be ignored. In addition, the generation of turbulence will be set to zero in the medium. This modelling strategy is enabled by turning on the 'Laminar Zone' option when defining the fluid properties. Enabling this option implies

that μ_t is zero. Disabling the option (the default) implies that turbulence will be computed in the porous region just as in the bulk fluid flow [6.3]'.

6.5 Deriving Porous Media Inputs Based on Superficial Velocity

When modelling porous media or porous jumps in Fluent it must be kept in 'mind that the porous cells are 100% open and that the values of $1/\alpha_{ij}$ and/ or $C_{2_{ij}}$ must be based on this assumption. Suppose the pressure drop variation with velocity through an actual device, which is only partial open to flow, is known [6.3]'. The following sub-sections (6.5.1, 6.5.2, 6.5.3) show examples of the computation of C_2 or $1/\alpha$ which are appropriate for particular Fluent models.

6.5.1 Using known Pressure Loss through a Perforated Plate

'Consider a perforated plate which has 25% area open to flow where the pressure drop through the plate is known to be 0.5 times the dynamic head in the plate. The loss factor K_L defined as:

$$\Delta p = K_L \left(\frac{1}{2} \rho v_{25\%open}^2 \right) \tag{6.10}$$

is therefore 0.5, based on the actual fluid velocity in the plate, i.e., the velocity through the 25% open area. To compute an appropriate value for C_2 , note that in a Fluent 6.3 model [6.3]':

1. 'The velocity through the perforated plate assumes that the plate is 100% open.
2. The loss coefficient must be converted into dynamic head loss per unit length of the porous region.

Noting item 1, the first step is to compute an adjusted loss factor $K_L^{'}$, which would be based on the velocity of a 100% open area:

$$\Delta p = K_L^{'} \left(\frac{1}{2} \rho v_{100\%open}^2 \right) \tag{6.11}$$

or, noting that for the same flow rate, $v_{25\%open} = 4 \times v_{100\%open}$

$$K_L^{'} = K_L \times \frac{v_{25\%open}^2}{v_{100\%open}^2} \tag{6.12}$$

$$= 0.5 \times \left(\frac{4}{1}\right)^2 = 8$$

The adjusted loss factor has a value of 8. Noting item 2, this is now converted into a loss coefficient per unit thickness of the perforated plate. Assuming that the plate has a thickness of 1.0 mm (10^{-3} m) [6.3]'. The inertial loss factor is then

$$C_2 = \frac{K_L^{'}}{thickness} \tag{6.13}$$

$$= 8/10^{-3} = 8000 \text{ m}^{-1}$$

Note that- for anisotropic media this information must be computed for each of the 2 (or 3) coordinate directions. This method was not used for simulating nets as porous media because a net is stretchable and therefore the area of the holes in the net cannot be calculated accurately.

6.5.2 Using an Empirical Equation to Derive Porous Media Inputs for Turbulent Flow through a Perforated Plate

Another example from the equation of Smith and Van Winkle [6.5] will be used to show how the porous media inputs can be calculated for pressure loss through a perforated plate with square-edged holes.

'The expression, which is claimed by the authors to apply for turbulent flow through square-edged holes on an equilateral triangular spacing, is' [6.6]

$$\dot{m} = CA_f \sqrt{\left(2\rho\Delta p\right) / \left(1 - \left(A_f / A_p\right)^2\right)} \tag{6.14}$$

where $\dot{m}$ = mass flow rate through the plate

A_f = the free area or total area of the holes

A_p = the area of the plate (solid and holes)

C = a coefficient that has been tabulated for various Reynolds-number ranges

D/t = the ratio of hole diameter to plate thickness

'For $t/D > 1.6$ and for $\mathrm{Re} > 4000$ the coefficient C takes a value of approximately 0.98, where the Reynolds number is based on hole diameter and velocity in the holes.

Rearranging above Equation 6.14 making use of the relationship

$$\dot{m} = \rho v A_p \tag{6.15}$$

and dividing by the plate thickness $\Delta x = t$, we obtain

$$\frac{\Delta p}{\Delta x} = \left(\frac{1}{2}\rho v^2\right)\frac{1}{C^2}\frac{\left(A_p/A_f\right)^2 - 1}{t} \tag{6.16}$$

where v is the superficial velocity (not the velocity in the holes). Comparing with Equation 6.8, it is seen that, for the direction normal to the plate, the constant C_2 can be calculated from [6.3]'

$$C_2 = \frac{1}{C^2}\frac{\left(A_p/A_f\right) - 1}{t} \tag{6.17}$$

This method is also not suitable for the present case as this method is only suitable for the square holes in a plate.

6.5.3 Deriving the Porous Coefficients Based on Experimental Pressure and Velocity Data

'Experimental data that is available in the form of pressure drop against velocity through a porous component can be extrapolated to determine the coefficients for the porous media. To affect a pressure drop across a porous medium of thickness Δn, the coefficients of the porous media are determined in the manner described below [6.3]'.

If for example the experimental data (fictitious) is [6.3]:

Velocity (m/s)	Pressure Drop (Pa)
20.0	78.0
50.0	487.0
80.0	1432.0
110.0	2964.0

then an xy curve can be plotted to create a trend line through these points yielding the following equation

$$\Delta p = 0.2829v^2 - 4.33539v \tag{6.18}$$

where Δp is the pressure drop and v is the velocity.

Note that a simplified version of the momentum equation, relating the pressure drop to the source term, can be expressed as

$$\nabla p = S_i \tag{6.19}$$

or

$$\Delta p = -S_i \Delta n \tag{6.20}$$

Hence, comparing Equation 6.18 to Equation 6.2 yields the following curve coefficients:

$$0.28296 = C_2 \frac{1}{2} \rho \Delta n \tag{6.21}$$

With $\rho = 1.225$ kg/m^3, and a porous media thickness, Δn, assumed to be 1m in this example, the inertial resistance factor, $C_2 = 0.462$.

Likewise,

$$-4.33539 = \frac{\mu}{\alpha} \Delta n \tag{6.22}$$

with $\mu = 1.7894 \times 10^{-5}$, the viscous inertial resistance factor (inverse of permeability), $\frac{1}{\alpha} = -242282$.

It is noted that this technique can be applied to the porous jump boundary condition. Similar to the case of a porous media, the thickness of the medium Δn has to be taken into account. This is the reason for using this method for calculating the permeability of the net and its use in for simulating nets in CFD.

6.6 Modelling Porous Media Based on Physical Velocity

As stated in Section 6.1, 'by default Fluent 6.3 calculates the superficial velocity based on volumetric flow rate. The superficial velocity in the governing equations can be represented as' [6.3]:

$$\vec{v}_{superficial} = \gamma \vec{v}_{physical} \tag{6.23}$$

where γ is the porosity of the media defined as the ratio of the volume occupied by the fluid to the total volume.

'The superficial velocity values within the porous region remain the same as those outside of the porous region. This limits the accuracy of the porous model in cases where there should be an increase in velocity throughout the porous region. For more accurate simulations of porous media flows, it becomes necessary to solve for the true or physical velocity throughout the flow-field rather than the superficial velocity [6.3]'.

Fluent calculates the physical velocity using the 'Porous Formulation' region of the 'Solver' panel. By default, the 'Superficial Velocity' option is turned on.

Using the physical velocity formulation, and assuming a general scalar ϕ , the governing equation in an isotropic porous media has the following form:

$$\frac{\partial(\gamma\rho\phi)}{\partial t} + \nabla\cdot(\gamma\rho\vec{v}\phi) = \nabla\cdot(\gamma\Gamma\nabla\phi) + \gamma S_\phi \tag{6.24}$$

Assuming isotropic porosity and single phase flow, the volume-averaged mass and momentum conservation equations are as follows:

$$\frac{\partial(\gamma\rho)}{\partial t} + \nabla\cdot(\gamma\rho\vec{v}) = 0 \tag{6.25}$$

$$\frac{\partial(\gamma\rho\vec{v})}{\partial t} + \nabla\cdot(\gamma\rho\vec{v}\vec{v}) = -\gamma\nabla p + \nabla\cdot(\gamma\vec{\tau}) + \gamma\vec{B}_f - \left(\frac{\mu}{\alpha} + \frac{C_2\rho}{2}|\vec{v}|\right)\vec{v} \tag{6.26}$$

The last term in Equation 6.26 represents the viscous and inertial drag forces imposed by the pore walls on the fluid.

'Note that even when the physical velocity is determined using Equation 6.26, the two resistance coefficients can still be derived using the superficial velocity as given in Section 6.6. Fluent 6.3 assumes that the inputs for these resistance coefficients are based

upon well-established empirical correlations usually based on superficial velocity. Therefore, Fluent 6.3 automatically converts the inputs for the resistance coefficients into those that are compatible with the physical velocity formulation [6.3]'.

'Note that the inlet mass flow is also calculated from the superficial velocity. Therefore, for the same mass flow rate at the inlet and the same resistance coefficients, for either the physical or the superficial velocity formulation, the same pressure drop across the porous media zone should be maintained' [6.3].

6.7 Solution Strategies for Porous Media

'In general, the standard solution procedures and solution parameter settings when in Fluent models include porous media. It may be found, however, that the rate of convergence is slow when the porous region through which the pressure drop is relatively large in the flow direction (e.g., the permeability, α is low or the inertial factor, C_2 is large). This slow convergence can occur because the porous media pressure drop appears as a momentum source term - yielding a loss of diagonal dominance - in the matrix of equations solved. The best remedy for poor convergence of a problem involving a porous medium is to supply a good initial guess for the pressure drop across the medium. This can be supplied by patching a value for the pressure in the fluid cells upstream and/or downstream of the medium. It is important to recall, when patching the pressure, that the pressures that have to be inputted should be defined as the gauge pressures used by the solver (i.e., relative to the operating pressure) [6.3]'.

'Another possible way to deal with poor convergence is to temporarily disable the porous media model (by turning off the 'Porous Zone' option in the Fluid Panel) and obtain an initial flow field without the effect of the porous region. With the porous media model turned off, Fluent will treat the porous zone as a fluid zone and calculate the flow field accordingly. Once an initial solution is obtained, or the calculation is proceeding steadily to convergence, the porous media model can be enabled and the calculation continued with the porous region included (This method is not recommended for porous media with high resistance) [6.3]'.

'Simulations involving highly anisotropic porous media may, at times, pose convergence troubles. These issues can be addressed by limiting the anisotropy of the porous media coefficients ($1/\alpha_{ij}$ and $C_{2_{i,j}}$) to two or three orders of magnitude. Even if

the medium's resistance in one direction is infinite, it is not necessary to set the resistance in that direction to be greater than 1000 times the resistance in the primary flow direction [6.3]'.

6.8 Wind-tunnel Tests on Nets

Two types of net (called Type A and Type B) were used here for the simulation as porous media and are shown in Figure 6.1. In the wind-tunnel a section of each net was placed within a rectangular frame and inserted into the wind-tunnel completely filling the cross section of the tunnel. The Type A net is a commonly used debris net for cladding scaffold structures during construction, for improvement of protection of both public and workforce from falling debris, and also to shield workforces from weather in the United Kingdom. It was manufactured from high density polythene monofilaments of thickness 0.42 mm. The Type B net was made by double folding the Type A net. The two nets were tested for drop in pressure versus velocity in the small wind-tunnel (as shown in Figure 6.2) of the School of Technology, Oxford Brookes University of cross-section 305 mm × 305 mm. 'This is a non-boundary-layer wind-tunnel, of the open-circuit type, constructed mainly in aluminium and supported by a tubular steel framework. The air enters the tunnel through a carefully shaped effuse, the entrance being covered by a protective screen. The working section is of Perspex, giving full visibility and the various models are supported from one of the side walls or by means of the three component balance, when provided. At the upstream end of the working section is a static tapping and a total head tube which may be traversed over the full height of the working section, whilst at the downstream end is a pitot static tube which may be similarly traversed [6.7]'.

'After the working section a diffuser leads to the axial flow fan unit and the air velocity is controlled by means of a double butterfly valve on the fan outlet. The fan discharges by way of a silencer. The maximum air velocity is such that pressure differences of the order of 30 cm of water are developed and these may be read with suitable accuracy by the simple manometer provided [6.8]'.

Type A Net **Type B Net**

Figure 6.1 Typical Type A and Type B Net

Figure 6.2 Typical Wind-tunnel in Oxford Brookes University

These nets were tested in the wind-tunnel to determine the drop in pressures versus the velocity so as to simulate the nets as porous media and to determine the coefficients for the porous media. The mean thicknesses of the nets were measured with the help of digital micrometer screw gauge. Their average approximate thicknesses were measured to be 0.42 mm and 0.65 mm for Type A and B nets respectively. The thickness of the Type B net was not double that of Type A, because of the interlocking of the fibers between adjacent weaves.

The experimental setup for the wind-tunnel test of the nets is shown in Figure 6.3

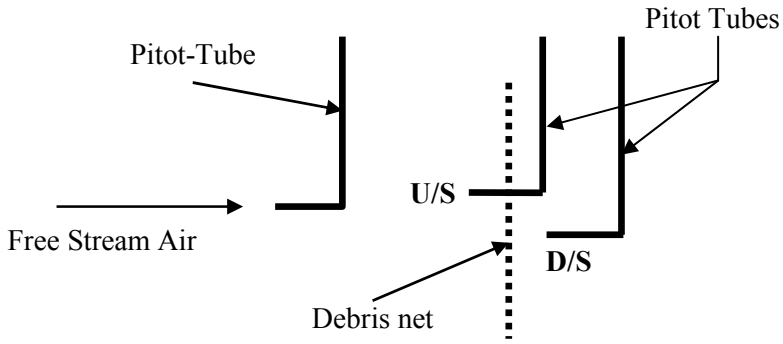

Figure 6.3 Experimental setup for wind-tunnel tests on nets

The experimental data for the Net Type A and Type B is given below in Table 6.1:

Table 6.1 Pressure drop versus wind speed across nets

Net Type A (two set of data taken together)		Net Type B	
Free Stream wind speed (m/s)	Pressure Drop (Pa)	Free stream wind Speed (m/s)	Pressure Drop (Pa)
2.9	5.0	3.0	16.0
3.2	10	4.5	37.0
4.7	17.0	9.6	111.0
6.8	29.0	14.4	216.0
8.6	47.0	19.0	386.0
10.9	84.0	22.7	535.0
13.0	96.0		
14.2	133.0		
16.5	165.0		
17.8	218.0		
20.6	245		

The xy curves for both Type A and Type B net have been plotted in Figures 6.4 and 6.5 to create trend lines through the points from Table 6.1 yielding the following equations:

For Type A Net $$\Delta p = 0.524v^2 + 1.082v \quad (6.27)$$

and

For Type B Net $$\Delta p = 1.238v^2 + 2.249v \quad (6.28)$$

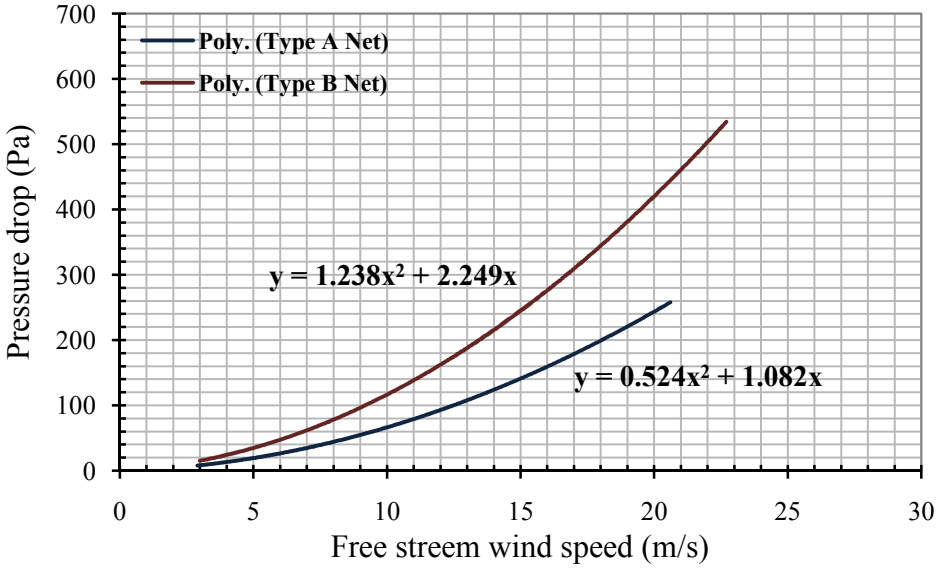

Figure 6.4 Free stream wind speed versus pressure drop across the nets

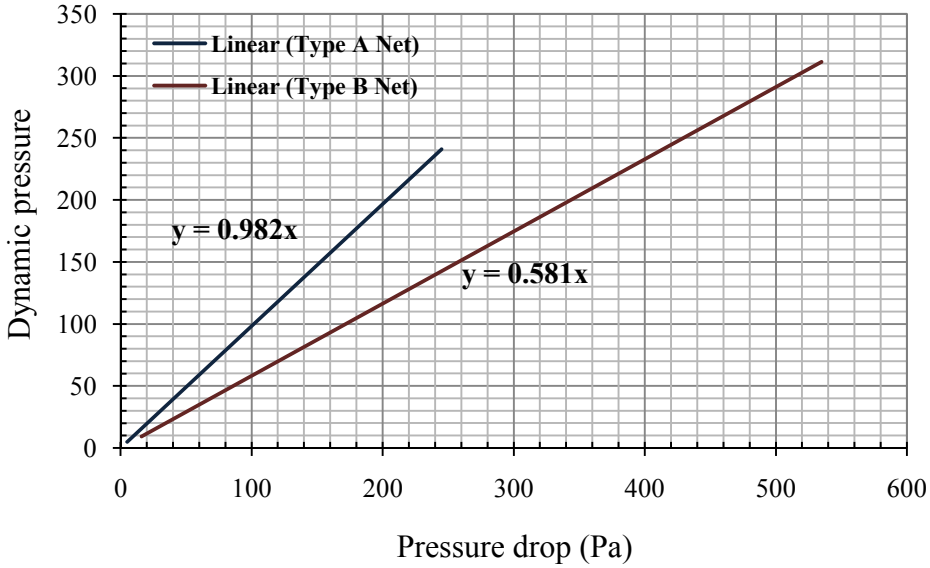

Figure 6.5 Pressure drop versus dynamic pressure across the nets

where Δp is the pressure drop and v is the velocity. Note that a simplified version of the momentum equation, relating the pressure drop to the source term, can be expressed as Equation 6.19 and 6.20.

Hence, comparing Equation 6.27 and Equation 6.28 with $\Delta p = -\left(\frac{\mu}{\alpha}v + C_2\frac{1}{2}\rho v^2\right)\Delta n$ yields the following curve coefficients:

For Type A Net $$0.524 = C_2\frac{1}{2}\rho\Delta n \qquad (6.29)$$

For Type B Net $$1.238 = C_2 \frac{1}{2} \rho \Delta n \quad (6.30)$$

with $\rho = 1.225$ kg/m^3, and a porous media thickness Δn equal to 0.42 mm and 0.65 mm for Type A and Type B net respectively. The inertial resistance factors are $C_2 = 2037 \, 1/m$ for Type A and $C_2 = 3110 \, 1/m$ for Type B respectively.

Likewise,

For Type A Net $$1.082 = \frac{\mu}{\alpha} \Delta n \quad (6.31)$$

For Type B Net $$2.249 = \frac{\mu}{\alpha} \Delta n \quad (6.32)$$

With $\mu = 1.7894 \times 10^{-5}$, the viscous inertial resistance factor (1/permeability) $\alpha = 6.946 \times 10^{-9} m^2$ and $5.172 \times 10^{-9} m^2$ for type A and type B nets respectively.

6.9 Theoretical Simulation of Nets in CFD

The thickness of the debris net is very small. It is very difficult to simulate the same thickness in CFD because it will lead to the size of the mesh being very-very small. Keeping this in mind the thickness of the net for CFD simulation was increased from 0.42 mm for Type A Net and 0.65 mm for Type B Net to 4 mm for both nets.

The values of α and C_2 were modified in proportion to the ratio of the actual thicknesses of the nets to those in the simulated nets developed for the CFD, so as to make the drop in pressure to be the same for both the wind-tunnel experiments and the theoretical equations developed for the CFD. The value of α was increased in proportion by 4/0.43 for Type A Net and 4/0.65 for Type B Net respectively. Whereas the value of inertial resistance C_2 was decreased to maintain the same drop in pressure in proportion to 0.43/4 and 0.65/4 for Type A Net and Type B Net respectively.

The computational domain as shown in Figure 6.4, covers 29 B (B is the outer dimension of the net clad scaffold) in stream (X) direction (-6 < x/B < 22), 13B in the lateral direction or normal (Y) direction (-6 < y/B < 6).

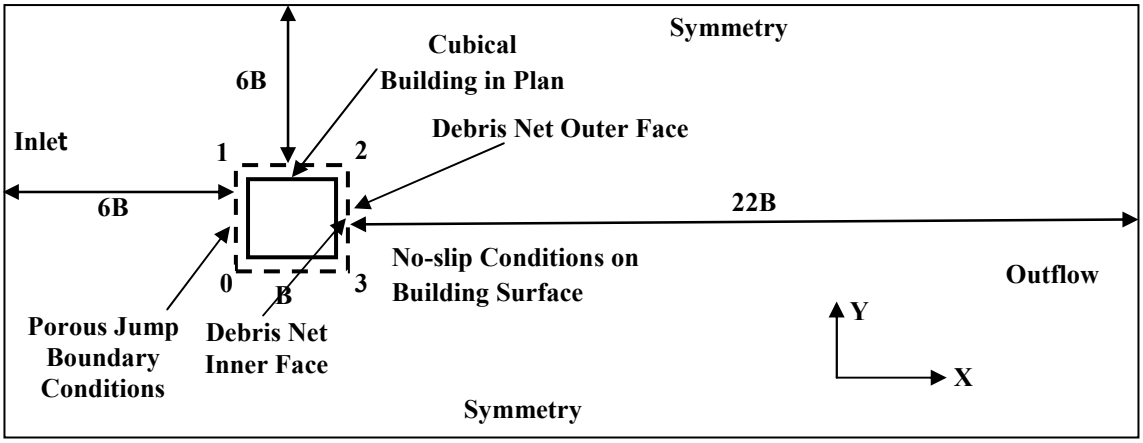

Note: 0, 1, 2 and 3 are the corners of the net and cubical the building, B is the width of net.

Figure 6.6 Computational domain and boundary conditions

The unsteady RNG $k-\varepsilon$ method was used for computations over a period of 4 seconds. The unsteady RNG $k-\varepsilon$ is most widely used method among academics and industries. It gives reasonable results on the windward and side faces. The time step was taken to be 0.001s and number of steps 4000. These were iterated to obtain the time averaged results with each time steps. The porous jump boundary condition was used for the net in all four directions. The inlet velocity for the 2D analysis was kept constant at 5 m/s. This will generate approximately the same wind speeds and pressures that occurs at 2/3 height in a 3D simulation, this height being approximately the stagnation height where there is little vertical fluid flow and then total flow is horizontal. A turbulence intensity of 15% and a integral length scale of 0.3 were kept constant for all the trials.

The pressure coefficients on the outer and inner face of net clad scaffold surrounding a cubical building are given in Figures 6.5 and 6.6. Figure 6.7 gives the difference of pressure coefficients of the outer and inner face of the nets. Note that the distances are given using the notation in Figure 6.4 where distance 0-1 is along the windward side, distance 1-2 is along a side wall and distance 2-3 is along the leeward side. Figure 6.8 gives the pressure coefficients on the walls of the building.

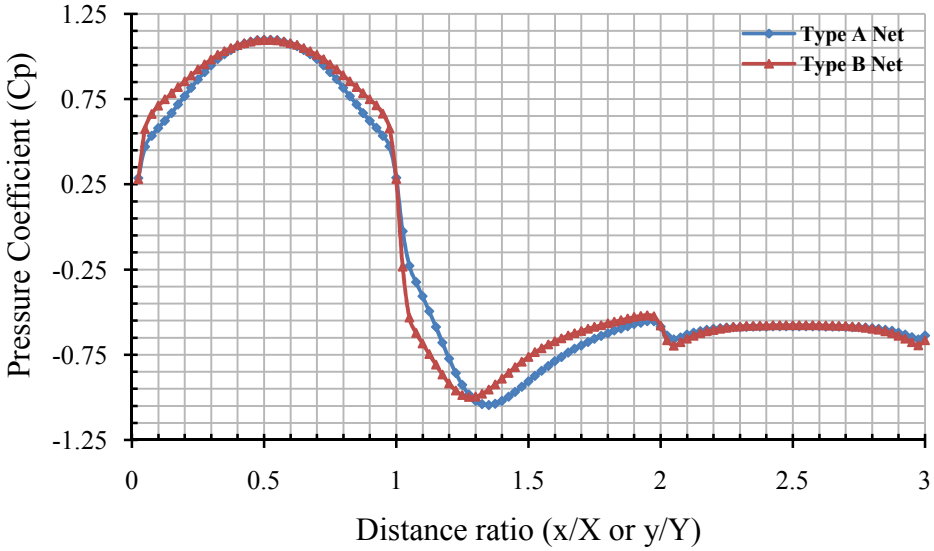

Figure 6.7 Pressure Coefficients on the outer face of the nets

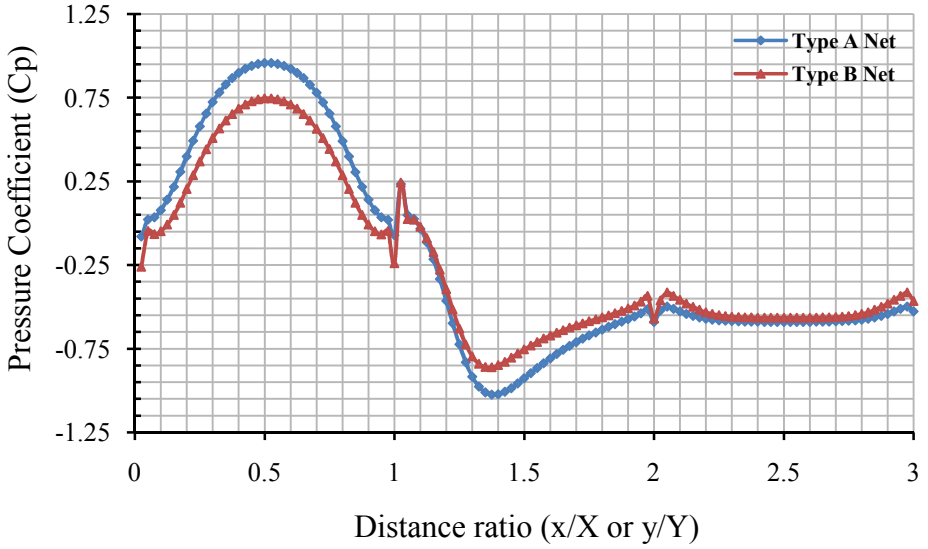

Figure 6.8 Pressure Coefficients on the inner face of the nets

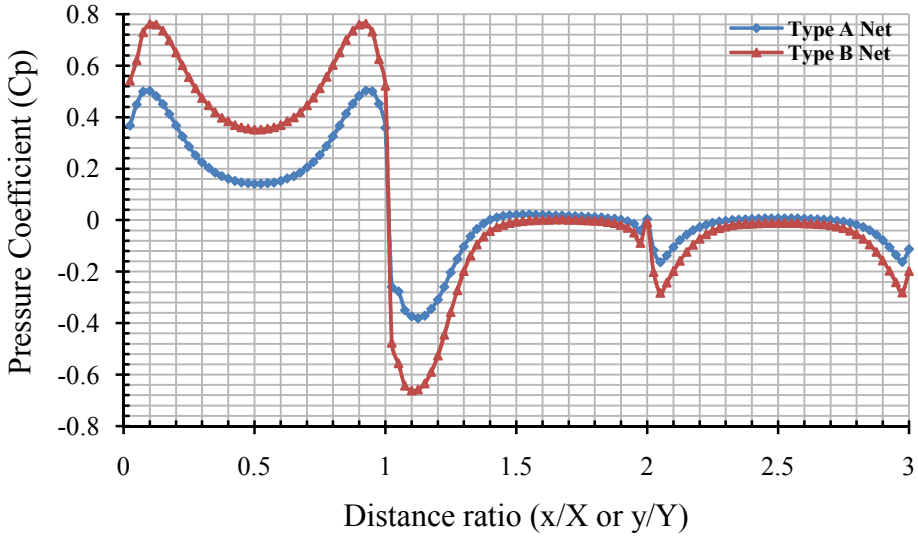

Figure 6.9 Difference in pressure coefficients between outer and inner face of the debris net

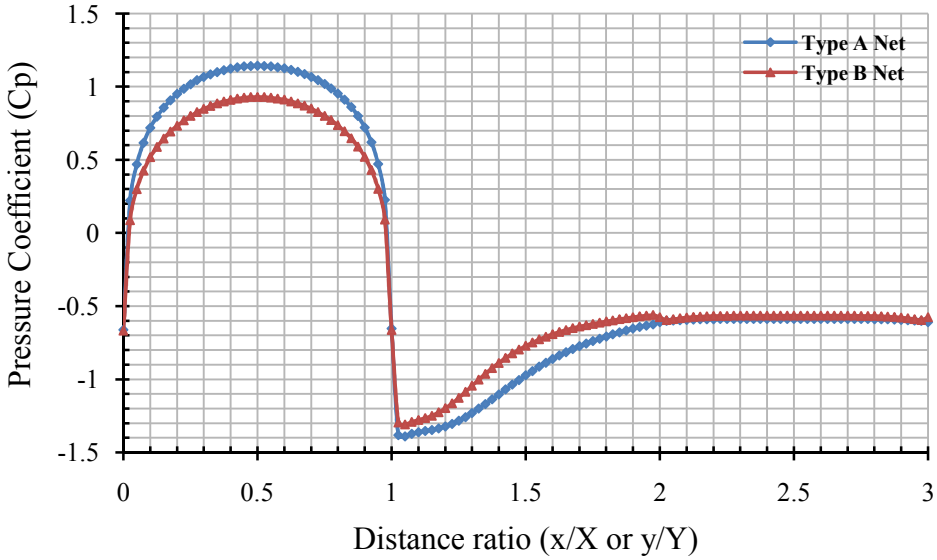

Figure 6.10 Variation of Pressure Coefficients on walls for Type A and Type B nets

Apart from the nets which were tested in the wind tunnel, a few arbitrary nets having permeability varying from $1.0\times10^{-6}m^2$ to $1.0\times10^{-10}m^2$ and having inertial constant C_2 (inertial resistance constant) equal to zero were also simulated with all other data kept the same as that used for Type A and Type B nets. A permeability of $1.0\times10^{-10}m^2$ corresponds to a nearly impermeable sheet and a permeability of $1.0\times10^{-6}m^2$ corresponds to a very permeable sheet (almost non-existing). The resulting pressure coefficients are shown in Figures 6.9-6.11. Figure 6.10 gives the effects of different permeability on the pressure coefficients on the faces of the building.

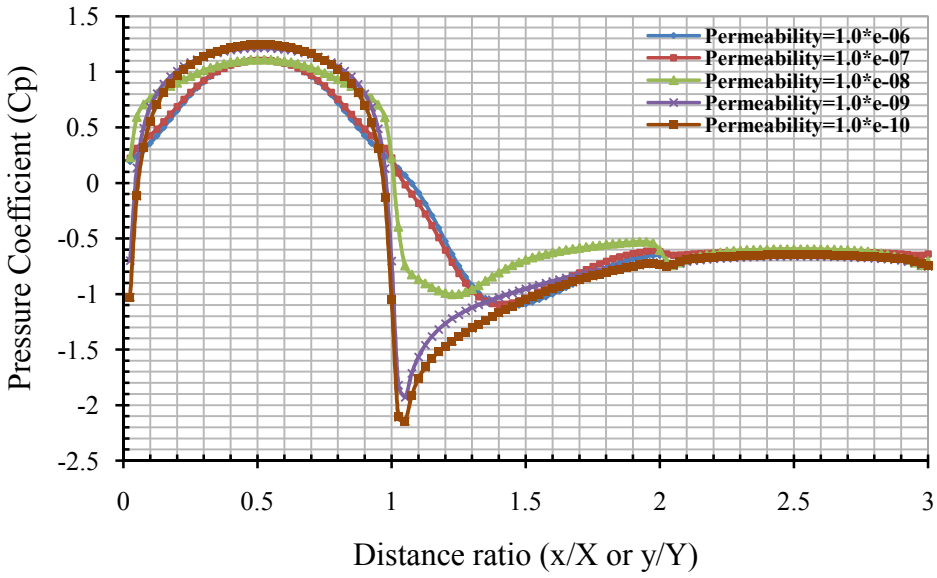

Figure 6.11 Pressure Coefficients on the outer face of the net at different permeabilities

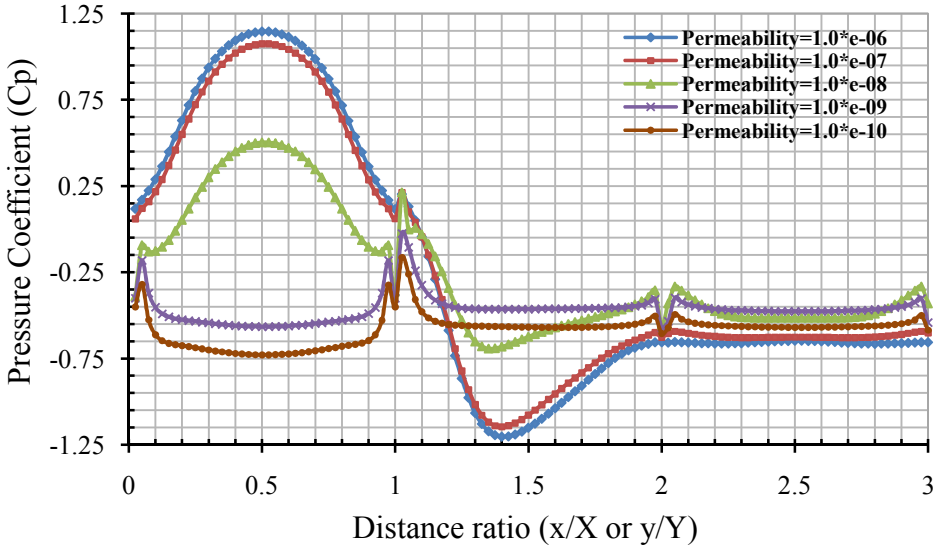

Figure 6.12 Pressure Coefficients on the inner face of the net at different permeabilities

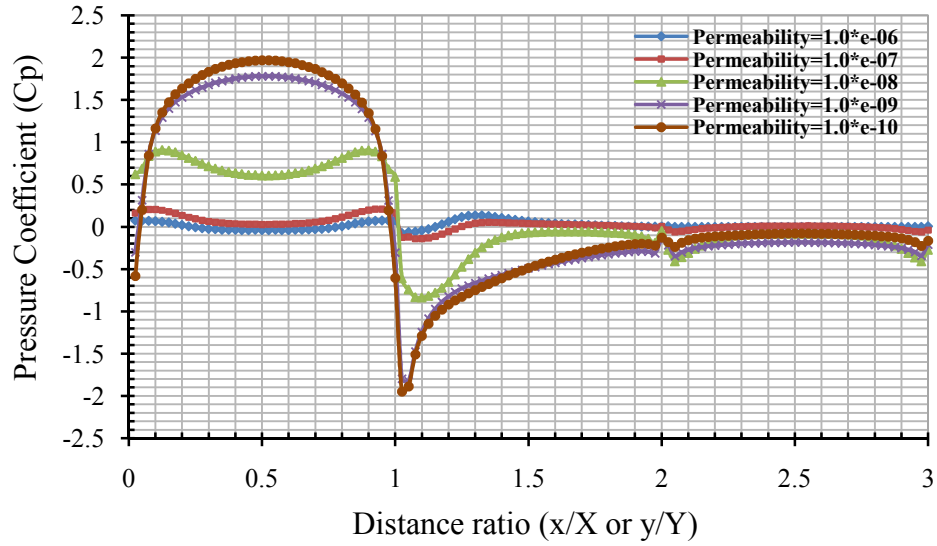

Figure 6.13 Difference in pressure coefficients between outer and inner face of the debris net

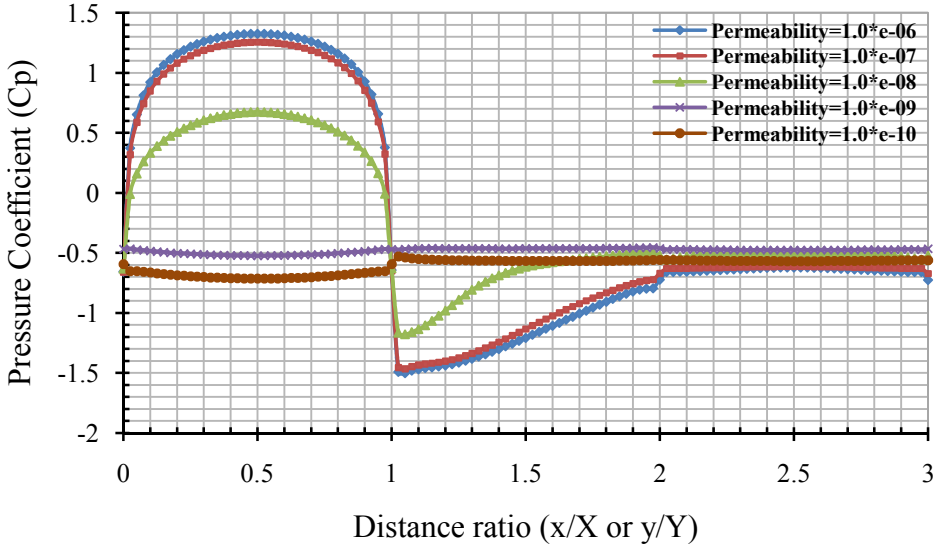

Figure 6.14 Pressure Coefficients on the outer wall of the building at different permeabilities

6.10 Discussions and Conclusions

Whilst performing the wind-tunnel experiments on the nets, the nets stretched because at high wind speed the nets took a curved shape which created a problem in placing the pitot tubes. Net Type B can be called representative of actual nets used in construction industries because it was stretched and was double folded. Studying Figures 6.5, 6.6 and 6.7 for the pressure coefficients on Type A and Type B nets, it can be seen that there is drop in pressures from 0.15 to nearly 0.48 in the middle and corner for Type A Net and 0.35 to nearly 0.75 in the middle and corner for Type B Net respectively. The drop in the pressure coefficient is inversely proportional to the permeability. When the permeability of the net decreases, suction pressure starts to be generated on the leeward side of the net.

Hence it can be concluded that when designing the net clad scaffolds, the wind load on the scaffolds should be considered to be 40% of the total wind load on the covered area of the scaffold. When the permeability decreases the inside pressure coefficient decreases and consequently becomes negative because of suction both on the inner face of the net and on the walls of the building (Figure 6.8).

The same patterns of results have been found for imaginary nets of permeabilities varying from 1.0×10^{-6} to 1.0×10^{-10} m^2. A full picture will be seen when the net is simulated as a three dimensional problem.

CHAPTER 7
Results and Discussions

7.1 Introduction

This chapter presents a detailed discussion on the results of wind-tunnel experiments on a model of the Silsoe Experimental Building (SEB) and on models of sheet clad/elevated sheet clad scaffolds (both on the outer and inner facade of the sheet clad/elevated sheet clad scaffolds) surrounding the SEB. Apart from wind-tunnel experiments on the above models, a computational simulation using computational fluid dynamics was also undertaken, using different CFD techniques available commercially so that a direct comparison of the results could be obtained. Before the CFD analyses were undertaken the accuracy of the most popular turbulence models described in Chapter 4 was also determined.

A model scale of 1:30 of the SEB was used for experiments in a wind-tunnel and the results obtained were compared with the full-scale data available from the research on the SEB by Richardson et al [7.1]. Pressure data obtained from the wind-tunnel experimental results on the model of SEB were compared to full-scale data with generally good agreement. The same model scale of 1:30 was used for computational analyses. The data obtained from wind-tunnel experiments and full-scale were also compared with various computational techniques available commercially and the conclusions are drawn on the use of the different techniques. The analyses undertaken on this model were only for validation purposes and to check the degree of accuracy of the various CFD models commercially available

To determine the wind forces on net/sheet clad scaffolds the SEB was used as a base model and a simulated scaffold erected around it. Although, sheet/net exhibits aero-elastic behaviour under wind load, an assumption was made to treat the sheeted scaffold as being made of static solid thin plates. Models were tested in a wind-tunnel and the same assumptions had been used for computational fluid dynamics analyses.

For the sheet clad scaffolds, two models were made, one with sheeting touching the ground and the other with an elevated sheet surrounding the SEB. These models were tested in a wind-tunnel to determine the pressure coefficients on the outer and inner

faces of the sheet. The simulated data from the wind-tunnel test were used as input for different computational techniques with agreement. A procedure was developed to extend the computational model to net clad scaffolds with the netting simulated as porous media with the netting properties obtained from wind-tunnel tests.

Overall results and conclusions will be given both in this Chapter and in Chapter 8 for all the models tested in this project based on the following criteria, which the author considers to be the essential requirements for a suitable wind engineering turbulence models:

- overall accuracy
- stability and ease of use in complex flow fields
- computational requirements and overheads

Although the accuracy of the model is the prime consideration, the model applicability is also of paramount importance. An accurate turbulence model that can-not be applied to say 5 out of 10 flow simulations, due to poor numerical stability, is of little use to the computational wind engineer. Steady state simulations using modern computer facilities make the issue of computational overheads only a relatively minor concern, nevertheless this point will be addressed as fast simulation times are preferred. Finally it is also preferable that the model has a general universality and so can be applied with equal success to other engineering disciplines and thus gains acceptance among the engineering community in general.

In any numerical simulation of fluid flow there are a number of checks that have to be made to assess the overall accuracy of the results obtained and to ensure that the CFD data is of a sufficiently high quality. The following work details these important checks and wherever necessary explains any assumptions that have been made.

The CFD package Fluent was used to obtain velocity, pressure, pressure coefficient and turbulent kinetic energy profiles, etc. for the cubical SEB and for sheet/net clad scaffolds surrounding the SEB. The results were used in the following checks and comparisons. To obtain the pressure data measurement lines were located approximately 5mm from the face of the various building and sheet/net shapes. All vector and contour plots shown are located along vertical centrelines, horizontal

centrelines and horizontally 2/3rd height of the SEB and on sheet/net clad scaffolds surrounding the SEB.

7.2 Wind-tunnel Experiments

Before starting wind-tunnel experiments on the models of Silsoe Experimental Building (SEB a cubical $6m \times 6m \times 6m$ test building) and on the Silsoe Building surrounded by sheet clad scaffolds [for the sheet clad scaffolds, two models were made, one with sheeting touching the ground and the other with an elevated sheet surrounding the SEB], a thorough study about the Silsoe site and on the full-scale results obtained from the research by Richardson et al [7.1] on the Silsoe Experimental Building was undertaken. To determine the wind forces on sheet clad scaffolds the SEB was used as a base model and a simulated scaffold erected around it. Although, normal sheeting exhibits aero-elastic behaviour under wind load, an assumption was made to treat the sheeted scaffold as being made of static solid thin plates. A 1:30 model scale of the SEB and SEB surrounded by sheet clad and elevated sheet clad scaffolds were used for experiments in the wind-tunnel. These models were tested in a wind-tunnel to determine the pressure coefficients on the outer and inner faces of the sheet. Pressure data obtained from the experimental results on 1:30 model of SEB were compared to full-scale data with generally good agreement.

Although not strictly a numerical accuracy check, there are a number of accuracy issues that are very important to this project when using scale models for wind-tunnel testing rather than prototype. This section will briefly highlight some of the more important aspects with regard to this project; for detailed information the interested reader is referred to Cook [7.2, 7.3].

There are certain apparent advantages for full-scale observations. Full-scale observations do not suffer from any scale mismatches due to Reynolds number, wind shear and turbulence intensities or from blockage effects. However, the main disadvantage of full-scale observations are that they are quite costly and time consuming. Also it is, impossible to control the approach flow conditions, e.g. the static and dynamic reference pressures, the thermal stratifications, etc., which will inevitably obscure details in the observed data [7.4]. Cook [7.2] stated that the error of measurements could possibly be larger in full scale observations than those occurring in well controlled wind-tunnel tests.

There are some serious matters to be considered when undertaking scale simulations in a wind-tunnel. One of the most important aspects is the effect of differing Reynolds numbers involved in the areas of flow recirculation over the building models. The scaling down of such regions of flow to wind-tunnel models will result in very small vortices that will be influenced to a much larger degree by the effects of fluid viscosity, thus reducing the strength of the predicted vortex. These so called Reynolds number vortex effects may result in unrealistically small roof and wake recirculation zones for the scaled building and thus errors in the prediction of pressures, etc.

Finally in this section, it is important to discuss the probable error in the mean pressure coefficient data used in this thesis for the model scale. Dr. Johnny Yue (Director RED Consultants, Hong Kong) stated that the predicted errors for a 259 second sampling time (equivalent to 1 hour in the field) were approximately $\pm 6-8$ percent. This predicted error was used, as a 'general rule of thumb', for all the data used in this project. Nonetheless, it is clear that this error will also be dependent on the location of the pressure tap, with the above mentioned error in an area of steady flow. The error may marginally increase in areas of unsteady flow, such as in the wake. The error is influenced by the time of observation, such as winter, rainy season etc. In the experiments undertaken during the research project it was either raining or the humidity of the air was 90-97% for all the experiments conducted. The main problem realized after the experiments had been completed whilst analysing the data was that some of the pressure taps became blocked during the experiment giving very absurd values. Moisture reduces the diameter of the pressure taps which also may influence the results.

7.2.1 Wind-tunnel Experiments on Silsoe Experimental Building (SEB)

The SEB was taken as the base model for study as the full-scale data, i.e. the velocity profile and longitudinal turbulence intensities from the Silsoe site, were available to be used both for the experiment (for simulation in a wind-tunnel) and for CFD analyses. The mean longitudinal wind speed profile measured in the wind-tunnel was in good agreement with the SRI full-scale profile with a power-law exponent of 0.17. The longitudinal turbulence intensity was slightly less than the Silsoe site full-scale data and has been discussed in Chapter 5. A manual iterative procedure was undertaken by changing the size and magnitude of the roughness to achieve the same turbulence at the model height during the simulation process but it was not possible to achieve exactly the same turbulence. The data for each wind direction were collected at 100 samples per

second per channel and the duration of each run was kept to 249 seconds. This was equivalent to one hour data in the field. The models were tested in the wind tunnel at every 15 degrees of angle to determine the pressure coefficients on its façade.

The pressure contours on the façade of the building and on roof are shown in figures from Figure 7.1 to Figure 7. 29. The full details of pressure coefficients (pressure contours maxima, minima, mean and r.m.s.) for two different terrains can be found in Report No.397, School of the Built-Environment, Oxford Brookes University, "Wind Tunnel Investigations of the Pressure Acting on sheet Clad Scaffolds", 2010 [7.5].

It was observed that the maximum suction pressure coefficients on the roof of the cubical SEB occurred when the direction of wind was at $\pm 45^0$ from the normal windward façade. It appears in most cases that it was the taps closest to the roof edge that experienced the highest suction. The maximum positive pressure on the windward face of the SEB occurred when the direction of the wind was perpendicular to its windward face. The maximum negative pressure on the side face of the SEB occurred when the direction of flow was parallel to the side face. The maximum negative pressure on the leeward face of the SEB occurred when the direction of wind was at $\pm 30^0$ from the windward façade.

Pressure Coefficient Contours on Roof of SEB

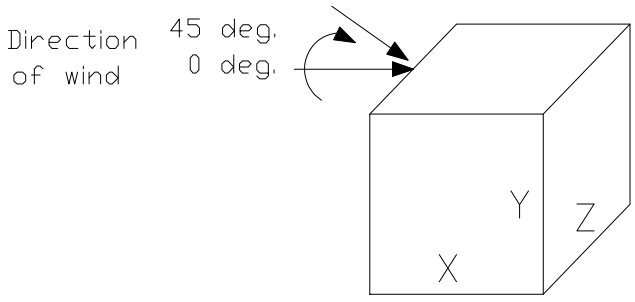

Figure 7.1 Angle of attack of wind on roof of the SEB , direction of which varies from 0^o to $+45^o$

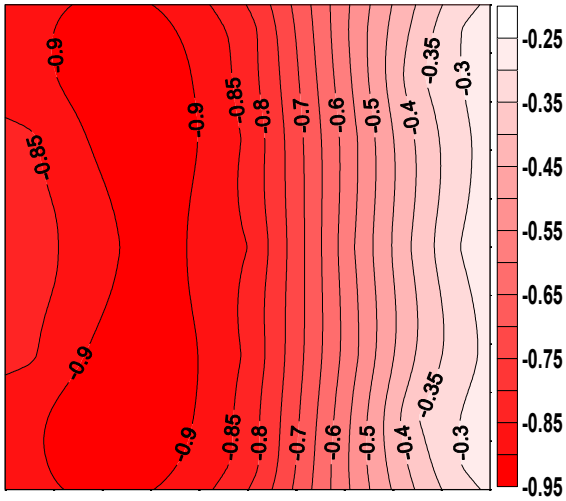

Figure 7.2 Pressure coefficient contours on the roof of the SEB when θ= 0°

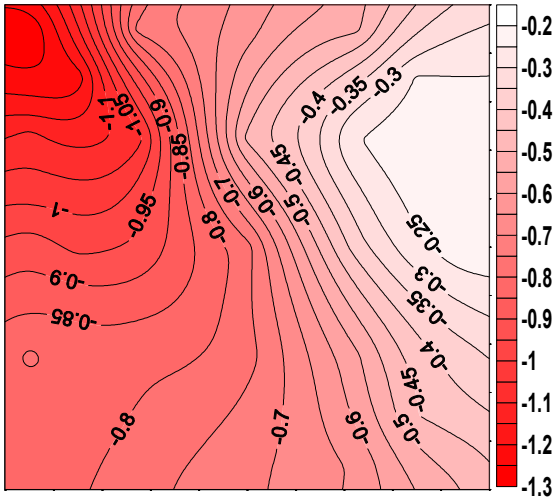

Figure 7.3 Pressure coefficient contours on the roof of the SEB when θ= 15°

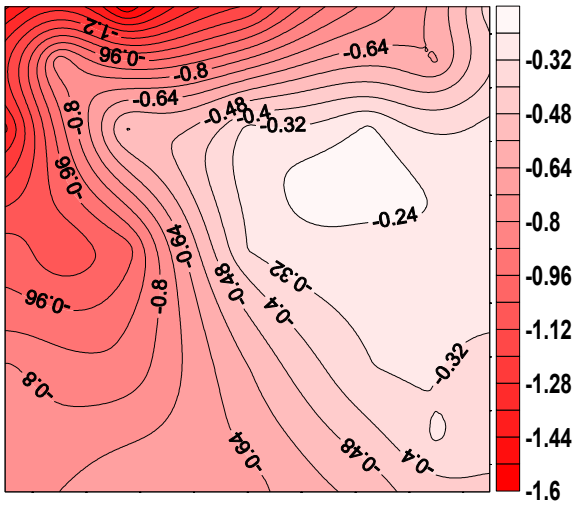

Figure 7.4 Pressure coefficient contours on the roof of the SEB when θ= 30°

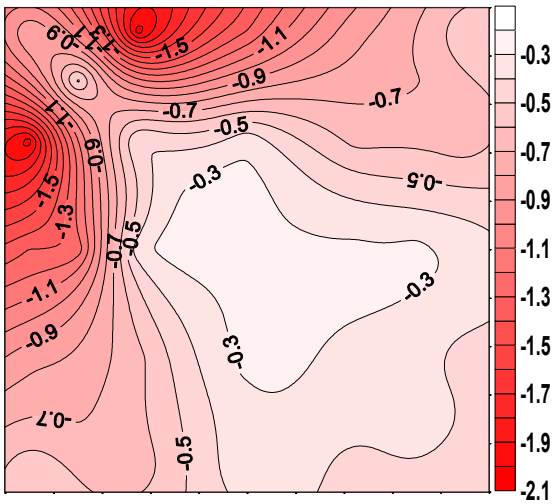

Figure 7.5 Pressure coefficient contours on the roof of the SEB when θ= 45°

Pressure Coefficient Contours on Windward Face of SEB

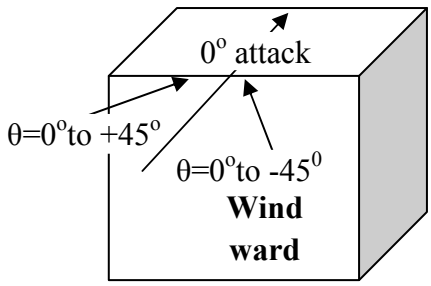

Figure 7.6 Angle of attack of wind on windward wall of SEB, direction of which varies from -45° to +45°

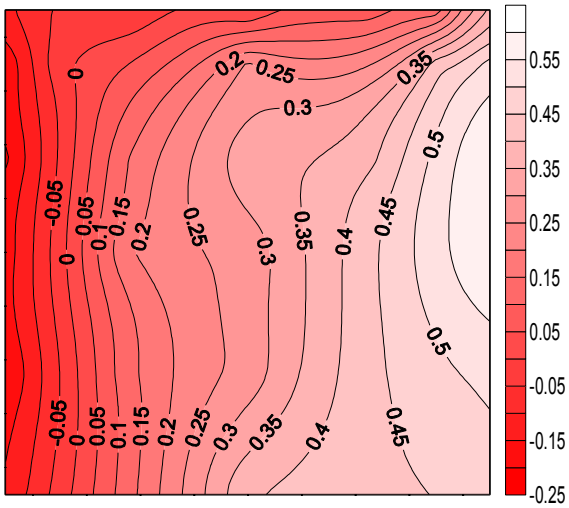

Figure 7.7 Pressure coefficient contours on the windward face of the SEB when θ= -45°

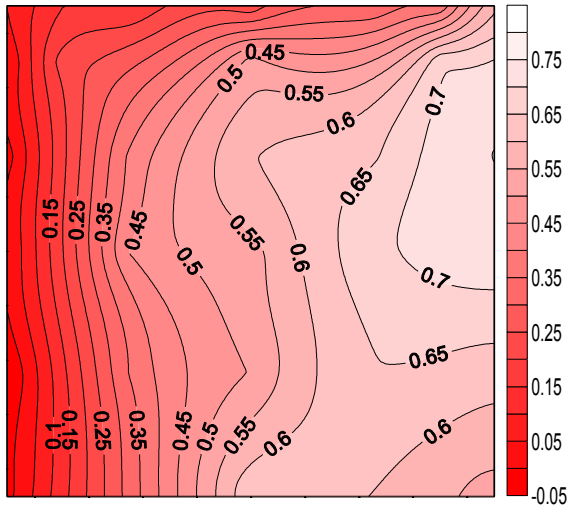

Figure 7.8 Pressure coefficient contours on the windward face of the SEB when θ= -30°

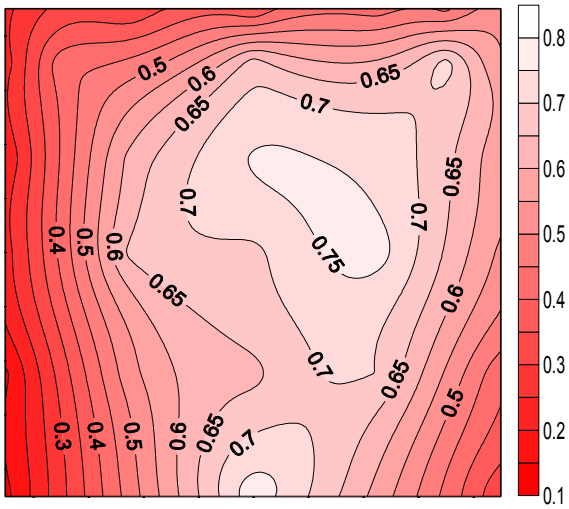

Figure 7.9 Pressure coefficient contours on the windward face of the SEB when θ= -15°

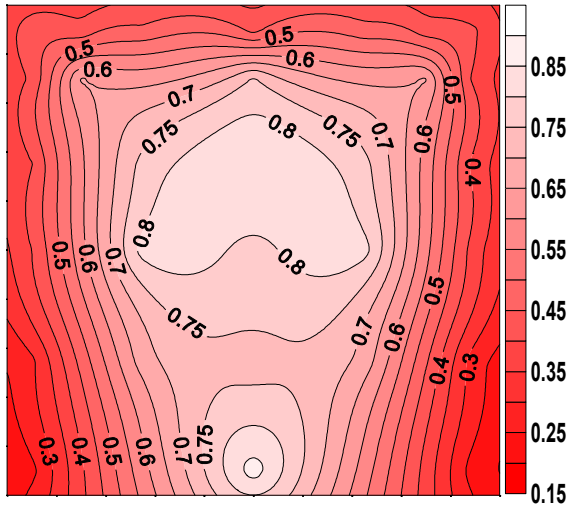

Figure 7.10 Pressure coefficient contours on the windward face of the SEB when θ=0°

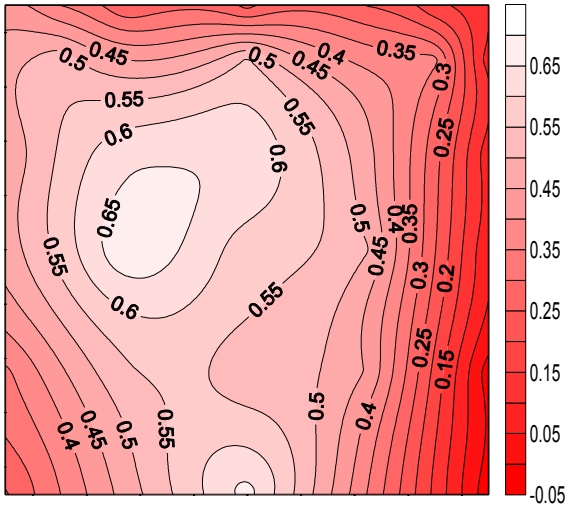

Figure 7.11 Pressure coefficient contours on the windward face of the SEB when θ=+15°

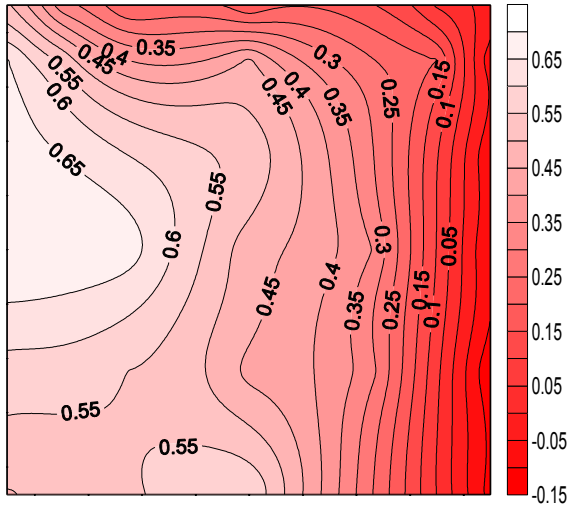

Figure 7.12 Pressure coefficient contours on the windward face of the SEB when θ=+30°

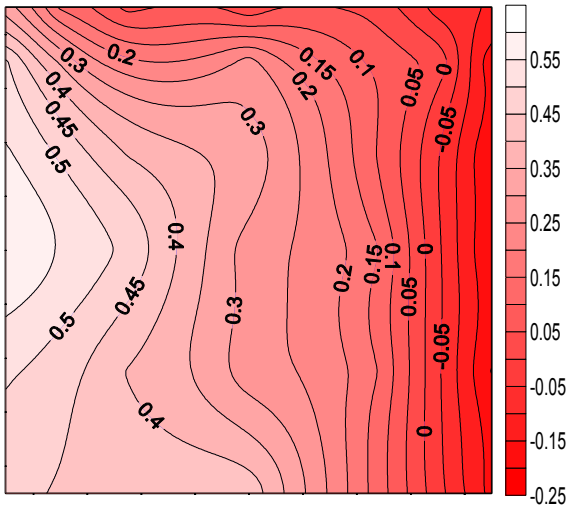

Figure 7.13 Pressure coefficient contours on the windward face of the SEB when θ=+45^o

Pressure Coefficient Contours on Side Face of SEB

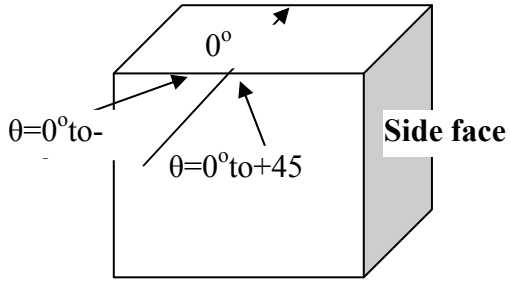

Figure 7.14 Angle of attack of wind on windward wall of SEB, direction of which varies from -45^o to +45^o

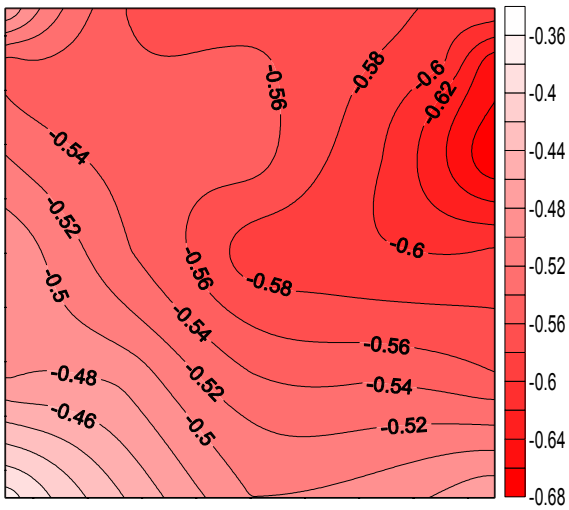

Figure 7.15 Pressure coefficient contours on the side face of the SEB when θ= -45^o

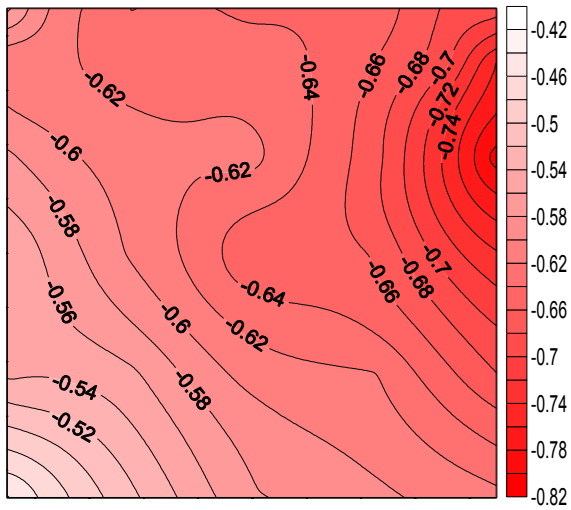

Figure 7.16 Pressure coefficient contours on the side face of the SEB when θ= -30^o

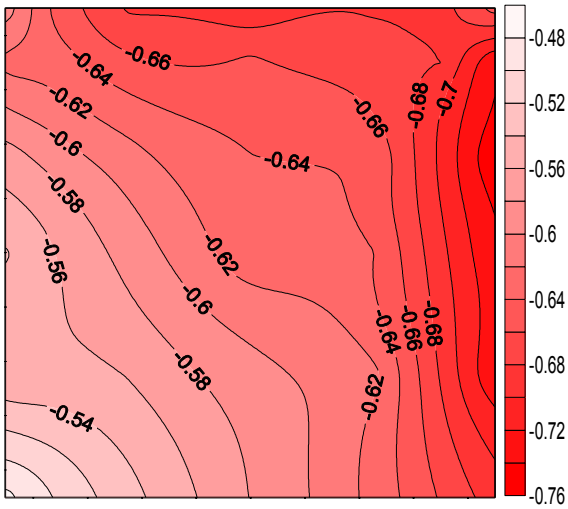

Figure 7.17 Pressure coefficient contours on the side face of the SEB when θ= -15°

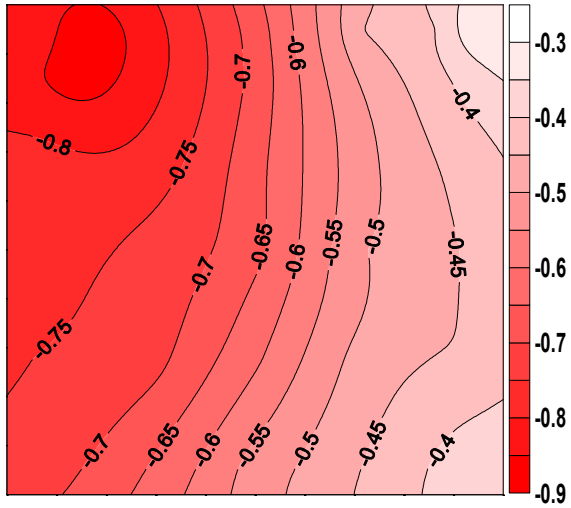

Figure 7.18 Pressure coefficient contours on the side face of the building when θ= 0°

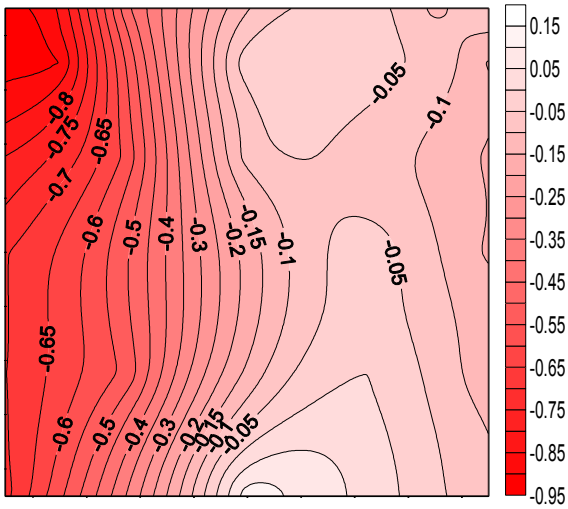

Figure 7.19 Pressure coefficient contours on the side face of the SEB when θ=+15°

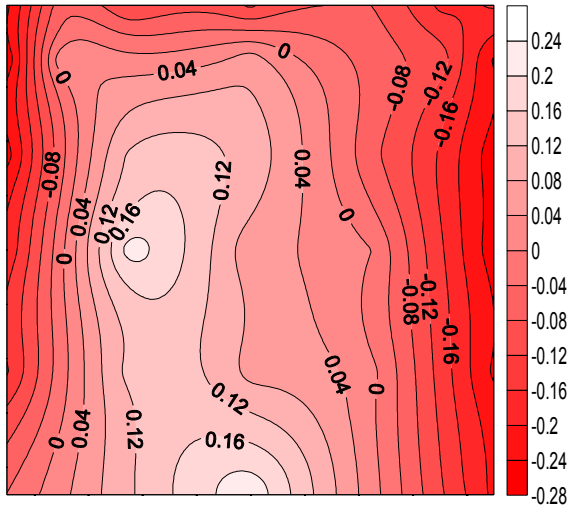

Figure 7.20 Pressure coefficient contours on the side face of the SEB when θ=+30°

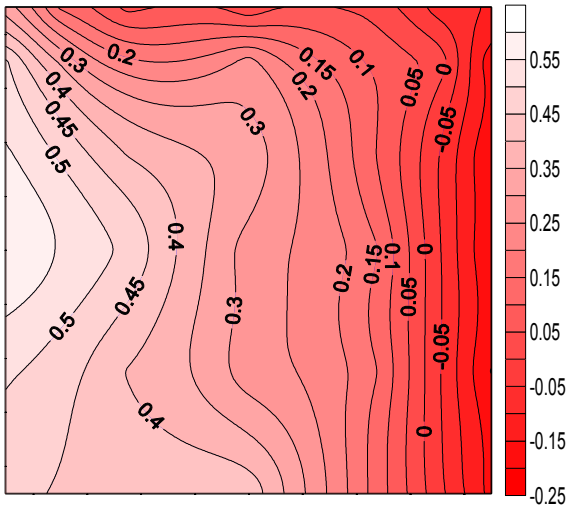

Figure 7.21 Pressure coefficient contours on the side face of the SEB when θ=+45°

Pressure Coefficient Contours on Leeward Face of SEB

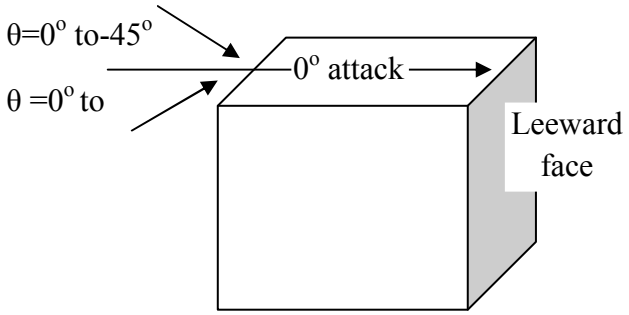

Figure 7.22 Angle of attack of wind on windward wall of SEB, direction of which varies from -45° to +45°

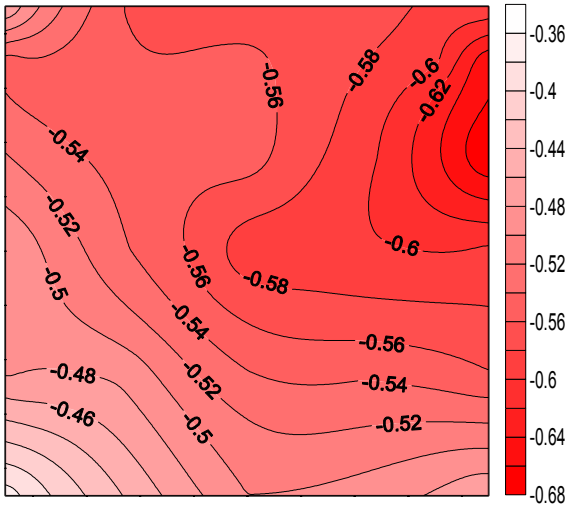

Figure 7.23 Pressure coefficient contours on the leeward face of the SEB when θ= -45°

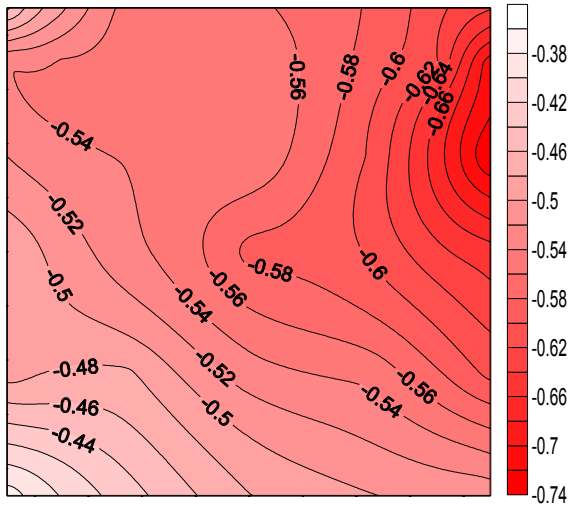

Figure 7.24 Pressure coefficient contours on the leeward face of the SEB when θ= -30°

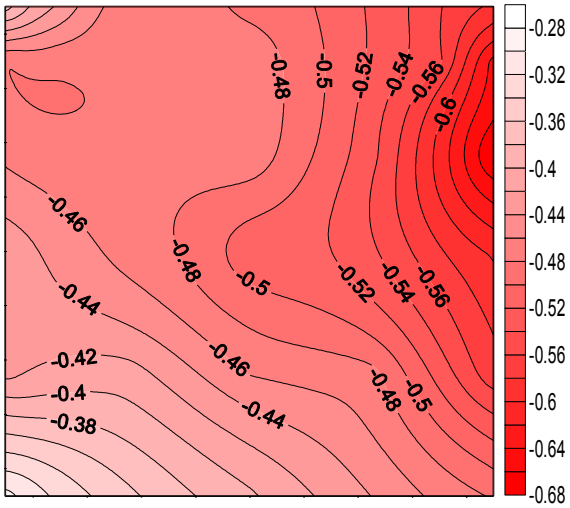

Figure 7.25 Pressure coefficient contours on the leeward face of the SEB when θ= -15°

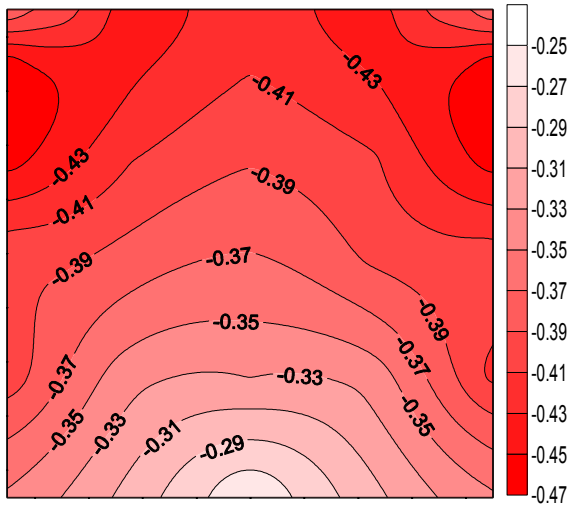

Figure 7.26 Pressure coefficient contours on the leeward face of the SEB when θ= 0°

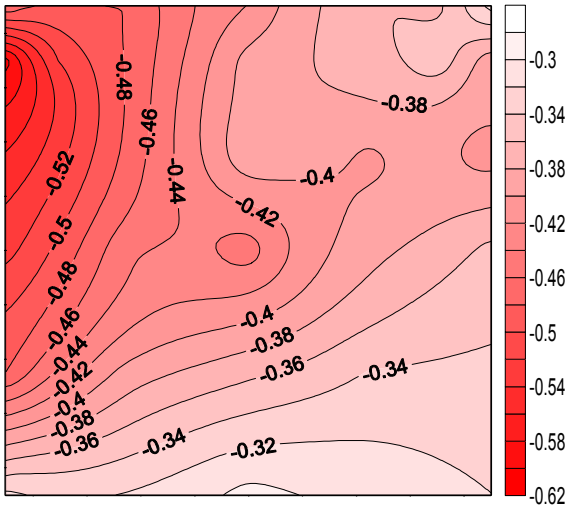

Figure 7.27 Pressure coefficient contours on the leeward face of the SEB when θ= +15°

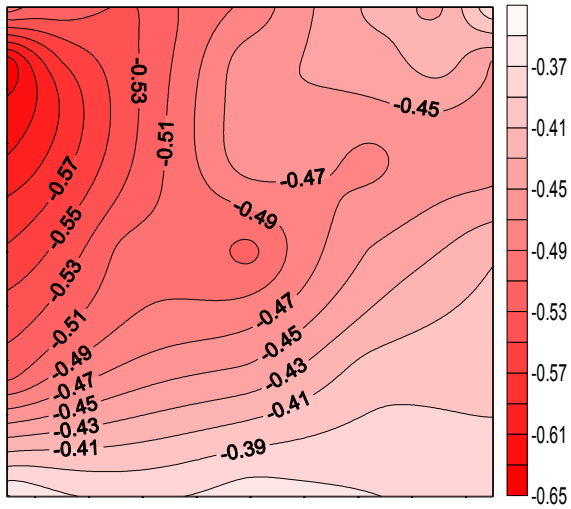

Figure 7.28 Pressure coefficient contours on the leeward face of the SEB when θ= +30°

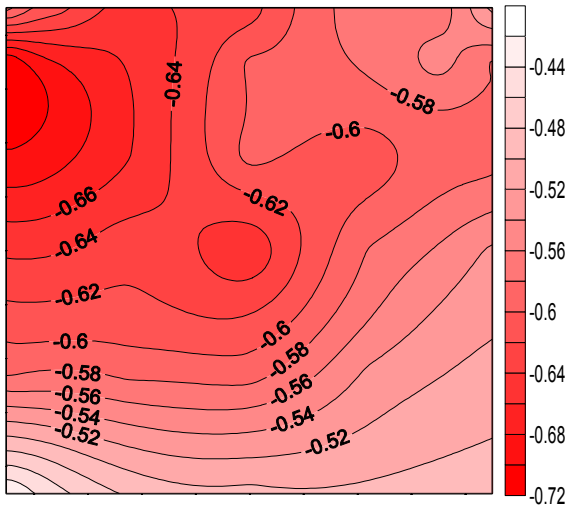

Figure 7.29 Pressure coefficient contours on the leeward face of the SEB when θ= +45°

7.2.2 Wind-tunnel Experiments on Sheet/Elevated Sheet Clad Scaffolds Surrounding SEB

To determine the pressure coefficients on sheet clad scaffolds, the SEB was used as a base model and a simulated scaffold erected around it. Two types of sheet clad scaffold were made, one touching the ground and the other with an elevated sheet (1 m from the ground on the prototype) surrounding the SEB to actually visualize the ground conditions. The models are shown in Figures 1.6 and 1.7. The top portions of the sheet clad scaffold were tapered from the inside and both top and bottom portions were tapered from the inside for the elevated sheet clad scaffold and can be seen in Figures 1.6 and 1.7. The same longitudinal wind velocity profile and longitudinal turbulence intensity were used as were used for SEB. The models were tested in the wind tunnel at every 15 degrees of angle to determine the pressure coefficients on its façade both

inside and outside. The pressure contours on the outer façade of the sheet clad scaffold (both elevated and touching the ground) are shown in Figures 7.30 to 7.77 and on the inner face of the sheet clad scaffold (both elevated and touching the ground) are shown in Figures 7.78 to 7.125. The full details of pressure coefficients (maxima, minima, mean and r.m.s.) for two different terrains and turbulences for both sheet clad scaffolds and elevated sheet clad scaffolds can be seen in the Report No.397, School of the Built-Environment, Oxford Brookes University [7.5].

The pressure coefficient contours on the outer façade of the sheet clad and elevated sheet clad scaffold show a similar trend. In the elevated sheet clad scaffolds the winds in the lower portion moved horizontally with separation of wind at the edges creating higher suction on the side faces. The wind did not move in the upward direction through the space in between scaffolds and structures as was initially thought would happen.

It was observed that the maximum positive pressure on the outer façade of the sheet clad scaffolds and the elevated sheet clad scaffolds occurred when the direction of wind was perpendicular to it. Also the maximum negative pressure on the side outer face of both sheet clad scaffolds and the elevated sheet clad scaffolds occurred when the direction of wind was parallel to its face. The maximum negative pressure on the leeward outer face of the sheet clad scaffolds and elevated sheet clad scaffolds occurred when the direction of wind was at $\pm 45^0$ from the windward face. This signifies that the patterns of pressure coefficients on the outer face of the sheet clad scaffolds and elevated sheet clad scaffolds were same.

The pressures on the inside face of the sheet clad and elevated sheet clad scaffold were negative (i.e. suction) but no definite trends of variation were found. This may be due to the local vortices of the trapped air between the wall façade and the scaffold sheet. However, the pressure coefficients on the inner face of the sheet clad scaffold are a little higher than those on the elevated scaffold.

Pressure Coefficient Contours on Windward Outer Face of the Sheet Clad Scaffold

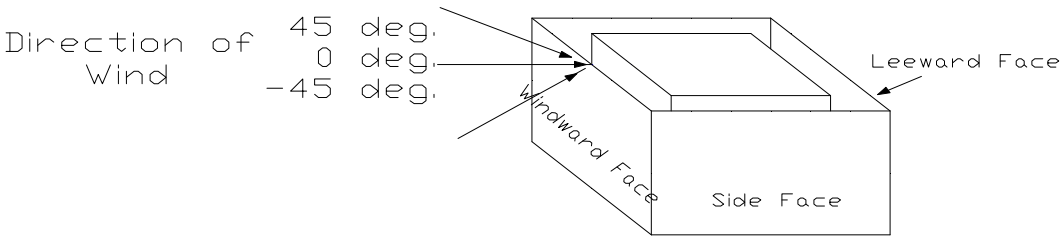

Figure 7.30 Angle of attack of wind on windward outer face of sheet clad scaffold surrounding SEB, direction of which varies from -45° to +45°

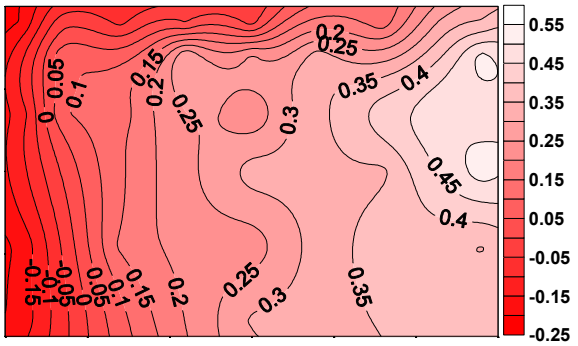

Figure 7.31 Pressure coefficient contours on the windward outer face of the sheet clad scaffold when θ= 45°

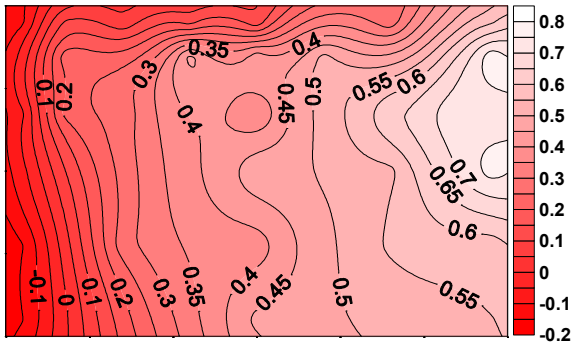

Figure 7.32 Pressure coefficient contours on the windward outer face of the sheet clad scaffold when θ= 30°

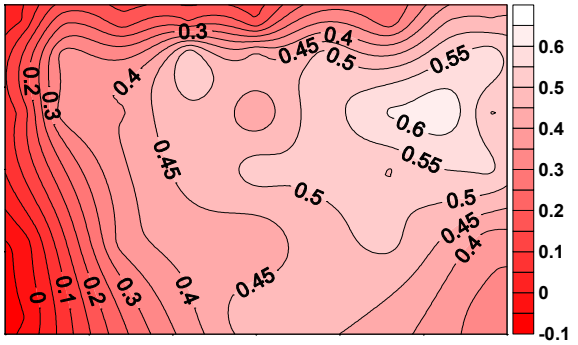

Figure 7.33 Pressure coefficient contours on the windward outer face of the sheet clad scaffold when θ= 15°

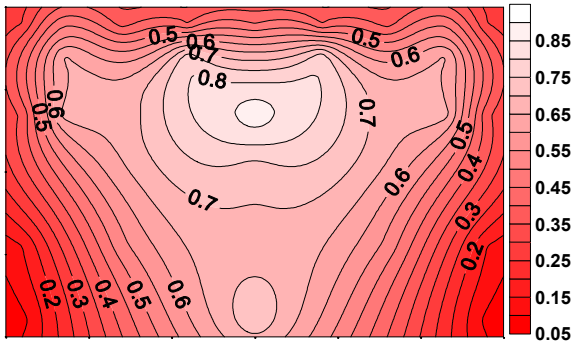

Figure 7.34 Pressure coefficient contours on the windward outer face of the sheet clad scaffold when θ= 0°

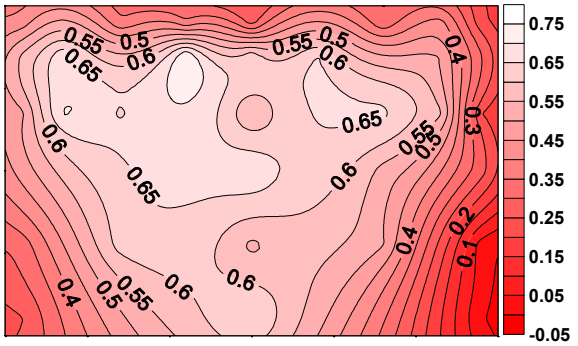

Figure 7.35 Pressure coefficient contours on the windward outer face of the sheet clad scaffold when θ= -15°

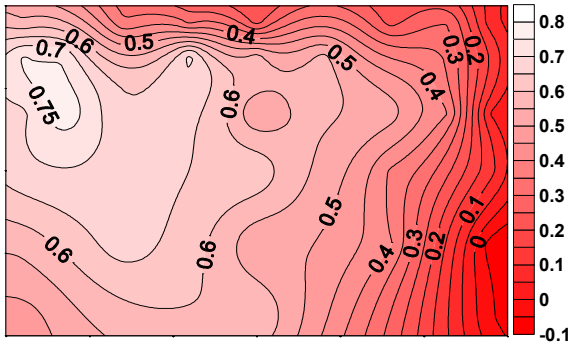

Figure 7.36 Pressure coefficient contours on the windward outer face of the sheet clad scaffold when θ= -30°

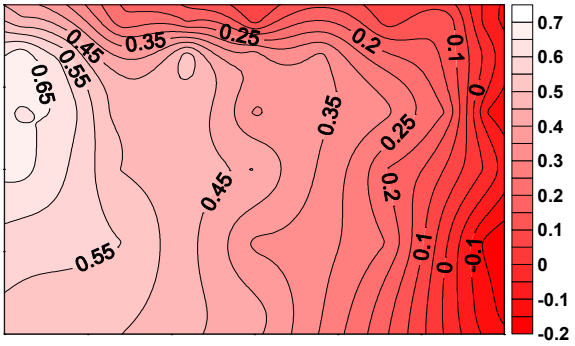

Figure 7.37 Pressure coefficient contours on the windward outer face of the sheet clad scaffold when θ= -45°

Pressure Coefficient Contours on the Side Outer Face of the Sheet Clad Scaffold

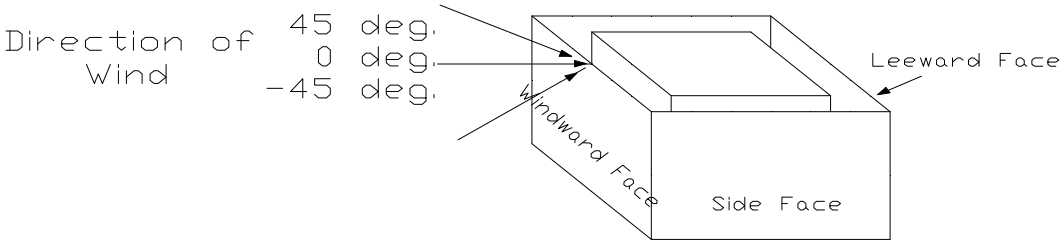

Figure 7.38 Angle of attack of wind on windward outer face of sheet clad scaffold surrounding SEB, direction of which varies from 45° to -45°

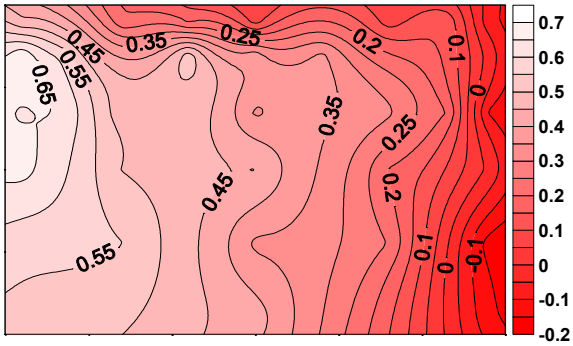

Figure 7.39 Pressure coefficient contours on the side outer face of the sheet clad scaffold when θ= 45°

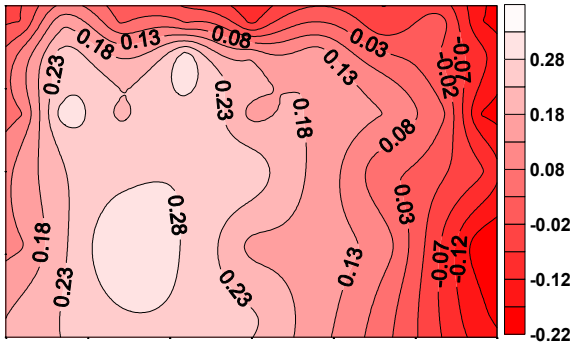

Figure 7.40 Pressure coefficient contours on the side outer face of the sheet clad scaffold when θ= 30°

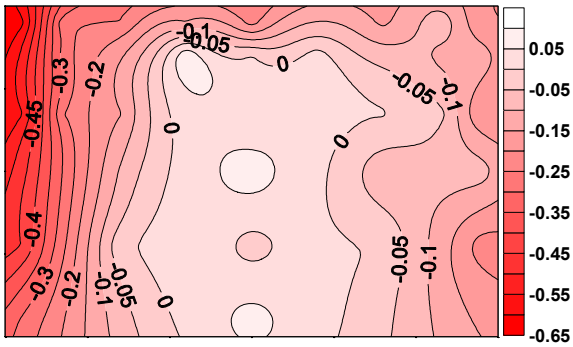

Figure 7.41 Pressure coefficient contours on the side outer face of the sheet clad scaffold when θ= 15°

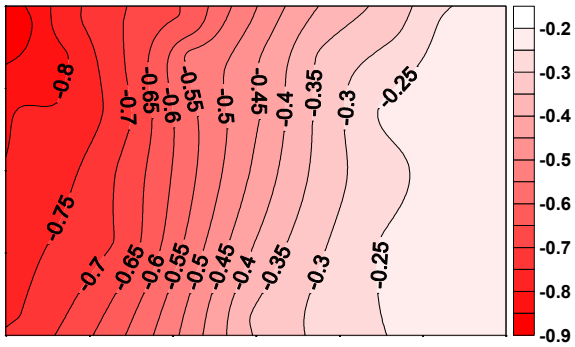

Figure 7.42 Pressure coefficient contours on the side outer face of the sheet clad scaffold when θ= 0°

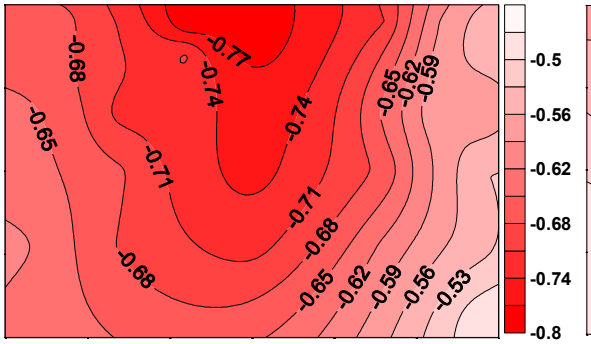

Figure 7.43 Pressure coefficient contours on the side outer face of the sheet clad scaffold when θ= -15°

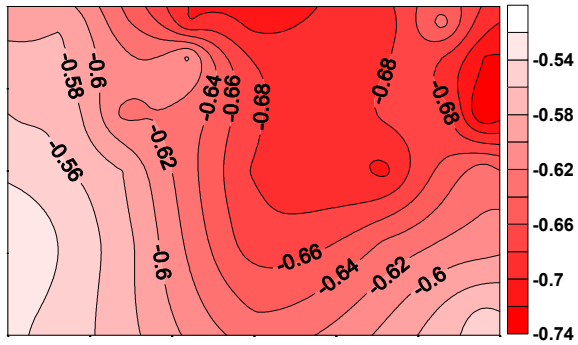

Figure 7.44 Pressure coefficient contours on the side outer face of the sheet clad scaffold when θ= -30°

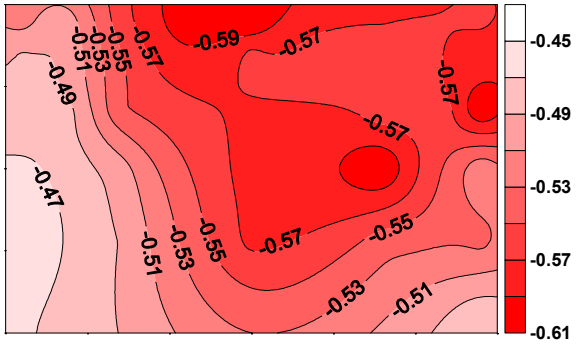

Figure 7.45 Pressure coefficient contours on the side outer face of the sheet clad scaffold when θ= -45°

Pressure Coefficient Contours on the Leeward Outer Face of the Sheet Clad Scaffold

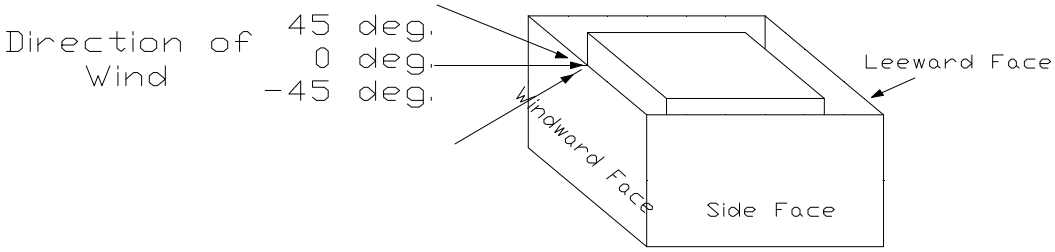

Figure 7.46 Angle of attack of wind on windward outer face of sheet clad scaffold surrounding SEB, direction of which varies from 45° to -45°

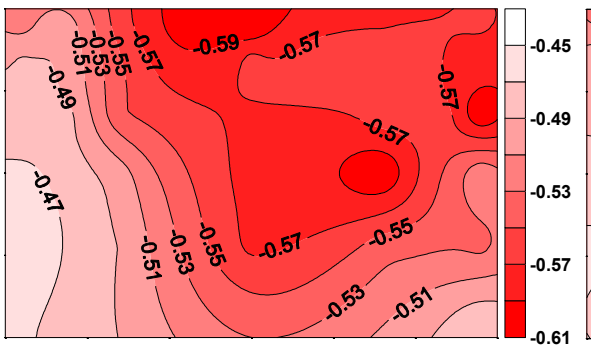

Figure 7.47 Pressure coefficient contours on the leeward outer face of the sheet clad scaffold when θ= 45°

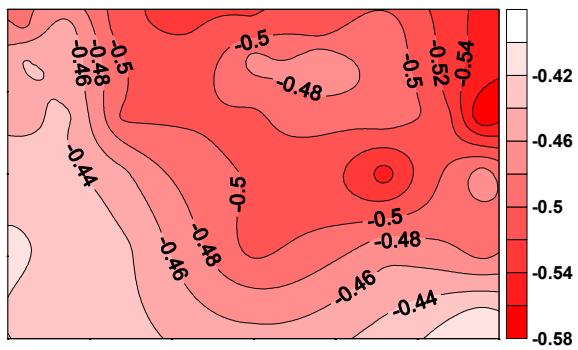

Figure 7.48 Pressure coefficient contours on the leeward outer face of the sheet clad scaffold when θ= 30°

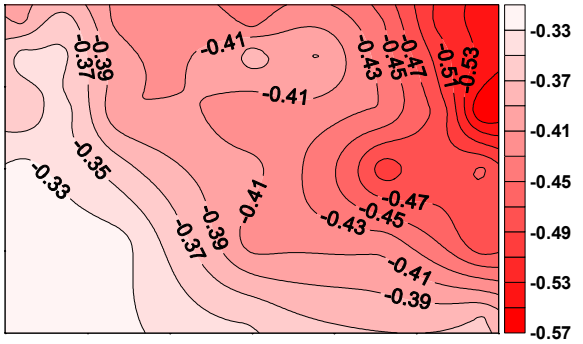

Figure 7.49 Pressure coefficient contours on the leeward outer face of the sheet clad scaffold when θ= 15°

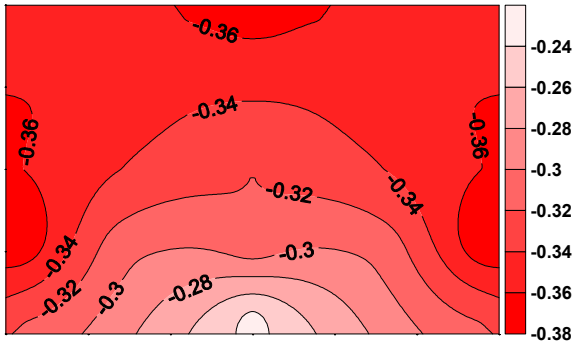

Figure 7.50 Pressure coefficient contours on the leeward outer face of the sheet clad scaffold when θ= 0°

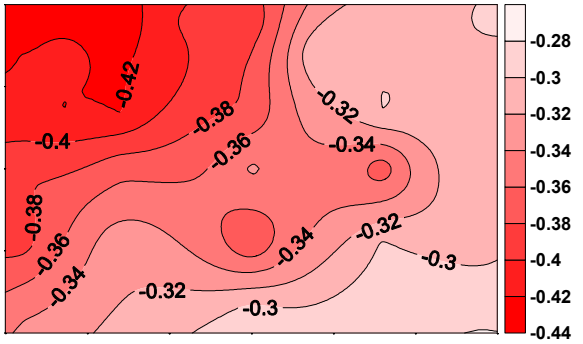

Figure 7.51 Pressure coefficient contours on the leeward outer face of the sheet clad scaffold when θ= -15°

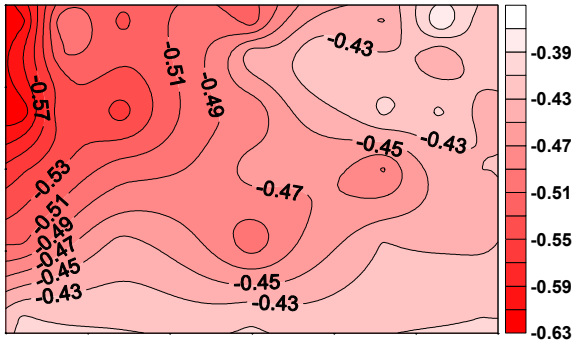

Figure 7.52 Pressure coefficient contours on the leeward outer face of the sheet clad scaffold when θ= -30°

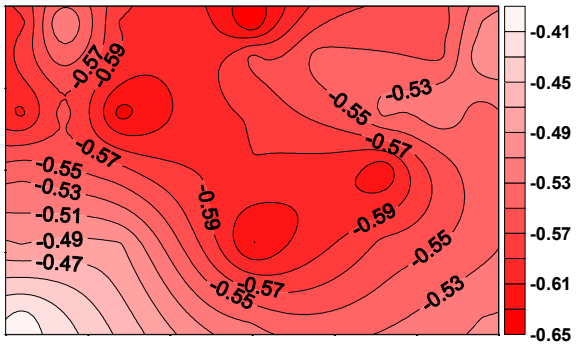

Figure 7.53 Pressure coefficient contours on the leeward outer face of the sheet clad scaffold when θ= -45°

Pressure Coefficient Contours on the Windward Outer Face of the Elevated Sheet Clad Scaffold

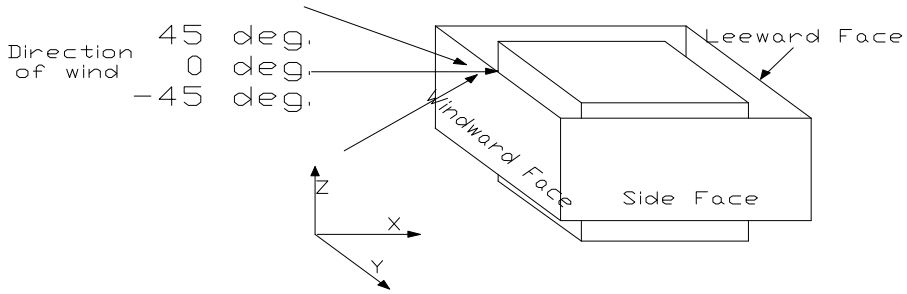

Figure 7.54 Angle of attack of wind on windward outer face of the elevated sheet clad scaffold surrounding SEB, direction of which varies from 45° to -45°

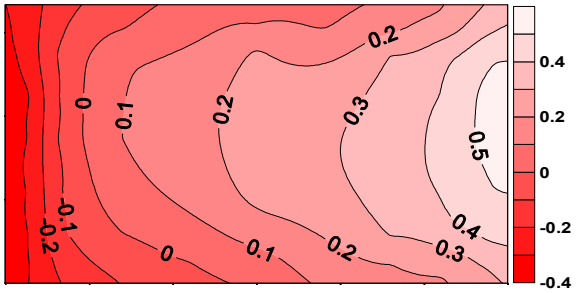

Figure 7.55 Pressure coefficient contours on the windward outer face of the elevated sheet clad scaffold when θ= 45°

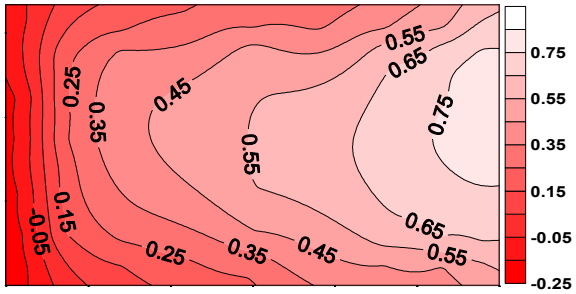

Figure 7.56 Pressure coefficient contours on the windward outer face of the elevated sheet clad scaffold when θ= 30°

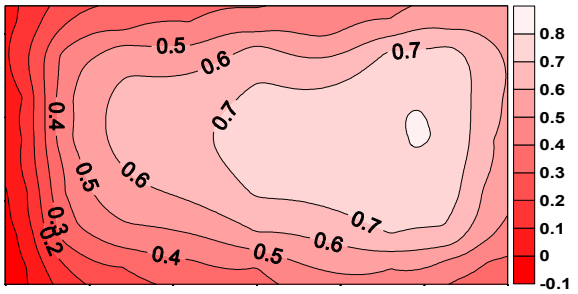

Figure 7.57 Pressure coefficient contours on the windward outer face of the elevated sheet clad scaffold when θ= 15°

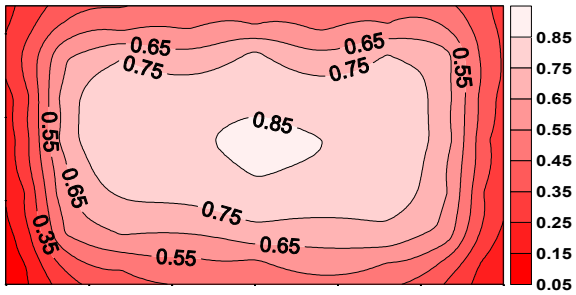

Figure 7.58 Pressure coefficient contours on the windward outer face of the elevated sheet clad scaffold when θ= 0°

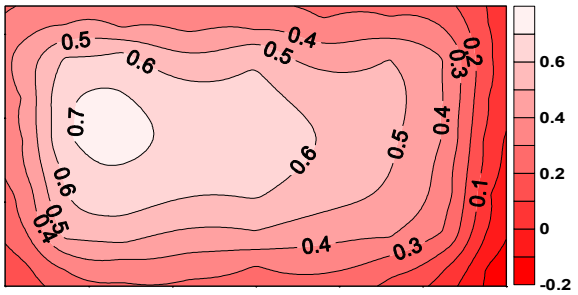

Figure 7.59 Pressure coefficient contours on the windward outer face of the elevated sheet clad scaffold when θ= -15°

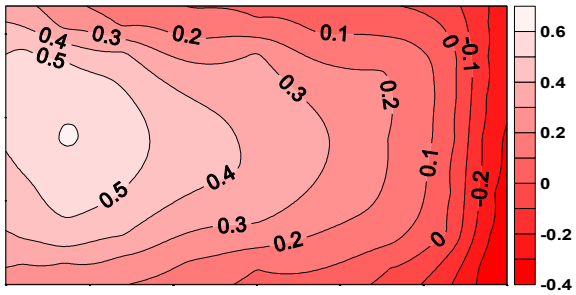

Figure 7.60 Pressure coefficient contours on the windward outer face of the elevated sheet clad scaffold when θ= -30°

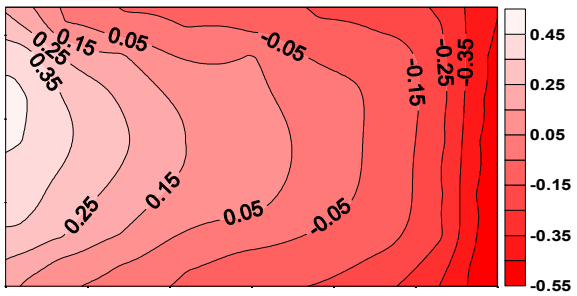

Figure 7.61 Pressure coefficient contours on the windward outer face of the elevated sheet clad scaffold when θ= -45°

Pressure Coefficient Contours on the Side Outer Face of the Elevated Sheet Clad Scaffold

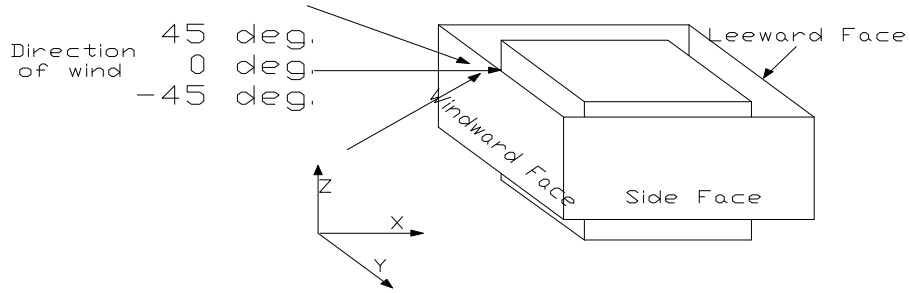

Figure 7.62 Angle of attack of wind on windward outer face of the elevated sheet clad scaffold surrounding SEB, direction of which varies from 45° to -45°

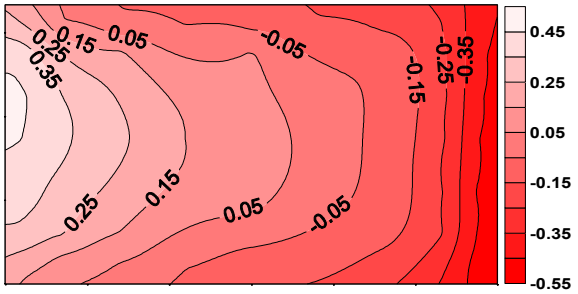

Figure 7.63 Pressure coefficient contours on the side outer face of the elevated sheet clad scaffold when θ= 45°

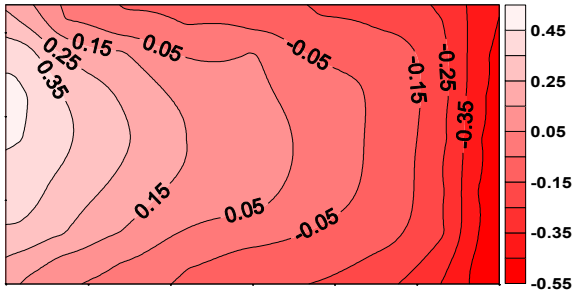

Figure 7.64 Pressure coefficient contours on the side outer face of the elevated sheet clad scaffold when θ= 30°

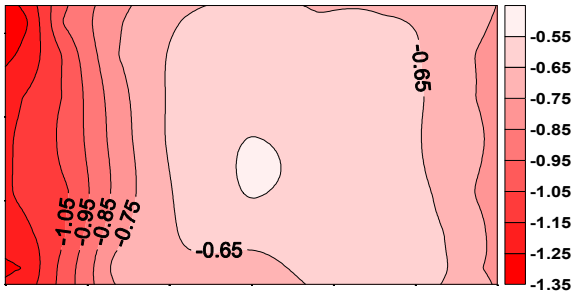

Figure 7.65 Pressure coefficient contours on the side outer face of the elevated sheet clad scaffold when θ= 15°

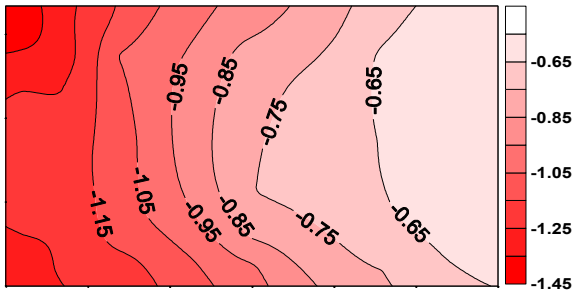

Figure 7.66 Pressure coefficient contours on the side outer face of the elevated sheet clad scaffold when θ= 0°

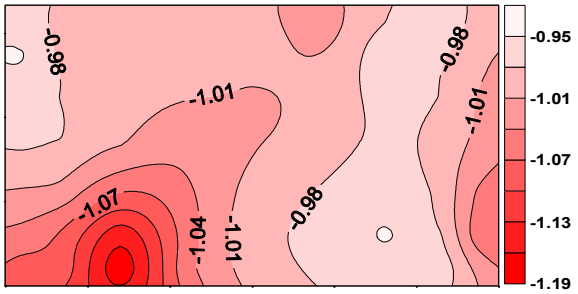

Figure 7.67 Pressure coefficient contours on the side outer face of the elevated sheet clad scaffold when θ= -15°

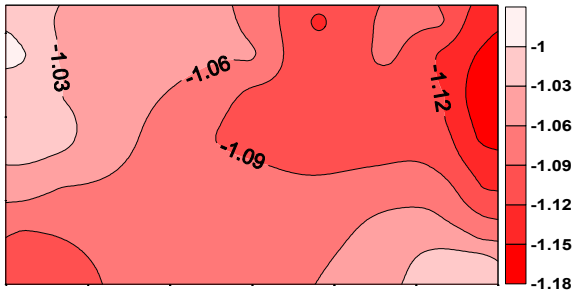

Figure 7.68 Pressure coefficient contours on the windward outer face of the elevated sheet clad scaffold when θ= -30°

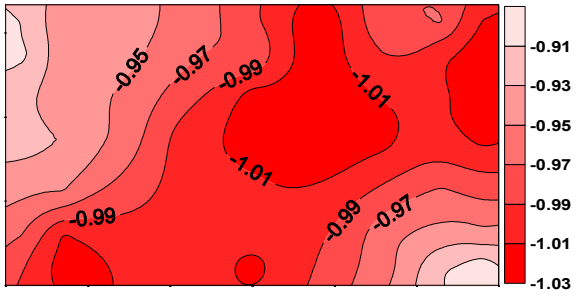

Figure 7.69 Pressure coefficient contours on the side outer face of the elevated sheet clad scaffold when θ= -45°

Pressure Coefficient Contours on the Leeward Outer Face of the Elevated Sheet Clad Scaffold

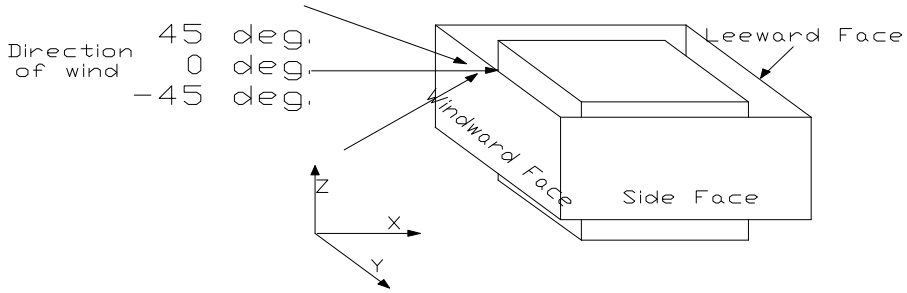

Figure 7.70 Angle of attack of wind on windward outer face of the elevated sheet clad scaffold surrounding SEB, direction of which varies from 45° to -45°

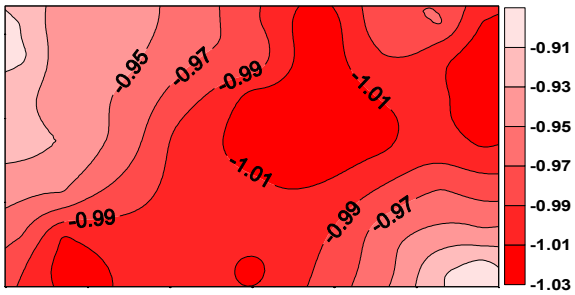

Figure 7.71 Pressure coefficient contours on the leeward outer face of the elevated sheet clad scaffold when θ= 45°

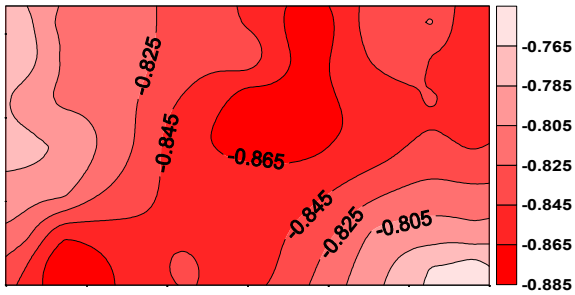

Figure 7.72 Pressure coefficient contours on the leeward outer face of the elevated sheet clad scaffold when θ= 30°

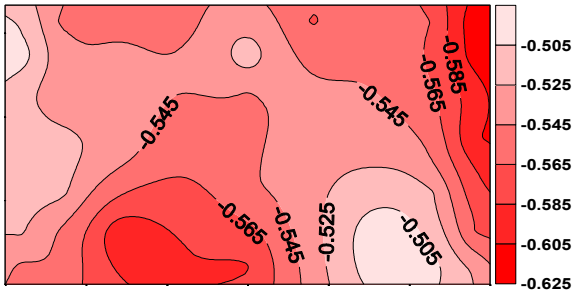

Figure 7.73 Pressure coefficient contours on the leeward outer face of the elevated sheet clad scaffold when θ= 15°

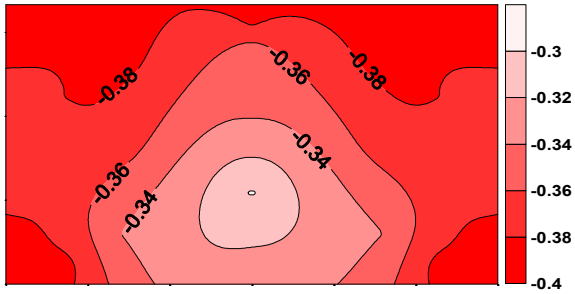

Figure 7.74 Pressure coefficient contours on the leeward outer face of the elevated sheet clad scaffold when θ= 0°

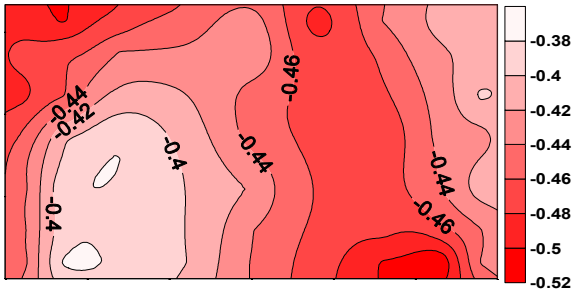

Figure 7.75 Pressure coefficient contours on the leeward outer face of the elevated sheet clad scaffold when θ= -15°

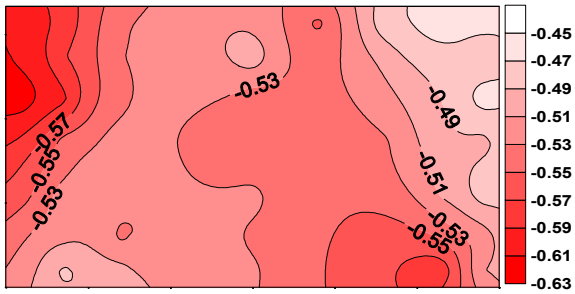

Figure 7.76 Pressure coefficient contours on the leeward outer face of the elevated sheet clad scaffold when θ= -30°

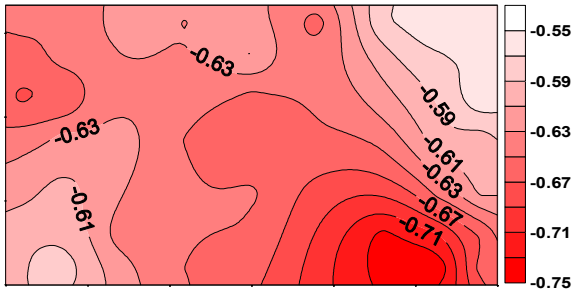

Figure 7.77 Pressure coefficient contours on the leeward outer face of the elevated sheet clad scaffold when θ= -45°

Pressure Coefficient Contours on the Windward Inner Face of the Sheet Clad Scaffold

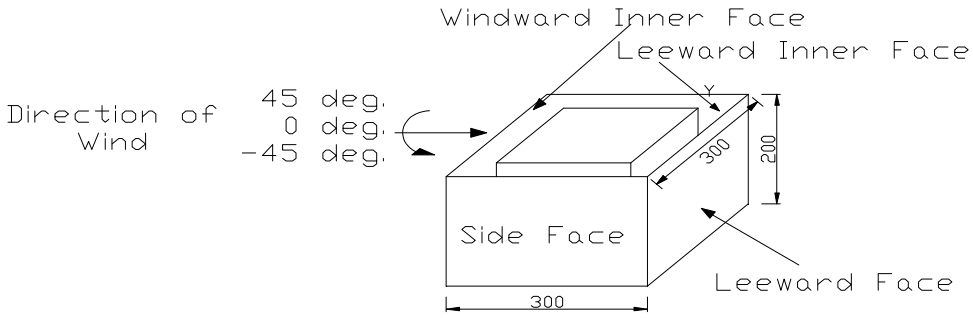

Figure 7.78 Angle of attack of wind on windward outer face of the sheet clad scaffold surrounding SEB, direction of which varies from 45° to -45°

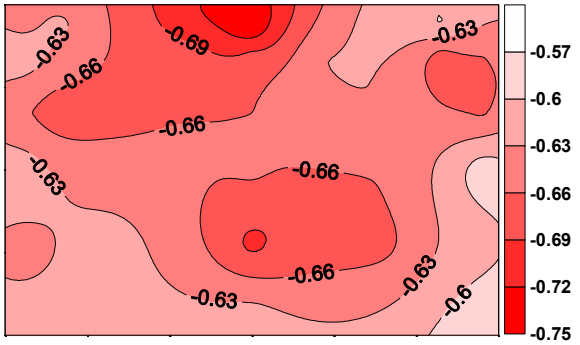

Figure 7.79 Pressure coefficient contours on the windward inner face of the sheet clad scaffold when θ= 45°

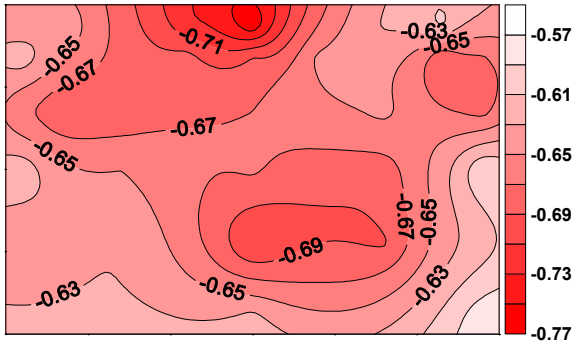

Figure 7.80 Pressure coefficient contours on the windward inner face of the sheet clad scaffold when θ= 30°

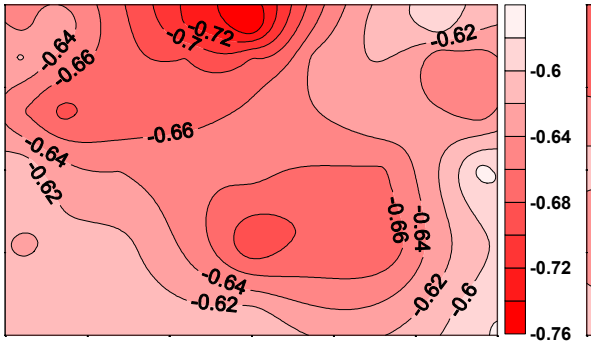

Figure 7.81 Pressure coefficient contours on the windward inner face of the sheet clad scaffold when θ= 15°

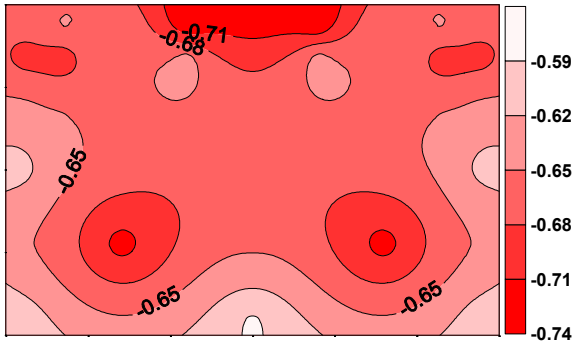

Figure 7.82 Pressure coefficient contours on the windward inner face of the sheet clad scaffold when θ= 0°

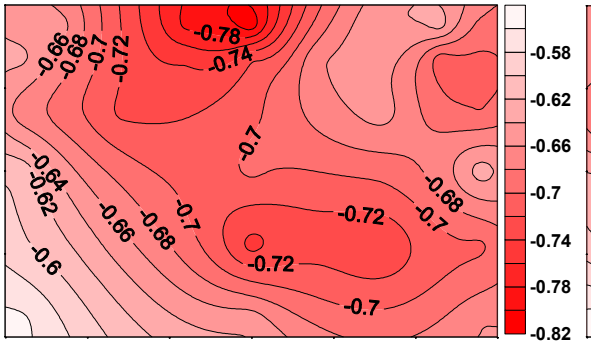

Figure 7.83 Pressure coefficient contours on the windward inner face of the sheet clad scaffold when θ= -15°

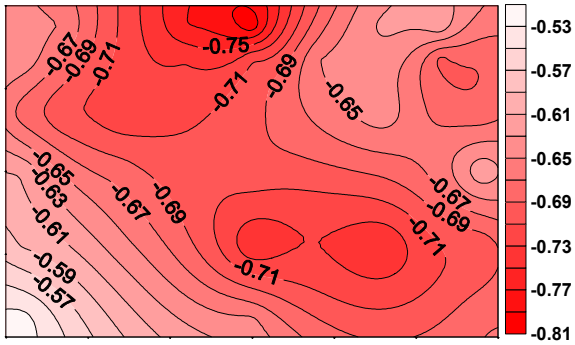

Figure 7.84 Pressure coefficient contours on the windward inner face of the sheet clad scaffold when θ= -30°

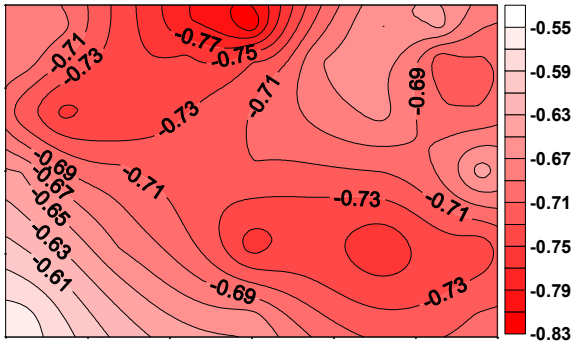

Figure 7.85 Pressure coefficient contours on the windward inner face of the sheet clad scaffold when θ= -45°

Pressure Coefficient Contours on the Side Inner Face of the Sheet Clad Scaffold

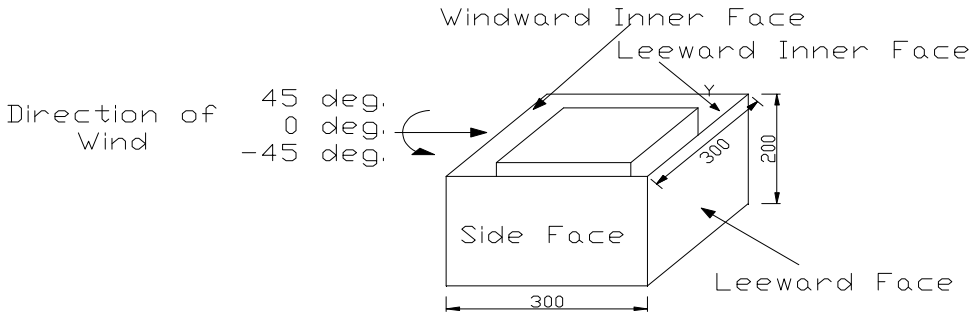

Figure 7.86 Angle of attack of wind on windward outer face of the sheet clad scaffold surrounding SEB, direction of which varies from 45° to -45°

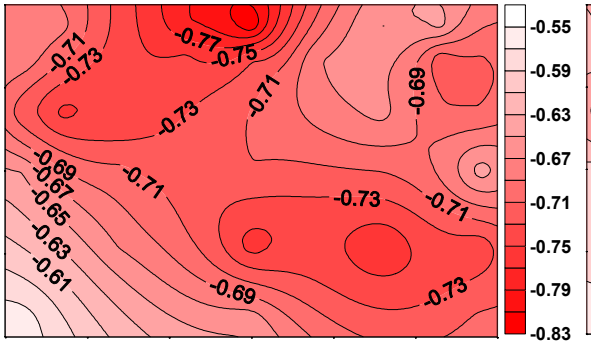

Figure 7.87 Pressure coefficient contours on the side inner face of the sheet clad scaffold when θ= 45°

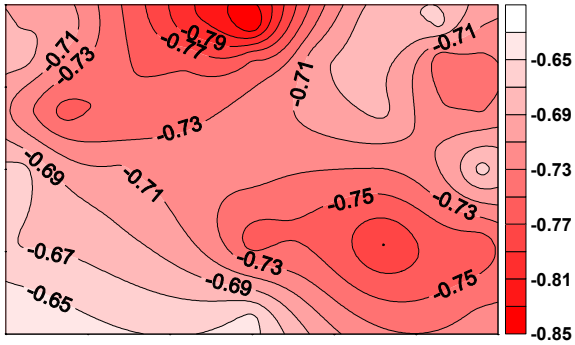

Figure 7.88 Pressure coefficient contours on the side inner face of the sheet clad scaffold when θ= 30°

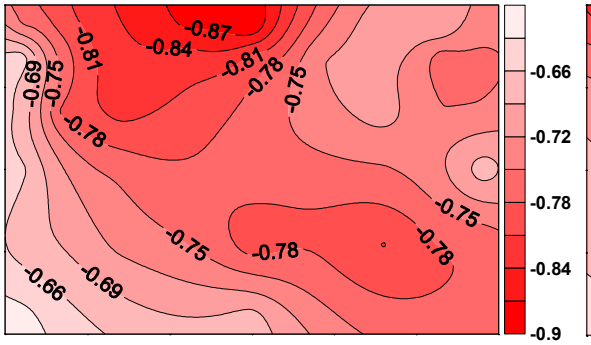

Figure 7.89 Pressure coefficient contours on the side inner face of the sheet clad scaffold when θ= 15°

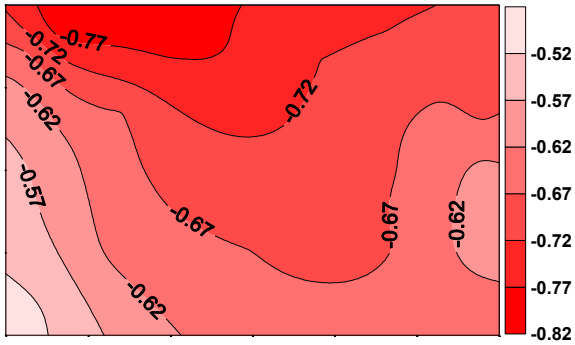

Figure 7.90 Pressure coefficient contours on the side inner face of the sheet clad scaffold when θ= 0°

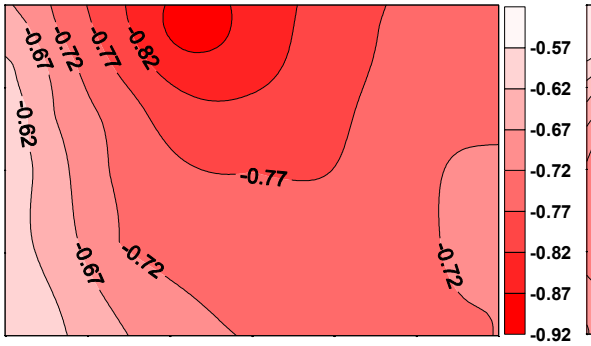

Figure 7.91 Pressure coefficient contours on the side inner face of the sheet clad scaffold when θ= -15°

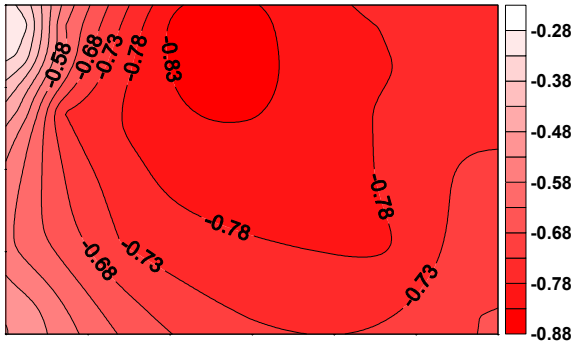

Figure 7.92 Pressure coefficient contours on the side inner face of the sheet clad scaffold when θ= -30°

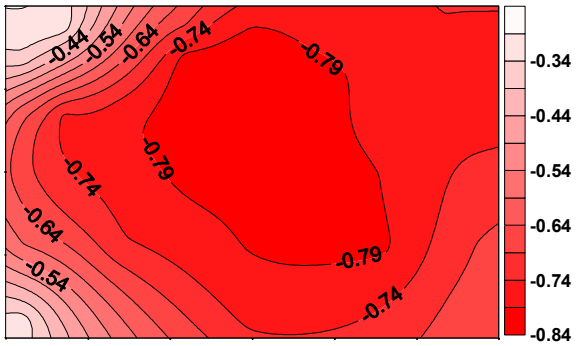

Figure 7.93 Pressure coefficient contours on the side inner face of the sheet clad scaffold when θ= -45°

Pressure Coefficient Contours on the Leeward Inner Face of the Sheet Clad Scaffold

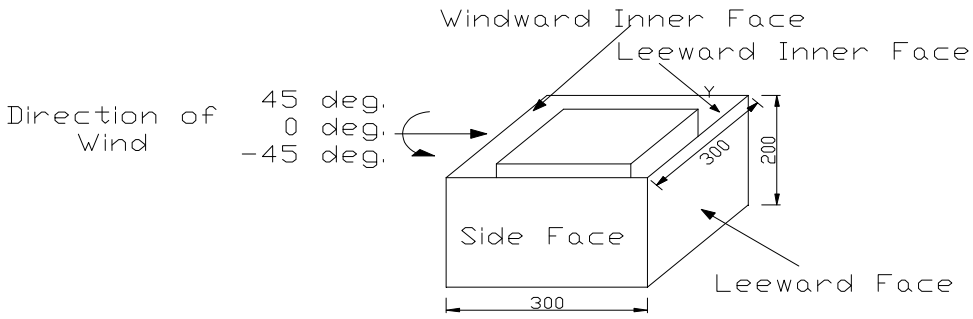

Figure 7.94 Angle of attack of wind on windward outer face of the elevated sheet clad scaffold surrounding SEB, direction of which varies from 45° to -45°

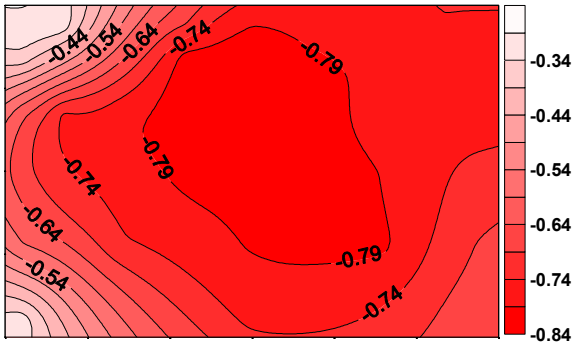

Figure 7.95 Pressure coefficient contours on the leeward inner face of the sheet clad scaffold when θ= 45°

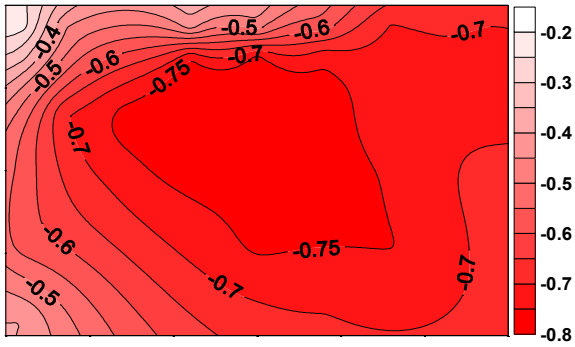

Figure 7.96 Pressure coefficient contours on the leeward inner face of the sheet clad scaffold when θ= 30°

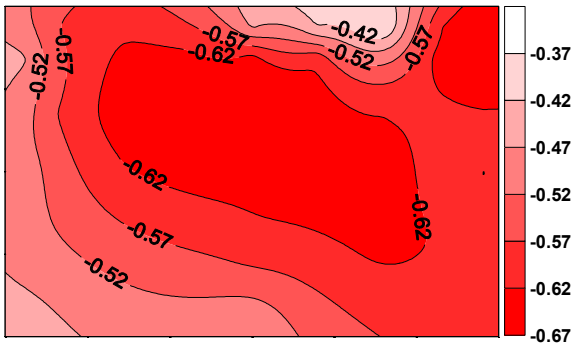

Figure 7.97 Pressure coefficient contours on the leeward inner face of the sheet clad scaffold when θ= 15°

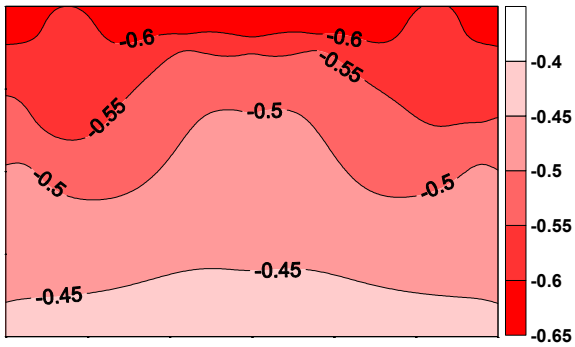

Figure 7.98 Pressure coefficient contours on the leeward inner face of the sheet clad scaffold when θ= 0°

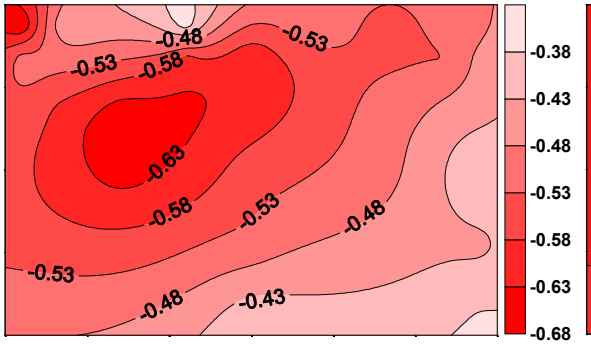

Figure 7.99 Pressure coefficient contours on the leeward inner face of the sheet clad scaffold when θ= -15°

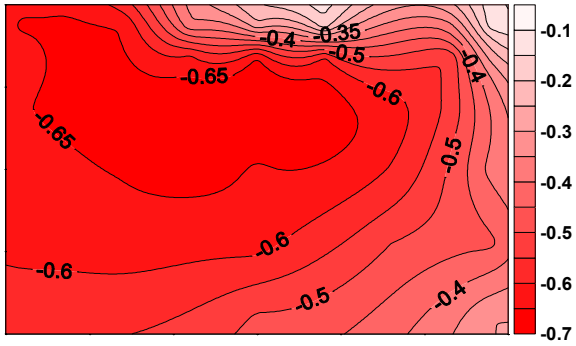

Figure 7.100 Pressure coefficient contours on the leeward inner face of the sheet clad scaffold when θ= -30°

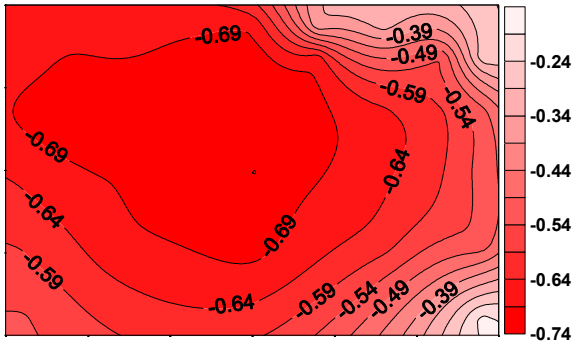

Figure 7.101 Pressure coefficient contours on the leeward inner face of the sheet clad scaffold when θ= -45°

Pressure Coefficient Contours on the windward Inner Face of the Elevated Sheet Clad Scaffold

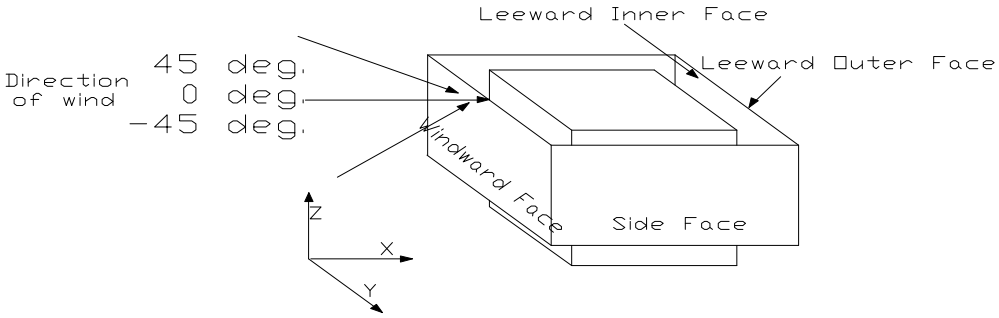

Figure 7.102 Angle of attack of wind on windward outer face of the elevated sheet clad scaffold surrounding SEB, direction of which varies from 45° to -45°

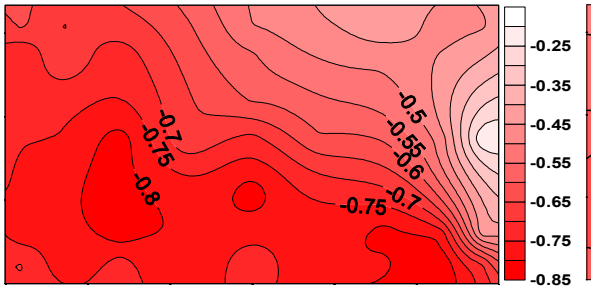

Figure 7.103 Pressure coefficient contours on the windward inner face of the elevated sheet clad scaffold when θ= 45°

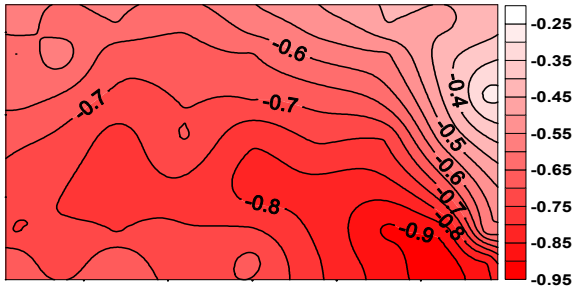

Figure 7.104 Pressure coefficient contours on the windward inner face of the elevated sheet clad scaffold when θ= 30°

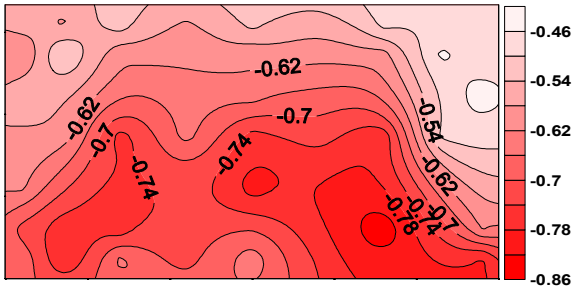

Figure 7.105 Pressure coefficient contours on the windward inner face of the elevated sheet clad scaffold when θ= 15°

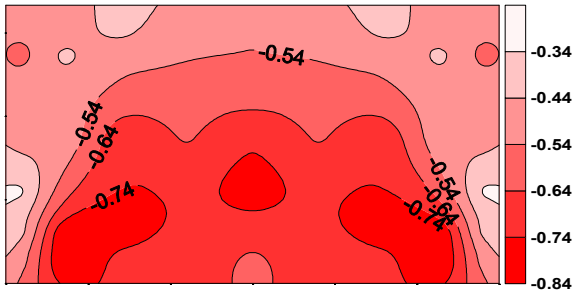

Figure 7.106 Pressure coefficient contours on the windward inner face of the elevated sheet clad scaffold when θ= 0°

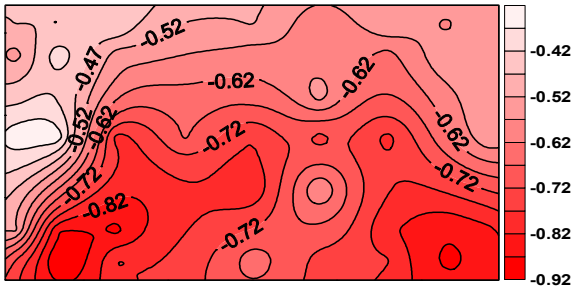

Figure 7.107 Pressure coefficient contours on the windward inner face of the elevated sheet clad scaffold when θ= -15°

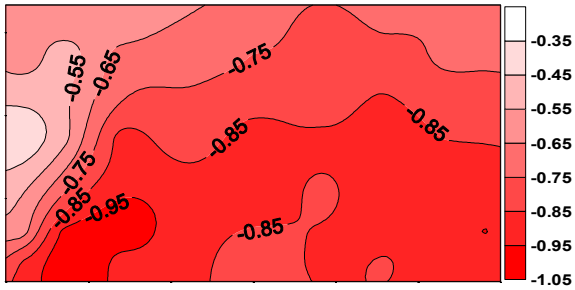

Figure 7.108 Pressure coefficient contours on the windward inner face of the elevated sheet clad scaffold when θ= -30°

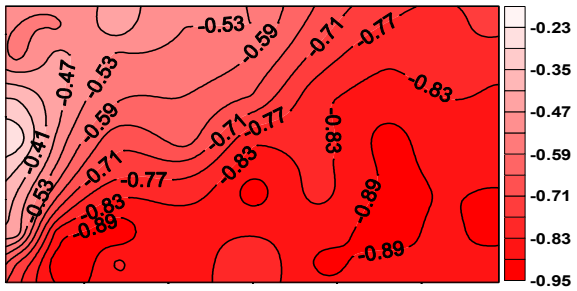

Figure 7.109 Pressure coefficient contours on the windward inner face of the elevated sheet clad scaffold when θ=-45°

Pressure Coefficient Contours on the Side Inner Face of the Elevated Sheet Clad Scaffold

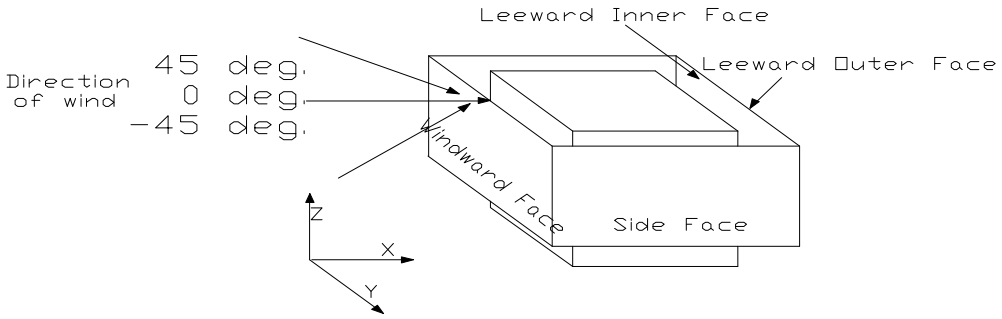

Figure 7.110 Angle of attack of wind on windward outer face of the elevated sheet clad scaffold surrounding SEB, direction of which varies from 45° to -45°

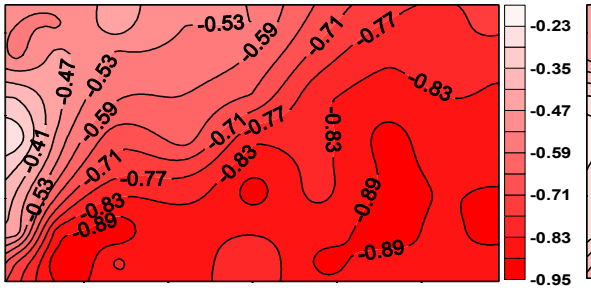

Figure 7.111 Pressure coefficient contours on the side inner face of the elevated sheet clad scaffold when θ= 45°

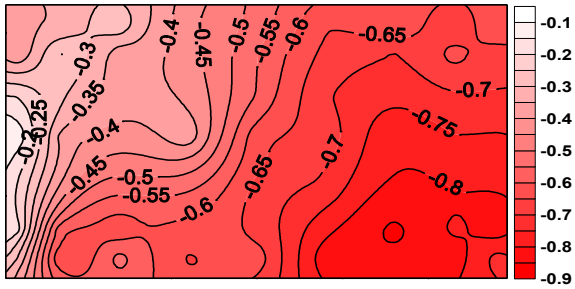

Figure 7.112 Pressure coefficient contours on the side inner face of the elevated sheet clad scaffold when θ= 30°

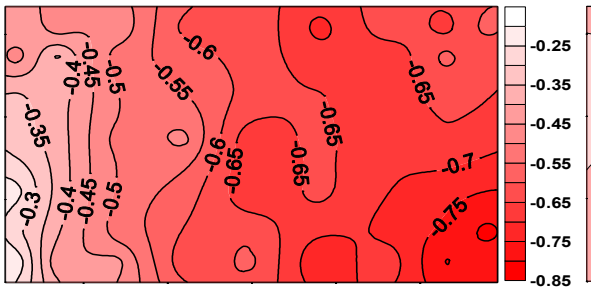

Figure 7.113 Pressure coefficient contours on the side inner face of the elevated sheet clad scaffold when θ= 15°

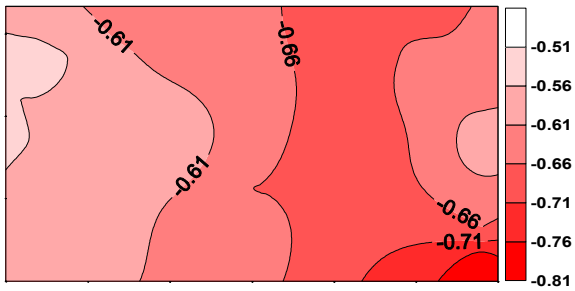

Figure 7.114 Pressure coefficient contours on the side inner face of the elevated sheet clad scaffold when θ= 0°

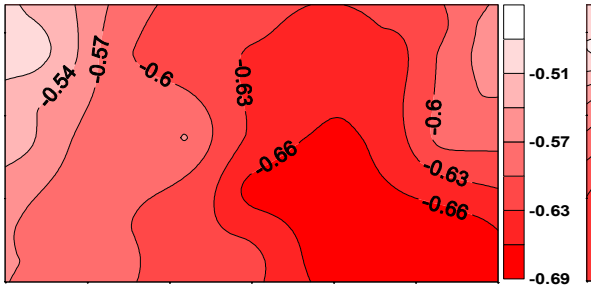

Figure 7.115 Pressure coefficient contours on the side inner face of the elevated sheet clad scaffold when θ= -15°

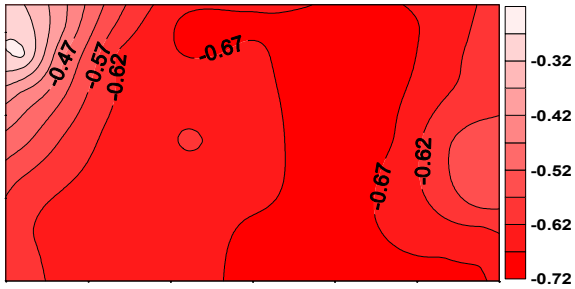

Figure 7.116 Pressure coefficient contours on the side inner face of the elevated sheet clad scaffold when θ= -30°

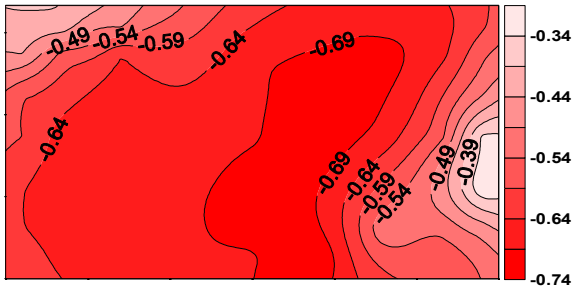

Figure 7.117 Pressure coefficient contours on the side inner face of the elevated sheet clad scaffold when θ= -45°

Pressure Coefficient Contours on the Leeward Inner Face of the Elevated Sheet Clad Scaffold

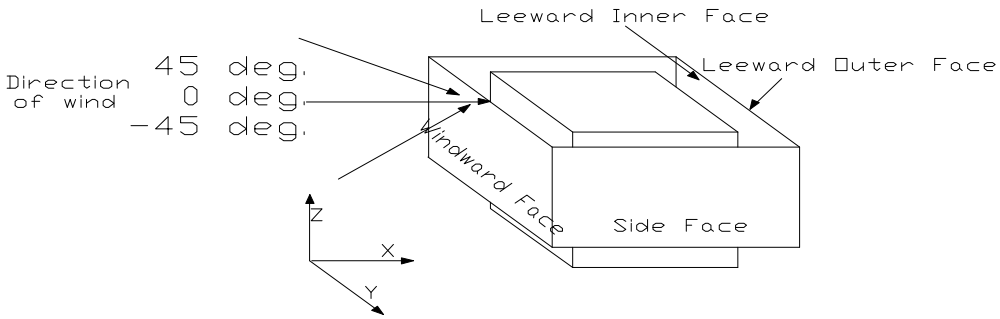

Figure 7.118 Angle of attack of wind on windward outer face of the elevated sheet clad scaffold surrounding SEB, direction of which varies from 45° to -45°

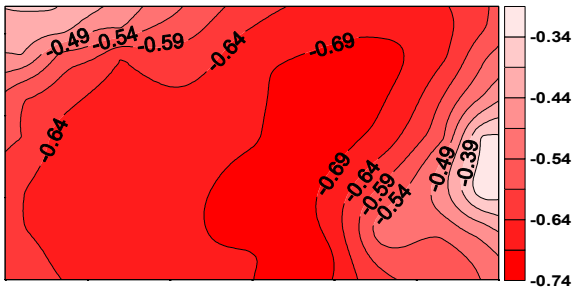

Figure 7.119 Pressure coefficient contours on the leeward inner face of the elevated sheet clad scaffold when θ= 45°

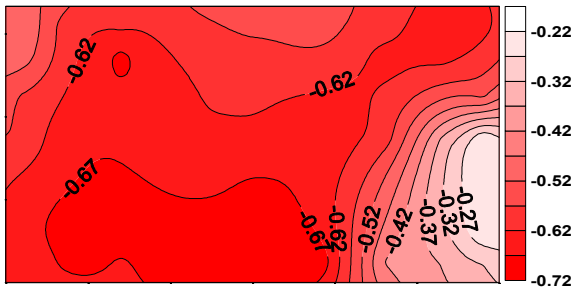

Figure 7.120 Pressure coefficient contours on the leeward inner face of the elevated sheet clad scaffold when θ= 30°

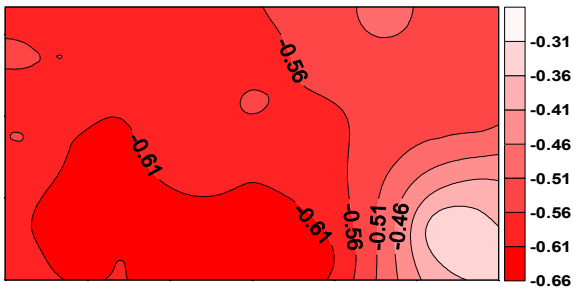

Figure 7.121 Pressure coefficient contours on the leeward inner face of the elevated sheet clad scaffold when θ= 15°

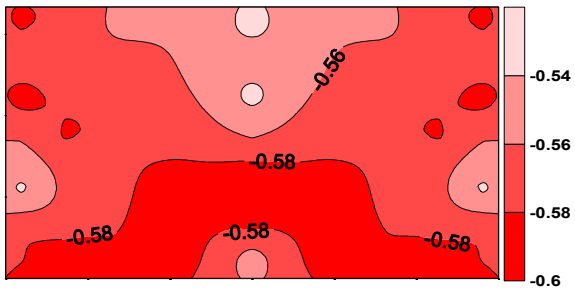

Figure 7.122 Pressure coefficient contours on the leeward inner face of the elevated sheet clad scaffold when θ= 0°

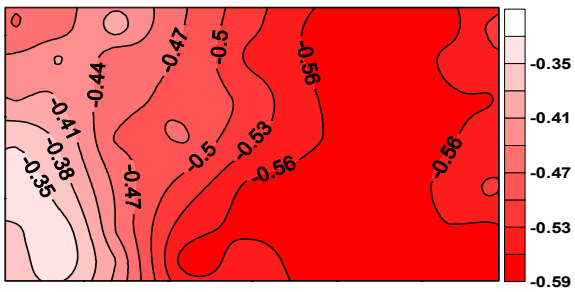

Figure 7.123 Pressure coefficient contours on the leeward inner face of the elevated sheet clad scaffold when θ= 15°

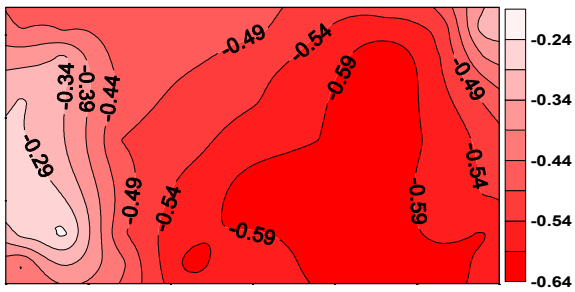

Figure 7.124 Pressure coefficient contours on the leeward inner face of the elevated sheet clad scaffold when θ= 30°

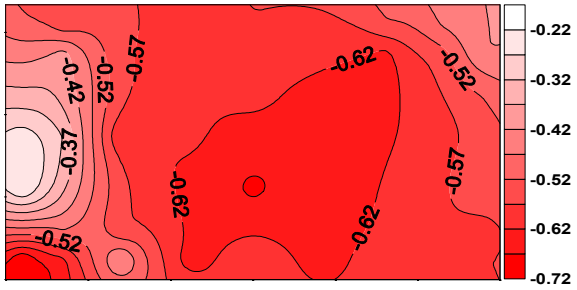

Figure 7.125 Pressure coefficient contours on the leeward inner face of the elevated sheet clad scaffold when θ= 45°

7.3 *Analysing the Models using Computational Fluid Dynamics Techniques*

Before analysing the models using Computational Fluid Dynamics (CFD) the conditions required were determined to enable accurate results to be obtained. The author tried to use exactly the same wind profile, turbulence and end conditions obtained from the wind-tunnel test for CFD analyses. Certain strategies were adopted when using Reynolds Stress Model for early convergence. In CFD analyses, to ensure that the results are independent of the number of elements, a number of mesh sizes were analysed and the optimum number of mesh arrangements used in further investigations. The details are discussed below:

7.3.1 *Geometry and Inlet Conditions*

It is important to specify the correct boundary conditions and domain dimensions for the CFD runs as in the case in actual wind-tunnel experimental studies. Therefore the sides, top and most importantly the inlet and outlet of the domain were positioned so as to minimise the interference with the flow field around the cube. The blockage ratio is defined as the ratio of the frontal area of the cube to the vertical cross sectional area of the computational domain and should not be greater than 3 percent [7.6]. The blockage ratio for these tests ranged from approximately 1.92 to 2.56 percent. Furthermore, symmetry boundaries were specified to further reduce the effect of the sides and top of the domain. The conditions of this boundary were:

1. no flux across the boundary
2. no scalar flux across the boundary

At the symmetry boundary the normal velocities were set to zero and the values of all other properties just outside the solution domain were equated to the nearest node just inside the domain [7.7]. The position of the outlet boundary is another important

consideration. The outlet boundary for flow simulation must be placed at a sufficient distance from the inlet and obstacles to the flow so that there are no flow gradients in the flow directions. The flow at the outlet must be in a state of equilibrium otherwise the interior solution to the flow problem will be influenced and the accuracy of the solutions will be compromised. Versteeg and Malalasekera recommended that the flow solution be compared for a number of different outlet positions to test sensitivity [7.8]. In the present study the position of the outlet was kept at 22.5 D or B (where D is the width of the model and B is the outer dimension of the sheet/net clad scaffold) from the model to avoid flow gradients in the flow direction.

The domain was meshed to allow a high degree of resolution of the flow with particular attention paid to areas of high flow gradients at the points of flow impingement and separation which occur in areas of sharp bends near to sides and the roof.

It is well known that in a numerical wind engineering simulation even minor changes to the inlet conditions can significantly modify the predicted flow field. It is of paramount importance that the conditions at the inlet of any CFD simulation match, as far as possible, those of the wind-tunnel (derived from full-scale data of the Silsoe site). In order to obtain CFD results that could be directly compared with the mean experimental values the ground roughness length was set to 0.01 m (prototype) to represent the fetch at the Silsoe site and the wall roughness length equal to 5.0 mm (prototype). Fully developed equilibrium atmospheric boundary layer flow profiles including variables such as stream-wise velocity, turbulent kinetic energy and Reynolds stress were specified at the inlet. These profiles allowed for sustainable equilibrium boundary layer when used in conjunction with the appropriate wall roughness length.

In modelling the atmospheric boundary layer there are a number of important rules to follow that have been defined by Jensen (1958), Ludwig and Sundaram (1969) [7.8] and Richards and Hoxey (1993) [7.9]. The classical approach, and the starting point, is to define a two-dimensional thermally neutral boundary layer in which Coriolis forces are ignored, with all flow variables in equilibrium. It is stated that in steady incompressible two dimensional flow modelling the existence of a homogeneous flow has the following properties:

1. the vertical velocity is zero
2. the pressure is constant
3. the shear stress is constant

i.e.

$$(\mu_l + \mu_t)\frac{\partial u}{\partial z} = \tau_0 = \rho u_*^2 \tag{7.1}$$

7.3.2 Inlet Conditions for the Reynolds Stress Turbulence Model

There are more stability and convergence difficulties when using RSM than any $k-\varepsilon$ models as it creates a high degree of coupling between the momentum equations and the turbulent stresses in the flow [7.9]. Therefore, when using RSM, special solution strategies were adopted in order to obtain a converged solution. The following strategies were generally adopted:

- The calculations were started using the standard $k-\varepsilon$ model until it converged, then the RSM algorithm was activated using the $k-\varepsilon$ solution data as a starting point for the RSM calculation.
- Low under-relaxation factors of 0.2 to 0.3 were used both for the velocities and for all of the stresses as the flows were highly swirling.
- Instead of the usual recommended residual of10^{-3}, 10^{-4} was used to apply tighter convergence criteria to ensure full convergence.

7.3.3 Velocity, Turbulent Kinetic Energy and Reynolds Stresses

The boundary layer data generated was incorporated into the CFD simulations by fitting curves to the first 24-36 m (prototype) of the profiles and entering the equations into a user defined C++ routine. The wind profiles at varying distance from the inlet are shown in Figure 7.126. The turbulent kinetic energies at varying distances from the inlet found by the standard $k-\varepsilon$ model and the Reynolds stress model are shown in Figures 7.127 and 7.128. As the distance from the model is reduced the production of turbulent kinetic energy is higher by the standard $k-\varepsilon$ than by the Reynolds stress model. Therefore using the available experimental boundary layer data it is apparent that the RSM predicted a more accurate match to experimentally obtained mean data. The turbulent kinetic energy calculated manually from the derived formula (discussed in Chapter 5) is quite similar to the Reynolds stress model. Figures 7.129 to 7.134 shows all the six Reynolds stresses at varying distances from inlet.

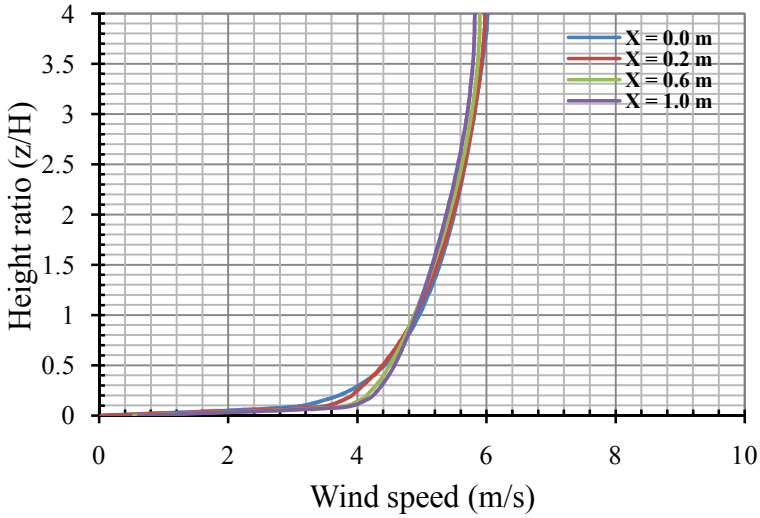

Figure 7.126 Wind speed at varying distances from inlet

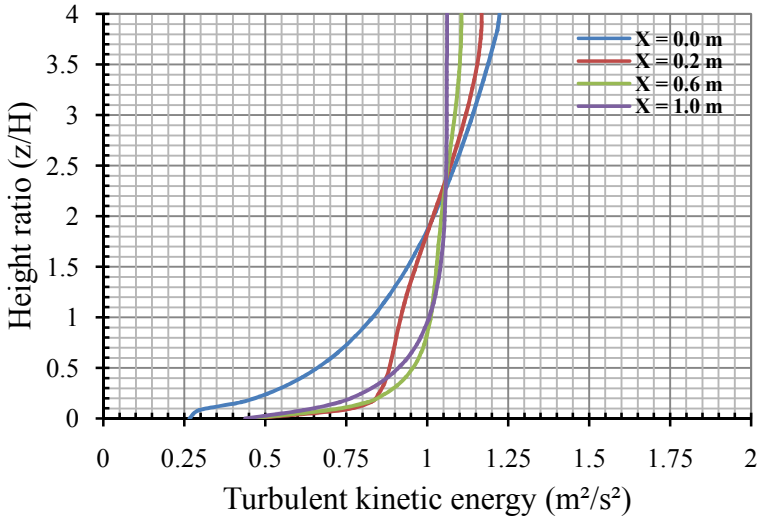

Figure 7.127 Turbulent kinetic energy at varying distances from inlet by standard $k-\varepsilon$ model

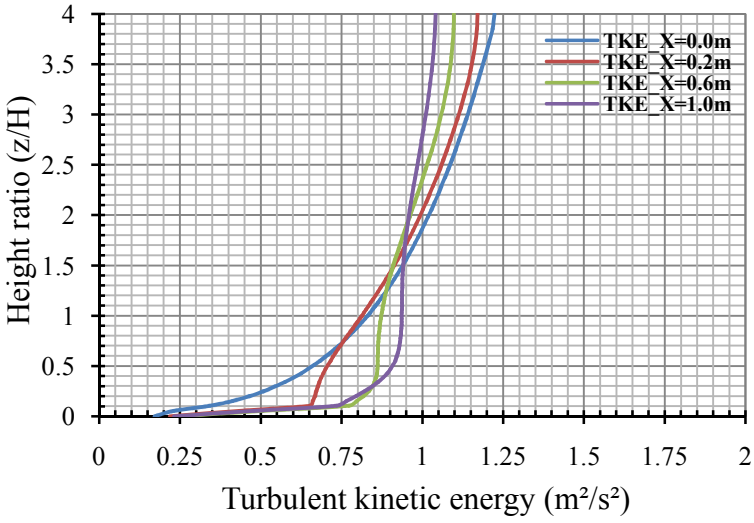

Figure 7.128 Turbulent kinetic energy at varying distances from inlet by Reynolds stress model

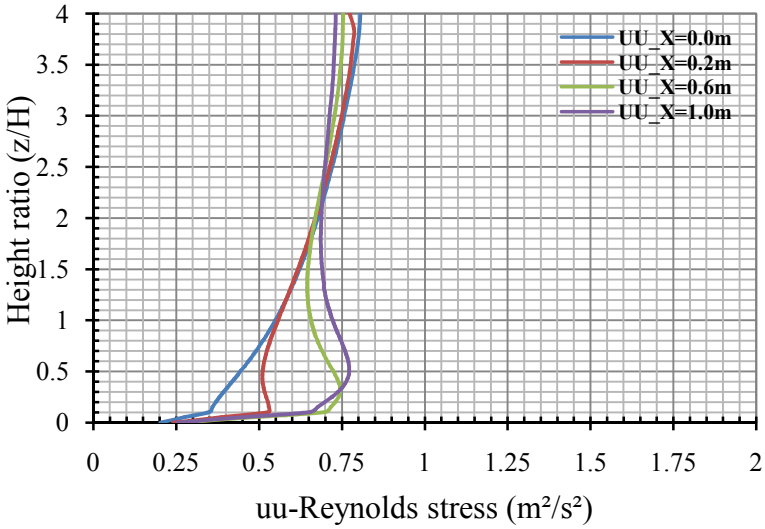

Figure 7.129 Variation of uu-Reynolds stress with height at varying distances from inlet

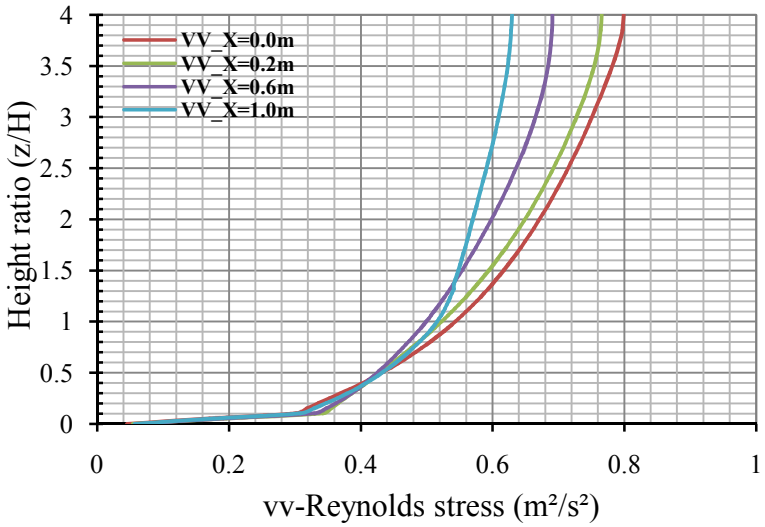

Figure 7.130 Variation of vv-Reynolds stress with height at varying distances from inlet

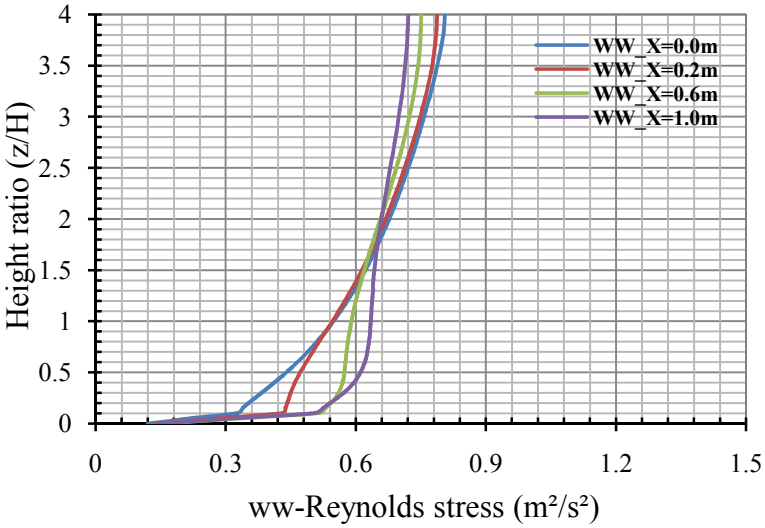

Figure 7.131 Variation of ww-Reynolds stress with height at varying distances from inlet

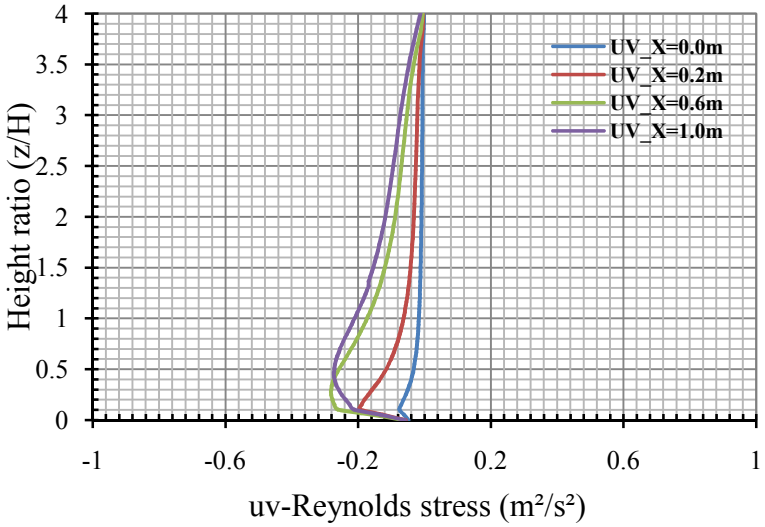

Figure 7.132 Variation of uv-Reynolds stress with height at varying distances from inlet

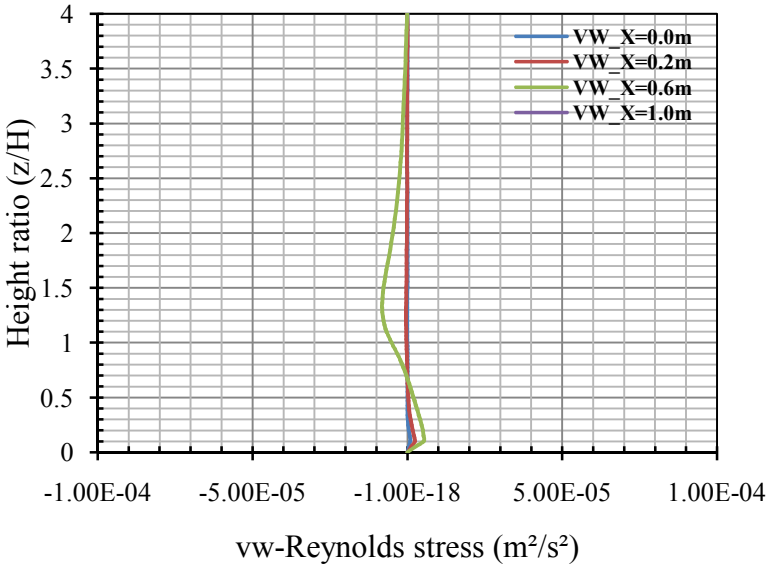

Figure 7.133 Variation of vw-Reynolds stress with height at varying distances from inlet

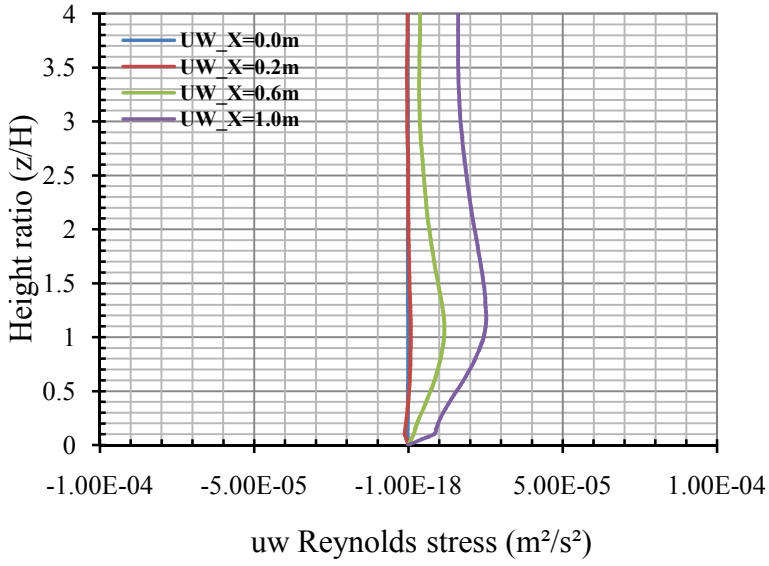

Figure 7.134 Variation of uw-Reynolds stress with height at varying distances from inlet

7.3.4 Variations on the Building Roughness Length

The roughness lengths on the building vary depending on the type of façade provided. For all CFD simulations a roughness length of 5 mm (prototype) was used. It was decided to undertake a small number of tests with modifications of roughness height varying from 0.0033 to 0.001 m. Figures 7.135 and 7.136 show the windward face and roof pressure distributions for the realizable $k-\varepsilon$ model. Interestingly it can be seen that for the computational tests the increase in turbulence due to higher roughness lengths has the effect of marginally increasing the front face stagnation pressure and increasing the roof front corner maximum negative pressure. This may in turn cause a shorter recirculation zone that reattaches half way along the roof and a steeper pressure gradient recovery. These effects, whereby the flow and pressure fields are modified as the incident wind turbulence increases are well documented in most of the books on CFD and is also explained in Chapter 4.

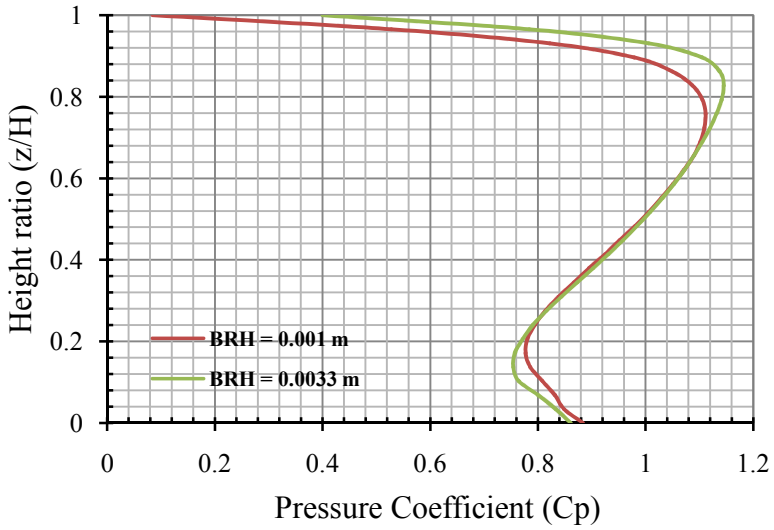

Figure 7.135 Pressure coefficients on the windward face of the building with different roughness heights

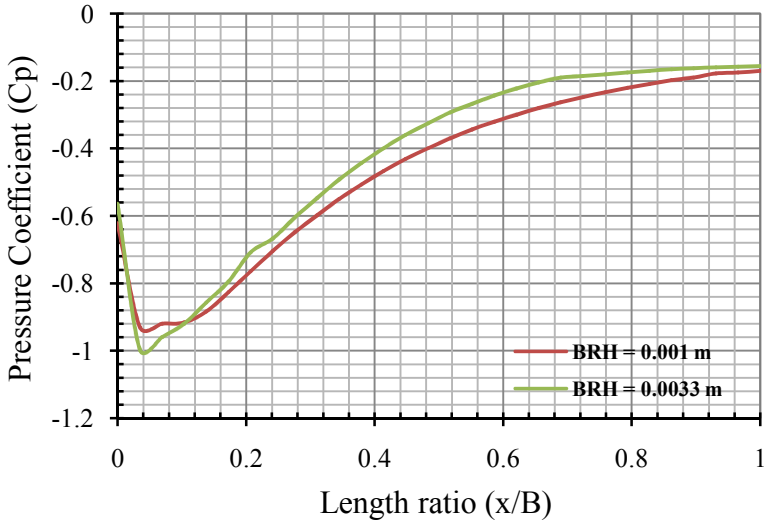

Figure 7.136 Pressure coefficients on the roof of the building with different roughness heights

7.3.5 Grid Refinement Tests

The level of grid refinement can have a significant effect on the accuracy of flow patterns produced by CFD simulations. All CFD simulations should therefore be able to adequately prove that a sufficiently fine mesh has been used. This was done by successive grid refinements until the flow field did not change significantly. Therefore extensive grid independence checks were undertaken with both the cubical SEB and the SEB surrounded by sheet clad scaffolds. The number of elements in the mesh for the cubical SEB and sheet clad scaffolds/elevated sheet clad scaffolds surrounding SEB started with approximately 1.75 million and finally ended with 4 million. All the models were checked for steady standard $k-\varepsilon$ model for the grid refinement before shifting to unsteady modelling.

7.4 Comparison of Full-scale, Wind-tunnel and CFD Results on SEB

The SEB (as shown in Figures 7.137 and 7.138) was taken as the base model for study as the full-scale data, i.e. the velocity profile and longitudinal turbulence intensities from the Silsoe site, were available to be used both for the experiment (for simulation in a wind-tunnel) and for CFD analyses. The mean longitudinal wind speed profile measured in the wind-tunnel was in good agreement with the SRI full-scale profile with a power-law exponent of 0.17. The longitudinal turbulence was slightly less than the Silsoe site full-scale data and has been discussed in Chapter 5.

Apart from CFD analyses by various techniques, the experimental results on SEB were also validated by the full-scale test data from the work of Richards and Hoxey [7.11].

The simulated wind speed profile and the turbulence achieved were used as inlet boundary conditions for CFD analyses. The integral length scales were also calculated at eave height of the model and used as initial data required. The computational domain covered 29**B** (**B** is any dimension of the SEB) in the stream (**X**) direction, 13**B** in the lateral or normal (**Y**) direction and 3**H** to 4**H** in the vertical direction, using the centre of plan of the building as the origin of coordinates. The reason for taking this domain is to keep the obstruction less than 3% and to eliminate the flow obstacle effect on the inflow and outflow boundary conditions.

The models used for the CFD analyses were (i) the Standard $k-\varepsilon$, (ii) the RNG (Renormalization group) $k-\varepsilon$, (iii) the Realizable $k-\varepsilon$, (iv) the Reynolds Stress and (v) Large Eddy Simulation (LES) models. All the above models were run for unsteady computations over a period of 4 seconds. The time step was taken to be 0.001 second and 4000 time steps performed. The time step for the LES was taken to be 0.0005 second and 5000 to 8000 times steps performed. These were iterated to obtain the time averaged results for each time step. A turbulence intensity of 18% and a length scale of 0.3 at the eave height were kept constant for all the trials.

It was found that Reynolds Stress method did not converge to an accurate solution when unstructured meshes were used. Therefore, structured meshes were created for the RSM and combinations of both structured and unstructured meshes were used for the remaining models to study the pressure coefficients on the façade of the SEB.

The CFD results presented thus far are not as good as might be hoped, although they do display the correct magnitude and trends in many cases. It was apparent that none of the models tested could accurately predict the experimentally obtained leeward pressure distribution [7.6].

A comparison of the results of experiments, full-scale and CFD analyses on the SEB can be seen in Figures 7.139 to 7.149. It can be seen from the study of the SEB that the standard $k-\varepsilon$ model over-predicted the pressure coefficients by approximately 20-25% at the flow stagnation point. The Large Eddy Simulation model predicted the most accurate results on the windward face. The remaining models, i.e. the Reynolds stress

model, the RNG $k-\varepsilon$ and the Realizable $k-\varepsilon$ showed similar patterns of the pressure coefficient distribution on the windward face with results which were approximately 10-15 percent higher than the experimentally obtained values. All the models analysed predicted lesser pressure coefficients on the trailing edge of the side face with the RNG $k-\varepsilon$ closer to the experimental data. In the leading edge of the side face the Standard $k-\varepsilon$ and the Realizable $k-\varepsilon$ predicted a little higher pressure coefficient whilst the LES value was near the experimental data. The reason may be due to the over production of the turbulent kinetic energy at the sharp edges, detail of which can be found in Chapter 4. It was again apparent that none of the models tested except the LES (which is near to the experimental value) could accurately predict the experimentally obtained leeward pressure distribution. It was also observed that the Reynolds stress method does not converge when unstructured meshes were used. Except for the Reynolds stress model, both structured and unstructured meshes were used. Structured meshes were created for the Reynolds stress model.

Figures 7.148 and 7.149 show the centreline pressure coefficient distributions for the roof along and across the flow direction. The Standard $k-\varepsilon$ and the Realizable $k-\varepsilon$ models predicted similar pressure distributions throughout the length and width. Except for the LES model, none of the models predicted pressure values near to the experimental value at the trailing edge. Most of the models except the RSM, predicted pressure values near to the experimental value at the leading edge. In the middle of the roof none of the methods predicted pressures close to the experimental values with the LES nearest to the experimental values with errors of 20-30%. All the models under-predicted the pressure coefficients moving down towards the trailing edge. It is apparent that none of the models tested except the LES could accurately predict the pressure distribution over the remainder of the roof even with the best CFD models calculating errors of 20-40%.

It should be noted that there are a few inconsistent experimental points both on the side wall and most noticeably on the roof of the cube that cannot be fully explained. These errors are most likely due to approach flow turbulence intensity variations. These possible errors should be the subject of further investigations.

The leeward pressure distribution can be seen in Figures 7.145 to 7.147. It was again apparent that none of the models tested could accurately predict the experimentally

obtained distribution. The best results were obtained from the Large Eddy Simulation although errors of approximately of 15-20 percent were still apparent. From the models the worst results were in error by up to 60-80%. It appears that the under prediction of negative pressures are a consequence of over-prediction of the wake recirculation and a corresponding lack of velocity deficit. These results confirm the need to accurately simulate the flow field around a bluff body, particularly the leeward wake region. No improvements were found with grid refinement. The flow patterns predicted by the present numerical study are shown in Appendix from Figures A.1 to A.16.

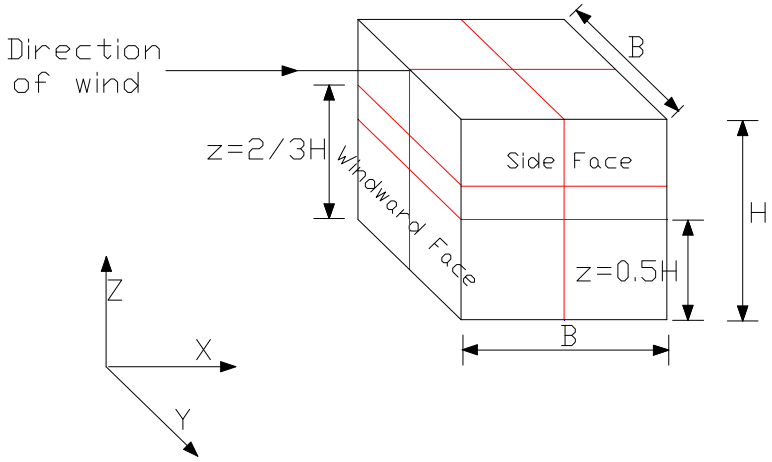

Figure 7.137 SEB showing windward and side face

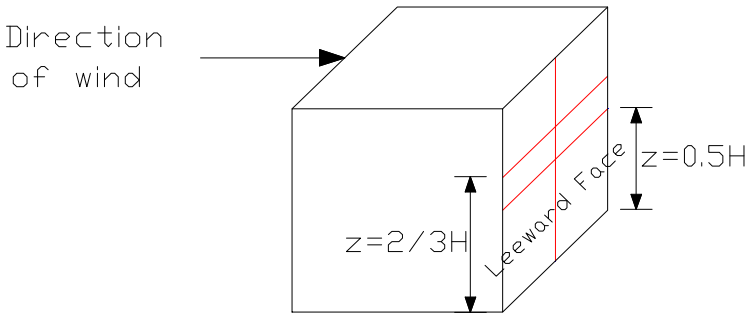

Figure 7.138 SEB showing leeward face

Note: The 'RED LINE' shown on the SEB is the position where the pressure coefficients measured

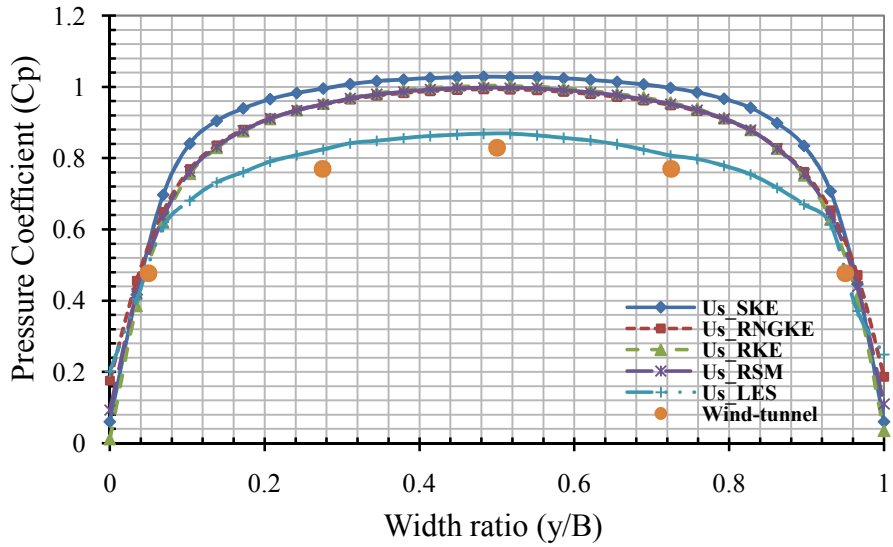

Figure 7.139 Pressure coefficients on the windward face of the SEB at z=0.5H

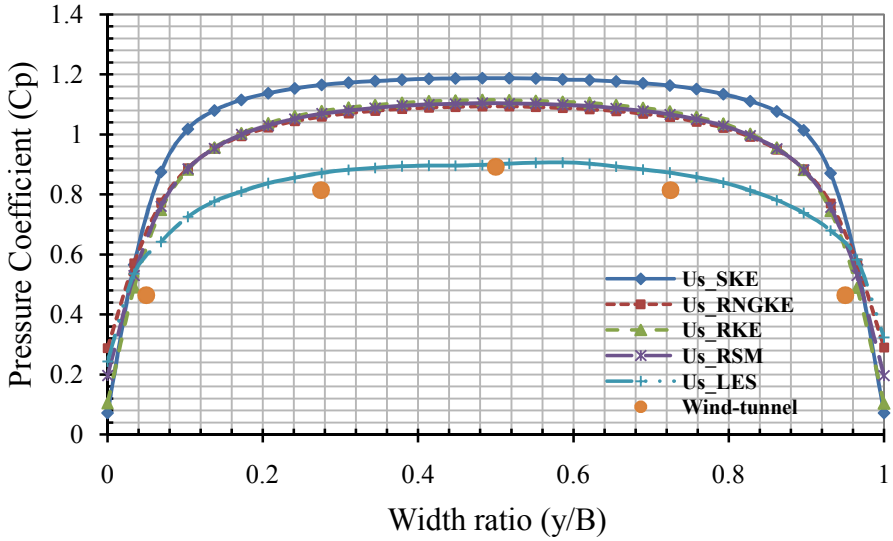

Figure 7.140 Pressure coefficients on the windward face of the SEB at z=2/3H

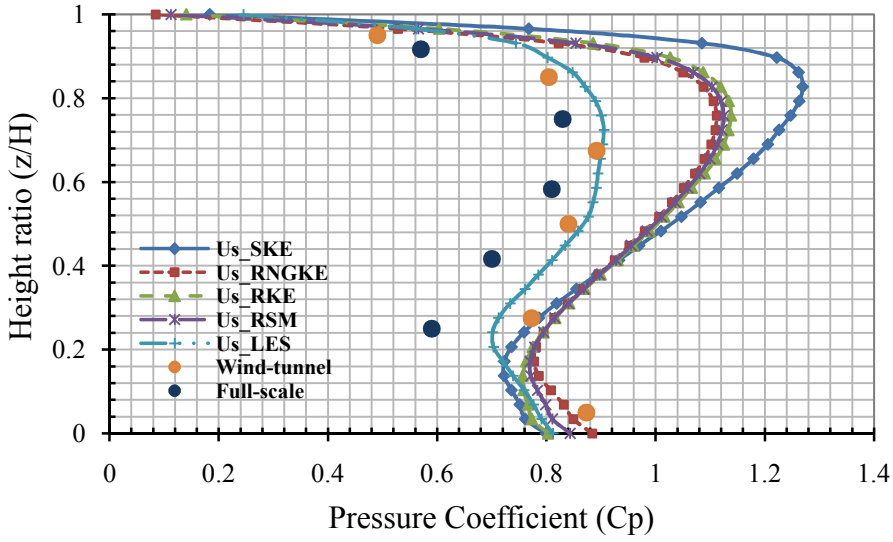

Figure 7.141 Pressure coefficients on the windward vertical face (mid-width) of the SEB

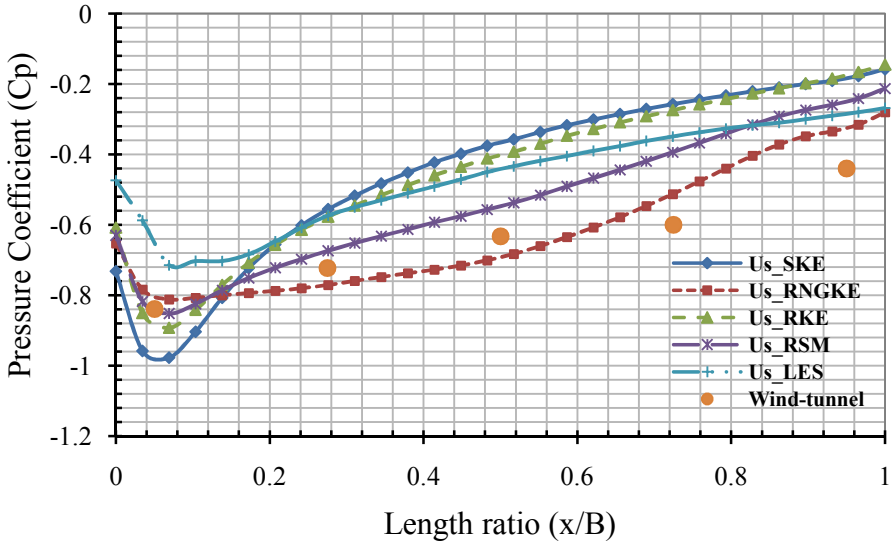

Figure 7.142 Pressure coefficients on the side face of the SEB at z=0.5H

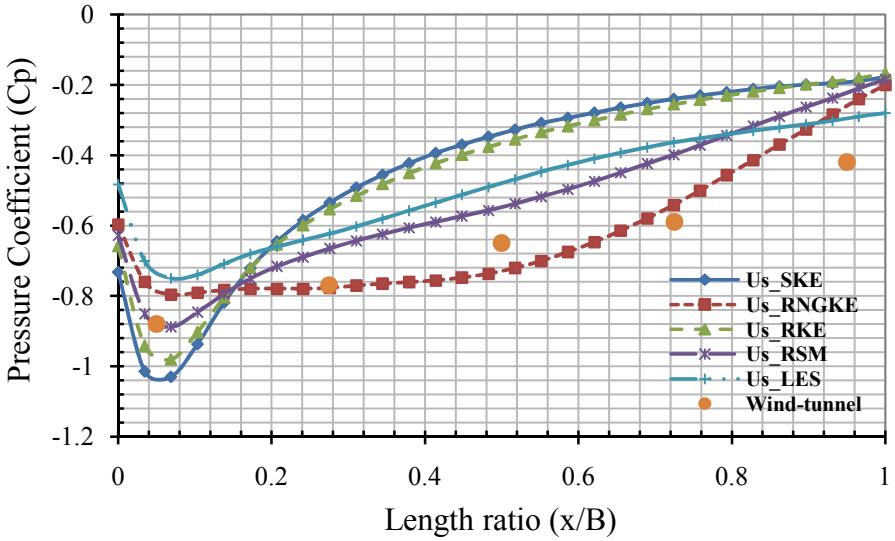

Figure 7.143 Pressure coefficients on the side face of the SEB at z=2/3H

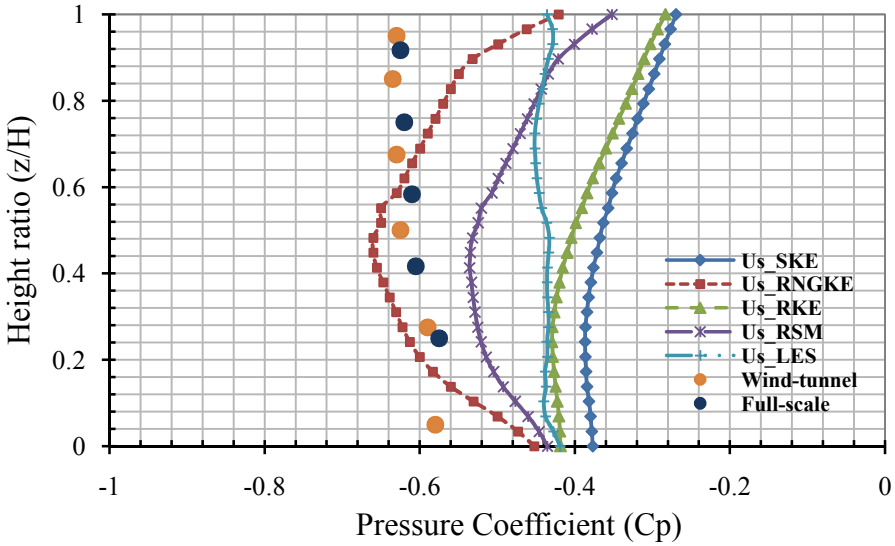

Figure 7.144 Pressure coefficients on the side vertical face (mid of width) of the SEB

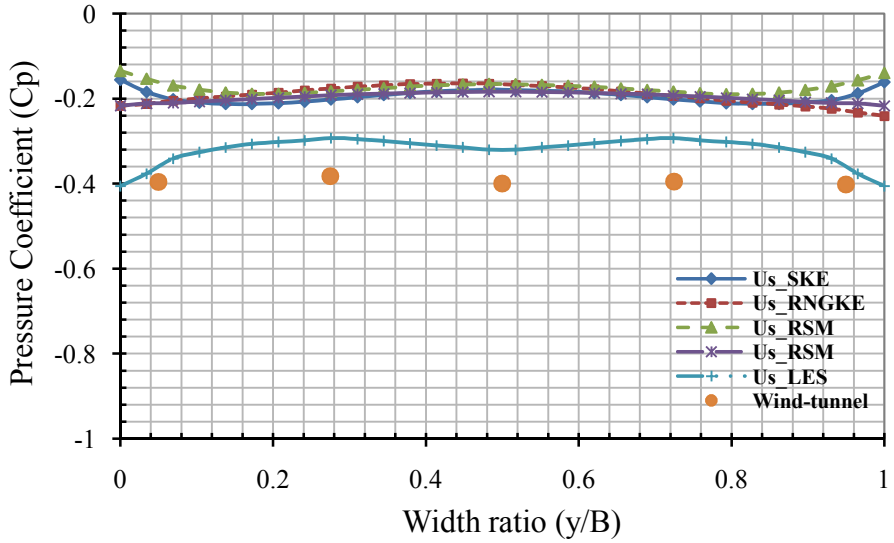

Figure 7.145 Pressure coefficients on the leeward outer face of the SEB at z=0.5H

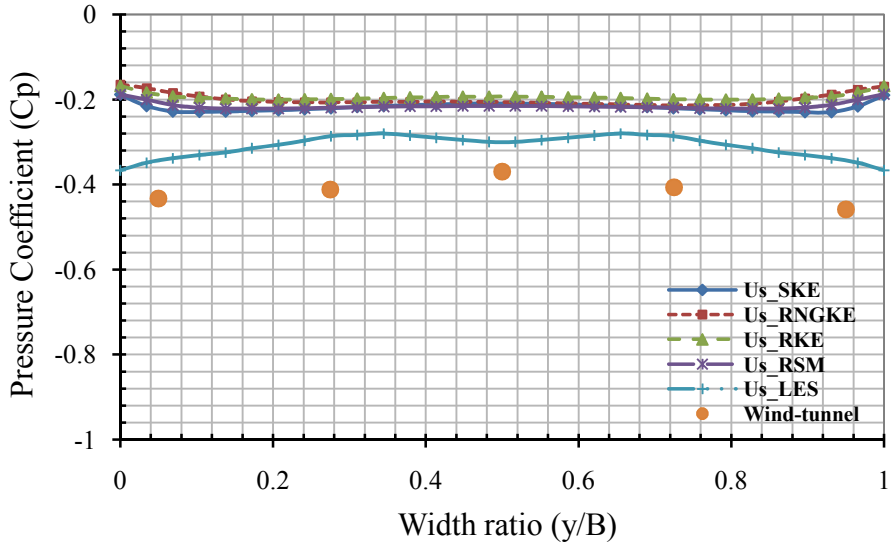

Figure 7.146 Pressure coefficients on the leeward outer face of the SEB at z=2/3H

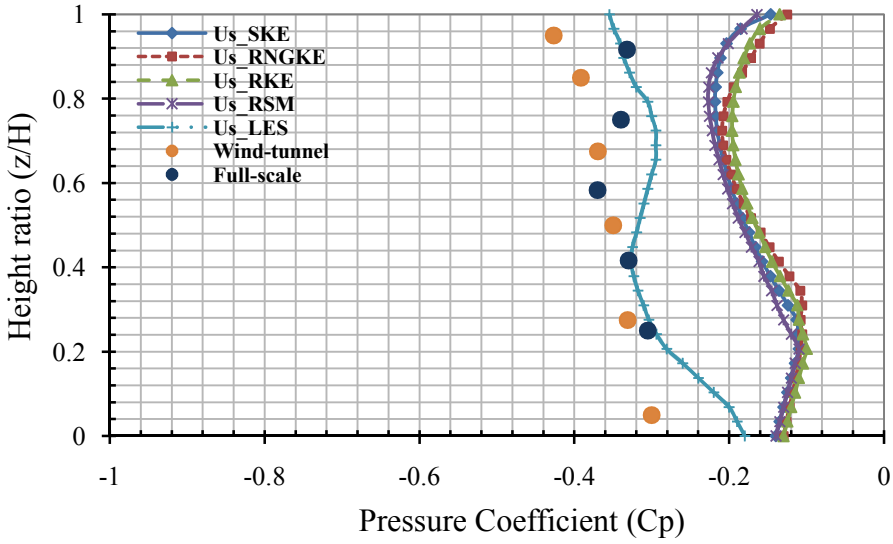

Figure 7.147 Pressure coefficients on the leeward vertical face at mid-width of the SEB

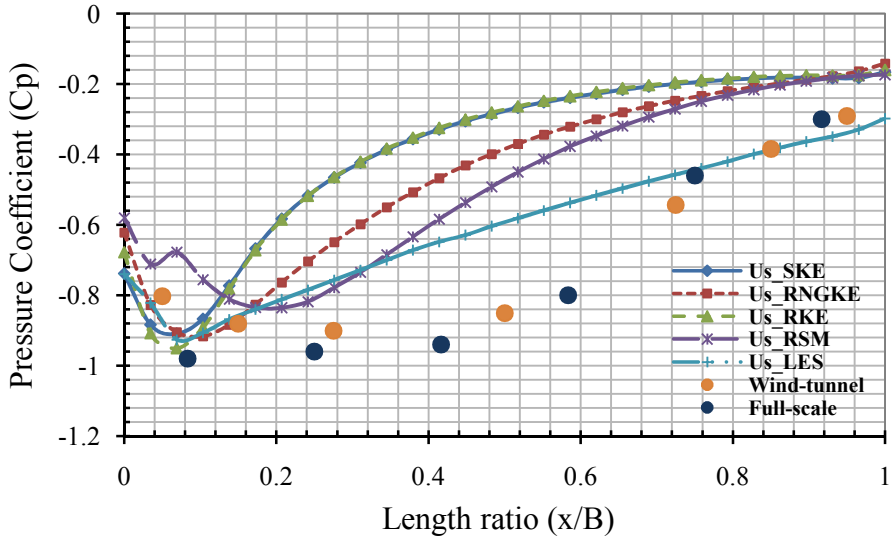

Figure 7.148 Pressure coefficients on the roof along the flow (mid of width) of the SEB

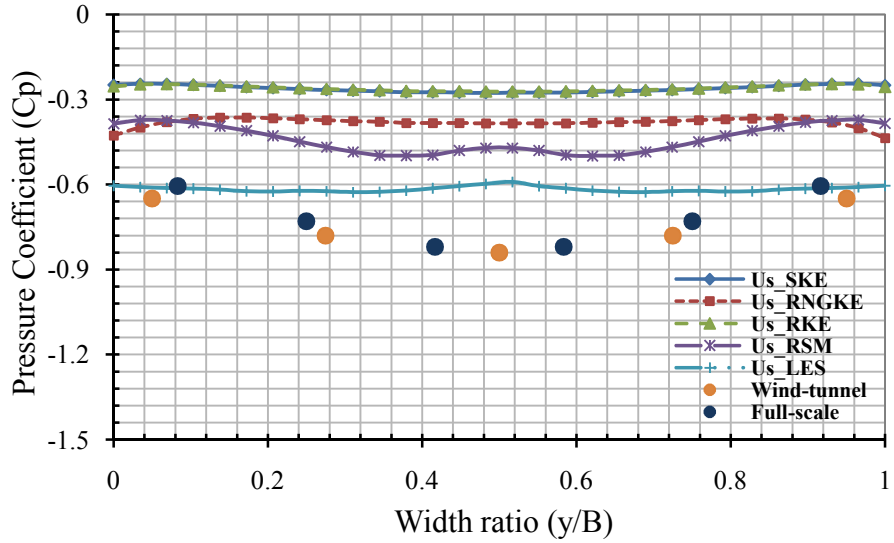

Figure 7.149 Pressure coefficients on the roof across the flow (mid of length) of the SEB

7.5 Comparison of Wind-tunnel and CFD Results on Sheet Clad Scaffolds Surrounding the SEB

Two types of sheet clad scaffold were made, one touching the ground and the other with an elevated sheet (1 m from the ground on the prototype) surrounding the SEB to actually visualize the ground conditions. The models are shown in Figures 7.150 and 7.151. The top portions of the sheet clad scaffold were tapered from the inside and both top and bottom portions were tapered from the inside for the elevated sheet clad scaffold and can be seen in Figures 1.6 and 1.7. The same longitudinal wind velocity profile and longitudinal turbulence intensity were used as were used for SEB.

Apart from experiments on the models, the models were also analysed by various CFD techniques and the same were validated against the wind-tunnel data. The simulated wind speed profile and the turbulence achieved were used as inlet boundary conditions for the CFD analyses. The integral length scales were also calculated at eave height of the model and also used as initial data required. The computational domain was long enough to eliminate the flow obstacle effect on the inflow and outflow boundary conditions.

The core region, i.e. that portion near the model was meshed with tetrahedral meshes with a quality value (a measure of the skewness of meshes) of the worst mesh less than 0.8. The farther ends were meshed with structured meshes as can be seen in Figures 5.28 and 5.29. Problems were encountered whilst meshing near to the top and the bottom of the sheet clad scaffold near to tapered portions.

The models used for the CFD analyses on the sheet clad scaffold were (i) Standard $k-\varepsilon$, (ii) RNG (Renormalization group) $k-\varepsilon$, (iii) Realizable $k-\varepsilon$ and the (v) Large Eddy Simulation (LES) models while for the elevated sheet clad scaffold only three methods i.e. the (i) Standard $k-\varepsilon$, (ii) RNG (Renormalization group) $k-\varepsilon$, (iii) Realizable $k-\varepsilon$ were used. The elevated sheet clad scaffold could not be successfully simulated with LES. This may be due a bad quality of mesh near to the tapered portions. The Reynolds stress method was not used because unstructured meshes were essential to model the boundary layers near to tapered portions. All the above models were run for unsteady computations over a period of 4 seconds. The time step was taken to be 0.001 second and 4000 time steps performed. The time step for LES was taken to be 0.0005 second and 5000 to 8000 times steps performed. These were iterated to obtain the time averaged results for each time step. A turbulence intensity of 18% and a length scale of 0.3 at the eave height were kept constant for all the trials.

The CFD results presented (from Figure 7.152 to Figure 7.205) thus far are not as good as might be hoped, although they do display the correct magnitude and trends in many cases. Once again the leeward pressure distribution could not accurately predict the experimentally obtained distribution.

It was also noted in the study of a sheet clad scaffold (both touching the ground and elevated sheet clad scaffolds) surrounding SEB that the standard $k-\varepsilon$ model over-predicted the pressure distribution by approximately 25-30% at the flow stagnation

point as can be seen in Figures 7.152 to 7.160 and in Figures 7.179 to 7.187. The remaining models all predicted relatively similar results with errors approximately 10-15 percent from the experimentally obtained values. The Large Eddy Simulation model produced the most accurate result on the windward face. The remaining models i.e. the RNG $k-\varepsilon$ and the Realizable $k-\varepsilon$, showed a similar pattern of the pressure coefficient distribution on the windward face. On the inside face of the windward sheeting all the models are close to the experimental value with the error near to 20%.

On the inside face of the windward sheet none of the CFD methods was near to the experimental values and the error was of the order of nearly 60%.

All the models predicted lesser pressure coefficients on the trailing edge of the side face (as shown in the Figures from 7.161 to 7.169 and 7.188 to 7.196) with RNG $k-\varepsilon$ closer to the experimental data. In the leading edge of the side face the Standard $k-\varepsilon$ and Realizable $k-\varepsilon$ predicted a higher pressure coefficient with an error of the order of 30-50%. The reason has already been explained in Chapter 4.

The experimental leeward pressure distribution was close to the RNG $k-\varepsilon$ and LES values for the models tested. The leeward pressure distribution for sheet clad and elevated sheet clad scaffolds can be seen in Figures 7.170 to 7.178 and Figures 7.197 to 7.205 respectively. It was again apparent that none of the models tested could accurately predict the experimentally obtained distribution. The best results were obtained from the Large Eddy Simulation although errors of approximately of 15-20 percent were still apparent. All the models predicted the worst result with errors of up to 80-100%. Once again it is apparent that the under-prediction of negative pressures is a consequence of over-prediction of the wake recirculation and the corresponding lack of velocity deficit and cannot be improved by mesh refinement. The flow patterns predicted by the present numerical study are shown in Figures A.17 to A.30.

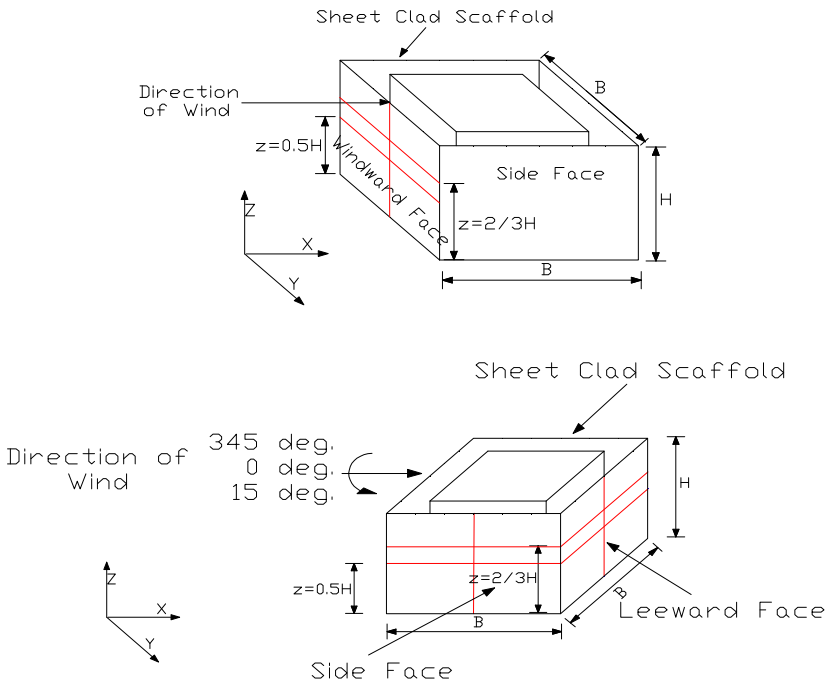

Figure 7.150 Sheet Clad Scaffold

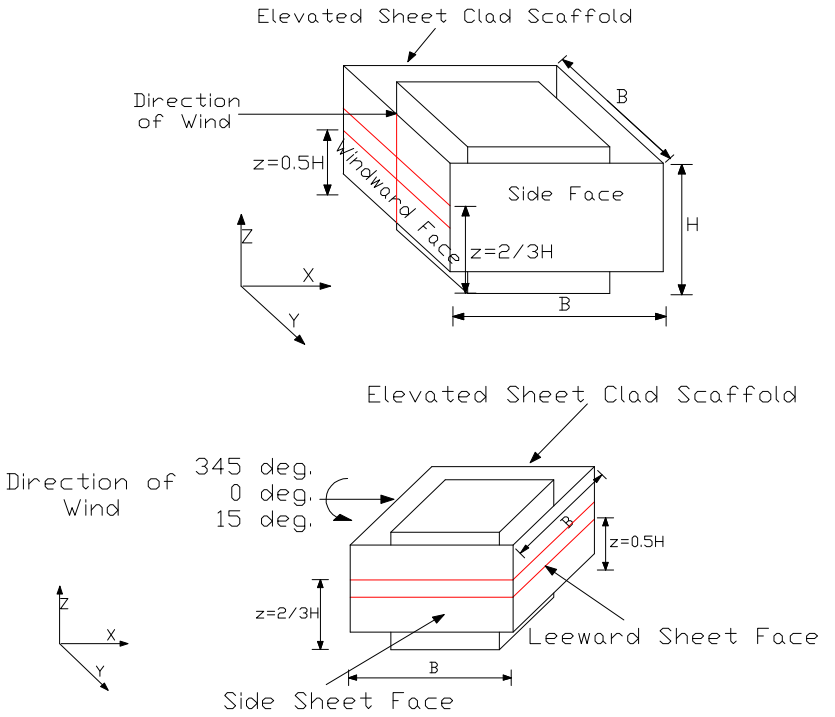

Figure 7.151 Elevated Sheet Clad Scaffold

Note: The 'RED LINE' shown on the sheet clad scaffold and elevated sheet clad scaffold surrounding SEB is the position where the pressure coefficients measured

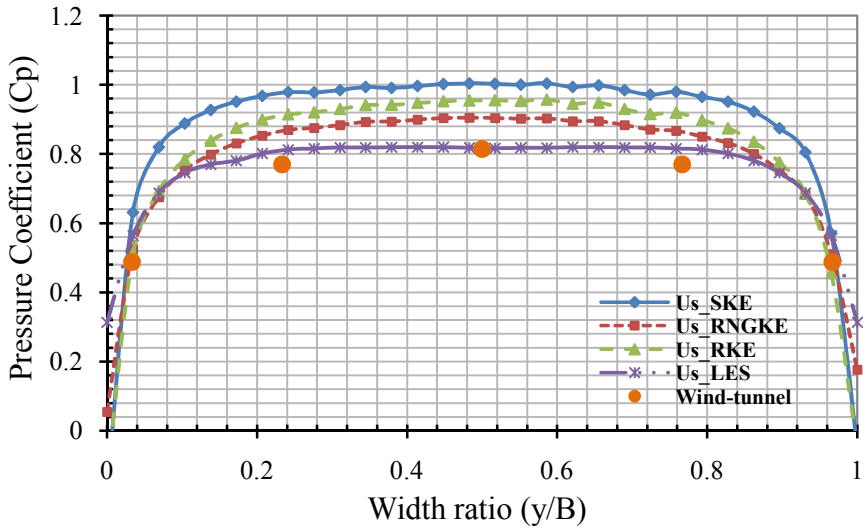

Figure 7.152 Pressure coefficients on the windward outer face of the sheet clad scaffold at mid height from the ground

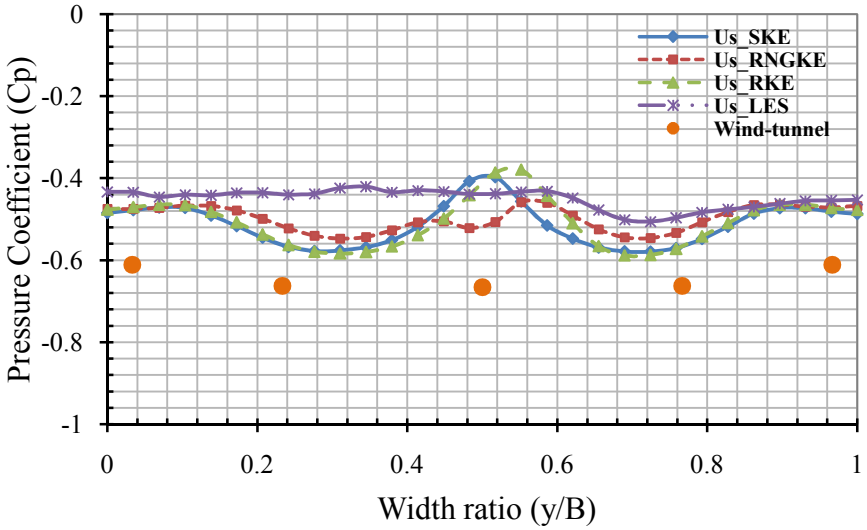

Figure 7.153 Pressure coefficients on the windward inner face of the sheet clad scaffold at mid height from the ground

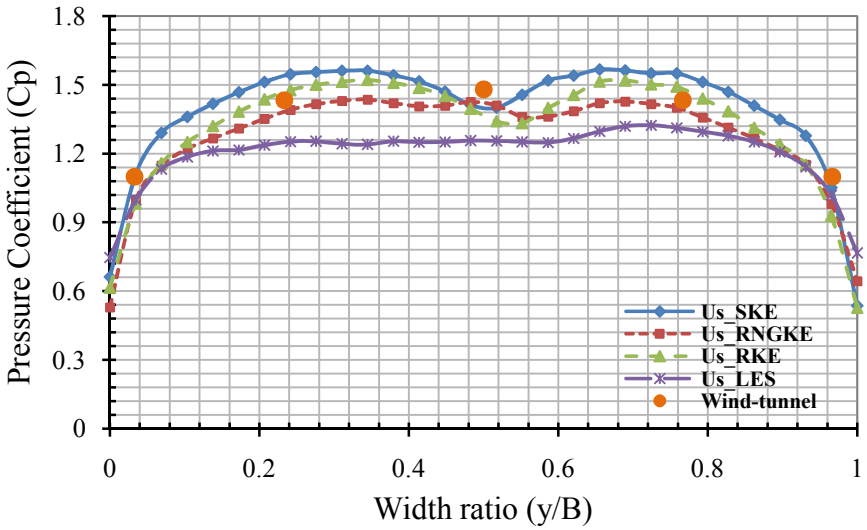

Figure 7.154 Difference of pressure coefficients of the windward outer and inner face of the sheet clad scaffold at mid height from the ground

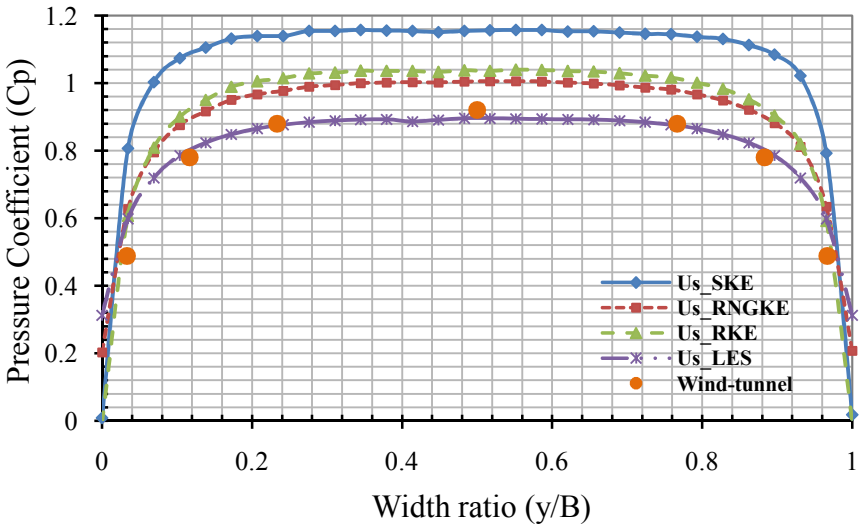

Figure 7.155 Pressure coefficients on the windward outer face of the sheet clad scaffold at two-third height from the ground

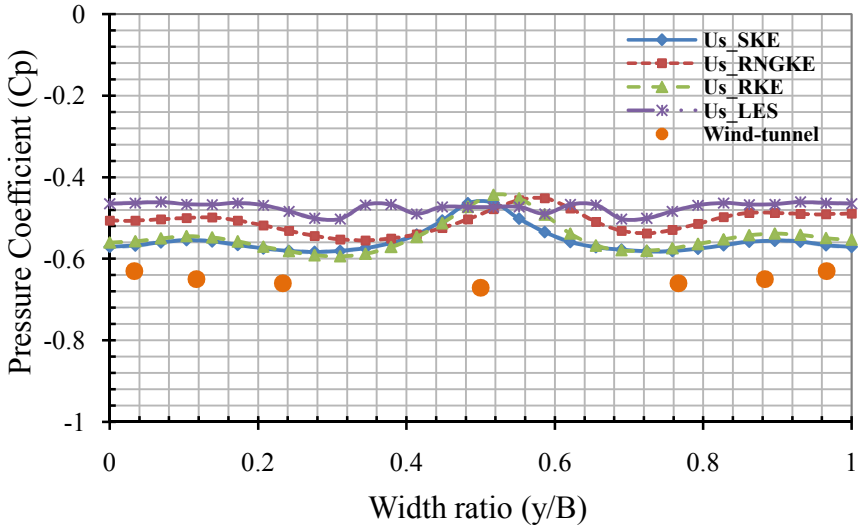

Figure 7.156 Pressure coefficients on the windward inner face of the sheet clad scaffold at two-third height from the ground

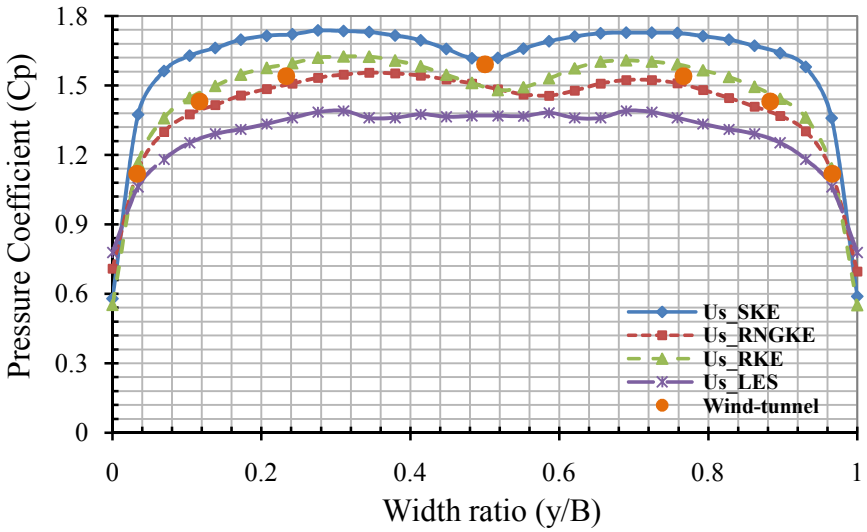

Figure 7.157 Difference of pressure coefficients of the windward outer and inner face of the sheet clad scaffold at two-third height from ground

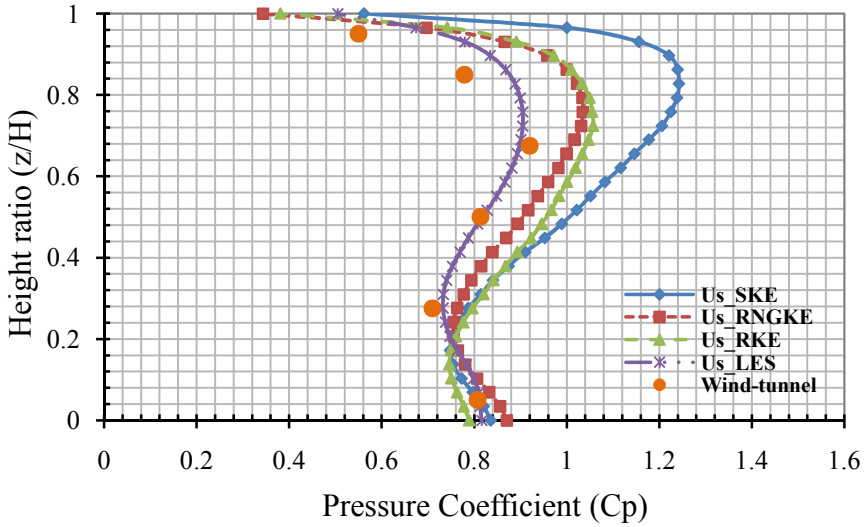

Figure 7.158 Pressure coefficients on the windward outer vertical face at mid-width of the sheet clad scaffold

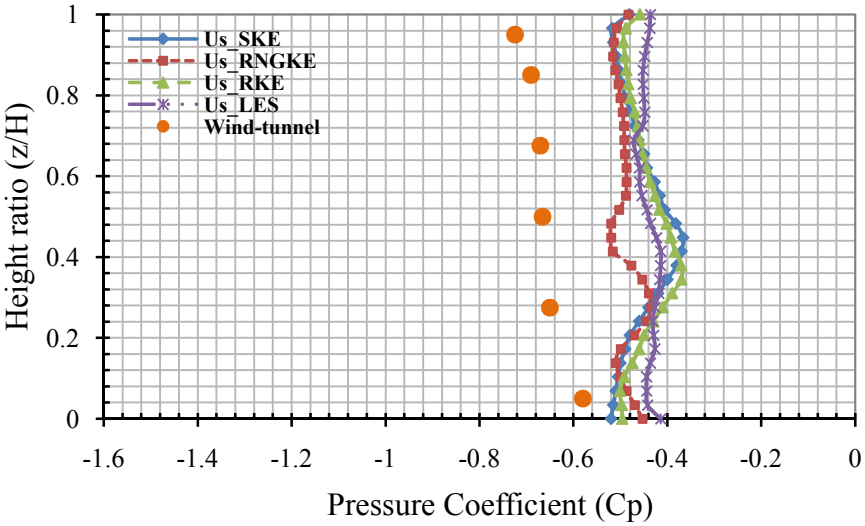

Figure 7.159 Pressure coefficients on the windward inner vertical face at mid-width of the sheet clad scaffold

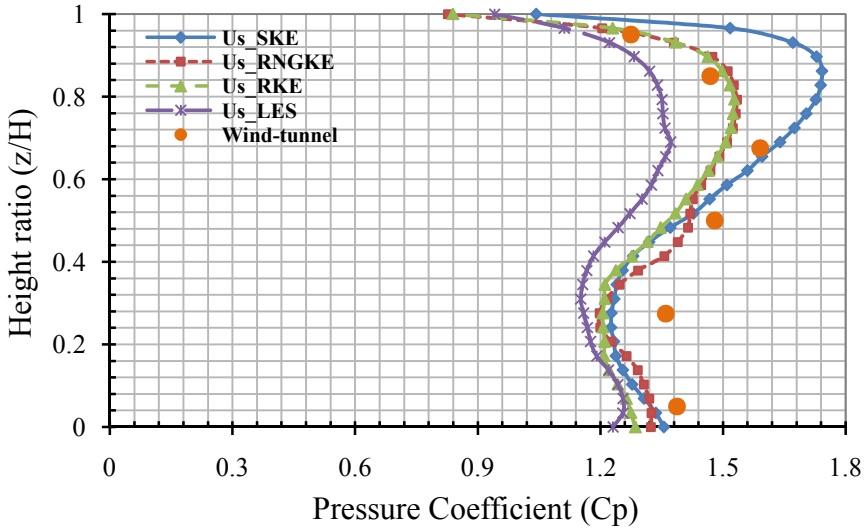

Figure 7.160 Difference of pressure coefficients of the windward outer and inner vertical face at mid-width of the sheet clad scaffold

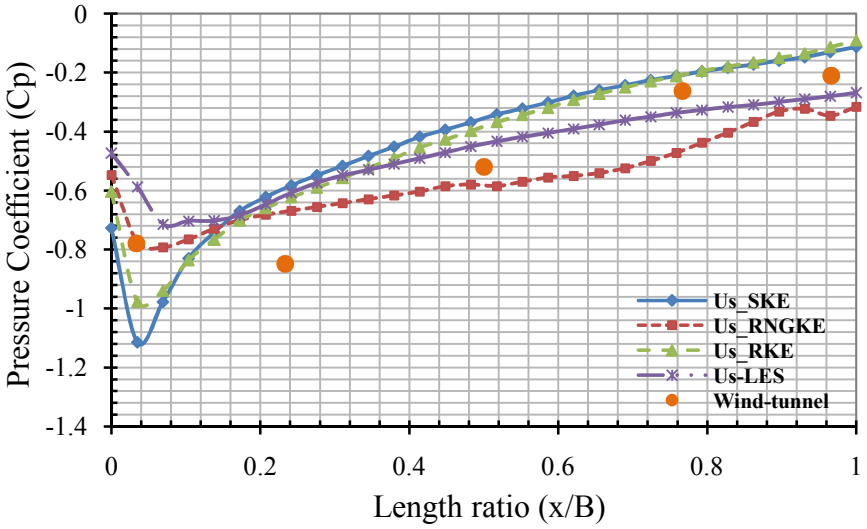

Figure 7.161 Pressure coefficients on the side outer face of the sheet clad scaffold at mid height from the ground

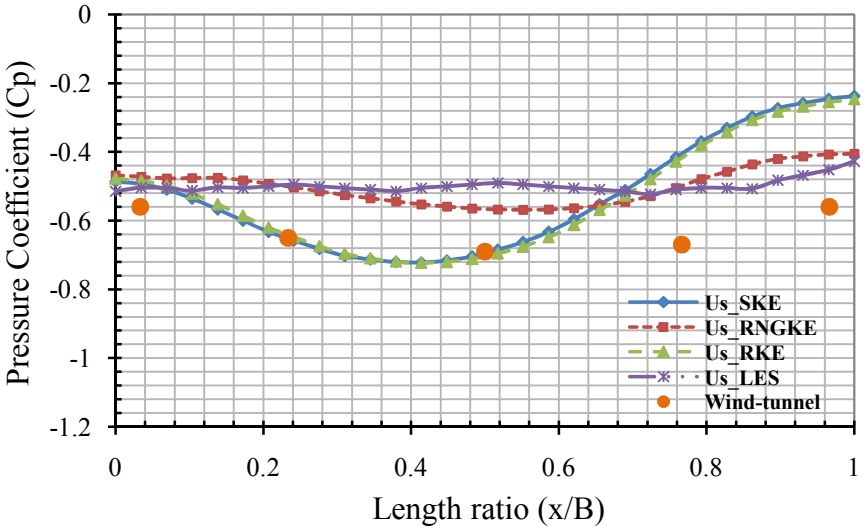

Figure 7.162 Pressure coefficients on the side inner face of the sheet clad scaffold at mid height from the ground

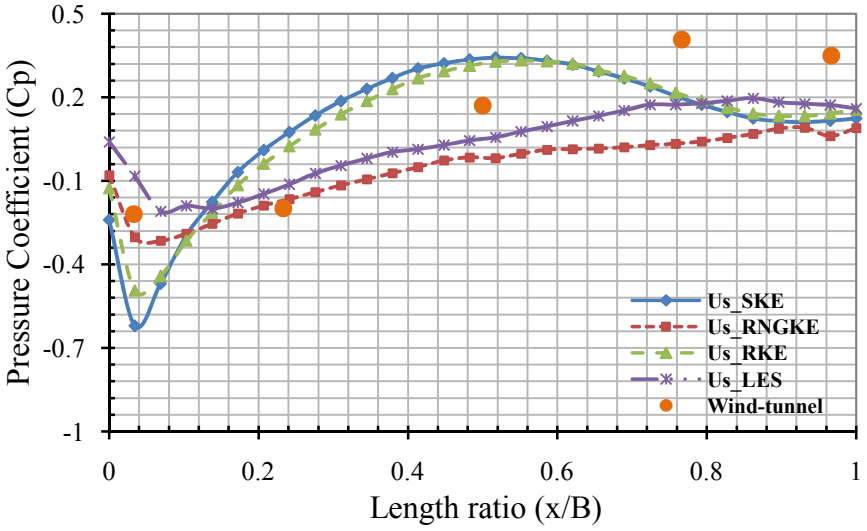

Figure 7.163 Difference of pressure coefficients of the side outer and inner face of the sheet clad scaffold at mid height from ground

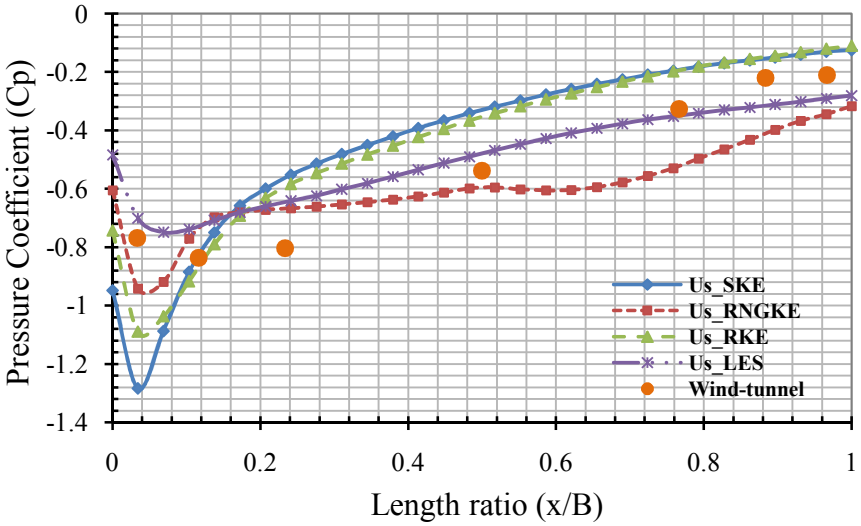

Figure 7.164 Pressure coefficients on the side outer face of the sheet clad scaffold at two-third height from the ground

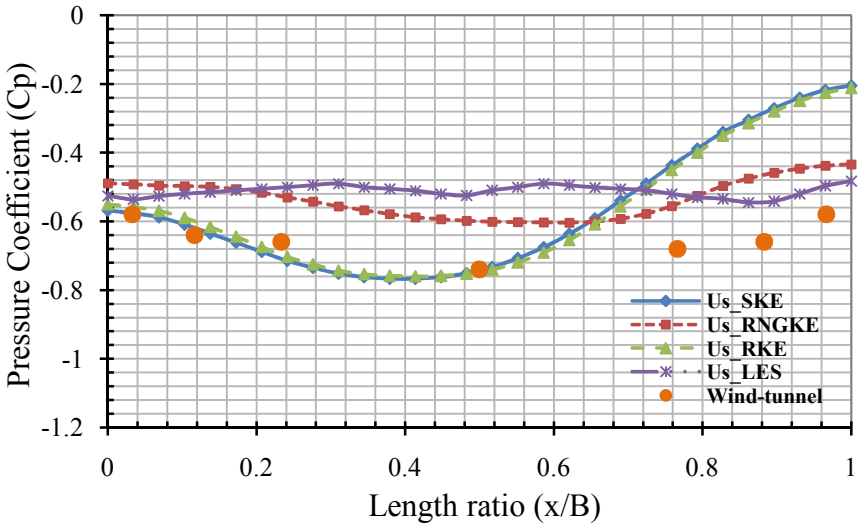

Figure 7.165 Pressure coefficients on the side inner face of the sheet clad scaffold at two-third height from the ground

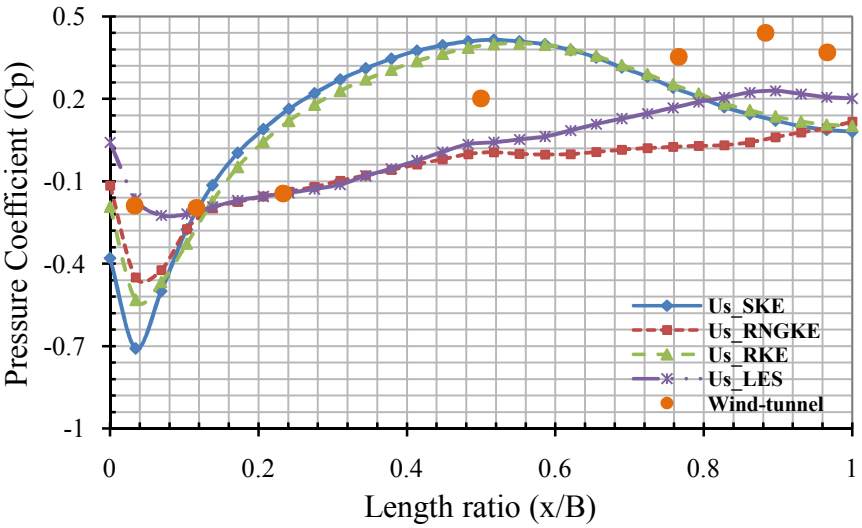

Figure 7.166 Difference of pressure coefficients of the side outer and inner face of the sheet clad scaffold at two-third height from ground

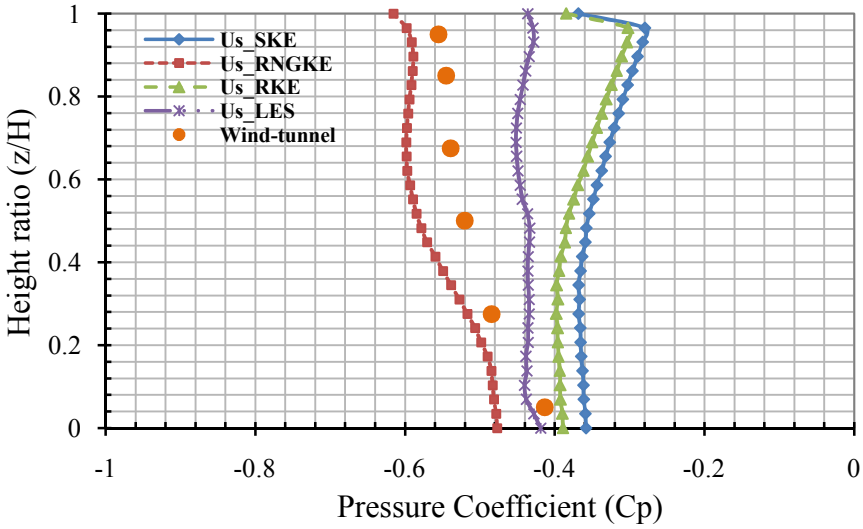

Figure 7.167 Pressure coefficients on the side outer vertical face at mid-length of the sheet clad scaffold

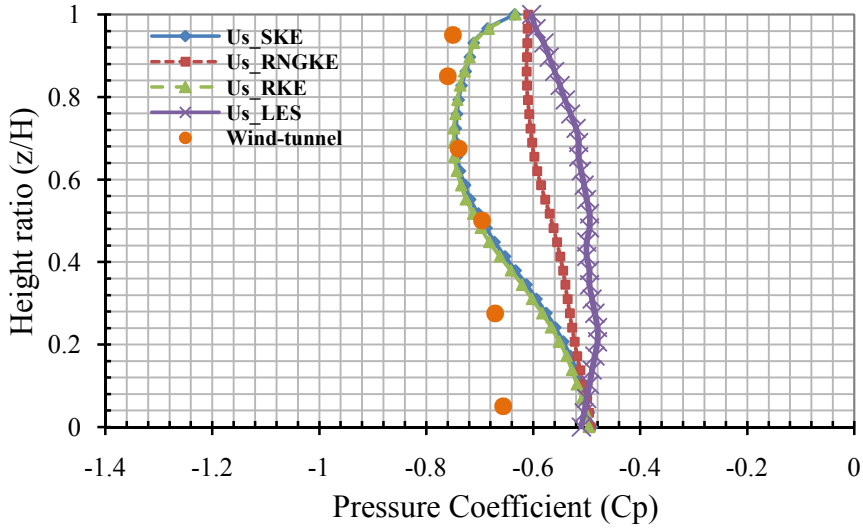

Figure 7.168 Pressure coefficients on the side inner vertical face at mid-length of the sheet clad scaffold

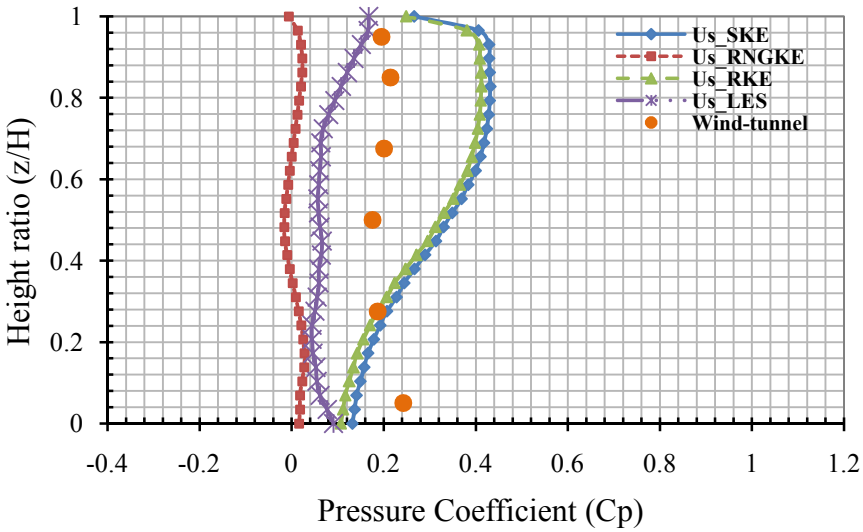

Figure 7.169 Difference of pressure coefficients of the side outer and inner vertical face at mid-length of the sheet clad scaffold

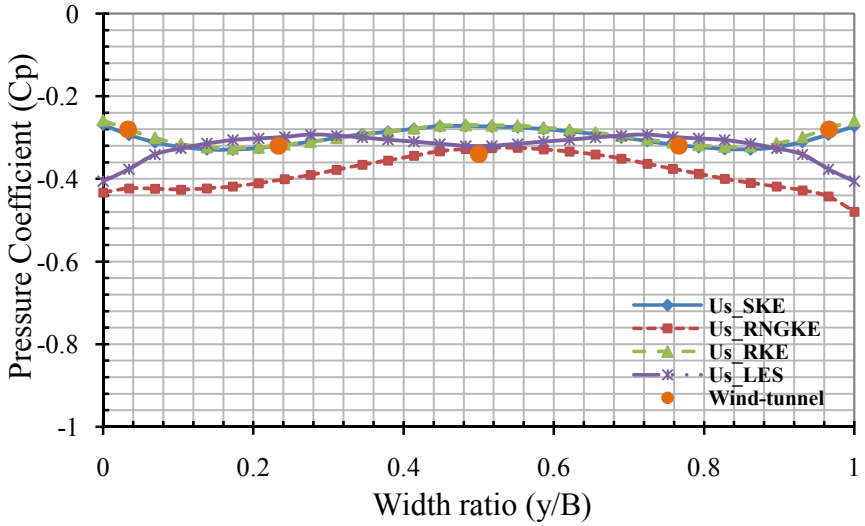

Figure 7.170 Pressure coefficients on the leeward outer face of the sheet clad scaffold at mid height from the ground

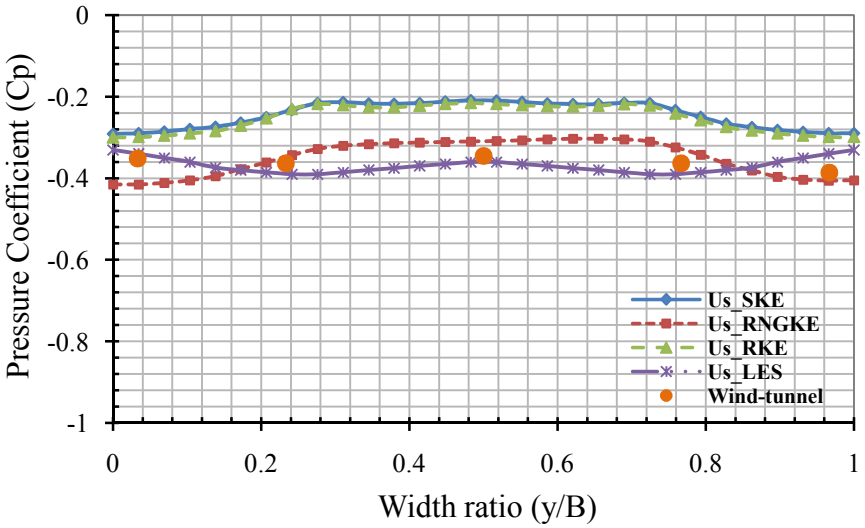

Figure 7.171 Pressure coefficients on the leeward inner face of the sheet clad scaffold at mid height from the ground

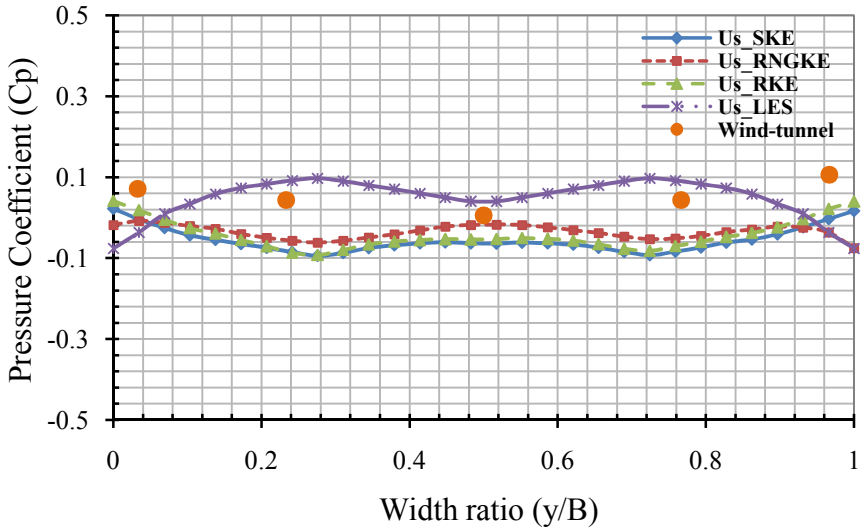

Figure 7.172 Difference of pressure coefficients of the leeward outer and inner face of the sheet clad scaffold at mid height from the ground

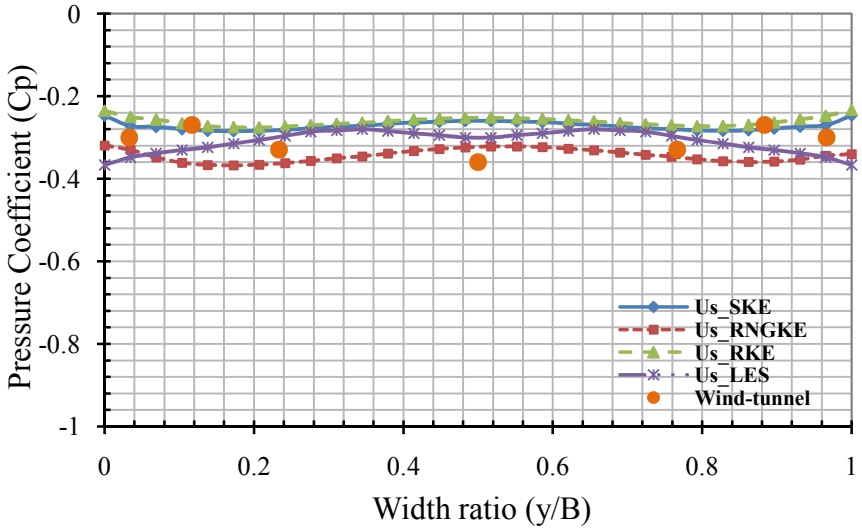

Figure 7.173 Pressure coefficients on the leeward outer face of the sheet clad scaffold at two-third height from the ground

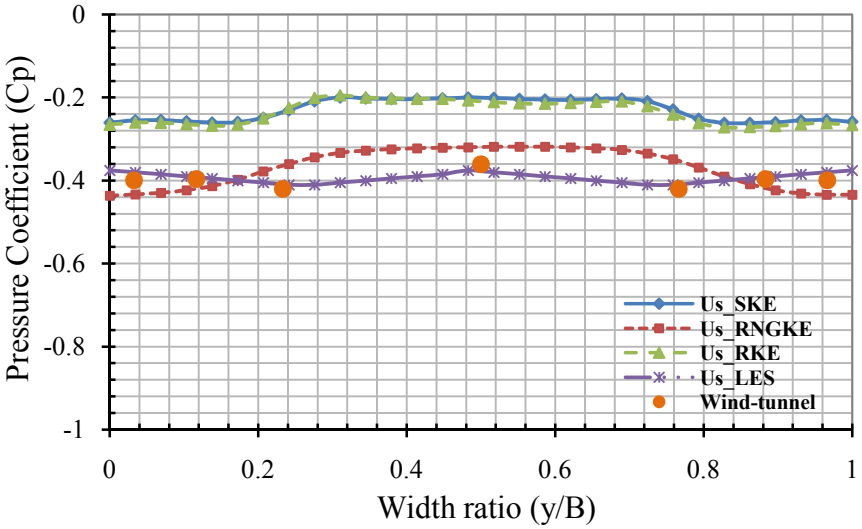

Figure 7.174 Pressure coefficients on the leeward inner face of the sheet clad scaffold at two-third height from the ground

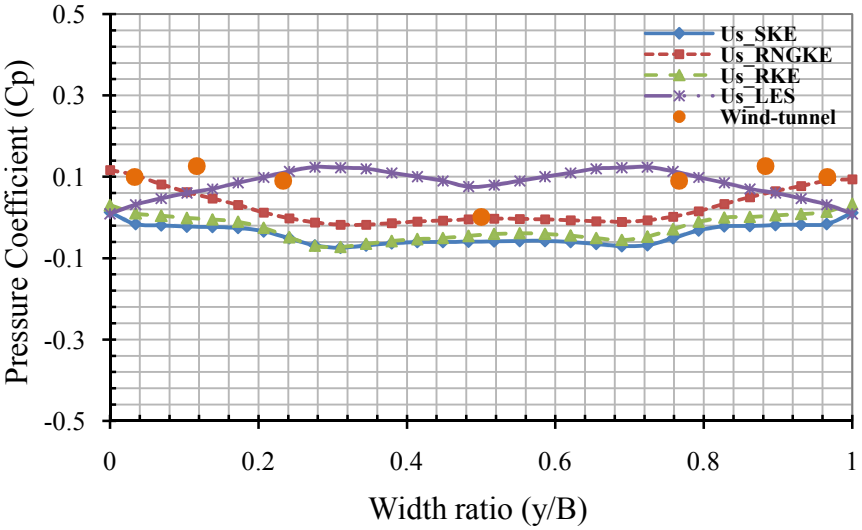

Figure 7.175 Difference of pressure coefficients of the leeward outer and inner face of the sheet clad scaffold at two-third height from the ground

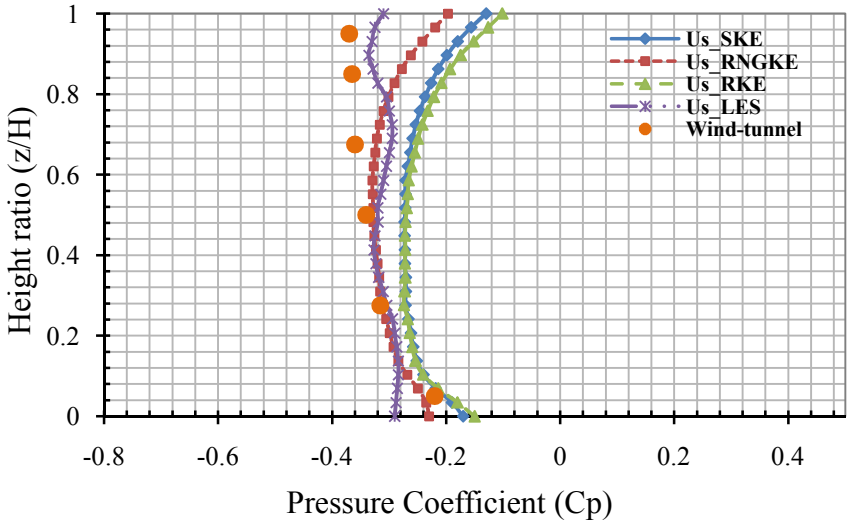

Figure 7.176 Pressure coefficients on the leeward outer vertical face at mid-width of the sheet clad scaffold

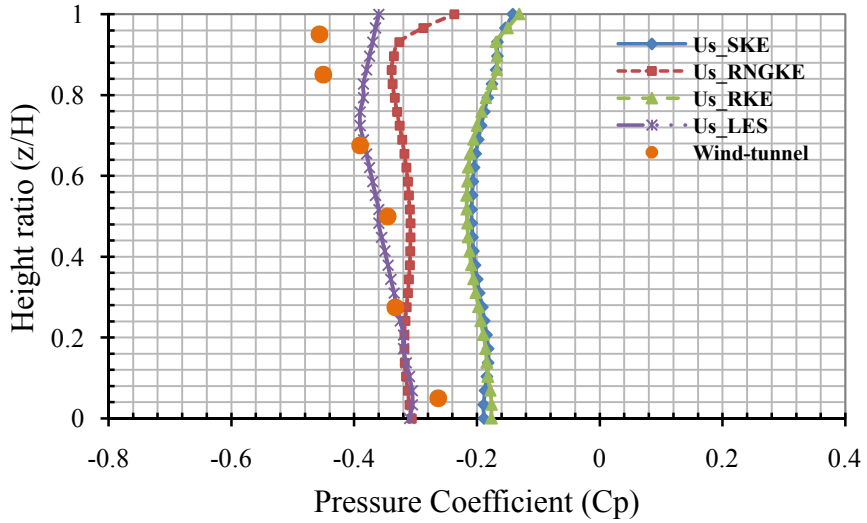

Figure 7.177 Pressure coefficients on the leeward inner vertical face at mid-width of the sheet clad scaffold

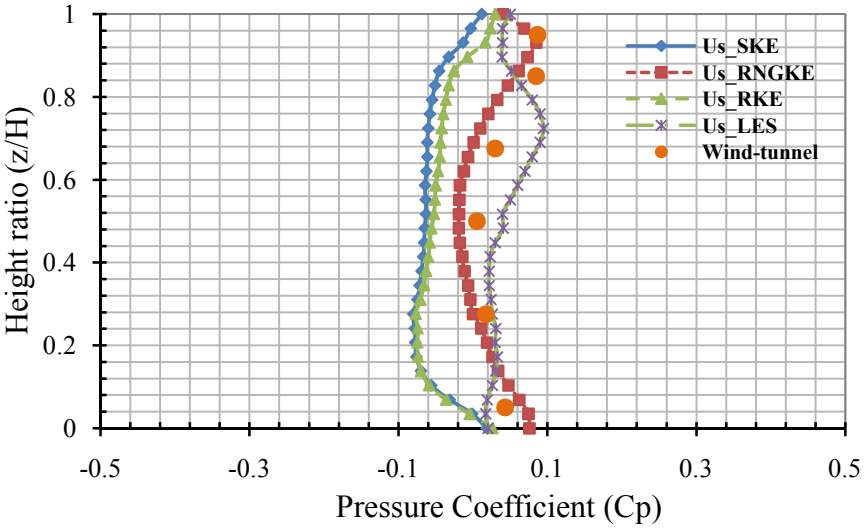

Figure 7.178 Difference of pressure coefficients of the leeward outer and inner vertical face at mid-width of the sheet clad scaffold

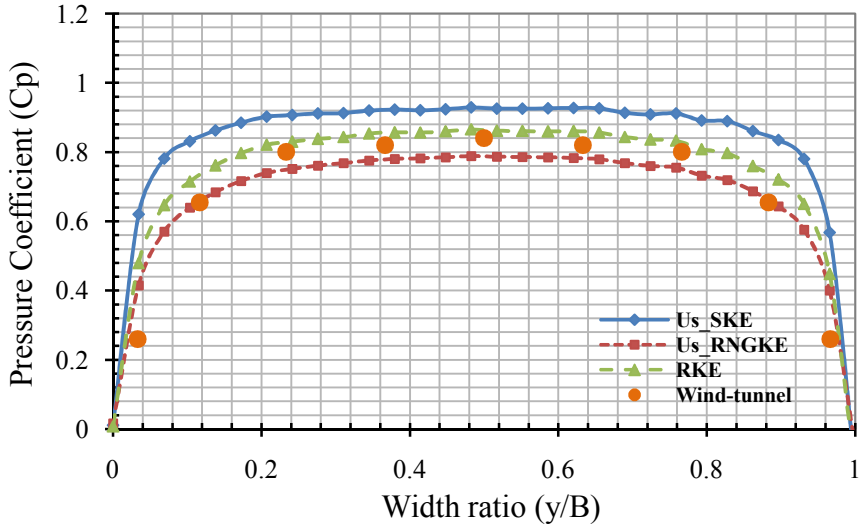

Figure 7.179 Pressure coefficients on the windward outer face of the elevated sheet clad scaffold at mid height from the ground

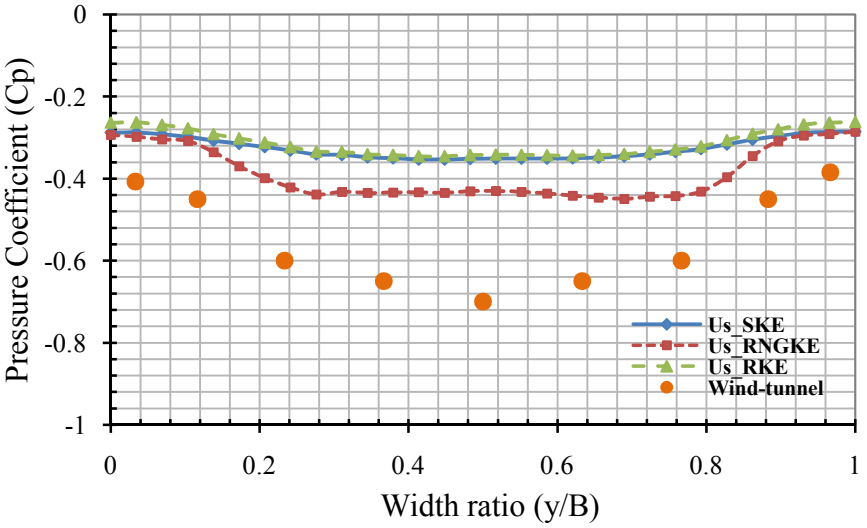

Figure 7.180 Pressure coefficients on the windward inner face of the elevated sheet clad scaffold at mid height from the ground

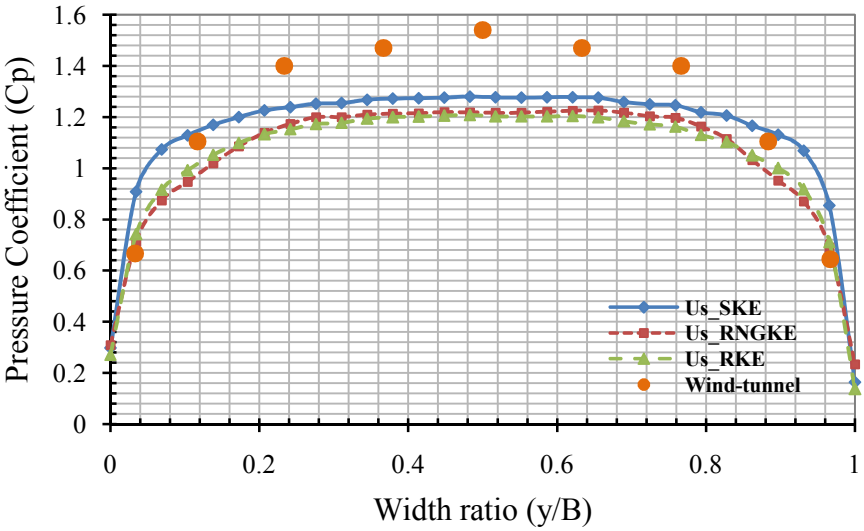

Figure 7.181 Difference of pressure coefficients of the windward outer and inner face of the elevated sheet clad scaffold at mid height from the ground

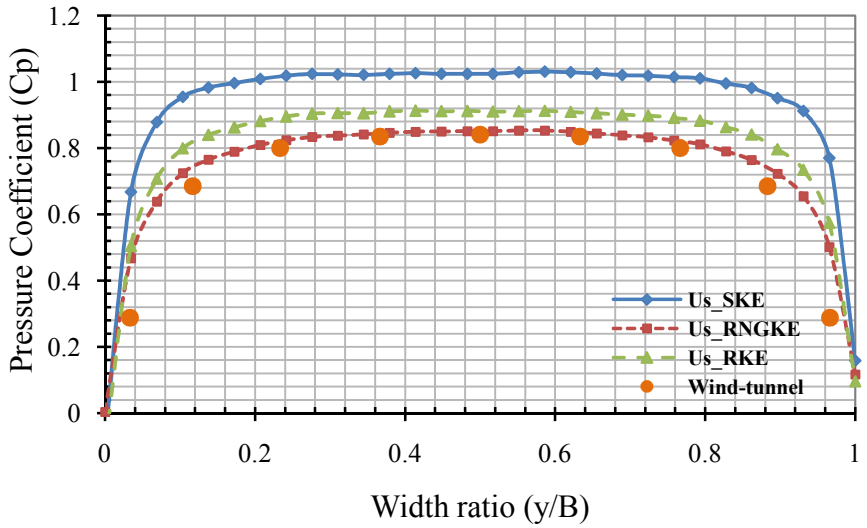

Figure 7.182 Pressure coefficients on the windward outer face of the elevated sheet clad scaffold at two-third height from the ground

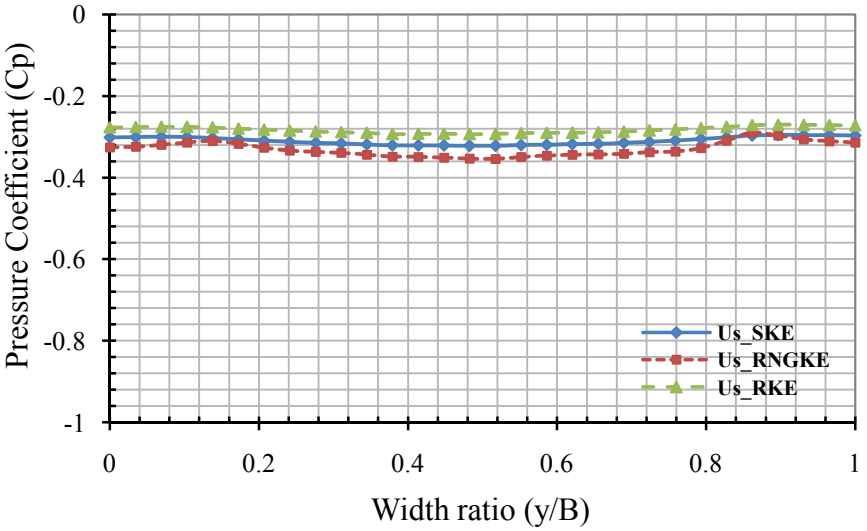

Figure 7.183 Pressure coefficients on the windward inner face of the elevated sheet clad scaffold at two-third height from the ground

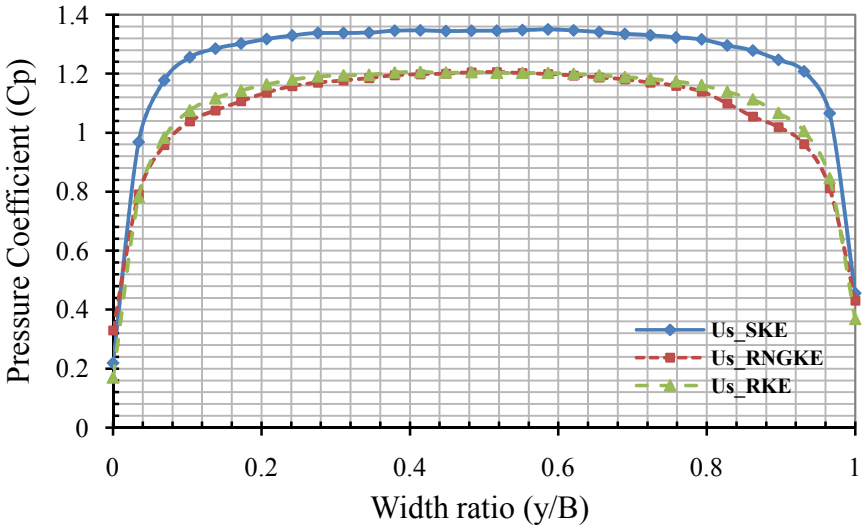

Figure 7.184 Difference of pressure coefficients of the windward outer and inner face of the elevated sheet clad scaffold at two-third height from the ground

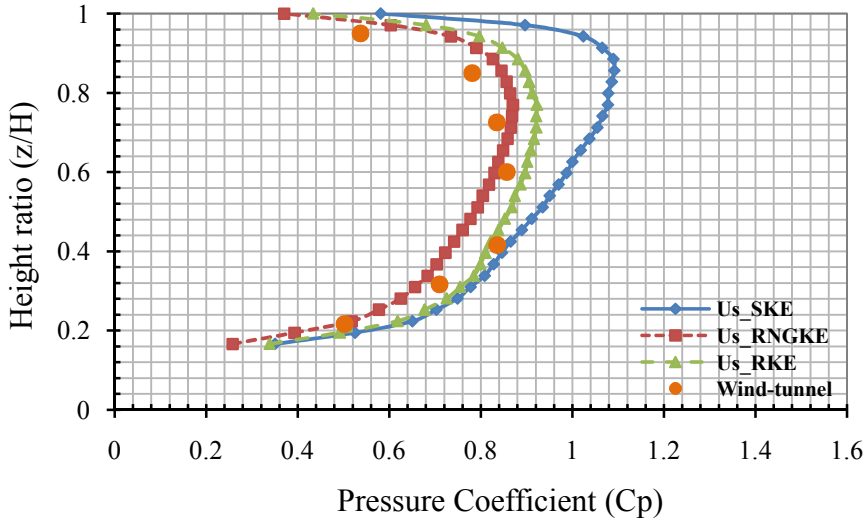

Figure 7.185 Pressure coefficients on the windward outer vertical face at mid-width of the elevated sheet clad scaffold

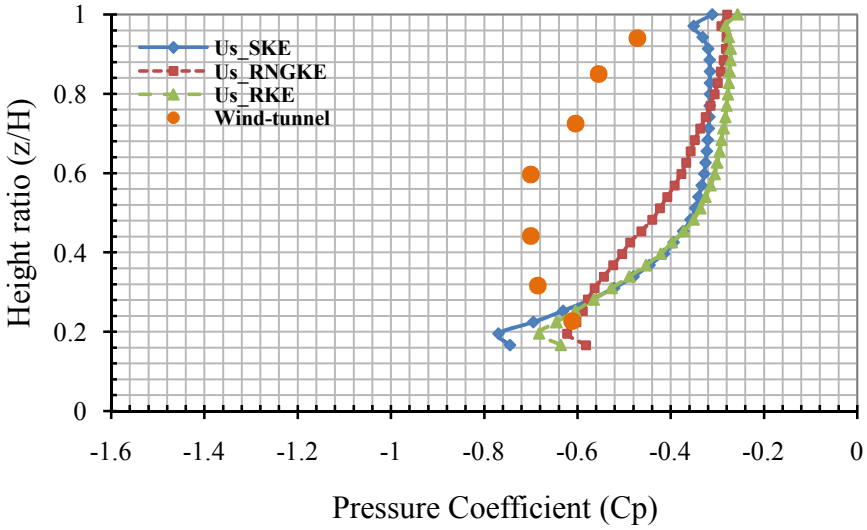

Figure 7.186 Pressure coefficients on the windward inner vertical face at mid-width of the elevated sheet clad scaffold

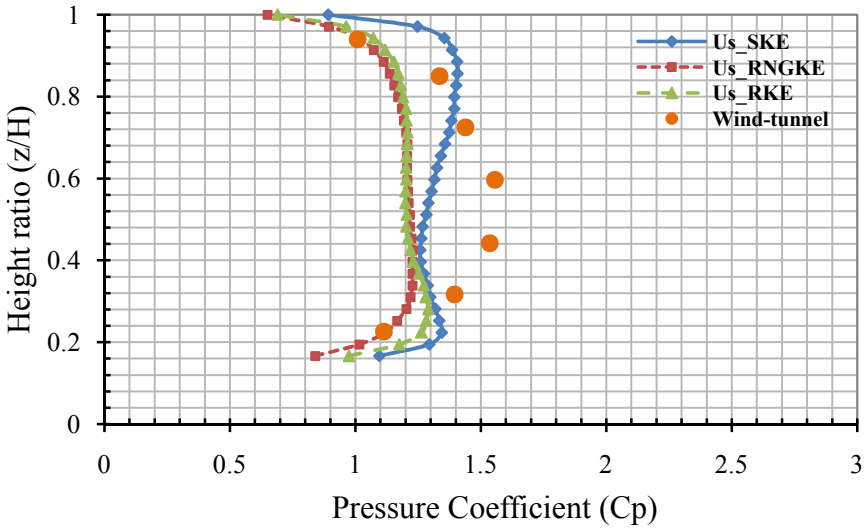

Figure 7.187 Difference of pressure coefficients of the windward outer and inner vertical face at mid-width of the elevated sheet clad scaffold

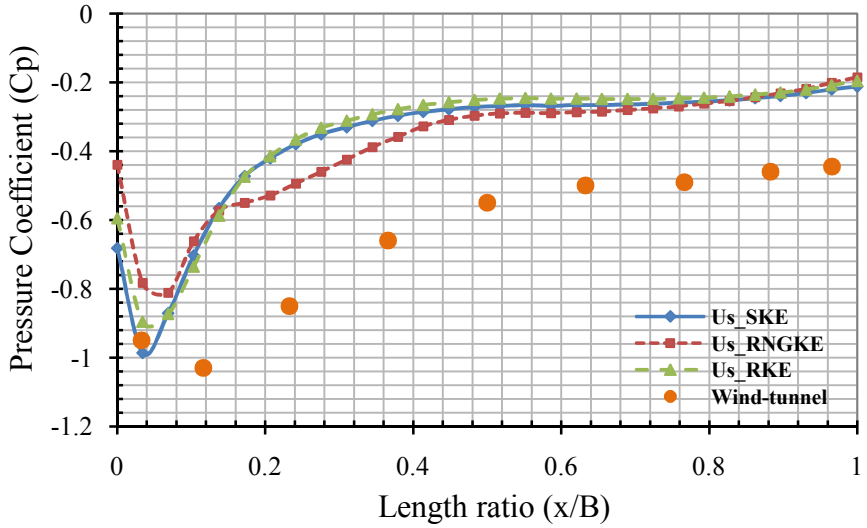

Figure 7.188 Pressure coefficients on the side outer face of the elevated sheet clad scaffold at mid height from the ground

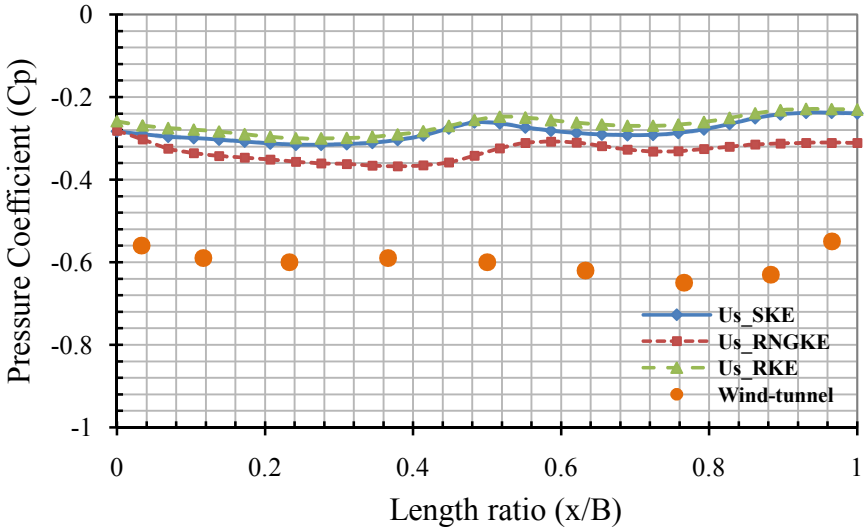

Figure 7.189 Pressure coefficients on the side inner face of the elevated sheet clad scaffold at mid height from the ground

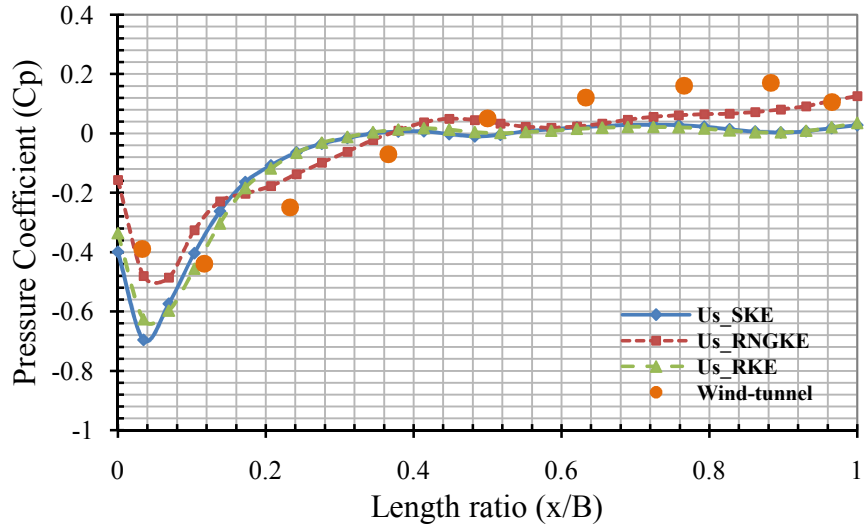

Figure 7.190 Difference of pressure coefficients of the side outer and inner face of the elevated sheet clad scaffold at mid height from the ground

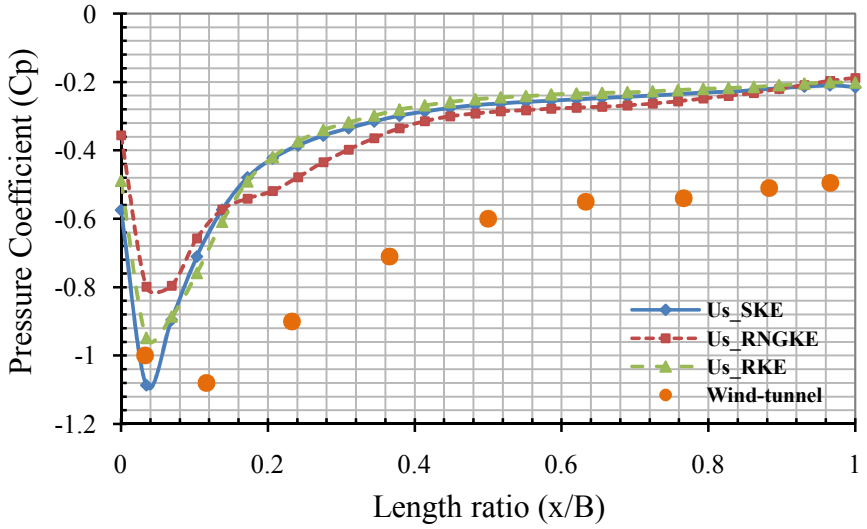

Figure 7.191 Pressure coefficients on the side outer face of the elevated sheet clad scaffold at two-third height from the ground

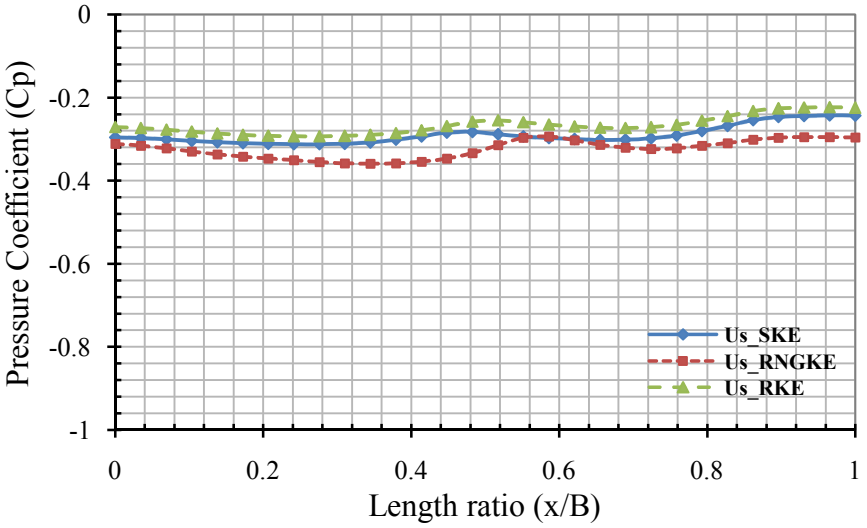

Figure 7.192 Pressure coefficients on the side inner face of the elevated sheet clad scaffold at two-third height from the ground

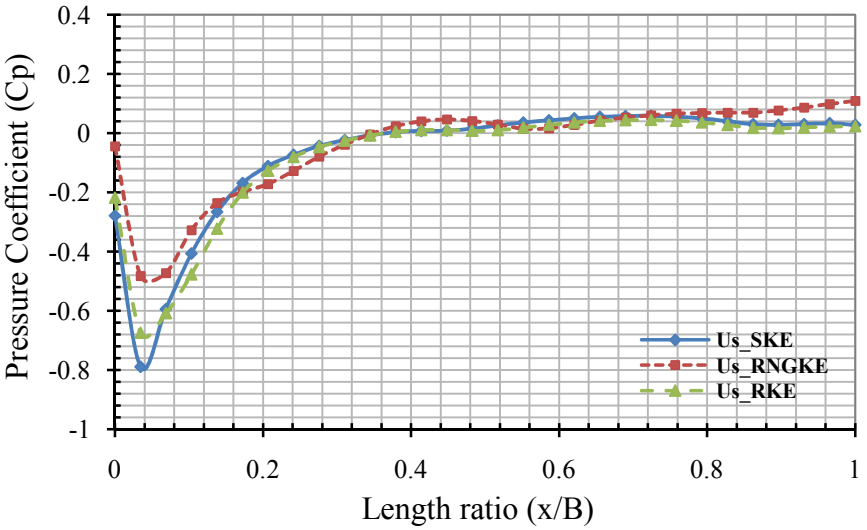

Figure 7.193 Difference of pressure coefficients of the side outer and inner face of the elevated sheet clad scaffold at two-third height from the ground

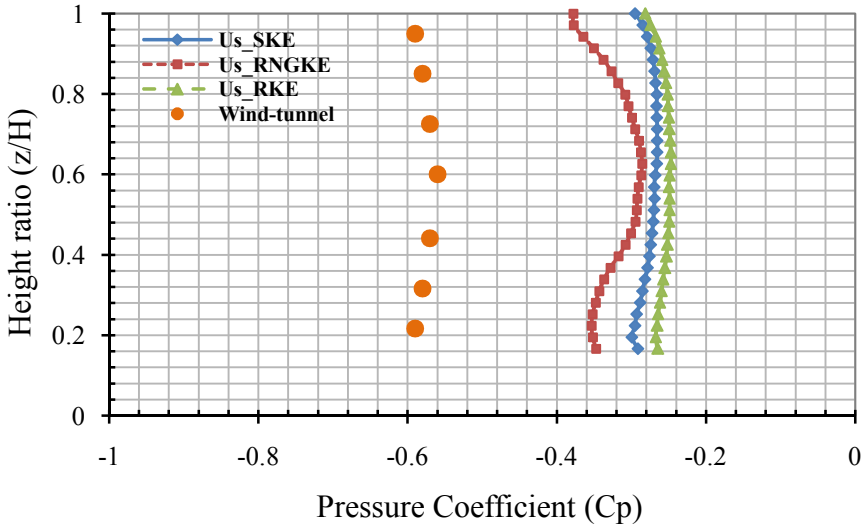

Figure 7.194 Pressure coefficients on the side outer vertical face at mid-length of the elevated sheet clad scaffold

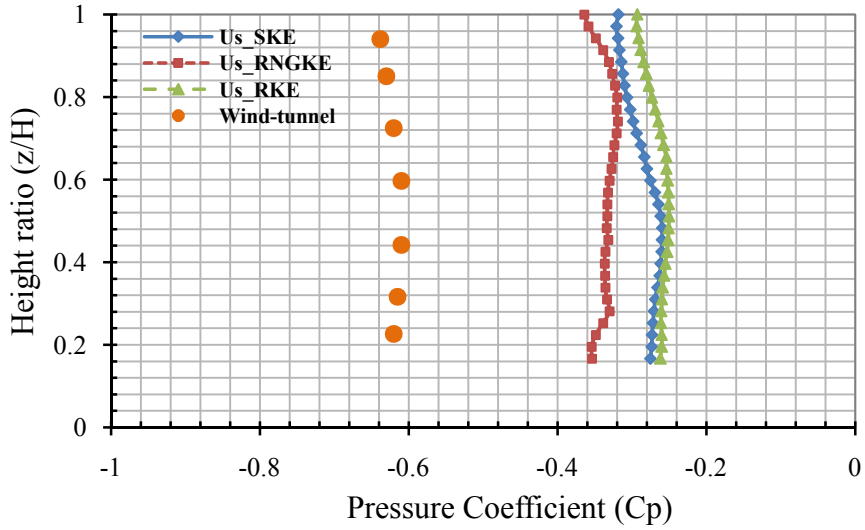

Figure 7.195 Pressure coefficients on the side inner vertical face at mid-length of the elevated sheet clad scaffold

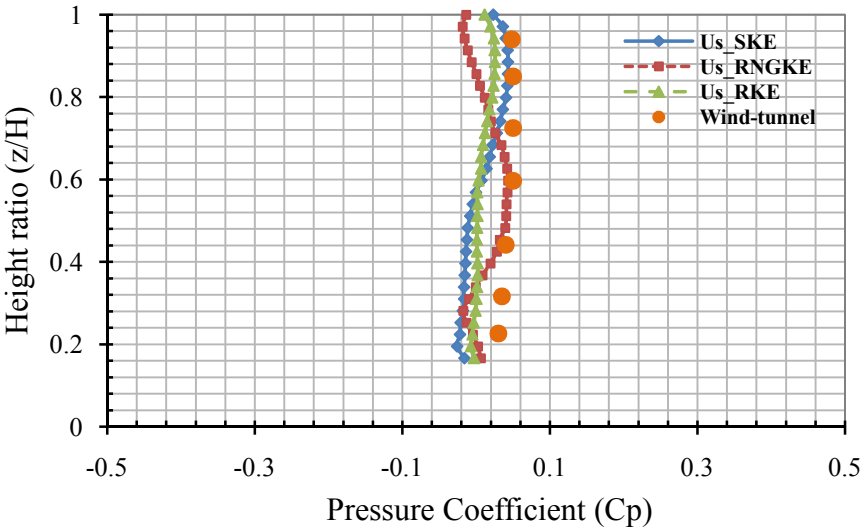

Figure 7.196 Difference of pressure coefficients of the side outer and inner vertical face at mid-length of the elevated sheet clad scaffold

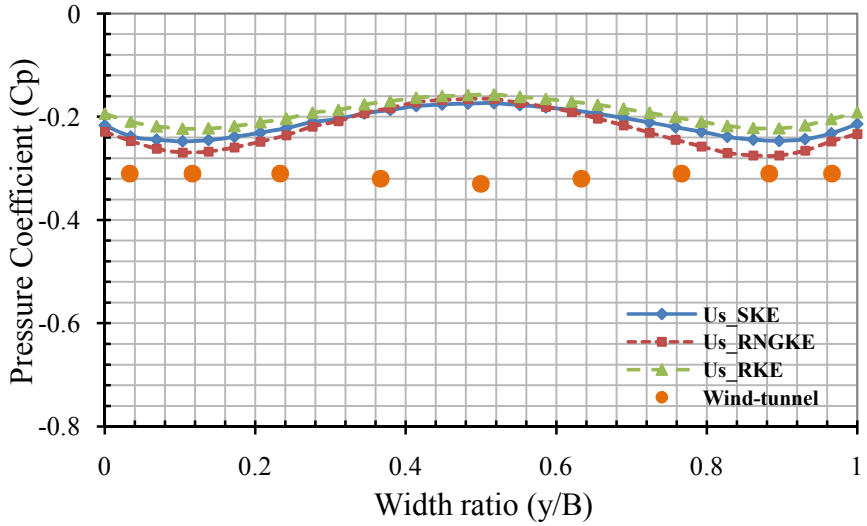

Figure 7.197 Pressure coefficients on the leeward outer face of the elevated sheet clad scaffold at mid height from the ground

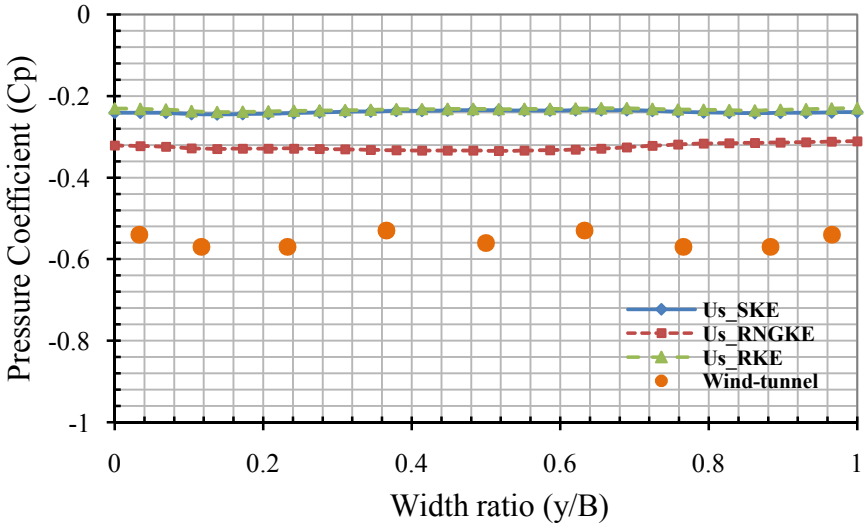

Figure 7.198 Pressure coefficients on the leeward inner face of the elevated sheet clad scaffold at mid height from the ground

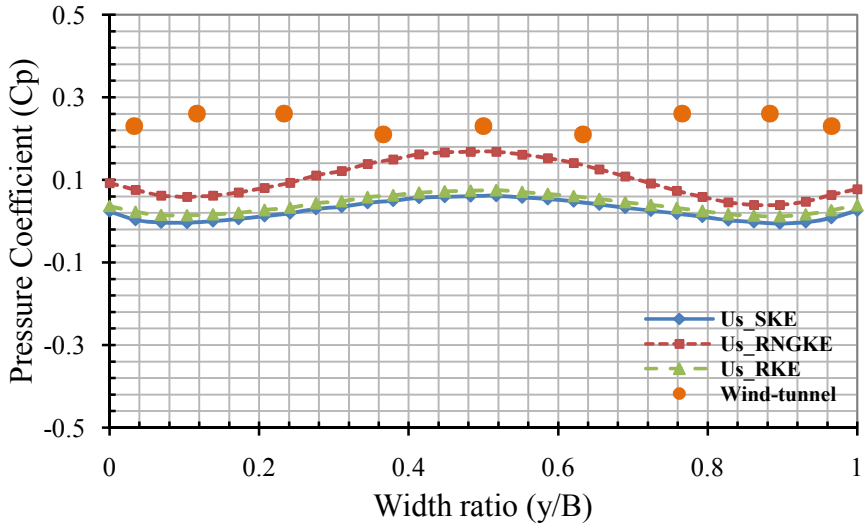

Figure 7.199 Difference of pressure coefficients on the leeward outer and inner face of the elevated sheet clad scaffold at mid height from the ground

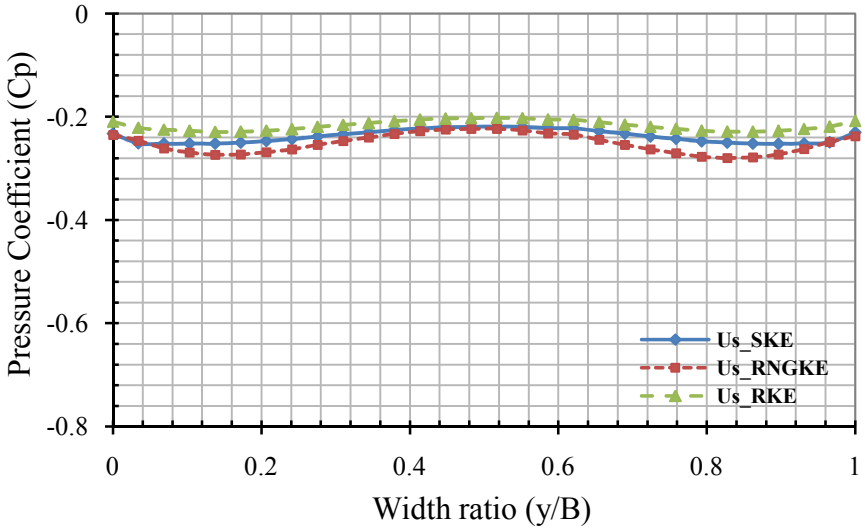

Figure 7.200 Pressure coefficients on the leeward outer face of the elevated sheet clad scaffold at two-third height from the ground

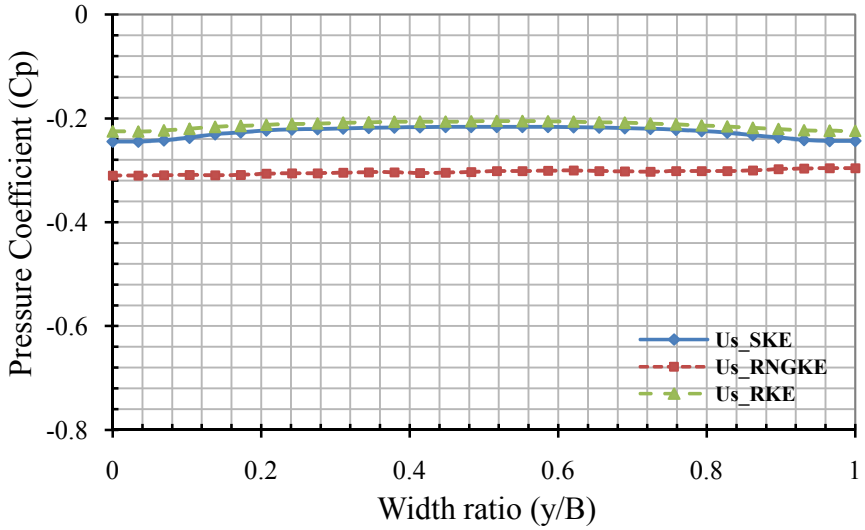

Figure 7.201 Pressure coefficients on the leeward inner face of the elevated sheet clad scaffold at two-third height from the ground

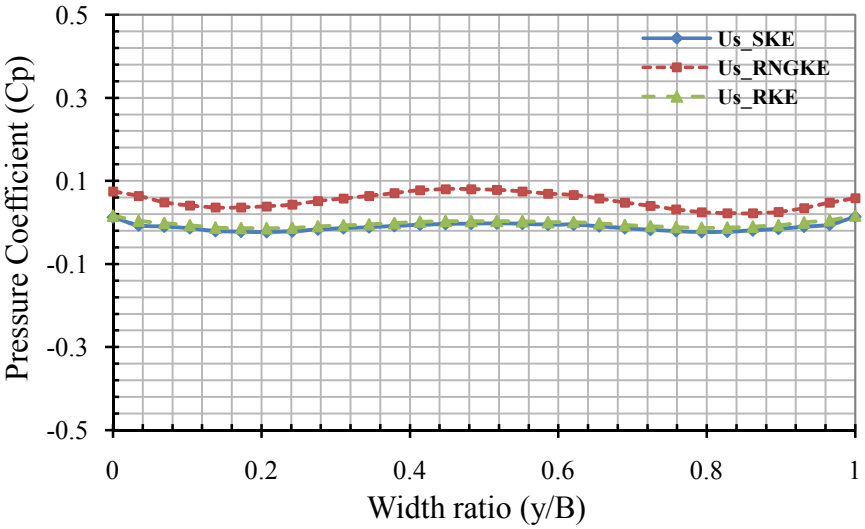

Figure 7.202 Difference of pressure coefficients on the leeward outer and inner face of the elevated sheet clad scaffold at two-third height from the ground

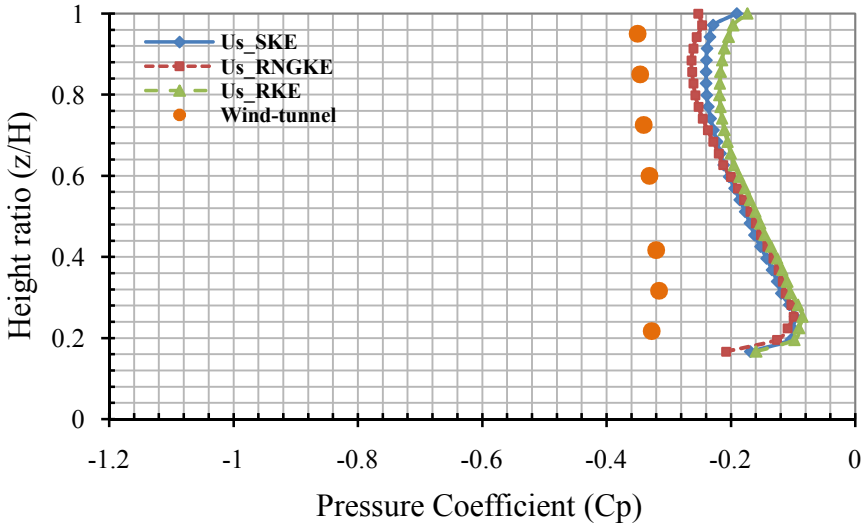

Figure 7.203 Pressure coefficients on the leeward outer vertical face at mid-width of the elevated sheet clad scaffold

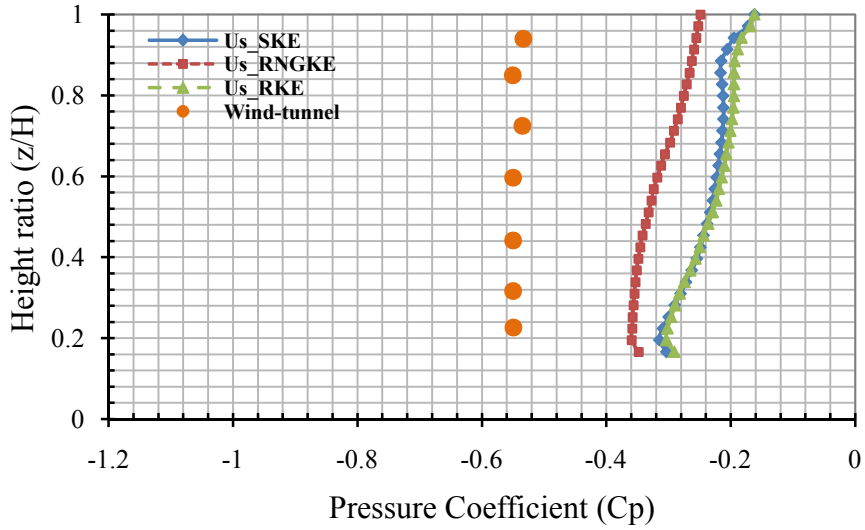

Figure 7.204 Pressure coefficients on the leeward inner vertical face at mid-width of the elevated sheet clad scaffold

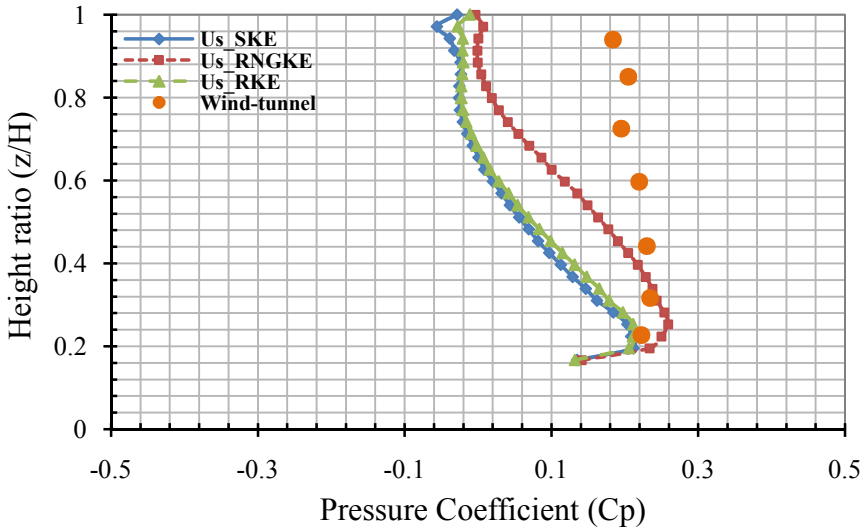

Figure 7.205 Difference of pressure coefficients on the leeward outer and inner vertical face at mid-width of the elevated sheet clad scaffold

7.6 CFD Results on Net Clad Scaffold Surrounding SEB

To determine the wind forces on net clad scaffolds the Silsoe building was used as a base model and a simulated scaffold erected around it. For the net clad scaffolds, two models were made, one touching the ground and the other with an elevated net (1m from the ground on prototype) surrounding the building and are shown in the Figure 7.206 and Figure 7.207 below.

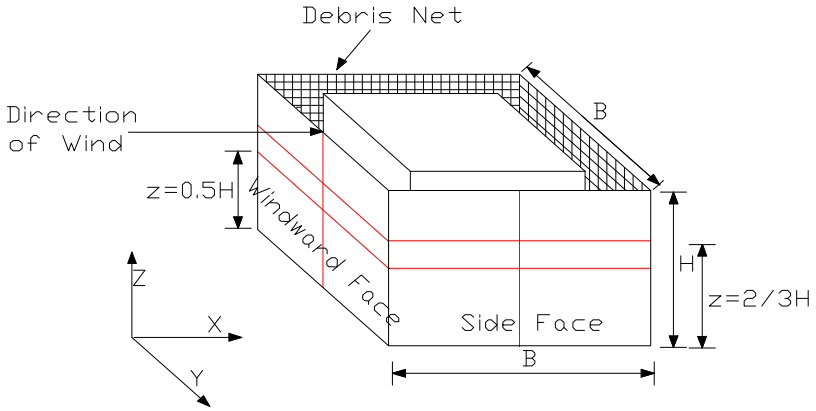

Figure 7.206 Net clad scaffold (touching the ground) surrounding SEB

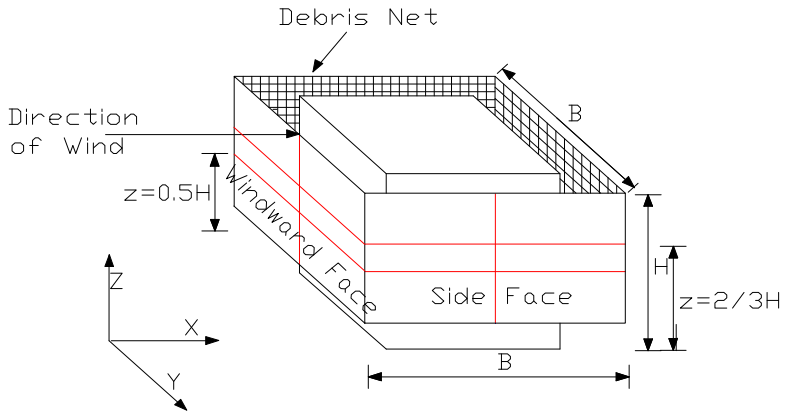

Figure 7.207 Elevated net clad scaffold surrounding SEB

Note: The 'RED LINE' shown on the net clad scaffold surrounding SEB is the position where the pressure coefficients measured

The simulated data from the wind-tunnel (as explained in Chapter 5 and Chapter 6) tests were used as input for different computational techniques used and a procedure was developed to extend the computational model to net clad scaffolds with the netting simulated as porous media. The netting properties such as its permeability and inertial resistance factor were obtained from wind-tunnel tests on nets as explained in Chapter 6. A structured mesh was generated for both cases of the net clad scaffold touching the

ground and for an elevated net clad scaffold. Two types of net (Type A Net and Type B Net) were used with thicknesses of 0.42 mm and 0.65 mm respectively.

The computational domain is shown in Figure 5.26, covers 29**B** (**B** is the outer dimension of the net clad scaffold) in the stream (**X**) direction (-6.5 < **x**/**B** < 22.5), 13**B** in the lateral or normal (**Y**) direction (-6.5 < **y**/**B** < 6.5) and 3**H or 4H** in the vertical direction, using the centre plan of the building as the origin of coordinates. For models with thin membranes a simplification called a "porous jump" was used to model the velocity/pressure drop characteristics and was applied to all the faces of the media.

Because of time constraints the LES simulations were not undertaken in this case. The unsteady RNG $k-\varepsilon$, Realizable $k-\varepsilon$ and Reynolds stress method were used for computations over a period of 4 seconds. The time step was taken to be 0.001s and 4000 time steps performed. These were iterated to obtain the time averaged results for each time step. The porous jump boundary condition was used for all nets in their respective directions. A turbulence intensity of 18% and a length scale of 0.3 at the eave height were kept constant for all the trials.

The pressure coefficients were plotted for both the cases (elevated net and net touching the ground) and for Type A Net and Type B Net on the inner and outer faces of the net and are shown in Figure 7.208 to Figure 7.315. The pressure coefficients were measured at 1/2 H and 2/3 H from the ground (parallel to the ground) on both the inner and outer faces. The pressure coefficients were also measured in the vertical direction in the middle of either width or depth of the scaffold (perpendicular to the ground) on both the inner and outer faces. The difference of pressure coefficients between outer and inner faces on all the façades of the net and for both type of nets is also plotted to determine the wind forces transferred from the net to the steel scaffold. Three different unsteady CFD models namely RNG $k-\varepsilon$, Realizable $k-\varepsilon$ and Reynolds stress model were used to determine the pressure coefficients on the outer and inner face of the net clad scaffolds. The pattern of the pressure coefficients by all the three models on the windward outer and inner face were almost the same. However, on the side face the suction (negative) pressure coefficients shown by RSM are more, followed by Realizable $k-\varepsilon$ and least by the RNG $k-\varepsilon$. Also on the leeward face the pressure coefficients shown by RSM are more than those found by the RNG and Realizable $k-\varepsilon$.

The drops in pressure coefficients are more for the Type B Net than for the Type A Net. This may be because Type B Net is denser than Type A Net. For Type B Net also the Reynolds stress model gives higher suction pressure than the RNG $k-\varepsilon$ and Realizable $k-\varepsilon$ models both on the side and leeward face. It was also observed that the Reynolds stress model showed a higher suction than the RNG $k-\varepsilon$ and the Realizable $k-\varepsilon$ model on the leeward side of the net. All plots, both for the net clad scaffold touching the ground and the elevated net clad scaffold and for Type A and Type B net respectively can be seen in figure from Figure 7.208 to Figure 7.315.

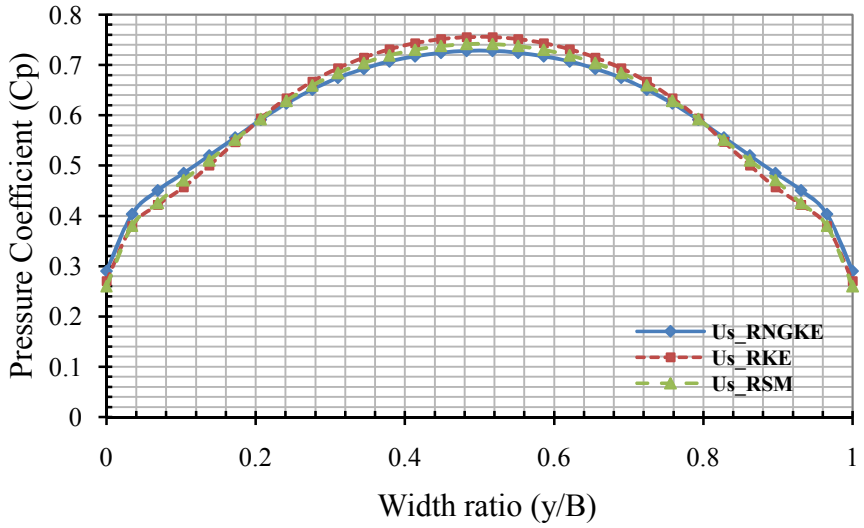

Figure 7.208 Pressure coefficients on the windward outer face of the net clad scaffold at mid height from the ground for Type A Net

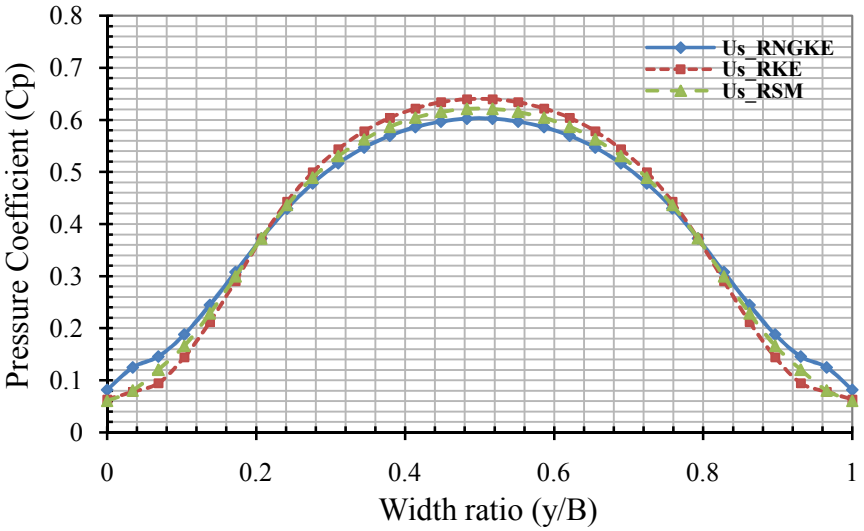

Figure 7.209 Pressure coefficients on the windward inner face of the net clad scaffold at mid height from the ground for Type A Net

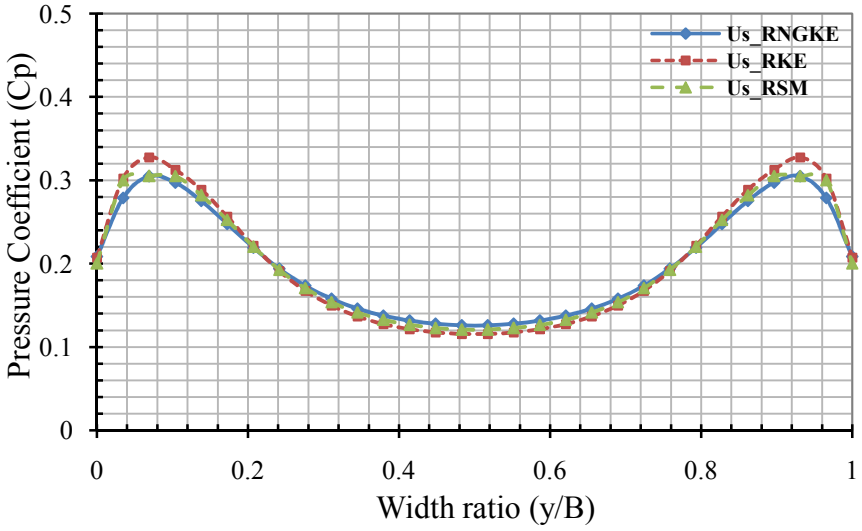

Figure 7.210 Difference of pressure coefficients of the windward outer and inner face of the net clad scaffold at mid height from the ground for Type A Net

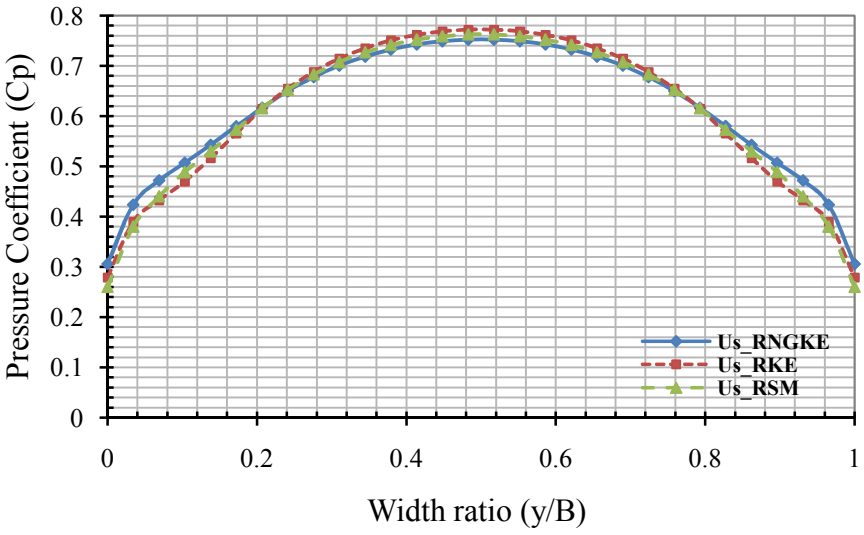

Figure 7.211 Pressure coefficients on the windward outer face of the net clad scaffold at two-third height from the ground for Type A Net

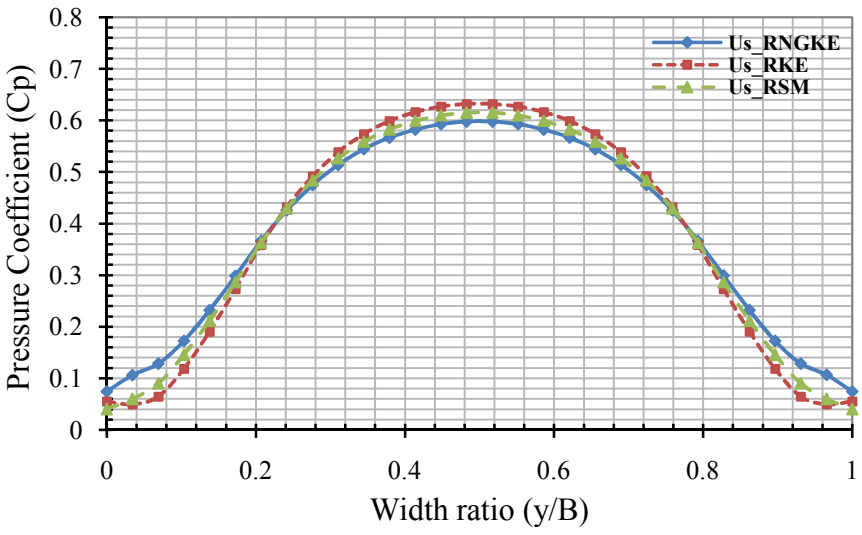

Figure 7.212 Pressure coefficients on the windward inner face of the net clad scaffold at two-third height from the ground for Type A Net

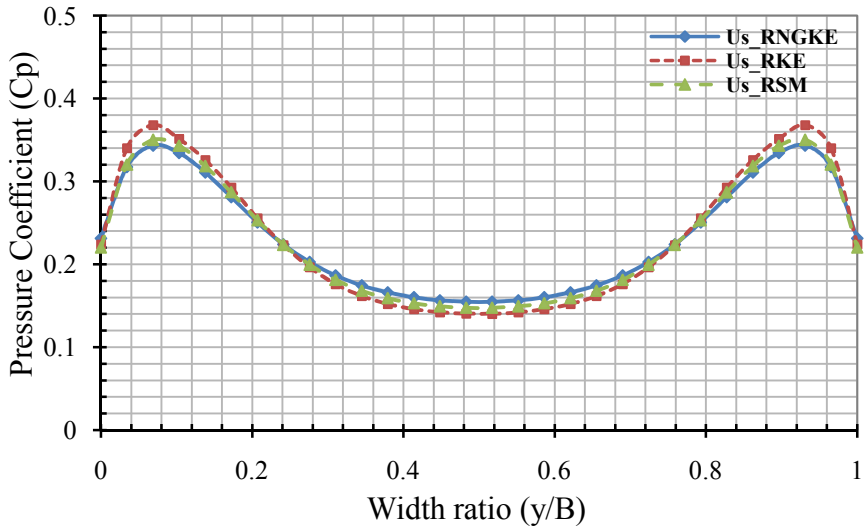

Figure 7.213 Difference of pressure coefficients of the windward outer and inner face of the net clad scaffold at two-third height from ground for Type A Net

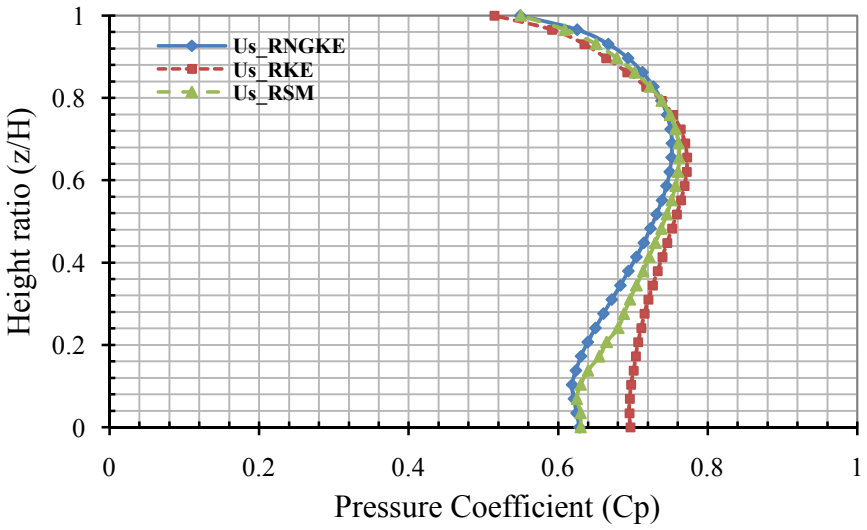

Figure 7.214 Pressure coefficients on the windward outer vertical face at mid-width of the net clad scaffold for Type A Net

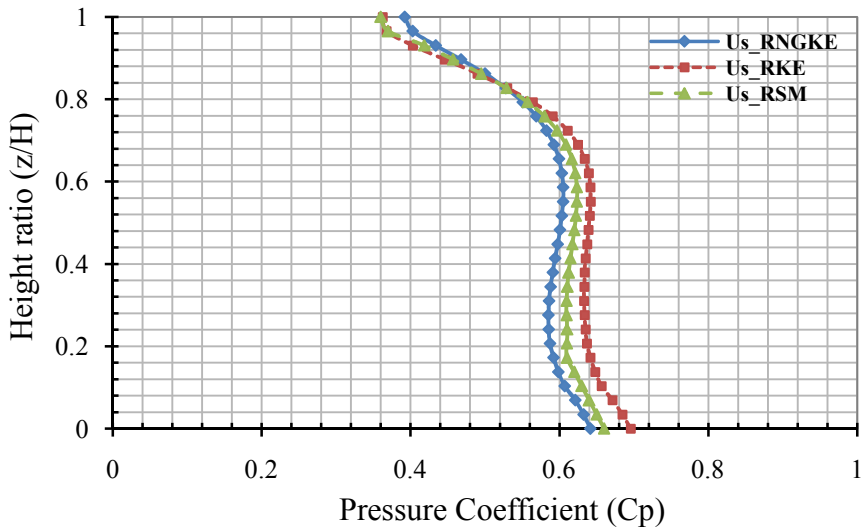

Figure 7.215 Pressure coefficients on the windward inner vertical face at mid-width of the net clad scaffold for Type A Net

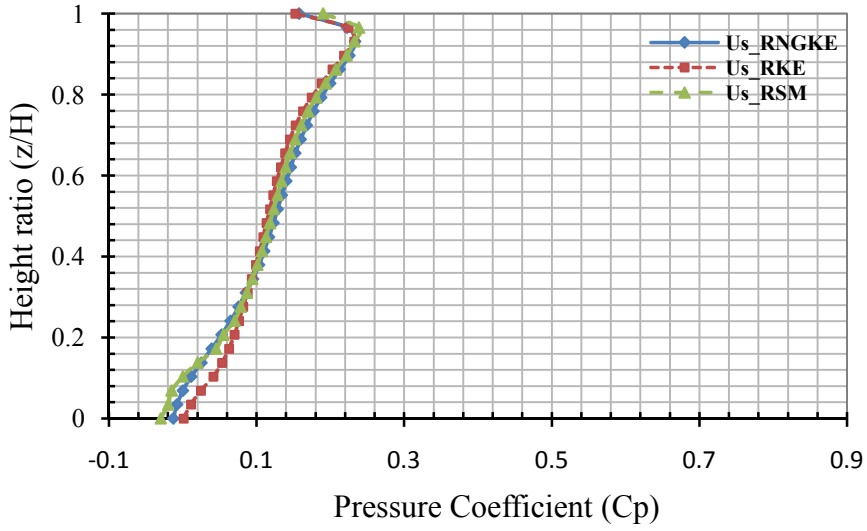

Figure 7.216 Difference of pressure coefficients of the windward outer and inner vertical face at mid-width of the net clad scaffold for Type A Net

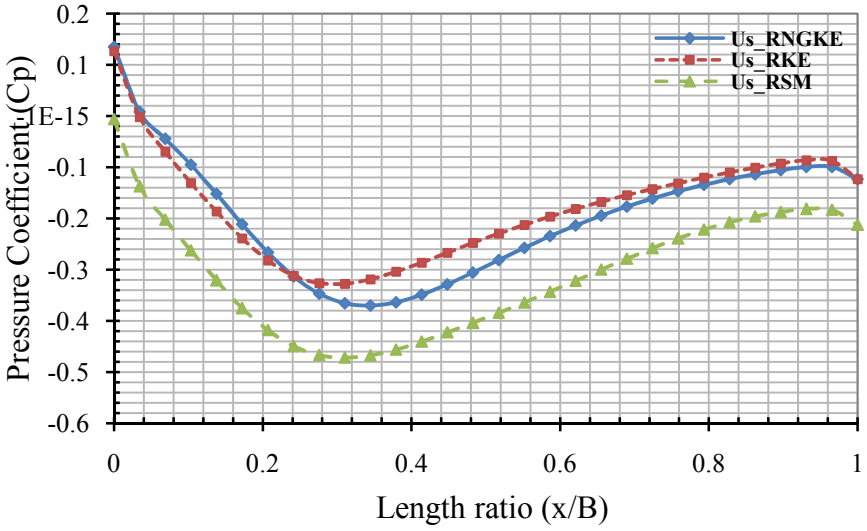

Figure 7.217 Pressure coefficients on the side outer face of the net clad scaffold at mid height from the ground for Type A Net

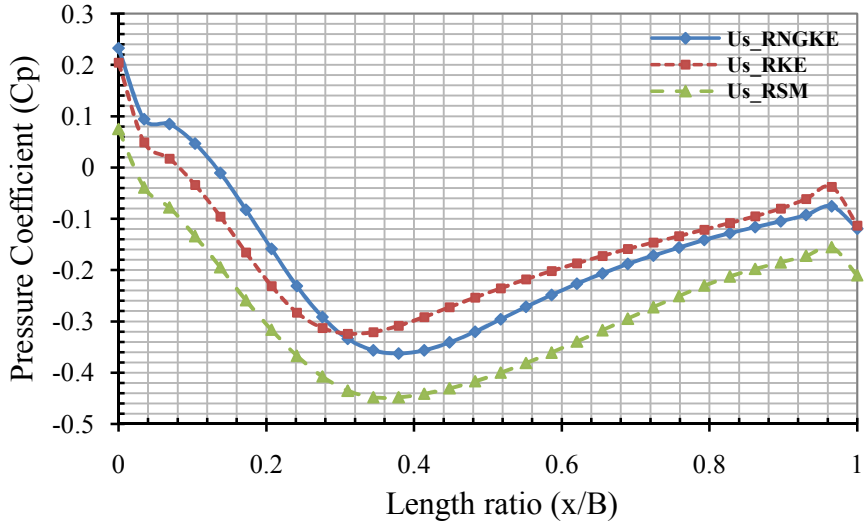

Figure 7.218 Pressure coefficients on the side inner face of the net clad scaffold at mid height from the ground for Type A Net

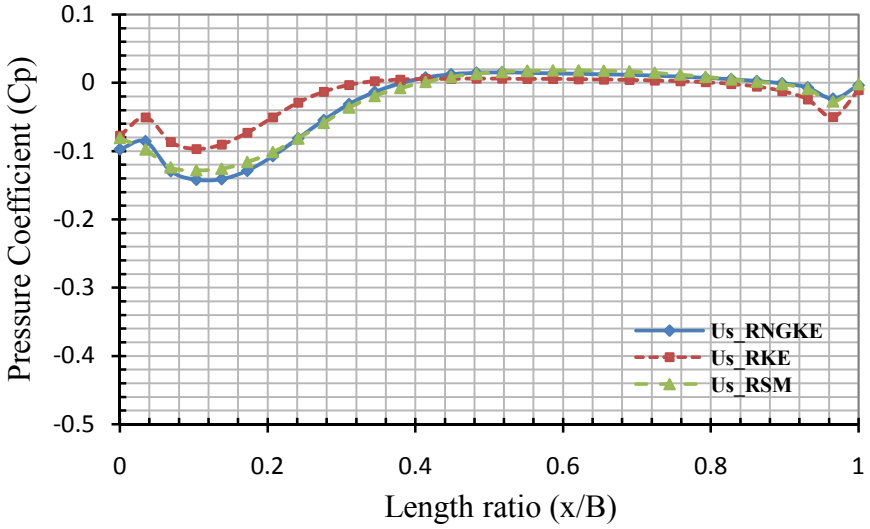

Figure 7.219 Difference of pressure coefficients of the side outer and inner face of the net clad scaffold at mid height from ground for Type A Net

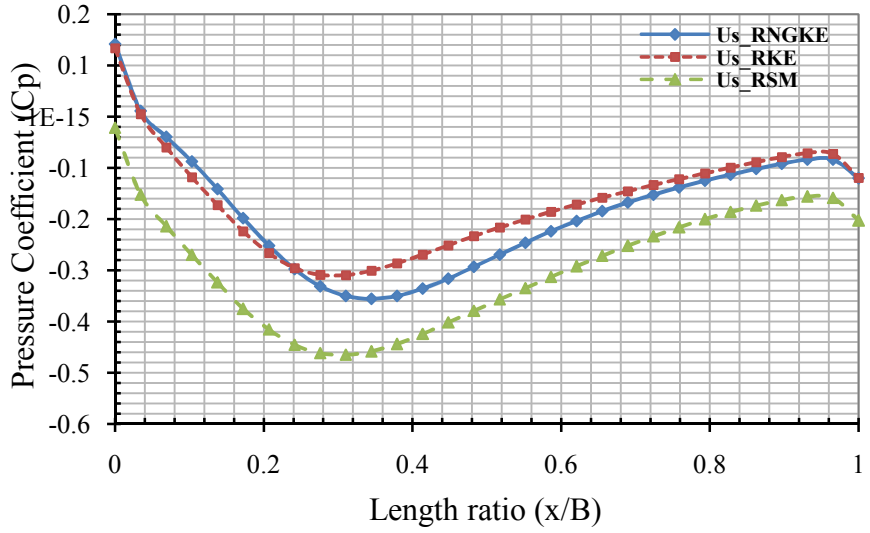

Figure 7.220 Pressure coefficients on the side outer face of the net clad scaffold at two-third height from the ground for Type A Net

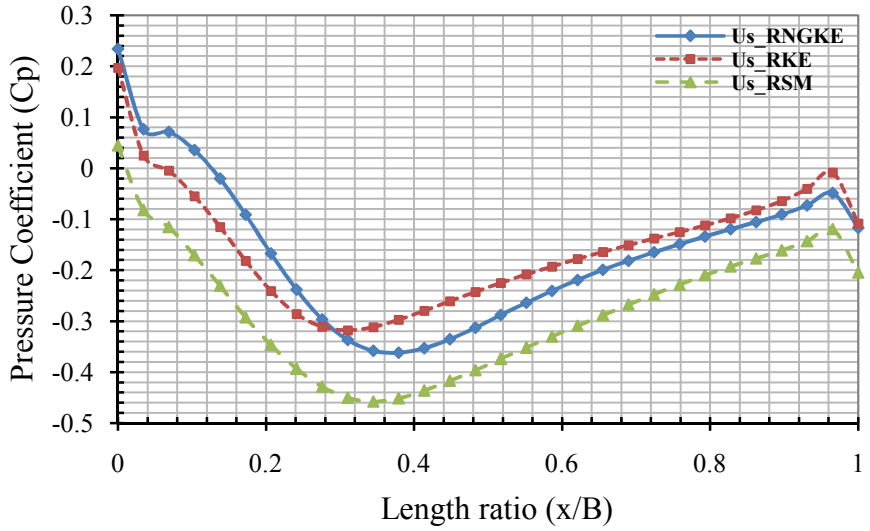

Figure 7.221 Pressure coefficients on the side inner face of the net clad scaffold at two-third height from the ground for Type A Net

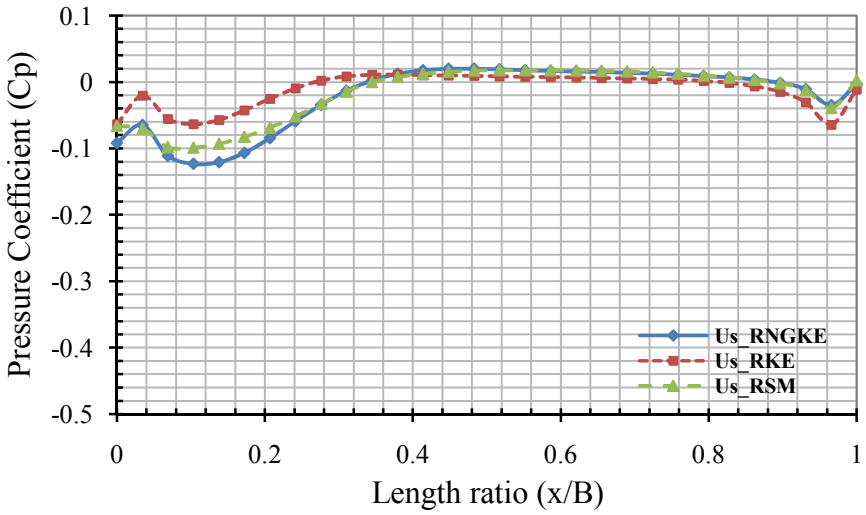

Figure 7.222 Difference of pressure coefficients of the side outer and inner face of the net clad scaffold at two-third height from ground for Type A Net

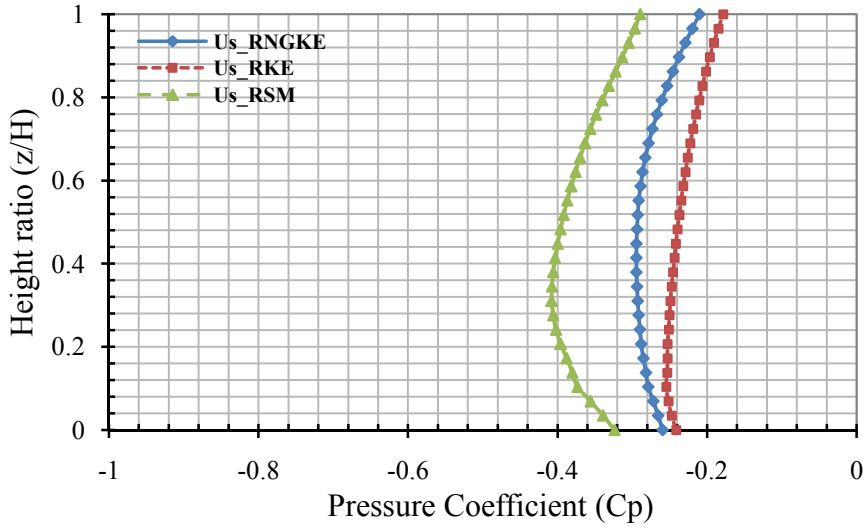

Figure 7.223 Pressure coefficients on the side outer vertical face at mid-length of the net clad scaffold for Type A Net

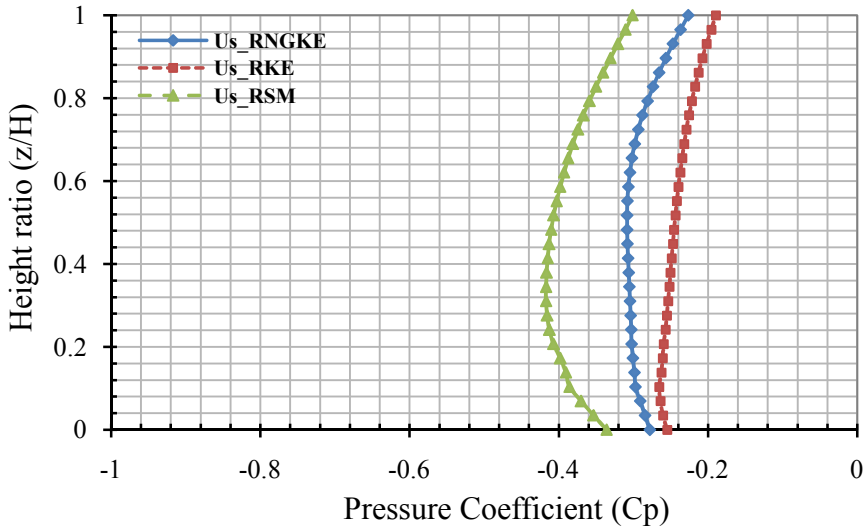

Figure 7.224 Pressure coefficients on the side inner vertical face at mid-length of the net clad scaffold for Type A Net

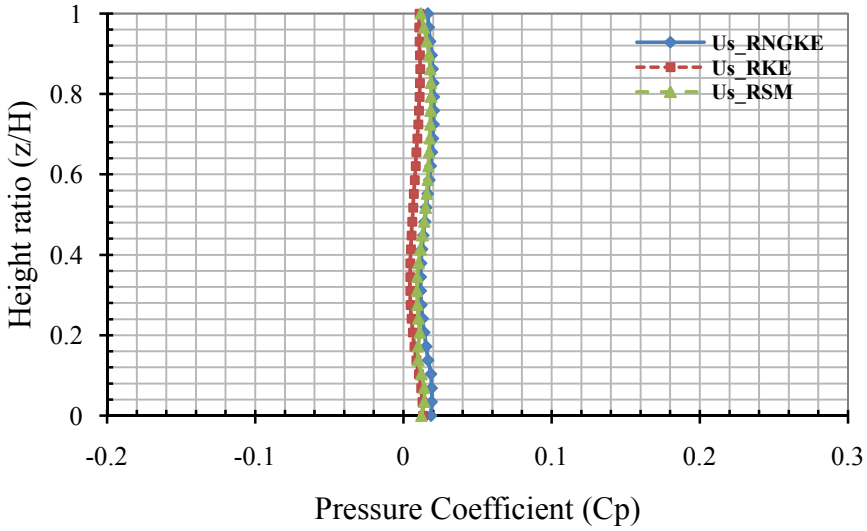

Figure 7.225 Difference of pressure coefficients of the side outer and inner vertical face at mid-length of the net clad scaffold for Type A Net

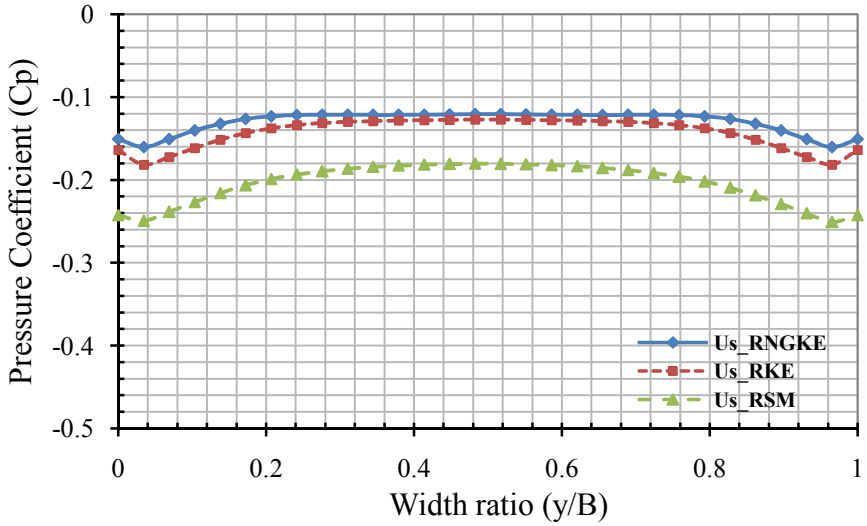

Figure 7.226 Pressure coefficients on the leeward outer face of the net clad scaffold at mid height from the ground for Type A Net

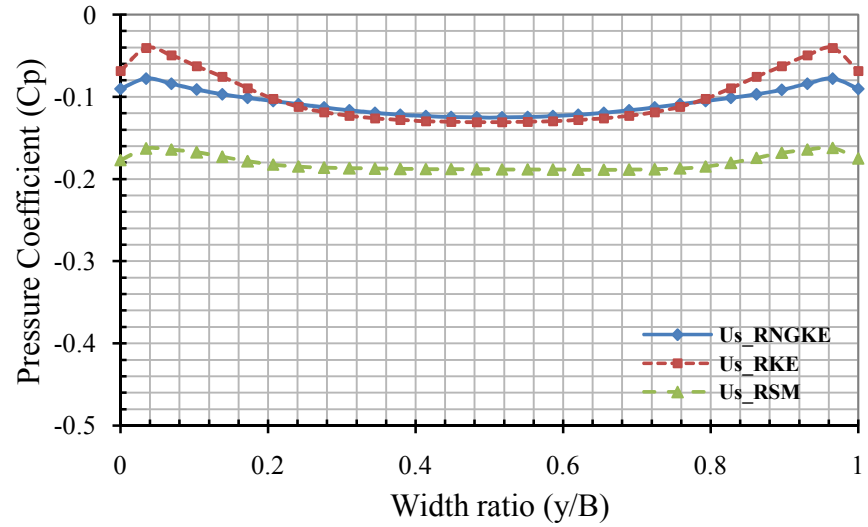

Figure 7.227 Pressure coefficients on the leeward inner face of the net clad scaffold at mid height from the ground for Type A Net

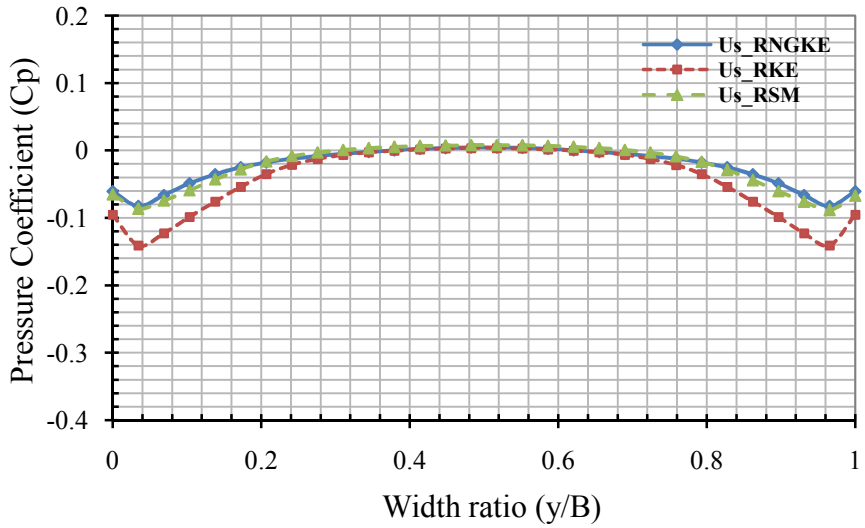

Figure 7.228 Difference of pressure coefficients of the leeward outer and inner face of the net clad scaffold at mid height from ground for Type A Net

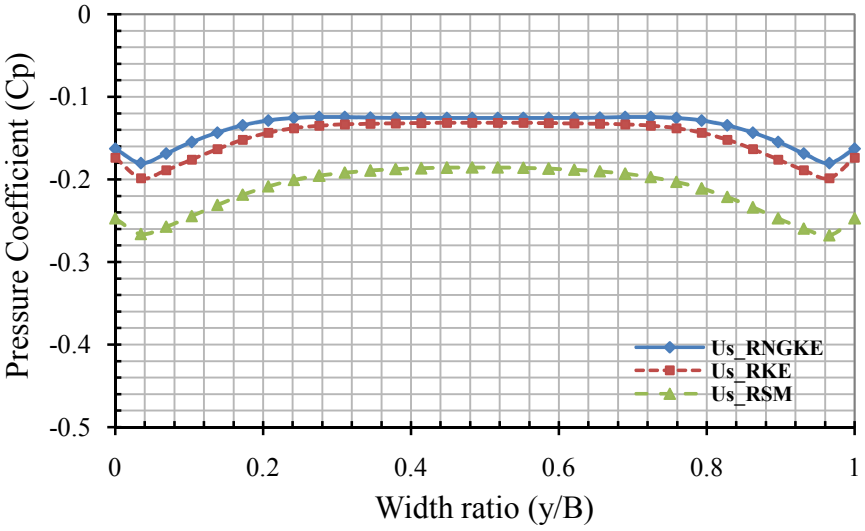

Figure 7.229 Pressure coefficients on the leeward outer face of the net clad scaffold at two-third height from the ground for Type A Net

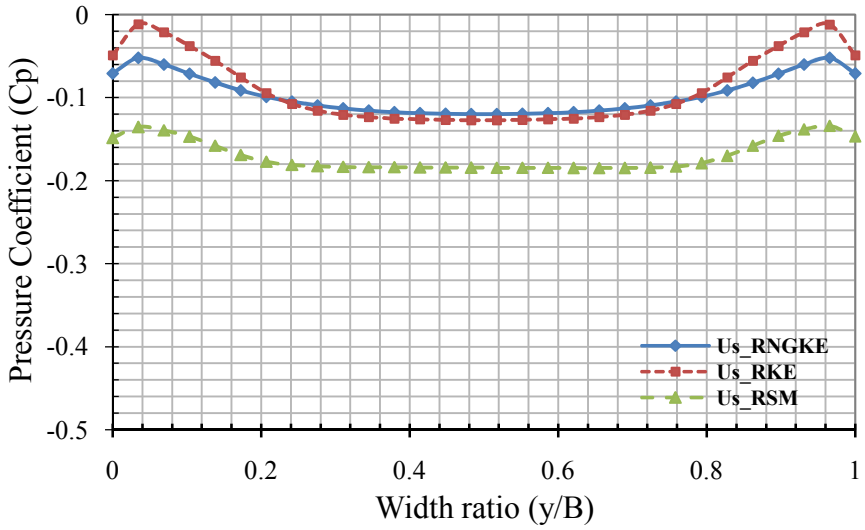

Figure 7.230 Pressure coefficients on the leeward inner face of the net clad scaffold at two-third height from the ground for Type A Net

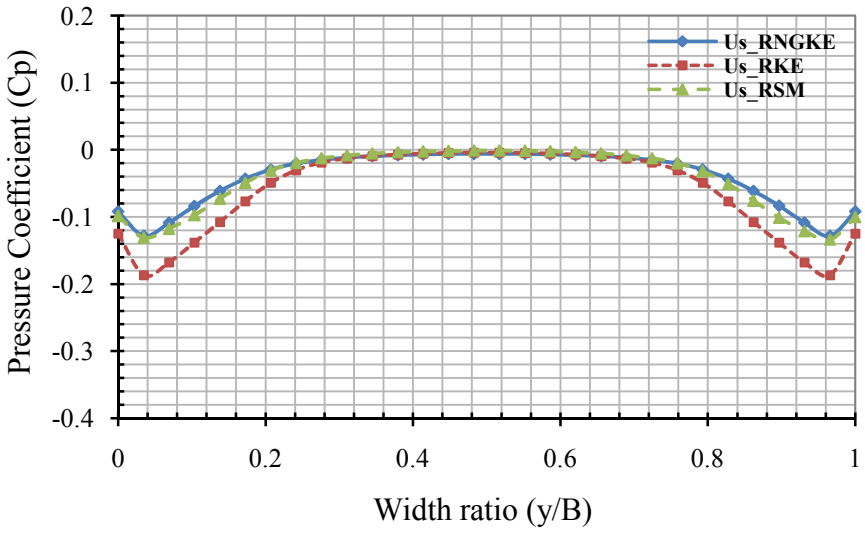

Figure 7.231 Difference of pressure coefficients of the leeward outer and inner face of the net clad scaffold at two-third height from ground for Type A Net

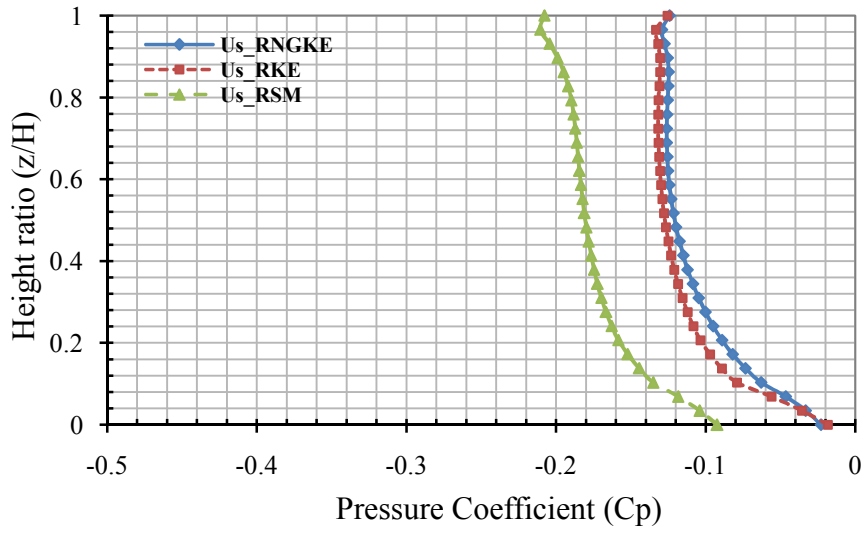

Figure 7.232 Pressure coefficients on the leeward outer vertical face at mid-width of the net clad scaffold for Type A Net

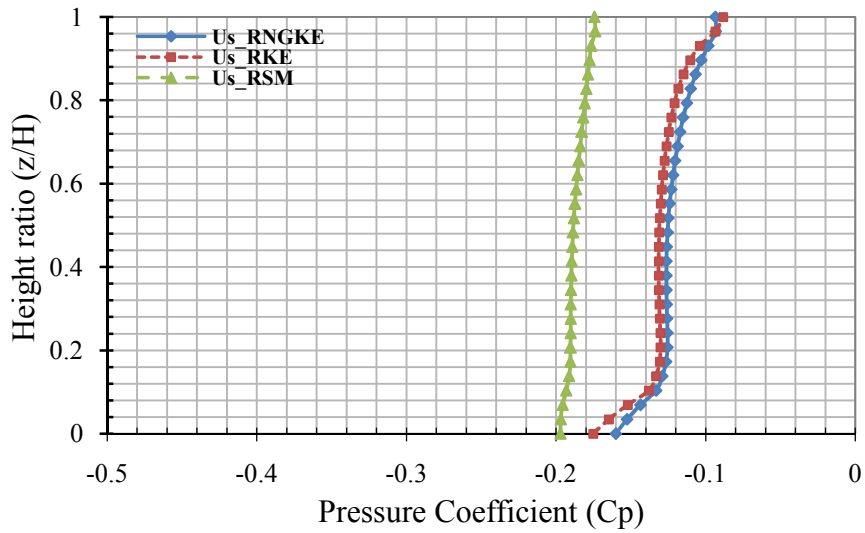

Figure 7.233 Pressure coefficients on the leeward inner vertical face at mid-width of the net clad scaffold for Type A Net

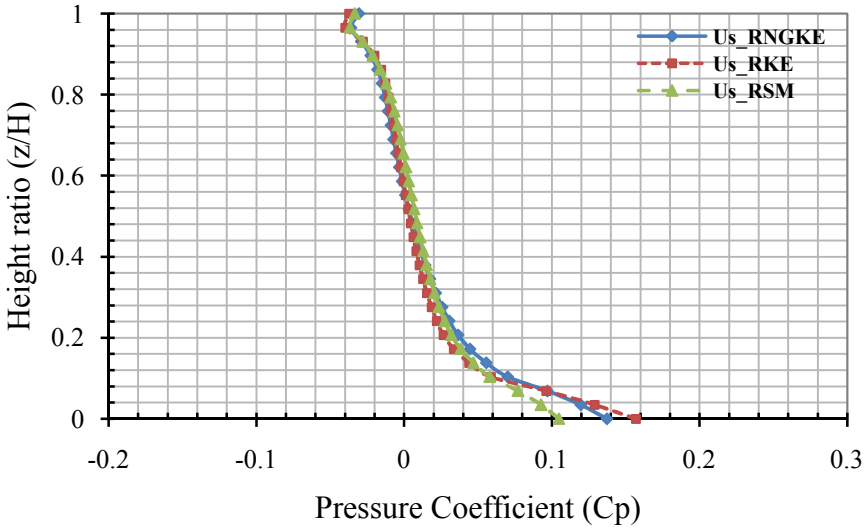

Figure 7.234 Difference of pressure coefficients of the leeward outer and inner vertical face at mid-width of the net clad scaffold for Type A Net

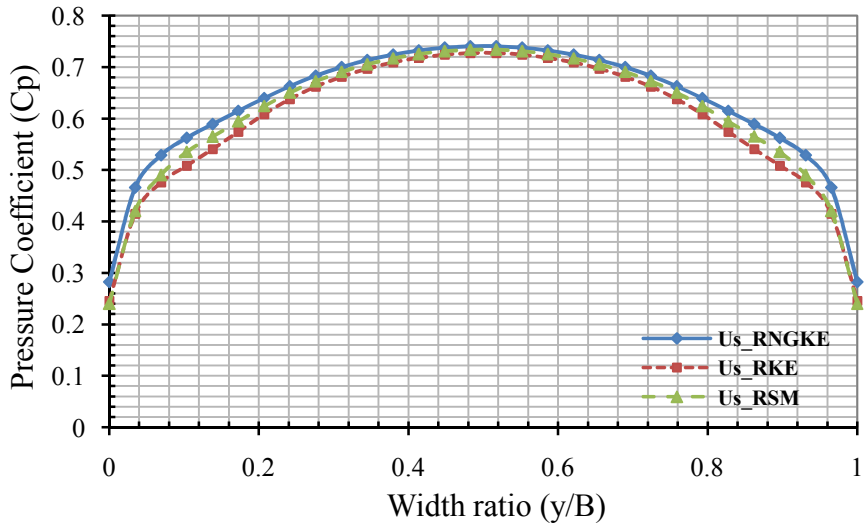

Figure 7.235 Pressure coefficients on the windward outer face of the net clad scaffold at mid height from the ground for Type B Net

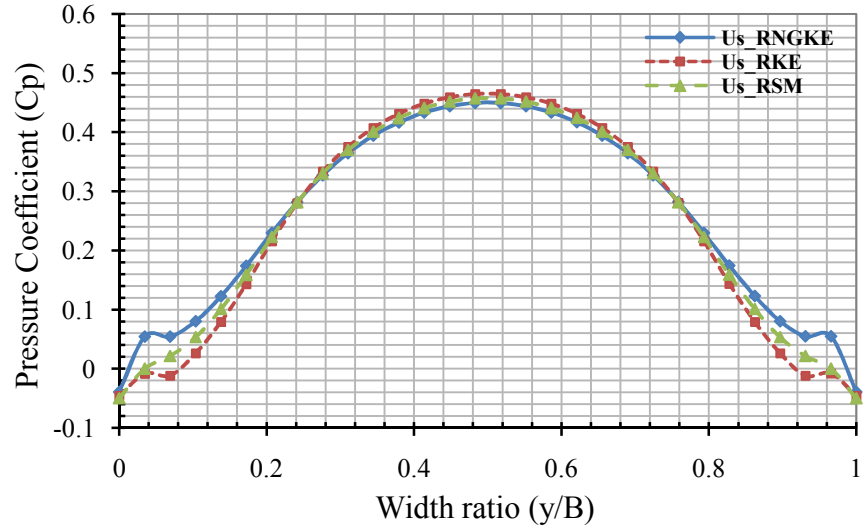

Figure 7.236 Pressure coefficients on the windward inner face of the net clad scaffold at mid height from the ground for Type B Net

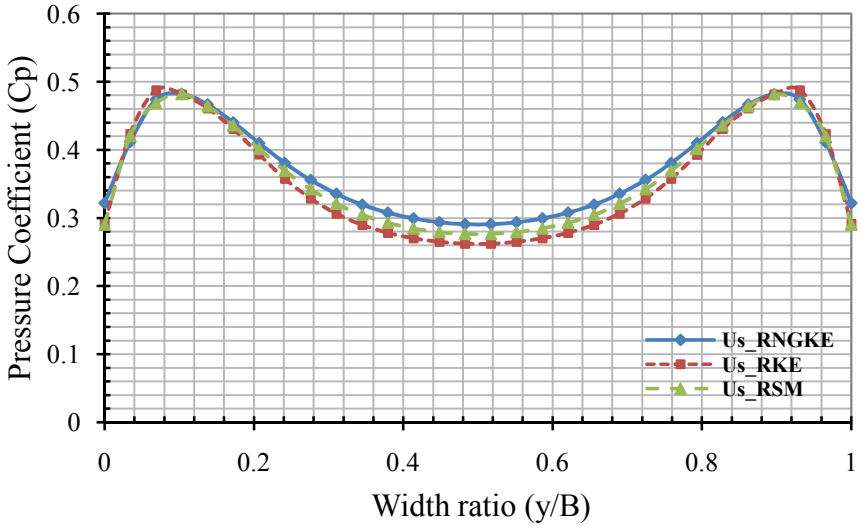

Figure 7.237 Difference of pressure coefficients of the windward outer and inner face of the net clad scaffold at mid height from ground for Type B Net

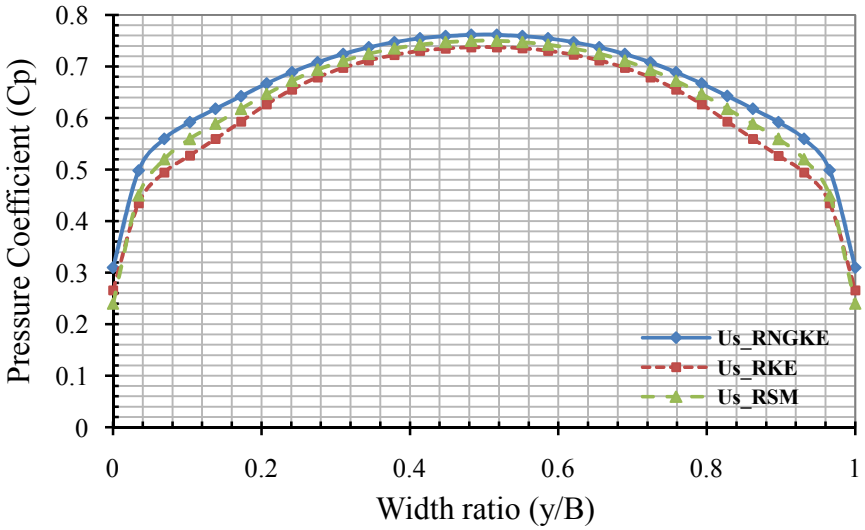

Figure 7.238 Pressure coefficients on the windward outer face of the net clad scaffold at two-third height from the ground for Type B Net

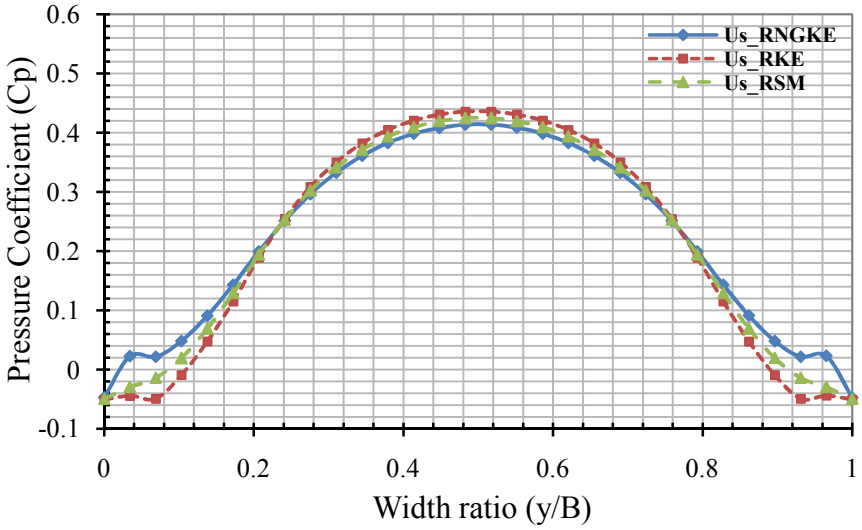

Figure 7.239 Pressure coefficients on the windward inner face of the net clad scaffold at two-third height from the ground for Type B Net

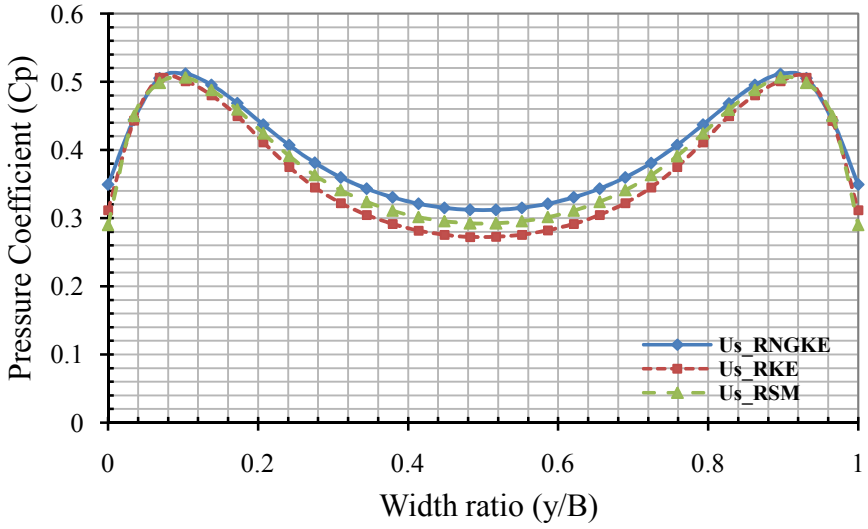

Figure 7.240 Difference of pressure coefficients of the windward outer and inner face of the net clad scaffold at two-third height from the ground for Type B Net

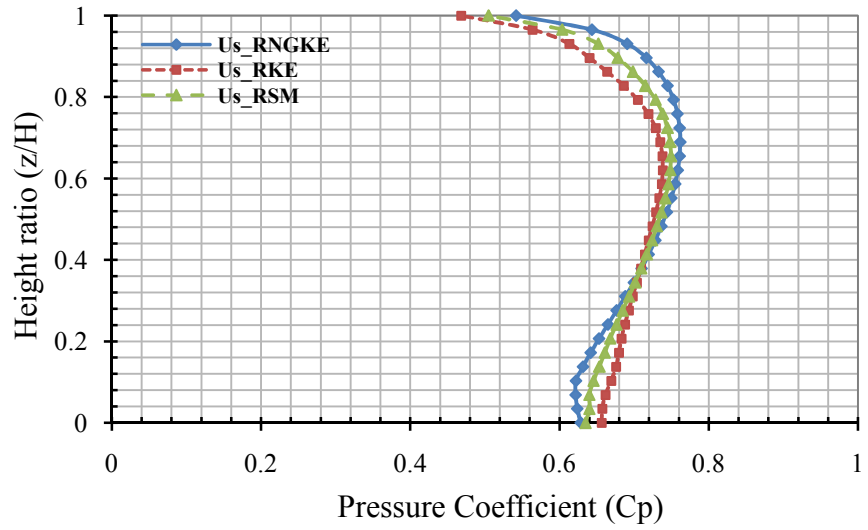

Figure 7.241 Pressure coefficients on the windward outer vertical face at mid-width of the net clad scaffold for Type B Net

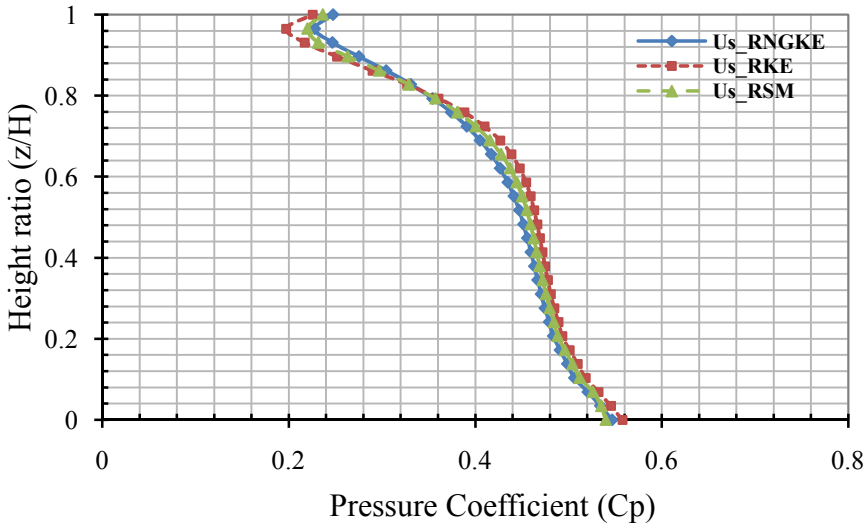

Figure 7.242 Pressure coefficients on the windward inner vertical face at mid-width of the net clad scaffold for Type B Net

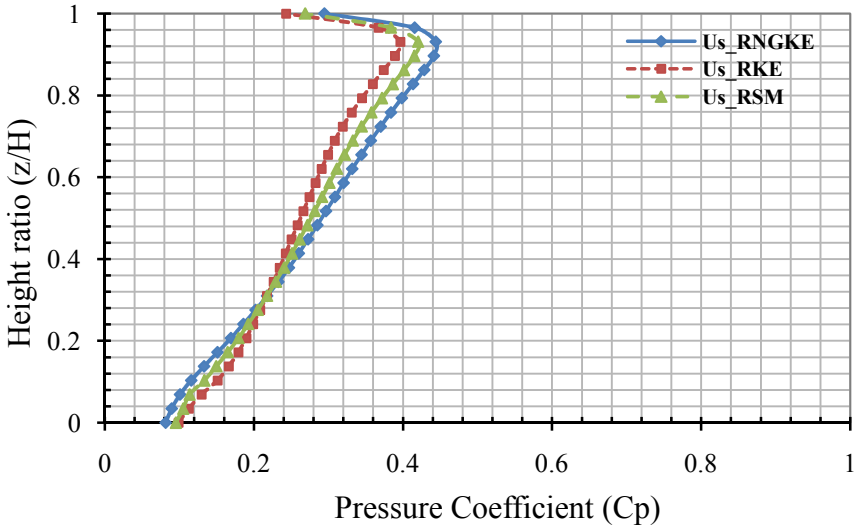

Figure 7.243 Difference of pressure coefficients of the windward outer and inner vertical face (mid of width) of the net clad scaffold for Type B Net

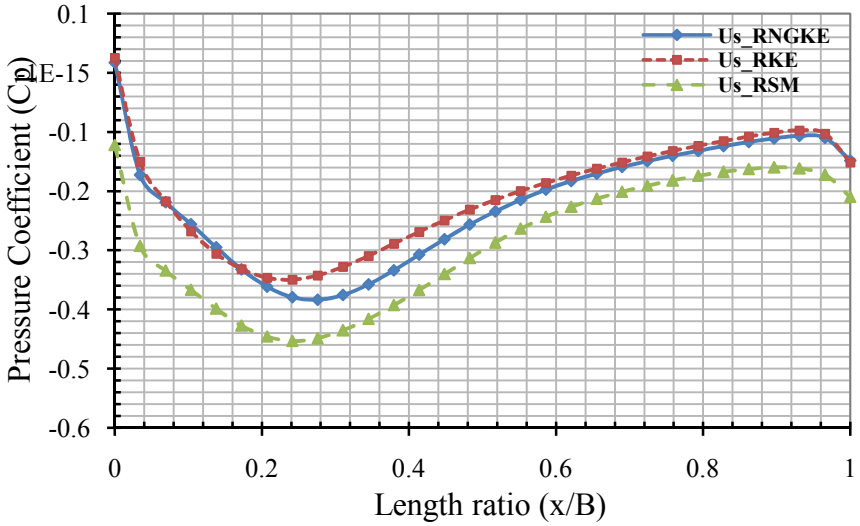

Figure 7.244 Pressure coefficient on the side outer face of the net clad scaffold at mid height from the ground for Type B Net

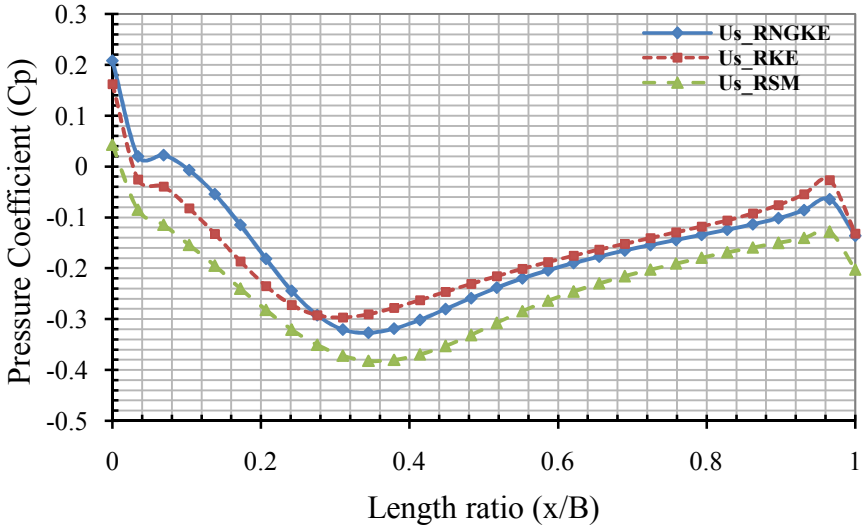

Figure 7.245 Pressure coefficient on the side inner face of the net clad scaffold at mid height from the ground for Type B Net

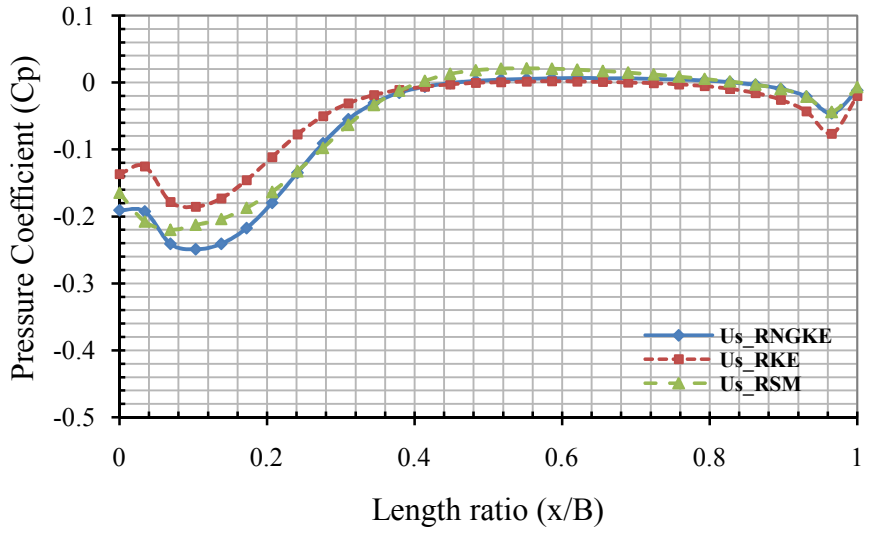

Figure 7.246 Difference of pressure coefficients of the side outer and inner face of the net clad scaffold at mid height from the ground for Type B Net

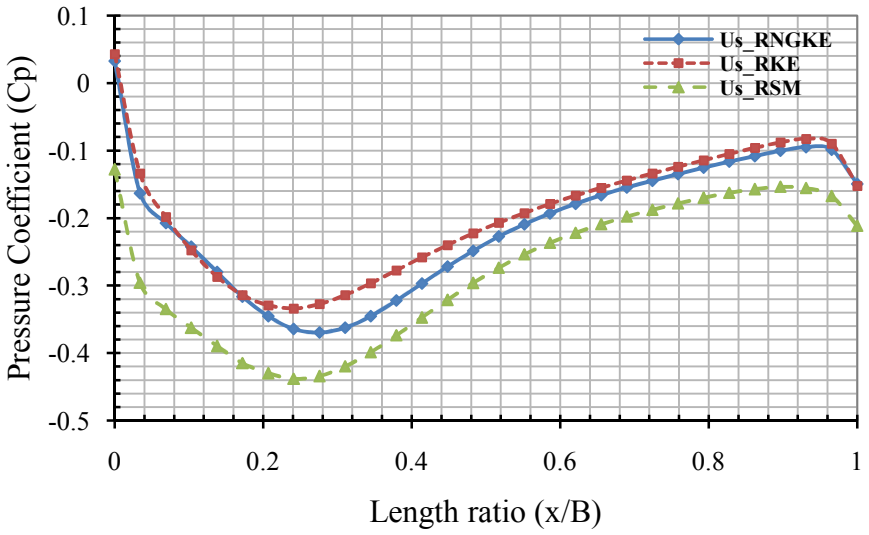

Figure 7.247 Pressure coefficient on the side outer face of the net clad scaffold at two-third height from the ground for Type B Net

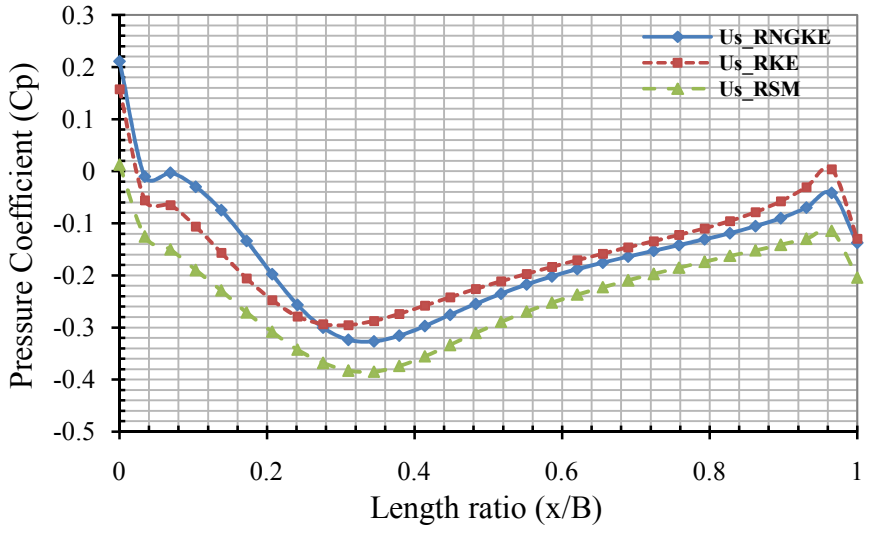

Figure 7.248 Pressure coefficient on the side inner face of the net clad scaffold at two-third height from the ground for Type B Net

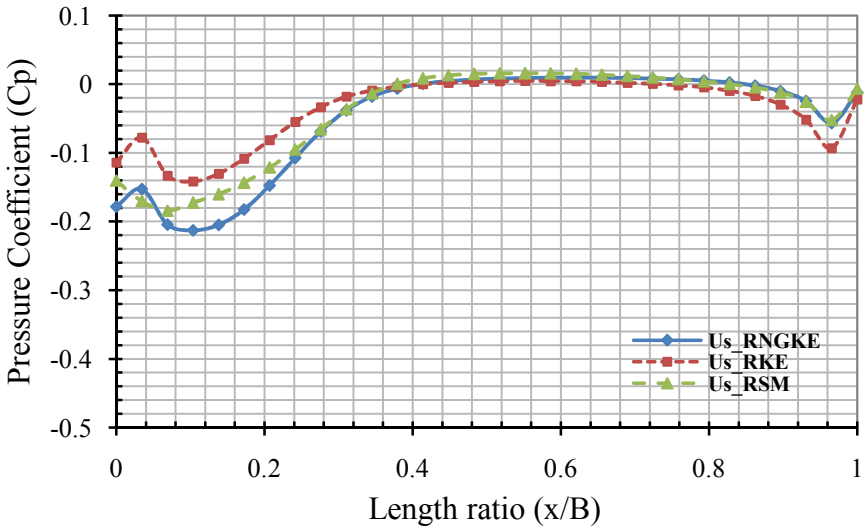

Figure 7.249 Difference of pressure coefficients of the side outer and inner face of the net clad scaffold at two-third height from the ground for Type B Net

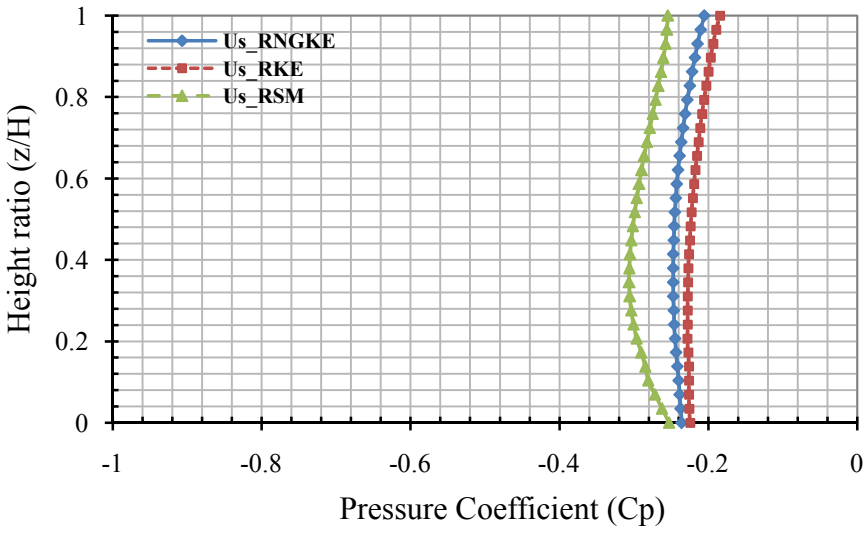

Figure 7.250 Pressure coefficients on the side outer vertical face at mid-length of the net clad scaffold for Type B Net

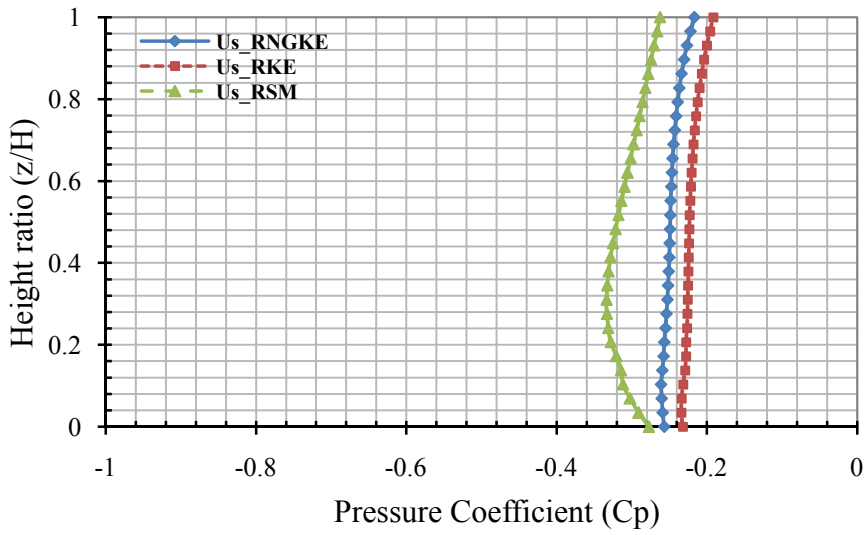

Figure 7.251 Pressure coefficients on the side inner vertical face at mid-length of the net clad scaffold for Type B Net

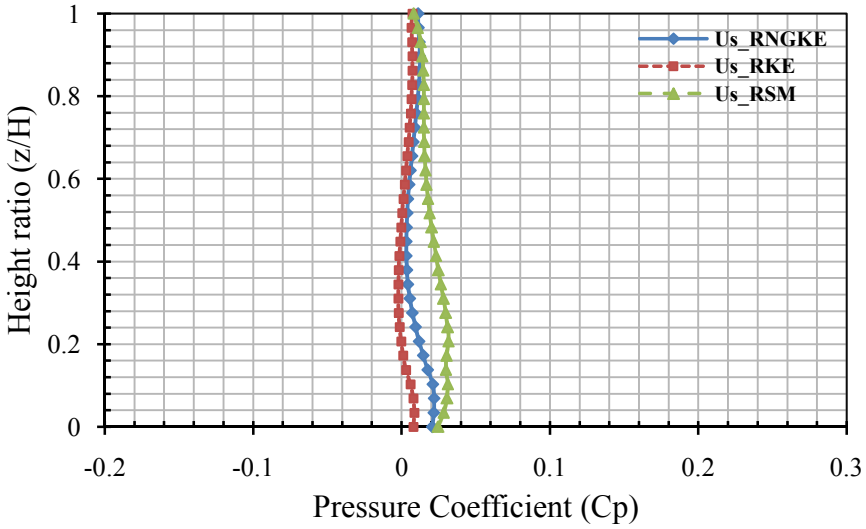

Figure 7.252 Difference of pressure coefficients of the side inner and outer vertical face at mid-length of the net clad scaffold for Type B Net

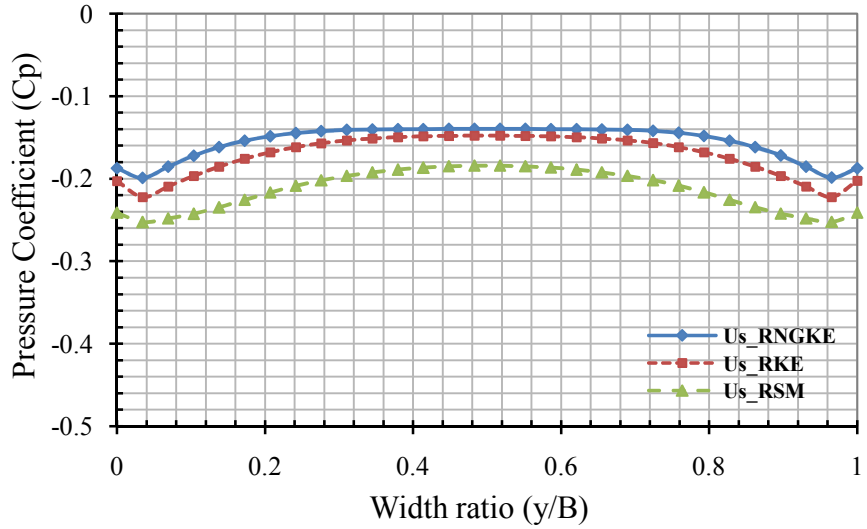

Figure 7.253 Pressure coefficients on the leeward outer face of the net clad scaffold at mid height from the ground for Type B Net

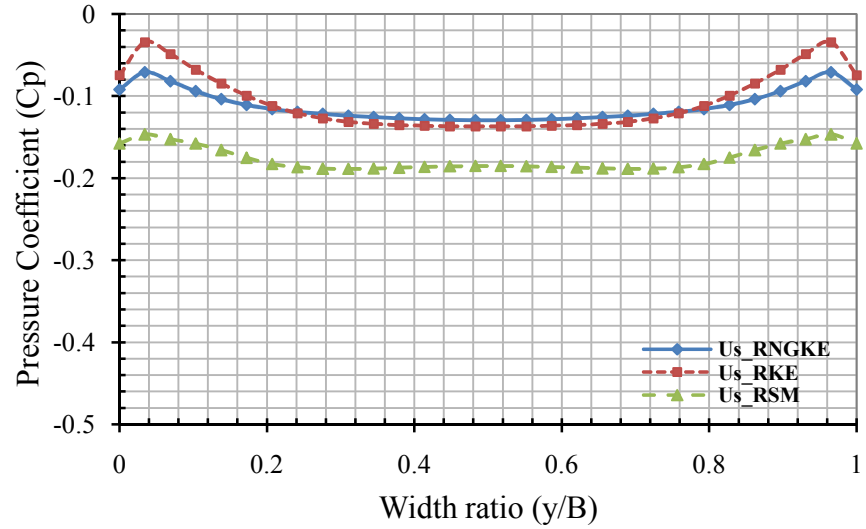

Figure 7.254 Pressure coefficients on the leeward inner face of the net clad scaffold at mid height from the ground for Type B Net

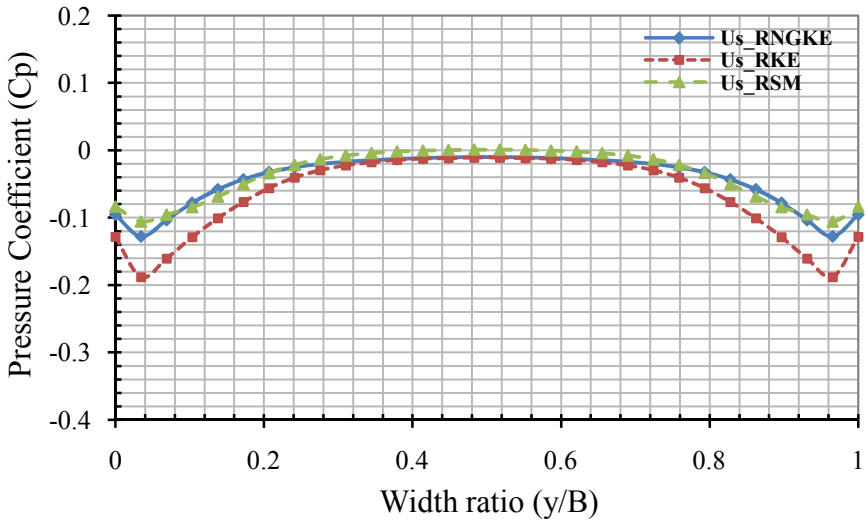

Figure 7.255 Difference of pressure coefficients of the leeward outer and inner face of the net clad scaffold at mid height from ground for Type B Net

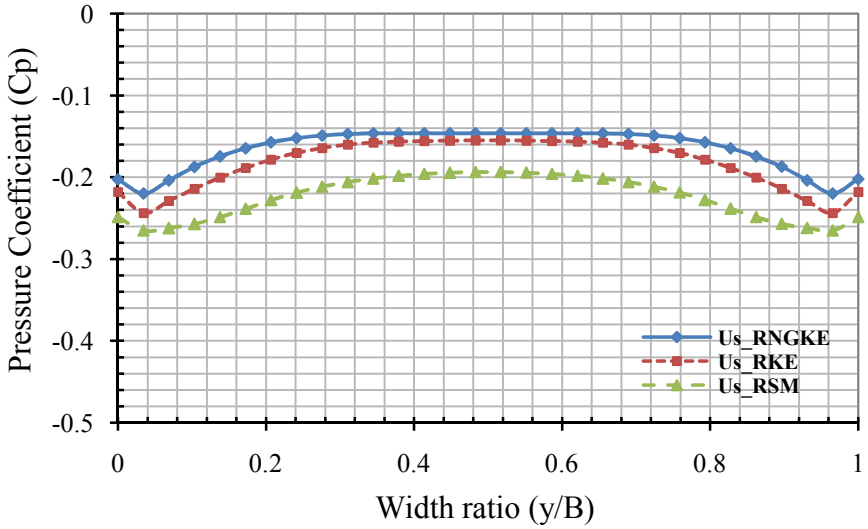

Figure 7.256 Pressure coefficients on the leeward outer face of the net clad scaffold at two-third height from the ground for Type B Net

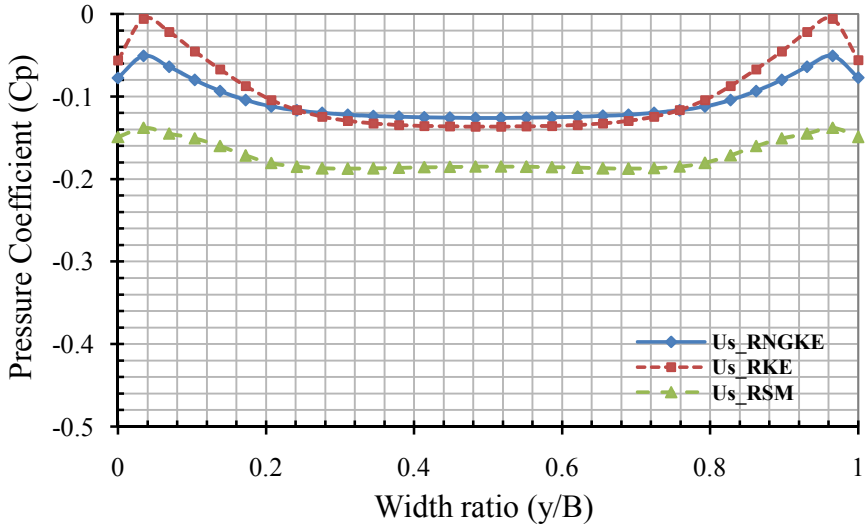

Figure 7.257 Pressure coefficients on the leeward inner face of the net clad scaffold at two-third height from the ground for Type B Net

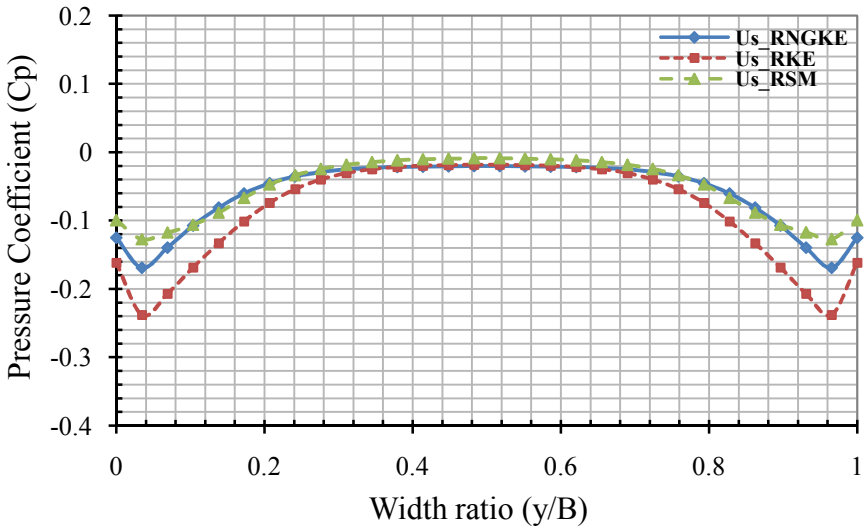

Figure 7.258 Difference of pressure coefficients of the leeward outer and inner face of the net clad scaffold at two-third height from the ground for Type B Net

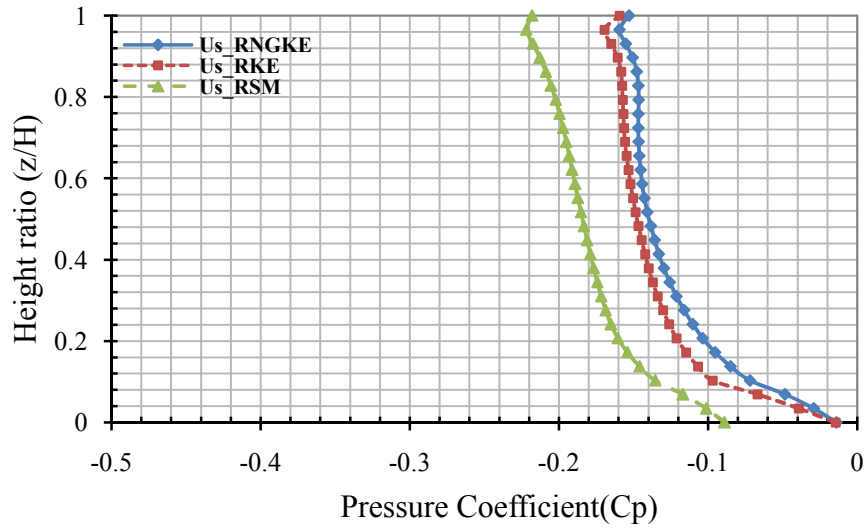

Figure 7.259 Pressure coefficients on the leeward outer vertical face at mid-width of the net clad scaffold for Type B Net

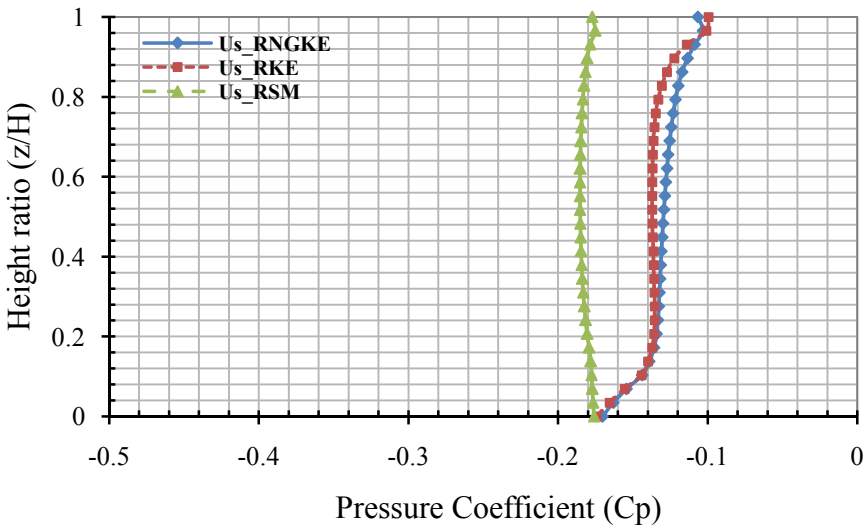

Figure 7.260 Pressure coefficients on the leeward inner vertical face at mid-width of the net clad scaffold for Type B Net

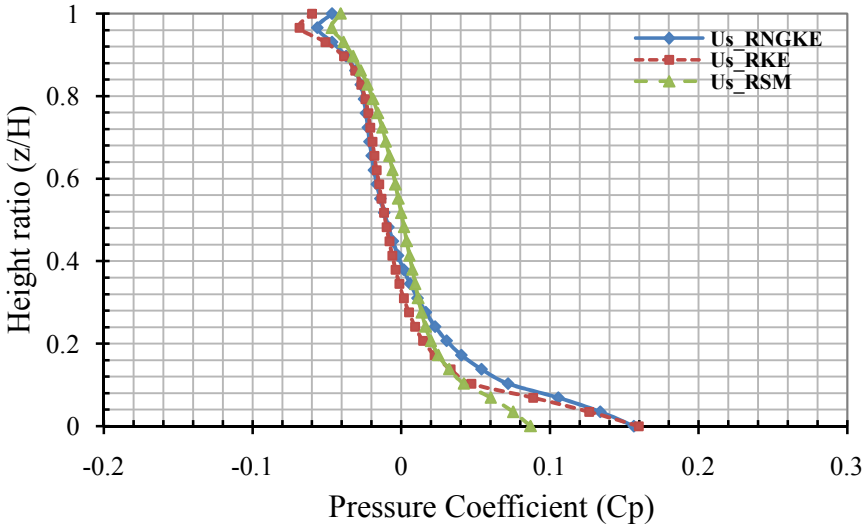

Figure 7.261 Difference of pressure coefficients of the leeward outer and inner vertical face at mid-width of the net clad scaffold for Type B Net

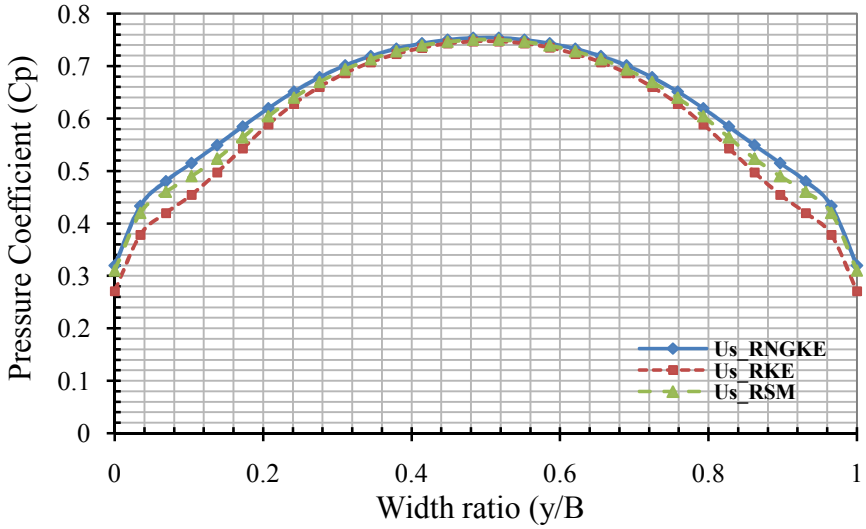

Figure 7.262 Pressure coefficients on the windward outer face of the elevated net clad scaffold at mid height from the ground for Type A Net

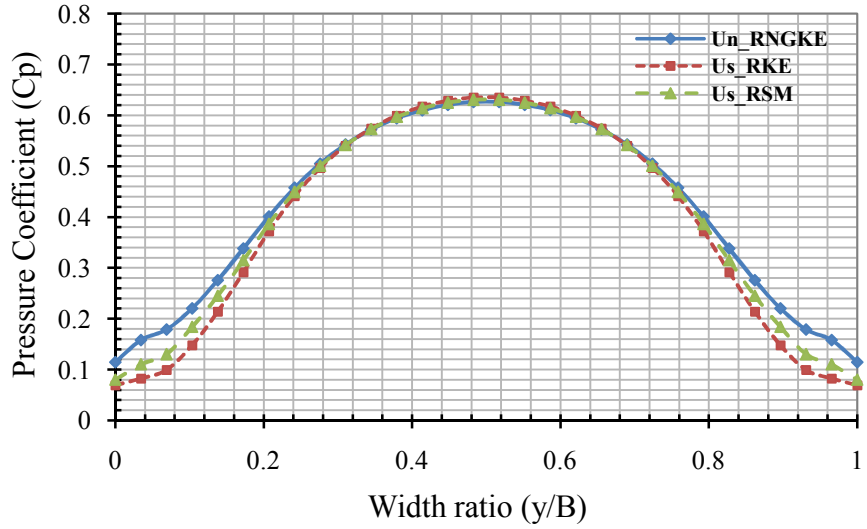

Figure 7.263 Pressure coefficients on the windward inner face of the elevated net clad scaffold at mid height from the ground for Type A Net

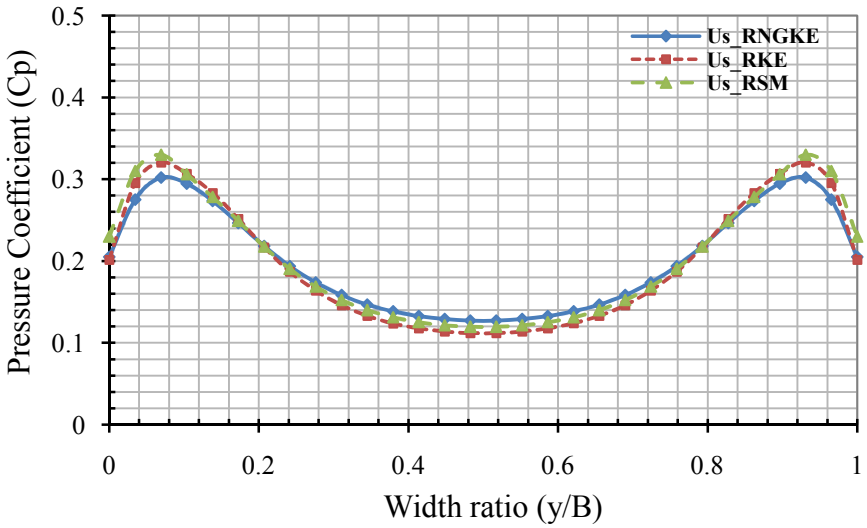

Figure 7.264 Difference of pressure coefficients of the windward outer and inner face of the elevated net clad scaffold at mid height from the ground for Type A Net

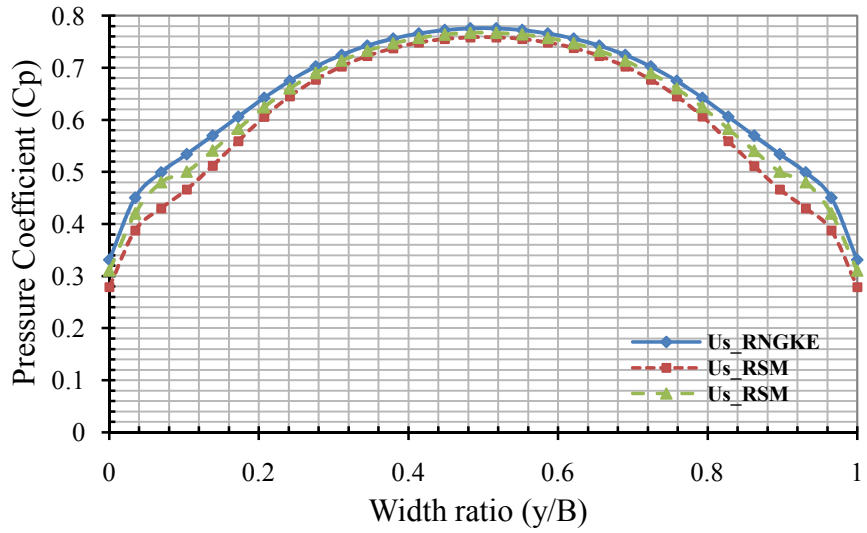

Figure 7.265 Pressure coefficients on the windward outer face of the elevated net clad scaffold at two-third height from the ground for Type A Net

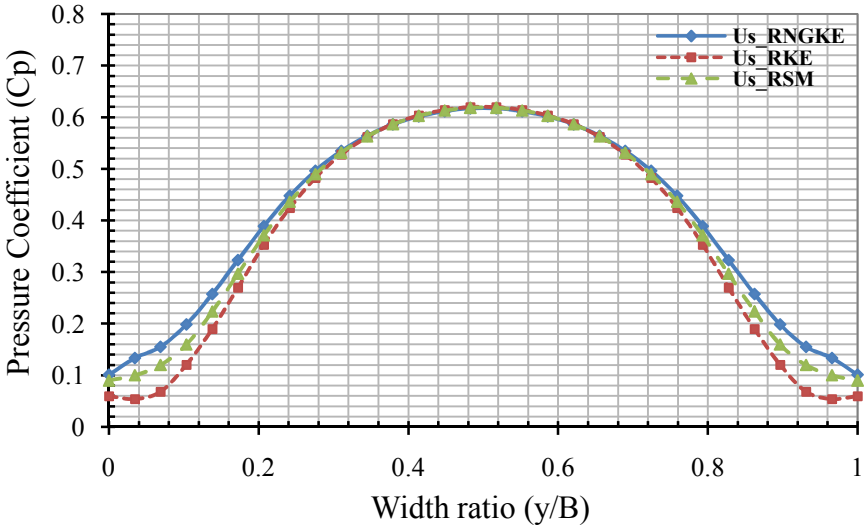

Figure 7.266 Pressure coefficients on the windward inner face of the elevated net clad scaffold at two-third height from the ground for Type A Net

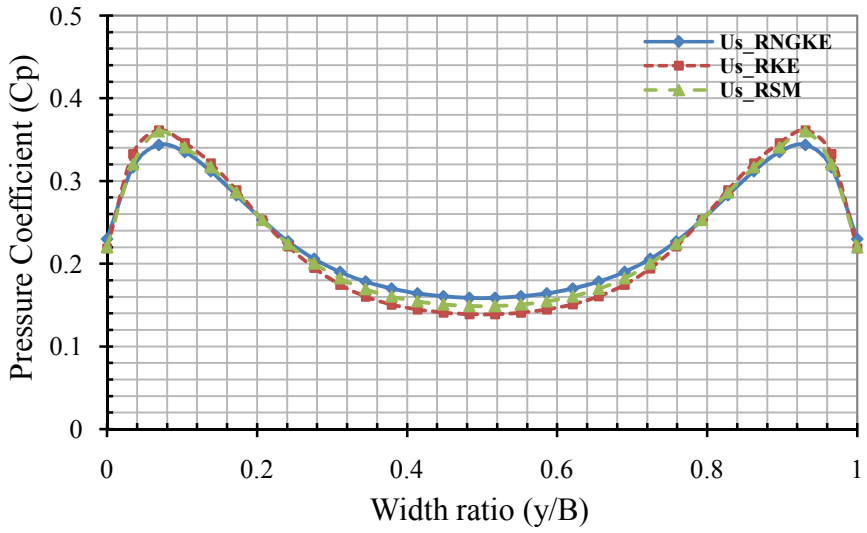

Figure 7.267 Difference of pressure coefficients of the windward outer and inner face of the elevated net clad scaffold at two-third height from ground for Type A Net

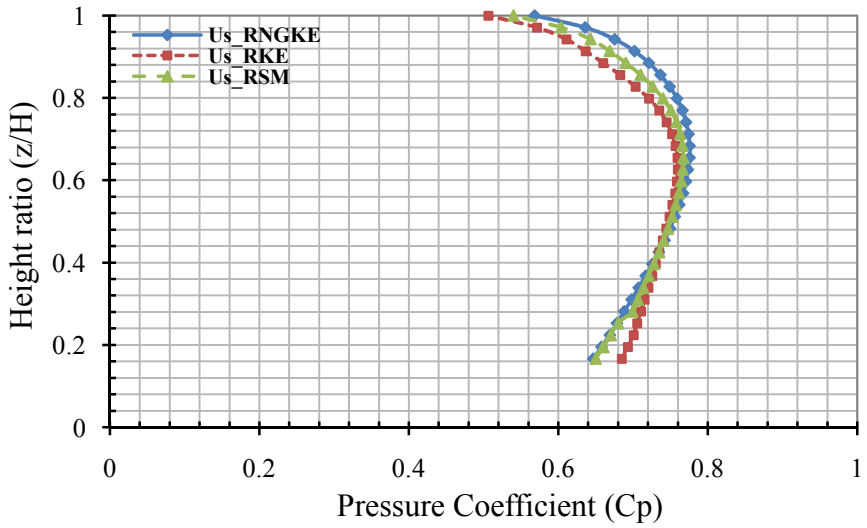

Figure 7.268 Pressure coefficients on the windward outer vertical face at mid-width of the elevated net clad scaffold for Type A Net

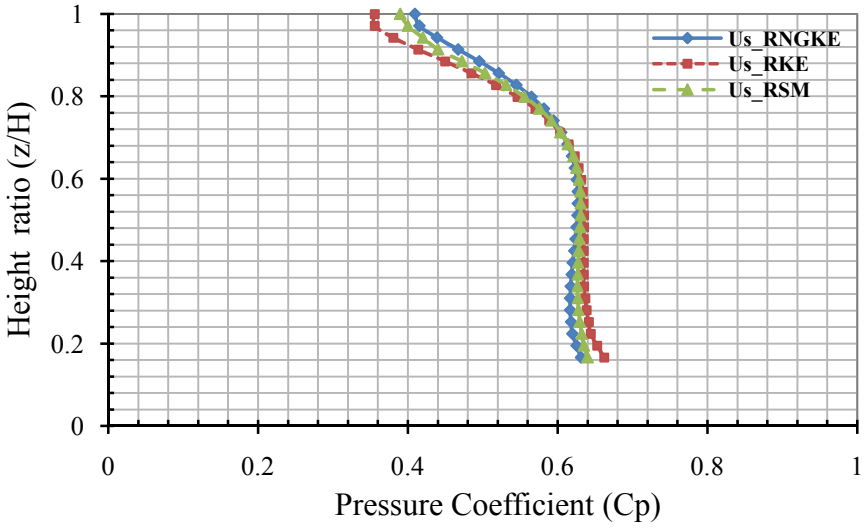

Figure 7.269 Pressure coefficients on the windward inner vertical face at mid-width of the elevated net clad scaffold for Type A Net

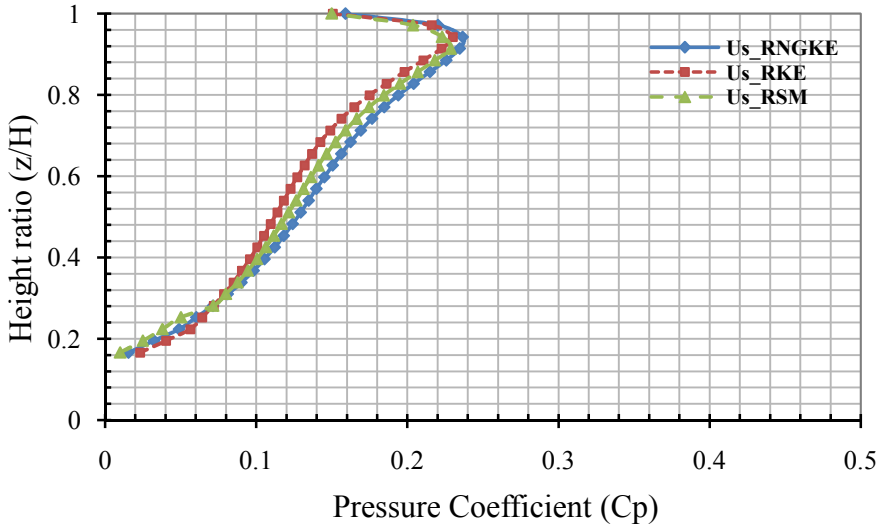

Figure 7.270 Difference of pressure coefficients of the windward outer and inner vertical face at mid-width of the elevated net clad scaffold for Type A Net

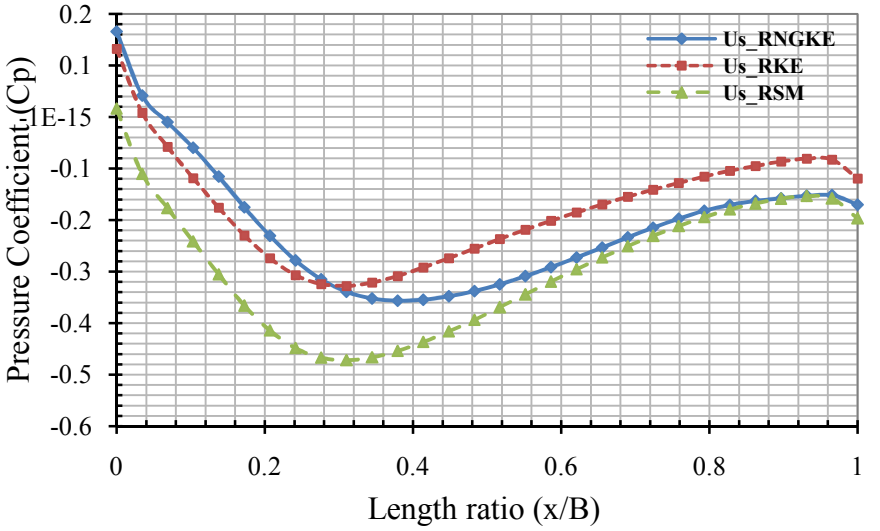

Figure 7.271 Pressure coefficients on the side outer face of the elevated net clad scaffold at mid height from the ground for Type A Net

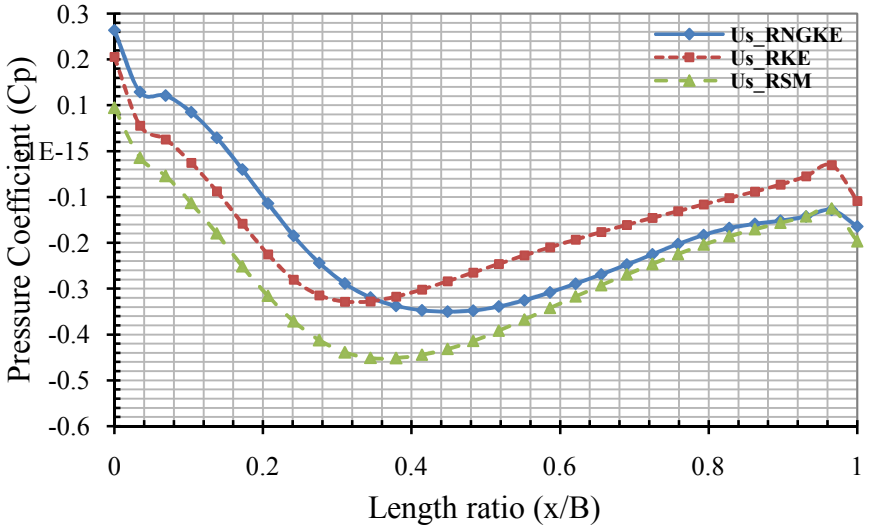

Figure 7.272 Pressure coefficients on the side inner face of the elevated net clad scaffold at mid height from the ground for Type A Net

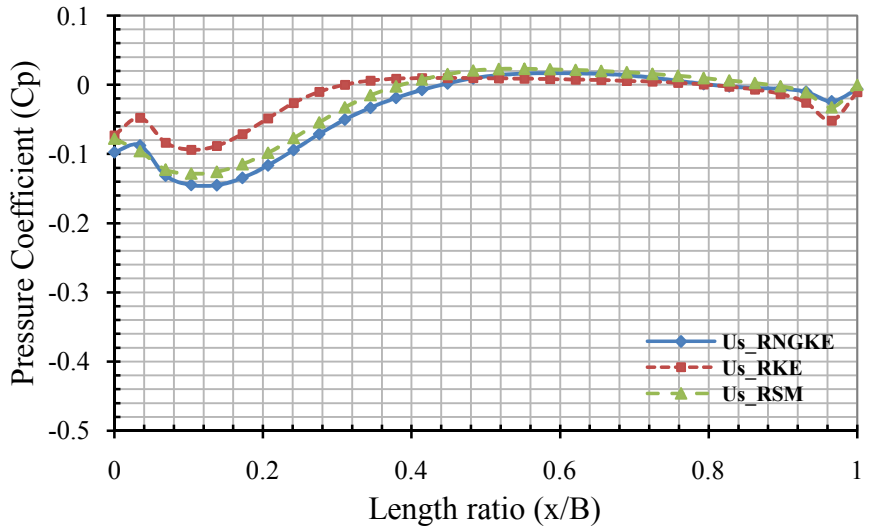

Figure 7.273 Difference of pressure coefficients of the side outer and inner face of the elevated net clad scaffold at mid height from ground for Type A Net

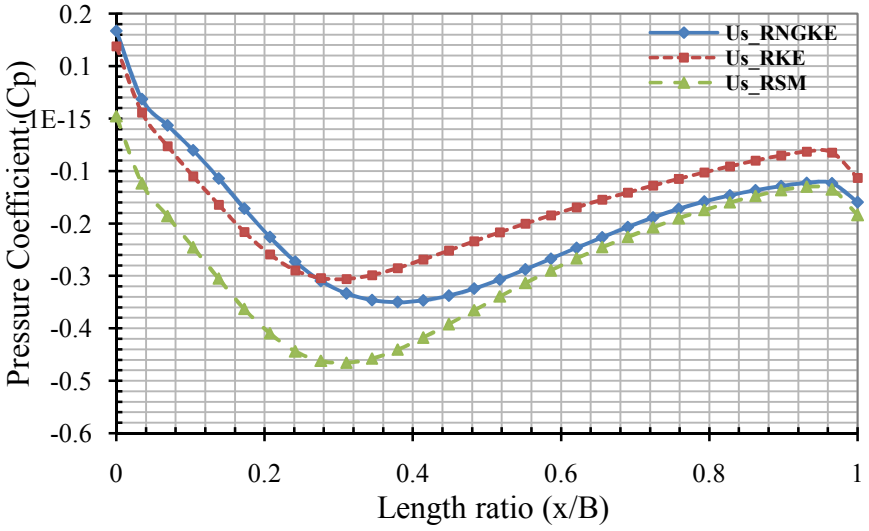

Figure 7.274 Pressure coefficients on the side outer face of the elevated net clad scaffold at two-third height from the ground for Type A Net

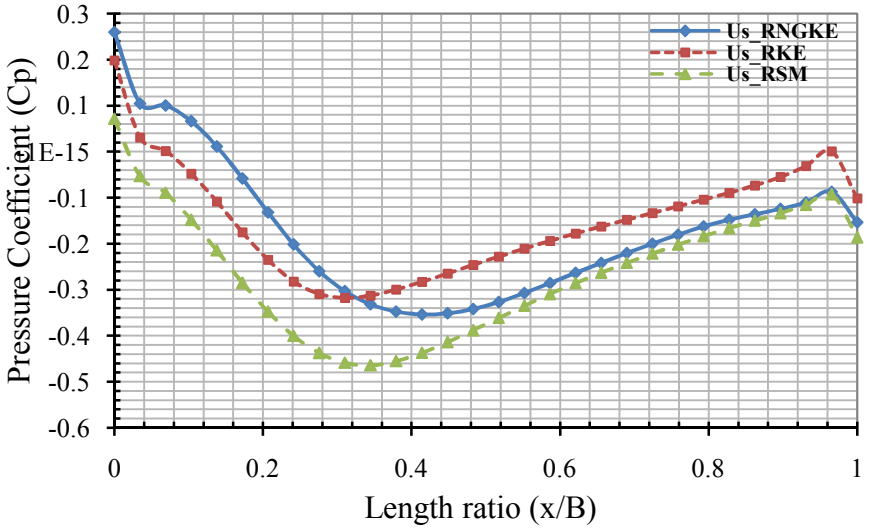

Figure 7.275 Pressure coefficients on the side inner face of the elevated net clad scaffold at two-third height from the ground for Type A Net

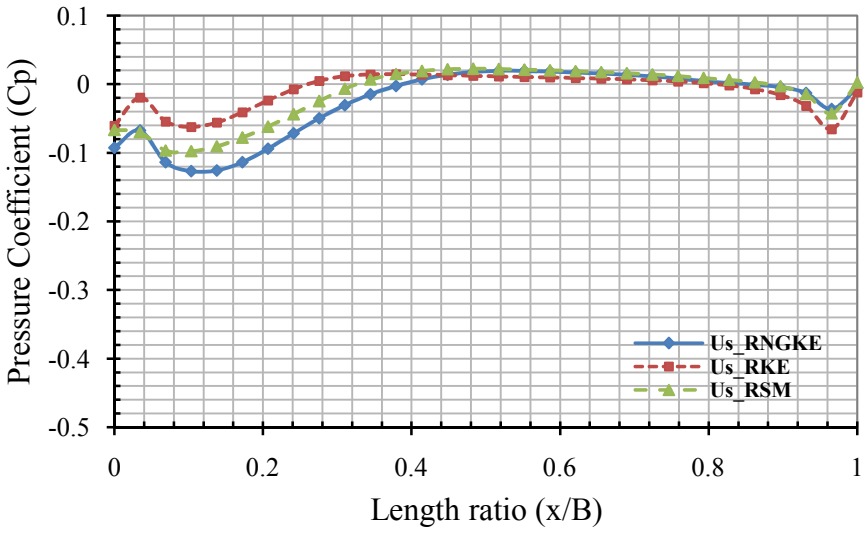

Figure 7.276 Difference of pressure coefficients of the side outer and inner face of the elevated net clad scaffold at two-third height from ground for Type A Net

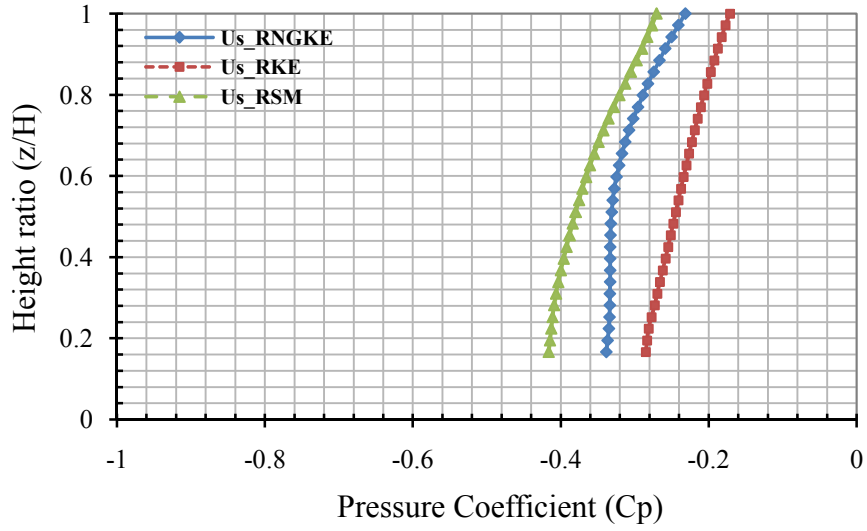

Figure 7.277 Pressure coefficients on the side outer vertical face at mid-length of the elevated net clad scaffold for Type A Net

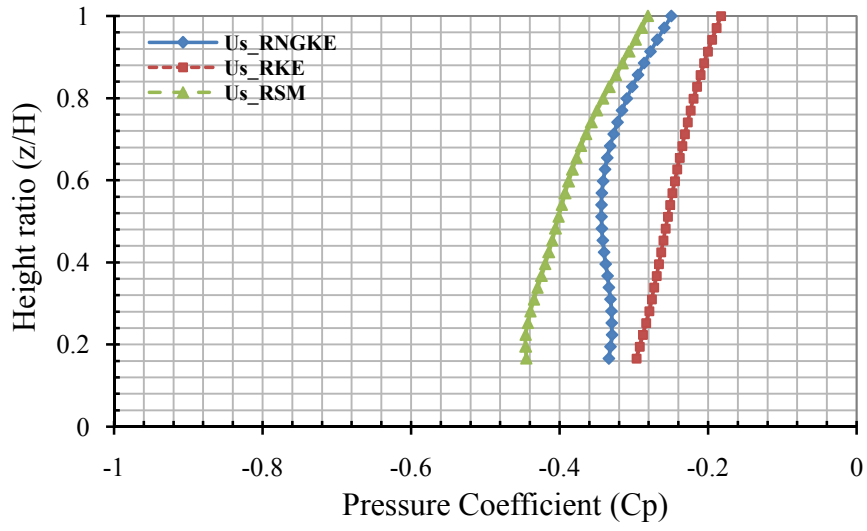

Figure 7.278 Pressure coefficients on the side inner vertical face at mid-length of the elevated net clad scaffold for Type A Net

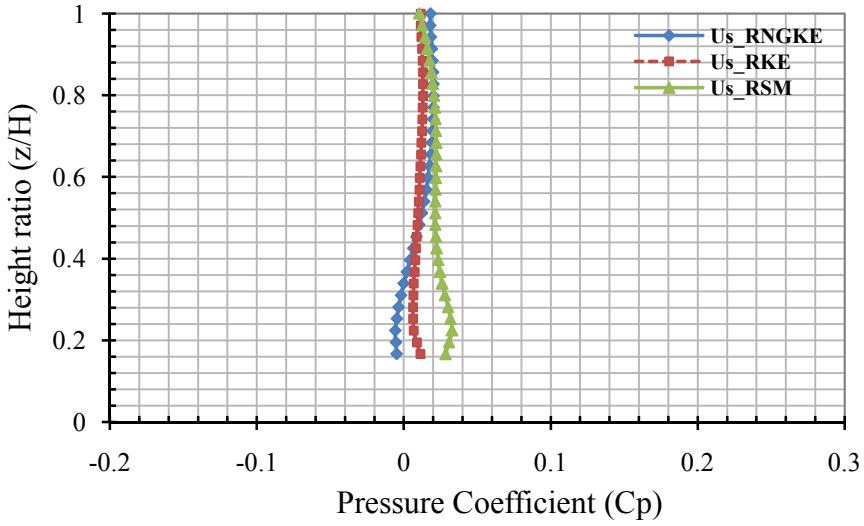

Figure 7.279 Difference of pressure coefficients on the side outer and inner vertical face at mid-length of the elevated net clad scaffold for Type A Net

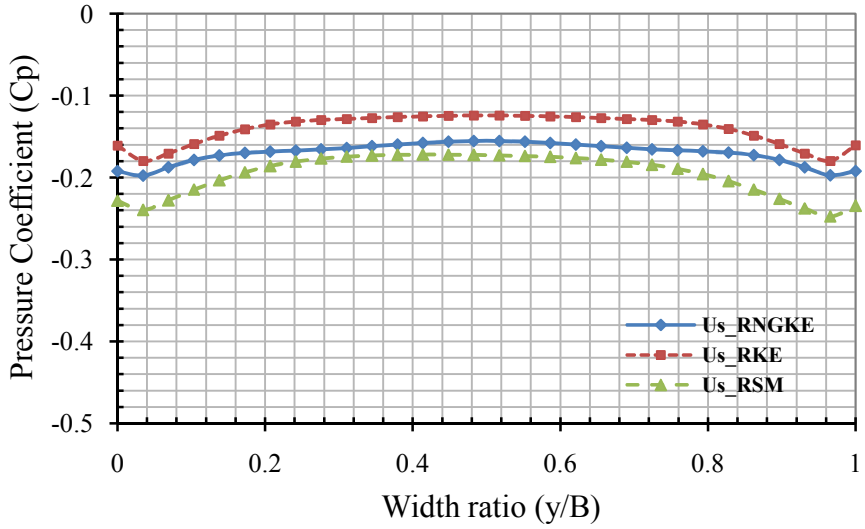

Figure 7.280 Pressure coefficients on the leeward outer face of the elevated net clad scaffold at mid height from the ground for Type A Net

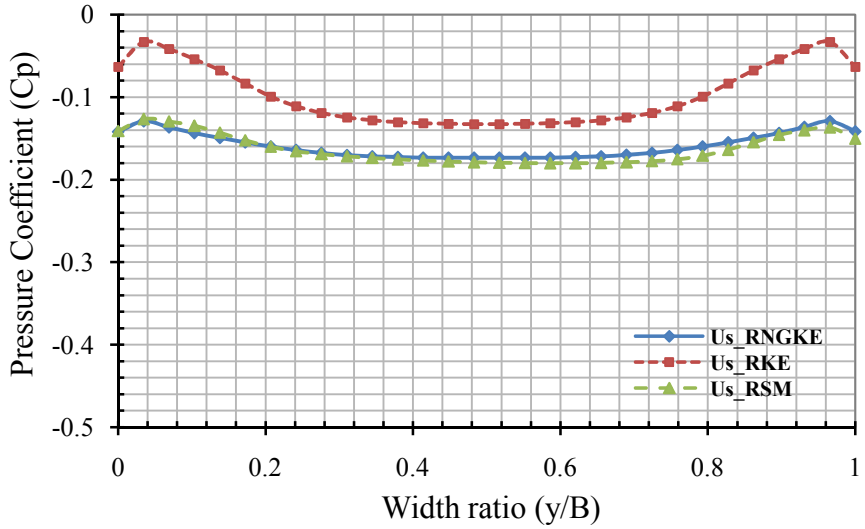

Figure 7.281 Pressure coefficients on the leeward inner face of the elevated net clad scaffold at mid height from the ground for Type A Net

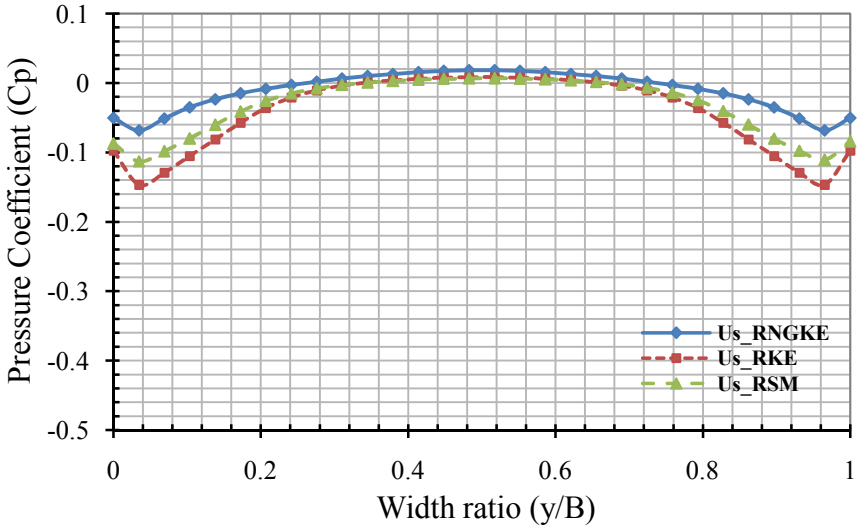

Figure 7.282 Difference of pressure coefficients of the leeward outer and inner face of the elevated net clad scaffold at mid height from ground for Type A Net

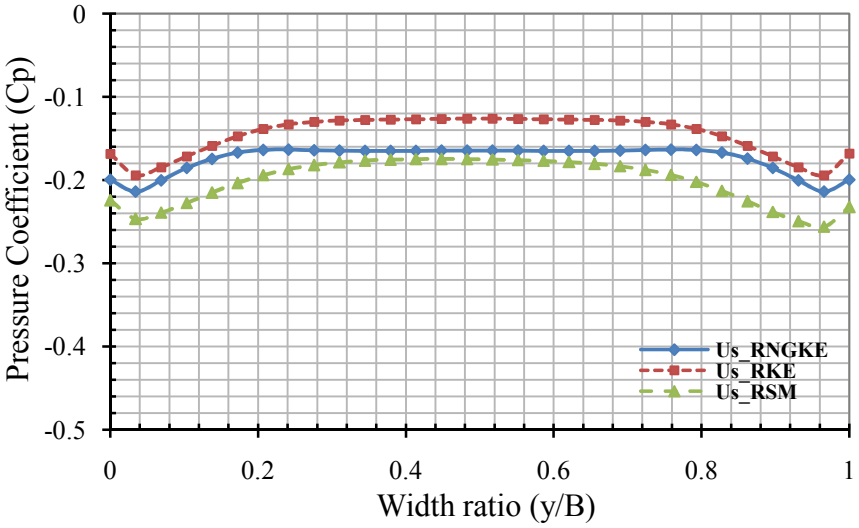

Figure 7.283 Pressure coefficients on the leeward outer face of the elevated net clad scaffold at two-third height from the ground for Type A Net

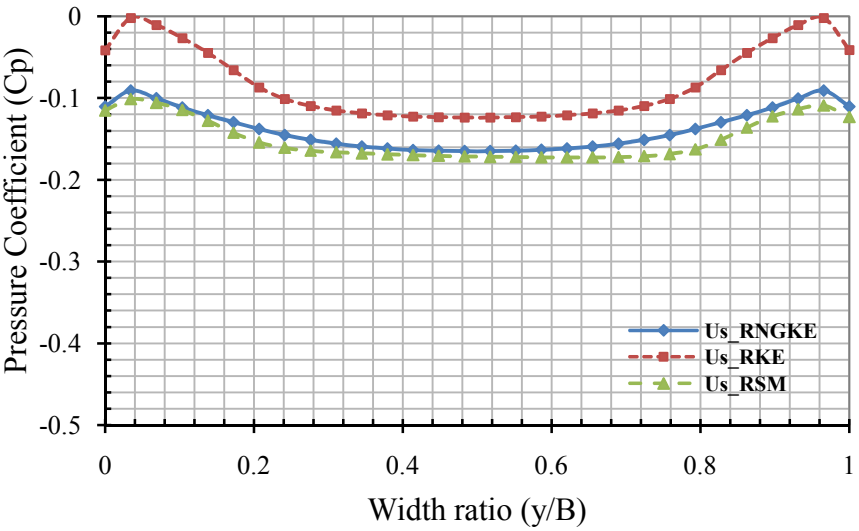

Figure 7.284 Pressure coefficients on the leeward inner face of the elevated net clad scaffold at two-third height from the ground for Type A Net

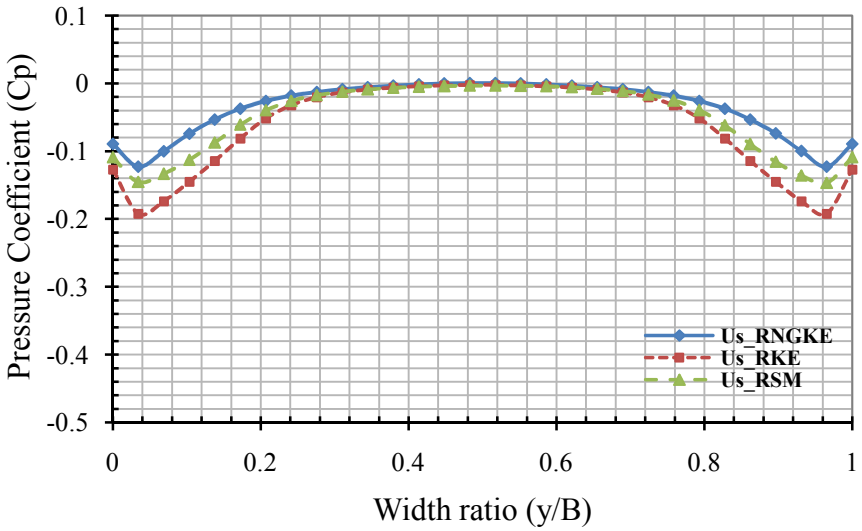

Figure 7.285 Difference of pressure coefficients of the leeward outer and inner face of the elevated net clad scaffold at two-third height from ground for Type A Net

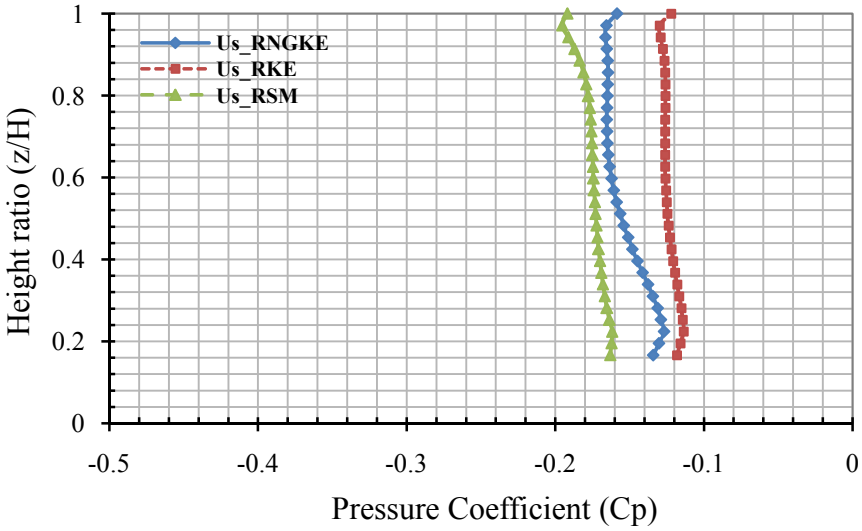

Figure 7.286 Pressure coefficients on the leeward outer vertical face at mid-width of the elevated net clad scaffold for Type A Net

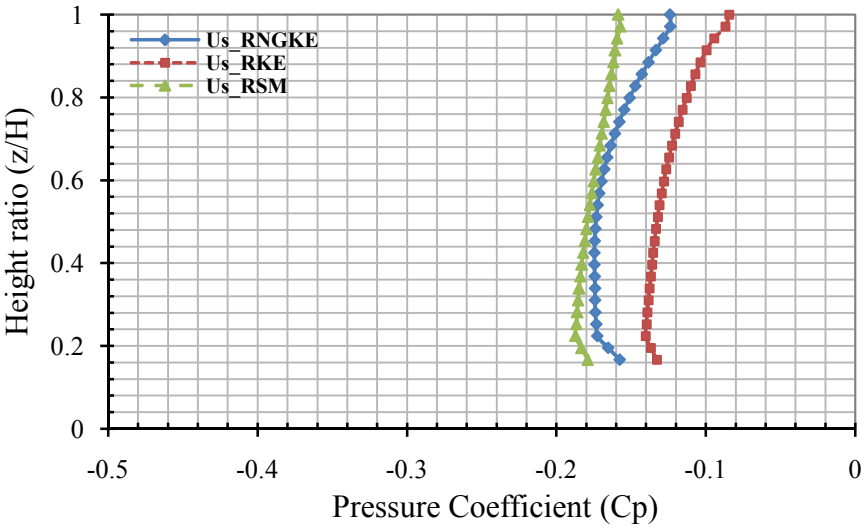

Figure 7.287 Pressure coefficients on the leeward inner vertical face at mid-width of the elevated net clad scaffold for Type A Net

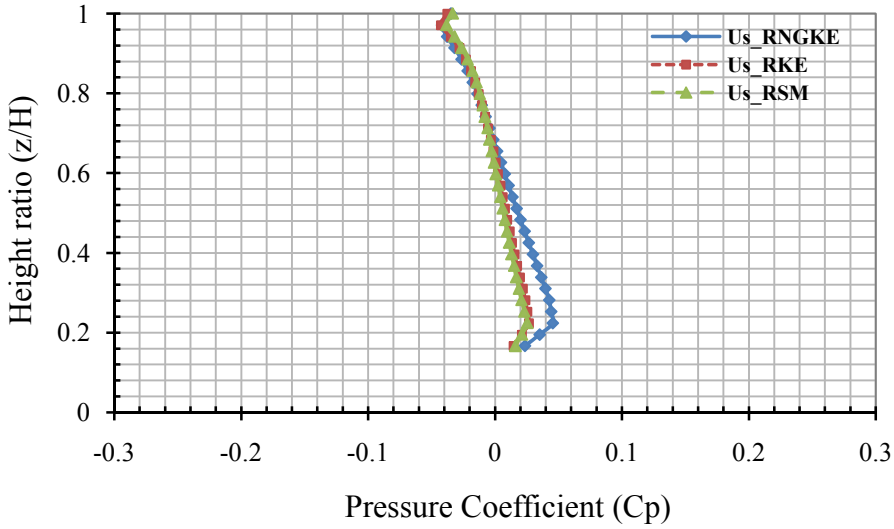

Figure 7.288 Difference of pressure coefficients of the leeward outer and inner vertical face at mid-width of the elevated net clad scaffold for Type A Net

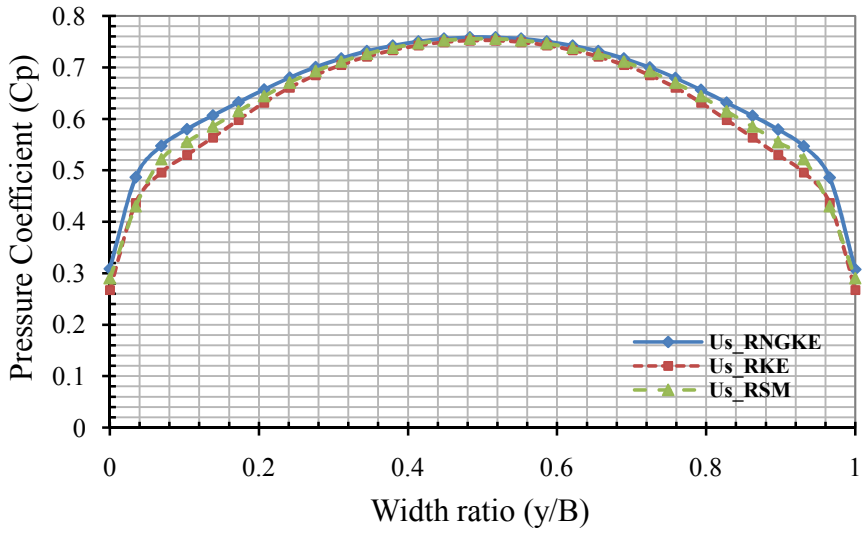

Figure 7.289 Pressure coefficients on the windward outer face of the elevated net clad scaffold at mid height from the ground for Type B Net

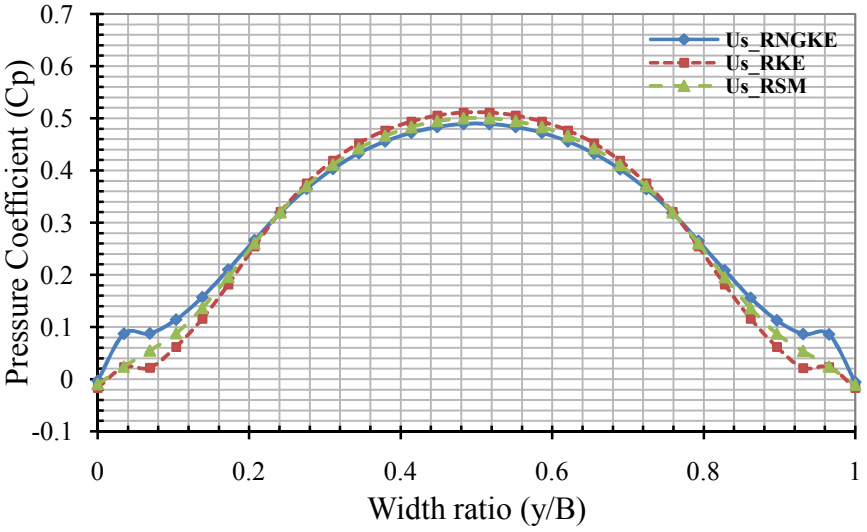

Figure 7.290 Pressure coefficients on the windward inner face of the elevated net clad scaffold at mid height from the ground for Type B Net

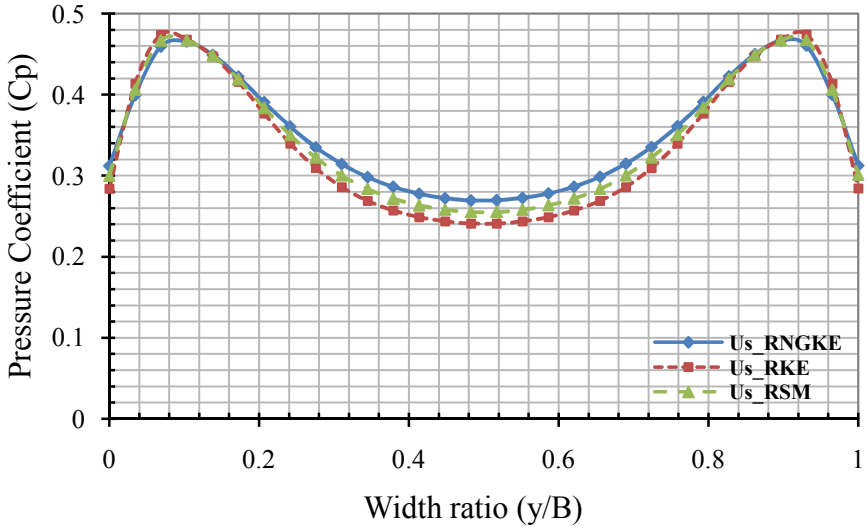

Figure 7.291 Difference of pressure coefficients of the windward outer and inner face of the elevated net clad scaffold at mid height from ground for Type B Net

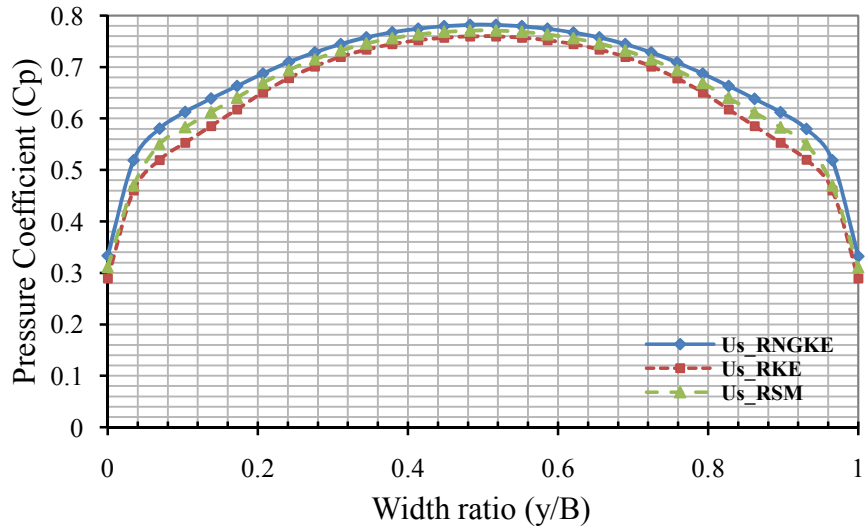

Figure 7.292 Pressure coefficients on the windward outer face of the elevated net clad scaffold at two-third height from the ground for Type B Net

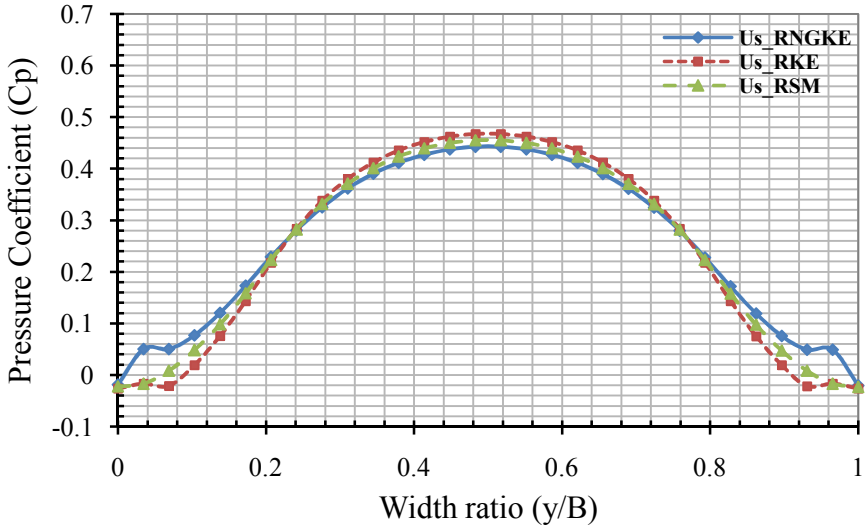

Figure 7.293 Pressure coefficients on the windward inner face of the elevated net clad scaffold at two-third height from the ground for Type B Net

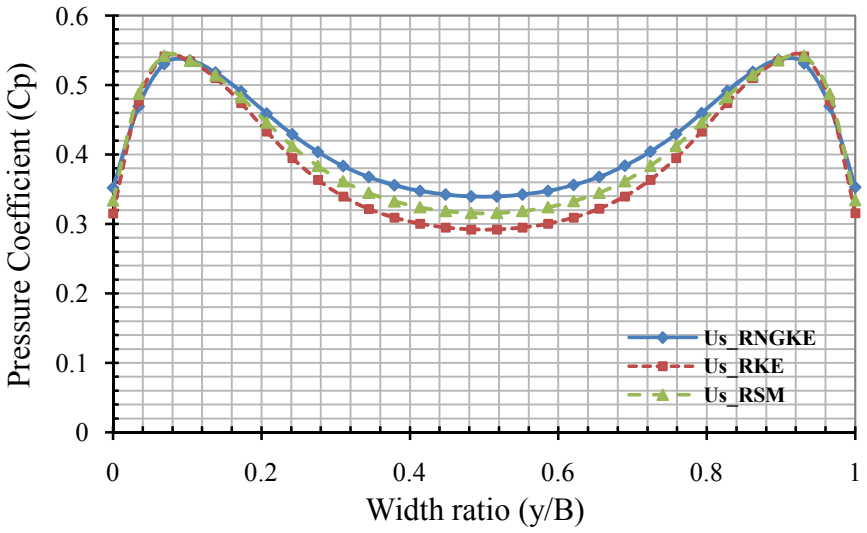

Figure 7.294 Difference of pressure coefficients of the windward outer and inner face of the elevated net clad scaffold at two-third height from the ground for Type B Net

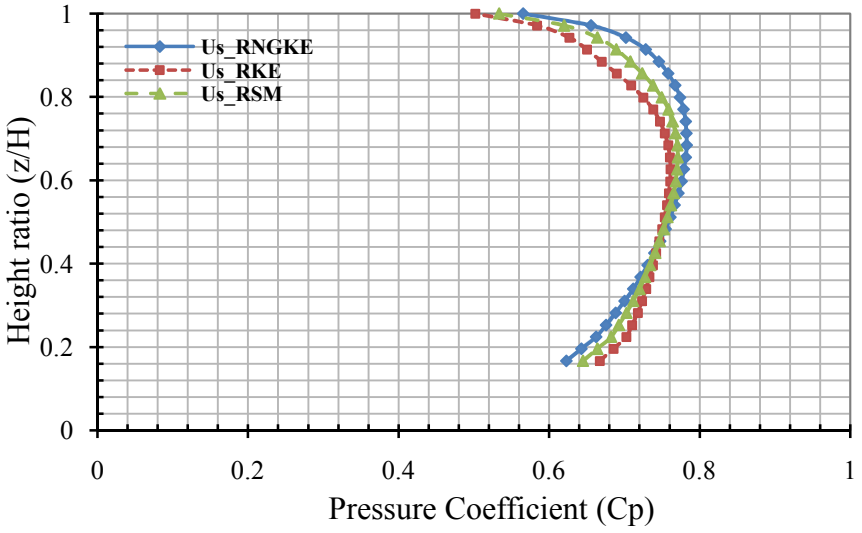

Figure 7.295 Pressure coefficients on the windward outer vertical face at mid-width of the elevated net clad scaffold for Type B Net

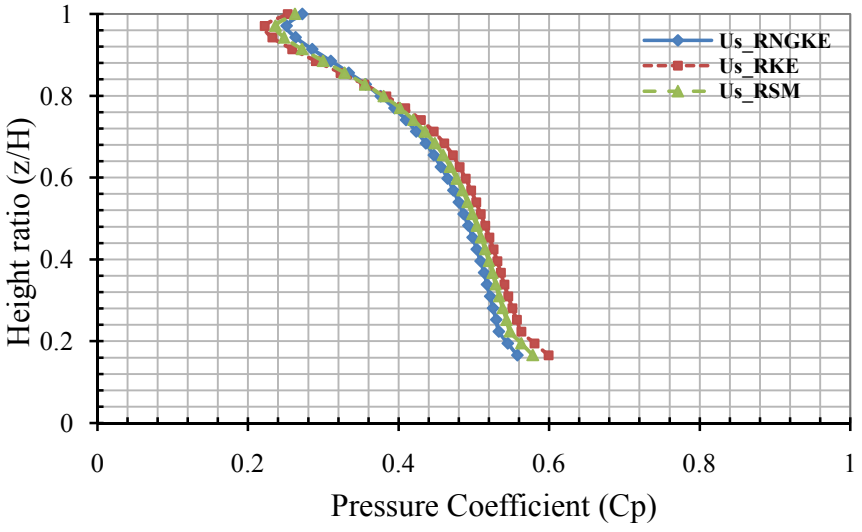

Figure 7.296 Pressure coefficients on the windward inner vertical face at mid-width of the elevated net clad scaffold for Type B Net

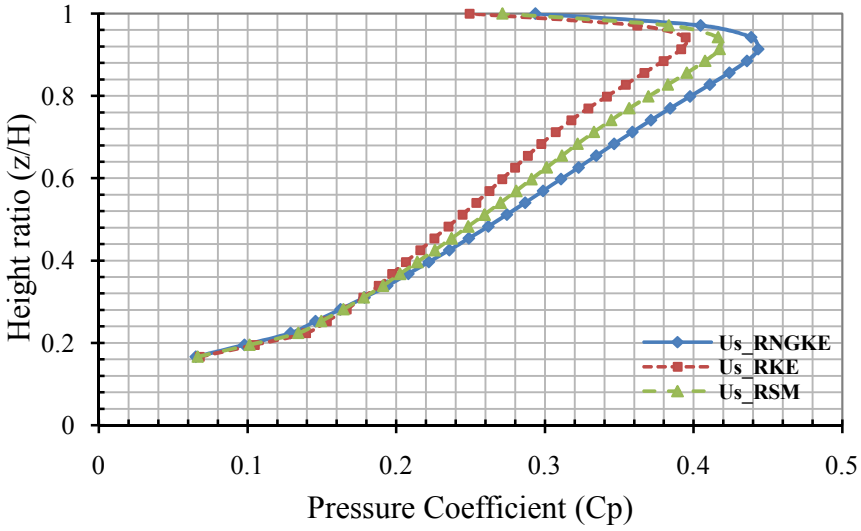

Figure 7.297 Difference of pressure coefficients of the windward outer and inner vertical face at mid-width of the elevated net clad scaffold for Type B Net

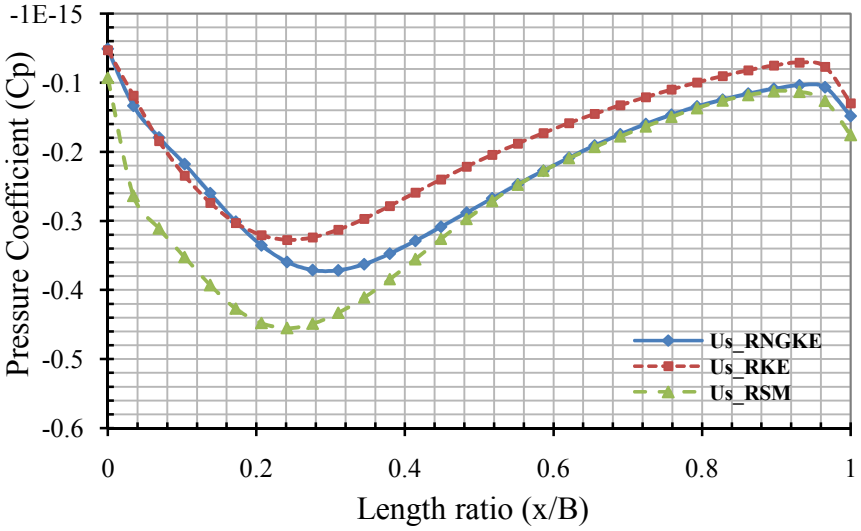

Figure 7.298 Pressure coefficient on the side outer face of the elevated net clad scaffold at mid height from the ground for Type B Net

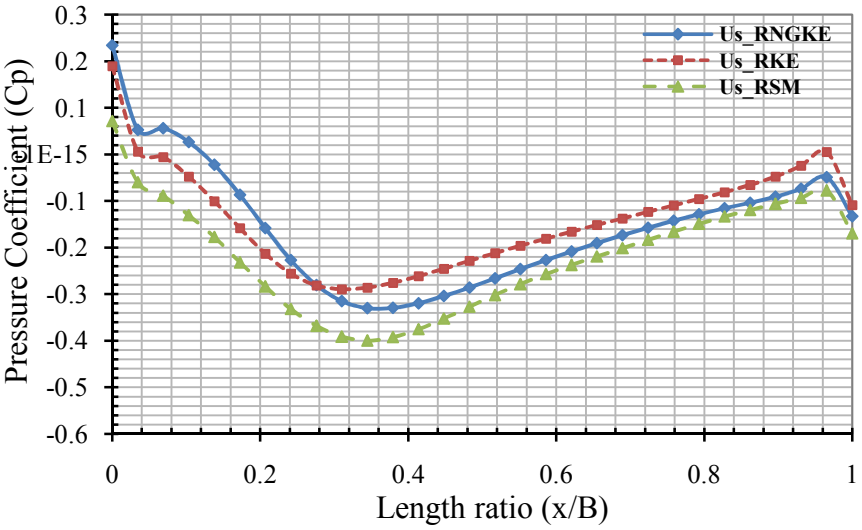

Figure 7.299 Pressure coefficient on the side inner face of the elevated net clad scaffold at mid height from the ground for Type B Net

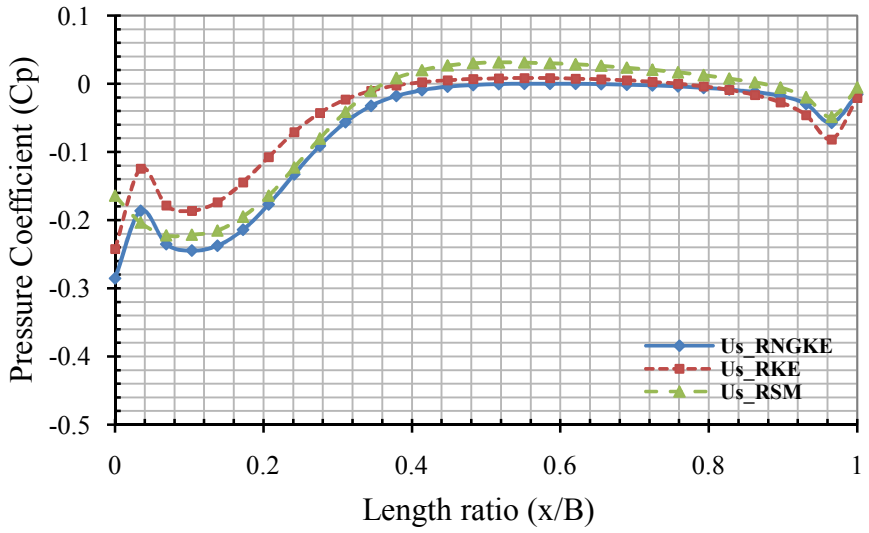

Figure 7.300 Difference of pressure coefficients of the side outer and inner face of the elevated net clad scaffold at mid height from the ground for Type B Net

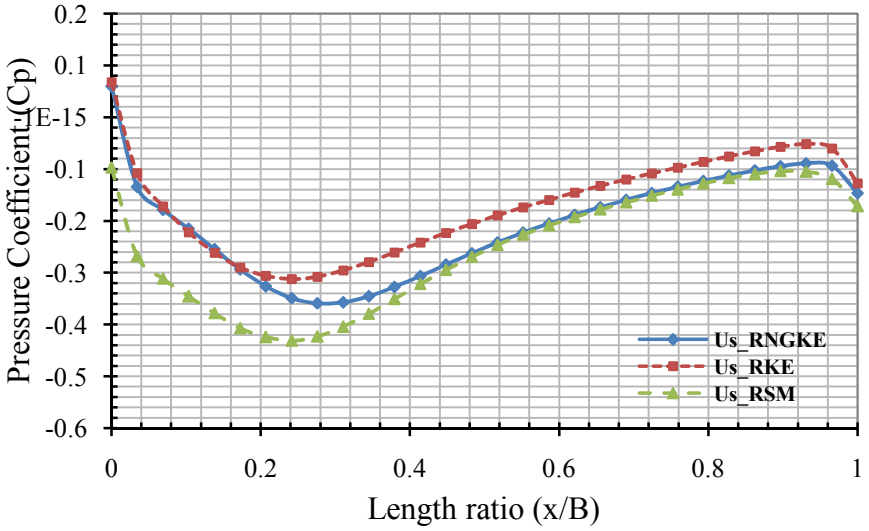

Figure 7.301 Pressure coefficient on the side outer face of the elevated net clad scaffold at two-third height from the ground for Type B Net

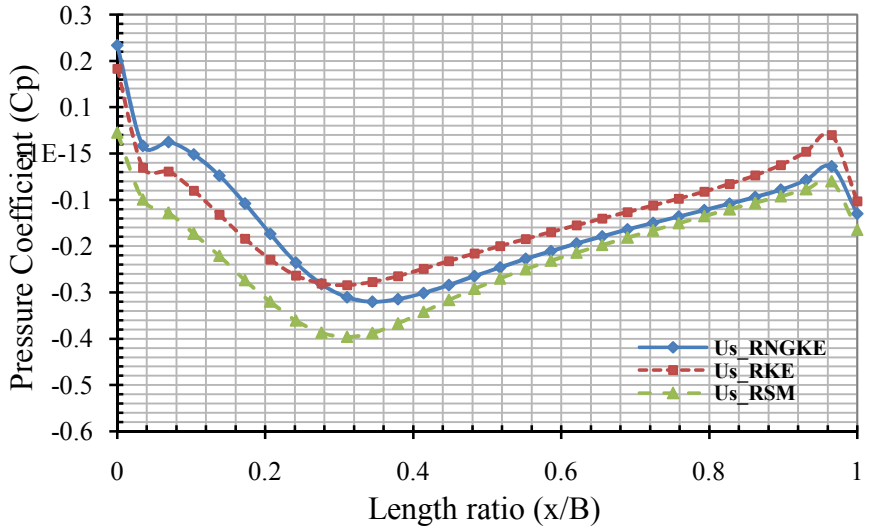

Figure 7.302 Pressure coefficient on the side inner face of the elevated net clad scaffold at two-third height from the ground for Type B Net

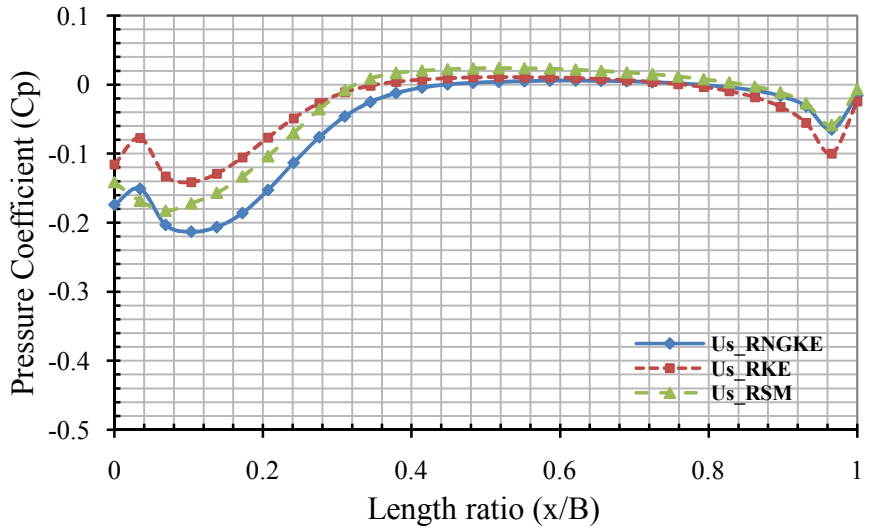

Figure 7.303 Difference of pressure coefficients of the side outer and inner face of the elevated net clad scaffold at two-third height from the ground for Type B Net

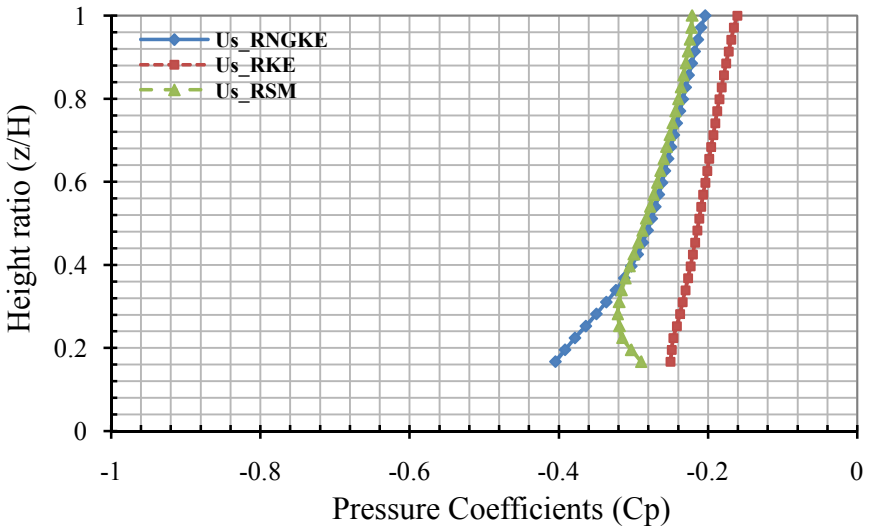

Figure 7.304 Pressure coefficients on the side outer vertical face at mid-length of the elevated net clad scaffold for Type B Net

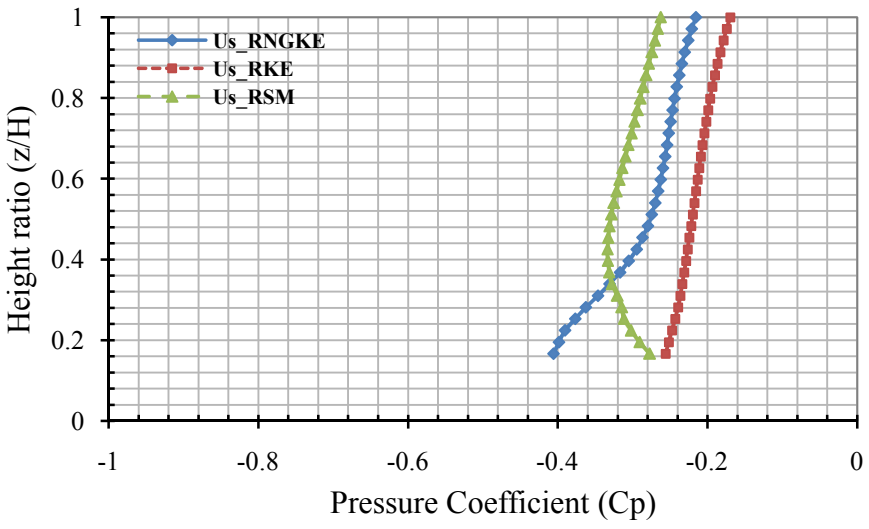

Figure 7.305 Pressure coefficients on the side inner vertical face at mid-length of the elevated net clad scaffold for Type B Net

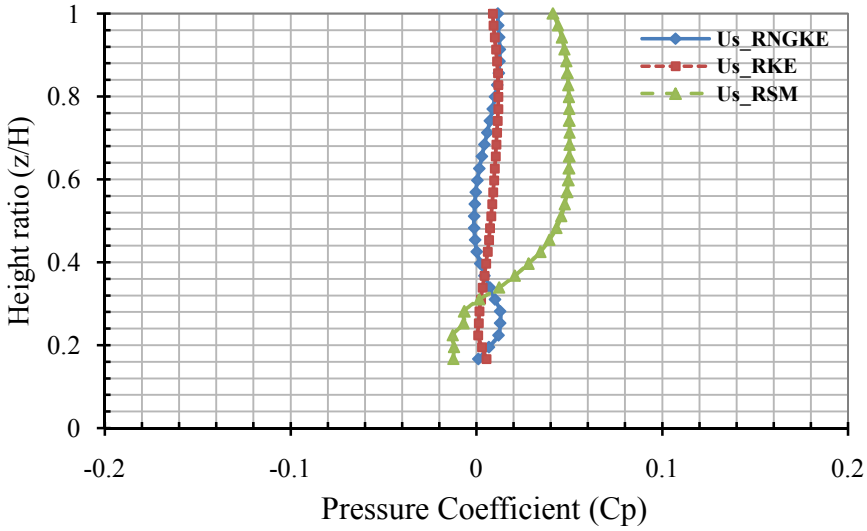

Figure 7.306 Difference of pressure coefficients of the side outer and inner vertical face at mid-length of the elevated net clad scaffold for Type B Net

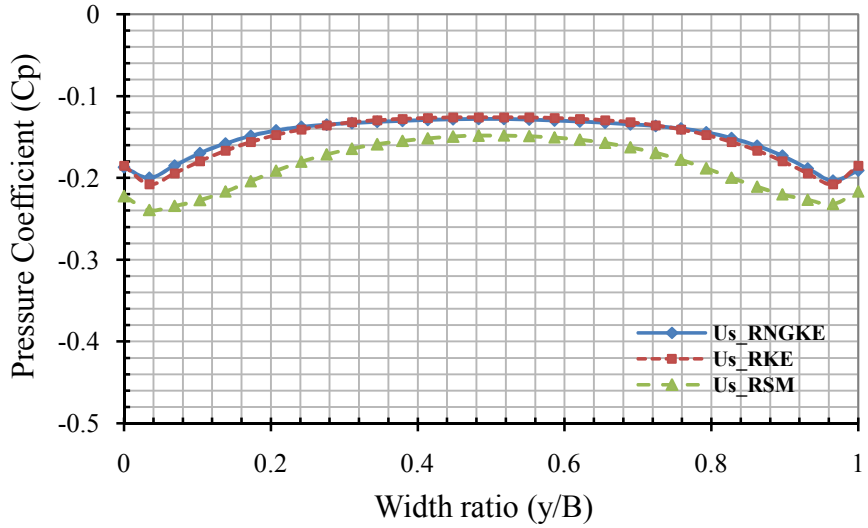

Figure 7.307 Pressure coefficients on the leeward outer face of the elevated net clad scaffold at mid height from the ground for Type B Net

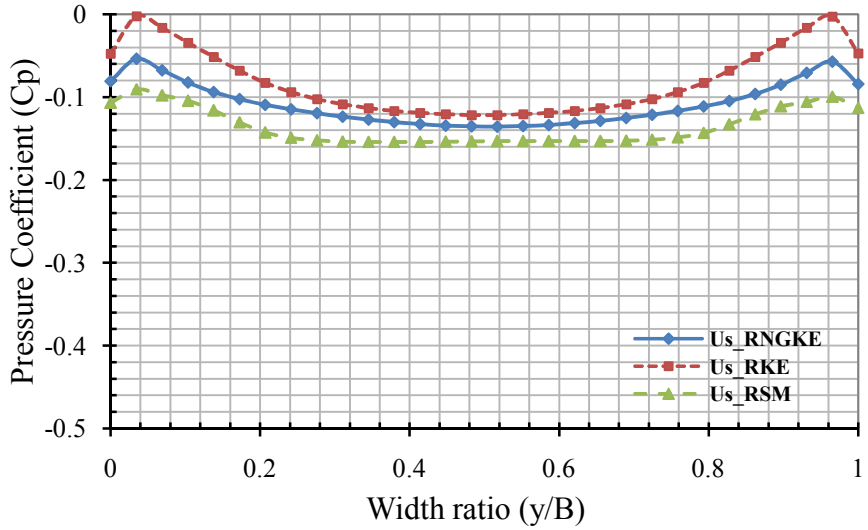

Figure 7.308 Pressure coefficients on the leeward inner face of the elevated net clad scaffold at mid height from the ground for Type B Net

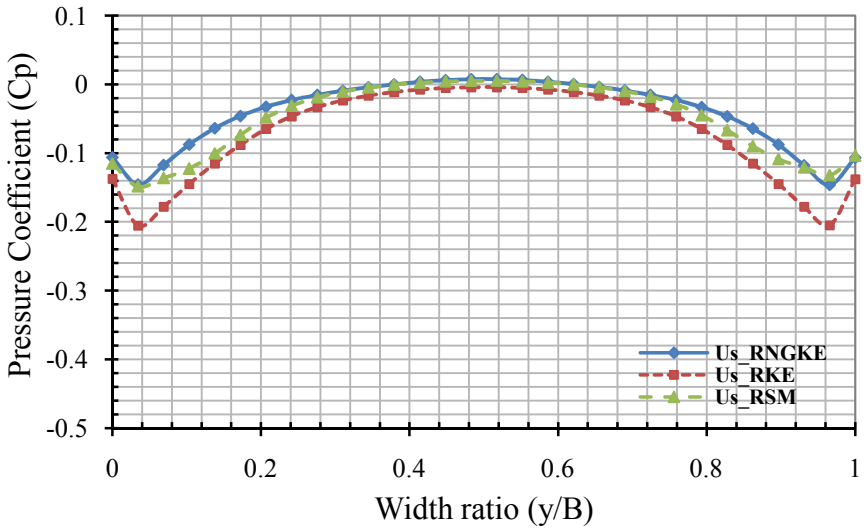

Figure 7.309 Difference of pressure coefficients of the leeward outer and inner face of the elevated net clad scaffold at mid height from ground for Type B Net

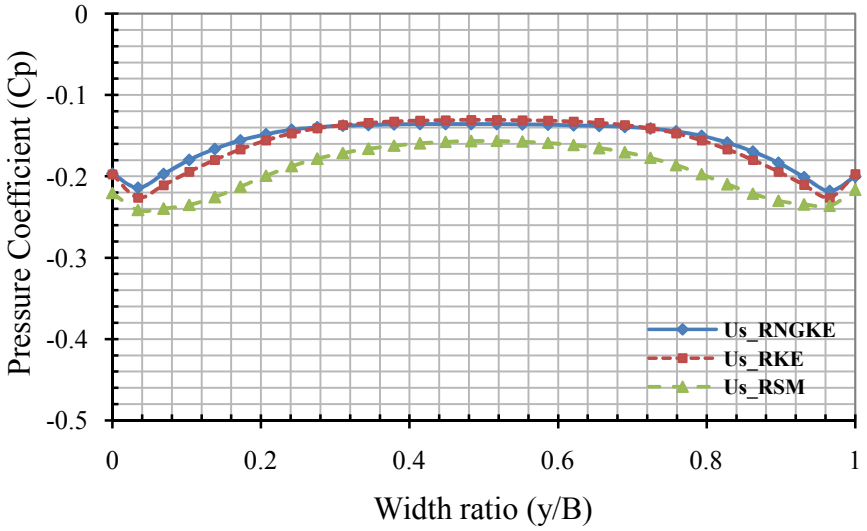

Figure 7.310 Pressure coefficients on the leeward outer face of the elevated net clad scaffold at two-third height from the ground for Type B Net

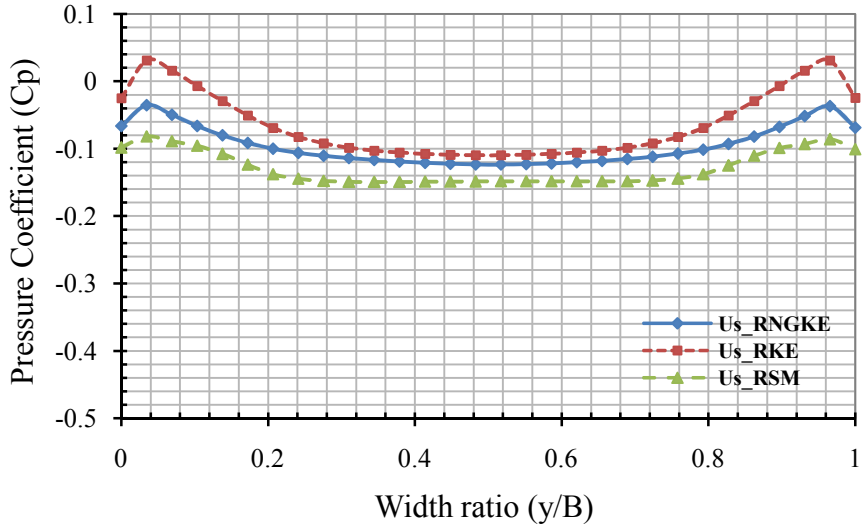

Figure 7.311 Pressure coefficients on the leeward inner face of the elevated net clad scaffold at two-third height from the ground for Type B Net

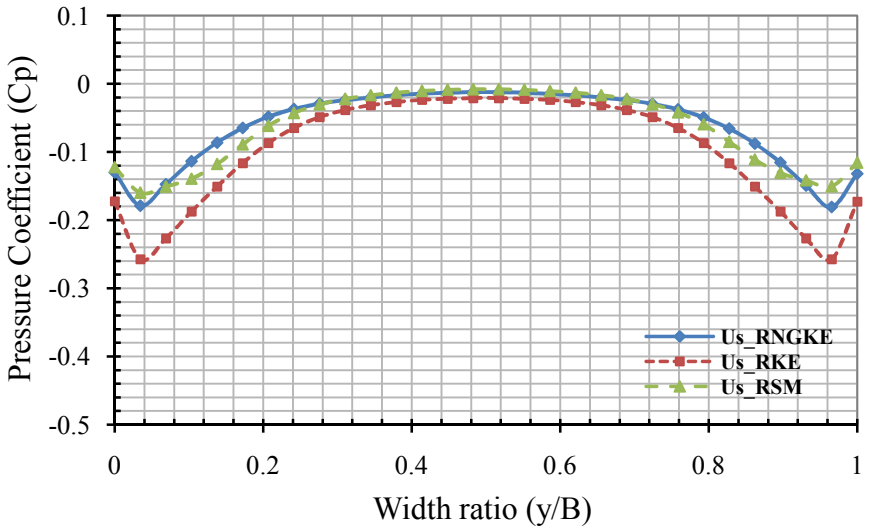

Figure 7.312 Difference of pressure coefficients of the leeward outer and inner face of the elevated net clad scaffold at two-third height from the ground for Type B Net

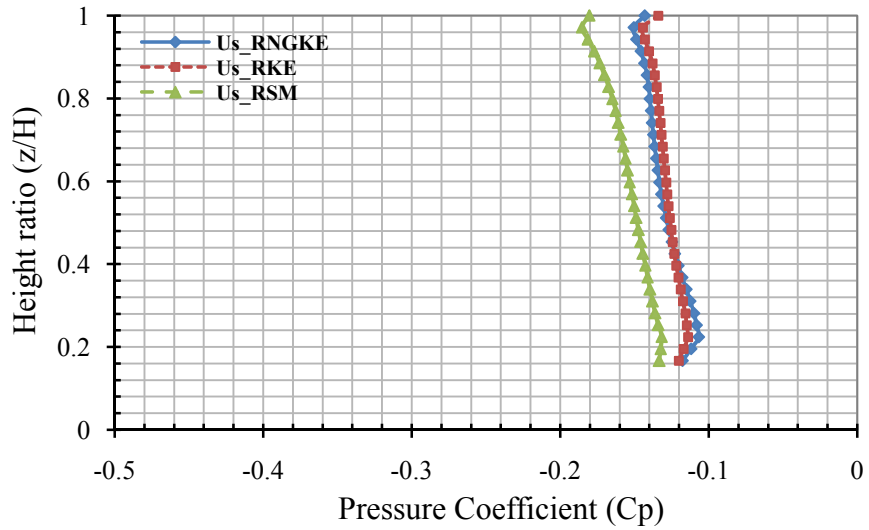

Figure 7.313 Pressure coefficients on the leeward outer vertical face at mid-width of the elevated net clad scaffold for Type B Net

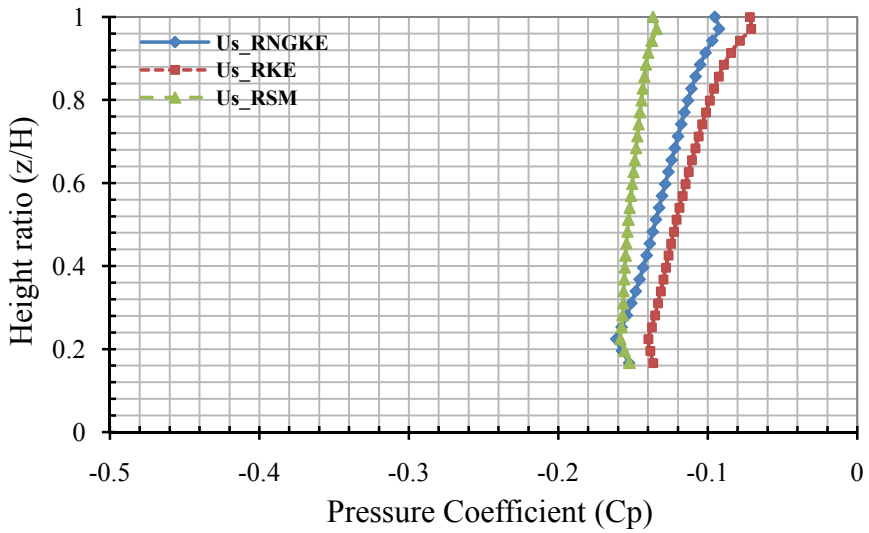

Figure 7.314 Pressure coefficients on the leeward inner vertical face at mid-width of the elevated net clad scaffold for Type B Net

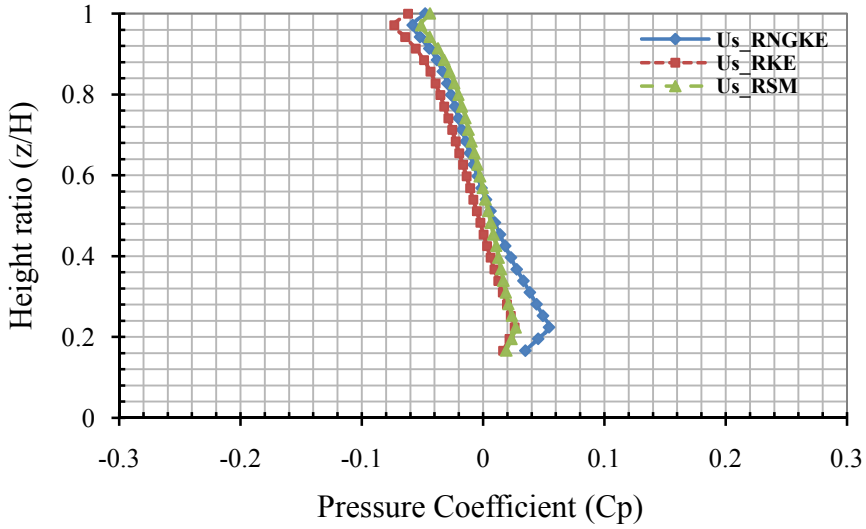

Figure 7.315 Difference of pressure coefficients of the leeward outer and inner vertical face at mid-width of the elevated net clad scaffold for Type B Net

The entire net clad scaffolds around the Silsoe Experimental Building were divided into different zones. The windward face was divided into three zones named as Zone A, Zone B and Zone C respectively. The side face was divided into two zones namely Zone D and Zone E respectively where as the leeward face was named as Zone F. The difference of pressure coefficients between inside and outside faces over different zones around the scaffolds were calculated for both types of scaffold (a net clad scaffold touching the ground and an elevated net clad scaffold) and integrated over the zones (by numerically integrating the pressure distributions along the curve for all the figures) to calculate the average pressure for two types of net used and are shown in Tables 7.1 to 7.8.

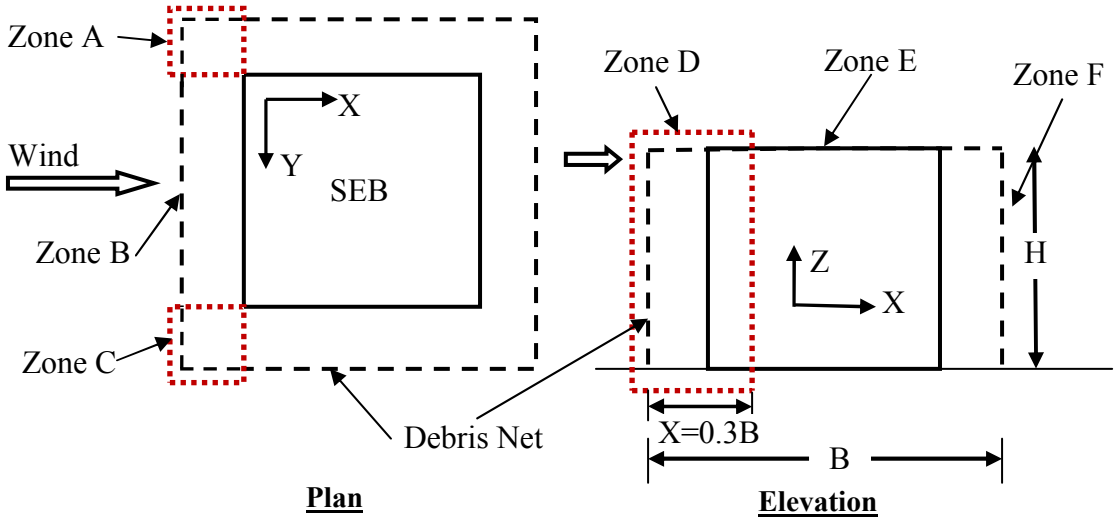

Figure 7.316 Net clad scaffolds touching the ground surrounding SEB

Table 7.1 Average pressure coefficient differences on net clad scaffolds for Type A Net at Z=0.5H

Net Clad Scaffold Surrounding the SEB (touching the ground)						
Net Type A, Z = 0.5H						
CFD Technique	Windward Face			Side Face		Leeward Face
	Zone A	Zone B	Zone C	Zone D	Zone E	Zone F
RNGKE	0.273	0.166	0.273	-0.108	0.003	-0.0235
RKE	0.288	0.1605	0.288	-0.063	-0.002	-0.0438
RSM	0.278	0.163	0.278	-0.102	0.003	-0.0238

Table 7.2 Average pressure coefficient differences on net clad scaffolds for Type B Net at Z=0.5H

Net Clad Scaffold Surrounding the SEB (touching the ground)						
Net Type B, Z = 0.5H						
CFD Technique	Windward Face			Side Face		Leeward Face
	Zone A	Zone B	Zone C	Zone D	Zone E	Zone F
RNGKE	0.431	0.343	0.431	-0.193	-0.007	-0.0441
RKE	0.429	0.318	0.429	-0.131	-0.012	-0.0665
RSM	0.425	0.331	0.425	-0.177	-0.001	-0.0380

Table 7.3 Average pressure coefficient differences on net clad scaffolds for Type A Net at Z=2/3H

Net Clad Scaffold Surrounding the SEB (touching the ground)						
Net Type A, Z = 2/3H						
CFD Technique	Windward Face			Side Face		Leeward Face
	Zone A	Zone B	Zone C	Zone D	Zone E	Zone F
RNGKE	0.307	0.196	0.307	-0.088	0.0072	-0.042
RKE	0.322	0.188	0.322	-0.037	-0.0007	-0.063
RSM	0.310	0.192	0.310	-0.074	0.0064	-0.044

Table 7.4 Average pressure coefficient differences on net clad scaffolds for Type B Net at Z=2/3H

Net Clad Scaffold Surrounding the SEB (touching the ground)						
Net Type B, Z = 2/3H						
CFD Technique	Windward Face			Side Face		Leeward Face
	Zone A	Zone B	Zone C	Zone D	Zone E	Zone F
RNGKE	0.461	0.367	0.461	-0.1622	-0.0037	-0.0615
RKE	0.449	0.333	0.449	-0.0972	-0.0109	-0.0874
RSM	0.447	0.350	0.447	-0.1392	-0.0003	-0.0522

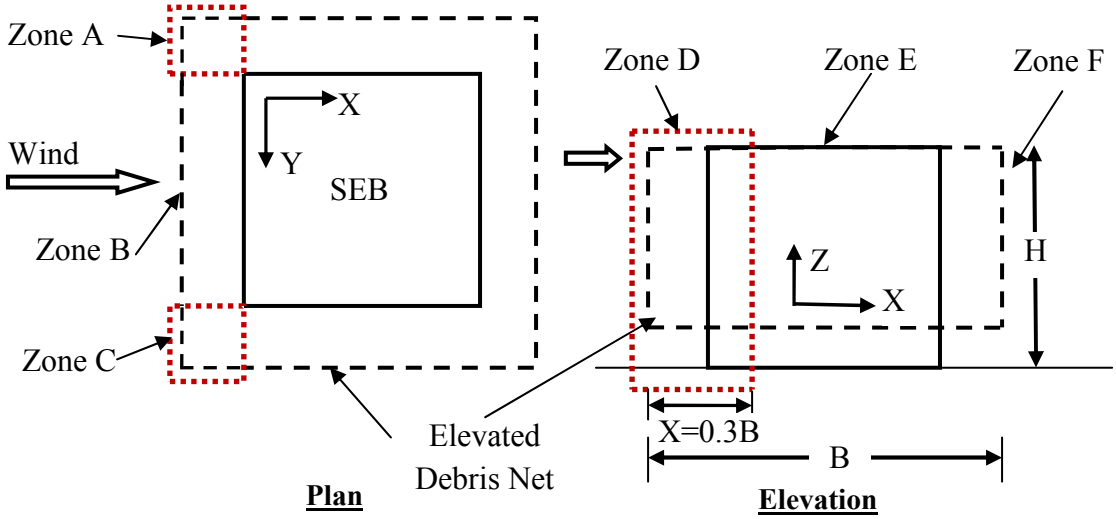

Figure 7.317 Elevated net clad scaffold surrounding SEB

Table 7.5 Average pressure coefficient differences on elevated net clad scaffolds for Type A Net at Z=0.5H

Elevated Net Clad Scaffold Surrounding the SEB						
Net Type A, Z = 0.5H						
CFD Technique	Windward Face			Side Face		Leeward Face
	Zone A	Zone B	Zone C	Zone D	Zone E	Zone F
RNGKE	0.2701	0.1667	0.2701	-0.1137	-0.00205	-0.01152
RKE	0.2815	0.1567	0.2815	-0.0604	-0.00065	-0.04411
RSM	0.2909	0.1616	0.2909	-0.0996	0.00568	-0.03362

Table 7.6 Average pressure coefficient differences on elevated net clad scaffolds for Type B Net at Z=0.5H

Elevated Net Clad Scaffold Surrounding the SEB						
Net Type B, Z = 0.5H						
CFD Technique	Windward Face			Side Face		Leeward Face
	Zone A	Zone B	Zone C	Zone D	Zone E	Zone F
RNGKE	0.4171	0.3228	0.4178	-0.20035	-0.01322	-0.04235
RKE	0.4174	0.2987	0.4175	-0.1411	-0.0085	-0.0721
RSM	0.4175	0.3107	0.4180	-0.1766	0.0087	-0.05055

Table 7.7 Average pressure coefficient differences on elevated net clad scaffolds for Type A Net at Z=2/3H

Elevated Net Clad Scaffold Surrounding the SEB						
Net Type A, Z = 2/3H						
CFD Technique	Windward Face			Side Face		Leeward Face
	Zone A	Zone B	Zone C	Zone D	Zone E	Zone F
RNGKE	0.3073	0.1989	0.3073	-0.09506	0.0028	-0.03686
RKE	0.3161	0.1867	0.3602	-0.0355	0.0006	-0.06507
RSM	0.3114	0.1928	0.3114	-0.07016	0.0085	-0.05166

Table 7.8 Average pressure coefficient differences on elevated net clad scaffolds for Type B Net at Z=2/3H

Elevated Net Clad Scaffold Surrounding the SEB						
Net Type B, Z = 2/3H						
CFD Technique	Windward Face			Side Face		Leeward Face
	Zone A	Zone B	Zone C	Zone D	Zone E	Zone F
RNGKE	0.4810	0.3919	0.4817	-0.16404	-0.00905	-0.06285
RKE	0.4756	0.3523	0.4757	-0.0949	-0.00785	-0.09824
RSM	0.4823	0.3721	0.4825	-0.1294	-0.00683	-0.06467

7.7 Flow Field Investigation

The flow pattern around a surface mounted cube has been well documented by Woo et al as shown in Figure 3.3 and by Huang et al [7.7]. The typical flow field features are summarized as: (1) a horse shoe vortex which originated from the separation as the flow from front of the cube bends horizontally the bluff body into the wake; (2) the flow separates at the front corners of the cube on the roof and side walls. A large separation region develops behind the cube which interacts with the horse-shoe vortex; (3) an arch vortex originating from the ground plate develops behind the cube. It was suggested by Martinuzi from his visualization studies that the flow around a cube will be different in a simulated wind-tunnel from a cube standing in an atmospheric boundary layer [7.7]. As reported by Davies et al the circulating flow region in a wind-tunnel test is contracted compared to full-scale tests [7.7]. Due to absence of flow data from both the experiments and the Silsoe cube this statement cannot be verified. The flow pattern predicted by the current numerical studies are shown in the Appendix in Figures A.1 to A.59.

The flow features suggested by Martinuzi et al [7.6] were captured by the author's numerical simulations in particular the location and shape of the arch vortex in the wake.

Instantaneous flow patterns predicted by the LES reveal that the detail flow structures are irregular and complex. The instantaneous flow field from the LES indicates that this vortex is unsteadily moving around the corner, which is in accordance with the drop of C_p predicted by the LES.

The turbulence is excessively over predicted by the standard $k-\varepsilon$ model, an unrealizable turbulent kinetic energy is seen near the sharp end. The over-production of

turbulent viscosity results in the prediction of small separation bubbles and a large downstream arch vortex.

7.13 Results Summary

Referring to the results on the SEB and Sheet/Net clad scaffolds it is clear that the standard $k-\varepsilon$ model cannot, in the majority of cases, adequately predict the flow fields and the pressure distribution around a bluff body. Nevertheless, there were a few notable exceptions where the flow remained attached to the bluff body and flow impingement was not so severe and the standard model performed acceptably. The most severe errors were due to the inaccurate and excessive prediction of turbulent kinetic energy levels, particularly at flow stagnation points. The results of which were to raise the maximum possible windward face stagnation pressure to a value greater than unity due to contributions from the three normal Reynolds stress turbulence components. In addition, the excessive values of turbulent kinetic energy predicted excessively mix and arrest the flow causing it to remain attached to the roof of the cube. This resulted in a poor flow field prediction and a sharp peak and large gradient of the negative pressure behind the upstream edge. It is also apparent that the excessive levels of the flow field result in a surprisingly short wake recirculation. Therefore, to conclude, the errors brought about by the isotropic eddy viscosity assumptions and the resulting simplifications, particularly with the production term in the turbulent kinetic energy transport equation are primarily responsible for this models poor performance.

Comparing the wind-tunnel tests with the results from the RNG $k-\varepsilon$ model and the standard $k-\varepsilon$ model, the RNG $k-\varepsilon$ model gave better a correlation. It was the only turbulence model that was able to predict the flow separation and reattachment on the roof of the cube which in turn produced an improved roof pressure distribution.

Reference [7.6] states that the RNG model incorporates revised model constants in the transport equations which cause the improvements. In addition, the turbulent energy dissipation equation, which has long been considered a source of inaccuracy in both $k-\varepsilon$ and the Reynolds stress model, has been revised. The ε equation now includes a strain dependent term to aid the model in dealing with flows that experiences large strain dependent term to aid the model in dealing with flows that experience large rates of deformation. These two factors are very important in helping the model to deal with impinging flow fields and lead to reduced eddy viscosity and turbulent kinetic energy.

The realizable $k-\varepsilon$ model satisfies certain mathematical constraints on the normal stresses, consistent with the physics of turbulent flows, combining the Boussinesq relationship with the eddy viscosity to obtain an expression for the normal Reynolds stress in an incompressible strained mean flow. These models have been validated for boundary layer flows, and separated flows on different models and perform substantially better than those of the standard $k-\varepsilon$ model.

The Reynolds stress model has far greater universality than the models based on the eddy viscosity concept due to its more rigorous and detailed mathematical formulation. The inclusion of a great number of equations allows for a far greater description of the physics of turbulent flow.

Despite the considerable abilities of this model it still has many inadequacies and there are many years of development work to be undertaken on the Reynolds stress model closure forms before it will show its real potential. At present the main areas identified as causing inaccuracies in flow predictions include the following:

- The modelled turbulence energy dissipation equation.
- The closure form of the pressure-strain tensor and the effect of wall reflection terms.
- Numerical instability and difficulties in obtaining converged solutions for the modelled partial differential equations in complex flows.
- Difficulties in convergence when unstructured meshes are used.

The LES technique, vigorously pursued in various countries has the advantage of producing time dependent flow information of very high quality and accuracy even in complex flow fields such as those used in the present study. It has succeeded in reproducing the properties of a highly anisotropic flow field in wind engineering problems. It is widely felt by researchers that the LES technique is a promising tool for the future. Overall for models, the LES method used gives results near to the experimental values.

This technique, although being more economical than DNS is still very resource intensive and as such is not yet much used outside of the research community. Further difficulties are apparent in the use of the sub-grid-scale model to dissipate the flow energy. The sub-grid-scale eddies are not simply dissipative but can contribute

significantly to turbulent mixing. Such processes as 'backscatter' can occur in which the small eddies combine with large eddies and transfer energy to them.

From the present study of the sheet clad scaffold pressure coefficients can be recommended for the design of scaffolds. The standard $k-\varepsilon$ and realizable $k-\varepsilon$ were not considered in determining the average values as their results were considered to be a little high. It is also notable that there was only a small difference in pressure values determined from elevated and non-elevated scaffolds and the author therefore does not distinguish between them. The author recommends that the following values in Table 7.9 of pressure coefficient for the design of sheet clad and elevated sheet clad scaffolds be used in the future.

Table 7.9 Recommended pressure coefficients on sheet/elevated sheet clad scaffolds

Net Clad Scaffold Surrounding the SEB (touching the ground)			
Design Pressure Coefficients	**Windward Face**	**Side Face**	**Leeward Face**
	1.3	**0.15 (suction) (outward)**	**-**

From the present study on net clad scaffolds, the following pressure coefficients recommended by the author for the design of scaffolds when cladded with nets. Hence the total pressure force on the scaffold will be the function of the effective net area in different zones multiplied by the coefficients of pressure recommended below in Tables 7.10. These values are derived by taking the average value of the results from Type A Nets and Type B Nets.

Table 7.10 Recommended pressure coefficients on net/elevated net clad scaffolds

Net Clad Scaffold Surrounding the SEB (touching the ground)						
Design Pressure Coefficients	**Windward Face**			**Side Face**		**Leeward Face**
	Zone A	**Zone B**	**Zone C**	**Zone D**	**Zone E**	**Zone F**
	0.37	**0.26**	**0.37**	**- 0.11 (outward)**	**-**	**-**

CHAPTER 8
Conclusions and Recommendations for Future Work

8.1 Introduction

The behaviour of fabric clad (net/sheet) on scaffold structures in a wind is extremely complex and aeroelastic in nature. However, both limitations in experiment and computational analyses compelled the choice of a rigid model which does not give information regarding the possibility of divergence or flutter, but can be used to predict the fluctuating wind pressures due to buffeting.

The wind forces ultimately acting on the scaffolds (transferring from covering materials to scaffolds) depends mainly on the air penetrability of the netting and of the building. Coverings made largely of windproof materials (sheeting) behave differently from wind penetrable coverings (net). Significant wind forces occur on the scaffolds even where the building façade is closed. In the present study buildings with closed facades were considered both for sheet and net clad scaffolds. The elevation of a net or sheet from the ground by a small amount (1 m in the simulations analysed in this thesis) however does not cause any major differences on the wind forces on the scaffolds as the wind moves horizontally (near the lower region) around the side of the building and does not pass through the gap between the facade of the building and the scaffolds.

The present design code for wind loads on scaffold structures are based on permanent structures. The present research, which is based on the experiment and computational analyses, proposes the replacement of the existing design pressure coefficients with ones suggested by the author.

8.2 Objectives Achieved

The following objectives of this project were successfully achieved:

- Determination of the pressure coefficients on sheeted scaffold structures by testing a scaled model in a wind-tunnel.
- Calculation of the permeability of nets commonly used in the construction industry.

- Development of a mathematical model of scaffolds subjected to wind loads using Computational Fluid Dynamics.
- Successfully simulating netting as a porous media and calculating the net pressure coefficients for the design of scaffold structures.
- Obtaining revised wind load pressures for scaffolds for inclusion in new/revised design codes and obtaining an understanding of the influence of the supporting structures.

8.3 Conclusions

Wind forces on the Silsoe Experimental Building (SEB) and sheet clad scaffolds (both elevated and touching the ground) surrounding the SEB with Reynolds number varying from 66,000 to 100,000 from wind-tunnel experiments and numerical simulations using Computational Fluid Dynamics techniques have been presented in this thesis and the details can be found in Chapter 7. The permeabilities of different nets were determined using wind-tunnel experiments on the netting. A purely numerical simulation of a net clad scaffold surrounding the SEB in atmospheric boundary layer using the permeabilities calculated from the wind-tunnel experiments is presented in Chapter 7. The effectiveness of the turbulence models and numerical treatments adopted for solving the practical problems with high Reynolds number were investigated in detail. Both structured and unstructured mesh arrangements were used, suitable for different turbulence models which can flexibly deal with the problem of a computational grid for surface mounted bluff bodies (refining meshes near the model edges and model surface neighbourhoods and also avoiding excessive grid-stretching). Numerical results showed that the height of the first cell of the boundary layer being 0.000084 m can ensure a wall unit $y^+ \cong 1$. Furthermore, grid dependent results were obtained by meshes with 1.75 million to 4 million grid numbers for the computations by the RANS models and the LES. The computational results were compared with the extensive experimental results with the following conclusions:

1. All the pressure coefficient contours drawn on different models on the outer face showed a definite pattern change as the angle of rotation changed. On the other hand, the pressure coefficients on the inner side of the sheet clad scaffold showed no definite pattern changes at different angles of rotation because little

movement of air was found between the building and the sheet clad scaffolds. The air between the building and the sheet clad scaffolds was almost stagnant.

2. The maximum positive pressure coefficients on the windward face of the SEB or on the sheet/elevated sheet clad scaffolds occurred when the direction of wind was normal to the windward face. The maximum negative pressure on the side face of the SEB or the sheet/elevated sheet clad scaffolds was when the direction of flow was parallel to the side face. The maximum negative pressure on the leeward face of the SEB or on the sheet/elevated sheet clad scaffolds occurred when the direction of wind was at $\pm 30^0$ from the windward façade. It was observed that the maximum suction pressure coefficients on the roof of the cubical SEB occurred when the direction of wind was at $\pm 45^0$ from the normal windward façade.
3. The pressure coefficients did not vary significantly from the corner to mid on the inside face of the sheet/elevated sheet clad scaffolds.
4. Two different types of terrain and inflow boundary conditions were modelled in wind-tunnel tests. The different terrains resulted in discrepancies between the mean pressure coefficients and the r.m.s. pressure coefficients between the tests showing the sensitivity of wind-tunnel results to different conditions. Full details are reported in [8.1].
5. It was found that the velocity profile mainly influenced the mean pressure coefficients and the turbulence intensity profile has a significant effect on the r.m.s. pressure coefficients(Report No. 397, School of the Built-Environment, Oxford Brookes University) [8.1].
6. Accurate modelling of the boundary conditions of incident flows such as the velocity profile and turbulence intensity profile in the numerical simulation is of great importance and must be successfully achieved in order to obtain good agreement between the numerical results and the experimental measurements.
7. Among the turbulence models used in this thesis, the LES with a dynamic SGS model (other SGS models have not been tested) provides satisfactory predictions for the mean pressure coefficients and reasonable results for the fluctuating pressure coefficients both for then SEB and for a sheet clad scaffold surrounding SEB. An elevated sheet clad scaffold surrounding the SEB could not be successfully simulated using LES because quality meshes could not achieved when using the meshing software GAMBIT.

8. The results, first reported in [8.2] by Huang et al, that the RNG $k-\varepsilon$ and Realizable $k-\varepsilon$ models were best choice among the RANS models for fast convergence were confirmed in this thesis. The models gave reasonable results for mean pressure coefficients being a little higher on the windward face and a little lower on the leeward face in most cases, but the duplication of the dynamic wind loads on the SEB and sheet/elevated sheet clad scaffolds was not complete due to model deficiencies.
9. CFD techniques are still advancing. The Large Eddy Simulation gives encouraging results and can be comparable with wind-tunnel measurements. The RANS models need improvements in the modelling of eddy viscosity concepts. Improvements are needed for CFD application in wind engineering, including grid generation strategies for complex solution domains. The application of higher order numerical schemes for space and time discretisation, more general and reliable sub-grid scale turbulence models for generation of inflow boundary turbulence characteristics, etc. is required for improved performance.
10. Almost all the flow regimes around the SEB and Sheet/elevated sheet clad scaffolds were correctly simulated by the present numerical simulations. Typical flow features around all the models simulated in the atmospheric boundary layers such as the recirculating flow region contraction in the building back face zone due to base suction were captured which can be seen in the figures in the Appendix.
11. The instantaneous flow fields captured when using LES techniques were irregular and complex at Reynolds numbers varying from 66,000 to 100,000 and can be seen in the Appendix.
12. The permeabilities of the nets were calculated from the graphs plotted between free stream velocity versus drop in pressure across the net (from wind-tunnel experiments) by assuming that the drop in pressure across the nets is proportional to the inertial resistance and inversely proportional to the permeability.
13. The difference in the pressure coefficients between the outer and the inner faces on all the façades of the net and for both type of nets (Type A Net and Type B Net) were plotted to determine the wind forces transferred from the net to the supporting scaffold. The nets were simulated as porous media.

14. The pattern of the pressure coefficients by all the three CFD models on the windward outer and inner faces were almost the same. However, on the side face the suction (negative) pressure coefficients shown by RSM are the highest, followed by the Realizable $k-\varepsilon$ and the least by the RNG $k-\varepsilon$ models. On the leeward face the pressure coefficients shown by RSM are higher than those found by the RNG and Realizable $k-\varepsilon$.
15. The drops in pressure coefficients are more for the Type B Net than for the Type A Net. This may be because Type B Net is denser than Type A Net.

8.4 Design Recommendations

The following are the pressure coefficients recommended for the future design of sheet clad scaffolding under wind load:

Table 8.1 Recommended pressure coefficients on sheet/elevated sheet clad scaffolds

Sheet Clad Scaffold Surrounding the SEB			
Design Pressure Coefficients	**Windward Face**	**Side Face**	**Leeward Face**
	1.3	**0.15 (suction) (outward)**	**-**

To calculate the wind forces transferred from the sheet to the scaffolds, the pressure coefficients are to be multiplied directly to the projected area of the sheet. There is no need to consider wind forces on the leeward face of the sheet clad scaffold as there is suction of nearly equal magnitude on both sides of the leeward sheet which cancels the pressures.

The different zones on net/elevated net clad scaffolds for taking pressure coefficient values are shown in Figures 7.336 and 7.337 and their zone values are given below.

Table 8.2 Recommended pressure coefficients on net/elevated net clad scaffolds

Net Clad Scaffold Surrounding the SEB (touching the ground)						
Design Pressure Coefficients	**Windward Face**			**Side Face**		**Leeward Face**
	Zone A	**Zone B**	**Zone C**	**Zone D**	**Zone E**	**Zone F**
	0.37	**0.26**	**0.37**	**- 0.11 (outward)**	**-**	**-**

To calculate the wind forces transferred from the net to the scaffolds, the pressure coefficients from different zones are to be multiplied directly to the projected area of the

net. Also there is no need to consider wind forces on the leeward face of the net clad or elevated net clad scaffold as there is suction of nearly equal magnitude on both sides of the leeward net which cancels the forces.

8.5 Recommendations for Future Work

The following are a few recommendations for future development in the present study;

(1) Further improvements are required for the development of turbulent viscosity for the RANS model and more reliable sub-grid-scale turbulence model.

(2) Aeroelastic wind-tunnel experiments are needed for a clear picture of wind flow around the sheet/net clad scaffolds and a true value of pressure coefficients on the sheet/net clad scaffolds.

(3) The models are required to be analysed both in the wind-tunnel and CFD for different aspect ratios of the façade of the scaffolds.

(4) The present studies on the sheet/net clad scaffold were on a low rise building. However, researches are required for sheet/net clad scaffolds on high rise buildings and buildings with different aspect ratios of height-width-depth.

(5) Researches are required on bare pole scaffolds surrounding a building and shielding effects on the scaffold tubes due to the presence of building.

(6) Researches are also required to be undertaken to determine effects of the interference of the neighbouring building near the sheet/net clad scaffolds on pressures and air flows.

(7) More detailed experimental work is required to further validate the inlet conditions for Reynolds stress turbulence models.

Chapter 1

[1.1] http://en.wikipedia.org/wiki/Scaffolding (Site visited 15.06.2009)

[1.2] Gurcharan Singh, 'Building Construction and Materials' 10th Edition, Standard Book House, Delhi-6, ISBN: 978-81-89401-21-4

[1.3] HSE (Health and Safety Executive), Proceedings of the Conference into Wind Loading on Temporary Structures, Buxton, HSE, UK, May 4th, 1994.

[1.4] http://www.cover-tech.com/curingblankets.htm (Site visited 16.06.2009)

[1.5] H.K. Versteeg, W. Malalasekera, 'An introduction to computational fluid dynamics – The finite volume method, 2nd Edition', Pearson Education Limited, ISBN: 978-0-13-127498-3, 2007.

[1.6] S. Murakami, 'Numerical turbulence simulation; Pictorial results', Research Institute of Industrial Technology, Tokyo University, Journal of Wind Engineering, Japan Association for Wind Engineering, Vol. 25, 1985.

[1.7]` N.G. Wright and G.J. Easom, 'Non-Linear $k-\varepsilon$ Turbulence Model Results for Flow over a Building at Full-Scale', Applied Mathematical Modelling 27(12): 1013-1033, 2003

[1.8] Fluent Users Guide: 6.3, 2006.

Chapter 2

[2.1] M.H.R. Godley and R.G. Beale, 'Sway stiffness of scaffold structures', The Structural Engineer, Vol. 75, No. 1 pp. 4-12, 1997.

[2.2] A. Maitra, 'Potential for reducing accidents by cladding scaffolds', Proceedings of the Conference into Wind Loading on Temporary Structures, Buxton, HSE, UK, May 4th, 1994.

[2.3] P. A. Blackmore, 'The history of wind damage in the UK', Proceedings of the Conference into Wind Loading on Temporary Structures, Buxton, HSE, UK, May 4th, 1994.

[2.4] BS 1139 – 5: 1990/ HD 1000: 1988 Metal Scaffolding – Specification for materials, dimensions, design loads and safety requirements for service and working scaffolds made of prefabricated elements.

[2.5] G. Maddocks, 'Current U.K. practice in cladding scaffolds', Proceedings of the Conference into Wind Loading on Temporary Structures, Buxton, HSE, UK, May 4th, 1994.

[2.6] BS 8093: 1991, ‘Code of practice for the use of safety nets, containment nets and sheets on constructional works’, 1991.

[2.7] DIN 4420- Part 1, ‘Work and guard scaffolding; general regulations; safety requirements; tests’, Beuth Verlag, Berlin (DIN 4420 Teil 1, Arbeits-und Schutzgerüste; Allgemeine Regelungen; Sicherheitstechnische Anforderungen; prüfungen), 1990.

[2.8] H. Nieser, ‘Current German practices in cladding temporary structures’, Proceedings of the Conference into Wind Loading on Temporary Structures, Buxton, HSE, UK, May 4th, 1994.

[2.9] C. J. K. Williams, ‘The structural design of fabric structures to resist wind loading’, Proceedings of the Conference into Wind Loading on Temporary Structures, Buxton, HSE, UK, May 4th, 74-82, 1994.

[2.10] R.E. Brand, ‘Falsework and access scaffolds in tubular steel’, McGraw-Hill 1975.

[2.11] The Concrete Society and The Institution of Structural Engineers, ‘Falsework a joint report’, TRCS 4, London, 1971.

[2.12] S.L. Bragg, ‘Final Report of the Advisory Committee on Falsework’, Her Majesties Stationary Office, London, 1975

[2.13] E. Lightfoot and D. Bhula, ‘The idealisation of scaffold couplers for performance tests and scaffold analysis’, Materieux et Constructions, 10, May-June, 159-167, 1977.

[2.14] E. Lightfoot and D. Bhula, ‘A test rig for scaffold couplers’, Materieux et Constructions, 10, May-June, 168-173, 1977.

[2.15] E. Lightfoot and G. Oliveto, ‘The collapse strength of tubular steel scaffold assemblies’, Proceedings of the institution of Civil Engineers, 63, Part 2, 311-329, 1977.

[2.16] H.S. Harung, E. Lightfoot and D.M. Duggan, ‘The strength of scaffold towers under vertical loading’, The Structural Engineering, Vol. 53, No. 1, pp. 31-39, 1975

[2.17] J. Weinhold, ‘Zur Frage der Geltung versuchsmaessig ermittelter Traglasten von Fassadengerusten (On the validity of experimentally determined load carrying capacities of façade scaffolds)’, Bauingineer, 60, 439-442, 1985.

[2.18] J. Linder and K.C. Frolich, ‘Statische Berechnungen zu Grossversuchen au Fassadengerusten (Structural analysis for full-scale tests on scaffold assemblies)’, Stahlbau, 5, 142-146, 1985.

[2.19] G.E. Vokel, ‘German assessment for the cuplock scaffold system within the comparison of the procedures in different European countries’, Report N25-15404, Part 1, Test Report for CENT/TC53-WG2-N008, 1990.

[2.20] M.H.R. Godley and R.G. Beale, ‘Sway stiffness of scaffold structures’, Structural Engineer, 75, No. 1, 4-12, 1997.

[2.21] CP3: Chapter V-2: 1972 Code of basic data for the design of buildings-Loading: Wind loads.

[2.22] BS 6399-2: 1997, 'Loading for Buildings – Code of practice for wind loads'.

[2.23] HSE (Health and Safety Executive), Proceedings of the Conference into Wind Loading on Temporary Structures, Buxton, HSE, UK, May 4th, 1994.

[2.24] P.A. Blackmore, 'The use of BS 6399: Part 2: wind loads, for the design of temporary structures', Proceedings of the Conference into Wind Loading on Temporary Structures, Buxton, HSE, 61-73, 1994.

[2.25] P.A. Blackmore, 'The history of wind damage in the UK', Proceedings of the Conference into Wind Loading on Temporary Structures, Buxton, HSE, 17-32, 1994.

[2.26] R. Hoxey, 'Full-scale studies of wind-loading on light-weight structures, windbreaks and walls at Silsoe Research Institute', Proceedings of the Conference into Wind Loading on Temporary Structures, Buxton, HSE, 83-98, 1994.

[2.27] P. Schnabel, 'Model experiments on covered scaffolding in wind tunnel', Proceedings of the Conference into Wind Loading on Temporary Structures, Buxton, HSE, 99-116, 1994.

[2.28] P. Schnabel, 'Final report on the research project Fluidic model experiments to determine wind loads on covered façade scaffolding (Abschlußbericht zum Forschungsvorhaben Strömungstechnische Modellversuche zur Ermittlung der Windlasten auf bekleidete Fassadengerüste)', Report A/18/91, LGA Bavaria, Munich, 1993.

[2.29] C. Wilson and E.J. Hollis, 'Research on the effects of wind loading on clad scaffold structures', Proceedings of the Conference into Wind Loading on Temporary Structures, Buxton, HSE, 117-136, 1994.

[2.30] K. Gylltoft, 'Wind loads on sheeted scaffolds, a field study', Swedish National Testing Institute, Technical Report SP-RAPP 1986:27, 1986.

[2.31] M. James, 'The design of flexible clad temporary structures - an intermediate view based on current design', Proceedings of the Conference into Wind Loading on Temporary Structures, Buxton, HSE, 99-116, 1994.

[2.32] K. F. Chung and W.K. Yu, 'Mechanical properties of structural bamboo for bamboo scaffolding', Engineering Structures, 24, pp. 429 442, 2002.

[2.33] K. F. Chung, W. K. Yu and S. L. Chan 'Mechanical properties and engineering data of structural bamboo', Proceedings of international seminar on Bamboo Scaffolds in Building Construction, An Alternative and Supplement to Metal Scaffolds, pp. 1-23, Hong Kong, 2002.

[2.34] K. F. Chung, S. L. Chan and W. K. Yu 'Practical design of bamboo scaffolds', Proceedings of international seminar on Bamboo Scaffolds in Building Construction, An Alternative and Supplement to Metal Scaffolds, pp. 65-88, Hong Kong, 2002.

[2.35] K.F. Chung, S.L. Chan and W.K. Yu 'Recent developments on bamboo scaffolding in building construction', Proceedings of international conference on Advances in Building Technology, Hong Kong, pp. 629-636, 2002.

[2.36] W.K. Yu, K.F. Chang and S.L. Chan, 'Column buckling of structural bamboo', Engineering Structures, 25, pp. 755-768, 2003

[2.37] W.K. Yu, K.F. Chung and S.L. Chan, 'Axial buckling of bamboo columns in bamboo scaffolds', Engineering Structures, 27, pp. 61-73, 2005.

[2.38] S.L. Chan, Z.H. Zhou, W.F. Chen, J.L. Peng, and A.D. Pan, 'Stability analysis of semi-rigid steel scaffolding', Engineering Structures, Vol. 17, No. 8, 568-574, 1995.

[2.39] J.L. Peng, T. Yen, W.F. Chen, S.L. Chan, 'Structural modelling and analysis of scaffold systems', Advances in Steel Structures, Hong Kong, 251-256. 1996

[2.40] J.L. Peng, A.D. Pan, D.V. Rosowsky, W.F. Chen, T. Yen and S.L. Chan, 'High clearance scaffold system during construction – I. Structural modelling and modes of failure', Engineering structures, Vol. 18, No. 3, 247-257, 1996a.

[2.41] J.L. Peng, A.D. Pan, D.V. Rosowsky, W.F. Chen, T. Yen and S.L. Chan, 'High clearance scaffold system during construction – II Structural modelling and modes of failure', Engineering Structures, Vol. 18, No. 3, 257-267, 1996b.

[2.33] M.H.R. Godley and R.G. Beale, 'Analysis of large proprietary access scaffold structures', Proceedings of Design of Temporary Structures as a Means of Access and as a Place of Work, London, 2001.

[2.43] M.H.R. Godley and R.G. Beale, 'Analysis of large proprietary access scaffold structures', Proc. Instn Civil Engrs Structs & Bldgs, 146, pp. 31-39, 2001.

[2.44] M.H.R. Godley and R.G. Beale, 'The K2 prefabricated scaffold system structural tests', Oxford Brookes University, Department of Civil Engineering, Report 340, 2001.

[2.45] C.C. Kao, 'Analysis of safety behaviour for steel scaffold and vertical shore - report', Department of Civil Engineering, National Taiwan University, Taiwan, 1981.

[2.46] T. Yen, W.F. Chen, Y.C. Lin, C.G. Go, M.S. Ju, Y.L. Huang, H.J. Chen, D.V. Rosowsky and A.D. Pan, 'Research of scaffold accident during construction period', (in Chinese), Labor Checking Report, The Council of Labor Affairs, Taipei, Taiwan, 156, 1993.

[2.47] T. Yen, W.F. Chen, Y.C. Lin, Y.L. Huang, H.J. Chen, 'Study of steel scaffold supports subjected to unsymmetrical loads and lateral loads' (in Chinese), Labor Checking Report IOSH 83-S222, The Council of Labor Affairs, Taipei, Taiwan, 197, 1994.

[2.48] T. Yen, W.F. Chen, Y.C. Lin, Y.L. Huang, H.J. Chen, 'Study of the interaction between wooden steel scaffolds and development of collapse warning system' (in Chinese), Labor Checking Report IOSH 84-S121, The Council of Labor Affairs, Taipei, Taiwan, 95, 1995.

[2.49] T. Yen, H.J. Chen, Y.L. Huang, W.F. Chen, R.C. Chi and Y.C. Lin, 'Design of scaffold shores for concrete building during construction', Journal of the Chinese Institute of Engineers, 20(6), 603-614, 1997.

[2.50] Y.L. Huang, H.J. Chen, D.V. Rosowsky and Y.G. Kao, 'Load carrying capacities and failure modes of scaffolding-shoring systems, Part 1: Modelling and Experiments', Structural Engineering and Mechanics, 10 (1), 53-66, 2000.

[2.51] Y.L. Huang, H.J. Chen, D.V. Rosowsky, 'Load carrying capacities and failure modes of scaffolding-shoring systems, Part 2: An analytical model and its closed form solution', Structural Engineering and Mechanics, 10 (1), 67-79, 2000.

[2.52] S.L. Chan, and A.Y.T. Chu, 'Design of metal scaffolds by simulation – An advanced technology in structural steel work design', Metal scaffolding (Falsework) – design, construction & safety, HKISC, pp. 24-40, 2003

[2.53] U.S. Department of Labour, 'Wind Effects on Scaffolding', Wisconsin Safety Newsletter, 1(1), 1-4, 2002.

[2.54] F. Yue, Y. Yuan, G.Q. Li, K.M. Ye, Z.M. Chen and Z.P. Wang, 'Wind load on integral-lift scaffolds for tall building construction', ASCE, Journal of Structural Engineering, 131(5), 816-824, 2005.

[2.55] A. Kaveh and H. Moez, 'Analysis of frames with semi-rigid joints: A graph-theoretical approach', Engineering Structures, Vol. 28, Issue 6, 2006, pp. 829-836, 2006.

[2.56] H. Irtaza, R.G. Beale, M.H.R. Godley, 'Determination of the effects of the wind load on bare tube access scaffold structures using computational fluid dynamics', Proceedings of the fifth International Conference on Advances in Steel Structures (ICASS 2007), Singapore, 637-642, 2007.

[2.57] R.G. Beale, 'Review of Research into scaffold structures', Civil Engineering Computations: Tools and Techniques, B.H.V. Topping, (Ed), Saxe-Coburg Publications, Scotland, Stirlingshire, Scotland, ISBN number 978-1-874672-32-6. 30p, pp. 271-293, 2007

[2.58] J.L. Peng, K.H. Chan, S.L. Chan and W.T. Chen, 'Experimental and analytical studies on steel scaffolds under eccentric loads', Journal of Constructional Steel Research, 65 (2), pp. 422-435, 2009.

[2.59] J.E. Cermak, 'Wind tunnel testing of structures', Journal of American Society of Civil Engineers, Volume 103, No. EM6, December 1977.

[2.60] 'Wind-tunnel studies of building and structures', by ASCE Aerospace division Task Committee on Wind-tunnel Studies of Building and Structures, Journal of Aerospace Engineering, Vol. 9, No. 1, January 1996.

[2.61] E. Simiu, 'Wind-tunnel testing and sector-by-sector approach to wind directionality effects', Journal of Structural Engineering, Vol. 131, No. 7, pp. 1143-1145, July 2005.

[2.62] S. Huang, Q.S. Li and S. Xu, 'Numerical evaluation of wind effects on tall steel building by CFD', Journal of Construction Steel Research, 63(5), 612-627, 2007.

Chapter 3

[3.1] E. Simiu and R.H. Scanlan, 'Wind effects on structures: An introduction to wind engineering', John Wiley & Sons, New York, 1996.

[3.2] R.M. Aynsley, W. Melbourne and B.J. Vickery, 'Architectural aerodynamics', Applied Sciences Publishers Ltd., London, 1977.

[3.3] L. Cochran and R. Derickson, 'Low-rise buildings and architectural aerodynamics', Architectural Science Review, September 2005.

[3.4] T. Von Kármán, 'The Wind and Beyond', Boston Little and Brown, CSU Call No. TL540.V67A3, 1967.

[3.5] A.G. Davenport, 'The response of supertall buildings to wind',Second Century of the Skyscraper Monograph by Council of Tall Buildings and the Urban Habitat, edited by C.S. Beedle, Van Nostrand Reinhold Company, 1988.

[3.6] L.S. Cochran, 'Early days of North American Wind Engineering: An Interview with Professor Cermak about Professor Davenport, Proceedings of the Engineering Symposium to Honour Alan G. Davenport for his forty years of Contributions, University of Western Ontario, London, Canada, June 2002.

[3.7] R.E. Fischer, 'Engineering for Architects'; McGraw Hill, 1980.

[3.8] J.O. Hinze, 'Turbulence - 2nd Edition', McGraw-Hill, New York, 1975.

[3.9] P. Bradshaw, 'An introduction to turbulence and its measurement - 1st Edition', The Common Wealth Library of Science Technology Engineering and Liberal Studies, Pergamon Press, New York, 1971.

[3.10] J.T. Lin and C.J. Apelt, 'Stratified flow over an obstacle; A numerical experiment', Technical Report for the Office of Naval Research, Washington D.C., report No. CER-69-70-JTL-CJA-25, 77 pages, CSU Call No. TA7.C6.1970 (ESBL), January 1970.

[3.11] S. Murakami, 'Numerical turbulence simulation; Pictorial results', Research Institute of Industrial Technology, Tokyo University, Journal of Wind Engineering, Japan Association for Wind Engineering, Vol. 25, 1985.

[3.12] S. Murakami, M. Shoji, A. Mochinda, Y. Ishida, Y. and Y. Hayashi, 'Numerical simulation of flow field around Texas Tech Building by Large Eddy Simulation', American Society of Civil Engineers, 10th Structural Congress, Texas, April 1992.

[3.13] H. Tennekes and J.L. Lumley, 'A first course in turbulence – 12th Edition', The MIT Press, 1989.

[3.14] H.W. Tieleman, 'Wind tunnel simulation of wind loading on low-rise structures', Journal of Wind Engineering and Industrial Aerodynamics, Vol. 91, Issues 12-15, pp. 1627-1649, 2003.

[3.15] C.J. Baker, 'Wind engineering – Past, present and future', Journal of Wind Engineering and Industrial Aerodynamics, Vol. 95, Issues 9-11, pp. 843-870, 2007.

[3.16] J.E. Cermak, 'Application of fluid mechanics to wind engineering', A Freeman Scholar Lecture, Journal of Fluids Engineering, American Society of Mechanical Engineers, Volume 97, No. 1, March 1975.

[3.17] N.J. Cook, 'The designer's guide to wind loading of building structures - Part 1', Butterworths publishing, London, 1985.

[3.18] T. Lawson, 'Building Aerodynamics', Imperial College Press, London, ISBN: 1-86094-187-7, 2001.

[3.19] R.P. Richards, R.P. Hoxey, B.D. Connell, D.P. Lander, 'Wind-tunnel modelling of Silsoe Cube', Journal of Wind Engineering and Industrial Aerodynamics, Vol. 95, 9-11, pp. 1384-1399, 2007.

[3.20] ESDU 85020, Issued October 1985, with amendments A to G, August 2001.

[3.21] C. Scruton, 'The Use of Wind Tunnels in Industrial Aerodynamics Research', National Physical Laboratories, Great Britain, NPL/Aero/411, p. 53, 1960.

[3.22] J.C. Kaimal, 'The Atmospheric Boundary Layer; Its Structure and Measurement', Indian Institute of Tropical Meteorology Visiting Professorship Program, Shivajinagar, Pune, February 1988.

[3.23] H.W. Tieleman, 'Problems associated with flow modelling procedures for low-rise structures', Summary papers for the Eighth International Conference on Wind Engineering, University of Western Ontario, July 1991.

[3.24] H.W. Tieleman, 'Wind tunnel simulation of wind loading on low-rise structures', Journal of Wind Engineering and Industrial Aerodynamics, Vol. 91, Issues 12-15, pp. 1627-1649, 2003.

[3.25] N.J. Cook, 'The designer's guide to wind loading of building structures - Part 1', Butterworths publishing, London, 1985.

[3.26] N.J. Cook, 'The designer's guide to wind loading of building structures - Part 2 Static structures', Butterworths publishing, London, 1990.

[3.27] H.W. Tieleman, D. Surry, J.X. Lin, 'Characteristics of mean and fluctuating pressure coefficients under corner (delta wing) vortices', Journal of wind engineering and industrial aerodynamics, Vol. 52, pp. 263-275, May 1994.

Chapter 4

[4.1] H.K. Versteeg, W. Malalasekera, 'An introduction to computational fluid dynamics: finite volume method – 2nd Edition', Pearson - Prentice Hall Publication, ISBN: 978-0-13-127498-3, 2007.

[4.2] S. Huang, Q.S. Li, S. Xu, 'Numerical evaluation of wind effects on a tall steel building by CFD', Journal of Constructional Steel, Vol. 63, Issue 5, pp. 612-627, 2007.

[4.3] D.M. Summers, T. Hanson and C.B. Wilson, 'Validation of computer simulation of wind over a building model', Journal of Building and Environment, Vol. 21, pp. 97-111, 1986.

[4.4] H.E. Mathews, 'Prediction of wind generated pressure distribution around buildings', Journal of Wind Engineering and Industrial Aerodynamics, Vol. 25, pp. 219-228, 1987.

[4.5] S. Murakami, A. Mochida, '3D Numerical simulation of airflow around a cubic model by means of $k-\varepsilon$ model', Journal of Wind Engineering and Industrial Aerodynamics, Elsevier, Amsterdam, Netherlands, Vol. 31, pp. 283-303, 1988.

[4.6] S. Murakami, A. Mochida, K. Hibi, '3D Numerical simulation of airflow around a cubic model by means of LES', Journal of Wind Engineering and Industrial Aerodynamics, Elsevier, Amsterdam, Netherlands, Vol. 25, pp. 291-305, 1987.

[4.7] S. Murakami, A. Mochida, 'Past, present and future of CWE: The view from 1999', The 10th ICWE, Copenhagen, Denmark, 1999.

[4.8] Acheson, D. J., Elementary Fluid Dynamics, Oxford Applied Mathematics and Computing Science Series, Oxford University Press, ISBN 0198596790, 1990.

[4.9] A.D. Young,' Boundary Layers', BSP Professional Books, Blackwell Scientific Publications Ltd, Oxford, UK, ISBN 0 632 02122 5, 1989.

[4.10] L. D. Landau, Lifshitz, E. M. (1987), Fluid mechanics, Course of Theoretical Physics, **6** (2nd revised ed.), Pergamon Press, ISBN 0 08 033932 8, OCLC 15017127, 1987.

[4.11] H. Schlichting and K. Gersten, 'Boundary layer theory', 8th Revised and Enlarged Edition, Springer Publications, USA, ISBN: 978-3540662709.

[4.12] Fluent 6.3 2006, Lecture notes.

[4.13] H. Tennekes and J.L. Lumley, 'A first course in turbulence', The MIT Press, Cambridge, UK, ISBN: 978-0262200196, 1972.

[4.14] S. Murakami, 'Overview of turbulence models applied in CWE', Institute of Industrial Science, University of Tokyo, Japan, 1997.

[4.15] C.T. Shaw, 'Using computational fluid dynamics', Prentice Hall, New York, USA, ISBN: 978-0139287145, 1992.

[4.16] B.E. Launder, Lecture notes of ICASE/LaRC Short course on Turbulence Modelling and Prediction, March 1994 in T.B. Gatski, M.Y. Hussaini and J.L. Lumley (1996), 'Simulation and modelling of turbulent flows', Oxford University Press, UK.

[4.17] Fluent 6.3 User's Guide, September 2006.

[4.18] T.B. Gatski, M.Y. Hussaini, and J.L. Lumley, 'Simulation and modelling of turbulent flows', ICASE/LaRC Series in Computational Science and Engineering, Oxford University Press, Oxford, UK, ISBN: 978-0195106435, 1996.

[4.19] B.E. Launder and D.B. Spalding, 'Lectures in mathematical models of turbulence', Academic Press, London, UK, ISBN: 0124380506, 1972.

[4.20] B.E. Launder and D.B. Spalding, 'The numerical computation of turbulent flows', Computational Methods in Applied Mechanics and Engineering, Vol. 3, pp. 537-566, 1974.

[4.21] S.Z. Shuja, B.S. Yilbas and M.O. Budai. 'Gas Jet impingement on a surface having a limited constant heat flux area: Various turbulence models', Numerical Heat Transfer Part A Applications, 8th January 1999.

[4.22] V.C. Patel, W. Rodi, G. Scheuerer, 'Turbulence models for near wall and low Reynolds number flows: A review', AIAA Journal, Vol. 23, No. 9, pp. 1308-1319, 1985.

[4.23] R.F. Mentor and H. Grotjans, 'Application of advance turbulence models to complex industrial flows', AEA Technology GmbH, Straudenfeldweg, 12 D-83624, Otterfing, Germany, 1999.

[4.24] D.C. Wilcox, 'Turbulence modelling for CFD', DCW Industries Inc. Canada, ISBN: 0963605100, 1994.

[4.25] V. Yakhot, S.A. Orszag, S. Thangam, T.B. Gatski and C.G. Speziale, 'Development of turbulence models for shear flows by a double expansion technique, Phys. Fluids A, Vol. 4, No. 7, pp. 1510-1520, 1992.

[4.26] B.E. Launder, G.J. Reece and W. Rodi, 'Progress in the development of a Reynolds-stress turbulence closure', Journal of fluid mechanics, Vol. 68, pt. 3, pp. 537-566, 1975.

[4.27] M.A. Leschziner, 'Modelling engineering flows with Reynolds stress turbulence closure', Journal of wind engineering and industrial aerodynamics, Vol. 35, pp. 21-47, Elsevier, Amsterdam, Netherlands, 1990.

[4.28] C.B. Jacobsen, 'Large eddy simulation of confined swirling flow: numerical part', Ph.D. Thesis submitted to Aalborg University, Institute of Energy Technology, 1997.

[4.29] M. Ciofalo and M.W. Collins, 'Large eddy simulations of turbulent flow in plane and rib-roughened channels', Proceedings of the 6th International Conference on Numerical Methods in Laminar and Turbulent Flows, Swansea, UK, July 1989.

[4.30] M. Germano, P. Piomelli, P. Moin and W.H. Cabot, 'A dynamic sub-grid-scale eddy viscosity model', Physics of Fluids A3, Vol. 7, pp. 1769-1765, 1991.

[4.31] Sowjanya Vijiapurapu. 'Simulation of turbulent flow in a ribbed pipe using Large Eddy Simulation', Numerical Heat Transfer Part A Applications, January 2007.

[4.32] S.E. Kin, 'Large eddy simulation using unstructured meshes and dynamic sub-grid-scale turbulence models', Technical Report AIAA-2004-2548, American Institute of Aeronautics and Astronautics, 34th Fluid Dynamics Conference and Exhibit, June 2004.

[4.33] F. Nicoud and F. Ducros, 'Sub-grid-scale stress modelling based on the square of the velocity gradient tensor', Flow, Turbulence and Combustion, 62(3): 183-200, 1999.

[4.34] B.N. Murthy, 'Assessment of standard k-@e, RSM and LES turbulence models in a baffled stirred vessel agitated by various impeller designs', Chemical Engineering Science, 11, 2008.

[4.35] C.G. Speziale, 'Analytical method for the derivation of Reynolds stress closures in turbulence', Annual review of fluid mechanics, Vol. 23, pp. 107-157, 1991.

[4.36] M. Tushiya, A. Mochida, Y. Ishida, S. Murakami and K. Konda, 'Development of new $k-\varepsilon$ model for flow and pressure field around a bluff body', 2nd International Symposium on Computational Wind Engineering, 1996.

[4.37] S. Murakami, A. Mochida, Y. Hayashi and S. Sakamoto, 'Numerical study on velocity pressure field and wind forces for bluff bodies by $k-\varepsilon$, ASM and LES', Journal of Wind Engineering and Industrial Aerodynamics', Vol. 41-44, pp. 2841-2852, Elsevier, 1992.

[4.38] N.G. Wright, 'Non-linear k-@e turbulence model results for flow over a building at full-scale', Applied Mathematical Modelling, 12, 2003.

[4.39] S. Murakami, 'Computational wind engineering', Journal of Wind Engineering and Industrial Aerodynamics', Vol. 35, pp. 4-6, Elsevier, 1990.

[4.40] S.A. Orzag, 'Lecture notes of ICASE/LaRC short course on Turbulence Modelling and Prediction, March 1994, in Gatski, T.B., Hussaini, M.Y. and Lumley, J.L. (1996). 'Simulation and modelling of turbulent flows', Oxford University Press, UK, 1994.

Chapter 5

[5.1] www.silsoeresearch.org.uk/envir-wind-waste/wind.html (Site visited 17.07.2009)

[5.2] H.W. Tieleman, D. Surry, K.C. Mehta, 'Full/model scale comparison of surface pressures on Texas Tech. experimental building', Journal of Wind Engineering and Industrial Aerodynamics, pp.1-23, 61, 1996.

[5.3] M. Kasperski and R. Hoxey, 'Extreme-value analysis for observed peak pressures on the Silsoe cube', Journal of Wind Engineering and Industrial Aerodynamics, pp. 994-1002, 96, 2008.

[5.4] P.J. Richards, R.P. Hoxey, B.D. Connell, D.P. Lander, 'Wind-tunnel modelling of Silsoe Cube', Journal of Wind Engineering and Industrial Aerodynamics, pp. 1384-1399, 95, 2007.

[5.5] P.J. Richards and R.P. Hoxey, 'Wind loads on the roof of a 6 m cube', Journal of Wind Engineering and Industrial Aerodynamics, pp. 984-993, 96, 2008.

[5.6] www.red.com.hk

[5.7] www.esterline.com (manual)

[5.8] N.J. Cook and J.R. Mayne, 'A novel working approach to the assessment of wind loads for equivalent static design a refined working approach to the assessment of wind loads for equivalent static design', Journal of Wind Engineering and Industrial Aerodynamics, Vol. 8, Issue 3, pp.299-301, 1981.

[5.9] S. Huang, Q.S. Li and S. Xu, 'Numerical evaluation of wind effects on tall steel building by CFD', Journal of Construction Steel Research, 63(5), 612-627, 2007.

[5.10] H. K. Versteeg and W. Malalasekera, 'An introduction to computational fluid dynamics – the finite volume method', 2nd Edition, Prentice Hall Publication, ISBN: 978-0-13-127498-3, 2007.

[5.11] Fluent 6.3 Inc. The user's guide 2006.

[5.12] D.C. Wilcox, 'Turbulence modelling for CFD', DCW Industries, Inc., La Canada, California, ISBN: 0-9636051-0-0, 1994.

[5.13] R. Smirnov, S. Shi, I. Celik, 'Random flow generation technique for large eddy simulations and particle-dynamics modelling', Journal of Fluids Engineering, 123: 359-71, 2001.

[5.14] H. Choi and P. Moin, 'Effects of the computational time step on numerical solutions of turbulent flow', Journal of Computational Physics, Vol. 113, Part 1, pp. 1-4, 1994.

[5.15] C.B. Jacobsen, 'Large eddy simulation of confined swirling flow: numerical part', PhD thesis submitted to Aalborg University, Institute of Energy Technology, 1997.

[5.16] H.W. Tieleman, 'Wind tunnel simulation of wind loading on low-rise structures', Journal of Wind Engineering and Industrial Aerodynamics, Vol. 91, Issues 12-15, pp. 1627-1649, 2003.

Chapter 6

[6.1] L.Z. Zhang, 'Flow maldistribution and thermal performance deterioration in a cross-flow air to air heat exchanger with plate-fin cores', International Journal of Heat and Mass Transfer, 09, 2009.

[6.2] S. Li, 'CFD model of apple atmospheric freeze drying at low temperature', Drying Technology, 07, 2007.

[6.3] Fluent Users Guide 6.3, 2006.

[6.4] R.F. Craig, 'Soil Mechanics, 6th edition', London: E & FN Spon, ISBN: 0419224505, 1997.

[6.5] Smith and Van Winkle, Am. Inst. Chem. Eng. J., 4:266-268, 1958.

[6.6] R. H. Perry, D. W. Green and J. O. Maloney, 'Perry's Chemical Engineers' Handbook', McGraw-Hill, New York, 6th edition, 1984.

[6.7] G. Singh, 'Building Construction and Materials' 10th Edition, Standard Book House, Delhi-6, ISBN: 978-81-89401-21-4.

[6.8] Plint and Partners Wind Tunnel Manual, Mechanical Engineering Departments, Oxford Brookes University, Oxford, UK.

Chapter 7

[7.1] G.M. Richardson and D. Surrey, 'The Silsoe building: a comparison of pressure coefficients and spectra at model and full-scale', Journal of Wind Engineering and Industrial Aerodynamics, Vol. 44, pp. 1055-1064, 1992.

[7.2] N.J. Cook, 'The designer's guide to wind loading on building structures: Part – I', Butterworths, London, England, 1986.

[7.3] N.J. Cook, 'The designer's guide to wind loading on building structures: Part – II', Butterworths, London, England, 1986.

[7.4] N. Holscher and H.J. Niemann, 'Towards quality assurance to wind-tunnel tests: A comparative testing program of the Windtechnologische Gesellschaft', Journal of Wind Engineering and Industrial Aerodynamics, Vol. 74-76, pp. 599-608, 1998.

[7.5] H. Irtaza, R.G. Beale and M.H.R. Godley, 'Experimental study on sheet clad scaffold', Report No. 397, School of the Built-Environment, Oxford Brookes University, ISBN 978-0-9556254-3-5, 2009.

[7.6] N.G. Wright and G.J. Easom, 'Non-Linear $k-\varepsilon$ Turbulence Model Results for Flow over a Building at Full-Scale', Applied Mathematical Modelling 27(12): 1013-1033, 2003.

[7.7] S. Huang, Q.S. Li and S. Xu, 'Numerical evaluation of wind effects on tall steel building by CFD', Journal of Construction Steel Research, 63(5), 612-627, 2007.

[7.8] H.K. Versteeg and W. Malalasekera, 'An introduction to computational fluid dynamics: The finite volume method', Second Edition, Pearson, Prentice Hall, 2007.

[7.9] P.J. Richards and R.P. Hoxey, 'Appropriate boundary conditions for computational wind engineering models using the $k-\varepsilon$ turbulence model', Journal of Wind Engineering and Industrial Aerodynamics, Vol. 46-47, pp. 145-153, 1993.

[7.10] Fluent Users Guide 6.3, 2006.

[7.11] P.J. Richards and R.P. Hoxey, 'Spectral models of the atmospheric surface layer', 10th ICWE, Copenhagen, June 1999.

Chapter 8

[8.1] H. Irtaza, R.G. Beale and M.H.R. Godley, 'Experimental study on sheet clad scaffold', Report No. 397, School of the Built-Environment, Oxford Brookes University, ISBN 978-0-9556254-3-5, 2009.

[8.2] S. Huang, Q.S. Li and S. Xu, 'Numerical evaluation of wind effects on tall steel building by CFD', Journal of Construction Steel Research, 63(5), 612-627, 2007.

1. Flow Pattern Around Silsoe Experimental Building

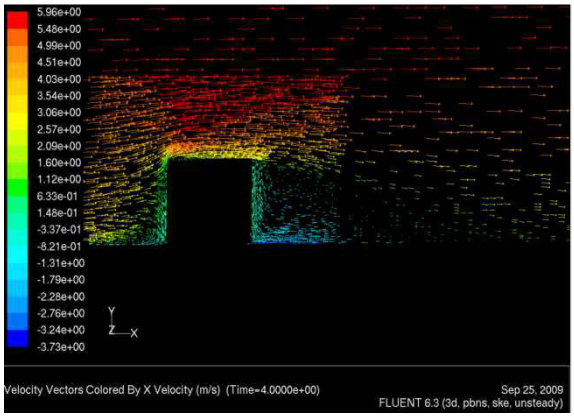

Figure A.1 Velocity vector showing the flow field in section, standard $k-\varepsilon$ model

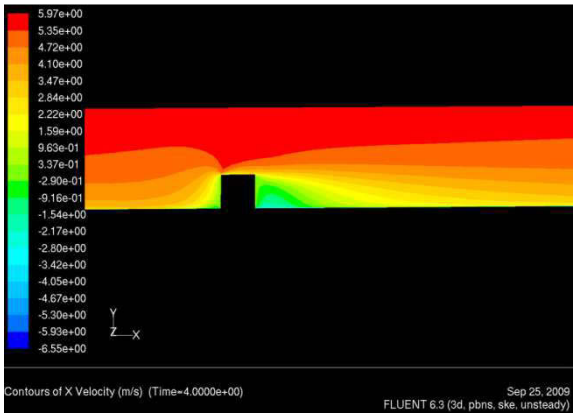

Figure A.2 X-velocity contour showing the flow field in section, standard $k-\varepsilon$ model

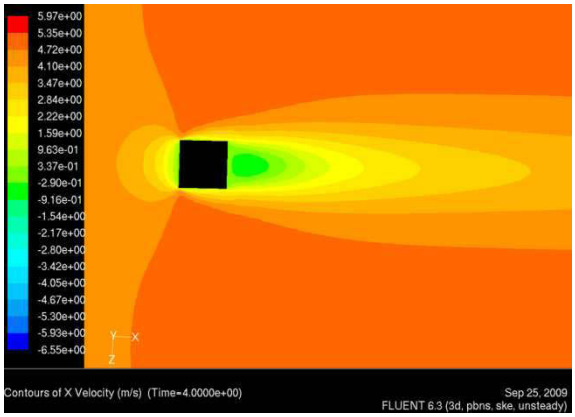

Figure A.3 X-velocity contour showing the flow field in plan, standard $k-\varepsilon$ model

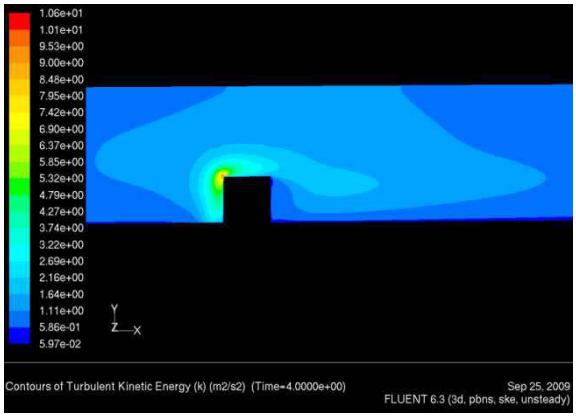

Figure A.4 Turbulent kinetic energy contour on SEB in section, standard $k-\varepsilon$ model

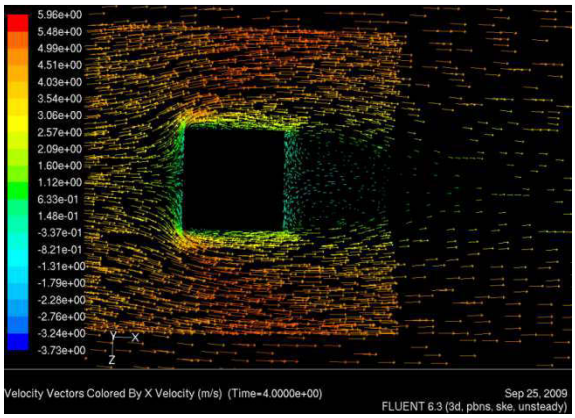

Figure A.5 Velocity vector showing the flow field in plan, standard $k-\varepsilon$ model

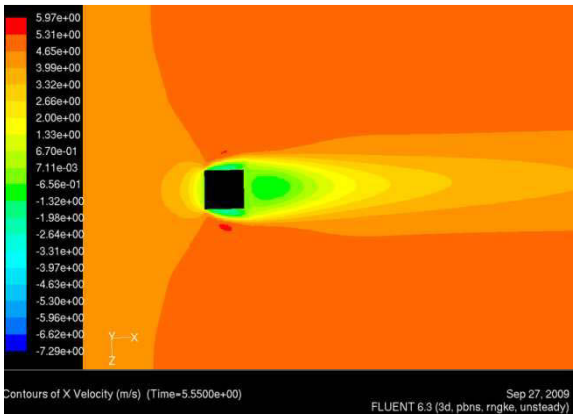

Figure A.6 X-velocity contours on SEB in plan, RNG $k-\varepsilon$ model

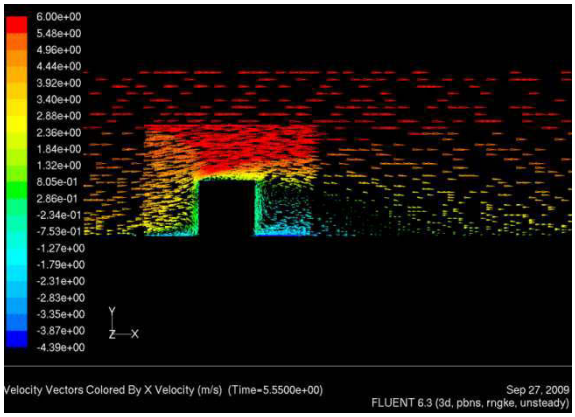

Figure A.7 Velocity vector showing the flow field in section, RNG $k-\varepsilon$ model

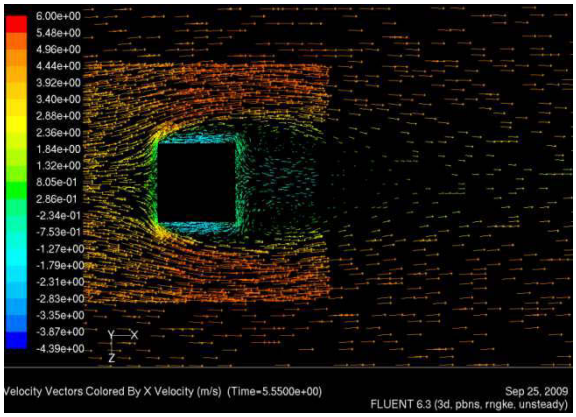

Figure A.8 Velocity vector showing the flow field in plan, RNG $k-\varepsilon$ model

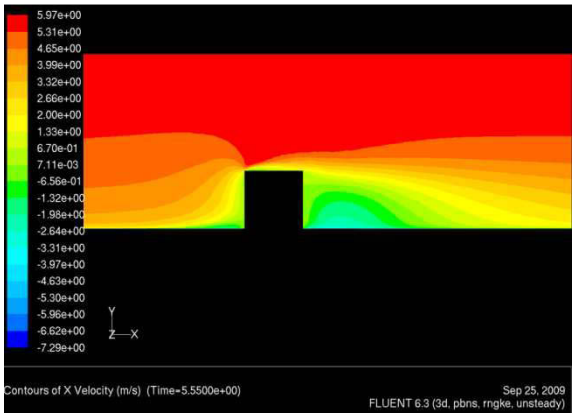

Figure A.9 X-velocity contour showing the flow field in section, RNG $k-\varepsilon$ model

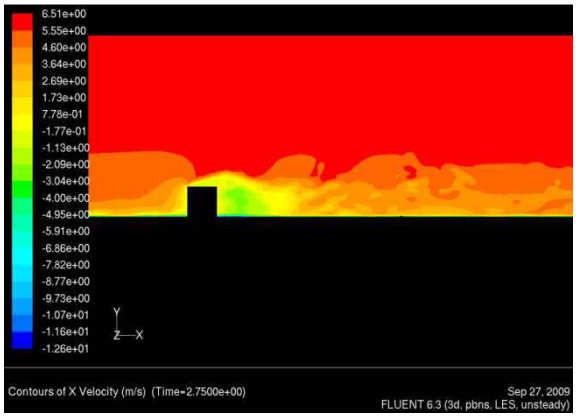

Figure A.10 Contours of X-velocity on SEB in section, LES model

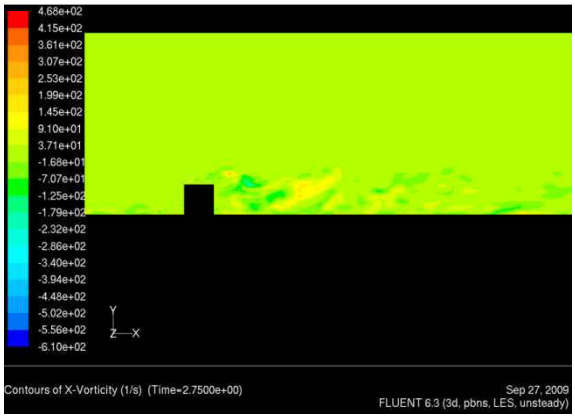

Figure A.11 Contours of X-vorticity on SEB in section, LES model

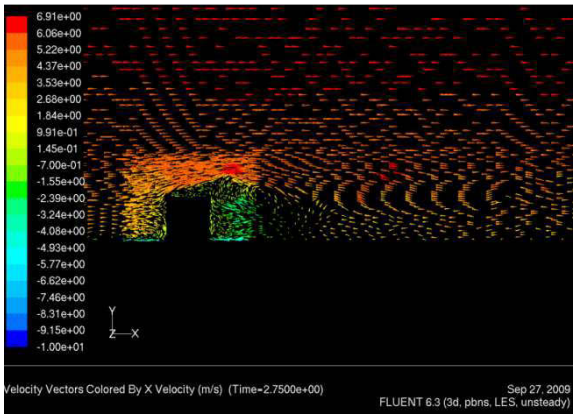

Figure A.12 Velocity vector on SEB in section, LES model

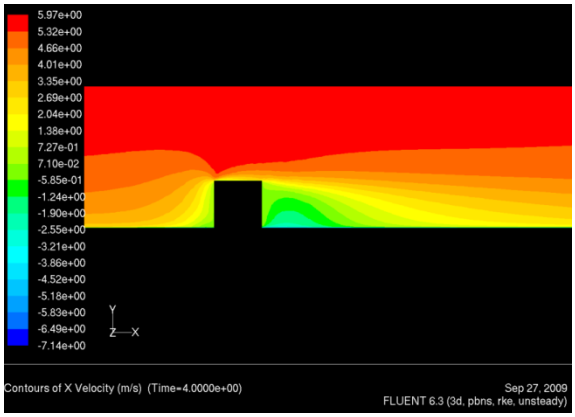

Figure A.13 Contours of X-velocity on SEB in section, Realizable $k-\varepsilon$ model

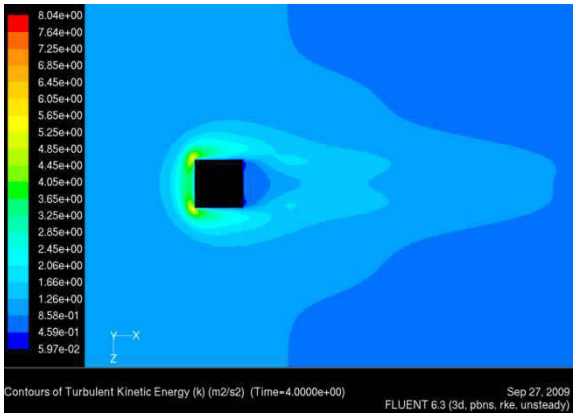

Figure A.14 Contours of turbulent kinetic energy on SEB in plan, Realizable $k-\varepsilon$ model

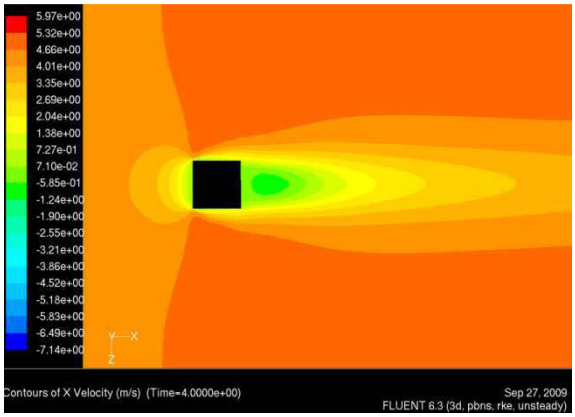

Figure A.15 Contours of X-velocity on SEB in plan, Realizable $k-\varepsilon$ model

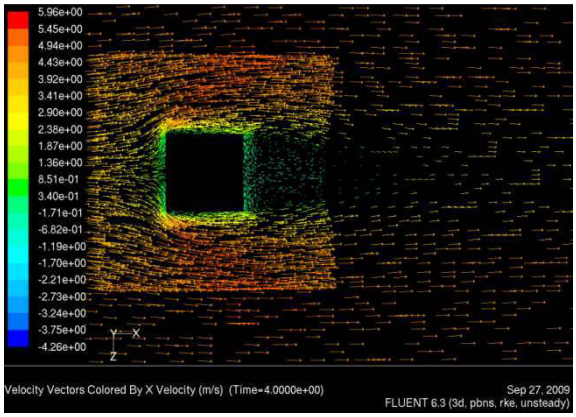

Figure A.16 Velocity vector on SEB in plan, Realizable $k-\varepsilon$ model

2. Flow Pattern Around Sheet Clad Scaffolds Surrounding Silsoe Experimental Building

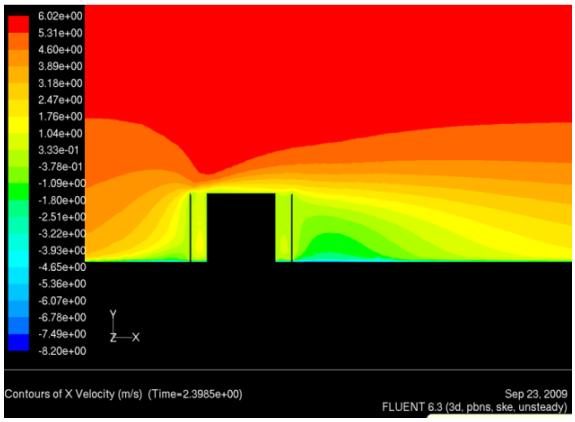

Figure A.17 X-velocity contours on sheet clad scaffold surrounding SEB in section, standard $k-\varepsilon$ model

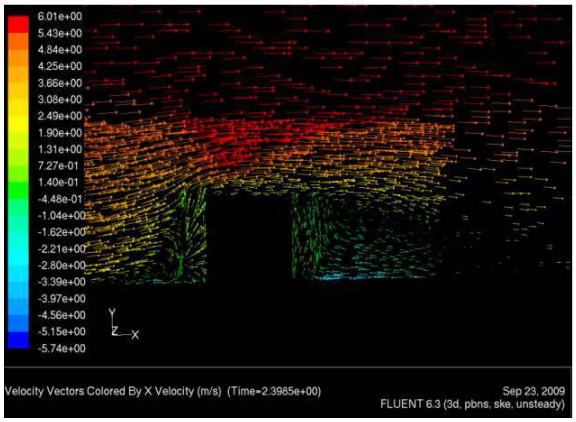

Figure A.18 X-velocity vectors on sheet clad scaffold surrounding SEB in section, standard $k-\varepsilon$ model

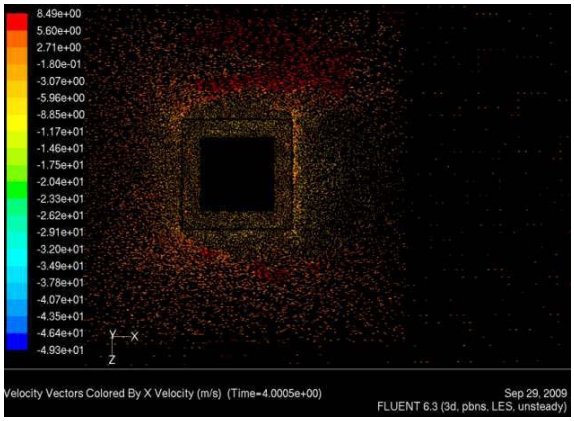

Figure A.19 X-velocity vectors on sheet clad scaffold surrounding SEB in plan, LES model

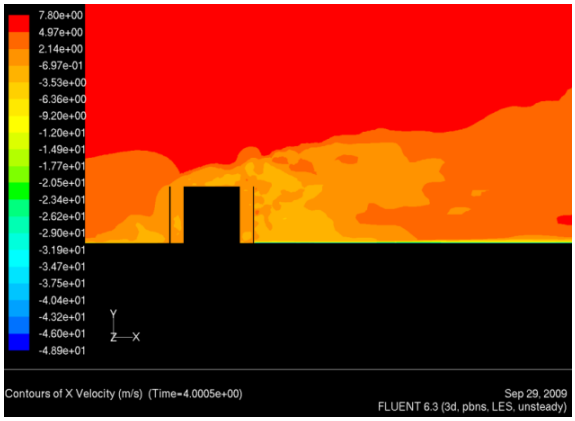

Figure A.20 X-velocity contours on sheet clad scaffold surrounding SEB in section, LES model

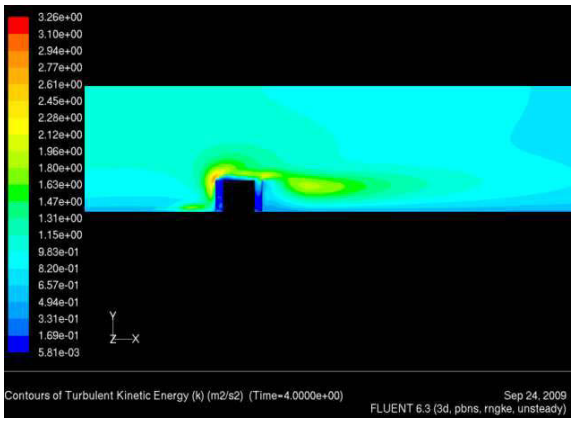

Figure A.21 Turbulent kinetic energy contours on sheet clad scaffold surrounding SEB in section, RNG $k-\varepsilon$ model

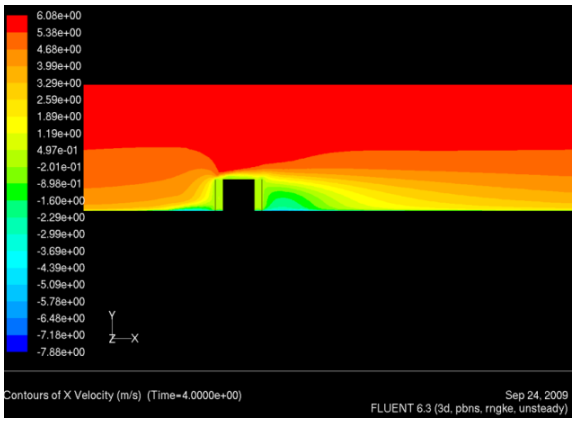

Figure A.22 X-velocity contours on sheet clad scaffold surrounding SEB in section, RNG $k-\varepsilon$ model

3. Flow Pattern Around Elevated Sheet Clad Scaffolds Surrounding Silsoe Experimental Building

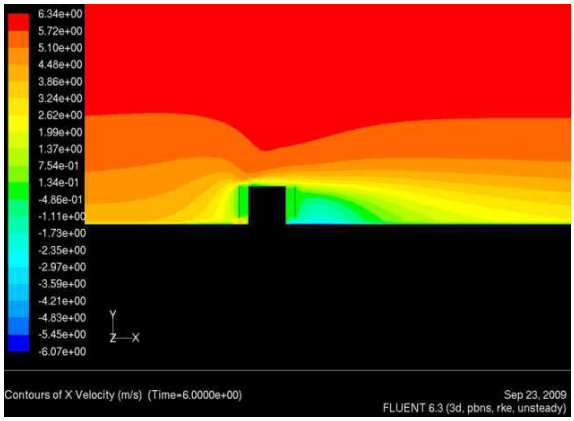

Figure A.23 X-velocity contours on elevated sheet clad scaffold surrounding SEB in section, Realizable $k-\varepsilon$ model

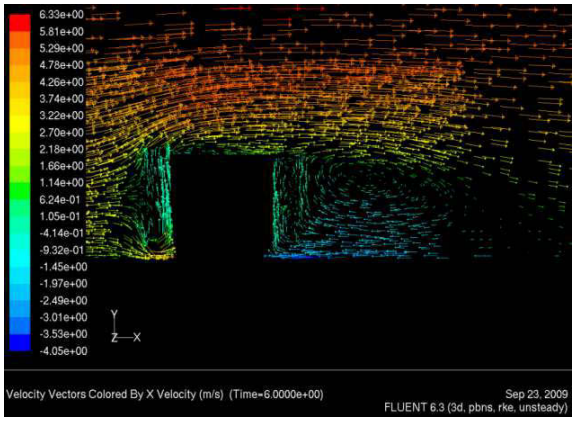

Figure A.24 Velocity vectors on elevated sheet clad scaffold surrounding SEB in section, Realizable $k-\varepsilon$ model

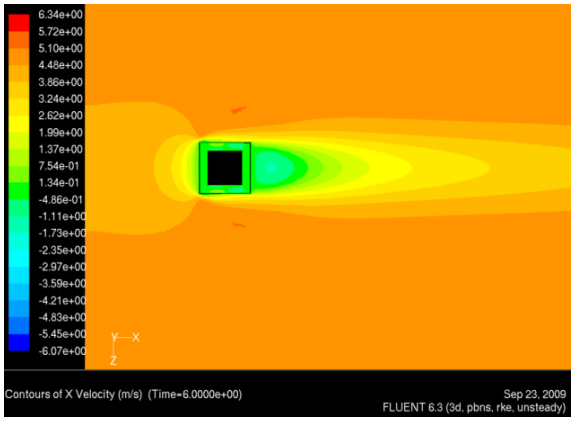

Figure A.25 X-velocity contours on elevated sheet clad scaffold surrounding SEB in plan, Realizable $k-\varepsilon$ model

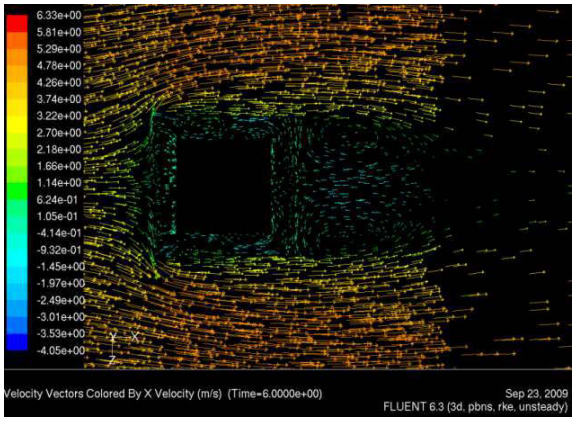

Figure A.26 Velocity vector on elevated sheet clad scaffold surrounding SEB in plan, Realizable $k-\varepsilon$ model

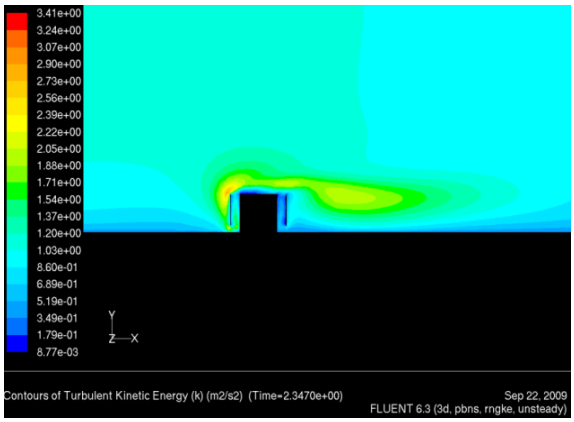

Figure A.27 Turbulent kinetic energy contours on elevated sheet clad scaffold surrounding SEB in plan, RNG $k-\varepsilon$ model

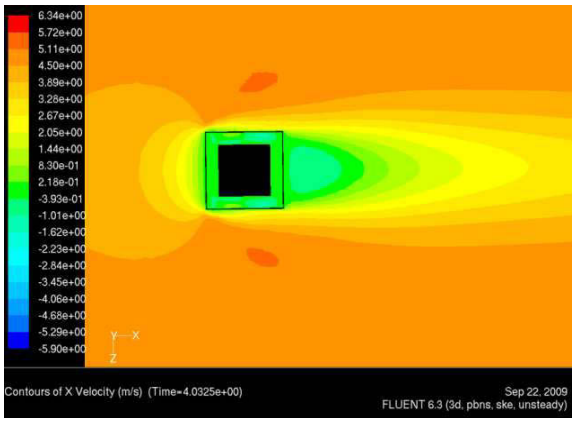

Figure A.28 X-velocity contours on elevated sheet clad scaffold surrounding SEB in plan, standard $k-\varepsilon$ model

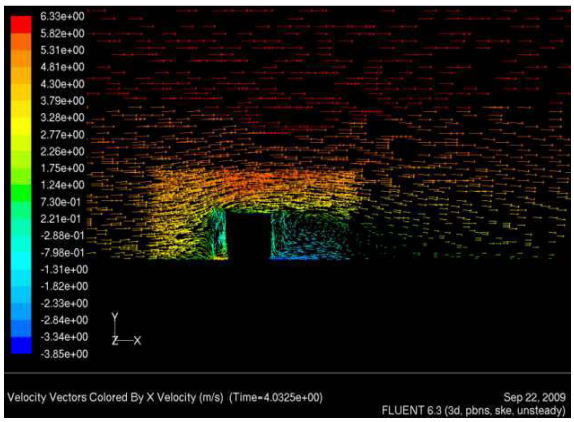

Figure A.29 Velocity vector on elevated sheet clad scaffold surrounding SEB in section, standard $k-\varepsilon$ model

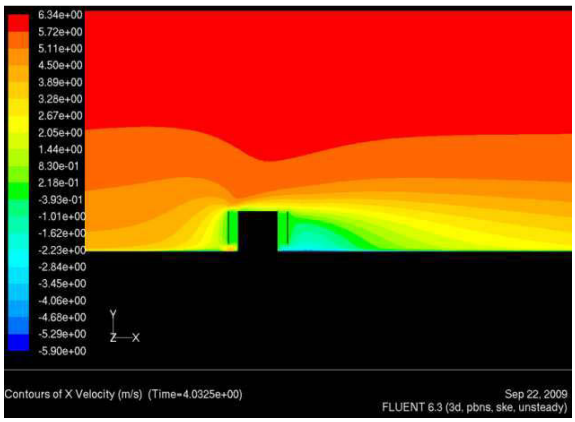

Figure A.30 X-velocity contours on elevated sheet clad scaffold surrounding SEB in section, standard $k-\varepsilon$ model

4. *Flow Pattern Around Net Clad Scaffolds Surrounding Silsoe Experimental Building*

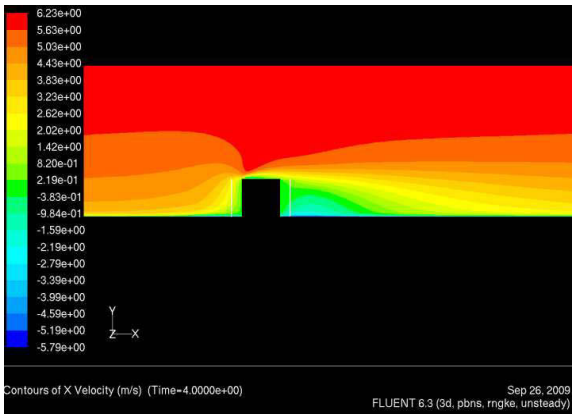

Figure A.31 X-velocity contours for Type A Net in section, RNG $k-\varepsilon$ model

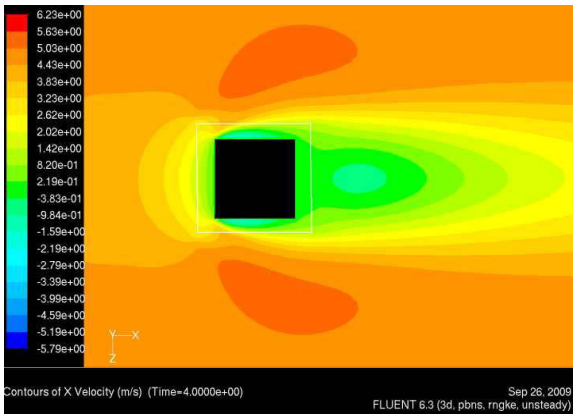

Figure A.32 X-velocity contours for Type A Net in plan, RNG $k-\varepsilon$ model

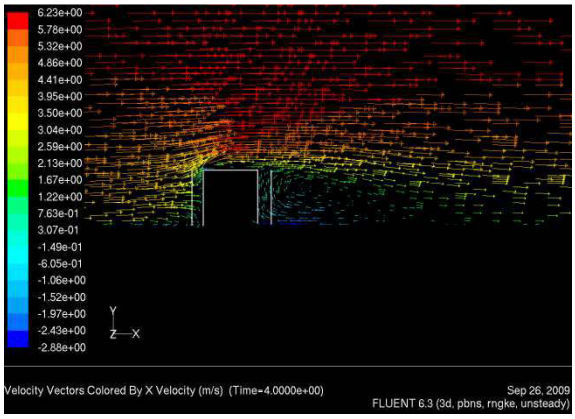

Figure A.33 Velocity vector for Type A Net in section, RNG $k-\varepsilon$ model

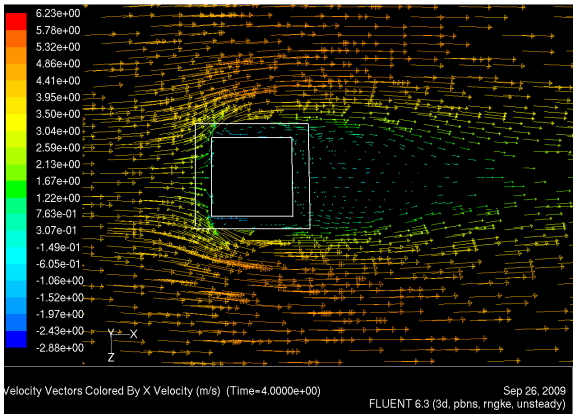

Figure A.34 Velocity vector for Type A Net in plan, RNG $k-\varepsilon$ model

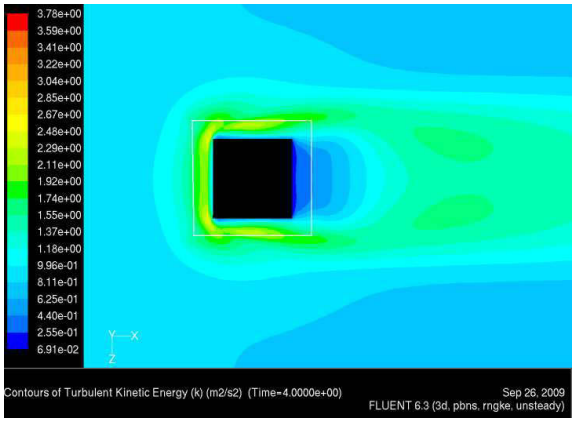

Figure A.35 Turbulent Kinetic energy contours for Type A Net in plan, RNG $k-\varepsilon$ model

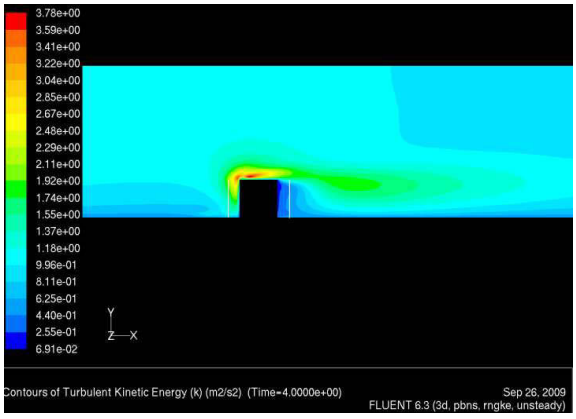

Figure A.36 Turbulent Kinetic energy contours for Type A Net in section, RNG $k-\varepsilon$ model

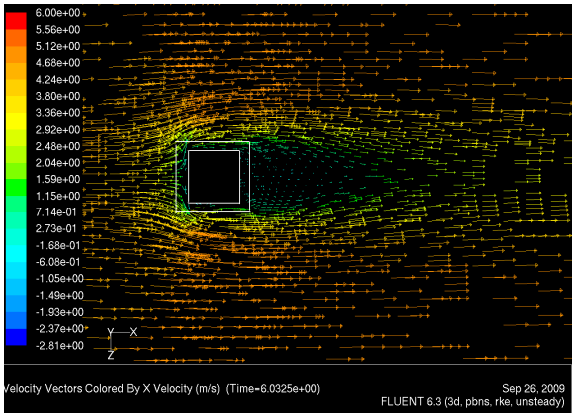

Figure A.37 Velocity vector for Type A Net in plan, Realizable $k-\varepsilon$ model

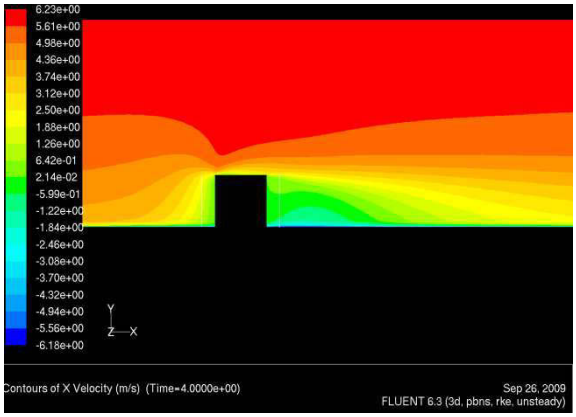

Figure A.38 X-velocity contours for Type A Net in section, Realizable $k-\varepsilon$ model

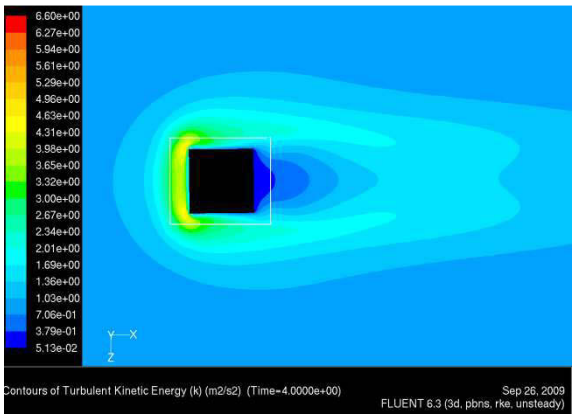

Figure A.39 Turbulent kinetic energy contours for Type A Net in plan, Realizable $k-\varepsilon$ model

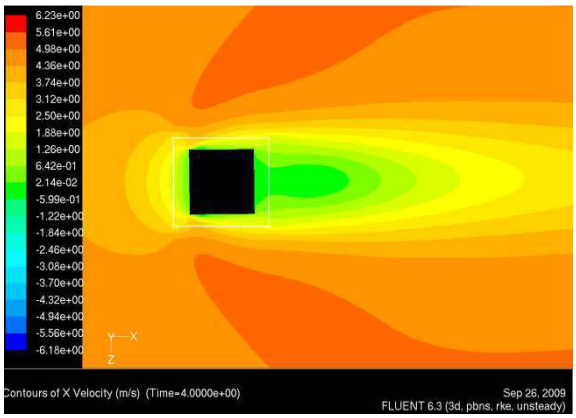

Figure A.40 X-velocity contours for Type A Net in plan, Realizable $k-\varepsilon$ model

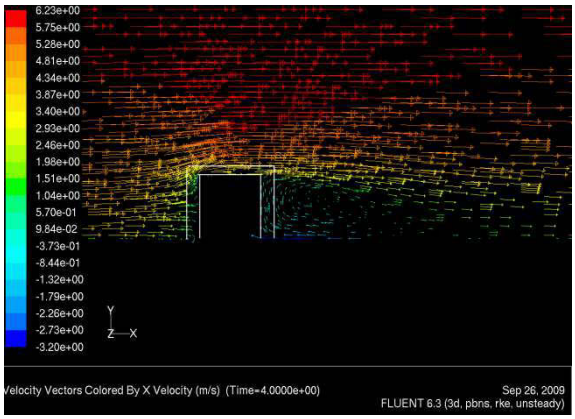

Figure A.41 Velocity vector for Type A Net in section, Realizable $k-\varepsilon$ model

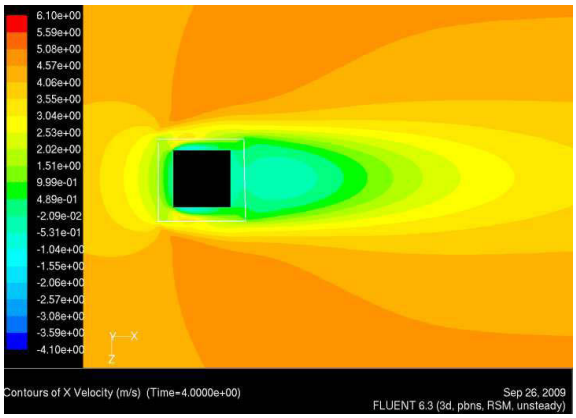

Figure A.42 X-velocity contours for Type A Net in plan, Reynolds stress model

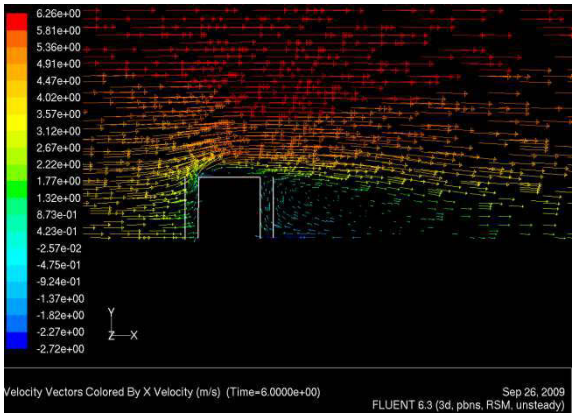

Figure A.43 Velocity vector for Type A Net in section, Reynolds stress model

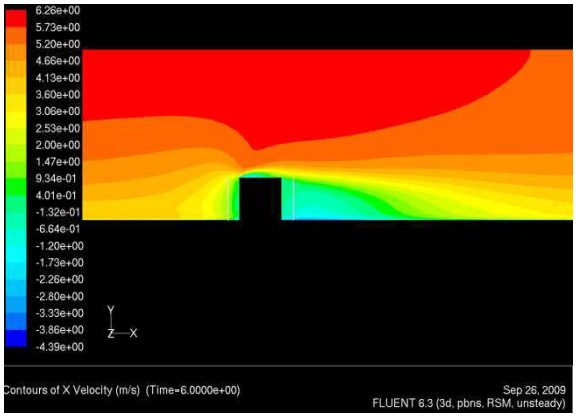

Figure A.44 X-velocity contours for Type A Net in section, Reynolds stress model

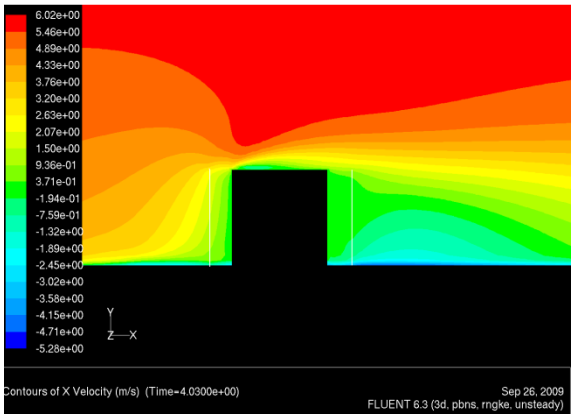

Figure A.45 X-velocity contours for Type B Net in section, RNG $k-\varepsilon$ model

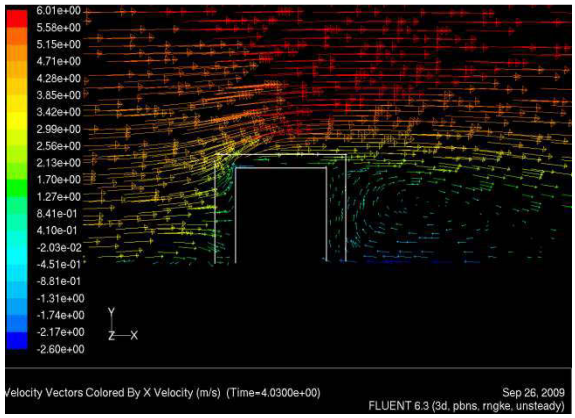

Figure A.46 Velocity vector for Type B Net in section, RNG $k-\varepsilon$ model

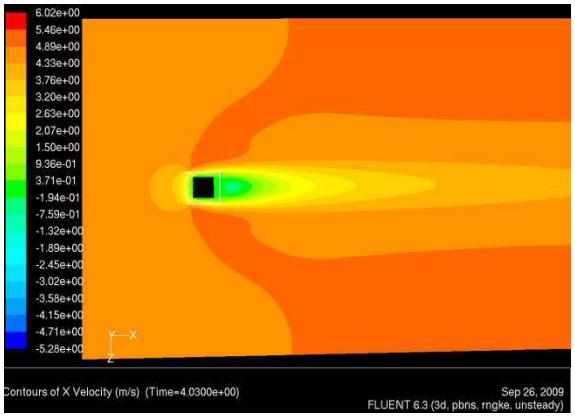

Figure A.47 X-velocity contours for Type B Net in plan, RNG $k-\varepsilon$ model

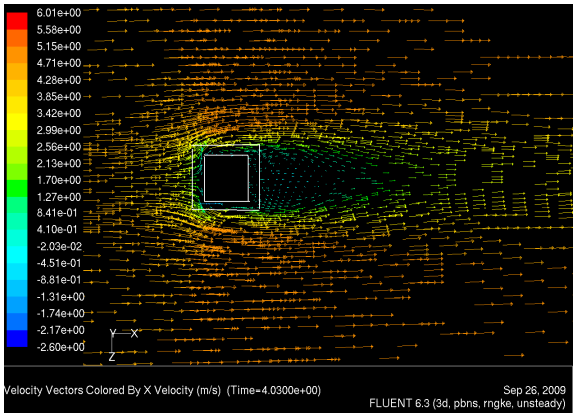

Figure A.48 Velocity vector for Type B Net in plan, RNG $k-\varepsilon$ model

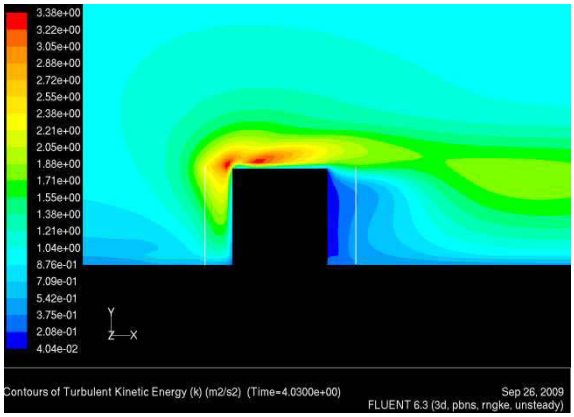

Figure A.49 Turbulent kinetic energy contours for Type B Net in section, RNG $k-\varepsilon$ model

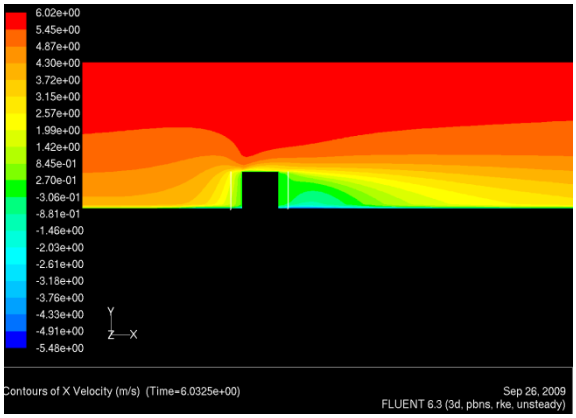

Figure A.50 X-velocity contours for Type B Net in section, Realizable $k-\varepsilon$ model

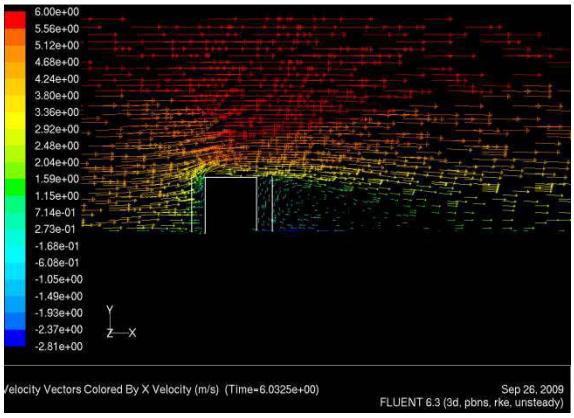

Figure A.51 Velocity vector for Type B Net in section, Realizable $k-\varepsilon$ model

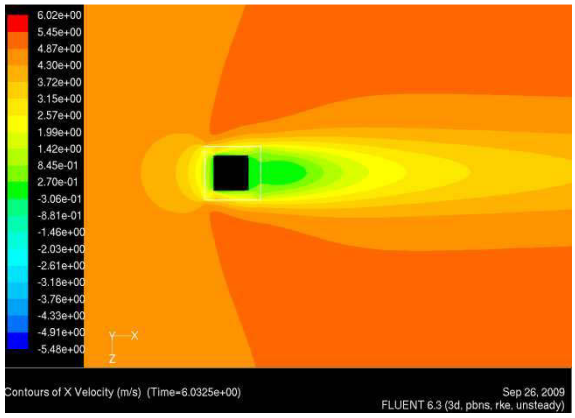

Figure A.52 X-velocity contours for Type B Net in plan, Realizable $k-\varepsilon$ model

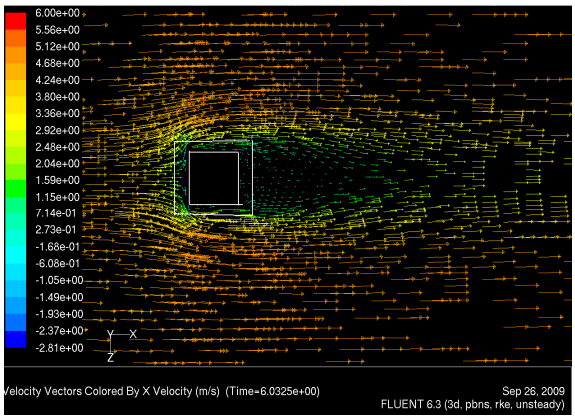

Figure A.53 Velocity vectors for Type B Net in plan, Realizable $k-\varepsilon$ model

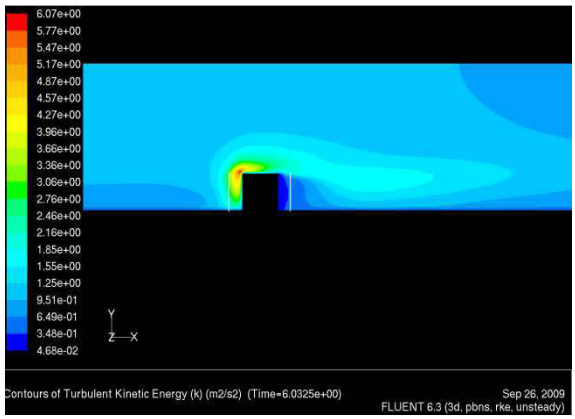

Figure A.54 Turbulent kinetic energy contours for Type B Net in section, Realizable $k-\varepsilon$ model

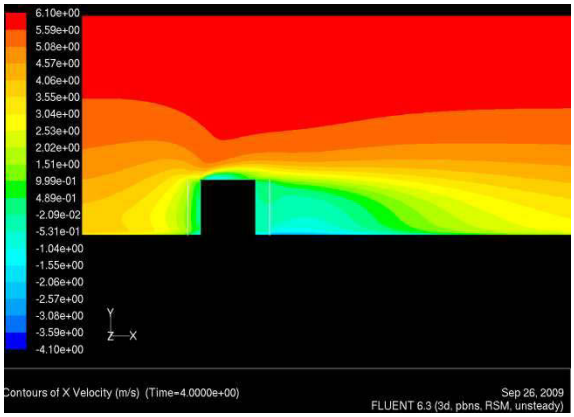

Figure A.55 X-velocity contours for Type B Net in section, Reynolds stress model

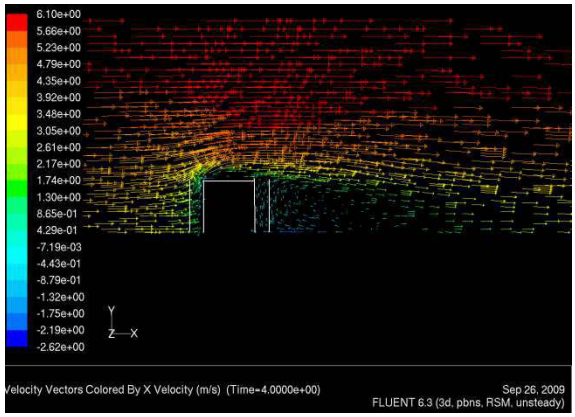

Figure A.56 Velocity vector for Type B Net in section, Reynolds stress model

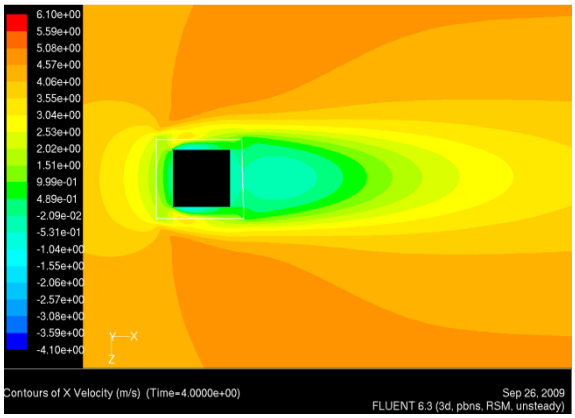

Figure A.57 X-velocity contours for Type B Net in plan, Reynolds stress model

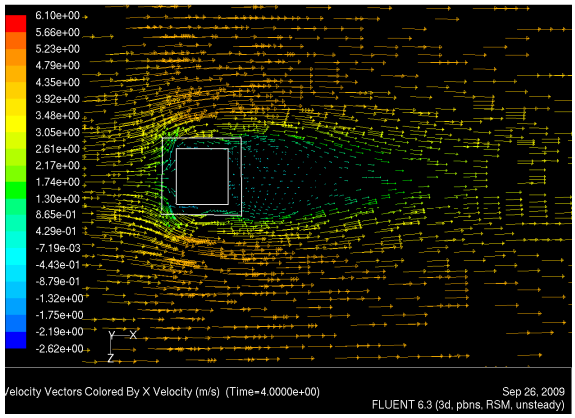

Figure A.58 Velocity vector for Type B Net in plan, Reynolds stress model

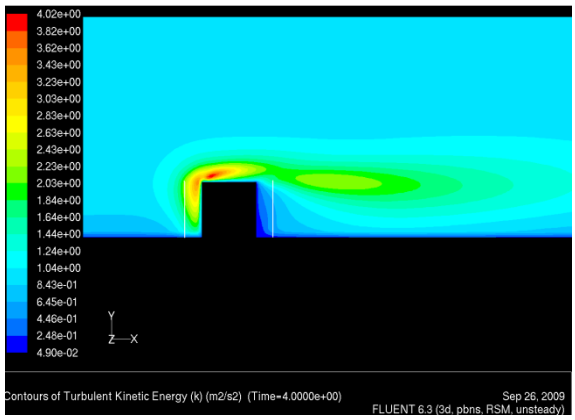

Figure A.59 Turbulent kinetic energy contours for Type B Net in section, Reynolds stress model